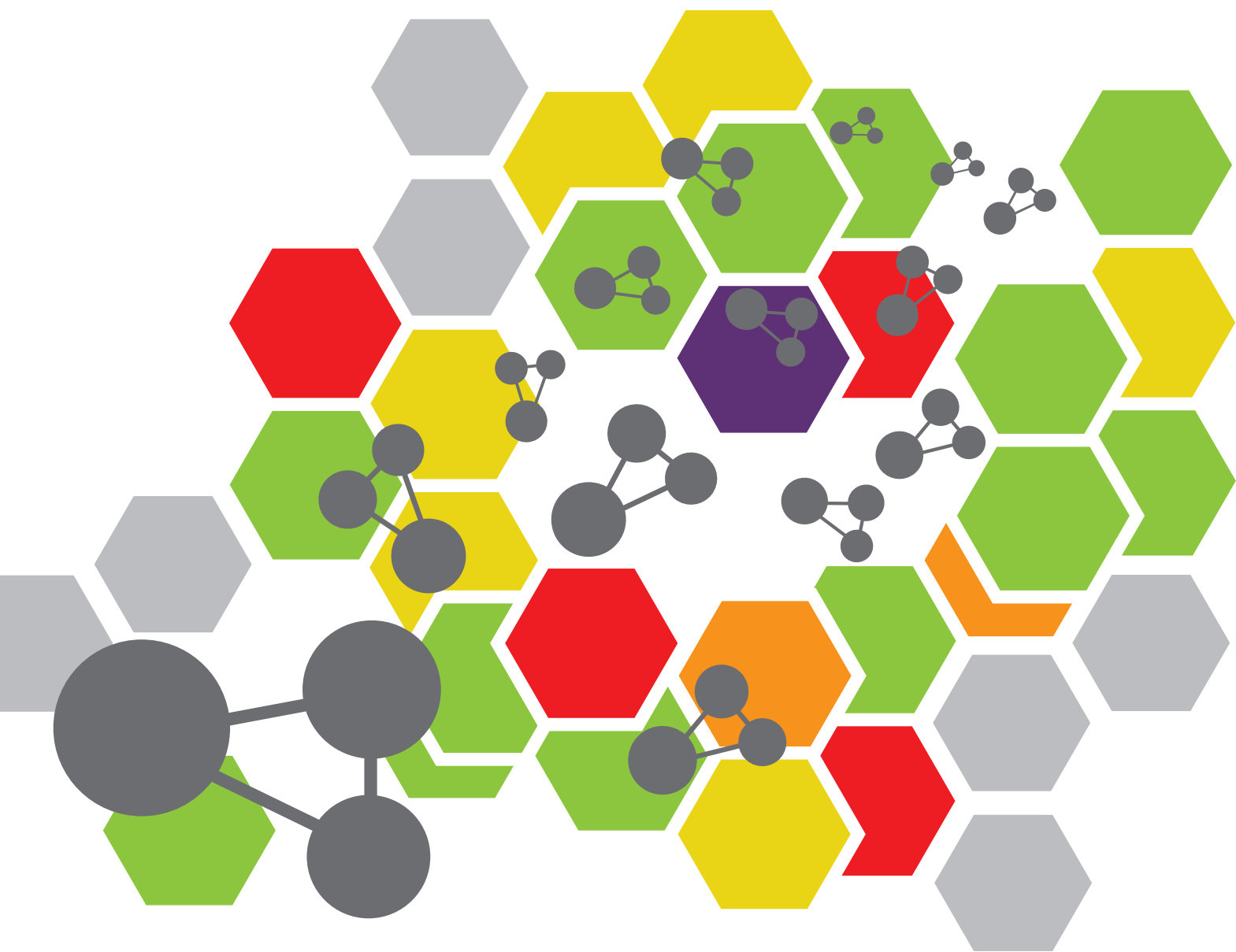


COMPUTATIONAL AND EXPERIMENTAL INSIGHTS IN REDOX-COUPLED PROTON PUMPING IN PROTEINS

EDITED BY: Vivek Sharma, Petra Imhof and Petra Hellwig
PUBLISHED IN: Frontiers in Chemistry





frontiers

Frontiers eBook Copyright Statement

The copyright in the text of individual articles in this eBook is the property of their respective authors or their respective institutions or funders. The copyright in graphics and images within each article may be subject to copyright of other parties. In both cases this is subject to a license granted to Frontiers.

The compilation of articles constituting this eBook is the property of Frontiers.

Each article within this eBook, and the eBook itself, are published under the most recent version of the Creative Commons CC-BY licence.

The version current at the date of publication of this eBook is CC-BY 4.0. If the CC-BY licence is updated, the licence granted by Frontiers is automatically updated to the new version.

When exercising any right under the CC-BY licence, Frontiers must be attributed as the original publisher of the article or eBook, as applicable.

Authors have the responsibility of ensuring that any graphics or other materials which are the property of others may be included in the CC-BY licence, but this should be checked before relying on the CC-BY licence to reproduce those materials. Any copyright notices relating to those materials must be complied with.

Copyright and source acknowledgement notices may not be removed and must be displayed in any copy, derivative work or partial copy which includes the elements in question.

All copyright, and all rights therein, are protected by national and international copyright laws. The above represents a summary only. For further information please read Frontiers' Conditions for Website Use and Copyright Statement, and the applicable CC-BY licence.

ISSN 1664-8714

ISBN 978-2-88971-575-6

DOI 10.3389/978-2-88971-575-6

About Frontiers

Frontiers is more than just an open-access publisher of scholarly articles: it is a pioneering approach to the world of academia, radically improving the way scholarly research is managed. The grand vision of Frontiers is a world where all people have an equal opportunity to seek, share and generate knowledge. Frontiers provides immediate and permanent online open access to all its publications, but this alone is not enough to realize our grand goals.

Frontiers Journal Series

The Frontiers Journal Series is a multi-tier and interdisciplinary set of open-access, online journals, promising a paradigm shift from the current review, selection and dissemination processes in academic publishing. All Frontiers journals are driven by researchers for researchers; therefore, they constitute a service to the scholarly community. At the same time, the Frontiers Journal Series operates on a revolutionary invention, the tiered publishing system, initially addressing specific communities of scholars, and gradually climbing up to broader public understanding, thus serving the interests of the lay society, too.

Dedication to Quality

Each Frontiers article is a landmark of the highest quality, thanks to genuinely collaborative interactions between authors and review editors, who include some of the world's best academicians. Research must be certified by peers before entering a stream of knowledge that may eventually reach the public - and shape society; therefore, Frontiers only applies the most rigorous and unbiased reviews.

Frontiers revolutionizes research publishing by freely delivering the most outstanding research, evaluated with no bias from both the academic and social point of view. By applying the most advanced information technologies, Frontiers is catapulting scholarly publishing into a new generation.

What are Frontiers Research Topics?

Frontiers Research Topics are very popular trademarks of the Frontiers Journals Series: they are collections of at least ten articles, all centered on a particular subject. With their unique mix of varied contributions from Original Research to Review Articles, Frontiers Research Topics unify the most influential researchers, the latest key findings and historical advances in a hot research area! Find out more on how to host your own Frontiers Research Topic or contribute to one as an author by contacting the Frontiers Editorial Office: frontiersin.org/about/contact

COMPUTATIONAL AND EXPERIMENTAL INSIGHTS IN REDOX-COUPLED PROTON PUMPING IN PROTEINS

Topic Editors:

Vivek Sharma, University of Helsinki, Finland

Petra Imhof, University of Erlangen Nuremberg, Germany

Petra Hellwig, Université de Strasbourg, France

Citation: Sharma, V., Imhof, P., Hellwig, P., eds. (2021). Computational and Experimental Insights in Redox-Coupled Proton Pumping in Proteins. Lausanne: Frontiers Media SA. doi: 10.3389/978-2-88971-575-6

Table of Contents

- 04 Editorial: Computational and Experimental Insights in Redox-Coupled Proton Pumping in Proteins**
Vivek Sharma, Petra Imhof and Petra Hellwig
- 06 The Ion-Translocating NrfD-Like Subunit of Energy-Transducing Membrane Complexes**
Filipa Calisto and Manuela M. Pereira
- 23 The Redox-Active Tyrosine is Essential for Proton Pumping in Cytochrome c Oxidase**
Margareta R. A. Blomberg
- 34 Quantification of Local Electric Field Changes at the Active Site of Cytochrome c Oxidase by Fourier Transform Infrared Spectroelectrochemical Titrations**
Federico Baserga, Jovan Dragelj, Jacek Kozuch, Hendrik Mohrmann, Ernst-Walter Knapp, Sven T. Stripp and Joachim Heberle
- 47 Ubiquinone Binding and Reduction by Complex I—Open Questions and Mechanistic Implications**
Etienne Galemou Yoga, Jonathan Schiller and Volker Zickermann
- 56 Mechanistic Insights on Heme-to-Heme Transmembrane Electron Transfer Within NADPH Oxydases From Atomistic Simulations**
Xiaojing Wu, Jérôme Hénin, Laura Baciou, Marc Baaden, Fabien Cailliez and Aurélien de la Lande
- 69 The High-Spin Heme b_L Mutant Exposes Dominant Reaction Leading to the Formation of the Semiquinone Spin-Coupled to the $[2Fe-2S]^+$ Cluster at the Q_o Site of *Rhodobacter capsulatus* Cytochrome bc_1**
Marcin Sarewicz, Sebastian Pintscher, Łukasz Bujnowicz, Małgorzata Wolska and Artur Osyczka
- 81 A Quinol Anion as Catalytic Intermediate Coupling Proton Translocation With Electron Transfer in *E. coli* Respiratory Complex I**
Franziska Nuber, Luca Mérono, Sabrina Oppermann, Johannes Schimpf, Daniel Wohlwend and Thorsten Friedrich
- 92 Modeling the Energy Landscape of Side Reactions in the Cytochrome bc_1 Complex**
Peter Husen and Ilia A. Solov'yov
- 106 Proton-Binding Motifs of Membrane-Bound Proteins: From Bacteriorhodopsin to Spike Protein S**
Ana-Nicoleta Bondar
- 114 A Voltammetric Perspective of Multi-Electron and Proton Transfer in Protein Redox Chemistry: Insights From Computational Analysis of *Escherichia coli* HypD Fourier Transformed Alternating Current Voltammetry**
Alister R. Dale-Evans, Martin J. Robinson, Henry O. Lloyd-Laney, David J. Gavaghan, Alan M. Bond and Alison Parkin
- 127 Protein Motifs for Proton Transfers That Build the Transmembrane Proton Gradient**
Divya Kaur, Umesh Khaniya, Yingying Zhang and M. R. Gunner



Editorial: Computational and Experimental Insights in Redox-Coupled Proton Pumping in Proteins

Vivek Sharma^{1*}, Petra Imhof² and Petra Hellwig³

¹University of Helsinki, Helsinki, Finland, ²Friedrich-Alexander-Universität (FAU) Erlangen-Nürnberg, Erlangen, Germany,

³Université de Strasbourg, Strasbourg, France

Keywords: cell respiration, photosynthesis, proton-coupled electron donor, molecular dynamics simulation, quantum chemical calculation, spectroscopy, mitochondria, reactive oxygen species (ROS)

Editorial on the Research Topic

Computational and Experimental Insights in Redox-Coupled Proton Pumping in Proteins

Elementary electron and proton transfer reactions commonly occur in chemistry and biology. Proteins involved in oxidative- and photo-phosphorylation carry out these reactions to generate energy in the form of ATP. Despite the simplicity of electron and proton transfer reactions, these pose extreme challenge to study either by experimental or computational approaches. In this special issue, we present a collection of reviews, original research articles as well as perspectives written by top-level experimental and computational experts working in the field of redox-active enzymes and associated fields. The special issue presents a current state-of-the-art in our understanding of the mechanism of bioenergetic enzymes, and at the same time provides important glimpses of theoretical and experimental methodological advances in the field.

The respiratory complex I, NADH:quinone (Q) oxidoreductase, is the first electron acceptor of the electron transport chain (ETC) in many organisms and pumps protons by conserving energy from the reduction of quinone to quinol (Parey et al., 2020). Despite recent major advances in structural characterization of this large complex (500–1 MDa), the molecular mechanism of redox-coupled proton pumping remains largely unknown and among other questions, the role of quinone/quinol binding in the electrostatic and conformational control of enzyme remains unclear (Hielscher et al., 2013; Haapanen and Sharma, 2021). One of the central elements of the coupling mechanism is the interface between the peripheral “arm” catalysing electron transfer and a membrane “arm” responsible for proton translocation. In this special issue, Yoga et al. and Nuber et al. have reviewed and discussed interesting aspects of quinone/quinol binding and its coupling to the conformational changes in this critical region of complex I. Yoga et al. reviewed the latest structural and computational data on the binding of quinone in the unique ~30 Å long quinone-binding tunnel of complex I, and discussed recent mechanistic models of proton pumping. Nuber et al. have highlighted the importance of movement of quinol (QH⁺) anion in the quinone tunnel and protonation/deprotonation reactions in the redox-coupled proton pumping mechanism of complex I.

The third complex in the ETC is complex III and is described by a well-known Q cycle (Crofts et al., 2017). Husen and Solov'yov gave new insights into the side-reactions of complex III, and by performing multiscale computational simulations they suggest how superoxide forms by reaction between dioxygen and semiquinone, and how it is released to the membrane-solvent environment. Thus, shedding light on the ROS (reactive oxygen species) generation by complex III of the ETC.

OPEN ACCESS

Edited by and Reviewed:

Antonio Monari,
UMR7019 Laboratoire de Physique et
Chimie Théoriques, France

*Correspondence:

Vivek Sharma
vivek.sharma@helsinki.fi

Specialty section:

This article was submitted to
Theoretical and Computational
Chemistry,
a section of the journal
Frontiers in Chemistry

Received: 22 August 2021

Accepted: 03 September 2021

Published: 15 September 2021

Citation:

Sharma V, Imhof P and Hellwig P
(2021) Editorial: Computational and
Experimental Insights in Redox-
Coupled Proton Pumping in Proteins.
Front. Chem. 9:762612.
doi: 10.3389/fchem.2021.762612

Sarewicz et al. by performing site-directed mutagenesis of heme b_L ligand and spectroscopic measurements provided new insights into the redox reactions of Q_o site of complex III.

The final electron acceptor, complex IV, acts as an electron sink in the ETC of many organisms, and efficiently pumps protons by conserving the free energy of oxygen reduction (Wikström and Sharma, 2018). The functional importance of a tyrosyl radical in the catalytic cycle of complex IV has been emphasized based on computations and experiments (Voicescu et al., 2009; Sharma et al., 2013). Blomberg, based on hybrid density functional theory calculations (Blomberg) discusses how highly conserved redox-active tyrosine remains deprotonated until the last steps of the catalytic cycle, a notion that is central to drive proton pumping even at high proton motive force. Baserga et al. performed advanced FTIR spectroelectrochemical titrations and provided a quantitative description of the changes in electric field at the active site of complex IV during its redox reactions.

Kaur and colleagues provide a holistic view on the proton binding motifs of the redox-active proton pumps. They highlight the central role played by *proton loading sites* (sites in protein that uptake and release protons) in maintaining pumping even at high proton motive force. Relatedly, Bondar presents a comparison of several proton translocating enzymes and their proton binding motifs, and emphasizes the importance of these in understanding mechanism of proton pumping enzymes. In the study of Calisto and Pereira, sequence and structural analysis of NrfD-like subunits is presented and their role in ion-translocation and quinone binding is discussed.

Other complex electron and proton translocating enzymes are presented, completing the picture on the complexity of coupled

electron and proton translocation in biological systems. Wu et al. reveal the complex electron transfer in NADPH oxidase 5 (NOX5), a member of a family of enzymes, dedicated to the production of reactive oxygen species. By computer simulations, they analysed the O_2 movement and electron tunneling pathways in the inter-heme electron-transfer steps that ultimately lead to production of superoxide in NOX5. Finally, Dale-Evans et al. describe the mechanism of HypD from *E. coli* by means of theoretical and computational studies on the voltametric current. Their data allowed them to specifically estimate the kinetic parameter and reveal a step-wise one-electron, one-proton transfer mechanism rather than a concerted two-electron redox reaction.

The work presented in this special issue highlights how experimental (spectroscopy, biochemistry, etc.) and computational (classical and quantum chemical simulations) studies in concert have greatly advanced our knowledge of proton-coupled electron transfer processes. Even with the broad range of exciting results and mechanistic understanding already obtained, the complexity of the systems involved in redox-coupled proton pumping is so high that novel developments at all levels will be needed in years and decades to come.

AUTHOR CONTRIBUTIONS

All authors listed have made a substantial, direct, and intellectual contribution to the work, and approved it for publication.

Tyrosine–Histidine Covalent Linkage in Cytochrome *c* Oxidase. *J. Phys. Chem. B* 113, 13429. doi:10.1021/jp9048742

Wikström, M., and Sharma, V. (2018). Proton Pumping by Cytochrome *c* Oxidase – A 40 Year Anniversary. *Biochim. Biophys. Acta* 1859, 692–698. doi:10.1016/j.bbabo.2018.03.009

Conflict of Interest: The authors declare that the research was conducted in the absence of any commercial or financial relationships that could be construed as a potential conflict of interest.

Publisher's Note: All claims expressed in this article are solely those of the authors and do not necessarily represent those of their affiliated organizations, or those of the publisher, the editors and the reviewers. Any product that may be evaluated in this article, or claim that may be made by its manufacturer, is not guaranteed or endorsed by the publisher.

Copyright © 2021 Sharma, Imhof and Hellwig. This is an open-access article distributed under the terms of the Creative Commons Attribution License (CC BY). The use, distribution or reproduction in other forums is permitted, provided the original author(s) and the copyright owner(s) are credited and that the original publication in this journal is cited, in accordance with accepted academic practice. No use, distribution or reproduction is permitted which does not comply with these terms.

REFERENCES

- Crofts, A. R., Rose, S. W., Burton, R. L., Desai, A. V., Kenis, P. J. A., and Dikanov, S. A. (2017). The Q-Cycle Mechanism of the bc_1 Complex: A Biologist's Perspective on Atomistic Studies. *J. Phys. Chem. B* 121, 3701–3717. doi:10.1021/acs.jpcc.6b10524
- Haapanen, O., and Sharma, V. (2021). Redox- and Protonation-State Driven Substrate-Protein Dynamics in Respiratory Complex I. *Curr. Opin. Electrochem.* 29, 100741. doi:10.1016/j.coelec.2021.100741
- Hielscher, R., Yegres, M., Voicescu, M., Gnannt, E., Friedrich, T., and Hellwig, P. (2013). Characterization of Two Quinone Radicals in the NADH:Ubiquinone Oxidoreductase from *Escherichia coli* by a Combined Fluorescence Spectroscopic and Electrochemical Approach. *Biochemistry* 52, 8993–9000. doi:10.1021/bi4009903
- Parey, K., Wirth, C., Vonck, J., and Zickermann, V. (2020). Respiratory Complex I – Structure, Mechanism and Evolution. *Curr. Opin. Struct. Biol.* 63, 1–9. doi:10.1016/j.sbi.2020.01.004
- Sharma, V., Karlin, K. D., and Wikström, M. (2013). Computational Study of the Activated O_H State in the Catalytic Mechanism of Cytochrome *c* Oxidase. *Proc. Nat. Acad. Sci. USA* 110, 16844–16849. doi:10.1073/pnas.1220379110
- Voicescu, M., El Khoury, Y., Martel, D., Heinrich, M., and Hellwig, P. (2009). Spectroscopic Analysis of Tyrosine Derivatives: On the Role of the



The Ion-Translocating NrfD-Like Subunit of Energy-Transducing Membrane Complexes

Filipa Calisto^{1,2} and Manuela M. Pereira^{1,2*}

¹ Instituto de Tecnologia Química e Biológica-António Xavier, Universidade Nova de Lisboa, Oeiras, Portugal,

² BiolSI-Biosystems & Integrative Sciences Institute, Faculdade de Ciências, Universidade de Lisboa, Lisboa, Portugal

OPEN ACCESS

Edited by:

Petra Hellwig,
Université de Strasbourg, France

Reviewed by:

Blanca Barquera,
Rensselaer Polytechnic Institute,
United States
Giovanni La Penna,
National Research Council (CNR), Italy

*Correspondence:

Manuela M. Pereira
mmpereira@fc.ul.pt

Specialty section:

This article was submitted to
Theoretical and Computational
Chemistry,
a section of the journal
Frontiers in Chemistry

Received: 03 February 2021

Accepted: 19 March 2021

Published: 13 April 2021

Citation:

Calisto F and Pereira MM (2021) The
Ion-Translocating NrfD-Like Subunit of
Energy-Transducing Membrane
Complexes. *Front. Chem.* 9:663706.
doi: 10.3389/fchem.2021.663706

Several energy-transducing microbial enzymes have their peripheral subunits connected to the membrane through an integral membrane protein, that interacts with quinones but does not have redox cofactors, the so-called NrfD-like subunit. The periplasmic nitrite reductase (NrfABCD) was the first complex recognized to have a membrane subunit with these characteristics and consequently provided the family's name: NrfD. Sequence analyses indicate that NrfD homologs are present in many diverse enzymes, such as polysulfide reductase (PsrABC), respiratory alternative complex III (ACIII), dimethyl sulfoxide (DMSO) reductase (DmsABC), tetrathionate reductase (TtrABC), sulfur reductase complex (SreABC), sulfite dehydrogenase (SoeABC), quinone reductase complex (QrcABCD), nine-heme cytochrome complex (NhcABCD), group-2 [NiFe] hydrogenase (Hyd-2), dissimilatory sulfite-reductase complex (DsrMKJOP), arsenate reductase (ArrC) and multiheme cytochrome *c* sulfite reductase (MccACD). The molecular structure of ACIII subunit C (ActC) and Psr subunit C (PsrC), NrfD-like subunits, revealed the existence of ion-conducting pathways. We performed thorough primary structural analyses and built structural models of the NrfD-like subunits. We observed that all these subunits are constituted by two structural repeats composed of four-helix bundles, possibly harboring ion-conducting pathways and containing a quinone/quinol binding site. NrfD-like subunits may be the ion-pumping module of several enzymes. Our data impact on the discussion of functional implications of the NrfD-like subunit-containing complexes, namely in their ability to transduce energy.

Keywords: NrfD-like, membrane protein, ion translocation, quinone/quinol binding site, CISM family, energy transduction

INTRODUCTION

All living organisms need energy to fuel life processes. External energy sources, light or chemical compounds, are converted to biologically usable forms of energy, such as adenosine triphosphate (ATP) or electrochemical gradients. According to Peter Mitchell's chemiosmotic hypothesis, the transmembrane difference of the electrochemical potential ($\Delta\tilde{\mu}$) can be established by energy-transducing membrane protein complexes that couple the energy released by light or chemical reactions (Gibbs energy change, ΔG) to the translocation of charges (electrons or ions) across the membrane (Mitchell, 1961). The energy stored in the form of the electrochemical potential can drive different energy-requiring reactions of the cells, such as synthesis of cellular components, solute transport or motility.

Energy transducing membrane complexes are usually composed of catalytic subunits and transmembrane proteins that perform translocation of charges, electrons or cations, across the membrane (Calisto et al., 2021). The most common membrane charge-translocating subunits so far observed in energy transduction complexes are the di-heme cytochrome *b*-like subunits and the so called NrfD-like subunits. The di-heme cytochrome *b*-like subunits are involved in the transport of electrons, whereas the NrfD-like subunits translocate ions. In this way this type of subunits is devoid of redox cofactors but contain ion-conducting pathways.

The NrfD-like subunits are present in many and diverse membrane complexes, widespread in Bacteria and Archaea, that can take part in oxygen, nitrogen, sulfur, arsenate or hydrogen metabolism (**Figure 1, Table 1**) (Rothery et al., 2008; Refojo et al., 2010, 2019; Marreiros et al., 2016). These subunits thus compose the NrfD family, which was named after the characterization of the periplasmic nitrite reductase (NrfABCD) complex, the first complex recognized to have a NrfD-like subunit (Simon, 2002; Rothery et al., 2008) (**Figure 1, NrfABCD**). Structures of representatives of the NrfD family were first obtained for the PsrC subunit from the *Thermus thermophilus* polysulfide reductase (PsrABC) complex (**Figures 1, 2, PsrABC**) and later for the ActC and ActF subunits from the respiratory alternative complex III (ACIII) from *Rhodothermus marinus* (**Figure 2, ACIII**) and *Flavobacterium johnsoniae* (Sousa et al., 2018; Sun et al., 2018) and for the photosynthetic ACIII from *Roseiflexus castenholzii* (Shi et al., 2020) (**Figure 1, ACIII**). The structural data showed these membrane subunits have 8 common transmembrane helices, organized in two four-helix bundles (TMHs 1–4 and TMHs 5–8) related by a 180° rotation around an axis perpendicular to the membrane (Sousa et al., 2018) (**Figure 3**), and contain one quinone/quinol-binding site close to the periphery of the membrane at the side at which the peripheral subunits are bound to. ActF does not contain any quinone/quinol binding site and it is the only NrfD-like subunit present in a complex in which another subunit of this type (which contains a quinone/quinol-binding site) is present. In addition, for all these subunits, putative ion-conducting pathways were proposed (Calisto et al., 2021). NrfD-like proteins also function as the link of the peripheral subunits to the membrane (**Figure 1**).

Besides *Escherichia coli* NrfABCD (Hussain et al., 1994; Clarke et al., 2007), ACIII and PsrABC complexes, the enzymes containing a NrfD-like subunits are dimethyl sulfoxide (DMSO) reductase (DmsABC), tetrathionate reductase (TtrABC), sulfur reductase complex (SreABC), sulfite dehydrogenase (SoeABC) and arsenate reductase (ArrABC) complexes, members of the so called complex iron-sulfur molybdoenzyme (CISM) family, which have a similar subunit composition to that of PsrABC complex (**Figure 1**) (Rothery and Weiner, 1993; Weiner et al., 1993; Berks, 1996; Hensel et al., 1999; Hinsley and Berks, 2002; Laska et al., 2003; Geijer and Weiner, 2004; Guiral et al., 2005; Duval et al., 2008; Dahl et al., 2013; Grimaldi et al., 2013; Tang et al., 2013; Steinmetz et al., 2014; Kurth et al., 2015; Boughanemi et al., 2020). The subunits and prosthetic groups of these enzymes are specified in **Table 1**. DmsABC is a quinol:DMSO

oxidoreductase with its peripheral DmsAB subunits facing the P-side of the membrane (Rothery and Weiner, 1993; Berks, 1996). TtrABC, expressed under anaerobic conditions in Proteobacteria (Marreiros et al., 2016), catalyzes the endergonic reduction of tetrathionate to thiosulfate with the concomitant oxidation of quinol to quinone. As DmsAB, TtrAB subunits are facing the P-side of the membrane (Hensel et al., 1999; Hinsley and Berks, 2002). SreABC, characterized in *Acidianus ambivalens*, was proposed to have quinol:sulfur oxidoreductase activity and SreAB were suggested to be located at the P-side of the membrane (Laska et al., 2003). SoeABC is a sulfite:quinone oxidoreductase complex described in *Aquifex aeolicus* and *Allochromatium vinosum* (Dahl et al., 2013; Boughanemi et al., 2020). SoeAB subunits were hypothesized to be located at the negative-side (N-side) of the membrane. ArrABC, involved in arsenate respiration, seems to have the peripheral ArrAB subunits at the P-side of the membrane (Stolz et al., 2006; Duval et al., 2008).

The multiheme cytochrome *c* sulfite reductase complex (MccACD), biochemically characterized from *W. succinogenes* and *Shewanella oneidensis* (Kern et al., 2011; Shirodkar et al., 2011) (**Figure 1, MccACD, Table 1**), the quinone reductase complex (QrcABCD), homologous to ACIII and present in sulfate-reducing bacteria, are other enzymes with NrfD-like subunits. Qrc catalyzes the transfer of electrons from a type-1 tetraheme cytochrome *c*₃ (TpIc₃) to quinone (**Figure 1, Qrc**) and so the peripheral subunits are facing the P-side of the membrane (Pereira et al., 2011; Venceslau et al., 2011). Group-2 [NiFe] hydrogenase (Hyd-2), produced under anaerobic conditions, is a hydrogen:quinone oxidoreductase complex with the peripheral subunits facing the P-side of the membrane (Laurinavichene et al., 2002; Sargent, 2016; Beaton et al., 2018) (**Figure 1, Hyd-2, Table 1**). The nine-heme cytochrome complex (NhcABCD), a TpIc₃:quinone oxidoreductase, is a member of a family of transmembrane complexes with multiheme cytochrome *c* subunit, described in *Desulfovibrio* species (Matias et al., 1999, 2005; Saraiva et al., 2001; Bento et al., 2003; Pereira et al., 2011) (**Figure 1, Nhc, Table 1**). The dissimilatory sulfite-reductase complex (DsrMKJOP) is a transmembrane complex with peripheral subunits at both sides of the membrane (Grein et al., 2010). DsrJ and DsrO subunits are anchored to the P-side of the membrane (Pires et al., 2006). DsrM is a di-heme cytochrome *b* membrane subunit (Pires et al., 2006). DsrK is facing the N-side of the membrane (Mander et al., 2002; Pires et al., 2006). DsrK is able to reduce the small protein DsrC, while DsrJ was suggested to interact with thiosulfate (Bamford et al., 2002; Denkmann et al., 2012; Venceslau et al., 2014) (**Figure 1, DsrMKJOP, Table 1**). Since DsrP and DsrM are membrane subunits with hypothetical quinone-binding sites, a quinone cycling of reduction and oxidation between DsrMK and DsrJOP was proposed to take place (Grein et al., 2013).

In this work we thoroughly analyze the primary structures of the members of the NrfD family and predicted the respective tertiary structures, the data provided allowed a deep and broad discussion on the presence of ion-conducting pathways and quinone/quinol-binding sites, which impacts on the function of the several complexes, namely in their ability to transduce energy.

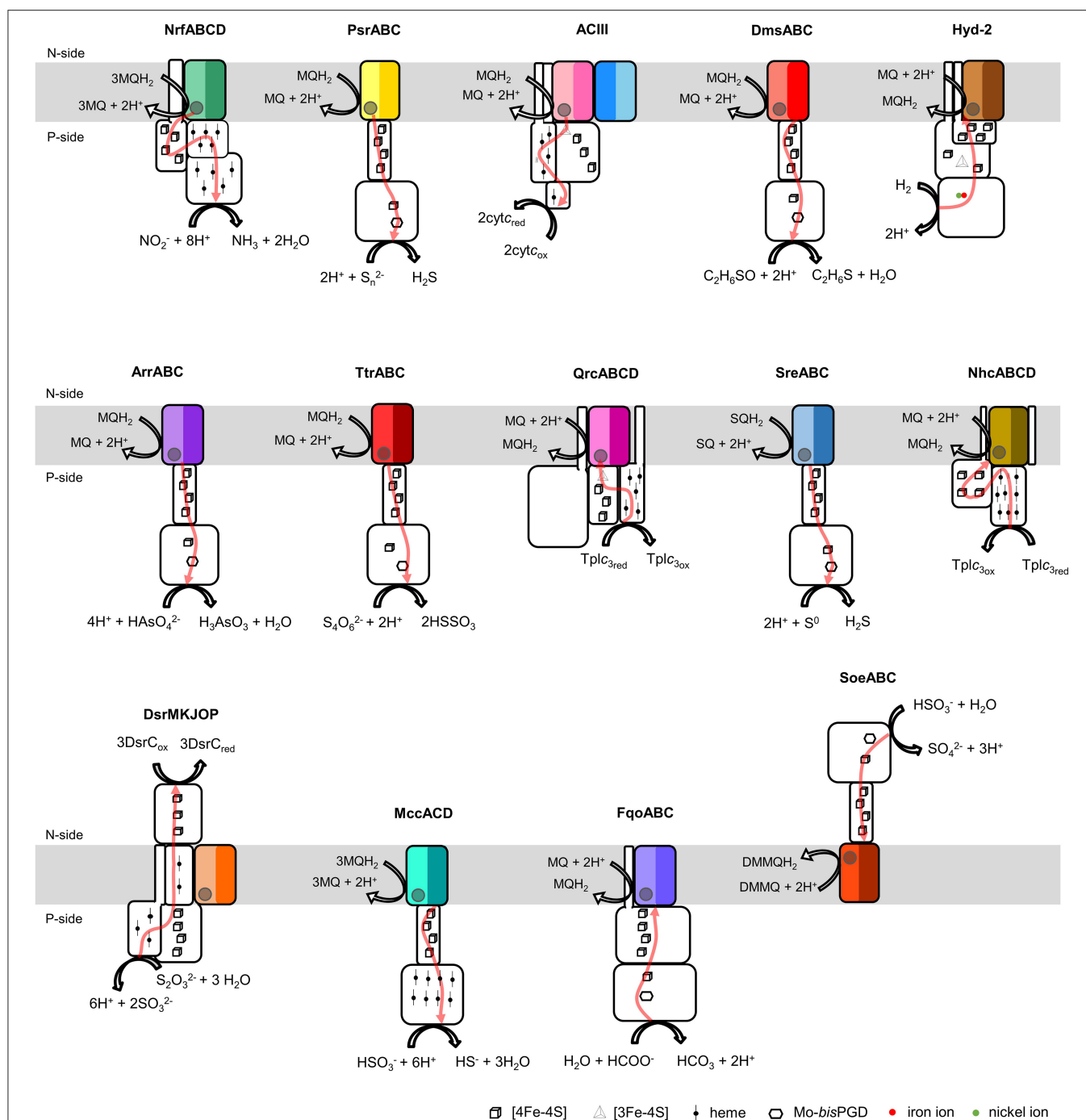




























FIGURE 1 | Composition and diversity of NrfD-like subunit-containing complexes. Schematic representation of periplasmic nitrite reductase (NrfABCD), polysulfide reductase (PsrABC), respiratory alternative complex III (ACIII), DMSO reductase (DmsABC), group-2 [Ni-Fe] hydrogenase (Hyd-2), arsenate reductase (ArrABC), tetrathionate reductase (TtrABC), quinone reductase complex (QrcABCD), sulfur reductase complex (SreABC), nine-heme cytochrome complex (NhcABCD), dissimilatory sulfite-reductase complex (DsrMKJOP), multiheme cytochrome c sulfite reductase (MccACD), formate:quinone oxidoreductase (FqoABC), sulfite dehydrogenase (SoeABC). P-side, positive-side of the membrane; N-side, negative-side of the membrane. The NrfD-like subunits (NrfD, PsrC, ActC, ActF, DmsC, HybB, ArrC, trrC, QrcD, SreC, NhcC, DsrP, MccD, fqcC, and SoeC) are colored, the two-color tones indicate the two structural repeats, each composed of a four-helix bundle (TMHs 1–4 and TMHs 5–8) and related by a 180° rotation around an axis perpendicular to the membrane. The circle, inside the colored subunits, indicates the presence of a quinone/quinol-binding site. The red arrows represent the pathway for electron transfer. The color code is used in all the following figures and in **Tables 1, 2**.

TABLE 1 | NrfD-like subunit-containing complexes.

Color code	Complex	Activity	NrfD-like subunit	Catalytic subunit	Iron-sulfur subunit	Other subunit
	Alternative complex III	Quinol:cytochrome <i>c</i> /HiPIP oxidoreductase	ActC	ActA (5x heme <i>c</i>)	ActB (1x [3Fe-4S] ^{1+/0} , 3x [4Fe-4S] ^{2+/1+})	ActD ActE (1x heme <i>c</i>)
			ActF			
	Polysulfide reductase	Quinol:polysulfide oxidoreductase	PsrC	PsrA (1x Mo- <i>bis</i> PGD, 1x [4Fe-4S] ^{2+/1+})	PsrB (4x [4Fe-4S] ^{2+/1+})	x
						
	Group-2 [NiFe] hydrogenase	Hydrogen:quinone oxidoreductase	HybB	HybC ([Ni-Fe])	HybO (1x [3Fe-4S] ^{1+/0} , 2x [4Fe-4S] ^{2+/1+}) HybA (4x [4Fe-4S] ^{2+/1+})	x
						
	DMSO reductase	QUINOL:DMSO OXIDOREDUCTASE	DmsC	DmsA (1x Mo- <i>bis</i> PGD, 1x [4Fe-4S] ^{2+/1+})	DmsB (4x [4Fe-4S] ^{2+/1+})	x
						
	Arsenate reductase	QUINOL:ARSENATE OXIDOREDUCTASE	ArrC	ArrA (1x Mo- <i>bis</i> PGD, 1x [4Fe-4S] ^{2+/1+})	ArrB (4x [4Fe-4S] ^{2+/1+})	x
						
	Dissimilatory sulfite-reductase complex	thiosulfate:DsrC oxidoreductase	DsrP	DsrJ (3x heme <i>c</i>) DsrK (1x [4Fe-4S] ^{3+/2+} , 3x [4Fe-4S] ^{2+/1+})	DsrO (4x [4Fe-4S] ^{2+/1+})	DsrM (2x heme <i>b</i>)
						
	Quinone reductase complex	Tpic ₃ :quinone oxidoreductase	QrcD	QrcA (6x heme <i>c</i>)	QrcC 1x [3Fe-4S] ^{1+/0} , 3x [4Fe-4S] ^{2+/1+})	QrcB
						
	Sulfur reductase complex	Quinol:sulfur oxidoreductase	SreC	SreA (1x Mo- <i>bis</i> PGD, 1x [4Fe-4S] ^{2+/1+})	SreB (4x [4Fe-4S] ^{2+/1+})	x
						
	Periplasmic nitrite reductase	Quinol:nitrite oxidoreductase	NrfD	NrfA (5x heme <i>c</i>)	NrfC (4x [4Fe-4S] ^{2+/1+})	NrfB (5x heme <i>c</i>)
						
	Tetrathionate reductase	Quinol:tetrathionate oxidoreductase	TtrC	TtrA (1x Mo- <i>bis</i> PGD, 1x [4Fe-4S] ^{2+/1+})	TtrB (4x [4Fe-4S] ^{2+/1+})	x
						
	Nine-heme cytochrome complex	Tpic ₃ :quinone oxidoreductase	NhcC	NhcA (9x heme <i>c</i>)	NhcB (4x [4Fe-4S] ^{2+/1+})	NhcD
						
	Sulfite dehydrogenase	Sulfite:quinone oxidoreductase	SoeC	SoeA (1x Mo- <i>bis</i> PGD, 1x [4Fe-4S] ^{2+/1+})	SoeB (4x [4Fe-4S] ^{2+/1+})	x
						
	Multiheme cytochrome <i>c</i> sulfite reductase	Quinol:sulfite oxidoreductase	MccD	MccA (8x heme <i>c</i>)	MccB (4x [4Fe-4S] ^{2+/1+})	x
						

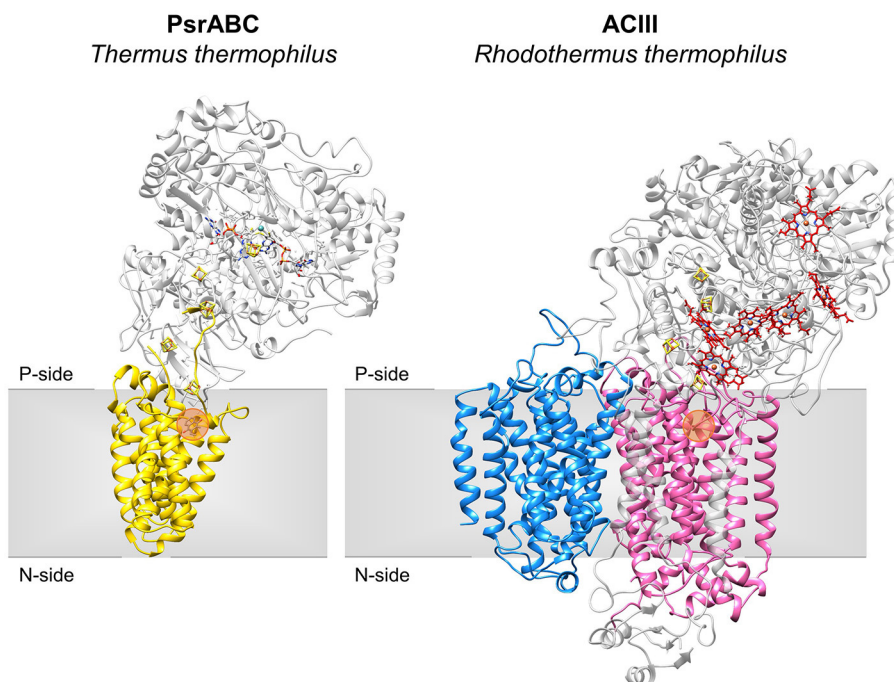


FIGURE 2 | Structures of NrfD-like subunit-containing complexes. Overall structure of PsrABC from *Thermus thermophilus* (left, PDB: 2VPZ) and Alternative Complex III from *Rhodothermus marinus* (right, PDB: 6FOK, ActH was not included for clarity). PsrC (yellow), ActC (pink) and ActF (blue) are NrfD-like subunits. The two complexes are oriented in relation to each other by the superimposition of the PsrC and ActC subunits. Iron-sulfur clusters represented by orange/yellow spheres; Cytochrome c-type hemes represented by red sticks; Mo-bisPGD cofactor represented by blue/red sticks with molybdenum shown as a blue sphere. Orange dots stand for the quinone-binding site. P-side, positive-side of the membrane; N-side, negative-side of the membrane.

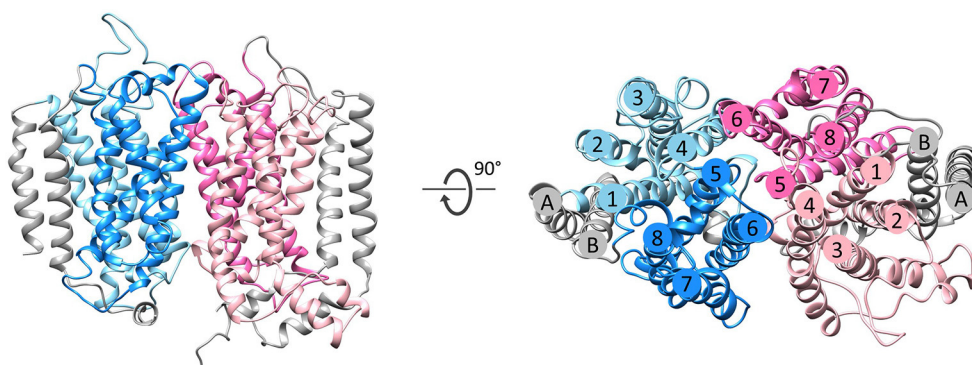


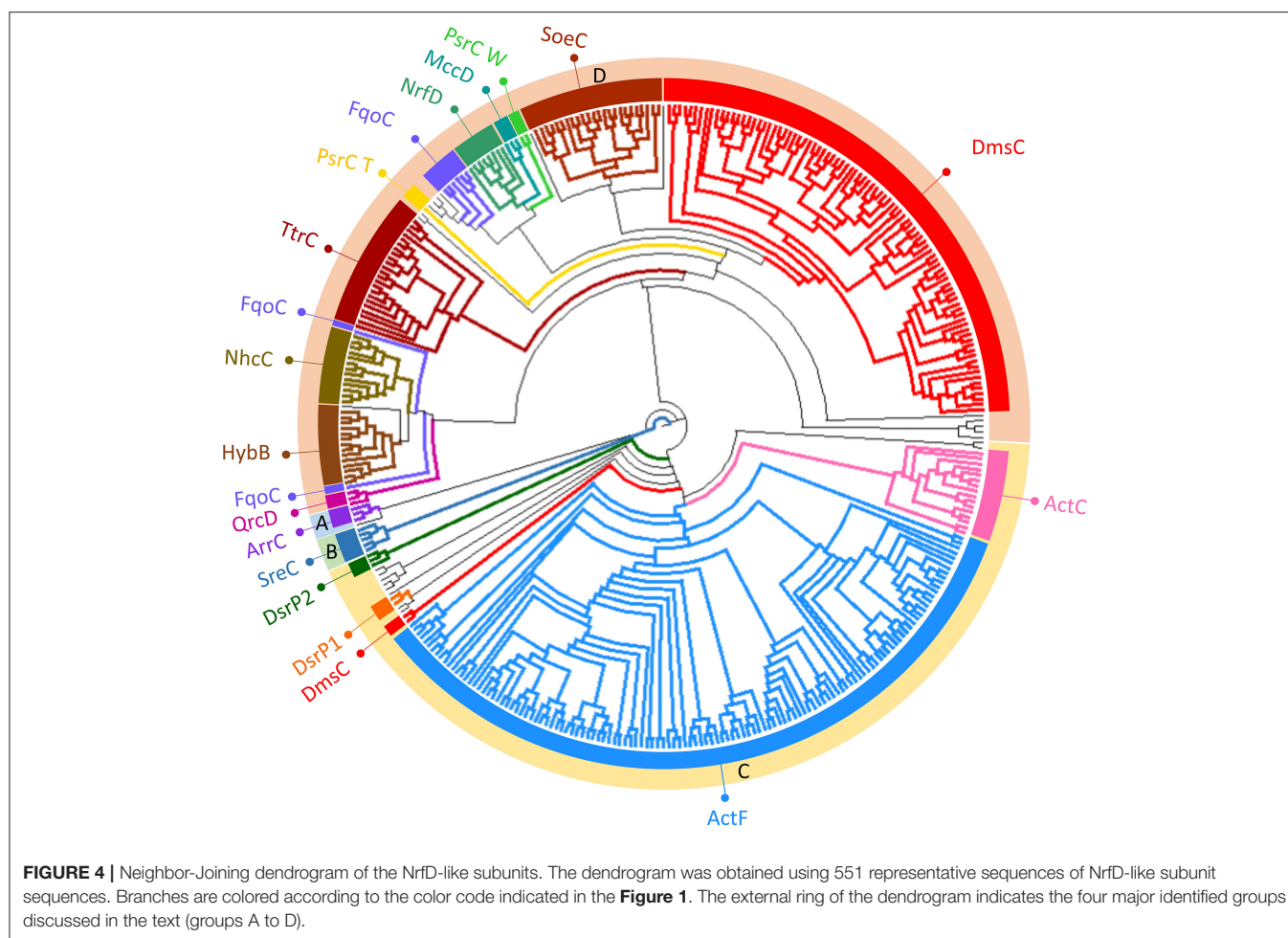
FIGURE 3 | Fold of homologous membrane subunits ActC and ActF. ActC (pink) and ActF (blue) seen from the membrane (left) and from the top (right). The N- and C-terminal helices (TMHs A-B), which form a helix dimer, are colored in gray. The four-helix bundles are shown in light pink/blue (TMHs 1–4) and dark pink/blue (TMHs 5–8).

RESULTS AND DISCUSSION

Taxonomic Distribution

NrfD-like subunits are the anchor protein of several modular complexes, which take part in a vast array of metabolisms, such as the oxygen, nitrogen, sulfur, arsenate and hydrogen cycles (Rothery et al., 2008; Refojo et al., 2010, 2019; Marreiros et al., 2016) (Figure 1). In this work, we performed sequence alignments and taxonomic profiling to investigate the

distribution of the NrfD-like subunit-containing complexes in microbial species. We gathered 4,545 NrfD-like amino acid sequences present in the genomes of 1,822 distinct species (96% Bacteria, 4% Archaea), with an average of 2.5 NrfD-like subunits per organism. In order to reduce the size of the obtained dataset, the 4,545 amino acid sequences were clustered according to their identity (50% identity) and 551 representative sequences were aligned, allowing to generate the correspondent Neighbor-Joining (NJ) dendrogram. From the

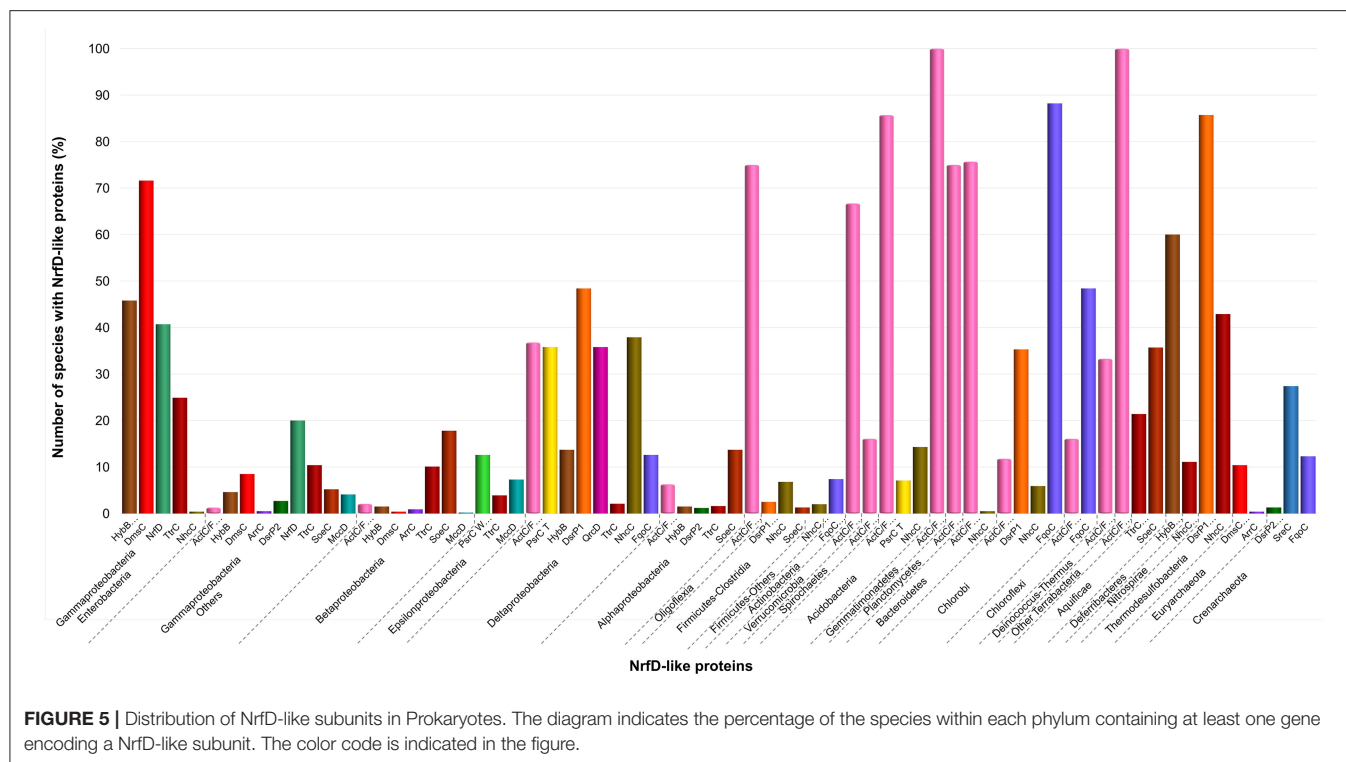


obtained dendrogram we were able to identify several branches belonging to different groups of NrfD-like subunit-containing complexes (**Figure 4**).

We observed that close to the root of the dendrogram, the sequences of NrfD-like subunits separated into four major groups (**Figure 4**, dendrogram groups A–D). The amino acid sequences of SreC (21 sequences) (**Figure 4**, group A) and ArrC (9 sequences) (**Figure 4**, group B) seem to be less related with the others NrfD-like subunits and constitute two distinct groups. The SreABC complex was biochemically characterized from the sulfur-dependent archaeon *A. ambivalens* (Laska et al., 2003) and genes coding for SreC subunit were only identified in archaea, in 21 species (27% of Crenarchaeota species) (**Figure 5**, SreC). ArrAB complex was described as a periplasmic complex, which is associated with the transmembrane ArrC subunit only in few microorganisms (Duval et al., 2008). In agreement, we identified nine genes coding for ArrC subunit, distributed in Gammaproteobacteria (four sequences), Betaproteobacteria (four sequences) and Euryarchaeota (one sequence) species (**Figure 5**, ArrC).

The third group (**Figure 4**, group C) englobes the amino acid sequences of ActC (521 sequences), ActF (521 sequences), DsrP

(88 sequences) and DmsC (42 sequences) subunits. Intriguingly, we identified two branches of DsrP amino acid sequences, which we called DsrP1 and DsrP2 (**Figure 4**). The amino acid sequence of DsrP subunit, biochemically characterized from *Desulfovibrio vulgaris* DsrMKJOP complex, was found in the DsrP1 branch (66 amino acid sequences of sulfate-reducing bacteria). Besides their presence in Deltaproteobacteria (46 species, 48%), genes coding for DsrP1 subunit were identified in species from Thermodesulfobacteria (6 species, 86%), Chlorobi (6 species, 35%) and Firmicutes-Clostridia (6 species, 3%) phyla (**Figure 5**, DsrP1). Genes coding for DsrP2 subunit were observed in 36 species of sulfur-oxidizing bacteria and from *Archaeoglobus* genus (23 species, 3% of Gammaproteobacteria; 10 species, 1% of Alphaproteobacteria; 3 species of 1% of Euryarchaeota species) (**Figure 5**, DsrP2). The amino acid sequences of ActC and ActF subunits (521 sequences) were naturally separated into two branches (**Figure 4**, ActC and ActF). Genes coding for ActC and ActF subunits were identified in species from Gammaproteobacteria-Others (11 species, 1%), Betaproteobacteria (10 species, 2%), Deltaproteobacteria (35 species, 37%), Alphaproteobacteria (46 species, 6%), Oligoflexia (nine species, 75%), Verrucomicrobia (10 species, 67%),



Spirochaetes (14 species, 16%), Acidobacteria (12 species, 86%), Gemmatimonadetes (three species, 100%), Planctomycetes (24 species, 75%), Bacteroidetes (290 species, 76%), Chlorobi (two species, 12%), Chloroflexi (six species, 16%), Deinococcus-Thermus (11 species, 33%) and Terrabacteria (three species, 100%) (**Figure 5**, ActC/F). Group C of the dendrogram also includes 42 amino acid sequences identified as DmsC subunit (**Figure 4**, group DmsC), namely the DmsC amino acid sequence from *Halobacterium* sp. strain NRC-1 (Müller and DasSarma, 2005). Genes coding for DmsC present in group C are all observed in 24 archaeal species from Euryarchaeota (10%) (**Figure 5**, DmsC).

The fourth group (**Figure 4**, group D) is composed of amino acid sequences of PsrC (48 sequences), DmsC (793 sequences), NrfD (411 sequences), TtrC (292 sequences), NhcC (81 sequences), HybB (320 sequences), QrcD (35 sequences), SoeC (239 sequences) and MccD (79 sequences) subunits. As observed before (Duarte et al., 2018), the amino acid sequences of PsrC subunit forms two separate branches, one represented by PsrC from *W. succinogenes* and the other pictured by PsrC from *T. thermophilus*. The amino acid sequence of PsrC subunit from *T. thermophilus* PsrABC complex, clusters within branch PsrC T with other 34 amino acid sequences (**Figure 4**, PsrC T) and PsrC from *W. succinogenes* PsrABC complex is present in branch PsrC W (**Figure 4**, PsrC W; 33 sequences). Genes coding for PsrC T subunits were found in 34 species (36%) from Deltaproteobacteria and one species (7%) from Acidobacteria, while genes coding for PsrC W subunits were observed in 26 species (13%) from Epsilonproteobacteria (**Figure 5**, PsrC T and PsrC W).

Genes coding for bacterial DmsC and NrfD subunits were identified in 80% (444 species) and 61% (383 species) of species from Gammaproteobacteria, respectively (**Figure 5**, DmsC and NrfD). Amino acid sequences of TtrC subunits were expected to be produced in 291 species, distributed in Proteobacteria (219 species, 35% Gammaproteobacteria; 47 species, 10% Betaproteobacteria; eight species, 4% Epsilonproteobacteria; two species, 2% Deltaproteobacteria; 12 species, 2% Alphaproteobacteria), Aquificae (three species, 21%) and Armatimonadetes (one species, 50%) phyla (**Figure 5**, TtrC). NhcC subunit coding genes were found in 64 bacteria species (36 from Deltaproteobacteria, 38%; 16 from Firmicutes-Clostridia, 9%; two from Acidobacteria, 14%; 2 from Bacteroidetes; one from Chlorobi, 6%; 1 from Nitrospirae, 11%; three from Thermodesulfobacteria, 43%) (**Figure 5**, NhcC). Genes coding for HybB subunit were observed in 314 species, 277 from Gammaproteobacteria (50%), 7 from Betaproteobacteria (2%), 13 from Deltaproteobacteria (4%), 11 from Alphaproteobacteria (2%), 2 from Acidobacteria (14%), 1 from Aquificae (7%) and three from Deferribacteres (60%) (**Figure 5**, HybB). The presence of genes coding for QrcD subunit was restricted to 35 species (36%) from Deltaproteobacteria (**Figure 5**, QrcD). Genes coding for SoeC subunit were present in 236 species from Proteobacteria (45 species from Gammaproteobacteria, 5%; 83 species from Betaproteobacteria, 18%; 100 species from Alphaproteobacteria, 14%), Firmicutes-Clostridia (three species, 1%) and Aquificae (five species, 36%) phyla (**Figure 5**, SoeC). While genes coding for MccD subunit were identified in 51 species (35 from Gammaproteobacteria, 4%; 15 from Epsilonproteobacteria, 7%) (**Figure 5**, MccD).

In group D of the dendrogram (Figure 4, FqoC), we were able to identify 110 amino acid sequences present in an uncharacterized complex, that we tentatively assigned as formate:quinone oxidoreductase complex (Figure 1, FqoABC). Our assignment is based on the observations that the complex is possibly composed of three subunits: two peripheral FqoAB subunits homologous to FdnGH subunits from *E. coli* formate dehydrogenase complex (Fdn-N) and a FqoC subunit, a NrfD-like subunit with eight predicted TMHs. Genes coding for FqoC were identified in 110 species present in three different dendrogram groups: FqoC1 includes genes coding for FqoC subunit from Actinobacteria (59 species, 7%), Chlorobi (15 species, 88%) and Crenarchaeota (9 species, 12%) phyla; FqoC2 gathers the genes coding for FqoC from Chloroflexi phylum (15 species, 48%); and FqoC3 includes genes coding for FqoC subunit from Deltaproteobacteria phylum (12 species, 13%) (Figure 5, FqoC).

Homology Models

The NrfD-like subunits are transmembrane proteins, with 8 to 10 TMHs, that interact with quinones but do not have redox cofactors. The structures of *T. thermophilus* PsrC and *R. marinus* ActC and ActF revealed details of the overall architecture of these NrfD-like subunits: the common 8 TMHs are organized in two four-helix bundles (TMHs 1–4 and TMHs 5–8), which form two structural repeats related by a 180° rotation around an axis perpendicular to the membrane layer plane (Jormakka et al., 2008; Sousa et al., 2018). Two additional TMHs (TMHs A-B), present in ActC and ActF, cross each other at an angle of ~45° at the periphery of each subunit (Sousa et al., 2018) (Figure 3). ActC and ActF subunits have their N- and C-terminal located at N-side of the membrane, while PsrC have both termini located at the P-side of the membrane. *T. thermophilus* PsrC and *R. marinus* ActC subunits contain one quinol-binding site at the P-side of the membrane of the first four-helix bundle (Jormakka et al., 2008; Sousa et al., 2018) (Figure 2).

We performed structural homology models of the NrfD-like subunits from *W. succinogenes* PsrABC, *E. coli* NrfABC, *E. coli* DmsABC, *E. coli* Hyd-2, *Salmonella enterica* TtrABC, *A. ambivalens* SreABC, *A. aeolicus* SoeABC, *D. vulgaris* QrcABCD, *D. vulgaris* DsrMKJOP1, *A. vinosum* DsrMKJOP2, *Desulfovibrio desulfuricans* NhcABCD, *Alkalilimnicola ehrlichii* ArrABC, *W. succinogenes* MccACD and *Chlorobaculum tepidum* FqoABC complexes. The homology models were calculated in Phyre2 without imposing any template. In all cases the randomly selected template was the structure from *R. marinus* ActC subunit. The homology models have confidence scores higher than 90%. The final models presented the common 8 TMHs organized in a similar arrangement as those of ActC, ActF and PsrC subunits. As in the case of *T. thermophilus* PsrC subunit, we predicted only 8 TMHs for *W. succinogenes* PsrC, *E. coli* DmsC, *E. coli* NrfD, *A. aeolicus* SoeC, *W. succinogenes* MccD and *C. tepidum* FqoC subunits. *S. enterica* TtrC subunit was predicted to have 9 TMHs, with the N-terminal at the P-side and the C-terminal at the N-side of the membrane, the extra TMH is equivalent to TMH B from ActC. The other NrfD-like subunits (*E. coli* HybB, *A. ehrlichii* ArrC, *D. vulgaris* DsrP1, *A. vinosum* DsrP2, *D. vulgaris* QrcD, *A.*

ambivalens SreC and *D. desulfuricans* NhcC) have 10 predicted TMHs, the two extra TMHs are equivalent to TMH A and B of ActC and ActF subunits. The models predict for all NrfD-like subunits the presence of the structural repeats, composed of the two four-helix bundles, harboring putative ion-conducting pathways and the existence of a quinone/quinol-binding site (Figure 1, Table 2).

Quinone-Binding Site

The crystal structures of *T. thermophilus* PsrC co-crystallized with either menaquinone-7 or ubiquinone-1 showed that the quinone-binding site is located in the first four-helix bundle of PsrC (TMHs 1–4) on the P-side of the membrane, in close proximity to the $[4\text{Fe-4S}]^{2+/1+}$ cluster of PsrB subunit (Jormakka et al., 2008). Highly conserved amino acid charged residues, present in this region, were suggested as essential for quinone-binding and coordination: His21^{PsrCT}, Asn18^{PsrCT} and Tyr130^{PsrCT} in *T. thermophilus* PsrC and His139^{ActC}, Asp169^{ActC} and Asp253^{ActC} in *R. marinus* ActC (Jormakka et al., 2008; Sousa et al., 2018) (Figure 6, ActC and PsrC T).

To further investigate structurally relevant elements and/or amino acid residues in the quinone-binding site, we analyzed the obtained structural homology models of the NrfD-like subunits and performed sequence alignment to identify the conserved residues involved in the binding and coordination of quinone/quinol molecule.

We identified for all NrfD-like subunits, with the exception of ActF subunit, the only NrfD-like that has been shown not to interact with quinones/quinols and part of a complex in which another NrfD-like subunit is present, the presence of quinone/quinol-binding site in the same spatial position of those observed for *T. thermophilus* PsrC and *R. marinus* ActC. These are all located in the first four-helix bundle (TMHs 1–4), close to the P-side of the membrane. In the case of SoeC the quinone/quinol-binding site is also present in the first four-helix bundle (TMHs 1–4) at the same special position of sites present in the other NrfD-like subunits, however it is expecting to be facing the N-site of membrane. This is because the catalytic subunit of SoeABC complex is predicted to be oriented toward the N-side of the membrane (Dahl et al., 2013; Boughanemi et al., 2020) (Figure 1) and thus SoeC would be expected to have an inverted orientation inside the membrane plane comparing to the other NrfD-like proteins.

We observed, within the predicted quinone/quinol-binding site of all NrfD-like subunits analyzed, the presence of 5, on average, amino acid residues (histidine, arginine, aspartate, glutamate, serine, tyrosine, threonine and asparagine) that may be involved in quinone/quinol-binding and stabilization in each protein (Figure 6, Table 2).

Although histidine, serine, glutamate, aspartate and tyrosine residues were described as being involved in the coordination of quinones in several quinone-interacting complexes, there seems to be no common pattern for quinone-binding (Abramson et al., 2000; Fisher and Rich, 2000; Zhang et al., 2002; Iwaki et al., 2003; Horsefield et al., 2006; Kleinschroth et al., 2008). Nevertheless, we noticed a conserved serine residue in all NrfD-like subunits, close to the entry of the quinone/quinol pocket

TABLE 2 | Amino acid residues conservation in NrfD-like subunit-containing complexes.

Color code	Complex	NrfD-like subunit	KEGG Template	Quinone-binding site (TMHs 1-4)	N-side ion-translocation half-channel (TMHs 1-4)	P-side ion-translocation half-channel (TMHs 5-8)	Residues conservation	*Amino acid residues variations	# TMH	# sequences
	Alternative Complex III	ActC	rmr:rmr_0223	His139, Ser164, Asp169, Asp253	His97, Thr100, Ser103, Arg114, Arg119, Glu122, Thr125, Tyr176, Ser180, Asp191, Arg196, Asp197, His247	Tyr270, Tyr323, Glu326, Glu338, Glu394, Arg395	>95%	x	10	521
		ActF	rmr:rmr_0226	x	Ser80, His88, Arg100, Glu103*, Tyr165, Thr170, Ser180*, Asp184*, Ser199, Tyr206	Ser227, Thr228, Tyr233*, Ser238, Tyr284, Tyr290, Glu300, Glu301, Arg308, His355*, Asp358*	>80%	*E103-73%, R/Y-7% *S180-71.9%, R/T/E-10% *D184-77%, E/K/S/Y-5% *Y233-76%, D/T/S-4% *H355-69%, R/T/E/S/K-14%*D358-75%, E/H/R-20%	10	516
	Polysulfide reductase	PsrC T	tth:tt_c0153	Asn18*, His21*, Glu67, Ser87, Tyr130	Arg48*, Thr50, Asp60, Thr102*, Tyr107, Arg114*, Ser124	Thr155, Ser183, Tyr190, Glu197*, Glu205*, Tyr210, Arg239	>80%, model sequence	*N18-73%, S-13% *H21-40%, Y-60% *R48-33%, S-53% *T102-13%, S-73% *R114-53%, K-40% *E197-33%, S/T-60% *E205-33%, T/S/R-67%	8	15
		PsrC W	wsu:ws0118	Tyr23, Asp76, Ser94, Tyr159, Thr160	Ser30, Lys41*, Asp52, Lys56, Tyr106, Glu146	Ser185, Ser188, Glu225, Tyr307, Tyr310, Arg305	>95%, model sequence	*K41-88%, E/R-12%	8	33
	Group-2 [NiFe] hydrogenase	HybB	eco:b2995	Asp58, Ser105, Asp109, Ser129, Glu133, Ser190	Thr63, Tyr77, Tyr84, His85, Arg89, Ser95, Tyr99, Tyr141, Glu148, Glu155, His184, Ser186, Ser187	Arg265, Glu268*, Glu291, Lys198, His200, Arg329	>95%	*E268-86%, D-13%	10	320
	DMSO reductase	DmsC	eco:b0896	Ser62, His65, Ser82, Glu87	Thr14, Glu39, Arg43, Ser90, Lys109, Thr116*, Ser111, Arg115, Thr122*	Thr135, Thr151, Thr158, Ser195, Ser199, Glu205, Asp222, Arg230, Glu267, Arg271, Tyr275	>80%, model sequence	*T116-15%, K/S/R/E/H-58% *T122-39%, S-19%	8	793
	Arsenate reductase	ArrC	aeh:mlg_0214	Tyr57, Glu107, Ser126	Ser64, Tyr83, Lys87, Arg88, Tyr135, Lys145, Asp153, Lys160*	Tyr198, Tyr200, Ser206, Arg256, Arg324, Ser279*	>95%	*K160-44%, H/R-44% *S279-56%, T-33%	10	9
	Dissimilatory sulfite-reductase complex	DsrP1	dvu:dvu1286	Tyr52, Asp106, Ser124, Asp129	Thr57, Tyr74, Glu89, Tyr136, Arg152, Lys162, Ser168*, His176, Thr179	Arg189, Thr194, Arg200, Ser204, Glu254, His266, Lys329	>95%	*S168-93%	10	66
		DsrP2	alv:alvin_1262	His57, Asp110, Ser128, Thr178	Ser68, Ser75, Tyr85, Ser92, Tyr137, Tyr147, Arg171, Thr175, Thr176	Ser204, Tyr248, His254, Tyr259, Tyr277*	>95%	*Y277-84%, H-9%	10	36

(Continued)

TABLE 2 | Continued

Color code	Complex	NrfD-like subunit	KEGG Template	Quinone-binding site (TMHs 1-4)	N-side ion-translocation half-channel (TMHs 1-4)	P-side ion-translocation half-channel (TMHs 5-8)	Residues conservation	*Amino acid residues variations	# TMH	# sequences
	Quinone reductase complex	QrcD	dvu:dvu0692	Asp70, Asp120*, Ser138, Glu142, Ser202	Arg87*, Tyr88, Asp93*, Tyr110, Tyr150, Glu157, Glu164, Arg166, His182, Ser196, His199, Ser196	Ser234, Tyr227, Tyr278, Glu319, Lys282, Asp285, Thr286, Tyr311, Arg358	>95%	*R87-53%, K/Y/S-47% *D93-68%, K/E-32% *D120-91%, E-9% *R166-62%, K-38%	10	35
	Sulfur reductase complex	SreC	aamb:d1866_07880	Tyr55, Ser110, Ser128, Arg129	Thr63, Ser66, Tyr68, Ser70, Glu73, Arg91, Glu93, Tyr137, Glu154, Lys155, Asp206	Glu222, Ser228 , Ser330, Ser235 , Tyr237, Thr311, Asp380, Tyr389	>80%, model sequence	x	10	21
	Periplasmic nitrite reductase	NrfD	eco:b4073	Asp15, Tyr21, His74, Ser92, Tyr162, Thr163	Ser28, Arg39*, Tyr104, His118*, Glu149*	Ser188, S191, Glu228, Lys246, Tyr260, Tyr311, Arg306	>80%, model sequence	*R39-65%, K-35% *H118-26%, K/D/E/T/S/R-47% *E149-78%, T/D/S-14% *K246-77%, S/R-16%	8	411
	Tetrathionate reductase	TtrC	sty:sty1737	Tyr26, Asp75, Ser93, Tyr146, Thr147, Glu150	Glu54, Thr63, Thr106, Lys119, Arg125, Thr129, Ser136	Arg157, Ser162*, Ser172*, Ser220, Arg280 , Lys292	>80%, model sequence	*S162-46%, T-41% *S172-66%, T-34%	9	292
	Nine-heme cytochrome complex	NhcC	dds:ddes_2040	Asp68, Asp119, Ser137, Glu141, Ser200	Tyr87*, Arg99, Thr104, Tyr109, Tyr149, Glu156, Glu163, Thr195, His197	Ser218, Ser228, Tyr278, Lys282, Glu306, Arg345	>80%	*Y87-58%, H-35%	10	81
	Sulfite dehydrogenase	SoeC	aae:aq_1231	Ser6, His65, Glu87, Thr132, Ser82, Ser85	Tyr25, Lys41, Ser47, Ser51, Thr97, Tyr106, Glu114, Thr116, Thr121, Ser128	Glu144*, Thr150, Arg224, Lys228, Glu239, Arg297 , His306	>80%, model sequence	*E144-46%, R/S-29%	8	239
	Multiheme cytochrome c sulfite reductase	MccD	wsu:ws0382	Tyr24, Asp75, Ser93, Tyr161, Thr162	Ser31, Arg42*, Lys55, Ser58, Ser61, Thr64, Tyr105, Ser109, Ser119, Tyr137, Arg141, Arg144* , Glu148, Thr151, Thr157	Ser187, Ser190, Glu227, Ser237, Lys246, Ser248, Tyr257, Arg306	>95%, model sequence	*R42-84%, K-11% *R144-87%, E/Y/K-13%	8	79
	Formate:quinone oxidoreductase	FqoC	cte:ct0494	Tyr16, Asp65, Ser81, Tyr147, Thr148	Thr26, Ser30, His34, Glu37*, Asp40, Arg41, Ser45*, Ser50, Tyr93, Tyr100, Glu127, Lys131, Ser138	Ser173, Glu212, Tyr219, Arg231, Glu235, His239, Glu259, Tyr295, Arg293	>80%, model sequence	*E37-13%, T/S/D-88% *S45-10%, R/K-90%	8	114

Amino acid residues, putatively involved in ion-conducting pathways and quinone/quinol-binding are represented in black (conserved residues in respective sequence alignments), gray (amino acid residues present in the model able to conduct protons, but not conserved in respective sequence alignments) and red (equivalent to Arg395^{ActC}).

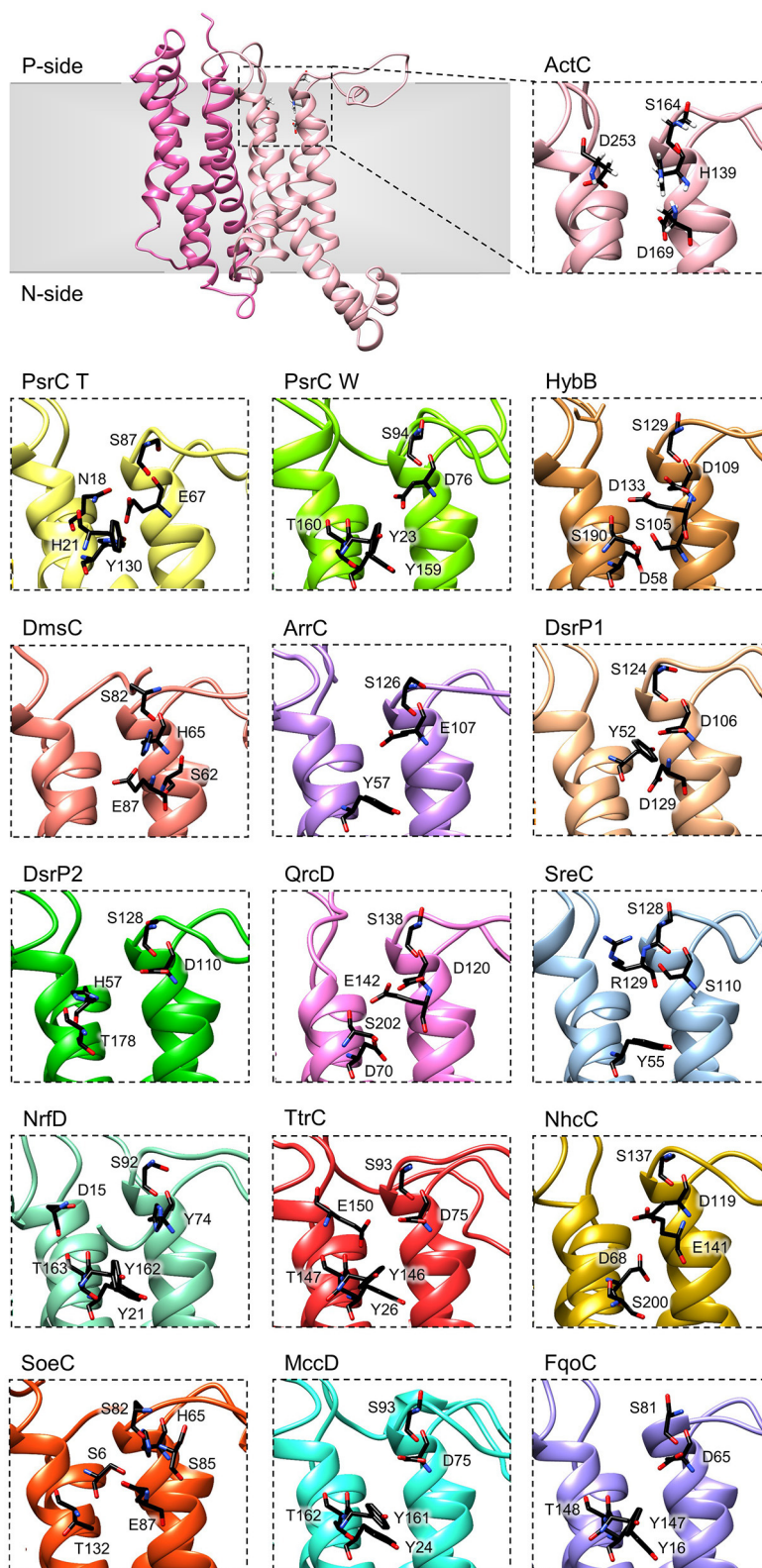


FIGURE 6 | Quinone-binding site. Zoomed views of structural models of NrfD-like subunits showing the respective putative quinone/quinol-binding sites, located close to the positive-side (P-side) of the membrane. The SoeC subunit is expected to be in an inverted orientation toward the membrane in relation to the other NrfD-like subunits and thus its quinone/quinol binding site is located close to the negative-side (N-side). The amino acid residues composing the different quinone/quinol-binding sites are indicated and depicted as sticks. Please note that all models are oriented with the P-side of the membrane at the top of each panel, except for SoeC that is oriented with the N-side of the membrane at the top of the respective panel.

(Ser164^{ActC}, Ser87^{PsrC-T}, Ser94^{PsrC-W}, Ser129^{HybB}, Ser82^{DmsC}, Ser126^{ArrC}, Ser124^{DsrP1}, Ser128^{DsrP2}, Ser138^{QrcD}, Ser128^{SreC}, Ser92^{NrfD}, Ser93^{TtrC}, Ser137^{NhcC}, Ser82^{SoeC}, Ser93^{MccD} and Ser81^{FqoC}). We hypothesized that this serine residue is involved in quinone coordination, since it is only absent in *R. marinus* ActF subunit, the only NrfD-like that has been shown not to interact with quinone (Sousa et al., 2018). Mutation of Ser94^{PsrC-W} residue in *W. succinogenes* PsrC caused partially inhibition of polysulfide respiration (Dietrich and Klimmek, 2002). We also identified in TMH 2, in the same spatial position in all NrfD-like subunits (again with the exception of ActF), the presence of a glutamate/aspartate/histidine/serine residue (Glu67^{PsrC-T}, Glu107^{ArrC}, Asp76^{PsrC-W}, Asp109^{HybB}, Asp106^{DsrP1}, Asp110^{DsrP2}, Asp120^{QrcD}, Asp75^{TtrC}, Asp119^{NhcC}, Asp75^{MccD}, Asp65^{FqoC}, His139^{ActC}, His65^{DmsC}, His65^{SoeC}, His74^{NrfD} and Ser110^{SreC}) that seems to be required for protonation/deprotonation of the quinone/quinol molecule (Table 2). Mutational studies support the relevance of this position. Replacement of Asp76^{PsrC-W} and His65^{DmsC} residues, in *W. succinogenes* PsrC and *E. coli* DmsC, respectively, blocked quinol oxidation (Rothery and Weiner, 1996; Zhao and Weiner, 1998; Geijer and Weiner, 2004) and lead to full inhibition of polysulfide respiration (Dietrich and Klimmek, 2002). In *T. thermophilus* PsrC structure, Tyr130^{PsrC-T} and His21^{PsrC-T} residues were proposed to act as ligands to menaquinone and pentachlorophenol, a quinone inhibitor (Jormakka et al., 2008), and, in fact, mutation of Tyr23^{PsrC-W} residue, the correspondent residue in *W. succinogenes* PsrC, also inhibit polysulfide respiration (Dietrich and Klimmek, 2002). Additional mutational studies, conducted in *E. coli* DmsABC (Rothery and Weiner, 1996; Zhao and Weiner, 1998), *W. succinogenes* PsrABC (Dietrich and Klimmek, 2002) and *E. coli* Hyd-2 (Lubek et al., 2019), also showed the importance of Glu87^{DmsC}, Tyr159^{PsrC-W}, Thr160^{PsrC-W} and Asp58^{HybB} residues for quinone/quinol coordination (Rothery and Weiner, 1996; Zhao and Weiner, 1998; Dietrich and Klimmek, 2002; Geijer and Weiner, 2004; Lubek et al., 2019).

Our models indicate that all NrfD-like proteins (except for ActF) are able to interact with quinones/quinols (Figures 1, 6).

Ion Translocation Pathways

NrfD-like subunit-containing complexes were hypothesized to be capable of ion-translocation across the membrane (Calisto et al., 2021) and, in fact, proton-conducting pathways have been identified in the structures of the PsrC, ActC and ActF subunits (Jormakka et al., 2008; Sousa et al., 2018; Sun et al., 2018; Shi et al., 2020). Proton-conducting pathways are formed by amino acid residues with side chains that can establish hydrogen bonds, constituting a hydrogen bond network. This allows proton transfer by a Grotthuss-type mechanism, which involves successive breaking and concomitant formation of hydrogen bonds (de Grotthuss, 1806; Cukierman, 2006).

In *R. marinus* ActC and ActF subunits, the putative ion-conducting pathway was suggested to be formed by two half-channels: a N-side half-channel in the first four-helix bundle (TMH 1–4) and a P-side half-channel in the second four-helix

bundle (TMH 5–8) (Sousa et al., 2018). ActC and ActF ion-conducting pathways are composed of conserved amino acid residues within all ACIII complexes (Sousa et al., 2018) (Figure 7, ActC; Table 2).

We were able to identify, in all NrfD-like subunits, amino acid residues that may constitute a N-side half-channel in the first four-helix bundle (TMH 1–4) and a P-side half-channel in the second four-helix bundle (TMH 5–8). The amino acid residues that compose these putative ion-conducting pathways are conserved within each subunit: ActC, ActF, HybB, ArrC, DsrP, QrcD, SreC, NrfD and NhcC subunits (Figure 7, Table 2). However, in PsrC, DmsC, TtrC, SoeC, MccD and FqoC subunits, the two half-channels were not so easy to define, as we observed less conserved residues.

In *T. thermophilus* PsrC structure, the putative ion-conducting pathway was suggested to be formed by a N-side half-channel in the second four-helix bundle (TMH 5–8) and a P-side half-channel in the first four-helix bundle (TMH 1–4) (Jormakka et al., 2008). Of the proposed residues in the N-side half-channel at TMH 5-8 (Glu224^{PsrC-T}, Thr220^{PsrC-T}, Arg177^{PsrC-T}) (Jormakka et al., 2008), only Arg177^{PsrC-T} residue is conserved among other PsrC T subunits. Mutation of Asp218^{PsrC-W}, the equivalent to Arg177^{PsrC-T} in *W. succinogenes* PsrC, and Ser192^{PsrC-W} residues, both located at TMH 5-8 in the N-side half-channel, resulted in inhibition or reduction of polysulfide respiration, respectively (Jormakka et al., 2008). Nevertheless, we identified conserved amino acid residues (Figure 7, PsrC T; Table 2) that could form two half-channels, resembling those identified in ActC and ActF subunits. Our identification is supported by substitution studies of amino acid residues located at TMH 1–4 on our proposed N-side half-channel (Tyr106^{PsrC-W} and Glu146^{PsrC-W}) and located at TMH 5-8 on the P-side half-channel (Glu225^{PsrC-W}, Ser185^{PsrC-W}, Ser188^{PsrC-W} and Tyr310^{PsrC-W}) of *W. succinogenes* PsrC model, resulted in strains with a compromised polysulfide respiration (Dietrich and Klimmek, 2002). These data suggest those residues may be important for proton translocation, since PsrABC catalyzes an endergonic reaction dependent of electrochemical potential (Dietrich and Klimmek, 2002; Calisto et al., 2021).

The presence of an ion-conducting pathway in HybB is also supported by the observations that replacement of Arg89^{HybB}, Tyr99^{HybB}, Glu148^{HybB} and His184^{HybB} in *E. coli* HybB (N-side half-channel TMH 5–8) significantly decreased hydrogen oxidation (Lubek et al., 2019). Addition of a protonophore increases hydrogen oxidation in these mutated strains (Lubek et al., 2019), showing that ion translocation and catalytic activity are coupled.

Previously for QrcD, only the N-side half-channel, present in the first four-helix bundle (TMH 1–4) as observed for ActC and ActF subunits, was proposed to be present (Duarte et al., 2018). This N-side half-channel was hypothesized to translocate protons from the N-side of the membrane to the quinone-binding site, for quinone reduction (Duarte et al., 2018). However, we identified conserved amino acid residues that could be part of a P-side half-channel in the second four-helix bundle (TMH 5–8) (Figure 7, QrcD; Table 2).

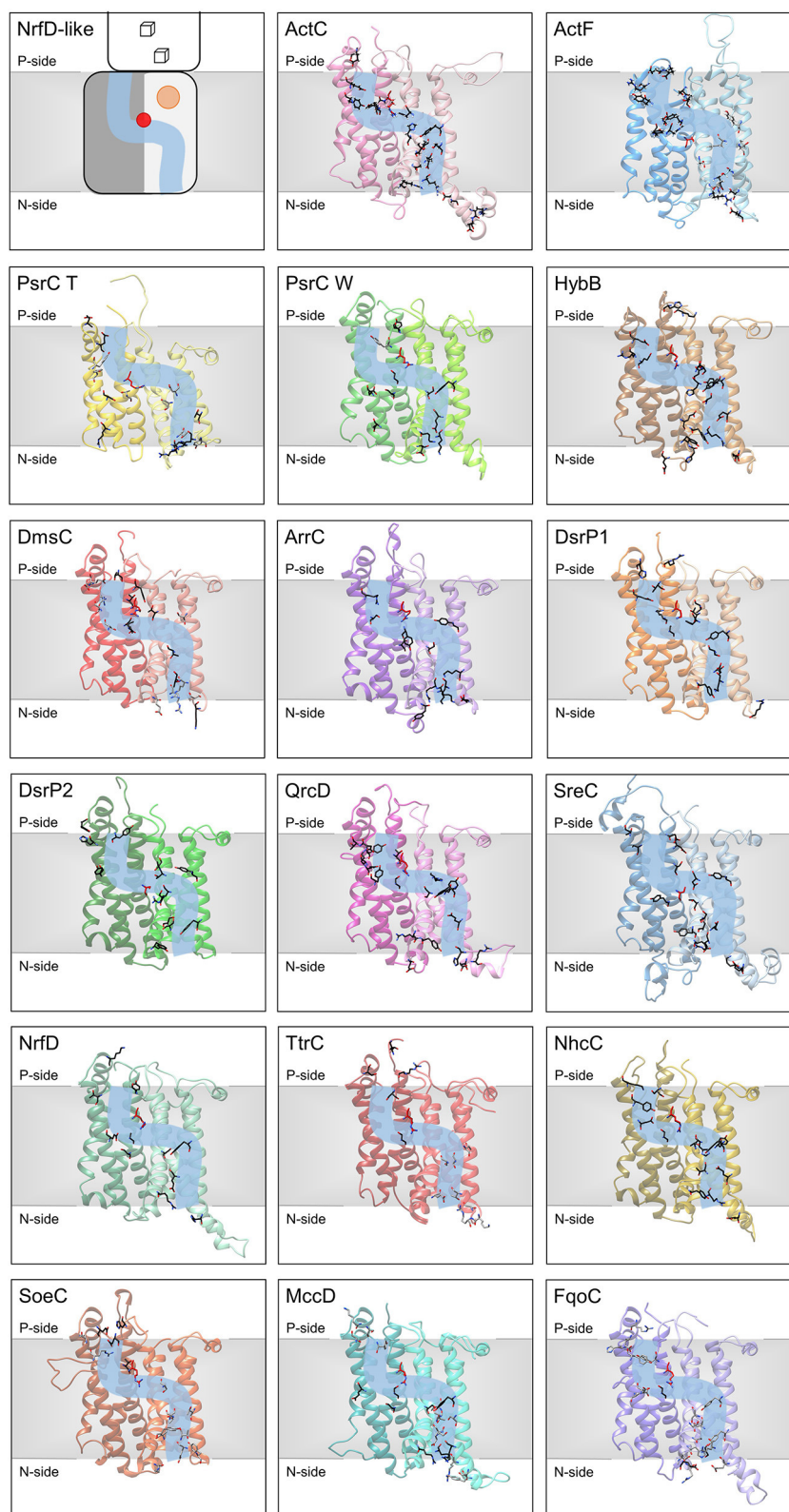


FIGURE 7 | Ion-translocation pathway. Structural models of NrfD-like subunits with amino acid residues putatively involved in ion-translocation. The top left side panel contains a general schematic representation of NrfD-like subunits. Each protein is composed by eight common TMH that form two four-helix bundle (TMHs 1–4, light
(Continued)

FIGURE 7 | gray [lighter colors in the following panels) and TMHs 5–8, dark gray (darker colors in the following panels)] related by a 180° rotation around an axis perpendicular to the membrane. The light blue line schematizes the ion-conducting pathway and the red dot indicates the presence of the arginine residue (Arg395^{ActC}), possibly acting as the gate of the pathway. The orange circle points to the quinone/quinol-binding site, which is in close proximity to the [4Fe-4S]^{+2/+1} cluster ([3Fe-4S]^{+1/+0} in ActC) (cube) present at the peripheral subunit. The other panels contain the structural models obtained for the 8 common TMHs, the amino acid residues, putatively involved ion-pathways are indicated and depicted as sticks along the light blue line and are highlighted in black (conserved residues in respective sequence alignments), gray (amino acid residues present in the model able to conduct protons, but not conserved in respective sequence alignments) and red (equivalent to Arg395^{ActC}). Please note that all models are oriented with the P-side of the membrane at the top of each panel, except for SoeC that is oriented with the N-side of the membrane at the top of the respective panel (see more in text and in legend of **Figure 6**).

Although the ion-conducting pathways present in the different NrfD-like subunits are not composed by the same amino acid residues, they are localized at the same spatial position. Noticeably, we identified a conserved arginine residue (Arg395^{ActC}, Arg239^{PsrC_T}, Arg305^{PsrC_W}, Arg329^{HybB}, Arg271^{DmsC}, Arg324^{ArrC}, Arg358^{QrcD}, Arg306^{NrfD}, Arg280^{TrcC}, Arg345^{NhcC}, Arg297^{SoeC}, Arg306^{MccD}, Arg293^{FqoC}) located in middle of the membrane (in TMH 8) in a position that coincides with that at which the two proton half-channels converge (**Figure 7**). In *Desulfovibrio vulgaris* DsrP this is occupied by a lysine (Lys329^{DsrP1}). We hypothesized that the residue at this position may perform a gate keeping role for proton translocation across the membrane. In fact, water molecules around Arg239^{PsrC_T} were observed in the structure of PsrC from *T. thermophilus* (Jormakka et al., 2008) and mutation of Arg305^{PsrC_W} resulted in inhibition of polysulfide respiration (Dietrich and Klimmek, 2002). Although, we hypothesized a relevant function for this arginine (or Lys329^{DsrP1}) residue, it is not conserved in ActF, DsrP2 and SreC. In these subunits the gating role may be performed by a conserved serine residue (Ser238^{ActF}, Ser204^{DsrP2} and Ser235^{SreC}), which is located in middle of the membrane in TMH 5, also coinciding with the convergence of the two half-channels (**Figure 7**).

The members of the NrfD family are transmembrane proteins (8 to 10 TMHs) characterized by the presence of structural repeats, composed of two four-helix bundles, harboring ion-translocation pathways and a quinone/quinol-binding site.

The quinone/quinol-binding site of NrfD-like subunits is located at the P-side of the membrane in the first four-helix bundle (TMHs 1–4), always in vicinity of the peripheral iron-sulfur subunit. The peripheral subunits of SoeABC complex are hypothesized to be located at the N-side (Dahl et al., 2013; Boughanemi et al., 2020) and thus SoeC would be expected to be in an inverted orientation in the membrane when comparing to the other NrfD-like proteins. In this way, its quinone-binding site would be present on the N-side of the membrane. We identified, in TMH 2 close to the entry of the quinone/quinol pocket, a serine residue (Ser164^{ActC}) that appears to be important for interaction with quinone/quinol molecule, since this serine residue is strictly conserved in all NrfD-like subunits that interact with quinone/quinol.

Our structural models reinforce the possible existence of ion-translocation pathways in all NrfD-like subunits and the contribution of the NrfD-like subunit-containing complexes to energy transduction. NrfD-like subunit-containing complexes may perform energy transduction by an indirect-coupling mechanism and may generate or consume electrochemical

potential (Calisto et al., 2021). *W. succinogenes* PsrABC activity was shown to be dependent on electrochemical potential (Dietrich and Klimmek, 2002), while QrcABCD activity was shown to be coupled to the formation of electrochemical potential (Duarte et al., 2018). The ion-translocation pathways, observed in NrfD-like subunits, are formed by amino acid residues that may establish hydrogen bonds, allowing proton translocation by a Grotthuss-type mechanism (de Grotthuss, 1806; Cukierman, 2006). A semiconserved arginine amino acid residue, located in the middle of the membrane at the intersection of the two ion half-channels, was here suggested to play an important role as gate keeper in ion-translocation. In ActF, DsrP2 and SreC the gating role may be performed by a conserved serine.

The data here presented indicate that NrfD-like subunits are possibly the ion translocating modules of different enzymes, involved in a vast array of metabolisms, such as the oxygen, nitrogen, sulfur, arsenate and hydrogen cycles. All NrfD-like subunits containing complexes may be thus energy transducing membrane machines that contribute to energy conservation in vast range of organisms and under multiple growth conditions.

MATERIALS AND METHODS

The selection of the complete NrfD-like subunits dataset was performed using protein BLAST (pBLAST) analysis tool (default parameters) running at KEGG's (Kyoto Encyclopedia of Genes and Genomes) database, which only contains data on fully sequenced genomes (Ogata et al., 1999; Kanehisa et al., 2006, 2008). The information used in this study was that available by October 2020.

Protein search was performed using the amino acid sequences of ActC and ActF from *R. marinus* (rmr:rmr_0223, rmr:rmr_0226), PsrC from *T. thermophilus* (tth:tt_c0153) and *W. succinogenes* (wsu:ws0118), NrfD (eco:b4073), DmsC (eco:b0896), and HybB (eco:b2995) from *E. coli*, TrcC from *S. enterica* (sty:sty1737), SreC from *A. ambivalens* (aamb:d1866_07880), SoeC from *A. aeolicus* (aae:aq_1231), QrcD (dvu:dvu0692) and DsrP (dvu:dvu1286) from *D. vulgaris*, NhcC from *D. desulfuricans* (dds:ddes_2040), ArrC from *A. ehrlichii* (aeh:mlg_0214) and MccD from *W. succinogenes* (wsu:ws0382). Results with *e*-value <0.01 were accepted for further analysis (ca. 4,545 protein sequences).

The 4,545 amino acid sequences were clustered according to their identity using the CD-HIT tool (50% identity) (Huang et al., 2010). The resulting 551 representative sequences were aligned using PROMALS3D (standard parameters, using *R. marinus* ActC as structural template, PDB: 6F04) (Pei et al., 2008).

The dendrogram was constructed using RAxML toll and the Neighbor-Joining (NJ) method at the CIPRES gateway portal (Miller et al., 2010). The obtained dendrogram was visualized and manipulated in Dendroscope (Huson et al., 2007).

To generate the structural models of NrfD-like subunits we used the amino acid sequence from *W. succinogenes* PsrC (wsu:ws0118), *E. coli* NrfD (eco:b4073), *E. coli* DmsC (eco:b0896), *E. coli* HybB (eco:b2995), *S. enterica* TtrC (sty:sty1737), *A. ambivalens* SreC (aamb:d1866_07880), *A. aeolicus* SoeC (aae:aq_1231), *D. vulgaris* QrcD (dvu:dvu0692), *D. vulgaris* DsrP1 (dvu:dvu1286), *Allochrochromatium vinosum* DsrP2 (alv:alvin_1262), *D. desulfuricans* NhcC (dds:ddes_2040), *A. ehrlichii* ArrC (aeh:mlg_0214), *W. succinogenes* MccD (wsu:ws0382) and *C. tepidum* FqoC (cte:ct0494) subunits. We developed the structural models using Phyre2 for predicting protein structure by homology modeling under intensive mode, and ActC *R. marinus* (PDB: 6F0K2) structure was selected as template (Kelley et al., 2015; Sousa et al., 2018). Protein structural model visualization and figure construction were performed using Chimera (Pettersen et al., 2004).

Quinone/quinol-binding sites and ion-translocation pathways were identified by sequence conservation analysis, after declustering the amino acid sequences from dendrogram branches, selected as containing ActC, ActF, PsrC, NrfD, DmsC, HybB, TtrC, SreC, SoeC, QrcD, DsrP, NhcC, ArrC, MccD and FqoC sequences. Sequence alignments were performed using

PROMALS3D for each dendrogram group and visualized using JalView software (Waterhouse et al., 2009).

DATA AVAILABILITY STATEMENT

The raw data supporting the conclusions of this article will be made available by the authors, without undue reservation.

AUTHOR CONTRIBUTIONS

FC and MP conceived the study, analyzed the results, and wrote the manuscript. All authors contributed to the article and approved the submitted version.

FUNDING

The work was funded by Fundação para a Ciência e a Tecnologia (PTDC/BIA-BQM/28827/2017 and PTDC/BIA-BQM/30528/2017). The project was further supported by UIDB/04046/2020 and UIDP/04046/2020 Centre grants from FCT, Portugal (to BioISI), by LISBOA-01-0145-FEDER-007660 cofunded by FEDER through COMPETE2020-POCI and by Fundação para a Ciência e a Tecnologia and by UIDB/04612/2020 and UIDP/04612/2020 research unit grants from FCT (to Mostmicro).

REFERENCES

- Abramson, J., Riistama, S., Larsson, G., Jasaitis, A., Svensson-Ek, M., Laakkonen, L., et al. (2000). The structure of the ubiquinol oxidase from *Escherichia coli* and its ubiquinone binding site. *Nat. Struct. Biol.* 7, 910–917. doi: 10.1038/82824
- Bamford, V. A., Bruno, S., Rasmussen, T., Appia-Ayme, C., Cheesman, M. R., Berks, B. C., et al. (2002). Structural basis for the oxidation of thiosulfate by a sulfur cycle enzyme. *EMBO J.* 21, 5599–5610. doi: 10.1093/emboj/cdf566
- Beaton, S. E., Evans, R. M., Finney, A. J., Lamont, C. M., Armstrong, F. A., Sargent, F., et al. (2018). The structure of hydrogenase-2 from *Escherichia coli*: implications for H₂-driven proton pumping. *Biochem. J.* 475, 1353–1370. doi: 10.1042/BCJ20180053
- Bento, I., Teixeira, V. H., Baptista, A. M., Soares, C. M., Matias, P. M., and Carrondo, M. A. (2003). Redox-Bohr and other cooperativity effects in the nine-heme cytochrome c from *Desulfovibrio desulfuricans* ATCC 27774: crystallographic and modeling studies. *J. Biol. Chem.* 278, 36455–36469. doi: 10.1074/jbc.M301745200
- Berks, B. C. (1996). A common export pathway for proteins binding complex redox cofactors? *Mol. Microbiol.* 22, 393–404. doi: 10.1046/j.1365-2958.1996.00114.x
- Boughanemi, S., Infossi, P., Giudici-Orticoni, M.-T., Schoepp-Cothenet, B., and Guiral, M. (2020). Sulfite oxidation by the quinone-reducing molybdenum sulfite dehydrogenase SoeABC from the bacterium *aquifex aeolicus*. *Biochim. Biophys. Acta Bioenerg.* 1861:148279. doi: 10.1016/j.bbabi.2020.148279
- Calisto, F., Sousa, F. M., Sena, F. V., Refojo, P. N., and Pereira, M. M. (2021). Mechanisms of energy transduction by charge translocating membrane proteins. *Chem. Rev.* 121, 1804–1844. doi: 10.1021/acs.chemrev.0c00830
- Clarke, T. A., Cole, J. A., Richardson, D. J., and Hemmings, A. M. (2007). The crystal structure of the pentahaem c-type cytochrome NrfB and characterization of its solution-state interaction with the pentahaem nitrite reductase NrfA. *Biochem. J.* 406, 19–30. doi: 10.1042/BJ20070321
- Cukierman, S. (2006). Et tu, grothuss! and other unfinished stories. *Biochim. Biophys. Acta Bioenerg.* 1757, 876–885. doi: 10.1016/j.bbabi.2005.12.001
- Dahl, C., Franz, B., Hensen, D., Kesselheim, A., and Zigann, R. (2013). Sulfite oxidation in the purple sulfur bacterium *Allochrochromatium vinosum*: identification of SoeABC as a major player and relevance of SoxYZ in the process. *Microbiology* 159, 2626–2638. doi: 10.1099/mic.0.071019-0
- de Grothuss, C. J. T. (1806). On the decomposition of water and the species held in solution by the aid of galvanic electricity. *Annu. Chem.* 58, 54–74.
- Denkmann, K., Grein, F., Zigann, R., Siemen, A., Bergmann, J., van Helmont, S., et al. (2012). Thiosulfate dehydrogenase: a widespread unusual acidophilic c-type cytochrome. *Environ. Microbiol.* 14, 2673–2688. doi: 10.1111/j.1462-2920.2012.02820.x
- Dietrich, W., and Klimmek, O. (2002). The function of methyl-menaquinone-6 and polysulfide reductase membrane anchor (PsrC) in polysulfide respiration of *Wolinella succinogenes*. *Eur. J. Biochem.* 269, 1086–1095. doi: 10.1046/j.0014-2956.2001.02662.x
- Duarte, A. G., Catarino, T., White, G. F., Lousa, D., Neukirchen, S., Soares, C. M., et al. (2018). An electrogenic redox loop in sulfate reduction reveals a likely widespread mechanism of energy conservation. *Nat. Commun.* 9:5448. doi: 10.1038/s41467-018-07839-x
- Duval, S., Ducluzeau, A.-L., Nitschke, W., and Schoepp-Cothenet, B. (2008). Enzyme phylogenies as markers for the oxidation state of the environment: the case of respiratory arsenate reductase and related enzymes. *BMC Evol. Biol.* 8:206. doi: 10.1186/1471-2148-8-206
- Fisher, N., and Rich, P. R. (2000). A motif for quinone binding sites in respiratory and photosynthetic systems. *J. Mol. Biol.* 296, 1153–1162. doi: 10.1006/jmbi.2000.3509
- Geijer, P., and Weiner, J. H. (2004). Glutamate 87 is important for menaquinol binding in DmsC of the DMSO reductase (DmsABC) from *Escherichia coli*. *Biochim. Biophys. Acta Biomembr.* 1660, 66–74. doi: 10.1016/j.bbamem.2003.10.016
- Grein, F., Pereira, I. A. C., and Dahl, C. (2010). Biochemical characterization of individual components of the *Allochrochromatium vinosum* DsrMKJOP transmembrane complex aids understanding of complex function *in vivo*. *J. Bacteriol.* 192, 6369–6377. doi: 10.1128/JB.00849-10

- Grein, F., Ramos, A. R., Venceslau, S. S., and Pereira, I. A. C. (2013). Unifying concepts in anaerobic respiration: insights from dissimilatory sulfur metabolism. *Biochim. Biophys. Acta Bioenerg.* 1827, 145–160. doi: 10.1016/j.bbabi.2012.09.001
- Grimaldi, S., Schoepp-Cothenet, B., Ceccaldi, P., Guigliarelli, B., and Magalon, A. (2013). The prokaryotic Mo/W-bisPGD enzymes family: a catalytic workhorse in bioenergetic. *Biochim. Biophys. Acta Bioenerg.* 1827, 1048–1085. doi: 10.1016/j.bbabi.2013.01.011
- Guiral, M., Tron, P., Aubert, C., Gloter, A., Iobbi-Nivol, C., and Giudici-Ortoni, M. T. (2005). A membrane-bound multienzyme, hydrogen-oxidizing, and sulfur-reducing complex from the hyperthermophilic bacterium *Aquifex aeolicus*. *J. Biol. Chem.* 280, 42004–42015. doi: 10.1074/jbc.M508034200
- Hensel, M., Hinsley, A. P., Nikolaus, T., Sawers, G., and Berks, B. C. (1999). The genetic basis of tetrathionate respiration in *Salmonella typhimurium*. *Mol. Microbiol.* 32, 275–287. doi: 10.1046/j.1365-2958.1999.01345.x
- Hinsley, A. P., and Berks, B. C. (2002). Specificity of respiratory pathways involved in the reduction of sulfur compounds by *Salmonella enterica*. *Microbiology* 148, 3631–3638. doi: 10.1099/00221287-148-11-3631
- Horsefield, R., Yankovskaya, V., Sexton, G., Whittingham, W., and Shiomi, K., Omura, S., et al. (2006). Structural and computational analysis of the quinone-binding site of complex II (succinate-ubiquinone oxidoreductase). *J. Biol. Chem.* 281, 7309–7316. doi: 10.1074/jbc.M508173200
- Huang, Y., Niu, B., Gao, Y., Fu, L., and Li, W. (2010). CD-HIT suite: a web server for clustering and comparing biological sequences. *Bioinformatics* 26, 680–682. doi: 10.1093/bioinformatics/btq003
- Huson, D. H., Richter, D. C., Rausch, C., DeZulian, T., Franz, M., and Rupp, R. (2007). Dendroscope: an interactive viewer for large phylogenetic trees. *BMC Bioinformatics* 8:460. doi: 10.1186/1471-2105-8-460
- Hussain, H., Grove, J., Griffiths, L., Busby, S., and Cole, J. (1994). A seven-gene operon essential for formate-dependent nitrite reduction to ammonia by enteric bacteria. *Mol. Microbiol.* 12, 153–163. doi: 10.1111/j.1365-2958.1994.tb01004.x
- Iwaki, M., Giotta, L., Akinku, A. O., Schägger, H., Fisher, N., Breton, J., et al. (2003). Redox-Induced Transitions in Bovine Cytochrome bc₁ Complex Studied by Perfusion-Induced ATR-FTIR Spectroscopy [†]. *Biochemistry* 42, 11109–11119. doi: 10.1021/bi0343020
- Jormakka, M., Yokoyama, K., Yano, T., Tamakoshi, M., Akimoto, S., Shimamura, T., et al. (2008). Molecular mechanism of energy conservation in polysulfide respiration. *Nat. Struct. Mol. Biol.* 15, 730–737. doi: 10.1038/nsmb.1434
- Kanehisa, M., Araki, M., Goto, S., Hattori, M., Hirakawa, M., Itoh, M., et al. (2008). KEGG for linking genomes to life and the environment. *Nucleic Acids Res.* 36, D480–D484. doi: 10.1093/nar/gkm882
- Kanehisa, M., Goto, S., Hattori, M., Aoki-Kinoshita, K. F., Itoh, M., Kawashima, S., et al. (2006). From genomics to chemical genomics: new developments in KEGG. *Nucleic Acids Res.* 34, D354–D357. doi: 10.1093/nar/gkj102
- Kelley, L. A., Mezulis, S., Yates, C. M., Wass, M. N., and Sternberg, M. J. E. (2015). The Phyre2 web portal for protein modeling, prediction and analysis. *Nat. Protoc.* 10, 845–858. doi: 10.1038/nprot.2015.053
- Kern, M., Klotz, M. G., and Simon, J. (2011). The Wolinella succinogenes mcc gene cluster encodes an unconventional respiratory sulphite reduction system. *Mol. Microbiol.* 82, 1515–1530. doi: 10.1111/j.1365-2958.2011.07906.x
- Kleinschroth, T., Anderka, O., Ritter, M., Stocker, A., Link, T. A., Ludwig, B., et al. (2008). Characterization of mutations in crucial residues around the Qo binding site of the cytochrome bc₁ complex from *Paracoccus denitrificans*. *FEBS J.* 275, 4773–4785. doi: 10.1111/j.1742-4658.2008.06611.x
- Kurth, J. M., Dahl, C., and Butt, J. N. (2015). Catalytic protein film electrochemistry provides a direct measure of the tetrathionate/thiosulfate reduction potential. *J. Am. Chem. Soc.* 137, 13232–13235. doi: 10.1021/jacs.5b08291
- Laska, S., Lottspeich, F., and Kletzin, A. (2003). Membrane-bound hydrogenase and sulfur reductase of the hyperthermophilic and acidophilic archaeon *Acidianus ambivalens*. *Microbiology* 149, 2357–2371. doi: 10.1099/mic.0.26455-0
- Laurinavichene, T. V., Zorin, N. A., and Tsygankov, A. A. (2002). Effect of redox potential on activity of hydrogenase 1 and hydrogenase 2 in *Escherichia coli*. *Arch. Microbiol.* 178, 437–442. doi: 10.1007/s00203-002-0471-x
- Lubek, D., Simon, A. H., and Pinsky, C. (2019). Amino acid variants of the HybB membrane subunit of *Escherichia coli* [NiFe]-hydrogenase-2 support a role in proton transfer. *FEBS Lett.* 593, 2194–2203. doi: 10.1002/1873-3468.13514
- Mander, G. J., Duin, E. C., Linder, D., Stetter, K. O., and Hedderich, R. (2002). Purification and characterization of a membrane-bound enzyme complex from the sulfate-reducing archaeon *Archaeoglobus fulgidus* related to heterodisulfide reductase from methanogenic archaea. *Eur. J. Biochem.* 269, 1895–1904. doi: 10.1046/j.1432-1033.2002.02839.x
- Marreiros, B. C., Calisto, F., Castro, P. J., Duarte, A. M., Sena, F. V., Silva, A. F., et al. (2016). Exploring membrane respiratory chains. *Biochim. Biophys. Acta Bioenerg.* 1857, 1039–1067. doi: 10.1016/j.bbabi.2016.03.028
- Matias, P. M., Coelho, R., Pereira, I. A. C., Coelho, A. V., Thompson, A. W., Sieker, L. C., et al. (1999). The primary and three-dimensional structures of a nine-haem cytochrome c from *Desulfovibrio desulfuricans* ATCC 27774 reveal a new member of the Hmc family. *Structure* 7, 119–130. doi: 10.1016/S0969-2126(99)80019-7
- Matias, P. M., Pereira, I. A. C., Soares, C. M., and Carrondo, M. A. (2005). Sulphate respiration from hydrogen in *Desulfovibrio* bacteria: a structural biology overview. *Prog. Biophys. Mol. Biol.* 89, 292–329. doi: 10.1016/j.pbimolbio.2004.11.003
- Miller, M. A., Pfeiffer, W., and Schwartz, T. (2010). “Creating the CIPRES science gateway for inference of large phylogenetic trees,” in *2010 Gateway Computing Environments Workshop (GCE)* (New Orleans, LA: IEEE), 1–8. doi: 10.1109/GCE.2010.5676129
- Mitchell, P. (1961). Coupling of phosphorylation to electron and hydrogen transfer by a chemi-osmotic type of mechanism. *Nature* 191, 144–148. doi: 10.1038/191144a0
- Müller, J. A., and DasSarma, S. (2005). Genomic analysis of anaerobic respiration in the archaeon *Halobacterium* sp. strain NRC-1: dimethyl sulfoxide and trimethylamine N-oxide as terminal electron acceptors. *J. Bacteriol.* 187, 1659–1667. doi: 10.1128/JB.187.5.1659-1667.2005
- Ogata, H., Goto, S., Sato, K., Fujibuchi, W., Bono, H., and Kanehisa, M. (1999). KEGG: kyoto encyclopedia of genes and genomes. *Nucleic Acids Res.* 27, 29–34. doi: 10.1093/nar/27.1.29
- Pei, J., Kim, B.-H., and Grishin, N. V. (2008). PROMALS3D: a tool for multiple protein sequence and structure alignments. *Nucleic Acids Res.* 36, 2295–2300. doi: 10.1093/nar/gkn072
- Pereira, I. A. C., Ramos, A. R., Grein, F., Marques, M. C., Silva, S. M., and Venceslau, S. S. (2011). A comparative genomic analysis of energy metabolism in sulfate reducing bacteria and archaea. *Front. Microbiol.* 2:69. doi: 10.3389/fmicb.2011.00069
- Pettersen, E. F., Goddard, T. D., Huang, C. C., Couch, G. S., Greenblatt, D. M., Meng, E. C., et al. (2004). UCSF Chimera—a visualization system for exploratory research and analysis. *J. Comput. Chem.* 25, 1605–1612. doi: 10.1002/jcc.20084
- Pires, R. H., Venceslau, S. S., Morais, F., Teixeira, M., Xavier, A. V., and Pereira, I. A. C. (2006). Characterization of the *Desulfovibrio desulfuricans* ATCC 27774 DsrMKJOP complex - a membrane-bound redox complex involved in the sulfate respiratory pathway. *Biochemistry* 45, 249–262. doi: 10.1021/bi0515265
- Refojo, P. N., Sena, F. V., Calisto, F., Sousa, F. M., and Pereira, M. M. (2019). The plethora of membrane respiratory chains in the phyla of life. *Adv. Microb. Physiol.* 74, 331–414. doi: 10.1016/bs.ampbs.2019.03.002
- Refojo, P. N., Sousa, F. L., Teixeira, M., and Pereira, M. M. (2010). The alternative complex III: a different architecture using known building modules. *Biochim. Biophys. Acta Bioenerg.* 1797, 1869–1876. doi: 10.1016/j.bbabi.2010.04.012
- Rothery, R. A., and Weiner, J. H. (1993). Topological characterization of *Escherichia coli* DMSO reductase by Electron paramagnetic resonance spectroscopy of an engineered [3Fe-4S] cluster. *Biochemistry* 32, 5855–5861. doi: 10.1021/bi00073a019
- Rothery, R. A., and Weiner, J. H. (1996). Interaction of an engineered [3Fe-4S] cluster with a menaquinol binding site of *Escherichia coli* DMSO reductase. *Biochemistry* 35, 3247–3257. doi: 10.1021/bi951584y
- Rothery, R. A., Workun, G. J., and Weiner, J. H. (2008). The prokaryotic complex iron-sulfur molybdoenzyme family. *Biochim. Biophys. Acta Biomembr.* 1778, 1897–1929. doi: 10.1016/j.bbamem.2007.09.002
- Saraiva, L. M., da Costa, P. N., Conte, C., Xavier, A. V., and LeGall, J. (2001). In the facultative sulphate/nitrate reducer *Desulfovibrio desulfuricans* ATCC 27774, the nine-haem cytochrome c is part of a membrane-bound redox complex mainly expressed in sulphate-grown cells. *Biochim. Biophys. Acta* 1520, 63–70. doi: 10.1016/S0167-4781(01)00250-0

- Sargent, F. (2016). The model [NiFe]-hydrogenases of *Escherichia coli*. *Adv. Microb. Physiol.* 68, 433–507. doi: 10.1016/bs.ampbs.2016.02.008
- Shi, Y., Xin, Y., Wang, C., Blankenship, R. E., Sun, F., and Xu, X. (2020). Cryo-EM structures of the air-oxidized and dithionite-reduced photosynthetic alternative complex III from *Roseiflexus castenholzii*. *Sci. Adv.* 6:eaba2739. doi: 10.1126/sciadv.aba2739
- Shirodkar, S., Reed, S., Romine, M., and Saffarini, D. (2011). The octahaem SirA catalyses dissimilatory sulfite reduction in *Shewanella oneidensis* MR-1. *Environ. Microbiol.* 13, 108–115. doi: 10.1111/j.1462-2920.2010.02313.x
- Simon, J. (2002). Enzymology and bioenergetics of respiratory nitrite ammonification. *FEMS Microbiol. Rev.* 26, 285–309. doi: 10.1111/j.1574-6976.2002.tb00616.x
- Sousa, J. S., Calisto, F., Langer, J. D., Mills, D. J., Refojo, P. N., Teixeira, M., et al. (2018). Structural basis for energy transduction by respiratory alternative complex III. *Nat. Commun.* 9:1728. doi: 10.1038/s41467-018-04141-8
- Steinmetz, P. A., Degreif-Dünnwald, P., and Unden, G. (2014). The aerobic and anaerobic respiratory chain of *Escherichia coli* and *Salmonella enterica*: enzymes and energetics. *EcoSal Plus* 6. doi: 10.1128/ecosalplus.ESP-0005-2013
- Stolz, J. F., Basu, P., Santini, J. M., and Oremland, R. S. (2006). Arsenic and selenium in microbial metabolism. *Annu. Rev. Microbiol.* 60, 107–130. doi: 10.1146/annurev.micro.60.080805.142053
- Sun, C., Benlekber, S., Venkatakrishnan, P., Wang, Y., Hong, S., Hosler, J., et al. (2018). Structure of the alternative complex III in a supercomplex with cytochrome oxidase. *Nature* 557, 123–126. doi: 10.1038/s41586-018-0061-y
- Tang, H., Rothery, R. A., and Weiner, J. H. (2013). A variant conferring cofactor-dependent assembly of *Escherichia coli* dimethylsulfoxide reductase. *Biochim. Biophys. Acta Bioenerg.* 1827, 730–737. doi: 10.1016/j.bbabi.2013.02.009
- Venceslau, S. S., Matos, D., and Pereira, I. A. C. (2011). EPR characterization of the new Qrc complex from sulfate reducing bacteria and its ability to form a supercomplex with hydrogenase and TplC3. *FEBS Lett.* 585, 2177–2181. doi: 10.1016/j.febslet.2011.05.054
- Venceslau, S. S., Stockdreher, Y., Dahl, C., and Pereira, I. A. C. (2014). The “bacterial heterodisulfide” DsrC is a key protein in dissimilatory sulfur metabolism. *Biochim. Biophys. Acta Bioenerg.* 1837, 1148–1164. doi: 10.1016/j.bbabi.2014.03.007
- Waterhouse, A. M., Procter, J. B., Martin, D. M. A., Clamp, M., and Barton, G. J. (2009). Jalview version 2-a multiple sequence alignment editor and analysis workbench. *Bioinformatics.* 25, 1189–1191. doi: 10.1093/bioinformatics/btp033
- Weiner, J. H., Shaw, G., Turner, R. J., and Trieber, C. A. (1993). The topology of the anchor subunit of dimethyl sulfoxide reductase of *Escherichia coli*. *J. Biol. Chem.* 268, 3238–3244. doi: 10.1016/S0021-9258(18)53684-X
- Zhang, J., Oettmeier, W., Gennis, R. B., and Hellwig, P. (2002). FTIR spectroscopic evidence for the involvement of an acidic residue in quinone binding in cytochrome bd from *Escherichia coli*. *Biochemistry* 41, 4612–4617. doi: 10.1021/bi011784b
- Zhao, Z., and Weiner, J. H. (1998). Interaction of 2-n-heptyl-4-hydroxyquinoline-N-oxide with dimethyl sulfoxide reductase of *Escherichia coli*. *J. Biol. Chem.* 273, 20758–20763. doi: 10.1074/jbc.273.33.20758
- Conflict of Interest:** The authors declare that the research was conducted in the absence of any commercial or financial relationships that could be construed as a potential conflict of interest.
- Copyright © 2021 Calisto and Pereira. This is an open-access article distributed under the terms of the Creative Commons Attribution License (CC BY). The use, distribution or reproduction in other forums is permitted, provided the original author(s) and the copyright owner(s) are credited and that the original publication in this journal is cited, in accordance with accepted academic practice. No use, distribution or reproduction is permitted which does not comply with these terms.



The Redox-Active Tyrosine Is Essential for Proton Pumping in Cytochrome c Oxidase

Margareta R. A. Blomberg*

Arrhenius Laboratory, Department of Organic Chemistry, Stockholm University, Stockholm, Sweden

OPEN ACCESS

Edited by:

Vivek Sharma,
University of Helsinki, Finland

Reviewed by:

Louis Noodleman,
The Scripps Research Institute,
United States

Alexei Stuchebrukhov,
University of California, Davis,
United States

*Correspondence:

Margareta R. A. Blomberg
margareta.blomberg@su.se

Specialty section:

This article was submitted to
Theoretical and
Computational Chemistry,
a section of the journal
Frontiers in Chemistry

Received: 10 December 2020

Accepted: 05 February 2021

Published: 14 April 2021

Citation:

Blomberg MRA (2021) The Redox-Active Tyrosine Is Essential for Proton Pumping in Cytochrome c Oxidase. *Front. Chem.* 9:640155. doi: 10.3389/fchem.2021.640155

Cellular respiration involves electron transport via a number of enzyme complexes to the terminal Cytochrome c oxidase (CcO), in which molecular oxygen is reduced to water. The free energy released in the reduction process is used to establish a transmembrane electrochemical gradient, via two processes, both corresponding to charge transport across the membrane in which the enzymes are embedded. First, the reduction chemistry occurring in the active site of CcO is electrogenic, which means that the electrons and protons are delivered from opposite sides of the membrane. Second, the exergonic chemistry is coupled to translocation of protons across the entire membrane, referred to as proton pumping. In the largest subfamily of the CcO enzymes, the A-family, one proton is pumped for every electron needed for the chemistry, making the energy conservation particularly efficient. In the present study, hybrid density functional calculations are performed on a model of the A-family CcOs. The calculations show that the redox-active tyrosine, conserved in all types of CcOs, plays an essential role for the energy conservation. Based on the calculations a reaction mechanism is suggested involving a tyrosyl radical (possibly mixed with tyrosinate character) in all reduction steps. The result is that the free energy released in each reduction step is large enough to allow proton pumping in all reduction steps without prohibitively high barriers when the gradient is present. Furthermore, the unprotonated tyrosine provides a mechanism for coupling the uptake of two protons per electron in every reduction step, i.e. for a secure proton pumping.

Keywords: cytochrome c oxidase, energy conservation, proton pumping, redox-active tyrosine, midpoint potentials, density functional theory

INTRODUCTION

Cytochrome c oxidase (CcO), the terminal enzyme in the respiratory chain, reduces molecular oxygen to water in an exergonic process. A significant part of the released free energy is converted into an electrochemical gradient across the membrane in which the enzyme is embedded. The gradient is used by another enzyme in the same membrane to transform ADP to ATP, which provides energy for many processes in the living cell. As shown in **Figure 1** the electrons needed for the oxygen reduction chemistry are delivered from soluble cytochrome c located on the P-side of the membrane, while the protons are delivered from the opposite side, the N-side. This means that the chemical reaction corresponds to charge motion across the membrane (electrogenic chemistry), which contributes to the creation of the electrochemical gradient. In 1977 Wikström discovered that the oxygen reduction is coupled to translocation of protons across the entire membrane, referred to

as proton pumping, which also contribute to the electrochemical gradient, and thereby increases the efficiency of the energy conservation (Wikström, 1977). The largest subgroup of CcOs, the A-family, which can be found in both mitochondria and bacteria, is known to pump four protons per oxygen molecule, i.e., one pumped proton per electron. The stoichiometry of the proton pumping is most likely lower in the other CcO families, the B- and the C-families (Han, et al., 2011; Von Ballmoos, et al., 2012). The proton pumping in the A family is the focus of the present study.

The active site in the A-family CcOs, the binuclear center (BNC), consists of a high-spin heme group of *a*-type, labeled heme *a*₃, a copper complex, labeled Cu_B and a redox-active tyrosine cross-linked to one of the histidine ligands on Cu_B. The electrons are delivered from soluble cytochrome *c* on the P-side of the membrane to the BNC via two electron transfer cofactors, a copper complex, Cu_A and a low-spin heme *a*. In the A-family CcOs two proton channels originating on the N-side of the membrane have been characterized, the D-channel leading to the center of the BNC, and the K-channel leading to the redox-active tyrosine, see **Figure 1**. The basic features of the reduction process are well known: Molecular oxygen binds to the reduced state of the BNC, the **R** state, with Fe_{a3}(II)-Cu_B(I)-TyrOH. The O-O bond is cleaved in the first step, yielding the **P_M** state, with Fe_{a3}(IV)=O-Cu_B(II)OH-TyrO[•]. The rest of the catalytic cycle consists of four proton coupled reduction steps leading back to the **R** state plus two new water molecules. Two or three protons for the chemistry are delivered via the D-channel, and the rest (one or two) via the K-channel. All protons to be pumped use the D-channel. It is now generally agreed that each reduction step in the A-family is coupled to proton pumping, also at a high gradient (Bloch et al., 2004; Ferguson, 2010; Kaila et al., 2010; Wikström and Hummer, 2012; Wikström et al., 2018). Although considerable knowledge about the proton pumping has been achieved (Brzezinski and Gennis, 2008; Popovic et al., 2010; Han et al., 2011; Blomberg and Siegbahn, 2015a; Rich, 2017; Wikström et al., 2018), the mechanistic details are still not agreed on. One of the remaining issues concerns the thermodynamics of the individual reduction steps. The exergonicity of a reduction step is determined by the proton coupled reduction potential (midpoint potential) of the active site cofactor that is reduced in the particular step. Experimental results indicate that two of the four BNC reduction potentials (Cu_B(II) and Fe_{a3}(III)) are too low to afford proton pumping (Wikström and Morgan, 1992; Kaila et al., 2010). A second remaining issue concerns how to achieve a secure coupling between the transfer of *one* electron to the BNC active site and the uptake of *two* protons, one for the chemistry and one to be pumped. An important element of such a coupling is the suggested proton loading site (PLS), a position in the vicinity of the BNC where the protons to be pumped are temporarily stored (Morgan et al., 1994; Rich et al., 1996). A third remaining issue concerns the gating of the protons, i.e. how to force the protons to move against the gradient and to avoid that they move back to the N-side, which is thermodynamically favorable as soon as there is a gradient across the membrane.

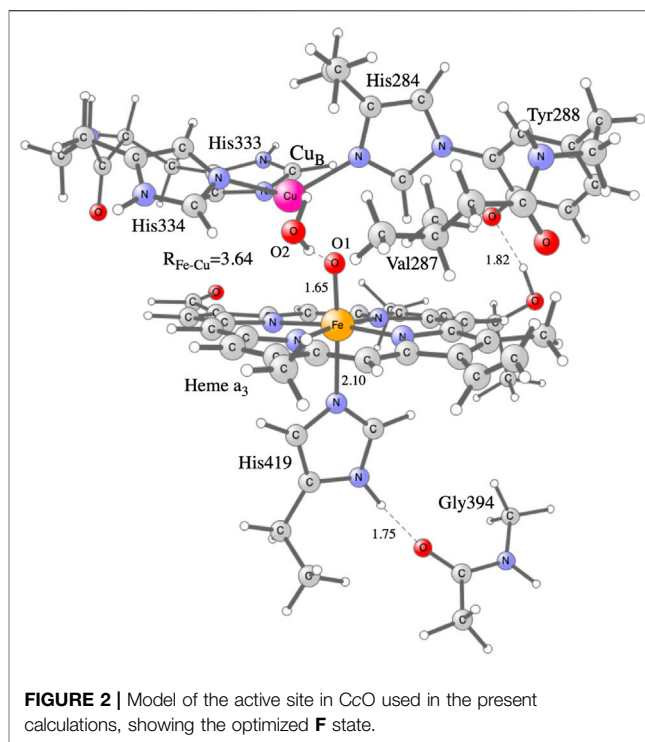
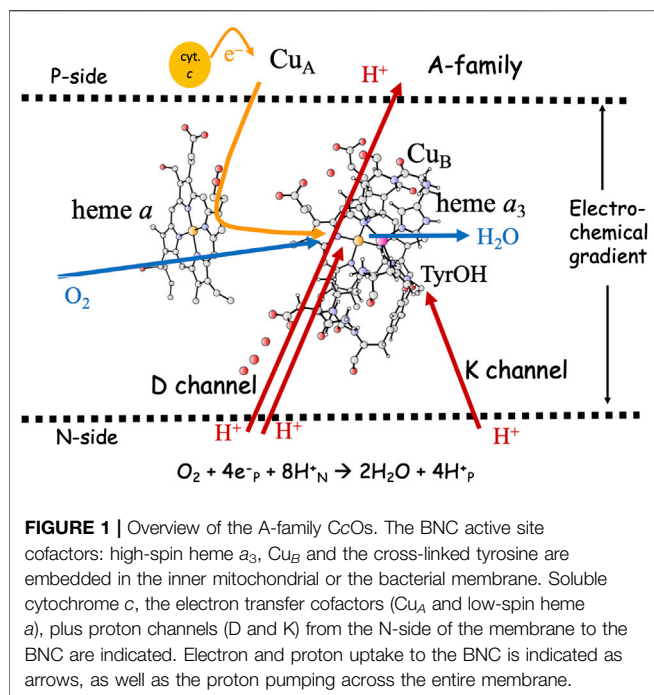
The focus of the present study is on the first two issues described in the preceding paragraph, the energetics of the

individual reduction steps and the coupling of electron and proton uptake. Quantum chemical calculations, using hybrid density functional theory (DFT), have been performed on a model of the BNC active site. To describe the overall energetics of each reduction step, both an electron and a proton are added to each main intermediate of the catalytic cycle. To describe the coupling of electron and proton uptake, the electron affinity of each main intermediate is calculated by adding only an electron. Clearly there are interesting details of the reduction processes which are not possible to describe with the present approach, but those are out of the scope of the present investigation. The results obtained with the present model support previous computational results showing that at least three of the BNC cofactors have high enough proton coupled reduction potentials for proton pumping (Blomberg, 2019). A mechanism is suggested, which allows proton pumping in all four reduction steps, and in which the redox-active tyrosine plays a special role (Blomberg, 2016). The computational results are also used to shed further light on a previously suggested mechanism for the coupling between electron and proton uptake, in which the conserved redox-active tyrosine plays an essential role (Blomberg, 2016; Blomberg, 2020a). The gating problem is shortly discussed.

COMPUTATIONAL DETAILS

Hybrid density functional theory (DFT) is an important tool in the studies of enzymatic reaction mechanisms, in particular employing the cluster approach, as described in recent reviews (Blomberg et al., 2014; Blomberg, 2020a). The cluster model of the active site in CcO used in the present study is the same as was used in a recent study on NO reduction in different CcOs (Blomberg, 2020b), see **Figure 2**. It is constructed on the basis of a crystal structure of the *Rhodobacter sphaeroides* aa₃ CcO (Qin et al., 2006). The model has about 170 atoms (depending on the state) and the total charge is +1 for the main intermediates in the catalytic cycle. To obtain the energetics of the catalytic cycle, plausible intermediate structures are optimized and their relative energies calculated. For the energetics of the proton coupled reduction steps the energy cost of an electron from soluble cytochrome *c* and a proton from bulk water is needed. Rather than using calculated values, the total energy of one electron and one proton is given a value that reproduces the overall energy of the reduction process, 2.2 eV, as obtained from experimental reduction potentials of the cytochrome *c* electron donor and the reduction of oxygen to water. This procedure has been described in more detail in several previous papers (Blomberg, 2016; Blomberg, 2019). To obtain the electron affinities, only an electron is added to the different intermediates. The calculated electron affinities are only compared to each other, therefore no explicit energy cost for just an electron is needed in the present context.

The B3LYP*-type of functionals are frequently used to describe metalloenzymes, and are found to generally give reliable results (Blomberg et al., 2014; Siegbahn and Blomberg, 2014). The dispersion corrected hybrid density functional



B3LYP-D3 (Becke, 1993; Grimme et al., 2010) was used here, together with a double zeta basis with polarization functions on all second row atoms, to optimize the geometries for the different intermediates. To obtain more accurate single point energies for the optimized structures, the B3LYP*-D3 functional (with 15% exact exchange) (Reiher et al., 2001), the lacv3p+ basis for the metal ions (Jaguar, 2018) and the large cc-pvtz (-f) basis set for the rest of the atoms were used. Polarization effects on the relative energies from the omitted protein that surrounds the cluster model were estimated using a self-consistent reaction field approach with a dielectric constant of 4.0 (Blomberg et al., 1998). For relative energies between intermediates with the same charge, small dielectric effects were obtained. Zero-point corrections for all structures were taken from the Hessians, calculated at the same level as the geometry optimizations, applying the harmonic approximation. The Gaussian 09 package (Gaussian, 2010) was used for geometry optimizations and Hessian calculations. The Jaguar (Jaguar, 2018) program was used for the polarization calculations and for the larger basis set. During the geometry optimizations the coordinates of a few atoms are fixed to the crystal structure, to maintain the steric effects of the surrounding protein, which means that accurate entropy effects cannot be obtained from the Hessians. The frozen atoms are the alpha carbons on each residue together with the two hydrogen atoms replacing the peptide links. An exception is the proximal His419 which has no frozen atoms, since it is kept in place by hydrogen bonding to the Gly394. Entropy effects were added to the relative energies only for the gaseous O_2 molecule, assuming that the entropy lost on binding is equal to the translational entropy for the free molecule (10.8 kcal/mol at room temperature). This approximation is supported by previous calculations where more explicit estimates of the entropy effects could be made

(Blomberg et al., 2004). For the binding enthalpy of a water molecule to bulk water an empirical value of 12 kcal/mol is used, which includes explicit zero point effects, and which is based on experimental thermodynamics and previous experience (Blomberg and Siegbahn, 2015a; Siegbahn, 2018). The reported energetic results are considered as free energies.

The use of the B3LYP* hybrid functional for the main results reported is based on previous experience showing that 15–20% exact exchange gives the best agreement with experiments for the calculated reduction potentials in CcO (Siegbahn and Blomberg, 2018), together with a recent study of the accuracy in calculated energy profiles for NO reduction in heme-copper oxidases showing that 15% exact exchange gives slightly better agreement with experiments (Blomberg, 2021). However, although it was showed that the reduction potentials in the heme-copper oxidases varies rather little with the fraction of exact exchange in the hybrid functional, it has been found in several studies on both CcO and cNOR that too small reduction potentials are obtained for the ferric heme (Blomberg, 2016; Blomberg and Siegbahn, 2016). Therefore a correction of 9 kcal/mol is used for the Fe(III)OH to Fe(II)OH_2 reduction step, which gives good agreement with experiments for both CcO and cNOR for the B3LYP* functional (Blomberg, 2019; Blomberg, 2020b). Clearly a corresponding (but opposite) correction has to be applied also on oxidation of the ferrous heme iron, i.e., when the oxygen molecule binds forming a ferric superoxide complex. Since it is expected that the main DFT-problem is concerned with the electronic part of the proton coupled reduction potential, the full correction of 9 kcal/mol is used for the calculated electron affinities of the **A** and **E** intermediates, which involve reduction from Fe(III) to Fe(II) . It is important to note that the best computational procedure that is

TABLE 1 | Driving forces, ΔG (eV), for the individual reduction steps in the catalytic cycle, as obtained from experiments (Kaila et al., 2010) and from the present calculations. Note that the first column shows only the cofactor reduced in each particular step, not the full BNC. Rate-limiting barriers, ΔG^\ddagger (eV), estimated from experimental information are also given for each step. The effects on the driving forces and the barrier heights of the presence of the electrochemical gradient across the membrane are also given.

Reduction process	No gradient			With gradient: 0.2 V Four protons pumped	
	ΔG (eV) exp	ΔG (eV) Calc	ΔG^\ddagger (eV) est	ΔG (eV) calc>	ΔG^\ddagger (eV) est
$P_M \rightarrow F$:					
TyrO $^\bullet \rightarrow$ TyrOH	-0.52	-0.55	+0.58	-0.15	+0.65
$F \rightarrow O_H$:					
Fe _{a3} (IV)=O \rightarrow Fe(III)OH	0.46	-0.43	+0.58	-0.03	+0.65
$O_H \rightarrow E$:					
Cu _B (II)OH \rightarrow Cu _B (I)OH ₂	-0.10	-0.80	+0.58	-0.40	+0.65
$E \rightarrow R$:					
Fe _{a3} (III)OH \rightarrow Fe _{a3} (II)OH ₂	-0.10	-0.10	+0.58	+0.30	+0.65
$R \rightarrow A$:					
O ₂ binding	-0.02 ^a	-0.02	+0.45	-0.02	+0.75
$A \rightarrow P_M$:					
O-O cleavage	-0.30 ^a	-0.30	+0.55	-0.30	+0.83
Sum	-1.50	-2.2		-0.60	

^aThe energetics of these reaction steps are taken from the calculations.

possible to use for the present type of systems, inevitably will have uncertainties of a few kcal/mol in the calculated relative energies, and therefore strong conclusions should not be drawn based on small energy differences.

RESULTS AND DISCUSSION

Energetics of the Individual Reduction Steps

The driving force of each reduction step in the catalytic cycle of O₂ reduction in CcO is determined by the difference in reduction potential between the BNC cofactor reduced in the particular step, and the ultimate electron donor, cytochrome *c*. It can be noted that the immediate electron donor to the BNC, low-spin heme *a*, has a reduction potential quite similar to cytochrome *c*, which means that the details in the energetics of the electron transfer process between the cofactors can be neglected when the overall energetics of the reduction processes is discussed. In **Table 1** the energetics of the reduction steps is summarized. The driving force of each reduction step, ΔG (eV), is obtained both from experimental information about the individual reduction potentials (Kaila et al., 2010), and from the presently calculated proton coupled reduction potentials. The table also includes estimated barriers, ΔG^\ddagger (eV), for each reduction step, and the effects on the energetics from the presence of the electrochemical gradient across the membrane. To complete the catalytic cycle also the energetics of the binding of molecular oxygen and the O-O bond cleavage are included in the table.

In **Table 1** the starting point for the reduction process is the P_M state, with Fe_{a3}(IV)=O-Cu_B(II)OH-TyrO $^\bullet$ obtained after the O-O bond cleavage. The first column in **Table 1** describes which cofactor is reduced in each step, and the order of the cofactor reductions follows the experimental assignments (Kaila et al., 2010). The second column in **Table 1** shows the exergonicity of

each reduction step obtained from the experimental reduction potentials (Kaila et al., 2010). The uneven distribution of the free energies over the reduction steps was noted at an early stage (Wikström and Morgan, 1992), and it was realized that the low driving force of two of the reduction steps was not compatible with the experimental observations that proton pumping occurs in all four reduction steps in the A family CcOs (Verkhovsky et al., 1999; Bloch et al., 2004). It was also pointed out that the sum of the driving forces based on the experimental reduction potentials would be significantly smaller than the overall exergonicity of the reduction process of 2.2 V, with more than half a volt missing (Kaila et al., 2010), see **Table 1**. The calculated proton coupled reduction potentials give a different picture, with the corresponding exergonicities shown as the third column in **Table 1**. The main difference is that the Cu_B(II) potential is significantly higher than the experimental value, resulting in a reasonable energy profile for the entire catalytic cycle with three significantly exergonic reduction steps (>0.4 eV) (Blomberg, 2016; Blomberg, 2019). The calculated Cu_B(II) potential is supported by more reliable CCSD(T) calculations on a smaller model of the copper-complex (Blomberg and Siegbahn, 2015a). The calculations show that the Cu_B(II) potential itself is high during catalytic turnover, with no need for involvement of any structurally excited state (Blomberg, 2020c). There is, however, still one reduction step with a very low exergonicity, Fe_{a3}(III)OH \rightarrow Fe_{a3}(II)OH₂ (0.1 eV). The fourth column in **Table 1** contains estimated barrier heights for the individual reaction steps, and since without gradient, all reaction steps are exergonic, the total barrier for each step is the same as the local barrier. The proton coupled reduction steps are rate limited by proton transfer (including the pump-protons), which based on experimental data, is estimated to occur on the millisecond time-scale. Using transition state theory, this corresponds to a barrier of about 0.58 eV (13.3 kcal/mol). From experiments the

TABLE 2 | Driving forces, ΔG (eV), for the individual reduction steps in the catalytic cycle, as obtained from the present calculations, assuming that the tyrosine is left unprotonated until the last reduction step. Note that the first column shows only the cofactor reduced in each particular step, not the full BNC. Rate-limiting barriers, $\Delta G^\#$ (eV), estimated from experimental information are also given for each step. The effects on the driving forces and the barrier heights of the presence of the electrochemical gradient across the membrane are also given.

Reduction process	No gradient		With gradient: 0.2 V Four protons pumped	
	ΔG (eV) calc	$\Delta G^\#$ (eV) est	ΔG (eV) calc	$\Delta G^\#$ (eV) est
P_M → F: Cu _B (II)OH → Cu _B (I)OH ₂	−0.80	+0.58	−0.40	+0.65
F → O_H: Fe _{a3} (IV)=O → Fe _{a3} (III)OH	−0.43	+0.58	−0.03	+0.65
O_H → E_H: Fe _{a3} (III)OHTyrO [•] → Fe _{a3} (II/III)OH ₂ TyrO ^{•/−}	−0.40	+0.58	−0.00	+0.65
E_H → R: Fe _{a3} (II/III)OH ₂ TyrO ^{•/−} → Fe _{a3} (II)OH ₂ TyrOH	−0.25	+0.58	+0.15	+0.65
R → A: O ₂ binding	−0.02	+0.45	−0.02	+0.60
A → P_M: O-O cleavage	−0.30	+0.55	−0.30	+0.68
Sum	−2.2		−0.60	

O₂ binding is known to occur in about 10 μs, corresponding to a barrier of about 0.45 eV (10.6 kcal/mol), and the O-O bond cleavage occurs in about 300 μs, corresponding to a barrier of about 0.55 eV (12.6 kcal/mol).

The main problem with a low exergonicity for a reaction step occurs when the electrochemical gradient is present across the membrane. Both the electrogenic chemistry and the proton pumping correspond to charge motion against the gradient across the entire membrane, which means that the exergonicity decreases in reaction steps involving these processes. The maximum electrochemical gradient is some 0.20–0.22 V (Wikström et al., 2018), and in the fifth column in **Table 1** the calculated driving forces of the reduction steps are given for the case of a gradient of 0.2 V. Each charge moved across the membrane decreases the exergonicity by 0.2 eV, and assuming that proton pumping occurs in all steps means that the exergonicity of all steps are decreased by 0.4 eV. The low reduction potential of the Fe_{a3}(III)OH cofactor, results in an endergonic E to R step (+0.30 eV) when a high gradient is present. Since the reduction steps are rate-limited by proton transfer against the gradient, the barriers are expected to increase, a slightly higher value of 0.65 eV (15 kcal/mol) is chosen here. The local barriers for O₂ binding and O-O bond cleavage are not expected to be affected by the gradient across the membrane. However, with an endergonic reaction step present, the total barriers increase for the succeeding reaction steps, since the total barrier has to be calculated relative to the preceding point with the lowest energy, i.e., the E state in this case. Therefore, the barriers for O₂ binding and O-O bond cleavage has to be calculated relative to the E state, and become 0.75 (0.30 + 0.45) and 0.83 (0.30−0.02 + 0.55) eV, respectively, when the gradient is present (see column six in **Table 1**). A barrier of 0.83 V (about 19 kcal/mol) corresponds to a very slow reaction, with only a few molecules reduced per minute, which is much slower than observed rates of at least a few hundreds per second in the working oxidase enzyme.

To avoid the strongly endergonic reaction step when the gradient is present over the membrane, and thereby the too high barriers, it was at an early stage suggested that the tyrosine should stay unprotonated until the R state is formed, a type of mechanism which has later been further clarified (Blomberg and Siegbahn, 2006; Blomberg, 2016). **Table 2** shows the energetics for such a mechanism, where the assignments of the reduction steps are based on the calculated reduction potentials. In this mechanism the E state, Cu_B(I)OH₂-Fe_{a3}(III)OH-TyrOH, is replaced by the E_H state, Cu_B(I)OH₂-Fe_{a3}(II/III)OH₂-TyrO^{•/−}, i.e., the proton was transferred to the center of the BNC rather than to the tyrosine when the O_H state was reduced. The result is that the reduction of Fe_{a3}(III) with a low potential is mixed with the reduction of TyrO[•] with a high potential, such that both the reduction steps between state O_H and state R have a reasonably large exergonicity, see the second column in **Table 2**. With this mechanism the E_H to R step is estimated to be only slightly endergonic, +0.15 eV, when the full gradient is present, see the fourth column in **Table 2**. The lower endergonicity of the E_H to R step decreases succeeding barriers as compared to the situation in **Table 1**. Thus, with this mechanism there is no barrier higher than 0.68 eV when a high gradient is present, see the fifth column in **Table 2**, and the oxygen reduction reaction can proceed with a reasonable rate also with a high gradient. It is noted that this mechanism requires that the E state, which has a lower energy than the E_H state, is avoided, i.e., that protonation of the tyrosine is avoided when the O_H state is reduced. In the A-family this is possible due to the presence of the D-channel for proton uptake (see **Figure 1**), but it also requires a high barrier for proton transfer within the BNC, from the center of the BNC where the D-channel ends, to the tyrosine (where the K-channel ends) (Blomberg and Siegbahn, 2015a; Blomberg, 2016). Experimental information supports the presence of such a barrier for proton transfer within the BNC (Vilhjálmsdóttir et al., 2020). The suggested mechanism implies that only one proton is taken up via the K-channel, in

the E_H to R step, which is in accordance with the experimental observation that the first reduction of the oxidized state actually does occur in mutants missing the essential lysine in the K-channel (Ganesan and Gennis, 2010). Furthermore, for the B- and the C-family CcOs, which have only one proton channel to the BNC, analogous to the K-channel in the A-family, i.e. ending at the redox-active tyrosine, it is not possible to avoid formation of the E state. This should be at least part of the explanation for a lower proton pumping stoichiometry in the B- and the C-families.

An alternative solution to the problem with too high barriers, could be that the stoichiometry of the proton pumping decreases when the gradient becomes high. Thus, if the E to R step in the mechanism shown in **Table 1**, at high gradient involved only electrogenic chemistry and no proton pumping, this step would be endergonic by only 0.10 eV, which would decrease the succeeding barriers by 0.2 eV compared to the values given in **Table 1**. Thus, if there exists such mechanism, removing the proton pumping in the E to R step at high gradient, the reaction could proceed with a reasonable rate also following the mechanism described in **Table 1**. It has also been suggested that only one proton is pumped during the O to R steps, and accordingly three protons pumped during the P to O steps. A detailed scheme for such a proton pumping scenario was constructed based on electrostatic repulsion and the electroneutrality principle (Michel, 1998; Michel, 1999). Another carefully constructed proton pumping scheme implying that only one proton is pumped during the O to R steps was based on electrostatic calculations (Popovic and Stuchebrukhov, 2004). However, as described in the following section, there are mechanistic aspects on the proton pumping that support the type of mechanism described in **Table 2**.

In summary, a reaction mechanism is suggested for O_2 reduction in the A-family CcOs (**Table 2**), in which all reduction steps are exergonic enough to allow proton pumping, also with a high gradient, and without making the overall reaction too slow.

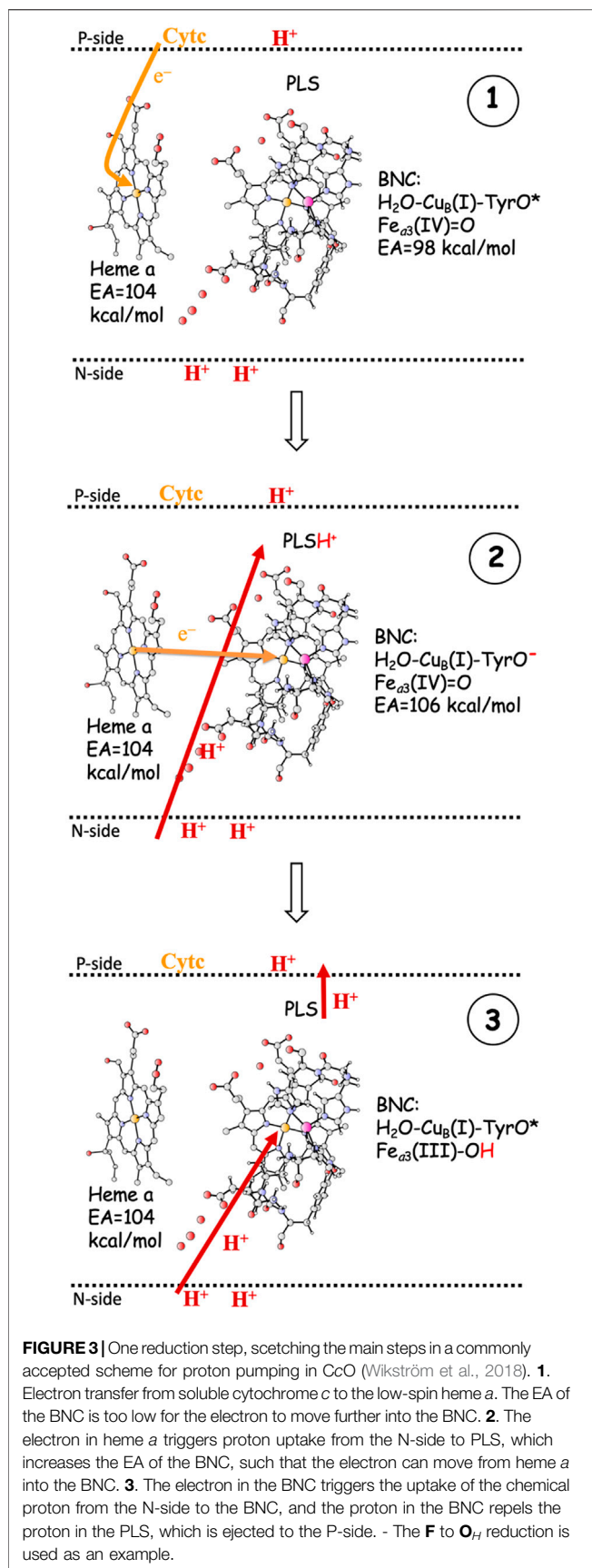
Coupling of Electron and Proton Transfer

As indicated in the introduction, the mechanisms for proton pumping in CcO are not yet fully understood. Many different mechanistic suggestions have been put forward, which are carefully described in a recent review by Wikström and coworkers (Wikström et al., 2018). The basic features of the most commonly accepted view of the proton pumping procedure are summarized in **Figure 3**, which describes one reduction step in terms of individual electron and proton transfer events (Wikström et al., 2003; Quenneville et al., 2006; Wikström et al., 2018; Blomberg, 2020a). A reduction step is initiated by electron transfer from soluble cytochrome c to the low-spin heme a , the immediate donor to the BNC, see panel 1 in **Figure 3**. At this point the electron affinity in the BNC is not large enough to make the electron move further, and the so called proton loading site (PLS) plays an important role (Morgan et al., 1994; Rich et al., 1996). The PLS is a site, not yet exactly known (Sugitani et al., 2008; Wikström et al., 2018), in the vicinity of both the BNC and the low-spin heme. The electron in the low-spin heme increases the proton affinity of the PLS, which triggers the uptake of a proton from the N-side. At

the same time, a proton in the PLS will increase the electron affinity of the BNC, which triggers the electron transfer from the low-spin heme to the BNC. It is not clear if this is a two-step procedure or a concerted one, but the result is a proton in the PLS and the electron in the BNC, see panel 2 in **Figure 3**. The electron in the BNC increases the proton affinity in the BNC, which triggers the uptake of the chemical proton. The proton in the BNC neutralizes the negative charge in the active site and the proton in the PLS is destabilized and expelled to the P-side of the membrane (Michel, 1998; Michel, 1999), see panel 3 in **Figure 3**.

The most crucial step in the pumping mechanism described in **Figure 3** is the one that leads from panel 1 to panel 2, i.e., the initial uptake of the proton to be pumped, and the most crucial property of the active site is the electron affinity (EA) of the BNC, which must be balanced so that the uptake of the pump-proton both is necessary and has a sufficient effect. Initially the EA of the BNC must be lower than the EA of the low-spin heme a , otherwise the proton in the PLS would not be needed for the electron transfer to the BNC to occur, and there would be no reliable proton pumping. However, the EA difference between the low-spin heme a and the BNC must not be too large, because then the effect of the proton in the PLS would not be sufficient to make the electron transfer to the BNC exergonic, which is essential for the state in panel 2 to be stable enough to be inevitably involved in the reduction process. Although the exact position of the PLS is not known, it is generally thought to be somewhere in the vicinity of the A-propionate of the high-spin heme a_3 (Sugitani et al., 2008; Blomberg and Siegbahn, 2012; Wikström et al., 2018). This means that the distance between the proton in the PLS and the BNC cofactor accepting the electron ($Fe_{a_3}(III/IV)$, $Cu_B(II)$, $TyrO^\bullet$) most likely is on the order of 10–15 Å. Assuming a dielectric constant of four (Blomberg et al., 1998), the Coulomb interaction energy between the PLS and one of the electron acceptors in the BNC would be on the order of 5–8 kcal/mol. This gives a hint of how much the EA of the BNC cofactors may increase by the proton in the PLS.

As described in the previous paragraph, the affinity for electron uptake (EA) for intermediates that are possible starting structures for the reduction steps is essential for the proton pumping. Using the BNC model described in the computational section, the EA of possible structures of the intermediates during the O_2 reduction process have been calculated by adding just an electron, and the results are summarized in **Figure 4**. The A-panel in **Figure 4** shows the type of reaction mechanism described in **Table 2** above. Characteristic of this mechanism is that the tyrosine is unprotonated (radical) in all intermediates except the R state, i.e., in all intermediates from which a reduction step is initiated. It is also characteristic that in each case the electron transfer initially yields a tyrosinate. It is therefore not surprising that all these states have a rather similar calculated EA, 103.0–107.6 kcal/mol, where one of the values, 103.0, is slightly lower than the other three, due to the involvement of $Fe_{a_3}(III)$ reduction (see above). As is also shown in **Figure 4A**, when the chemical proton arrives in the BNC, the electron moves from the tyrosinate to another cofactor in the BNC (except for the E_{HR} to R step). For example, in the F_R state, the new electron is on the tyrosine and the high-



spin heme is still in the $\text{Fe}_{a3}(\text{IV})$ state, but when the proton has reached the BNC, forming the O_H state, the high-spin heme turns into $\text{Fe}_{a3}(\text{III})$. This scheme for reduction of the **F** state agrees with experimental observations (Björck and Brzezinski, 2018).

In the B-panel of **Figure 4** alternative structures are shown for intermediates that could be the starting point for each of the four reduction steps. Characteristic for these states is that they all have the tyrosine protonated, and also that they all have significantly lower calculated EAs compared to those involved in the suggested mechanism shown in the A-panel in the same figure, 80.6–90.3 kcal/mol, as compared to 103.0–107.6 kcal/mol. The difference in EA at each reduction level ranges between about 15 and 25 kcal/mol. These two sets of calculated EAs cannot be considered as absolute values, but they are comparable to each other, since they are obtained for the same model, with the same charge, in the same environment. Preferably they should also be compared to the corresponding calculated value for the immediate electron donor, the low-spin heme *a*. Unfortunately this cannot be done in a reliable way, since both the model and the environment would be different for a calculated low-spin heme *a* EA, as compared to the BNC, which may lead to incomparable absolute values. However, there is experimental information which can be used to estimate the level of EA values needed in the BNC for the electron transfer to occur at the right stage. In a joint experimental and theoretical study of the fully reduced state of CcO, it was shown that the electron present in the low-spin heme was not transferred to the BNC in the **A** state, $\text{Fe}_{a3}(\text{III}) \text{O}_2^- \text{Cu}_B(\text{I})\text{-TyrOH}$, but only after the so called **I_P** state, $\text{Fe}_{a3}(\text{III}) \text{OOH-Cu}_B(\text{I})\text{-TyrO}^*$ with a calculated EA of 105.0 kcal/mol (using the present model) had been formed. This shows that the calculated EA of 90.3 kcal/mol for the **A** state (**Figure 4B**) is too low for electron transfer from the low-spin heme, while a value of 105 kcal/mol works. Furthermore, it is known that after O-O bond cleavage the **P_M** state is formed, and also that the succeeding reduction step is coupled to proton pumping. In addition, after the O-O bond cleavage there is only one possible type of structure, the **P_M** state shown in **Figure 4A**, which means that the calculated EA of this state indicates what is needed for a reduction mechanism that is coupled to proton pumping. Therefore, it can be concluded that only the intermediates with an unprotonated tyrosine and a high EA, similar to that of the **P_M** state, shown in **Figure 4A**, can be securely coupled to proton pumping. It should be noted here that even though all intermediates that initiate a reduction step, in **Figure 4A** are described as having a tyrosyl radical, at least in some cases there may be a partial electron transfer from e.g., $\text{Cu}_B(\text{I})$ to form a mixture with tyrosinate. This is the reason for using the notation unprotonated tyrosine rather than tyrosyl radical in the text. The point is that due to the “extra” proton in the center of the BNC, as compared to putting the proton on the tyrosine, also e.g. $\text{Cu}_B(\text{II})$ has a high EA, similar to that of the tyrosyl radical. The fact that no tyrosyl radical in the BNC has been observed experimentally may indicate that there is a larger involvement of the tyrosinate electronic structure than the present model calculations suggest. Furthermore, these intermediates with an unprotonated tyrosine are not expected to be very long-lived, compare (Blomberg, 2020c).

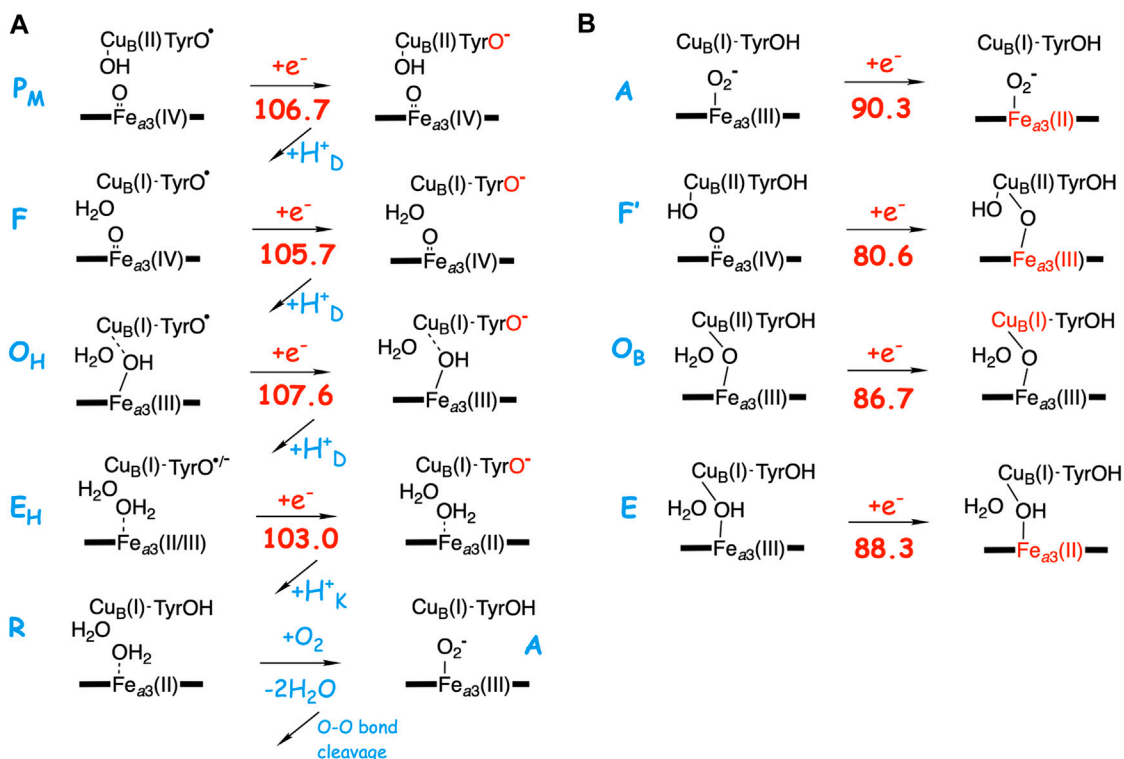


FIGURE 4 | Calculated electron affinities (EA, kcal/mol) of possible intermediates in the catalytic cycle of the A-family CcOs. **(A)** The mechanism for O₂ reduction suggested in **Table 2** with calculated EAs for the intermediates that initiate each of the reduction steps. **(B)** Calculated EAs for alternative structures for each reduction step.

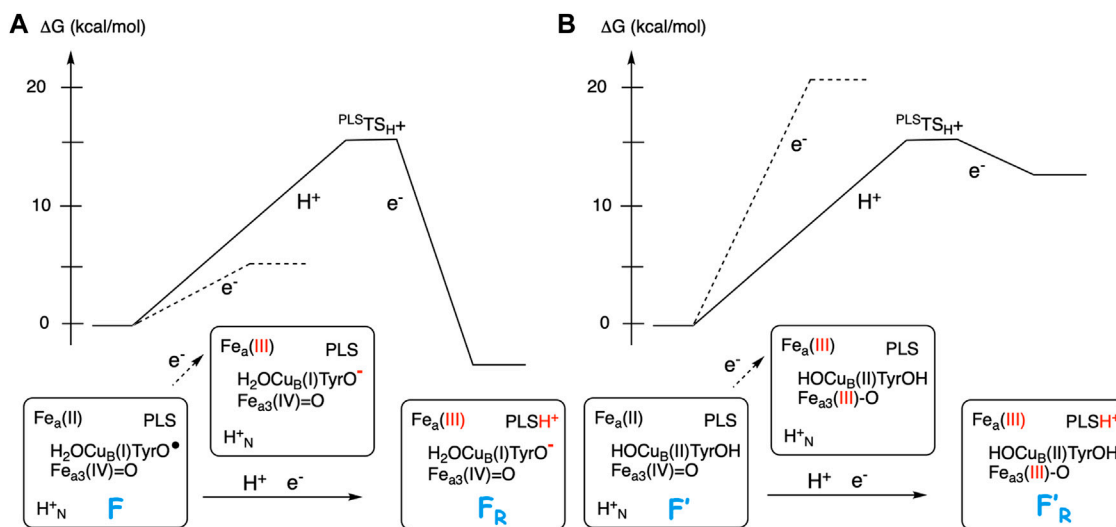


FIGURE 5 | Sketch of energy profiles for coupled electron transfer from heme *a* to the BNC and proton transfer from the N-side to PLS (full curves). The dotted lines correspond to only electron transfer from heme *a* to the BNC. **(A)** For the **F** state, with a high EA, the coupled reaction is exergonic. **(B)** For the **F'** state, with a low EA, the coupled reaction is endergonic.

Figure 5 illustrates the energetics of the coupled electron and proton transfer during the first part of a reduction step, using the **F** (A-panel) and the **F'** (B-panel) intermediates as an example. For

the **F** state a pure electron transfer from the low-spin heme *a* to the tyrosyl radical is only slightly endergonic (dotted curve in **Figure 5A**). Therefore, when the electron transfer is coupled to

proton transfer from the N-side of the membrane to the PLS, a rather small change (5–8 kcal/mol) in EA of the BNC makes the coupled process exergonic (full curve in **Figure 5A**). On the other hand, for the **F'** state with a very low initial EA, a pure electron transfer from the low-spin heme *a* to Fe_{a3}(IV) is strongly endergonic (dotted curve in **Figure 5B**). A proton in PLS increases the EA of the BNC, but in this case also the coupled reaction will be endergonic (full curve in **Figure 5B**), and both the electron and the proton will return back before the next step in the forward reaction, the transfer of the chemical proton to the BNC occurs. In that kind of situation, it is more likely that there is a coupled proton and electron transfer to the BNC, without proton pumping, a mechanism suggested for O₂ reduction in cNOR (Blomberg and Ådelroth, 2017), and also for NO reduction in CcO (Blomberg and Ådelroth, 2018). Characteristic of the two latter processes is that there is no tyrosyl radical present in any of the intermediates, in the first case because there is no tyrosine available in the active site of cNOR, and in the second case because the active site tyrosine is not involved when NO is reduced in CcO.

Finally, to check the accuracy of the calculated EA values reported in **Figure 4** the corresponding values are calculated using a fraction of 20% exact exchange in the hybrid B3LYP functional, and the results are reported in **Supplementary Figure S1** in the **Supplementary Material**. The difference in calculated EA between 15 and 20% exact exchange is in all cases less than 2 kcal/mol, supporting the large difference in EA between the two sets of structures discussed above. In summary, it is concluded that the redox-active tyrosine plays an essential role for the proton pumping in CcO, which is in accordance with the observation that it is conserved in the active site of all types of CcOs (Hemp et al., 2006).

Gating Barriers

Both the electrogenic chemistry and the proton pumping imply that protons must move against the gradient, i.e. in the direction that is thermodynamically unfavorable. This means that there has to be barriers in the proton pathways, some of which must be flexible. Furthermore, the proton uptake must always occur from the N-side and not from the P-side. This means that there must be a barrier for proton uptake from the P-side, both to the PLS and to the BNC, which is always higher than the barriers for proton uptake from the N-side via the D- and the K-channels. At the same time, the barrier between the PLS and the P-side must be low enough for the pump-protons to be expelled to the P-side. No specific proton pathway has been characterized between the PLS and the P-side, and therefore it is difficult to suggest gating mechanisms in this region. For the protons taken up from the N-side there are mainly two situations that has to be handled by barriers with a varying height. First, when the proton is taken up for the PLS, transfer to the BNC must be avoided. One suggestion is that there is an unfavorable alignment of water molecules toward the BNC at this point of the reaction, the so-called “water-gated” mechanism (Wikström et al., 2003). Another suggestion involves thermodynamic considerations, in which the endergonicity

of proton transfer to the BNC before the electron has arrived in the BNC is an important part of the barrier that prevents the proton from going to the BNC rather than to the PLS (Siegbahn and Blomberg, 2007; Blomberg and Siegbahn, 2012).

The most discussed gating situation is probably how to prevent the proton in the PLS to leak back to the N-side when the chemical proton has arrived in the BNC. One suggestion is that the transition state in the D-channel, where all pumped protons are transferred, has a positive character, which means that it is low when there is an uncompensated electron in the vicinity, such as in the low-spin heme *a*, thus allowing the proton to be taken up in the first place. But when the electron is neutralized by the proton in the BNC, the barrier is high, and the proton that is expelled from the PLS cannot return to the N-side, and has to go to the P-side (Siegbahn and Blomberg, 2007; Blomberg and Siegbahn, 2010; Blomberg and Siegbahn, 2012). The positive character of the transition state is achieved by the traveling proton itself, and excludes an initial deprotonation of the glutamic acid at the BNC end of the D-channel. Other suggestions involve charge separation processes for the proton transfer in the D-channel in which the glutamic acid becomes deprotonated, and also motion of the glutamic side chain between different positions (Kaila et al., 2008).

The present computational approach cannot be applied to large enough models to reliably describe the different gating situations in the CcOs. Although there have been theoretical studies performed on significantly larger portions of the CcO enzyme than the models used in the present study, see e.g., (Goyal et al., 2015; Reidelbach and Imhof, 2020), it has not yet been possible to conclusively quantify the different gating suggestions.

CONCLUSION

Cellular energy conservation occurs in the respiratory chain, where one of the members, Cytochrome *c* oxidase (CcO), reduces molecular oxygen. The CcOs belonging to the A-family are particularly efficient in converting the released free energy in the reduction process to an electrochemical gradient across the membrane. Apart from the electrogenic reduction chemistry, which contributes to the gradient, there is also proton pumping across the entire membrane in every reduction step. The fact that every single electron transfer into the active site for the oxygen reduction is coupled to the motion of two positive charges (protons) across the membrane, requires intricate mechanisms and special energetic preconditions. Quantum chemical calculations suggest a mechanism for the oxygen reduction process that solves some of the pending issues. The main characteristic of the suggested mechanism is that the redox-active tyrosine in the active site, which is conserved in all types of CcOs, and which becomes a neutral tyrosyl radical in the O–O bond cleavage step, stays unprotonated in all intermediates from which the reduction steps are initiated, see **Table 2** and **Figure 4A**. This means that the proton goes to the center of the BNC rather than to the tyrosine in each step, and the tyrosine stays as

a radical or with some tyrosinate character mixed in. One consequence of such a mechanism is that the free energy released in the oxygen reduction process becomes smoother distributed over the reduction steps, which is needed to avoid too high barriers during the reduction process when the gradient is present. Another consequence is that the affinity for electron transfer to the active site from the immediate donor, the low-spin heme, is adjusted to a value that *both* is small enough to require the uptake of a proton to a pump-loading site, *and* is large enough to secure an exergonic process for the combined uptake of the pump-proton and the electron transfer to the active site, see panel 2 in **Figure 3**. In this way the tyrosine plays an essential role for a secure proton pumping in all reduction steps.

DATA AVAILABILITY STATEMENT

The original contributions presented in the study are included in the article/**Supplementary Material**, further inquiries can be directed to the corresponding author.

REFERENCES

- Becke, A. D. (1993). Density-functional thermochemistry. III. The role of exact exchange. *J. Chem. Phys.* 98, 5648–5652. doi:10.1063/1.464913
- Björck, M. L., and Brzezinski, P. (2018). Control of transmembrane charge transfer in cytochrome c oxidase by the membrane potential. *Nat. Commun.* 9, 3187. doi:10.1038/s41467-018-05615-5
- Bloch, D., Belevich, I., Jasaitis, A., Ribacka, C., Puustinen, A., Verkhovsky, M. I., et al. (2004). The catalytic cycle of cytochrome c oxidase is not the sum of its two halves. *Proc. Natl. Acad. Sci. U.S.A.* 101, 529–533. doi:10.1073/pnas.0306036101
- Blomberg, M. R. A., Blomberg, M. R. A., and Siegbahn, P. E. M. (2004). A theoretical study of myoglobin working as a nitric oxide scavenger. *J. Biol. Inorg. Chem.* 9, 923–935. doi:10.1007/s00775-004-0585-5
- Blomberg, M. R. A., Borowski, T., Him, F., Liao, R. Z., and Siegbahn, P. E. M. (2014). Quantum chemical studies of mechanisms for metalloenzymes. *Chem. Rev.* 114, 3601–3658. doi:10.1021/cr400388t
- Blomberg, M. R. A. (2016). Mechanism of oxygen reduction in cytochrome c oxidase and the role of the active site tyrosine. *Biochemistry* 55, 489–500. doi:10.1021/acs.biochem.5b01205
- Blomberg, M. R. A., and Ådelroth, P. (2017). The mechanism for oxygen reduction in cytochrome c dependent nitric oxide reductase (cNOR) as obtained from a combination of theoretical and experimental results. *Biochim. Biophys. Acta* 1858, 884–894. doi:10.1016/j.bbabi.2017.08.005
- Blomberg, M. R. A., and Ådelroth, P. (2018). Mechanisms for enzymatic reduction of nitric oxide to nitrous oxide - a comparison between nitric oxide reductase and cytochrome c oxidase. *Biochim. Biophys. Acta* 1859, 1223–1234. doi:10.1016/j.bbabi.2018.09.368
- Blomberg, M. R. A. (2019). Active site midpoint potentials in different cytochrome c oxidase families: a computational comparison. *Biochemistry* 58, 2028–2038. doi:10.1021/acs.biochem.9b00093
- Blomberg, M. R. A. (2020a). Activation of O₂ and NO in heme-copper oxidases - mechanistic insights from computational modelling and NO in heme-copper oxidases-mechanistic insights from computational modelling. *Chem. Soc. Rev.* 49, 7301–7330. doi:10.1039/d0cs00877j
- Blomberg, M. R. A. (2020b). Role of the two metals in the active sites of heme copper oxidases-A study of NO reduction in cbb3 cytochrome c oxidase cytochrome c oxidase. *Inorg. Chem.* 59, 11542–11553. doi:10.1021/acs.inorgchem.0c01351
- Blomberg, M. R. A. (2020c). The structure of the oxidized state of cytochrome c oxidase - experiments and theory compared. *J. Inorg. Biochem.* 206, 111020. doi:10.1016/j.jinorgbio.2020.111020
- Blomberg, M. R. A., and Siegbahn, P. E. M. (2010). A quantum chemical study of the mechanism for proton-coupled electron transfer leading to proton pumping in cytochrome c oxidase. *Mol. Phys.* 108, 2733–2743. doi:10.1080/00268976.2010.523017
- Blomberg, M. R. A., Siegbahn, P. E. M., and Babcock, G. T. (1998). Modeling electron transfer in biochemistry: a quantum chemical study of charge separation in Rhodobacter sphaeroides and photosystem II. *J. Am. Chem. Soc.* 120, 8812–8824. doi:10.1021/ja9805268
- Blomberg, M. R. A., and Siegbahn, P. E. M. (2015a). How cytochrome c oxidase can pump four protons per oxygen molecule at high electrochemical gradient. *Biochim. Biophys. Acta* 1847, 364–376. doi:10.1016/j.bbabi.2014.12.005
- Blomberg, M. R. A., and Siegbahn, P. E. M. (2016). Improved free energy profile for reduction of NO in cytochrome c dependent nitric oxide reductase (cNOR). *J. Comput. Chem.* 37, 1810–1818. doi:10.1002/jcc.24396
- Blomberg, M. R. A., and Siegbahn, P. E. M. (2006). Quantum chemistry applied to the mechanisms of transition metal containing enzymes-Cytochrome c oxidase, a particularly challenging case. *J. Comput. Chem.* 27, 1373–1384. doi:10.1002/jcc.20448
- Blomberg, M. R. A., and Siegbahn, P. E. M. (2012). The mechanism for proton pumping in cytochrome c oxidase from an electrostatic and quantum chemical perspective. *Biochim. Biophys. Acta* 1817, 495–505. doi:10.1016/j.bbabi.2011.09.014
- Blomberg, M. R. A. (2021). The importance of exact exchange - a methodological investigation of NO reduction in heme-copper oxidases. *J. Chem. Phys.* 154. doi:10.1063/5.0035634
- Brzezinski, P., and Gennis, R. B. (2008). Cytochrome c oxidase: exciting progress and remaining mysteries. *J. Bioenerg. Biomembr.* 40, 521–531. doi:10.1007/s10863-008-9181-7
- Ferguson, S. J. (2010). ATP synthase: from sequence to ring size to the P/O ratio. *Proc. Natl. Acad. Sci. U.S.A.* 107, 16755–16756. doi:10.1073/pnas.1012260107
- Ganesan, K., and Gennis, R. B. (2010). Blocking the K-pathway still allows rapid one-electron reduction of the binuclear center during the anaerobic reduction of the aa3-type cytochrome c oxidase from Rhodobacter sphaeroides-type cytochrome c oxidase from Rhodobacter sphaeroides. *Biochim. Biophys. Acta* 1797, 619–624. doi:10.1016/j.bbabi.2010.03.012
- Gaussian (2010). *Revision C.01*. Wallingford, CT: Gaussian Inc.
- Goyal, P., Yang, S., and Cui, Q. (2015). Microscopic basis for kinetic gating in cytochrome c oxidase: insights from QM/MM analysis. *Chem. Sci.* 6, 826–841. doi:10.1039/c4sc01674b
- Grimme, S., Anthony, J., Ehrlich, S., and Krieg, H. (2010). A consistent and accurate *ab initio* parametrization of density functional dispersion correction (DFT-D) for the 94 elements H-Pu. *J. Chem. Phys.* 132, 154104. doi:10.1063/1.3382344

AUTHOR CONTRIBUTIONS

Since I am the only author I did everything.

FUNDING

This work was supported by the Swedish Research Council (grant number 2016–03721). The computations were performed on resources provided by the Swedish National Infrastructure for Computing (SNIC) at the National Supercomputer Center at Linköping University (NSC) partially funded by the Swedish Research Council through grant agreement no. 2018–05973.

SUPPLEMENTARY MATERIAL

The Supplementary Material for this article can be found online at: <https://www.frontiersin.org/articles/10.3389/fchem.2021.640155/full#supplementary-material>.

- Han, H., Hemp, J., Pace, L. A., Ouyang, H., Ganesan, K., and Hyeob Roh, J. (2011). Adaptation of aerobic respiration to low O₂ environments environments. *Proc. Natl. Acad. Sci. U.S.A.* 108, 14109–14114. doi:10.1073/pnas.1018958108
- Hemp, J., Robinson, D. E., Ganesan, K. B., Martinez, T. J., Kelleher, N. L., and Gennis, R. B. (2006). Evolutionary migration of a post-translationally modified active-site residue in the proton-pumping heme-copper oxygen reductases. *Biochemistry* 45, 15405–15410. doi:10.1021/bi062026u
- Jaguar (2018). New York, NY: Schrödinger, LLC.
- Kaila, V. R. I., Verkhovsky, M. I., Hummer, G., and Wikström, M. (2008). Glutamic acid 242 is a valve in the proton pump of cytochrome c oxidase. *Proc. Natl. Acad. Sci. U.S.A.* 105, 6255–6259. doi:10.1073/pnas.0800770105
- Kaila, V. R. I., Verkhovsky, M. I., and Wikström, M. (2010). Proton-coupled electron transfer in cytochrome oxidase. *Chem. Rev.* 110, 7062–7081. doi:10.1021/cr1002003
- Michel, H. (1998). The mechanism of proton pumping by cytochrome c oxidase. *Annu. Rev. Biophys.* 95, 12819–12824. doi:10.1073/pnas.95.22.12819
- Michel, H. (1999). CytochromecOxidase: catalytic cycle and mechanisms of proton pumping—A discussion†. *Biochemistry* 38, 15129–15140. doi:10.1021/bi9910934
- Morgan, J. E., Verkhovsky, M. I., and Wikström, M. r. (1994). The histidine cycle: a new model for proton translocation in the respiratory heme-copper oxidases. *J. Bioenerg. Biomemb.* 26, 599–608. doi:10.1007/bf00831534
- Popovic, D. M., Leontyev, I. V., Beech, D. G., and Stuchebrukhov, A. A. (2010). Similarity of cytochrome c oxidases in different organisms. *Proteins* 78, 2691–2698. doi:10.1002/prot.22783
- Popovic, D. M., and Stuchebrukhov, A. A. (2004). Proton pumping mechanism and catalytic cycle of cytochrome c oxidase: Coulomb pump model with kinetic gating. *FEBS Lett.* 566, 126–130. doi:10.1016/j.febslet.2004.04.016
- Qin, L., Hiser, C., Mulichak, A., Gavarito, R. M., and Ferguson-Miller, S. (2006). Identification of conserved lipid/detergent-binding sites in a high-resolution structure of the membrane protein cytochrome c oxidase. *Proc. Natl. Acad. Sci. U.S.A.* 103, 16117–16122. doi:10.1073/pnas.0606149103
- Quenneville, J., Popovic, D. M., and Stuchebrukhov, A. A. (2006). Combined DFT and electrostatics study of the proton pumping mechanism in cytochrome c oxidase. *Biochim. Biophys. Acta* 1757, 1035–1046. doi:10.1016/j.bbabo.2005.12.003
- Reidlbach, M., and Imhof, P. (2020). Proton transfer in the D-channel of cytochrome c oxidase modeled by a transition network approach. *Biochim. Biophys. Acta* 1864, 129614. doi:10.1016/j.bbag.2020.129614
- Reiher, M., Salomon, O., and Hess, B. A. (2001). Reparameterization of hybrid functionals based on energy differences of states of different multiplicity. *Theor. Chem. Acc.* 107, 48–55. doi:10.1007/s00214-001-0300-3
- Rich, P. R., Meunier, B., Mitchell, R., and Moody, A. J. (1996). Coupling of charge and proton movement in cytochrome c oxidase. *Biochim. Biophys. Acta* 1275, 91–95. doi:10.1016/0005-2728(96)00055-2
- Rich, P. R. (2017). Mitochondrial cytochrome c oxidase: catalysis, coupling and controversies. *Biochem. Soc. Trans.* 45, 813–829. doi:10.1042/bst20160139
- Siegbahn, P. E. M., and Blomberg, M. R. A. (2007). Energy diagrams and mechanism for proton pumping in cytochrome c oxidase. *Biochim. Biophys. Acta* 1767, 1143–1156. doi:10.1016/j.bbabo.2007.06.009
- Siegbahn, P. E. M., and Blomberg, M. R. A. (2014). Energy diagrams for water oxidation in photosystem II using different density functionals. *J. Chem. Theor. Comput.* 10, 268–272. doi:10.1021/ct401039h
- Siegbahn, P. E. M., and Blomberg, M. R. A. (2018). A systematic DFT approach for studying mechanisms of redox active enzymes. *Front. Chem.* 6, 644. doi:10.3389/fchem.2018.00644
- Siegbahn, P. E. M. (2018). The S2 to S3 transition for water oxidation in PSII (photosystem II), revisited to S transition for water oxidation in PSII (photosystem II), revisited. *Phys. Chem. Chem. Phys.* 20, 22926–22931. doi:10.1039/c8cp03720e
- Sugitani, R., Medvedev, E. S., and Stuchebrukhov, A. A. (2008). Theoretical and computational analysis of the membrane potential generated by cytochrome c oxidase upon single electron injection into the enzyme. *Biophys. Acta* 1777, 1129–1139. doi:10.1016/j.bbabo.2008.05.006
- Von Ballmoos, C., Ädelroth, P., Gennis, R. B., and Brzezinski, P. (2012). Proton transfer in ba3 cytochrome c oxidase from *Thermus thermophilus* cytochrome c oxidase from *Thermus thermophilus*. *Biochim. Biophys. Acta* 1817, 650–657. doi:10.1016/j.bbabo.2011.11.015
- Verkhovsky, M. I., Jasaitis, A., Verkhovskaya, M. L., Morgan, J. E., and Wikström, M. (1999). Proton translocation by cytochrome c oxidase. *Nature* 400, 480–483. doi:10.1038/22813
- Vilhjálmsdóttir, J., Albertsson, I., Blomberg, M. R. A., Ädelroth, P., and Brzezinski, P. (2020). Proton transfer in uncoupled variants of cytochrome c oxidase. *FEBS Lett.* 594, 813–822. doi:10.1002/1873-3468.13679
- Wikström, M., and Hummer, G. (2012). Stoichiometry of proton translocation by respiratory complex I and its mechanistic implications. *Proc. Natl. Acad. Sci. U.S.A.* 109, 4431–4436. doi:10.1073/pnas.1120949109
- Wikström, M. K. F. (1977). Proton pump coupled to cytochrome c oxidase in mitochondria. *Nature* 266, 271–273. doi:10.1038/266271a0
- Wikström, M., Krab, K., and Sharma, V. (2018). Oxygen activation and energy conservation by CytochromecOxidase. *Chem. Rev.* 118, 2469–2490. doi:10.1021/acs.chemrev.7b00664
- Wikström, M., and Morgan, J. E. (1992). The dioxygen cycle. Spectral, kinetic, and thermodynamic characteristics of ferryl and peroxy intermediates observed by reversal of the cytochrome oxidase reaction. *J. Biol. Chem.* 267, 10266–10273. doi:10.1016/s0021-9258(19)50013-8
- Wikström, M., Verkhovsky, M. I., and Hummer, G. (2003). Water-gated mechanism of proton translocation by cytochrome c oxidase. *Biochim. Biophys. Acta* 1604, 61–65. doi:10.1016/s0005-2728(03)00041-0

Conflict of Interest: The author declares that the research was conducted in the absence of any commercial or financial relationships that could be construed as a potential conflict of interest.

Copyright © 2021 Blomberg. This is an open-access article distributed under the terms of the Creative Commons Attribution License (CC BY). The use, distribution or reproduction in other forums is permitted, provided the original author(s) and the copyright owner(s) are credited and that the original publication in this journal is cited, in accordance with accepted academic practice. No use, distribution or reproduction is permitted which does not comply with these terms.



Quantification of Local Electric Field Changes at the Active Site of Cytochrome c Oxidase by Fourier Transform Infrared Spectroelectrochemical Titrations

Federico Baserga¹, Jovan Dragelj^{2,3}, Jacek Kozuch¹, Hendrik Mohrmann¹, Ernst-Walter Knapp², Sven T. Stripp¹ and Joachim Heberle^{1*}

¹ Department of Physics, Experimental Molecular Biophysics, Freie Universität Berlin, Berlin, Germany, ² Macromolecular Modelling Group, Institute of Chemistry and Biochemistry, Freie Universität Berlin, Berlin, Germany, ³ Modeling of Biomolecular Systems, Technische Universität Berlin, Berlin, Germany

OPEN ACCESS

Edited by:

Petra Hellwig,
Université de Strasbourg, France

Reviewed by:

Bernd Ludwig,
Goethe University Frankfurt, Germany
Qiang Cui,
Boston University, United States

*Correspondence:

Joachim Heberle
joachim.heberle@fu-berlin.de

Specialty section:

This article was submitted to
Theoretical and Computational
Chemistry,
a section of the journal
Frontiers in Chemistry

Received: 18 February 2021

Accepted: 24 March 2021

Published: 27 April 2021

Citation:

Baserga F, Dragelj J, Kozuch J, Mohrmann H, Knapp E-W, Stripp ST and Heberle J (2021) Quantification of Local Electric Field Changes at the Active Site of Cytochrome c Oxidase by Fourier Transform Infrared Spectroelectrochemical Titrations. *Front. Chem.* 9:669452. doi: 10.3389/fchem.2021.669452

Cytochrome c oxidase (CcO) is a transmembrane protein complex that reduces molecular oxygen to water while translocating protons across the mitochondrial membrane. Changes in the redox states of its cofactors trigger both O₂ reduction and vectorial proton transfer, which includes a proton-loading site, yet unidentified. In this work, we exploited carbon monoxide (CO) as a vibrational Stark effect (VSE) probe at the binuclear center of CcO from *Rhodobacter sphaeroides*. The CO stretching frequency was monitored as a function of the electrical potential, using Fourier transform infrared (FTIR) absorption spectroelectrochemistry. We observed three different redox states (R₄CO, R₂CO, and O), determined their midpoint potential, and compared the resulting electric field to electrostatic calculations. A change in the local electric field strength of +2.9 MV/cm was derived, which was induced by the redox transition from R₄CO to R₂CO. We performed potential jump experiments to accumulate the R₂CO and R₄CO species and studied the FTIR difference spectra in the protein fingerprint region. The comparison of the experimental and computational results reveals that the key glutamic acid residue E286 is protonated in the observed states, and that its hydrogen-bonding environment is disturbed upon the redox transition of heme a₃. Our experiments also suggest propionate A of heme a₃ changing its protonation state in concert with the redox state of a second cofactor, heme a. This supports the role of propionic acid side chains as part of the proton-loading site.

Keywords: vibrational Stark effect, carbon monoxide, proton transfer, electrostatic potential, redox chemistry, electron transfer, infrared spectroscopy

INTRODUCTION

The eukaryotic respiratory chain exploits electron-rich substrates to pump protons from the mitochondrial matrix into the intermembrane space; the resulting proton gradient provides energy for adenosine triphosphate (ATP) production (Mitchell, 1966). The terminal oxidase of the mitochondrial respiratory chain receives electrons from cytochrome c and is referred to as

“complex IV,” or cytochrome *c* oxidase (CcO) (Wikstrom, 1977). While we know that CcO catalyzes the reduction of molecular oxygen (O_2) to water, the molecular mechanism by which the enzyme couples O_2 reduction and proton translocation are not entirely understood.

Cytochrome *c* oxidase is a transmembrane protein complex naturally found in many organisms (García-Horsman et al., 1994). Bacterial CcOs are typically less complex than their eukaryotic relatives, which simplifies the biotechnological production. The terminal oxidase from *Rhodobacter sphaeroides* (RsCcO) is often used as a model organism for eukaryotic isoenzymes, since its active site shares high-sequence identity to mammalian oxidases, e.g., from *Bos taurus* (BtCcO) (Hosler et al., 1992; García-Horsman et al., 1994). RsCcO comprises four subunits: subunit I is fundamental to the function of the enzyme as it harbors the two cofactors heme a and heme a_3 . The latter forms the catalytic binuclear center (BNC), together with a copper ion (Cu_B) that is coordinated by three histidine residues (Pereira et al., 2001).

Reduction of O_2 is catalyzed at the BNC, where O_2 binds to the central iron of heme a_3 and Cu_B . Other ligands are able to coordinate heme a_3 or Cu_B as well, in particular carbon monoxide (CO), nitric oxide, cyanide, and isocyanate (Jain and Kassner, 1984; Brzezinski and Malmström, 1985; Mitchell and Rich, 1994; Brunori, 2001). **Figure 1** shows the BNC of BtCcO in the oxidized form, overlaid by the fully reduced CO-inhibited form.

The catalytic cycle of O_2 reduction comprises several redox intermediates. In the reductive phase, cytochrome *c* provides electrons through direct electron transfer to the dinuclear copper site (Cu_A), which is located close to the surface of CcO. Cu_A represents the start of a “conductive wire” leading to heme a, heme a_3 , and, finally, to Cu_B (Hill, 1993; Sezer et al., 2015). The number of electrons at the four cofactors of CcO determines the three redox states, which are stable after reducing the enzyme. Starting from the oxidized state (O) (Michel et al., 1998), the two-electron-reduced state (R_2) is formed in which Cu_A and heme a are oxidized, while heme a_3 and Cu_B are both reduced (Greenwood et al., 1974; Brzezinski and Malmström, 1985). At strongly negative electric potential all four cofactors are reduced (FR or R_4) (Hellwig et al., 1998; Brzezinski and Gennis, 2008). The O state dominates in the presence of O_2 ; whereas the R_2 and R_4 states can be stabilized through chemical reduction (Namslawer et al., 2002; Schäfer et al., 2018). The R_4 and O states have been analyzed *via* x-ray diffraction crystallography (Yoshikawa et al., 1998), electron

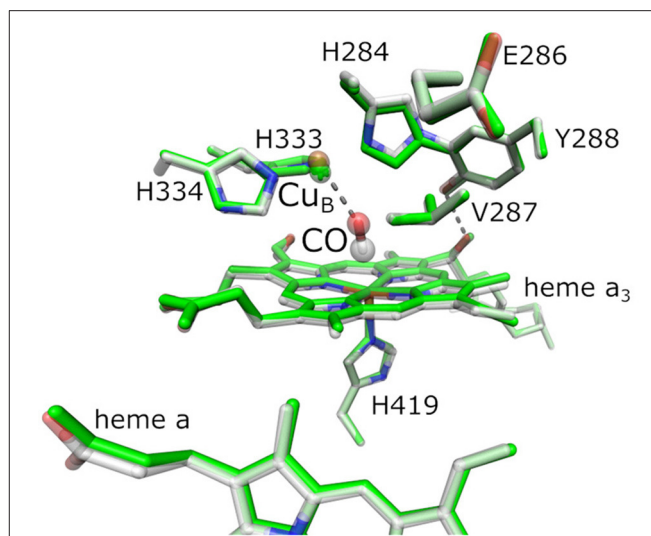


FIGURE 1 | Active site of bovine cytochrome *c* oxidase (BtCcO) in the oxidized state (2DYR, in green) and in the fully reduced, CO-inhibited state (3AG1, with colored atoms). The binuclear center (BNC) comprehends heme a_3 , the copper ion Cu_B , and a number of conserved residues as labeled. The highlighted residues H334, H333, H284, E286, Y288, V287, and H419 are labeled according to the RsCcO nomenclature and are analogous to the actual residues H291, H290, H240, E242, Y244, V241, and H376 in BtCcO shown here.

paramagnetic resonance (EPR) spectroscopy (Sharpe et al., 2008), resonance Raman (RR) spectroscopy (Woodruff et al., 1981), and Fourier transform infrared (FTIR) spectroscopy (Heitbrink et al., 2002). The intermediates of the physiologically relevant R_2 state are more difficult to trap using chemical methods, and demand transient methods like UV/Vis flow-flash spectroscopy (Gibson and Greenwood, 1963; Brzezinski and Malmström, 1985; Brzezinski and Gennis, 2008; Schäfer et al., 2018). However, UV/Vis spectroscopy is insensitive to protonation states of amino acid side chains, which are critical to understanding proton transfer, hydrogen-bonding changes, and other mechanistic details of CcO catalysis.

Cytochrome *c* oxidase pumps protons across the mitochondrial membrane against an electrochemical gradient. The protons necessary for the catalytic reaction are delivered *via* conserved amino acid trajectories referred to as “D” and “K” pathways, with the “chemical protons” for O_2 reduction being provided exclusively through the latter (Ädelroth and Gennis RB, 1998). In the K pathway, the proton uptake correlates with the initial reduction of Cu_A and heme a. The proton translocation against the transmembrane proton gradient is driven by the so-called proton-loading site (PLS), which couples with the redox-reaction occurring at the BNC (Belevich et al., 2007). It has been proposed that the PLS is located next to the propionate groups of either heme a or heme a_3 (Kaila et al., 2011; Sezer et al., 2017). In the D pathway, a glutamate residue controls the proton flux (E286 in RsCcO, cf. **Figure 1**) that also plays a key role in proton translocation (Ädelroth et al., 1997; Nyquist et al., 2003). The carboxylic side chain of E286 was shown to be protonated in the O, R_2 , and R_4 states of the redox cycle (Nyquist

Abbreviations: ATR, attenuated total reflection; BNC, binuclear center formed by heme a_3 and Cu_B ; BtCcO, cytochrome *c* oxidase from *Bos Taurus*; CcO, cytochrome *c* oxidase; DPPC, 1,2-dipalmitoyl-sn-glycero-3-phosphocholine; E286, glutamate 286 of *Rhodobacter sphaeroides*; FTIR, Fourier transform infrared spectroscopy; O, state in which all redox cofactors are oxidized; PLS, proton loading site; PRA a_3 , ring A propionate of heme a_3 ; PRD a_3 , ring D propionate of heme a_3 ; PdCcO, cytochrome *c* oxidase from *Paracoccus denitrificans*; R_2 , two-electron reduced state in which Cu_A and heme a are oxidized, while the binuclear center is reduced; R_2 CO, two-electron reduced state with carbon monoxide ligating heme a_3 ; R_4 , fully reduced state in which all metal cofactors are reduced; R_4 CO, fully reduced state with carbon monoxide ligating heme a_3 ; RsCcO, cytochrome *c* oxidase from *Rhodobacter sphaeroides*; VSE, vibrational Stark effect.

et al., 2003). A possible proton transfer scenario from E286 to the PLS may involve the reduction of heme a and the BNC (Belevich et al., 2006). Belevich et al. (2007) showed a correlation between membrane electrostatic potential and redox changes upon electron injection and suggested that redox changes at heme a, as well as pKa differences, are key factors.

Fourier transform infrared difference spectroscopy allows addressing changes in protonation states and hydrogen-bonding patterns (Lorenz-Fonfria, 2020), but transient techniques are difficult to apply due to the lack of specific triggers (Schleeger et al., 2009). Alternatively, *operando* FTIR spectroscopy, in combination with electrochemical titrations, can facilitate the detection of elusive species in order to assign vibrational bands to different redox states, specific amino acid side chains, or redox sites (Hellwig et al., 1998; Gorbikova et al., 2006; Dodia et al., 2013). Introducing an internal probe like CO as an axial ligand to heme a₃ provides complementary feedback of functional relevance. As is clear from X-ray crystallography (Figure 1), the presence of CO does not introduce significant structural changes at the BNC when compared to the oxidized protein, rendering CO a molecular reporter and O₂ surrogate (Yoshikawa et al., 1998). Due to its high frequency and a large dipole moment, the C≡O stretching vibration is easily detected by IR spectroscopy. Furthermore, the CO ligand exhibits a high Stark-tuning rate, enabling to report on the changes in the local electrostatic field through an electrochromic shift (vibrational Stark effect, VSE) (Park et al., 1999; Boxer, 2009).

In this work, we use *operando* FTIR difference spectroelectrochemistry in attenuated total reflection (ATR) configuration (Nyquist et al., 2004; Senger et al., 2017) to investigate CO-inhibited R_sCcO. This approach facilitates CO gas binding and redox titrations from the fully reduced to the oxidized state. We determined the midpoint potential, acquired the difference spectra, and discussed the changes in the hydrogen-bonding pattern and protonation for each of the identified redox states. The measured VSE of the CO ligand is compared to electrostatic computations, calculating electric field changes at the BNC for different redox and protonation states.

MATERIALS AND METHODS

Sample Preparation

Wild-type CcO from *R. sphaeroides* was expressed, purified, and stored in phosphate buffer [10 mM phosphate, pH 8, with 0.1% n-dodecyl-β-D-maltosid (DDM)] at −80°C. Ahead of the experiment, the samples were inserted into liposomes to simulate the physiological environment of the enzyme (Robinson and Capaldi, 1977). We prepared two 1 mg/ml solutions of dipalmitoylphosphatidylcholine (DPPC) vesicles, as well as isotopically carbon-substituted ¹³C₄₀-DPPC (Cambridge Isotope Laboratories) vesicles in 50 mM phosphate buffer (pH 8) with 100 mM NaCl. The vesicles were extruded through a filter with pore size of 100 nm. After washing the DDM-solubilized CcO with the same phosphate buffer, we reconstituted the sample in the lipid vesicles by detergent removal upon addition of 30 mg of biobeads over a period of 12 h. The molar ratio of lipids per CcO molecule was ~200:1.

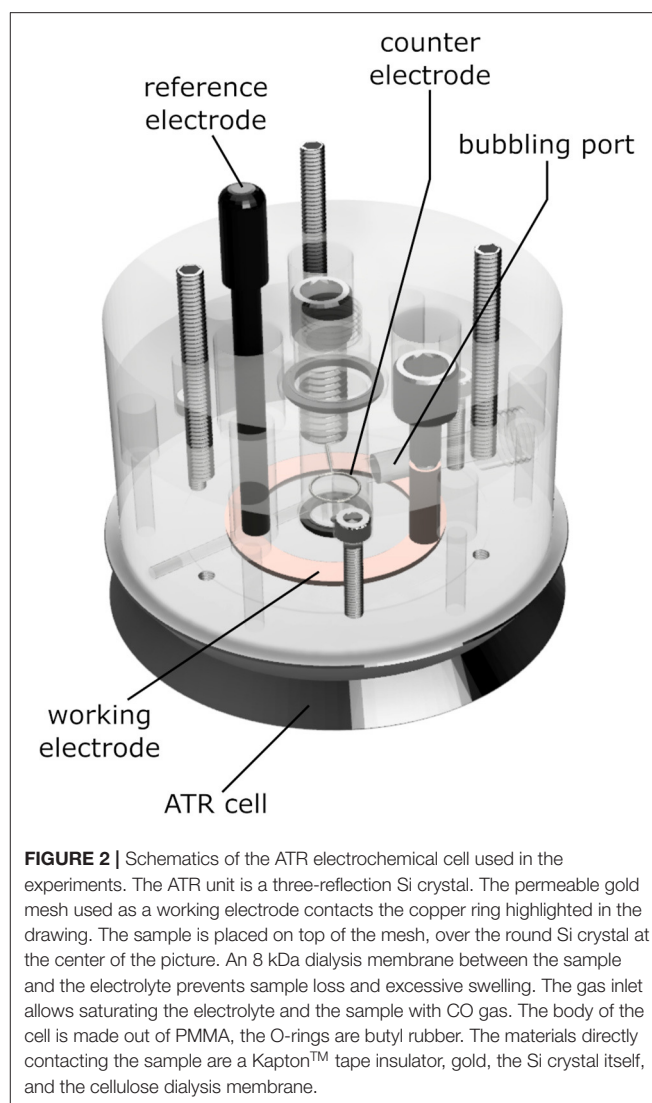


FIGURE 2 | Schematics of the ATR electrochemical cell used in the experiments. The ATR unit is a three-reflection Si crystal. The permeable gold mesh used as a working electrode contacts the copper ring highlighted in the drawing. The sample is placed on top of the mesh, over the round Si crystal at the center of the picture. An 8 kDa dialysis membrane between the sample and the electrolyte prevents sample loss and excessive swelling. The gas inlet allows saturating the electrolyte and the sample with CO gas. The body of the cell is made out of PMMA, the O-rings are butyl rubber. The materials directly contacting the sample are a Kapton™ tape insulator, gold, the Si crystal itself, and the cellulose dialysis membrane.

The resulting samples were washed four times with the final buffer and pelleted by centrifugation, yielding two different samples: DPPC-reconstituted CcO and ¹³C₄₀-DPPC-reconstituted CcO in H₂O buffer (50 mM phosphate, pH 8, with 100 mM NaCl). The samples in D₂O were prepared by *in situ* buffer exchange directly on the ATR crystal.

Electrochemistry

We constructed an electrochemical cell (depicted in Figure 2) that allows ATR/FTIR measurements while purging a buffer reservoir on top of the sample with gas, basing our design on previous works (Dodia et al., 2013). The cell consists of a transparent acrylic body that can be screwed onto a Silicon ATR cell (Pike Technologies, WI, United States). The body of the cell has holes for a buffer reservoir, an Ag/AgCl reference electrode, an annular copper working electrode, a platinum counter electrode, and a gas-bubbling port.

The ATR crystal and its stainless-steel base were insulated using 95 μm thick Kapton tape (DuPont, DE, United States)

in an annular shape. We deposited 5 μl of reconstituted CcO (15–20 μM , corresponding to 20–27 ng of protein) onto a 9 μm gold mesh (Goodfellow, PA, United States), adhered on top of the Si reflection element of the ATR setup. All experiments were performed anaerobically (*vide infra*). The sample was dried while monitoring the water bands of its absolute spectra. For samples measured in excess aqueous solution, we placed an 8 kDa dialysis membrane atop of the sample directly after drying to avoid excessive film swelling and subsequent sample loss. Then, we mounted the cell on top of the assembly and filled it with 3 ml of electrolyte buffer, i.e., 50 mM phosphate (pH 8) with 300 mM NaCl and 40 μM mediators (Hellwig et al., 1998). For the samples in D_2O , we deposited 2 μl of pure D_2O on top of the dry sample and redried it to facilitate buffer substitution in the protein. We then placed the dialysis membrane atop this film and filled the reservoir with D_2O buffer [50 mM phosphate at $\text{pH}^* 7.9$ (Krazel and Bal, 2004), with 300 mM NaCl and 40 μM mediators]. We connected the electrodes in the cell to an Autolab potentiostat (Metrohm, Germany) and set the potential to -500 mV vs. Ag/AgCl while slowly purging the buffer solution with CO. The Ag/AgCl reference electrode was stored in saturated KCl before and after use. CO binding was performed over a period of about 1 h. The CO absorption was stable over 12 h; after which, a background spectrum was recorded at a reducing potential of -500 mV vs. Ag/AgCl. For the redox titration, the electrode potential was increased in steps of 25 mV every 450 s until a potential of $+600\text{ mV}$ (vs. Ag/AgCl) was ultimately reached.

FTIR Spectroscopy

All infrared absorption data were recorded on a Vertex 70 spectrometer, equipped with an MCT detector (Bruker, Germany). The spectrometer with the electrochemical cell was placed in a vinyl anaerobic chamber (COY lab products, MI, United States). Spectra were recorded in the frequency range of $4000\text{--}800\text{ cm}^{-1}$ at a spectral resolution of 2 cm^{-1} with at least 300 coadditions.

First, we monitored the binding of CO to CcO by recording the characteristic vibrational band of the $\text{C}\equiv\text{O}$ stretching vibration that peaks at $1,964\text{ cm}^{-1}$ at -500 mV vs. Ag/AgCl at pH 8 (Mitchell et al., 1996). After performing the redox titration, we measured reduced-minus-oxidized spectra belonging to the two states identifiable from the analysis of the CO band shift in its fingerprint region, i.e., $1,950\text{--}1,980\text{ cm}^{-1}$ (Dodson et al., 1996; Mitchell et al., 1996; Iwaki and Rich, 2007). The only correction applied to our spectra was a Lorentzian Fourier filter, excluding components broader than 150 cm^{-1} , acting essentially as a baseline correction (Supplementary Figure 1). The final difference spectra show characteristic protein bands, cofactor bands, as well as the CO rebinding with its band shift.

Preparing the Crystal Structure for Electrostatic Energy Computations

The crystal structure of RsCcO [PDB code: 2GSM (Qin et al., 2006)] was used and supplemented by hydrogen atoms, using CHARMM (Brooks et al., 2009). The atomic charges of the cofactors (heme a, heme a_3 , Cu_A , and Cu_B) were retrieved from previous work (Woelke et al., 2013). For the protein moiety,

atomic partial charges were taken from the CHARMM force field. The CO ligand at heme a_3 was placed using a structural overlay with the heme a_3 of the BtCcO crystal structure as shown in Figure 1 [PDB code: 3AG1 (Muramoto et al., 2010)]. The environment of the BNC in BtCcO is virtually identical to the one of RsCcO (Supplementary Figure 2). In the bovine structure, the Fe–C–O angle is 169° . This angle is nearly identical to the angle of 170° in the myoglobin crystal structure from sperm whale [PDB code: 3E5O (Tomita et al., 2009)]. The distances of Fe–C and Fe–O in BtCcO are $d_{\text{Fe–C}} = 1.67\text{ \AA}$ and $d_{\text{Fe–O}} = 2.40\text{ \AA}$, respectively. They differ slightly from the values in the myoglobin crystal structure, which are $d_{\text{Fe–C}} = 1.88\text{ \AA}$ and $d_{\text{Fe–O}} = 2.99\text{ \AA}$ (Tomita et al., 2009). In addition, we modeled an idealized geometry of CO bound to heme a_3 , with a Fe–C–O angle of 180° and $d_{\text{Fe–C}} = 1.70\text{ \AA}$. The side chain of E286 is in the “down” conformation in the crystal structure, pointing away from the propionic side chain of heme a_3 , PRDa₃. We performed energy minimization for the side chain of E286 to obtain a chemically reasonable structure in this case.

Electric Field Computation Based on Crystal and Modeled Structures

We compared different redox states (oxidation of heme a or both heme a and Cu_A) and protonation equilibria. In the following, the electric field at a point \vec{r} generated by point charges q_i in positions \vec{r}_i is defined as:

$$\vec{E}_{\text{theory}}(\vec{r}) = \frac{1}{4\pi\epsilon_r\epsilon_0} \sum_i^N q_i \frac{\vec{r} - \vec{r}_i}{|\vec{r} - \vec{r}_i|^3} \quad (1)$$

where ϵ_0 is the vacuum permittivity, with $\epsilon_0 = 8.85 \cdot 10^{-12}\text{ C/Vm}$ and ϵ_r is the dielectric constant in the vicinity of the probe, which was set to $\epsilon_r = 4.0$ (Kieseritzky and Knapp, 2008; Meyer and Knapp, 2015). In the present application, the positions of the hydrogen atoms were added to the crystal structure of CcO with HBUILD of CHARMM (Brooks et al., 2009) and energy minimized for oxidized cofactors (Cu_A^{2+} , Fe^{3+} of both heme a and heme a_3 , Cu_B^{2+}), with most residues in standard protonation states, except for deprotonated K354 and protonated D407. The histidine tautomeric states were determined as in previous works (Woelke et al., 2013). The hydrogen atoms of heme a, the BNC, E286, the propionates of ring D (PRDa₃) and ring A (PRAa₃) at heme a_3 , as well as the histidines H333 and H334 that ligate Cu_B , were energy minimized for the different charge states (Supplementary Figure 3). The geometry of all other atoms was not optimized. The atomic point charges q_i of these molecules vary according to the redox state of the enzyme, and it was necessary to consider them in order to compute the change of electric field in the transition between oxidized and reduced states. The change in the electric field at the CO in the direction of the CO bond, given by the unit vector \vec{p} , is described by:

$$\vec{p} \cdot \Delta \vec{E}(\vec{r}) = \vec{p} \cdot [\vec{E}_{\text{ox}}(\vec{r}) - \vec{E}_{\text{red}}(\vec{r})], \quad (2)$$

where \vec{r} corresponds to the center of the CO bond.

Considering water molecules explicitly in computations of electrostatic energies can pose modeling challenges. Therefore, water is usually considered implicitly by filling its bulk volume with a dielectric medium of $\epsilon_r = 80$. The crystal water molecules were not removed in our electrostatic computations, and their atoms were not subjected to charge-state-specific geometry optimization. In the presence of explicit water, its volume can be treated as the protein volume, using a dielectric constant of $\epsilon_r = 4.0$. For the membrane volume, the same value of the dielectric constant is appropriate. The outer solvation layer of CcO is more than 22 Å away from the CO probe, such that the dielectric constant is also in this part $\epsilon_r = 4.0$. Hence, a homogeneous dielectric medium can be used to describe the redox-induced variation of electrostatic field at the CO ligand of heme a_3 .

The changes of the electrostatic field at CO ligated to heme a_3 are mainly governed by the variation of the atomic charges of heme a with its redox state. Since the charge changes are distributed over many heme atoms, only moderate conformational changes may occur as a result of the change in the heme a redox state, justifying why only specific hydrogen atoms (which are generally more mobile) were geometrically optimized. In the same spirit, using only geometry optimization and no molecular dynamics simulation, computations of heme redox potential were performed for artificial cytochrome b , with an accuracy of 20 mV (Popović et al., 2001). The agreement with experimentally measured heme redox potential is similar also for large proteins (Voigt and Knapp, 2003).

RESULTS

Response of the C≡O Stretching Vibration to Changes in Redox Potential

We recorded an FTIR spectrum of fully reduced, CO-inhibited CcO at an electric potential of -500 mV vs. Ag/AgCl, which was used as a reference for the following spectra. Then, the electrode potential was increased in steps of 25 mV, and a series of potential-induced difference spectra were acquired in the range of the C≡O stretching vibration (**Figure 3A**). A positive band at $1,968\text{ cm}^{-1}$ evolves in the range of $+50$ to $+200$ mV. This feature develops into a single negative peak at $1,964\text{ cm}^{-1}$ for potentials higher than $+300$ mV. Such behavior indicates the presence of three different redox species.

In order to analyze this redox behavior rigorously, the potential-dependent difference spectra were transformed into absolute spectra, where the total contributions from the observed states are readily visible (**Figure 3B**). This data set was fit, using two Voigtian components with peak maxima at 1963.7 and 1967.2 cm^{-1} . The blueshift of the CO peak is characteristic of the formation of the $R_2\text{CO}$ state (Dodson et al., 1996; Iwaki and Rich, 2007), i.e., the state in which the BNC is reduced, but the other metal centers in CcO are oxidized (Brzezinski and Malmström, 1985). The identifiable states are: (I) a state where CO is initially bound under reducing conditions [$R_4\text{CO}$ with $\nu(\text{C}\equiv\text{O}) = 1963.7\text{ cm}^{-1}$], (II) a state in which the majority of the sample has undergone the CO band shift [$R_2\text{CO}$ with $\nu(\text{C}\equiv\text{O}) = 1967.2\text{ cm}^{-1}$], and (III) a state in which the CO ligand finally

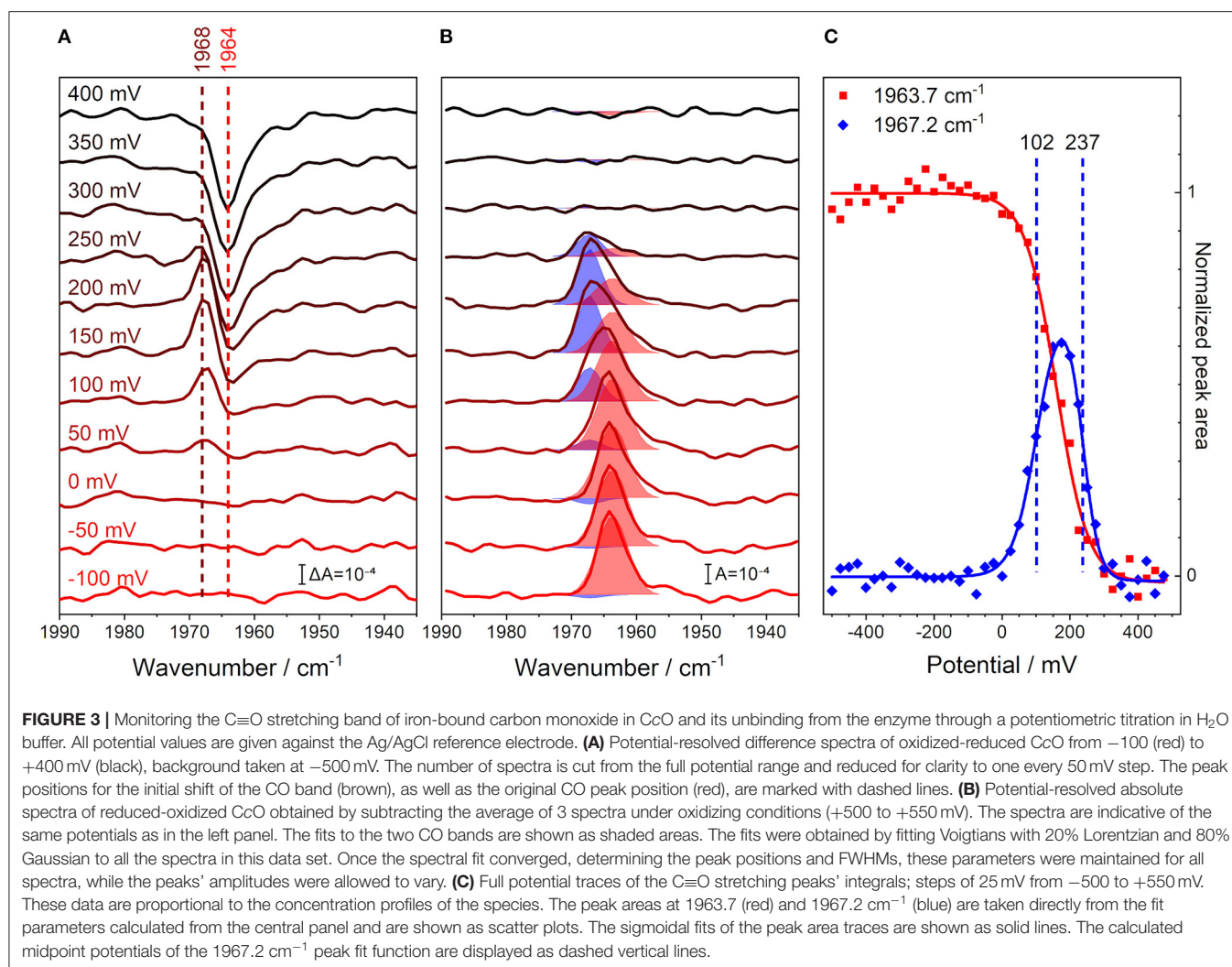
dissociates from the BNC (O) (Dodson et al., 1996; Cooper and Brown, 2008).

Plotting the relative abundance of the two CO-inhibited species against the applied electrode potential illustrates the depletion and formation of the $R_4\text{CO}$, $R_2\text{CO}$, and O states (**Figure 3C**). The analysis of the potential-dependent traces provides midpoint potentials of $+102 \pm 11$ mV for the $R_4\text{CO} \rightarrow R_2\text{CO}$ transition and $+237 \pm 6$ mV for the $R_2\text{CO} \rightarrow \text{O}$ transition, which we will discuss below (these values are almost invariant to the specific fit procedure; see **Supplementary Figure 4**). It should be noted that the second transition involves the dissociation of the CO ligand. However, rebinding of the CO ligand to heme a_3 was a reversible process under the conditions and at the time scales of the experiment (**Supplementary Figure 5**). Even though the $R_2\text{CO}$ state is stable and exhibits an easily identifiable CO band, it is not possible to accumulate a pure $R_2\text{CO}$ state under any conditions. In fact, the $R_2\text{CO}$ state only represents 60% of the total species at its maximum of $+175$ mV (**Figure 3C**). The O state is accumulated at highly positive electrode potentials and is indicative of complete oxidation of the BNC. Evidently, it is impossible to exclude the contribution of a one-electron-reduced BNC component in the O state since the unbound CO probe cannot report any longer on the electronic state of its surroundings.

The frequency of the C≡O vibration can be used to quantify electrostatic changes in the local environment *via* the VSE (Park et al., 1999; Boxer, 2009), under the condition that the redox state of heme a_3 remains unchanged. As such, the spectral shift from 1963.7 to 1967.2 cm^{-1} can be interpreted in terms of an altered electric field projected on the CO bond upon the $R_4\text{CO} \rightarrow R_2\text{CO}$ redox transition. In the case of CcO, the CO ligand adopts a well-defined conformation when bound to heme a_3 (as indicated by its narrow bandwidth), with an angle given by the BNC coordinates (Muramoto et al., 2010). Thus, one can interpret the frequency shift of the CO probe using the linear VSE equation:

$$\Delta\nu = |\Delta\vec{\mu}| \cdot \Delta E \quad (3)$$

where $|\Delta\vec{\mu}| = 2.4/f\text{ cm}^{-1}/(\text{MV}/\text{cm})$ is the Stark tuning rate of CO bound to a heme iron (Park et al., 1999) and $\Delta E = \vec{p} \cdot \Delta\vec{E}$ is the change in the local electric field projected onto the CO bond axis \vec{p} (see **Supplementary Figure 6** for the convention on the electric field direction) (Park et al., 1999; Suydam and Boxer, 2003). The factor f is the local field correction and is required when experimentally ascertaining the local electric field in a protein. This parameter is a result of the specific experimental design of vibrational Stark spectroscopy which provided the Stark-tuning rate, and has been suggested to be ~ 2 in recent work (Fried and Boxer, 2015; Schneider and Boxer, 2016). Using our experimentally determined blueshift of $\Delta\nu = +3.5\text{ cm}^{-1}$ for the redox titration, we infer that the change in electrostatic field experienced by the CO probe along its bond axis is $\Delta E = +2.9\text{ MV}/\text{cm}$.



Evaluating Protonation Changes Upon Reduction by Electrostatic Energy Computation

We performed electrostatic computations to disentangle the various contributions to the electric field changes. The calculated electric field changes projected onto the CO bond ($\vec{p} \cdot \Delta \vec{E}$) are compared to the electric field change of +2.9 MV/cm as derived from the measured blueshift of +3.5 cm⁻¹ upon oxidation of CcO. The experimentally determined electric field is a result of the individual contributions resulting from the change in oxidation states of the cofactors, as well as the protonation states of E286, the propionates of heme a₃ (PRDa₃ and PRAa₃), and the residues H333/H334 and Y288. Here, we used electrostatic energy computations by solving the Poisson-Boltzmann equation to evaluate pK_a values. This approach allows isolating the different contributions to the electric field changes. Alternatively, MD simulations with polarizable force fields were successfully used to match the electrostatics determined from MD simulation to experimental results (Welborn and Head-Gordon, 2019; Wu et al., 2020).

The charge changes displayed in **Table 1** are organized such that the charge increases by one elementary unit for all the considered transitions. The possible contributions of H333, H334, and Y288 are so large that any change in their protonation states can be ruled out for the present experiments. Our electrostatic computations also account for the two different side-chain conformations of E286. It has been discussed that this flexibility allows E286 to act as a proton valve near the entrance of the D-pathway (Belevich et al., 2006; Kaila et al., 2008, 2011; Woelke et al., 2013). In the reported crystal structures of wild-type CcO, E286 is in the “down” conformation, where the carboxylic group points toward the entrance of the D-pathway (**Supplementary Figure 3**) (Yoshikawa et al., 1998). However, in the structure of the N131D mutant of *PdCcO*, E278 (equivalent to E286 in *RsCcO*) adopts an alternative rotamer conformation with the carboxylic acid group pointing toward the P side of the membrane (Dürr et al., 2008). We modeled the alternative “up” conformation of protonated E286, as suggested by molecular dynamics simulations (Kaila et al., 2008). We also considered the two charge-neutral protonation states, namely, E286H¹ and E286H² with hydrogen atoms at O¹ and O², respectively.

TABLE 1 | Electrostatics computations.

Group	Transition	Fe–C–O angle 169°	Fe–C–O angle 180°
heme a	Fe ²⁺ → Fe ³⁺	0.82	0.83
Cu _A	Cu ¹⁺ → Cu ²⁺	0.13	0.07
E286 (down)	E286 [−] → E286H ¹	−1.61	−1.49
E286 (down)	E286 [−] → E286H ²	−1.50	−1.38
E286 (up)	E286 [−] → E286H ¹	−2.24	−2.10
E286 (up)	E286 [−] → E286H ²	−1.94	−1.83
PRDa ₃	PRD [−] → PRDH ¹	0.52	0.19
PRDa ₃	PRD [−] → PRDH ²	0.79	0.52
PRAa₃	PRA[−] → PRAH¹	2.17	1.69
PRAa₃	PRA[−] → PRAH²	1.85	1.37
Y288	Y288 [−] → Y288H	−7.28	−6.97
H334	H334 → H334 ⁺ H ^δ	−11.45	−11.71
H333	H333 → H333 ⁺ H ^δ	−11.87	−12.06

Electric field changes of CO bound to the iron of heme a₃ and Cu_B are computed at the CO-bond center projected onto the CO bond \vec{p} . The values for $\vec{p} \cdot \Delta \vec{E}$ are given in units of MV/cm. While CO is bound, heme a₃ and Cu_B are kept in the reduced state with Fe²⁺ and Cu_B⁺. The electric field changes are induced by oxidation of heme a and Cu_A, and changes in the protonation states of E286, the propionic acids PRDa₃ and PRAa₃, as well as of the histidines H333 and H334. The two histidines, ligated to Cu_B, are doubly deprotonated in the deprotonated state. Furthermore, two orientations of E286 were considered with the proton attached either at O1 or O2 of the carboxylic acids. The computed electric field changes that are compatible with the measured value of 2.9 MV/cm are highlighted by bold digits.

Computing the oxidation of heme a and Cu_A yielded electric field changes of +0.82 and +0.13 MV/cm, respectively (Table 1). Upon oxidation of heme a, experimental data suggest a protonation of a heme a₃ propionate, and corresponding computed electric field changes range from +0.52 to +2.17 MV/cm (Table 1). Initially, the propionate side chains of both hemes have been considered as candidates for acting as the PLS (Behr et al., 1998). More recent studies have favored the propionates of heme a₃ (Kaila et al., 2011; Sezer et al., 2017). Adding the contributions of heme a and Cu_A oxidation and PRDa₃ protonation yields a result which is in moderate agreement (i.e., a similar sign but deviant magnitude) with the measured electric field, regardless of the CO geometry. Instead, considering the oxidation of heme a and Cu_A together with the protonation of PRAa₃ is in line with our experimental data (+3.12 or +2.59 MV/cm, depending on the modeled CO angle vs. +2.9 MV/cm of the experimental estimate). In contrast, protonation changes of E286, H333, and H334 lead to negative field changes and disagree with the present experiment.

Protein Response to Changes in the Applied Electric Potential

Analyzing CO-inhibited CcO, we pinpointed the transition potentials between the R₄CO, R₂CO, and O states. After the equilibration in the O state, we applied rapid potential jumps, leading to the R₂CO and R₄CO states. Each potential jump was followed by a longer equilibration period of ~30 min at the oxidizing potential. Given the different choice of background, it is important to remember that the following data show the process

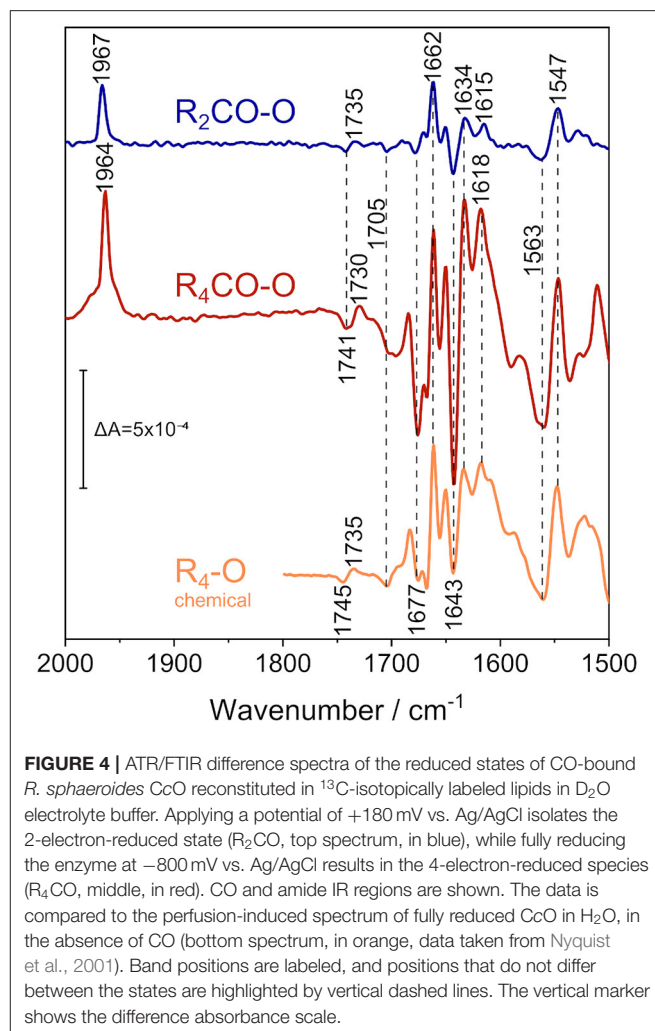


FIGURE 4 | ATR/FTIR difference spectra of the reduced states of CO-bound *R. sphaeroides* CcO reconstituted in ¹³C-isotopically labeled lipids in D₂O electrolyte buffer. Applying a potential of +180 mV vs. Ag/AgCl isolates the 2-electron-reduced state (R₂CO, top spectrum, in blue), while fully reducing the enzyme at −800 mV vs. Ag/AgCl results in the 4-electron-reduced species (R₄CO, middle, in red). CO and amide IR regions are shown. The data is compared to the perfusion-induced spectrum of fully reduced CcO in H₂O, in the absence of CO (bottom spectrum, in orange, data taken from Nyquist et al., 2001). Band positions are labeled, and positions that do not differ between the states are highlighted by vertical dashed lines. The vertical marker shows the difference absorbance scale.

opposite to Figure 3, i.e., protein reduction instead of oxidation. The steady-state spectra of Figure 4 show that CO easily rebinds to the protein after oxidation, if reducing conditions are provided (for more details, see Supplementary Figure 5).

We recorded FTIR difference spectra of CO-inhibited CcO reconstituted in DPPC. Instead of the native lipid, we used the ¹³C₄₀-labeled isotopomer of DPPC (Hübner and Mantsch, 1991) to avoid any possible spectral overlap with the C=O stretching vibration of glutamic acid and aspartic acid, absorbing at around 1,740 cm^{−1}. Furthermore, the ester carbonyl bands of DPPC can shift with electric field changes (Zawisza et al., 2007). FTIR difference spectroscopy has been conducted with the sample immersed in D₂O buffer to avoid spectral interference from the water bending vibration at 1,640 cm^{−1} (for a comprehensive overview of the differences that these isotope substitutions entail, see Supplementary Figures 7–9).

In these experiments, we used the FTIR spectrum of oxidized CcO (O) as a reference. The O state spectrum was accumulated at +600 mV. A rapid potential jump from +600 to +180 mV was applied to the sample. This resulted in the formation of the R₂CO state, and the R₂CO-O difference spectrum was recorded

(top spectrum in **Figure 4**). In R_2CO , the BNC is reduced, but heme a and Cu_A are oxidized. Since CO was present in our spectroelectrochemical cell, the reduction of the BNC resulted in immediate binding of CO to heme a_3 , as evident from the band at $1,967\text{ cm}^{-1}$.

The electrochemically-induced FTIR difference spectrum between the fully reduced and oxidized states (R_4CO-O , **Figure 4**, middle spectrum) was recorded at -800 mV . It is noted that this spectrum is almost identical to the R_4-O spectrum of the fully reduced state generated by the presence of the chemical reductant sodium dithionite (Nyquist et al., 2001) (**Figure 4**, bottom spectrum), despite the presence of the CO ligand in the former (as evident from the band at $1,964\text{ cm}^{-1}$). The strongest bands have been assigned to cofactor redox transitions (Babcock and Salmeen, 1979; Woodruff et al., 1981; Kozuch et al., 2013). The insensitivity of the difference bands to H/D agrees with this assignment. The only exception is the sigmoidal band pair at $1,741/1,730\text{ cm}^{-1}$. This band feature was assigned to the change in hydrogen bonding of the $C=O$ group of the carboxylic side chain of E286 (Nyquist et al., 2001), which absorbs at $1,745/1,735\text{ cm}^{-1}$ in H_2O (see R_4-O spectrum in **Figure 4**). CcO from *Paracoccus denitrificans* (PdCcO) exhibits the same vibrational changes in potentiometric titrations (Hellwig et al., 1998; Gorbikova et al., 2006).

A negative band at $1,705\text{ cm}^{-1}$ appears in both the R_4CO and R_2CO states. This band has been tentatively assigned to the $C=O$ stretching vibration of a carboxylic side chain of an aspartic or glutamic acid (Hellwig et al., 1999b). Also, the propionic acid side chain of heme a_3 in the ba_3 enzyme from *Thermus thermophilus* was proposed (Koutsoupakis et al., 2011). The negative band indicates that such carboxylic side chain is protonated in the oxidized state of CcO and deprotonated upon reduction of the BNC in the R_2CO and R_4CO states.

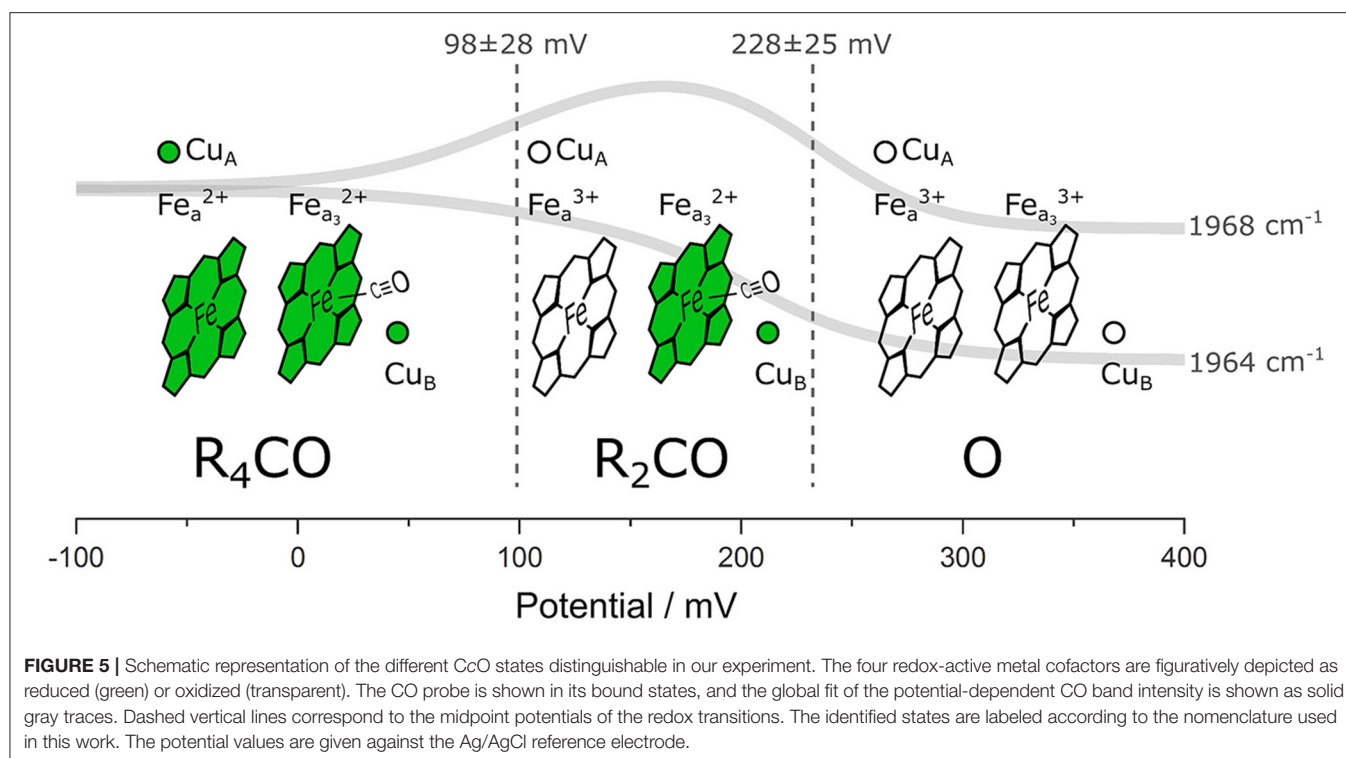
Bands between $1,700$ and $1,620\text{ cm}^{-1}$ are either due to peptide backbone vibrations (amide I) or to vibrational bands of the redox cofactors. The first of such features is the negative band at $1,677\text{ cm}^{-1}$, possibly indicative of amide I (Dodia et al., 2013) or of propionic acid A of heme a_3 (Behr et al., 1998, 2000). This band is weak in the R_2CO state and may well be due to contamination by the R_4CO state, as apparent from our analysis of the potential dependence using bound CO as a sensor (**Figure 3C**). The band position also does not change upon H/D exchange (**Supplementary Figure 7**). Given these considerations, we favor the assignment to the $\nu(C=O)$ of one of the hemes' propionics. The intense positive peak at $1,662\text{ cm}^{-1}$ originates in the $O \rightarrow R_2CO$ transition, since its intensity and frequency barely change upon transition to the R_4CO state. Thus, this positive feature probably correlates only with heme a_3 reduction and is not the peak-shifted counterpart of the negative feature found at $1,677\text{ cm}^{-1}$. The band has previously been assigned either to amide I (Gorbikova et al., 2006), or to the heme a_3 formyl $\nu(C=O)$ in the cofactor's reduced state (Heibel et al., 1993; Hellwig et al., 1999a,b; Nyquist et al., 2001). This band is also not influenced by H/D exchange in our experiment, and it appears to show a single unconvoluted peak. Therefore, it is unlikely to be due to amide I and is, thus, assigned to heme a_3 formyl.

The majority of difference bands between $1,700$ and $1,500\text{ cm}^{-1}$ have been assigned to heme a and heme a_3 , facilitating the direct readout of the cofactor redox states. The most intense negative peak at $1,643\text{ cm}^{-1}$, for example, is found mainly in the R_4CO state. It was previously assigned to the formyl groups of the oxidized heme a (Babcock and Salmeen, 1979; Hellwig et al., 1999a; Kozuch et al., 2013). Surprisingly, this band is also present in the R_2CO spectrum (**Figure 4**, top spectrum), albeit with a less intense negative peak. It is likely that the feature at $1,643\text{ cm}^{-1}$ correlates with heme a reduction in the $R_2CO \rightarrow R_4CO$ transition. However, even when considering R_4CO contamination in the R_2CO state (*vide supra*), we cannot exclude the possibility that this band originates from the R_2CO state. Reduced heme a exhibits a characteristic band, which is the $\nu_{10}(C=C)$ vibration at $1,634\text{ cm}^{-1}$ (Heibel et al., 1993; Kozuch et al., 2013); for which, the same considerations apply. Another band that changes in absorbance in the two reduced states can be identified at $1,618\text{ cm}^{-1}$ in the R_4CO spectrum and at $1,615\text{ cm}^{-1}$ in the R_2CO spectrum. These peaks are assigned to the vinyl $\nu(C=C)$ of reduced heme a_3 (Heibel et al., 1993; Hellwig et al., 1999a; Dodia et al., 2013). The small peak shift of 3 cm^{-1} indicates that the heme a_3 ring reacts in response to the change in the internal electric field as a result of the reduction of heme a.

The low-energy region between $1,570$ and $1,540\text{ cm}^{-1}$ shows mainly two strong bands, a broad negative band at $1,563\text{ cm}^{-1}$ and a positive one at $1,547\text{ cm}^{-1}$. The latter and the formyl band at $1,662\text{ cm}^{-1}$ are the only two bands that do not exhibit a strong change in absorbance between R_2CO and R_4CO , which links their appearance to heme a_3 reduction. While isotopic labeling hinted toward the asymmetric carboxylate stretching mode $\nu_{as}(COO^-)$ of the deprotonated $PRDa_3$ (Behr et al., 1998, 2000), resonance Raman experiments have shown that bands at similar positions can also be assigned to the heme a ν_{11} vibration (Heibel et al., 1993; Kozuch et al., 2013). The assignment of the negative band at $1,563\text{ cm}^{-1}$ is ambiguous as well: Resonance Raman studies assign this frequency to the ν_{38x} mode of oxidized heme a_3 (Kozuch et al., 2013); however, the band could also be due to the $\nu_{as}(COO^-)$ mode of heme propionate(s) (Hellwig et al., 1999a,b) in the O state. In this scenario, proton transfer between heme propionic acid side chains in the $O \rightarrow R_2CO$ transition would justify the presence of the $1,563$ and $1,547\text{ cm}^{-1}$ bands in our spectra.

DISCUSSION

We performed ATR/FTIR spectroelectrochemistry on lipid-reconstituted CcO in the presence of CO. Exploiting the CO ligand as a VSE probe, we identified three states corresponding to different electrode potentials applied to the protein film (**Figure 5**): (I) the fully reduced state R_4CO (in which all four metal centers are reduced), (II) the mixed-valence state R_2CO with two electrons (reduced heme a_3 and Cu_B), and (III) the oxidized state O (all four metal centers are oxidized) in which CO is dissociated from the BNC. It was not possible to trap a pure R_2CO state under our experimental conditions, and we can also not exclude a possible one-electron component



in what we denote as the O state. It is important to notice that this hypothetical one-electron-reduced state, analogous to the E state of CcO under turnover conditions, would imply the partial reduction of Cu_B at the BNC (Belevich and Verkhovsky, 2008). However, all four redox centers of CcO are oxidized at the potentials higher than +300 mV vs. Ag/AgCl (ca. +500 mV vs. SHE) (Wilson et al., 1976). It is also evident that the midpoint potentials derived from sigmoidal fitting (102 and 237 mV, **Figure 3C**) and global fitting of the difference spectra (98 and 228 mV, **Supplementary Figure 4A**) are identical within the error margin (34 and 25 mV, respectively, **Supplementary Figure 4A**). Other studies (Gorbikova et al., 2006) also show a possible intermediate state by following oxidation of the cofactors through specific marker bands. In fact, the potential traces of the two CO peaks exhibit similar behavior as vibrational bands found in potentiometric titrations of PdCcO in the absence of CO (Hellwig et al., 1999a; Gorbikova et al., 2006). The difference between the midpoint potentials of CO-bound CcO and the potentials relative to the CO-free enzyme is small [23 mV (Dodson et al., 1996)]. However, the midpoint potential of the R₄CO → R₂CO transition is higher in RsCcO than reported (Hellwig et al., 1999a; Gorbikova et al., 2006). We relate these differences to the probe's selectivity, allowing us to observe electrochemical transitions whose trace is otherwise very convoluted.

We quantified the local electric field by measuring the frequency shift of the CO vibration and by performing electrostatic computations. We derived a +2.9 MV/cm change in the total electric field projected on the CO bond, induced by the redox transition from R₄CO to R₂CO (in which heme a and

Cu_A are oxidized). As elegantly elaborated by Kaila et al. (2010), electric fields can orient charged and polar residues (including water molecules) to generate a proton pathway with low energetic barriers. Thus, the quantification of the electric field magnitude achieved here represents an essential requirement to gauge the driving force of proton transfer in the vicinity of the BNC.

The primary cause of the Stark shift can be attributed to the redox transition of heme a, which contributes with an electric field of +0.82 MV/cm projected onto the CO ligand according to the electrostatic calculations. In comparison, the simultaneous oxidation of the distant Cu_A accounts for a much smaller extent of +0.13 MV/cm. These redox transitions can induce further protonation and/or structural changes whose electrostatic contributions are shown in **Table 1**. Combining the electric field changes due to oxidation of heme a and Cu_A and simultaneous protonation of PRA₃ (+3.12 or +2.59 MV/cm for CO angles of 169° or 180°, respectively) agrees with the change in the electric field that was experimentally determined (+2.9 MV/cm). Comparing this result with the behavior of the band at 1,677 cm⁻¹ in our spectra, we may refer to PRA₃ as a deprotonation site in the physiological O → R transition, most likely involving E286 as a relay site. Combining the oxidation of heme a with any other transition shown in **Table 1** results in less agreement with our experimental findings. For example, the computed values of the change in the electric field related to changes in the protonation state of E286 are negative, which indicates that this transition does not take place. The E286 ν(C=O) peak shift between the oxidized state and the two reduced states corroborates this prediction. This observation also excludes the possibility of a protonation/deprotonation event,

since the carboxylate group has symmetric and antisymmetric COO^- stretching vibrations that appear at around 1,570 and 1,400 cm^{-1} (Zscherp et al., 1999; Barth, 2007). The collected data hint at E286 being protonated in all the observed states. Even though our sample does not undergo catalytic turnover in the absence of O_2 , we think that the same assumptions apply to the physiological O and R_2 states of CcO, as well as to the R_4 state (Nyquist et al., 2003).

The major change that E286 undergoes upon reduction is a change in its hydrogen-bonding environment (Nyquist et al., 2004; Barth, 2007). It has been recently computed that E286 is connected to a water cavity when it adopts the “up” conformation (Son et al., 2017). In the “down” conformation, on the contrary, it is close to the terminal water molecule of the D-pathway [W6560 in oxidized RsCcO crystals (Tomita et al., 2009)]. Our data suggest a picture in which E286 is hydrogen bonded either to one of such water molecules, or to some unidentified residue. The hydrogen bond is weakest in the oxidized state and gets progressively stronger when lowering the electrode potential [redshifts of the $\nu(\text{C}=\text{O})$ peak are 6 cm^{-1} and 11 cm^{-1} for the R_2CO and R_4CO states, respectively]. Depending on the exact origin of this shift, the interpretation hints to E286 changing its conformation from “up” to “down” during oxidation of heme a, or *vice versa*. The hydrogen-bonding environment experienced by E286 may also depend on its conformation relative to the propionic acid side chain of heme a_3 . These findings add to the current knowledge (Nyquist et al., 2001, 2003; Heitbrink et al., 2002) and suggest that the reduction of heme a_3 (happening after the first proton pumping step following the E state, under physiological conditions) already influences the hydrogen-bonding environment of E286.

Finally, the potentiostatic FTIR difference spectra in D_2O show very few band shifts that are typical for protein backbone deuteration. Adding our interpretation and previous assignments to this fact, we suppose that almost all the assigned bands appearing in the window between 1,710 and 1,500 cm^{-1} in **Figure 4** are either cofactor bands or representatives of “buried” backbone motifs. However, residues in the vicinity of the BNC which are not accessible to bulk solvent ought to be scarce when CcO cycles through reduced and oxidized states (Busenlehner et al., 2006). Our observations relate cofactor bands to the redox transition responsible for their appearance and are especially interesting when analyzing bands that have previously been ambiguous (Hellwig et al., 1999a,b; Dodia et al., 2013), as they indicate that the $\text{C}=\text{O}$ -stretching features in the area between 1,710 and 1,640 cm^{-1} are most likely due to propionic acid or formyl bands. Moreover, bands below 1,710 cm^{-1} do not show frequency shifts between the two reduced states, with the vinyl mode of reduced heme a_3 found at 1,615 and 1,618 cm^{-1} being the only exception. The exact reason for this shift is currently unknown, but it is reasonable to assume that the protonation state of PRAa_3 can change the coupling mode of the $\nu(\text{C}\alpha=\text{C}\beta)$ of the same porphyrin ring, influencing its vibrational frequency. There are only two bands that correlate with heme a_3 reduction, which are the bands at 1,662 and 1,547 cm^{-1} .

While it is difficult to assign the latter, the former is due to the formyl $\text{C}=\text{O}$ stretching vibration of reduced heme a_3 . In fact, this is the only intense band at a frequency compatible with $\text{C}=\text{O}$ groups among the ones that are associated with the transition at +237 mV, and it lacks a respective shifted band in the oxidized state. This feature may be representative of a strong perturbation of the environment close to the formyl side chain of heme a_3 upon reduction (which takes place during the physiological $\text{E} \rightarrow \text{R}$ transition). It is not immediately clear whether the band at 1,643 cm^{-1} correlates with the same redox transition, or if it is indicative of a separate process involving only the formyl side chain of heme a. In general, our data show that the ligand interaction sphere of heme a_3 is already disturbed in the $\text{O} \rightarrow \text{R}_2\text{CO}$ transition, with possible propionate protonation/deprotonation events indicative of proton transfer close to the cofactor. This scenario would not involve heme a but only heme a_3 . Its formyl side chain may be responsive to these changes, resulting in the 1,662 cm^{-1} positive band. Adding this information to the probable protonation of PRAa_3 upon heme a oxidation, our analysis supports the assignment of the proton-loading site to the propionates of heme a_3 (Behr et al., 1998; Kaila et al., 2011; Sezer et al., 2017).

DATA AVAILABILITY STATEMENT

The original contributions presented in the study are included in the article/**Supplementary Material**, further inquiries can be directed to the corresponding author.

AUTHOR CONTRIBUTIONS

FB performed FTIR measurements, analyzed the spectroscopic data, and wrote the paper. JD constructed the CcO models and computed the electric field changes. JK, HM, and STS analyzed and discussed the data. E-WK and JH conceived the study. All authors discussed the results and contributed to the writing of the paper.

FUNDING

This work was funded by the Deutsche Forschungsgemeinschaft (SFB 1078, project A1 and C2).

ACKNOWLEDGMENTS

We thank Jessica Stapel for sample preparation and Petko Chernev (Uppsala Universitet) for kindly providing data analysis software. We acknowledge support by the Open Access Publication Initiative of Freie Universität Berlin.

SUPPLEMENTARY MATERIAL

The Supplementary Material for this article can be found online at: <https://www.frontiersin.org/articles/10.3389/fchem.2021.669452/full#supplementary-material>

REFERENCES

- Ädelroth, P., and Gennis RB, Brzezinski, P. (1998). Role of the pathway through K(I-362) in proton transfer in cytochrome *c* oxidase from *R. sphaeroides*. *Biochemistry* 37, 2470–2476. doi: 10.1021/bi971813b
- Ädelroth, P., Svensson Ek, M., Mitchell, D. M., Gennis, R. B., and Brzezinski, P. (1997). Glutamate 286 in cytochrome *aa₃* from *Rhodobacter sphaeroides* is involved in proton uptake during the reaction of the fully-reduced enzyme with dioxygen. *Biochemistry* 36, 13824–13829. doi: 10.1021/bi9629079
- Babcock, G. T., and Salmeen, I. (1979). Resonance raman spectra and optical properties of oxidized cytochrome oxidase. *Biochemistry* 18, 2493–2498. doi: 10.1021/bi00579a009
- Barth, A. (2007). Infrared spectroscopy of proteins. *Biochim. Biophys. Acta* 1767, 1073–1101. doi: 10.1016/j.bbabi.2007.06.004
- Behr, J., Hellwig, P., Mänte, W., and Michel, H. (1998). Redox dependent changes at the heme propionates in cytochrome *c* oxidase from *Paracoccus denitrificans*: direct evidence from FTIR difference spectroscopy in combination with heme propionate ¹³C labeling. *Biochemistry* 37, 7400–7406. doi: 10.1021/bi9731697
- Behr, J., Michel, H., Mänte, W., and Hellwig, P. (2000). Functional properties of the heme propionates in cytochrome *c* oxidase from *Paracoccus denitrificans*. Evidence from FTIR difference spectroscopy and site-directed mutagenesis. *Biochemistry* 39, 1356–1363. doi: 10.1021/bi991504g
- Belevich, I., Bloch, D. A., Belevich, N., Wikström, M., and Verkhovsky, M. I. (2007). Exploring the proton pump mechanism of cytochrome *c* oxidase in real time. *Proc. Natl. Acad. Sci. U.S.A.* 104, 2685–2690. doi: 10.1073/pnas.0608794104
- Belevich, I., and Verkhovsky, M. I. (2008). Molecular mechanism of proton translocation by cytochrome *c* oxidase. *Antiox Redox Signal.* 10, 1–30. doi: 10.1089/ars.2007.1705
- Belevich, I., Verkhovsky, M. I., and Wikström, M. (2006). Proton-coupled electron transfer drives the proton pump of cytochrome *c* oxidase. *Nature* 440, 829–832. doi: 10.1038/nature04619
- Boxer, S. G. (2009). Stark realities. *J. Phys. Chem. B* 113, 2972–2983. doi: 10.1021/jp8067393
- Brooks, B. R., Brooks, I. I. C. L., Mackerell, A. D. Jr., Nilsson, L., Petrella, R. J., Roux, B., et al. (2009). CHARMM: the biomolecular simulation program. *J. Comput. Chem.* 30, 1545–1614. doi: 10.1002/jcc.21287
- Brunori, M. (2001). Nitric oxide, cytochrome-*c* oxidase and myoglobin. *Trends Biochem. Sci.* 26, 21–23. doi: 10.1016/S0968-0004(00)01698-4
- Brzezinski, P., and Gennis, R. B. (2008). Cytochrome *c* oxidase: exciting progress and remaining mysteries. *J. Bioenerg. Biomemb.* 40, 521–531. doi: 10.1007/s10863-008-9181-7
- Brzezinski, P., and Malmström, B. G. (1985). The reduction of cytochrome *c* oxidase by carbon monoxide. *FEBS Lett.* 187, 111–114. doi: 10.1016/0014-5793(85)81224-2
- Busenlehner, L. S., Salomonsson, L., Brzezinski, P., and Armstrong, R. N. (2006). Mapping protein dynamics in catalytic intermediates of the redox-driven proton pump cytochrome *c* oxidase. *Proc. Natl. Acad. Sci. U.S.A.* 103, 15398–15403. doi: 10.1073/pnas.0601451103
- Cooper, C. E., and Brown, G. C. (2008). The inhibition of mitochondrial cytochrome oxidase by the gases carbon monoxide, nitric oxide, hydrogen cyanide and hydrogen sulfide: chemical mechanism and physiological significance. *J. Bioenerg. Biomemb.* 40:533. doi: 10.1007/s10863-008-9166-6
- Dodia, R., Maréchal, A., Bettini, S., Iwaki, M., and Rich, P. R. (2013). IR signatures of the metal centres of bovine cytochrome *c* oxidase: assignments and redox-linkage. *Biochem. Soc. Trans.* 41, 1242–1248. doi: 10.1042/BST20130087
- Dodson, E. D., Zhao, X.-J., Caughey, W., and Elliott, M. C. (1996). Redox dependent interactions of the metal sites in carbon monoxide-bound cytochrome *c* oxidase monitored by infrared and UV/visible spectroelectrochemical methods. *Biochemistry* 35, 444–452. doi: 10.1021/bi951313n
- Dürr, K. L., Koepke, J., Hellwig, P., Müller, H., Angerer, H., Peng, G., et al. (2008). A D-pathway mutation decouples the *Paracoccus denitrificans* cytochrome *c* oxidase by altering the side-chain orientation of a distant conserved glutamate. *J. Mol. Biol.* 384, 865–877. doi: 10.1016/j.jmb.2008.09.074
- Fried, S. D., and Boxer, S. G. (2015). Measuring electric fields and noncovalent interactions using the vibrational stark effect. *Acc. Chem. Res.* 48, 998–1006. doi: 10.1021/ar500464j
- García-Horsman, J. A., Barquera, B., Rumbley, J., Ma, J., and Gennis, R. B. (1994). The superfamily of heme-copper respiratory oxidases. *J. Bacteriol.* 176, 5587–5600. doi: 10.1128/JB.176.18.5587-5600.1994
- Gibson, Q., and Greenwood, C. (1963). Reactions of cytochrome oxidase with oxygen and carbon monoxide. *Biochem. J.* 86:541. doi: 10.1042/bj0860541
- Gorbikova, E. A., Vuorilehto, K., Wikström, M., and Verkhovsky, M. I. (2006). Redox titration of all electron carriers of cytochrome *c* oxidase by fourier transform infrared spectroscopy. *Biochemistry* 45, 5641–5649. doi: 10.1021/bi060257v
- Greenwood, C., Wilson, M. T., and Brunori, M. (1974). Studies on partially reduced mammalian cytochrome oxidase. Reactions with carbon monoxide and oxygen. *Biochem. J.* 137, 205–215. doi: 10.1042/bj1370205
- Heibel, G. E., Hildebrandt, P., Ludwig, B., Steinruecke, P., Soulimane, T., and Buse, G. (1993). Comparative resonance raman study of cytochrome *c* oxidase from beef heart and *Paracoccus denitrificans*. *Biochemistry* 32, 10866–10877. doi: 10.1021/bi00091a042
- Heitbrink, D., Sigurdson, H., Bolwien, C., Brzezinski, P., and Heberle, J. (2002). Transient binding of CO to Cu_B in cytochrome *c* oxidase is dynamically linked to structural changes around a carboxyl group: a time-resolved step-scan fourier transform infrared investigation. *Biophys. J.* 82(1 Pt 1), 1–10. doi: 10.1016/S0006-3495(02)75368-X
- Hellwig, P., Behr, J., Ostermeier, C., Richter, O.-M. H., Pfützner, U., Odenwald, A., et al. (1998). Involvement of glutamic acid 278 in the redox reaction of the cytochrome *c* oxidase from *Paracoccus denitrificans* investigated by FTIR spectroscopy. *Biochemistry* 37, 7390–7399. doi: 10.1021/bi9725576
- Hellwig, P., Grzybek, S., Behr, J., Ludwig, B., Michel, H., and Mänte, W. (1999a). Electrochemical and ultraviolet/visible/infrared spectroscopic analysis of heme *a* and *a₃* redox reactions in the cytochrome *c* oxidase from *Paracoccus denitrificans*: separation of heme *a* and *a₃* contributions and assignment of vibrational modes. *Biochemistry* 38, 1685–1694. doi: 10.1021/bi982282+
- Hellwig, P., Soulimane, T., Buse, G., and Mänte, W. (1999b). Similarities and dissimilarities in the structure-function relation between the cytochrome *c* oxidase from bovine heart and from *Paracoccus denitrificans* as revealed by FT-IR difference spectroscopy. *FEBS Lett.* 458, 83–86. doi: 10.1016/S0014-5793(99)01133-3
- Hill, B. C. (1993). The sequence of electron carriers in the reaction of cytochrome *c* oxidase with oxygen. *J. Bioenerg. Biomemb.* 25, 115–120. doi: 10.1007/BF00762853
- Hosler, J. P., Fetter, J., Tecklenburg, M., Espe, M., Lerma, C., and Ferguson-Miller, S. (1992). Cytochrome *aa₃* of *Rhodobacter sphaeroides* as a model for mitochondrial cytochrome *c* oxidase. Purification, kinetics, proton pumping, and spectral analysis. *J. Biol. Chem.* 267, 24264–24272. doi: 10.1016/S0021-9258(18)35760-0
- Hübner, W., and Mantsch, H. H. (1991). Orientation of specifically ¹³C=O labeled phosphatidylcholine multilayers from polarized attenuated total reflection FT-IR spectroscopy. *Biophys. J.* 59, 1261–1272. doi: 10.1016/S0006-3495(91)82341-4
- Iwaki, M., and Rich, P. R. (2007). An IR study of protonation changes associated with heme–heme electron transfer in bovine cytochrome *c* oxidase. *J. Am. Chem. Soc.* 129, 2923–2929. doi: 10.1021/ja067779i
- Jain, A., and Kassner, R. (1984). Cyanate binding to the ferric heme octapeptide from cytochrome *c*. A model for anion binding to high spin ferric hemoproteins. *J. Biol. Chem.* 259, 10309–10314. doi: 10.1016/S0021-9258(18)90965-8
- Kaila, V. R., Sharma, V., and Wikström, M. (2011). The identity of the transient proton loading site of the proton-pumping mechanism of cytochrome *c* oxidase. *Biochim. Biophys. Acta* 1807, 80–84. doi: 10.1016/j.bbabi.2010.08.014
- Kaila, V. R., Verkhovsky, M. I., Hummer, G., and Wikström, M. (2008). Glutamic acid 242 is a valve in the proton pump of cytochrome *c* oxidase. *Proc. Natl. Acad. Sci. U.S.A.* 105, 6255–6259. doi: 10.1073/pnas.0800770105
- Kaila, V. R., Verkhovsky, M. I., and Wikström, M. (2010). Proton-coupled electron transfer in cytochrome oxidase. *Chem. Rev.* 110, 7062–7081. doi: 10.1021/cr1002003
- Kieseritzky, G., and Knapp, E. W. (2008). Optimizing pKa computation in proteins with pH adapted conformations. *Proteins* 71, 1335–1348. doi: 10.1002/prot.21820
- Koutsoumpakis, C., Kolaj-Robin, O., Soulimane, T., and Varotsis, C. (2011). Probing protonation/deprotonation of tyrosine residues in cytochrome *ba₃* oxidase from *Thermus thermophilus* by time-resolved step-scan

- fourier transform infrared spectroscopy. *J. Biol. Chem.* 286, 30600–30605. doi: 10.1074/jbc.M111.252213
- Kozuch, J., von der Hocht, I., Hilbers, F., Michel, H., and Weidinger, I. M. (2013). Resonance raman characterization of the ammonia-generated oxo intermediate of cytochrome *c* oxidase from *Paracoccus denitrificans*. *Biochemistry* 52, 6197–6202. doi: 10.1021/bi400535m
- Krazel, A., and Bal, W. (2004). A formula for correlating pKa values determined in D₂O and H₂O. *J. Inorg. Biochem.* 98, 161–166. doi: 10.1016/j.jinorgbio.2003.10.001
- Lorenz-Fonfria, V. A. (2020). Infrared difference spectroscopy of proteins: from bands to bonds. *Chem. Rev.* 120, 3466–3576. doi: 10.1021/acs.chemrev.9b00449
- Meyer, T., and Knapp, E.-W. (2015). pK_a values in proteins determined by electrostatics applied to molecular dynamics trajectories. *J. Chem. Theory Comput.* 11, 2827–2840. doi: 10.1021/acs.jctc.5b00123
- Michel, H., Behr, J., Harrenga, A., and Kannt, A. (1998). Cytochrome *c* oxidase: structure and spectroscopy. *Annu. Rev. Biophys. Biomol. Struct.* 27, 329–356. doi: 10.1146/annurev.biophys.27.1.329
- Mitchell, D. M., Shapleigh, J. P., Archer, A. M., Alben, J. O., and Gennis, R. B. (1996). A pH-dependent polarity change at the binuclear center of reduced cytochrome *c* oxidase detected by FTIR difference spectroscopy of the CO adduct. *Biochemistry* 35, 9446–9450. doi: 10.1021/bi960392f
- Mitchell, P. (1966). Chemiosmotic coupling in oxidative and photosynthetic phosphorylation. *Biol. Rev. Camb. Philos. Soc.* 41, 445–501. doi: 10.1111/j.1469-185X.1966.tb01501.x
- Mitchell, R., and Rich, P. R. (1994). Proton uptake by cytochrome *c* oxidase on reduction and on ligand binding. *Biochim. Biophys. Acta* 1186, 9–26. doi: 10.1016/0005-2728(94)90130-9
- Muramoto, K., Ohta, K., Shinzawa-Itōh, K., Kanda, K., Taniguchi, M., Nabekura, H., et al. (2010). Bovine cytochrome *c* oxidase structures enable O₂ reduction with minimization of reactive oxygens and provide a proton-pumping gate. *Proc. Natl. Acad. Sci. U.S.A.* 107, 7740–7745. doi: 10.1073/pnas.0910410107
- Namslauer, A., Brändén, M., and Brzezinski, P. (2002). The rate of internal heme-heme electron transfer in cytochrome *c* oxidase. *Biochemistry* 41, 10369–10374. doi: 10.1021/bi025976y
- Nyquist, R. M., Ataka, K., and Heberle, J. (2004). The molecular mechanism of membrane proteins probed by evanescent infrared waves. *ChemBiochem* 5, 431–436. doi: 10.1002/cbic.200300687
- Nyquist, R. M., Heitbrink, D., Bolwien, C., Gennis, R. B., and Heberle, J. (2003). Direct observation of protonation reactions during the catalytic cycle of cytochrome *c* oxidase. *Proc. Natl. Acad. Sci. U.S.A.* 100:8715. doi: 10.1073/pnas.1530408100
- Nyquist, R. M., Heitbrink, D., Bolwien, C., Wells, T. A., Gennis, R. B., and Heberle, J. (2001). Perfusion-induced redox differences in cytochrome *c* oxidase: ATR/FT-IR spectroscopy. *FEBS Lett.* 505, 63–67. doi: 10.1016/S0014-5793(01)02769-7
- Park, E. S., Andrews, S. S., Hu, R. B., and Boxer, S. G. (1999). Vibrational stark spectroscopy in proteins: a probe and calibration for electrostatic fields. *J. Phys. Chem. B* 103, 9813–9817. doi: 10.1021/jp992329g
- Pereira, M. M., Santana, M., and Teixeira, M. (2001). A novel scenario for the evolution of haem-copper oxygen reductases. *Biochim. Biophys. Acta* 1505, 185–208. doi: 10.1016/S0005-2728(01)00169-4
- Popović, D. M., Zarić, S. D., Rabenstein, B., and Knapp, E.-W. (2001). Artificial cytochrome *b*: computer modeling and evaluation of redox potentials. *J. Am. Chem. Soc.* 123, 6040–6053. doi: 10.1021/ja003878z
- Qin, L., Hiser, C., Mulichak, A., Garavito, R. M., and Ferguson-Miller, S. (2006). Identification of conserved lipid/detergent-binding sites in a high-resolution structure of the membrane protein cytochrome *c* oxidase. *Proc. Natl. Acad. Sci. U.S.A.* 103, 16117–16122. doi: 10.1073/pnas.0606149103
- Robinson, N. C., and Capaldi, R. A. (1977). Interaction of detergents with cytochrome *c* oxidase. *Biochemistry* 16, 375–381. doi: 10.1021/bi00622a006
- Schäfer, J., Dawitz, H., Ott, M., and Ädelroth, P., Brzezinski P (2018). Regulation of cytochrome *c* oxidase activity by modulation of the catalytic site. *Sci. Rep.* 8, 1–10. doi: 10.1038/s41598-018-29567-4
- Schleeger, M., Wagner, C., Vellekoop, M. J., Lendl, B., and Heberle, J. (2009). Time-resolved flow-flash FT-IR difference spectroscopy: the kinetics of CO photodissociation from myoglobin revisited. *Anal. Bioanal. Chem.* 394, 1869–1877. doi: 10.1007/s00216-009-2871-0
- Schneider, S. H., and Boxer, S. G. (2016). Vibrational stark effects of carbonyl probes applied to reinterpret IR and raman data for enzyme inhibitors in terms of electric fields at the active site. *J. Phys. Chem. B* 120, 9672–9684. doi: 10.1021/acs.jpcc.6b08133
- Senger, M., Laun, K., Wittkamp, F., Duan, J., Haumann, M., Happe, T., et al. (2017). Proton-coupled reduction of the catalytic [4Fe-4S] cluster in [FeFe]-hydrogenases. *Angew. Chem. Int.* 56, 16503–16506. doi: 10.1002/anie.201709910
- Sezer, M., Kiel, P., Kuhlmann, U., Mohrmann, H., Schulz, C., Heinrich, D., et al. (2015). Surface enhanced resonance Raman spectroscopy reveals potential induced redox and conformational changes of cytochrome *c* oxidase on electrodes. *J. Phys. Chem. B* 119, 9586–9591. doi: 10.1021/acs.jpcc.5b03206
- Sezer, M., Woelke, A.-L., Knapp, E. W., Schlesinger, R., Mroginski, M. A., and Weidinger, I. M. (2017). Redox induced protonation of heme propionates in cytochrome *c* oxidase: Insights from surface enhanced resonance Raman spectroscopy and QM/MM calculations. *Biochim. Biophys. Acta* 1858, 103–108. doi: 10.1016/j.bbabi.2016.10.009
- Sharpe, M. A., Krzyaniak, M. D., Xu, S., McCracken, J., and Ferguson-Miller, S. (2008). EPR evidence of cyanide binding to the Mn (Mg) center of cytochrome *c* oxidase: support for Cu_A-Mg involvement in proton pumping. *Biochemistry* 48, 328–335. doi: 10.1021/bi801391r
- Son, C. Y., Yethiraj, A., and Cui, Q. (2017). Cavity hydration dynamics in cytochrome *c* oxidase and functional implications. *Proc. Natl. Acad. Sci. U.S.A.* 114, E8830–E8836. doi: 10.1073/pnas.1707922114
- Suydam, I. T., and Boxer, S. G. (2003). Vibrational stark effects calibrate the sensitivity of vibrational probes for electric fields in proteins. *Biochemistry* 42, 12050–12055. doi: 10.1021/bi0352926
- Tomita, A., Sato, T., Ichianagi, K., Nozawa, S., Ichikawa, H., Chollet, M., et al. (2009). Visualizing breathing motion of internal cavities in concert with ligand migration in myoglobin. *Proc. Natl. Acad. Sci. U.S.A.* 106, 2612–2616. doi: 10.1073/pnas.0807774106
- Voigt, P., and Knapp, E.-W. (2003). Tuning heme redox potentials in the cytochrome *c* subunit of photosynthetic reaction centers. *J. Biol. Chem.* 278, 51993–52001. doi: 10.1074/jbc.M307560200
- Welborn, V. V., and Head-Gordon, T. (2019). Fluctuations of electric fields in the active site of the enzyme ketosteroid isomerase. *J. Am. Chem. Soc.* 141, 12487–12492. doi: 10.1021/jacs.9b05323
- Wikstrom, M. K. F. (1977). Proton pump coupled to cytochrome *c* oxidase in mitochondria. *Nature* 266, 271–273. doi: 10.1038/266271a0
- Wilson, D. F., Erecińska, M., and Owen, C. S. (1976). Some properties of the redox components of cytochrome *c* oxidase and their interactions. *Arch. Biochem. Biophys.* 175, 160–172. doi: 10.1016/0003-9861(76)90495-1
- Woelke, A. L., Galstyan, G., Galstyan, A., Meyer, T., Heberle, J., and Knapp, E.-W. (2013). Exploring the possible role of Glu286 in CcO by electrostatic energy computations combined with molecular dynamics. *J. Phys. Chem. B* 117, 12432–12441. doi: 10.1021/jp407250d
- Woodruff, W. H., Dallinger, R. F., Antal, T. M., and Palmer, G. (1981). Resonance Raman spectroscopy of cytochrome oxidase using solet excitation: selective enhancement, indicator bands, and structural significance for cytochromes *a* and *a*₃. *Biochemistry* 20, 1332–1338. doi: 10.1021/bi00508a045
- Wu, Y., Fried, S. D., and Boxer, S. G. (2020). A preorganized electric field leads to minimal geometrical reorientation in the catalytic reaction of ketosteroid isomerase. *J. Am. Chem. Soc.* 142, 9993–9998. doi: 10.1021/jacs.0c00383
- Yoshikawa, S., Shinzawa-Itōh, K., Nakashima, R., Yaono, R., Yamashita, E., Inoue, N., et al. (1998). Redox-coupled crystal structural changes in bovine heart cytochrome *c* oxidase. *Science* 280, 1723–1729. doi: 10.1126/science.280.5370.1723
- Zawisza, I., Bin, X., and Lipkowski, J. (2007). Potential-driven structural changes in Langmuir–blodgett DMPC bilayers determined by in situ spectroelectrochemical PM IRRAS. *Langmuir* 23, 5180–5194. doi: 10.1021/la063190l
- Zscherp, C., Schlesinger, R., Tittor, J., Oesterhelt, D., and Heberle, J. (1999). *In situ* determination of transient pK_a changes of internal amino acids of

bacteriorhodopsin by using time-resolved attenuated total reflection Fourier-transform infrared spectroscopy. *Proc. Natl. Acad. Sci. U.S.A.* 96, 5498–5503. doi: 10.1073/pnas.96.10.5498

Conflict of Interest: The authors declare that the research was conducted in the absence of any commercial or financial relationships that could be construed as a potential conflict of interest.

Copyright © 2021 Baserga, Dragelj, Kozuch, Mohrmann, Knapp, Stripp and Heberle. This is an open-access article distributed under the terms of the Creative Commons Attribution License (CC BY). The use, distribution or reproduction in other forums is permitted, provided the original author(s) and the copyright owner(s) are credited and that the original publication in this journal is cited, in accordance with accepted academic practice. No use, distribution or reproduction is permitted which does not comply with these terms.



Ubiquinone Binding and Reduction by Complex I—Open Questions and Mechanistic Implications

Etienne Galemou Yoga^{1,2}, Jonathan Schiller^{1,2} and Volker Zickermann^{1,2*}

¹ Institute of Biochemistry II, University Hospital, Goethe University, Frankfurt, Germany, ² Centre for Biomolecular Magnetic Resonance, Institute for Biophysical Chemistry, Goethe University, Frankfurt, Germany

OPEN ACCESS

Edited by:

Petra Imhof,
University of Erlangen
Nuremberg, Germany

Reviewed by:

Leonid Sazanov,
Institute of Science and Technology
Austria (IST Austria), Austria
Freddy Fernandes Guimaraes,
Universidade Federal de Goiás, Brazil
Oscar Juarez,
Illinois Institute of Technology,
United States

*Correspondence:

Volker Zickermann
zickermann@med.uni-frankfurt.de

Specialty section:

This article was submitted to
Theoretical and Computational
Chemistry,
a section of the journal
Frontiers in Chemistry

Received: 26 February 2021

Accepted: 06 April 2021

Published: 30 April 2021

Citation:

Galemou Yoga E, Schiller J and
Zickermann V (2021) Ubiquinone
Binding and Reduction by Complex
I—Open Questions and Mechanistic
Implications. *Front. Chem.* 9:672851.
doi: 10.3389/fchem.2021.672851

NADH: ubiquinone oxidoreductase (complex I) is the first enzyme complex of the respiratory chain. Complex I is a redox-driven proton pump that contributes to the proton motive force that drives ATP synthase. The structure of complex I has been analyzed by x-ray crystallography and electron cryo-microscopy and is now well-described. The ubiquinone (Q) reduction site of complex I is buried in the peripheral arm and a tunnel-like structure is thought to provide access for the hydrophobic substrate from the membrane. Several intermediate binding positions for Q in the tunnel were identified in molecular simulations. Structural data showed the binding of native Q molecules and short chain analogs and inhibitors in the access pathway and in the Q reduction site, respectively. We here review the current knowledge on the interaction of complex I with Q and discuss recent hypothetical models for the coupling mechanism.

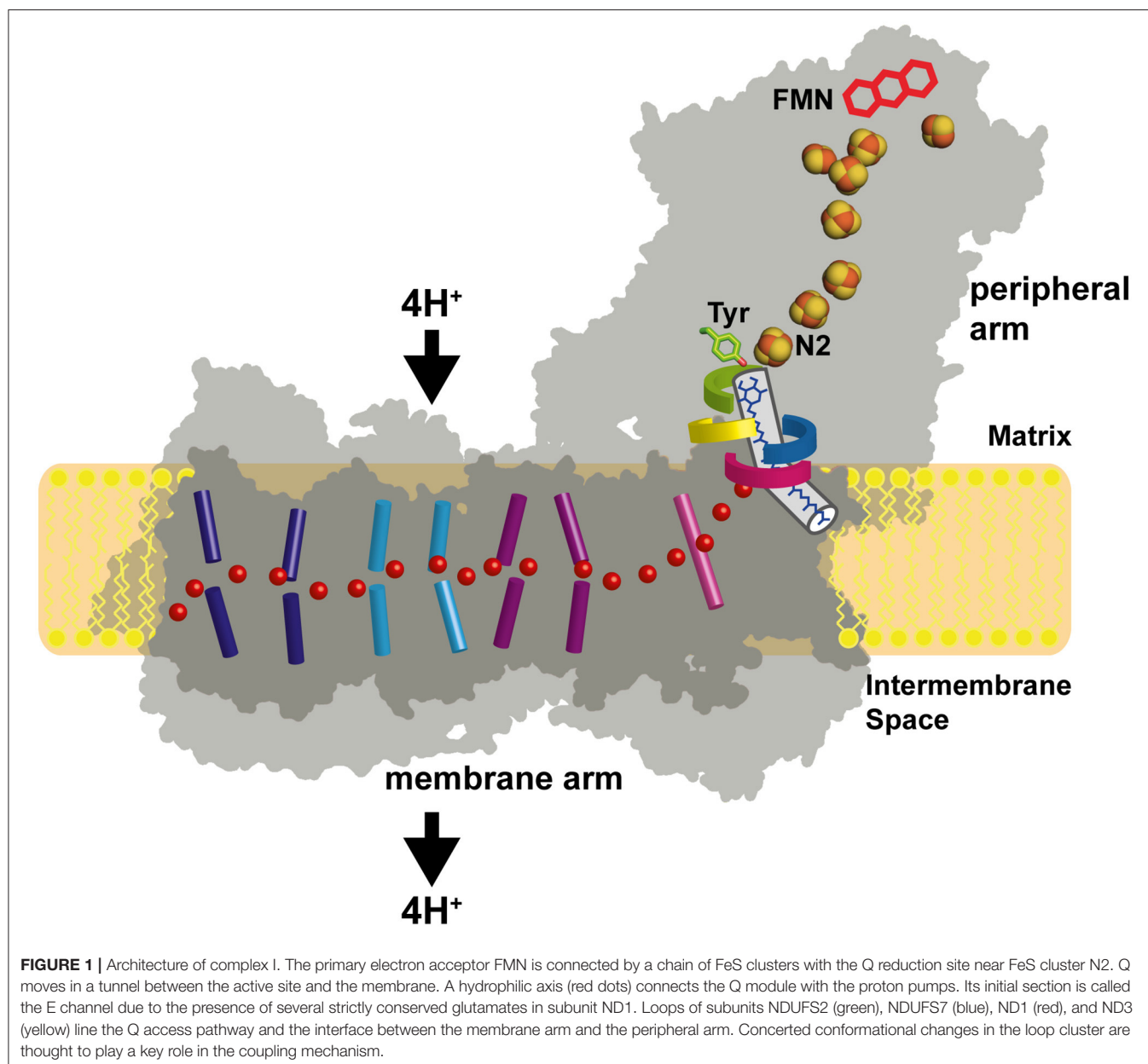
Keywords: respiratory chain, NADH dehydrogenase, oxidative phosphorylation, proton pumping, electron transfer, semiquinone, inhibitor

INTRODUCTION

Respiratory complex I (also known as NADH dehydrogenase or NDH-1) is a very large membrane protein found in the inner mitochondrial membrane and in the plasma membrane of aerobic bacteria (Hirst, 2013; Sazanov, 2015; Galemou Yoga et al., 2020a). Complex I couples electron transfer from NADH to quinone (Q) to the translocation of protons across the bioenergetic membrane. Note that some bacterial species utilize menaquinone instead of ubiquinone. With a pump stoichiometry of 4 H⁺ per NADH consumed, complex I contributes substantially to the proton motive force that drives ATP synthase. A large variety of compounds are known to inhibit complex I activity by interfering with Q reduction (Murai and Miyoshi, 2016). The catalytic reaction of complex I is fully reversible. In the presence of a reduced Q pool and a sufficiently high membrane potential, complex I can reduce NAD⁺ by reverse electron transfer (RET), e.g., during reperfusion after ischemia (Chouchani et al., 2014). Mitochondrial complex I from many species can switch reversibly from an active A-form to a deactive D-form (Kotlyar and Vinogradov, 1990). The A/D transition is thought to limit the release of detrimental oxygen species under conditions that promote RET (Drose et al., 2016). Complex I dysfunction is associated with neuromuscular and neurodegenerative diseases (Rodenburg, 2016; Fiedorczuk and Sazanov, 2018). The structure of complex I has been determined by x-ray crystallography (Baradaran et al., 2013; Zickermann et al., 2015) and by electron cryo-microscopy (cryo-EM) (Fiedorczuk et al., 2016; Zhu et al., 2016; Agip et al., 2019; Parey et al., 2019, 2020; Grba and Hirst, 2020; Kampjut and Sazanov, 2020; Soufari et al., 2020; Klusch et al., 2021). Cryo-EM structures of the related NADH dehydrogenase-like

(*ndh*) complex or “photosynthetic complex I” have been reported recently (Laughlin et al., 2019; Schuller et al., 2019; Pan et al., 2020). The L-shaped architecture of complex I is highly conserved and consists of a peripheral arm (PA) and a membrane arm (MA) (**Figure 1**). Fourteen complex I subunits are conserved from bacteria to human. These so-called central subunits harbor all bioenergetic core functions of the enzyme complex. Eukaryotic complex I is much larger than its bacterial counterpart and comprises some 30 additional accessory subunits. The central subunits can be divided into three functional modules. The NADH oxidation module (N module) and the ubiquinone reduction module (Q module) constitute the PA, whereas the proton pumping module (P module) forms the MA of the enzyme. Eight to nine FeS clusters are found in the PA depending

on the species. Seven of them connect the primary electron acceptor FMN to the Q reduction site, which is formed by the NDUFS2 and NDUFS7 subunits. Five FeS clusters typically give rise to electron paramagnetic resonance (EPR) signals, namely N1b, N2, N3, N4, and N5 (Ohnishi, 1998; Hirst and Roessler, 2016). Cluster N2 is the last cluster of the electron transfer chain in the PA and the immediate electron donor for Q. The membrane arm of complex I consists of seven central subunits. The three largest subunits ND2, ND4, and ND5 are related to each other and to subunits of bacterial Mrp type sodium proton antiporters (Mathiesen and Högerhäll, 2002). A hydrophilic axis (Baradaran et al., 2013) of titratable residues extending from subunit ND1 at the PA/MA interface to subunit ND5 at the distal end of the MA is thought to play a key role in energy transmission



from the Q module to the pump sites. Its connection with the Q module is also called the E channel due to the presence of strictly conserved glutamate residues in ND1. We have proposed that a concerted rearrangement of loops in subunits NDUFS2, ND1, and ND3 is critical for converting the energy released during Q reduction into pump strokes (Zickermann et al., 2015). Indeed, there is now increasing experimental evidence for conformational changes in the Q module and at the PA/MA interface (Agip et al., 2018; Cabrera-Orefice et al., 2018; Galemou Yoga et al., 2019; Grba and Hirst, 2020; Gutierrez-Fernandez et al., 2020; Kampjut and Sazanov, 2020).

In this review, we focus on the progress in the understanding of Q binding and reduction by complex I and its mechanistic implications.

THE Q REDUCTION SITE AND THE ACCESS PATHWAY FOR THE SUBSTRATE FROM THE MEMBRANE

The position of the Q reduction site in complex I is unique among energy-converting Q-reactive enzymes because cluster N2, the immediate electron donor for Q, resides at around 30 Å above the membrane surface (Figures 1, 2A) (Zickermann et al., 2003). Site-directed mutagenesis studies identified critical residues for Q and inhibitor binding in subunits NDUFS2 and NDUFS7 of the PA (Fendel et al., 2008; Tocilescu et al., 2010b; Sinha et al., 2015). A strictly conserved tyrosine of NDUFS2 was identified to bind the Q head group (Tocilescu et al., 2010a). The x-ray structure of complex I from *Thermus thermophilus* provided structural evidence for the coordination of Q by this tyrosine and by a histidine residue in the loop connecting the first and the second strand of the N-terminal β -sheet of NDUFS2 (Figure 2B) (Baradaran et al., 2013; Gutierrez-Fernandez et al., 2020). This Q binding site is connected by a ~ 35 Å long tunnel with the membrane bilayer (Baradaran et al., 2013). Site-directed mutagenesis of several residues in the Q access pathway drastically impaired Q reductase activity (Angerer et al., 2012). The entry portal of the Q tunnel is formed by transmembrane helices (TMHs) 1 and 6 and surface helix $\alpha 1$ of subunit ND1. Exchange of an alanine residue in helix $\alpha 1$ interferes with Q reduction kinetics (Zickermann et al., 1998) and is one of the most prevalent causes for Leber's hereditary optic neuropathy (Howell et al., 1991). It has recently been suggested that the entry to the tunnel is so narrow that a conformational change is required to enable the passage of a Q molecule (Wang et al., 2021). The middle of the tunnel is characterized by a highly charged region formed by residues of the TMH5-6 loop of subunit ND1 and a long loop of NDUFS7. Recently, site-directed mutagenesis combined with molecular dynamics simulations identified the critical role of the NDUFS7 loop for binding and the dynamics of Q in the tunnel (Galemou Yoga et al., 2019). Fedor et al. (2017) investigated the impact of the isoprenoid chain length on the kinetics of Q reduction and showed that in contrast to short-chain Q analogs, the dissociation of the long-chain Q10 is not rate-limiting. Movement in the narrow tunnel is thought to be guided by the ~ 50 -Å long isoprenoid chain of

Q10 that still reaches into the membrane bilayer when the Q head group is bound at its reduction site near cluster N2. The dynamics of Q in the tunnel have been further studied in three computational approaches (Warnau et al., 2018; Haapanen et al., 2019; Hoias Teixeira and Menegon Arantes, 2019). Free energy profiles consistently suggested the presence of up to five different transient Q binding sites along the Q tunnel. We here follow the nomenclature for intermediate binding sites introduced by Haapanen and Sharma (denoted by Arabic numbers in Figure 2) (Haapanen et al., 2019). Interestingly, these sites largely match with Q binding and in complex I structures determined under different conditions (denoted by Roman numbers in Figure 2). Site 1 is close to cluster N2 at the deepest end of the Q tunnel. Hydrogen bonding of the Q head group with the conserved tyrosine residue (Figure 2B) was reported for crystal structures of complex I from *T. thermophilus*, which was soaked with the short-chain Q analog decyl benzoquinone (DBQ) (Baradaran et al., 2013; Gutierrez-Fernandez et al., 2020). A distance of around 5 Å between the Q head group and tyrosine was recently observed in ovine complex I (Figure 2C) (Kampjut and Sazanov, 2020). This position is similar to the Q binding site identified in the cryo-EM structure of complex I from *Yarrowia lipolytica* captured under turnover (Parey et al., 2018). Although the Q head group has moved away from the tyrosine, this binding position is still assigned to site 1. The two different binding modes might reflect the reduction of Q (Kampjut and Sazanov, 2020) and/or different functional states of the site (see below) (Parey et al., 2018). Site 3 is located approximately in the middle of the Q tunnel and shows some correlation with a bound plastoquinone (PL9) modeled in the recent cryo-EM structure of photosynthetic complex I from *Thermosynechococcus elongatus* (Figure 2D) (Pan et al., 2020). Site 4 is situated in the charged region in the kink of the tunnel at the PA/MA interface. A native Q9 molecule has been observed at this position in complex I from *Y. lipolytica* purified in the detergent lauryl maltose neopentylglycol (LMNG) (Figure 2E) (Parey et al., 2019). Native Q molecules were found in a similar position in plant complex I (Soufari et al., 2020; Klusch et al., 2021). In contrast, a detergent molecule was modeled at this position in complex I from *Y. lipolytica* purified in dodecyl maltoside (DDM) (Grba and Hirst, 2020). Obviously, the more bulky LMNG is unable to enter the narrow opening of the Q tunnel. In the closed state of ovine complex I during turnover, a second DBQ molecule was modeled close to site 4 (Figure 2F). Note that the simultaneous presence of Q molecules in site 2 and site 4 seems only possible because DBQ was used as a substrate. Steric clashes between two Q10 molecules would render a comparable scenario highly unlikely under physiological conditions (Kampjut and Sazanov, 2020). In the open state of ovine complex I with NADH bound, a DBQ molecule was also observed in site 4. It is interesting to note the conformational change of the NDUFS7 loop in this structure (residue R₂ in Figure 2G). A rearrangement of this loop connected with Q dynamics has been proposed previously (Galemou Yoga et al., 2019). Site 5 is closer to the Q tunnel entrance and binding of Q in this site was observed in the open conformation of ovine complex I during turnover (Figure 2H) (Kampjut and Sazanov, 2020).

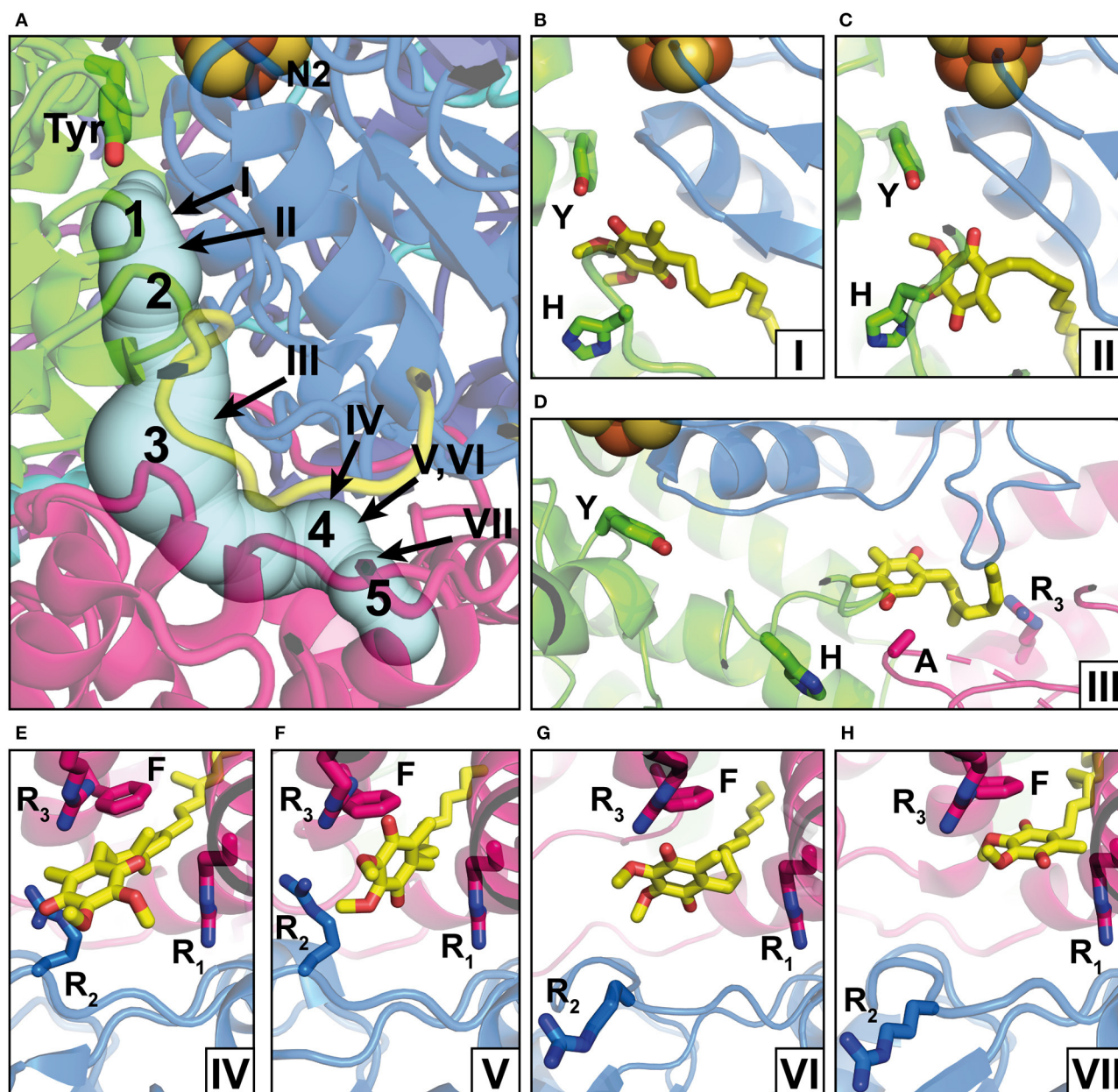


FIGURE 2 | Q binding positions. **(A)** The Q reduction site in the peripheral arm of complex I (PDB: 6RFR) is formed by subunits NDUFS2 (green) and NDUFS7 (blue). A tunnel for Q access from the membrane traverses subunit ND1 (pink). The tunnel was calculated using the CAVER3 software (Chovancova et al., 2012) (starting point conserved Y144, PDB: 6RFR, probe radius 1.3 Å). Intermediate Q binding positions determined by computational methods are indicated by Arabic numbers according to Haapanen et al. (2019). The positions of Q molecules (head group) modeled into X-ray or cryo-EM structures are indicated by Roman numbers and are shown in detailed views in separate panels; the direction of view is consistent for panels in the same row. **(B)** DBQ bound to complex I from *T. thermophilus* (PDB: 6IOD) (Y, Y87; H, H38); **(C)** DBQ bound to complex I from *Ovis aries* in the closed state during turnover (PDB: 6ZKC) (Y, Y108; H, H59); **(D)** PL9 bound to ndh complex I from *T. elongatus BP-1* (PDB: 6KHJ) (Y, Y72; H, H23; A, A237; R₃, R329); **(E)** Q9 bound to complex I from *Y. lipolytica* (PDB: 6RFR) (R₁, R27; R₂, R108, R₃, R297; F, F228); **(F)** DBQ bound to complex I from *O. aries* in the closed state during turnover (PDB: 6ZKC) (R₁, R25; R₂, R77, R₃, R274; F, F224); **(G)** DBQ bound to complex I from *O. aries* in the open state with NADH bound in the N module (PDB 6ZKH) (R₁, R25; R₂, R77, R₃, R274; F, F224); **(H)** DBQ bound to complex I from *O. aries* in the open state during turnover (PDB 6ZKD) (R₁, R25; R₂, R77, R₃, R274; F, F224).

Taken together, the evidence for a single narrow Q access pathway in complex I seems to be compelling. However, it should be noted that Uno et al. (2020) showed inhibitor-sensitive

reduction of Q analogs which are too bulky to enter the Q tunnel. It is currently unclear how these results can be reconciled with the structural data and more work is needed to resolve this issue.

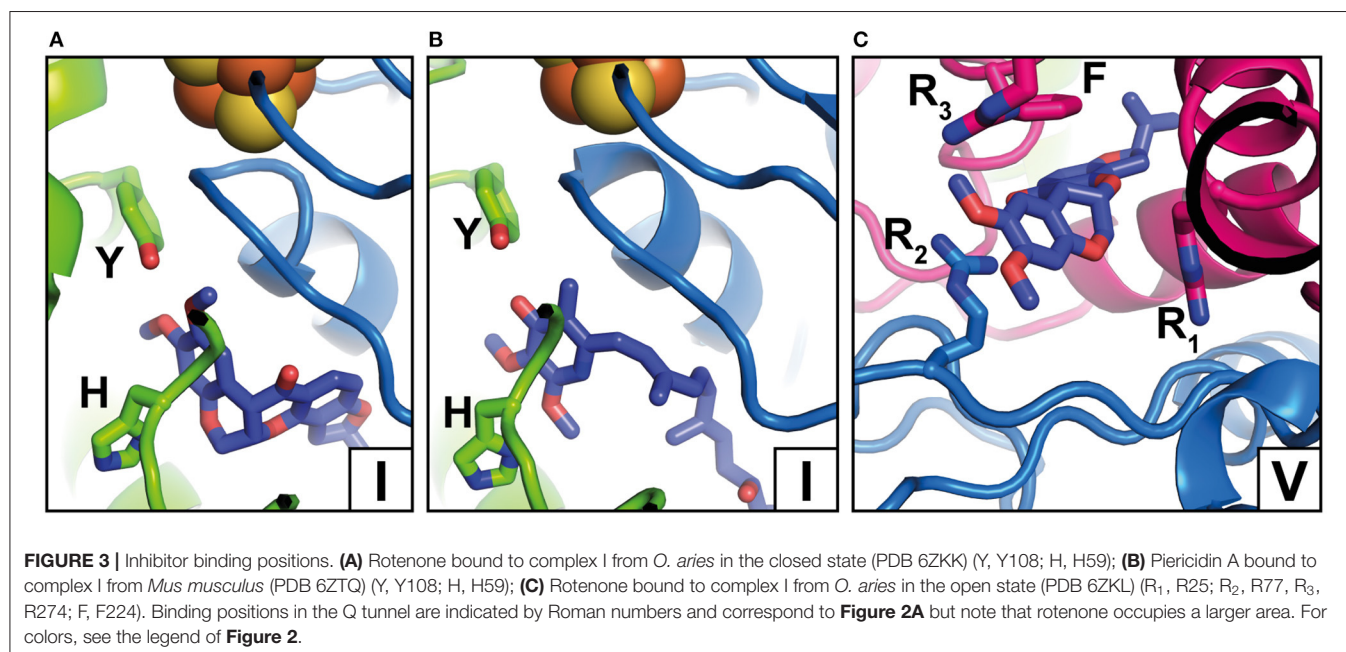
INHIBITOR BINDING SITES IN COMPLEX I

Complex I is known to be sensitive to a variety of inhibitors such as piericidins, rotenoids, or quinazolines (Degli Esposti, 1998; Murai and Miyoshi, 2016). Inhibitor binding to complex I was characterized by Scatchard analysis (Gutman et al., 1970), fluorescence quench titrations (Okun et al., 1999), mutagenesis (Darrouzet et al., 1998; Fendel et al., 2008; Tocilescu et al., 2010b; Sinha et al., 2015), and chemical biology approaches (Murai and Miyoshi, 2016; Uno et al., 2018). In recent years, an increasing number of complex I structures with bound inhibitors have become available (Figure 3) (Baradaran et al., 2013; Zickermann et al., 2015; Bridges et al., 2020; Gutierrez-Fernandez et al., 2020; Kampjut and Sazanov, 2020). The binding of three different inhibitors to complex I from *T. thermophilus* was recently analyzed by the Sazanov group (Gutierrez-Fernandez et al., 2020). The crystal structure of the enzyme with bound aureothin, pyridaben, and piericidin A revealed that these inhibitors bind at site 1 at the deepest end of the Q tunnel with their head groups interacting with the essential tyrosine residue near cluster N2. In the crystal structure of complex I from *Y. lipolytica*, the Q antagonist inhibitor 2-decyl-4-quinazoliny amine (DQA) was modeled near the $\beta 1\beta 2$ loop of the 49 kDa subunit (Zickermann et al., 2015). More recently, the Hirst group determined the cryo-EM structure of mouse complex I with bound piericidin A (Bridges et al., 2020). Interestingly, two piericidin molecules were found in the Q tunnel. The first inhibitor molecule was bound in site 1 (Figure 3B) in agreement with the position observed in complex I from *T. thermophilus*, while the second molecule was observed at site 4 (not shown). This suggests that the binding of piericidin is cooperative and that piericidin competes with Q for two different binding sites in the Q tunnel. Since rotenone is much bulkier than other Q site inhibitors such as DQA or Piericidin, it has been hypothesized that it cannot enter and

transit the narrow Q tunnel. However, in ovine complex I, two rotenone molecules were modeled in the Q tunnel at sites 1 (Figure 3A) and 4 (Figure 3C), respectively. Surprisingly, a third rotenone molecule was found in the ND4 subunit. Note that rotenone has been shown to inhibit Na^+/H^+ antiporter activity of inactive complex I (Roberts and Hirst, 2012). The binding of rotenone in the ND4 site could explain this observation. Rotenone binding in the Q tunnel suggests either that the entrance of the Q tunnel undergoes a reorganization to allow access of the bulky molecule or that rotenone can access the Q site *via* alternative pathways (Uno et al., 2018).

Q REDUCTION AND MECHANISTIC IMPLICATIONS

It is generally accepted that the energy for driving the proton pumps is released in the Q module and there is increasing evidence showing that the concerted rearrangement of a cluster of four loops surrounding the Q binding site and at the interface of PA and MA (Figure 1) is a central element of the coupling mechanism (Zickermann et al., 2015; Cabrera-Orefice et al., 2018; Parey et al., 2018; Galemou Yoga et al., 2019, 2020b; Kampjut and Sazanov, 2020). Full reduction of Q requires the uptake of two electrons and two protons. The delivery of electrons by a single electron donor and the observation of semiquinone radicals by EPR spectroscopy (Magnitsky et al., 2002) fostered the idea that reaction intermediates accumulate in a stepwise reaction sequence from Q to QH_2 . Early on, the formation of negatively charged quinone species has been proposed to be a key step in the catalytic cycle (Euro et al., 2008). However, note that more recently the assignment of semiquinone EPR signals to complex I has been questioned (Wright et al., 2020). In any case, the timing



of charge movements and charge compensation reactions in the Q reduction site is thought to be of utmost importance for the coupling mechanism. Over the years, a number of mechanistic schemes for redox-linked proton translocation have been proposed and a selection of recent models is discussed below.

The stabilization of negatively charged intermediates of Q redox chemistry ($Q^{\cdot-}$ and $QH^{\cdot-}$) plays a central role in the two-state stabilization-change mechanism proposed by Brandt (Brandt, 2011). This mechanism assumes two different functional states of the Q binding site. Electron transfer from cluster N2 to Q or $QH^{\cdot-}$ is only possible in the so-called E state. Proton transfer to $Q^{\cdot-}$ or $QH^{\cdot-}$ is only possible in the so-called P state. Stabilization of the anionic species generated in the E state provides the energy for proton pumping and is tightly linked with transition from the E to the P state. Full reduction of Q to QH_2 includes two E-to-P state transformations. This does not necessarily mean the execution of two separate pump events because transient storage of electrostatic or conformational energy would still allow pumping in a single step. The cycling between the E and P states is thought to involve a conformational rearrangement of the Q reduction site (Zickermann et al., 2015; Cabrera-Orefice et al., 2018). In fact, we have observed a different mode of Q binding in the cryo-EM structure of complex I from *Y. lipolytica* captured during steady-state activity as compared with Q binding observed in native complex I from *T. thermophilus* (Parey et al., 2018). Different conformations of the $\beta 1\beta 2$ loop of NDUFS2 in both structures further support the idea of a two-state mechanism associated with concerted loop rearrangements. Recent structures of ovine (Kampjut and Sazanov, 2020) and *T. thermophilus* (Gutierrez-Fernandez et al., 2020) confirm a different mode of Q binding to site 1 (Figures 2B,C). Nevertheless, more work is needed to establish an unequivocal link between the hypothetical E and P states with the protein structure.

Based on structural information with increasing resolution, molecular modeling and molecular dynamics simulation approaches have been established as powerful tools to study complex I function (Hummer and Wikström, 2016). In initial quantum mechanics/molecular mechanics (QM/MM) simulations of Q reduction, Sharma et al. (2015) placed a Q molecule into the Q reduction site and tested the impact of different Q redox states. In case simulations were performed with a Q^{2-} , i.e., assuming a two-electron reduction, fast proton transfer from the coordinating tyrosine and histidine residues was observed resulting in the formation of QH_2 . Prior to the proton transfer reaction, the histidine residue forms a salt bridge with a conserved aspartate residue of NDUFS2 that is located further toward subunit ND1. Breaking this ion pair by the redox-coupled proton transfer to Q triggers a conformational change of the $\beta 1\beta 2$ loop and subsequent flipping of the aspartate side chain is associated with rearrangements of conserved acidic residues in the ND1 subunit. Electrostatic pKa calculations suggested that these changes result in proton uptake from the N side and are thus thought to trigger the loading of the proton pump. Note that the initial formation of Q^{2-} is an essential prerequisite for

this mechanism because no proton transfer reactions were observed when oxidized Q or semiquinone states were modeled in the site.

In a later study, Gamiz-Hernandez et al. (2017) reported that the negative charge of cluster N2 shifts the midpoint potential of ubiquinone to a value in the range of -300 mV. This value is unusually low but is in agreement with the values reported earlier based on freeze-quench reduction kinetics (Verkhovskaya et al., 2008) and electrometric calculations (Verkhovskaya and Wikström, 2014). Remarkably, such a dramatic shift in potential would result in an annihilation of the redox potential difference between NADH and a Q molecule in site 1 and would consequently render Q reduction isoenergetic (Wikström et al., 2015; Gamiz-Hernandez et al., 2017; Kaila, 2018). Since, in this scenario, there is a redox potential difference between Q in site 1 and Q in the membrane ($+90$ mV), the release in free energy is thought to be associated with the movement of Q between site 1 and the exit of the Q tunnel (Wikström et al., 2015; Kaila, 2018). The binding of QH_2 close to the entry of the E channel, corresponding approximately to site 4, is suggested to “push” out protons previously loaded on acidic ND1 residues by the mechanism described above (Kaila, 2018; Mühlbauer et al., 2020). However, the molecular details of that energy conversion step remain obscure.

The association of complex I with a tightly bound Q molecule was first reported by Verkhovsky et al. (2012) for the enzyme from *Escherichia coli*. Later, native Q molecules were observed in the cryo-EM structures of complex I from *Y. lipolytica* (Parey et al., 2019) and *Brassica oleracea* (Soufari et al., 2020) and free energy calculations suggested that a large energy barrier restricts the movement of Q from the tunnel into the membrane bilayer (Warnau et al., 2018; Haapanen et al., 2019; Hoias Teixeira and Menegon Arantes, 2019). Wikström et al. (2015) have discussed the function of a Q molecule trapped in the Q tunnel to shuttle electrons between cluster N2 and a substrate Q molecule of the membrane Q pool. Haapanen et al. (2019) proposed that the two-electron reduction of a “shuttling Q” by FeS cluster N2 and proton transfer from the nearby tyrosine leads to the formation of a $QH^{\cdot-}$ molecule and tyrosinate in site 1. The repulsion of negative charges is thought to drive the movement of $QH^{\cdot-}$ to site 4. A substrate Q molecule in site 5 is reduced by electron transfer from the shuttling Q, while the proton released in site 4 is suggested to enter the E channel and to push out protons loaded on antiporter-like subunits. A shuttling Q is known to operate in photosystem II and in bacterial photoreaction centers (Müh et al., 2012). However, for complex I, unambiguous experimental evidence for a comparable mechanistic concept, e.g., the observation of a spin-spin coupled state between two SQ species by EPR spectroscopy, is still lacking.

The recent high-resolution structure of the ovine complex I reported by Kampjut and Sazanov (Kampjut and Sazanov, 2020) has offered a detailed view on Q binding and conformational changes in loops in the Q module and in ND1. Q reduction is thought to involve proton transfer from the Q coordinating histidine and tyrosine residues but in contrast to any previously proposed models, the authors of this study hypothesize that for the re-protonation of site 1, the protons are extracted

from two acidic residues in membrane-intrinsic subunit ND4L. The resulting negative charge in this subunit is suggested to subsequently trigger a series of events in the hydrophilic axis that ultimately lead to proton translocation to the P side. However, proton transfer from the membrane interior to site I is at variance with two recent studies, which identified putative proton access pathways from the N side (Galemou Yoga et al., 2020b; Grba and Hirst, 2020).

Taken together, the recent surge in high-resolution structural information in combination with molecular simulations and functional studies has greatly advanced the general understanding of complex I. However, conceptually different mechanisms for redox-linked proton translocation are currently discussed. Cryo-EM techniques including tomography as well as computational approaches will become even more powerful in the future. The identification of further intermediates is an

avenue for research to comprehensively understand the catalytic cycle of respiratory complex I.

AUTHOR CONTRIBUTIONS

EG, JS, and VZ wrote the paper. All authors contributed to the article and approved the submitted version.

FUNDING

This work was supported by the Deutsche Forschungsgemeinschaft (DFG grant ZI552/4-2 to VZ).

ACKNOWLEDGMENTS

We thank Vivek Sharma for the discussions.

REFERENCES

- Agip, A. A., Blaza, J. N., Bridges, H. R., Viscomi, C., Rawson, S., Muench, S. P., et al. (2018). Cryo-EM structures of complex I from mouse heart mitochondria in two biochemically defined states. *Nat. Struct. Mol. Biol.* 25, 547–556. doi: 10.1038/s41594-018-0073-1
- Agip, A. A., Blaza, J. N., Fedor, J. G., and Hirst, J. (2019). Mammalian respiratory complex I through the lens of cryo-EM. *Annu. Rev. Biophys.* 48, 165–184. doi: 10.1146/annurev-biophys-052118-115704
- Angerer, H., Nasiri, H. R., Niedergesass, V., Kerscher, S., Schwalbe, H., and Brandt, U. (2012). Tracing the tail of ubiquinone in mitochondrial complex I. *Biochim. Biophys. Acta* 1817, 1776–1784. doi: 10.1016/j.bbabi.2012.03.021
- Baradaran, R., Berrisford, J. M., Minhas, G. S., and Sazanov, L. A. (2013). Crystal structure of the entire respiratory complex I. *Nature* 494, 443–448. doi: 10.1038/nature11871
- Brandt, U. (2011). A two-state stabilization-change mechanism for proton-pumping complex I. *Biochim. Biophys. Acta* 1807, 1364–1369. doi: 10.1016/j.bbabi.2011.04.006
- Bridges, H. R., Fedor, J. G., Blaza, J. N., Di Luca, A., Jussupow, A., Jarman, O. D., et al. (2020). Structure of inhibitor-bound mammalian complex I. *Nat. Commun.* 11:5261. doi: 10.1038/s41467-020-18950-3
- Cabrera-Orefice, A., Yoga, E. G., Wirth, C., Siegmund, K., Zwicker, K., Guerrero-Castillo, S., et al. (2018). Locking loop movement in the ubiquinone pocket of complex I disengages the proton pumps. *Nat. Commun.* 9:4500. doi: 10.1038/s41467-018-06955-y
- Chouchani, E. T., Pell, V. R., Gaude, E., Aksentijevic, D., Sundier, S. Y., Robb, E. L., et al. (2014). Ischaemic accumulation of succinate controls reperfusion injury through mitochondrial ROS. *Nature* 515, 431–435. doi: 10.1038/nature13909
- Chovancova, E., Pavelka, A., Benes, P., Strnad, O., Brezovsky, J., Kozlikova, B., et al. (2012). CAVER 3.0: a tool for the analysis of transport pathways in dynamic protein structures. *PLoS. Comput. Biol.* 8:e1002708. doi: 10.1371/journal.pcbi.1002708
- Darrouzet, E., Issartel, J. P., Lunardi, J., and Dupuis, A. (1998). The 49-kDa subunit of NADH-ubiquinone oxidoreductase (Complex I) is involved in the binding of piericidin and rotenone, two quinone-related inhibitors. *FEBS Lett.* 431, 34–38. doi: 10.1016/S0014-5793(98)00719-4
- Degli Esposti, M. (1998). Inhibitors of NADH-ubiquinone reductase: an overview. *Biochim. Biophys. Acta* 1364, 222–235. doi: 10.1016/S0005-2728(98)00029-2
- Drose, S., Stepanova, A., and Galkin, A. (2016). Ischemic A/D transition of mitochondrial complex I and its role in ROS generation. *Biochim. Biophys. Acta* 1857, 946–957. doi: 10.1016/j.bbabi.2015.12.013
- Euro, L., Belevich, G., Verkhovsky, M. I., Wikström, M., and Verkhovskaya, M. (2008). Conserved lysine residues of the membrane subunit Nuom are involved in energy conversion by the proton-pumping NADH:ubiquinone oxidoreductase (Complex I). *Biochim. Biophys. Acta* 1777, 1166–1172. doi: 10.1016/j.bbabi.2008.06.001
- Fedor, J. G., Jones, A. J. Y., Di, L. A., Kaila, V. R. I., and Hirst, J. (2017). Correlating kinetic and structural data on ubiquinone binding and reduction by respiratory complex I. *Proc. Natl. Acad. Sci. U.S.A.* 114, 12737–12742. doi: 10.1073/pnas.1714074114
- Fendel, U., Tocilescu, M. A., Kerscher, S., and Brandt, U. (2008). Exploring the inhibitor binding pocket of respiratory complex I. *Biochim. Biophys. Acta* 1777, 660–665. doi: 10.1016/j.bbabi.2008.04.033
- Fiedorczuk, K., Letts, J. A., Degliesposti, G., Kaszuba, K., Skehel, M., and Sazanov, L. A. (2016). Atomic structure of the entire mammalian mitochondrial complex I. *Nature* 538, 406–410. doi: 10.1038/nature19794
- Fiedorczuk, K., and Sazanov, L. A. (2018). Mammalian mitochondrial complex I structure and disease-causing mutations. *Trends Cell Biol.* 28, 835–867. doi: 10.1016/j.tcb.2018.06.006
- Galemou Yoga, E., Angerer, H., Parey, K., and Zickermann, V. (2020a). Respiratory complex I - Mechanistic insights and advances in structure determination. *Biochim. Biophys. Acta* 1861:148153. doi: 10.1016/j.bbabi.2020.148153
- Galemou Yoga, E., Haapanen, O., Wittig, I., Siegmund, K., Sharma, V., and Zickermann, V. (2019). Mutations in a conserved loop in the PSST subunit of respiratory complex I affect ubiquinone binding and dynamics. *Biochim. Biophys. Acta* 1860, 573–581. doi: 10.1016/j.bbabi.2019.06.006
- Galemou Yoga, E., Parey, K., Djurabekova, A., Haapanen, O., Siegmund, K., Zwicker, K., et al. (2020b). Essential role of accessory subunit LYRM6 in the mechanism of mitochondrial complex I. *Nat. Commun.* 11:6008. doi: 10.1038/s41467-020-19778-7
- Gamiz-Hernandez, A. P., Jussupow, A., Johansson, M. P., and Kaila, V. R. I. (2017). Terminal electron-proton transfer dynamics in the quinone reduction of respiratory complex I. *J. Am. Chem. Soc.* 139, 16282–16288. doi: 10.1021/jacs.7b08486
- Grba, D. N., and Hirst, J. (2020). Mitochondrial complex I structure reveals ordered water molecules for catalysis and proton translocation. *Nat. Struct. Mol. Biol.* 27, 892–900. doi: 10.1038/s41594-020-0473-x
- Gutierrez-Fernandez, J., Kaszuba, K., Minhas, G. S., Baradaran, R., Tambalo, M., Gallagher, D. T., et al. (2020). Key role of quinone in the mechanism of respiratory complex I. *Nat. Commun.* 11:4135. doi: 10.1038/s41467-020-17957-0
- Gutman, M., Singer, T. P., and Casida, J. E. (1970). Studies on the respiratory chain-linked reduced nicotinamide adenine dinucleotide dehydrogenase. XVII. Reaction sites of piericidin A and rotenone. *J. Biol. Chem.* 245, 1992–1997. doi: 10.1016/S0021-9258(18)63196-5
- Haapanen, O., Djurabekova, A., and Sharma, V. (2019). Role of second quinone binding site in proton pumping by respiratory complex I. *Front. Chem.* 7:221. doi: 10.3389/fchem.2019.00221
- Hirst, J. (2013). Mitochondrial complex I. *Annu. Rev. Biochem.* 82, 551–575. doi: 10.1146/annurev-biochem-070511-103700

- Hirst, J., and Roessler, M. M. (2016). Energy conversion, redox catalysis and generation of reactive oxygen species by respiratory complex I. *Biochim. Biophys. Acta* 1857, 872–883. doi: 10.1016/j.bbabo.2015.12.009
- Hois Teixeira, M., and Menegon Arantes, G. (2019). Balanced internal hydration discriminates substrate binding to respiratory complex I. *Biochim. Biophys. Acta* 1860, 541–548. doi: 10.1016/j.bbabo.2019.05.004
- Howell, N., Bindoff, L. A., McCullough, D. A., Kubacka, I., Poulton, J., Mackey, D., et al. (1991). Leber hereditary optic neuropathy: identification of the same mitochondrial ND1 mutation in six pedigrees. *Am. J. Hum. Genet.* 49, 939–950.
- Hummer, G., and Wikström, M. (2016). Molecular simulation and modeling of complex I. *Biochim. Biophys. Acta* 1857, 915–921. doi: 10.1016/j.bbabo.2016.01.005
- Kaila, V. R. I. (2018). Long-range proton-coupled electron transfer in biological energy conversion: towards mechanistic understanding of respiratory complex I. *J. R. Soc. Interface* 15:20170916. doi: 10.1098/rsif.2017.0916
- Kampjut, D., and Sazanov, L. A. (2020). The coupling mechanism of mammalian respiratory complex I. *Science* 370:eabc4209. doi: 10.1126/science.abc4209
- Klusck, N., Senkler, J., Yildiz, Ö., Kühlbrandt, W., and Braun, H. P. (2021). A ferredoxin bridge connects the two arms of plant mitochondrial complex I. *Plant Cell*. doi: 10.1093/plcell/koab092
- Kotlyar, A. B., and Vinogradov, A. D. (1990). Slow active/inactive transition of the mitochondrial NADH-ubiquinone reductase. *Biochim. Biophys. Acta* 1019, 151–158. doi: 10.1016/0005-2728(90)90137-S
- Laughlin, T. G., Bayne, A. N., Trempe, J. F., Savage, D. F., and Davies, K. M. (2019). Structure of the complex I-like molecule NDH of oxygenic photosynthesis. *Nature* 566, 411–414. doi: 10.1038/s41586-019-0921-0
- Magnitsky, S., Touloukhonova, L., Yano, T., Sled, V. D., Högerhäll, C., Grivennikova, V. G., et al. (2002). EPR characterization of ubisemiquinones and iron-sulfur cluster N2, central components of the energy coupling in the NADH-ubiquinone oxidoreductase (complex I) *in situ*. *J. Bioenerg. Biomembr.* 34, 193–208. doi: 10.1023/A:1016083419979
- Mathiesen, C., and Högerhäll, C. (2002). Transmembrane topology of the NuoL, M and N subunits of NADH:quinone oxidoreductase and their homologues among membrane-bound hydrogenases and bona fide antiporters. *Biochim. Biophys. Acta* 1556, 121–132. doi: 10.1016/S0005-2728(02)00343-2
- Müh, F., Glockner, C., Hellmich, J., and Zouni, A. (2012). Light-induced quinone reduction in photosystem II. *Biochim Biophys Acta* 1817, 44–65. doi: 10.1016/j.bbabo.2011.05.021
- Mühlbauer, M. E., Saura, P., Nuber, F., Di Luca, A., Friedrich, T., and Kaila, V. R. I. (2020). Water-Gated Proton Transfer Dynamics in Respiratory Complex I. *J. Am. Chem. Soc.* 142, 13718–13728. doi: 10.1021/jacs.0c02789
- Murai, M., and Miyoshi, H. (2016). Current topics on inhibitors of respiratory complex I. *Biochim. Biophys. Acta* 1857, 884–891. doi: 10.1016/j.bbabo.2015.11.009
- Ohnishi, T. (1998). Iron-sulfur clusters/semiquinones in complex I. *Biochim. Biophys. Acta* 1364, 186–206. doi: 10.1016/S0005-2728(98)00027-9
- Okun, J. G., Lummen, P., and Brandt, U. (1999). Three classes of inhibitors share a common binding domain in mitochondrial complex I (NADH:ubiquinone oxidoreductase). *J. Biol. Chem.* 274, 2625–2630. doi: 10.1074/jbc.274.5.2625
- Pan, X., Cao, D., Xie, F., Xu, F., Su, X., Mi, H., et al. (2020). Structural basis for electron transport mechanism of complex I-like photosynthetic NAD(P)H dehydrogenase. *Nat. Commun.* 11:610. doi: 10.1038/s41467-020-14456-0
- Parey, K., Brandt, U., Xie, H., Mills, D. J., Siegmund, K., Vonck, J., et al. (2018). Cryo-EM structure of respiratory complex I at work. *Elife* 7:45. doi: 10.7554/eLife.39213.045
- Parey, K., Haapanen, O., Sharma, V., Kofeler, H., Zullig, T., Prinz, S., et al. (2019). High-resolution cryo-EM structures of respiratory complex I: mechanism, assembly, and disease. *Sci. Adv.* 5:eaa9484. doi: 10.1126/sciadv.aax9484
- Parey, K., Wirth, C., Vonck, J., and Zickermann, V. (2020). Respiratory complex I — structure, mechanism and evolution. *Curr. Opin. Struct. Biol.* 63, 1–9. doi: 10.1016/j.sbi.2020.01.004
- Roberts, P. G., and Hirst, J. (2012). The deactive form of respiratory complex I from mammalian mitochondria is a Na⁺/H⁺ antiporter. *J. Biol. Chem.* 287, 34743–34751. doi: 10.1074/jbc.M112.384560
- Rodenburg, R. J. (2016). Mitochondrial complex I-linked disease. *Biochim. Biophys. Acta* 1857, 938–945. doi: 10.1016/j.bbabo.2016.02.012
- Sazanov, L. A. (2015). A giant molecular proton pump: structure and mechanism of respiratory complex I. *Nat. Rev. Mol. Cell. Biol.* 16, 375–388. doi: 10.1038/nrm3997
- Schuller, J. M., Birrell, J. A., Tanaka, H., Konuma, T., Wulffhorst, H., Cox, N., et al. (2019). Structural adaptations of photosynthetic complex I enable ferredoxin-dependent electron transfer. *Science* 363, 257–260. doi: 10.1126/science.aau3613
- Sharma, V., Belevich, G., Gamiz-Hernandez, A. P., Rog, T., Vattulainen, I., Verkhovskaya, M. L., et al. (2015). Redox-induced activation of the proton pump in the respiratory complex I. *Proc. Natl. Acad. Sci. U.S.A.* 112, 11571–11576. doi: 10.1073/pnas.1503761112
- Sinha, P. K., Castro-Guerrero, N., Patki, G., Sato, M., Torres-Bacete, J., Sinha, S., et al. (2015). Conserved amino acid residues of the NuoD segment important for structure and function of *Escherichia coli* NDH-1 (complex I). *Biochemistry* 54, 753–764. doi: 10.1021/bi501403t
- Soufari, H., Parrot, C., Kuhn, L., Waltz, F., and Hashem, Y. (2020). Specific features and assembly of the plant mitochondrial complex I revealed by cryo-EM. *Nat. Commun.* 11:5195. doi: 10.1038/s41467-020-18814-w
- Tocilescu, M. A., Fendel, U., Zwicker, K., Droese, S., Kerscher, S., and Brandt, U. (2010a). The role of a conserved tyrosine in the 49-kDa subunit of complex I for ubiquinone binding and reduction. *Biochim. Biophys. Acta* 1797, 625–632. doi: 10.1016/j.bbabo.2010.01.029
- Tocilescu, M. A., Zickermann, V., Zwicker, K., and Brandt, U. (2010b). Quinone binding and reduction by respiratory complex I. *Biochim. Biophys. Acta* 1797, 1883–1890. doi: 10.1016/j.bbabo.2010.05.009
- Uno, S., Kimura, H., Murai, M., and Miyoshi, H. (2018). Exploring the quinone/inhibitor-binding pocket in mitochondrial respiratory complex I by chemical biology approaches. *J. Biol. Chem.* 294, 679–696. doi: 10.1074/jbc.RA118.006056
- Uno, S., Masuya, T., Shinzawa-Itoh, K., Lasham, J., Haapanen, O., Shiba, T., et al. (2020). Oversized ubiquinones as molecular probes for structural dynamics of the ubiquinone reaction site in mitochondrial respiratory complex I. *J. Biol. Chem.* 295, 2449–2463. doi: 10.1074/jbc.RA119.012347
- Verkhovskaya, M., and Wikström, M. (2014). Oxidoreduction properties of bound ubiquinone in complex I from *Escherichia coli*. *Biochim. Biophys. Acta* 1837, 246–250. doi: 10.1016/j.bbabo.2013.11.001
- Verkhovskaya, M. L., Belevich, N., Euro, L., Wikström, M., and Verkhovskiy, M. I. (2008). Real-time electron transfer in respiratory complex I. *Proc. Natl. Acad. Sci. U.S.A.* 105, 3763–3767. doi: 10.1073/pnas.0711249105
- Verkhovskiy, M., Bloch, D. A., and Verkhovskaya, M. (2012). Tightly-bound ubiquinone in the *Escherichia coli* respiratory complex I. *Biochim. Biophys. Acta* 1817, 1550–1556. doi: 10.1016/j.bbabo.2012.04.013
- Wang, P., Dhananjayan, N., Hagrass, M. A., and Stuchebrukhov, A. A. (2021). Respiratory complex I: bottleneck at the entrance of quinone site requires conformational change for its opening. *Biochim. Biophys. Acta* 1862:148326. doi: 10.1016/j.bbabo.2020.148326
- Warnau, J., Sharma, V., Gamiz-Hernandez, A. P., Di Luca, A., Haapanen, O., Vattulainen, I., et al. (2018). Redox-coupled quinone dynamics in the respiratory complex I. *Proc. Natl. Acad. Sci. U.S.A.* 115, E8413–E8420. doi: 10.1073/pnas.1805468115
- Wikström, M., Sharma, V., Kaila, V. R., Hosler, J. P., and Hummer, G. (2015). New perspectives on proton pumping in cellular respiration. *Chem. Rev.* 115, 2196–2221. doi: 10.1021/cr500448t
- Wright, J. J., Fedor, J. G., Hirst, J., and Roessler, M. M. (2020). Using a chimeric respiratory chain and EPR spectroscopy to determine the origin of semiquinone species previously assigned to mitochondrial complex I. *BMC Biol.* 18:54. doi: 10.1186/s12915-020-00768-6
- Zhu, J., Vinothkumar, K. R., and Hirst, J. (2016). Structure of mammalian respiratory complex I. *Nature* 536, 354–358. doi: 10.1038/nature19095
- Zickermann, V., Barquera, B., Wikström, M., and Finel, M. (1998). Analysis of the pathogenic human mitochondrial mutation ND1/3460, and mutations of strictly conserved residues in its vicinity, using the bacterium *Paracoccus denitrificans*. *Biochemistry* 37, 11792–11796. doi: 10.1021/bi9810555
- Zickermann, V., Bostina, M., Hunte, C., Ruiz, T., Radermacher, M., and Brandt, U. (2003). Functional implications from an unexpected position of the 49-kDa subunit of NADH:ubiquinone oxidoreductase. *J. Biol. Chem.* 278, 29072–29078. doi: 10.1074/jbc.M302713200

Zickermann, V., Wirth, C., Nasiri, H., Siegmund, K., Schwalbe, H., Hunte, C., et al. (2015). Mechanistic insight from the crystal structure of mitochondrial complex I. *Science* 347, 44–49. doi: 10.1126/science.1259859

Conflict of Interest: The authors declare that the research was conducted in the absence of any commercial or financial relationships that could be construed as a potential conflict of interest.

Copyright © 2021 Galemou Yoga, Schiller and Zickermann. This is an open-access article distributed under the terms of the Creative Commons Attribution License (CC BY). The use, distribution or reproduction in other forums is permitted, provided the original author(s) and the copyright owner(s) are credited and that the original publication in this journal is cited, in accordance with accepted academic practice. No use, distribution or reproduction is permitted which does not comply with these terms.



Mechanistic Insights on Heme-to-Heme Transmembrane Electron Transfer Within NADPH Oxydases From Atomistic Simulations

OPEN ACCESS

Edited by:

Petra Imhof,
University of Erlangen
Nuremberg, Germany

Reviewed by:

Albert Poater,
University of Girona, Spain
Daniele Narzi,
University of L'Aquila, Italy

*Correspondence:

Fabien Cailliez
fabien.cailliez@universite-paris-saclay.fr
Aurélien de la Lande
aurelien.de-la-lande@
universite-paris-saclay.fr

†Present address:

Xiaoqing Wu,
Department of Physics and
Astronomy, University College
London, London, United Kingdom

Specialty section:

This article was submitted to
Theoretical and Computational
Chemistry,
a section of the journal
Frontiers in Chemistry

Received: 07 January 2021

Accepted: 06 April 2021

Published: 04 May 2021

Citation:

Wu X, Hénin J, Baciou L, Baaden M,
Cailliez F and de la Lande A (2021)
Mechanistic Insights on
Heme-to-Heme Transmembrane
Electron Transfer Within NADPH
Oxydases From Atomistic Simulations.
Front. Chem. 9:650651.
doi: 10.3389/fchem.2021.650651

Xiaoqing Wu^{1,2†}, Jérôme Hénin^{1,2}, Laura Baciou³, Marc Baaden^{1,2}, Fabien Cailliez^{3*} and Aurélien de la Lande^{3*}

¹ CNRS, Université de Paris, UPR 9080, Laboratoire de Biochimie Théorique, Paris, France, ² Institut de Biologie Physico-Chimique-Fondation Edmond de Rothschild, PSL Research University, Paris, France, ³ Institut de Chimie Physique, Université Paris Saclay, CNRS (UMR 8000), Orsay, France

NOX5 is a member of the NADPH oxidase family which is dedicated to the production of reactive oxygen species. The molecular mechanisms governing transmembrane electron transfer (ET) that permits to shuttle electrons over the biological membrane have remained elusive for a long time. Using computer simulations, we report conformational dynamics of NOX5 embedded within a realistic membrane environment. We assess the stability of the protein within the membrane and monitor the existence of cavities that could accommodate dioxygen molecules. We investigate the heme-to-heme electron transfer. We find a reaction free energy of a few tenths of eV (ca. -0.3 eV) and a reorganization free energy of around 1.1 eV (0.8 eV after including electrostatic induction corrections). The former indicates thermodynamically favorable ET, while the latter falls in the expected values for transmembrane inter-heme ET. We estimate the electronic coupling to fall in the range of the μ eV. We identify electron tunneling pathways showing that not only the W378 residue is playing a central role, but also F348. Finally, we reveal the existence of two connected O₂-binding pockets near the outer heme with fast exchange between the two sites on the nanosecond timescale. We show that when the terminal heme is reduced, O₂ binds closer to it, affording a more efficient tunneling pathway than when the terminal heme is oxidized, thereby providing an efficient mechanism to catalyze superoxide production in the final step. Overall, our study reveals some key molecular mechanisms permitting reactive oxygen species production by NOX5 and paves the road for further investigation of ET processes in the wide family of NADPH oxidases by computer simulations.

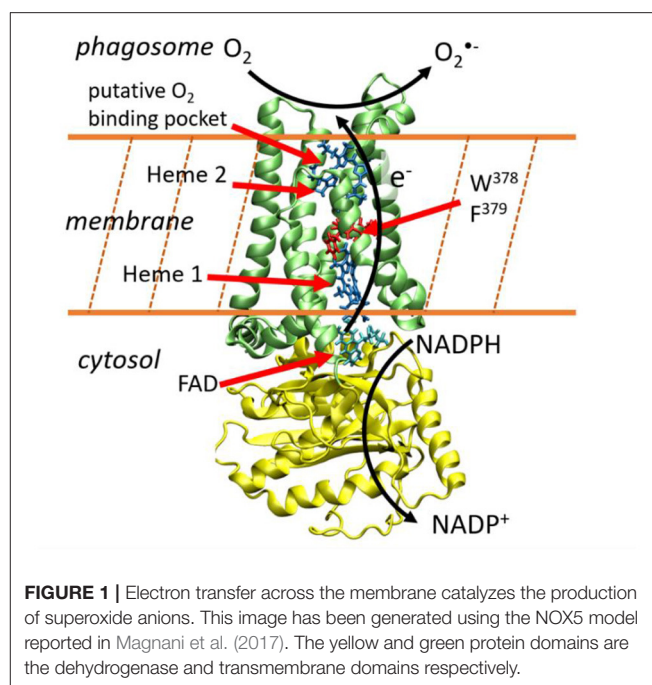
Keywords: Marcus theory of electron transfer, reaction free energies, NADPH oxydase, molecular dynamics simulations (MD simulations), membrane protein, electron tunneling

INTRODUCTION

NADPH oxidases (NOX) encompass a family of membrane enzymes dedicated to the production of cellular reactive oxygen species (ROS) in a regulated manner (Geiszt and Leto, 2004; Bedard and Krause, 2007). NOX enzymes have conserved structures common to all family members. In Humans, seven isoenzymes are expressed: NOX1 to NOX5, Duox1 and Duox2. This family is subdivided into two groups; one according to the ability of the NOX to form a heterodimer with p22^{phox} (NOX1-4), the other according to the presence of calcium-binding EF-hand type motifs in its sequence (NOX5 and Duox1/2). These enzymes are expressed in many tissues, including kidney, fibroblasts, osteoclasts, and thyroid, where they produce ROS, albeit generally at diverse levels, in response to stimuli such as growth factors, cytokines or calcium. They are involved in a great number of physiological functions, such as host defense, post-translational proteins processing, inter- and intra-cellular signaling, regulation of gene expression and cell differentiation. Aberrant levels of NADPH-oxidase derived ROS, either too low or too high, can disturb the balance of cellular homeostasis, ultimately resulting in pathological states. NOX are widely distributed in different kingdoms of life including animals (in particular mammals), plants and lower organisms and their expression is specific to each kingdom of life (Bedard et al., 2007; Sumimoto, 2008; Hajjar et al., 2017).

Whereas the members of the NADPH oxidase family differ in their tissue distribution, mode of activation and physiological functions, they all share the capacity to generate ROS. Among them, superoxide is produced by NOX1-3 and NOX5, and H₂O₂ is produced by NOX4 and Duox enzymes. NOX are flavohemoproteins and electron transporters consisting in a N-terminus region of six transmembrane helices that bind two non-identical heme groups and a cytosolic C-terminus region (dehydrogenase domain) where an NAD(P)H and a Flavin Adenosine Diphosphate (FAD)-binding site are localized. This transmembrane protein permits to shuttle electrons brought by NADPH molecules from the cytosol toward the internal part of the phagosome (Figure 1). Directional electron transfers are catalyzed by a series of redox molecules encapsulated within the protein matrices that serve as stepping stones for the electrons. On the cytosolic side, FAD is the primary electron acceptor and gets a hydride anion, *i.e.* two electrons and one proton, from NADPH. It is hypothesized that electrons are then shuttled one-by-one to the first heme (Heme1), then to the second heme (Heme2), before being finally transferred to a dioxygen molecule to form the superoxide anion. Redox potentials of hemes in NOX2, which is the most studied member of the NADPH oxidase family and is considered as the prototype of NOX family, have been measured (Cross et al., 1995). To the best of our knowledge, there have been no reports of kinetic measurements of these intrinsic ET steps which are presumably faster than other rate-limiting steps of the overall NOX machinery (*e.g.*, sub-units association or NADPH binding).

This sketchy description of transmembrane ET is supported by various biochemical data, notably by recent 3D structures. In 2017, Magnani et al. reported the first X-ray diffraction



structures of the dehydrogenase and transmembrane domains of NOX5 from *Cylindrospermum stagnale*. This cyanobacteria NOX5 exhibits 40% sequence homology with human NOX5 (Magnani et al., 2017). Very recently, cryo-EM structures of mouse Duox1-DuoxA1 have been reported (Sun, 2020). NOX5 and Duox catalyze superoxide and hydrogen peroxide production, respectively. Their 3D-structures are well conserved and present two well-aligned hemes in the transmembrane domain (Figure 1). A phenylalanine residue (379 in NOX5 and 1097 in DUOX1-DUOX1A1) is located midway between the two hemes suggesting this residue could play an important role to sustain inter-heme electron tunneling. These ET path schemes in NOX enzymes are valuable hypotheses but should be taken with caution as reasoning on single structures to predict tunneling pathways, ignoring structural fluctuations, has often proven to be misleading (Prytkova et al., 2007; de la Lande et al., 2010, 2013; Beratan et al., 2015). Putative binding pockets for O₂ molecules have been identified which could serve to maintain molecular oxygen close to Heme2, thus facilitating its reduction (Magnani et al., 2017; Sun, 2020).

Globally, we start to accumulate structural insights on NOX enzymes. However, little is known about the thermodynamics and kinetics of the succession of electron transfer steps within NOX. In this article, we report the first microscopic simulations of NOX5 within a realistic lipid membrane. Our aim is twofold. First, we aim at building a realistic model of NOX5 at the atomic level. We report molecular dynamics simulations of several hundreds of nanoseconds to assess its stability in a fully hydrated lipid bilayer environment. Second, we report a computational study of the inter-heme electron transfer step including evaluations of the ET free energy, of reorganization free energies and of tunneling pathways. We further reveal that O₂

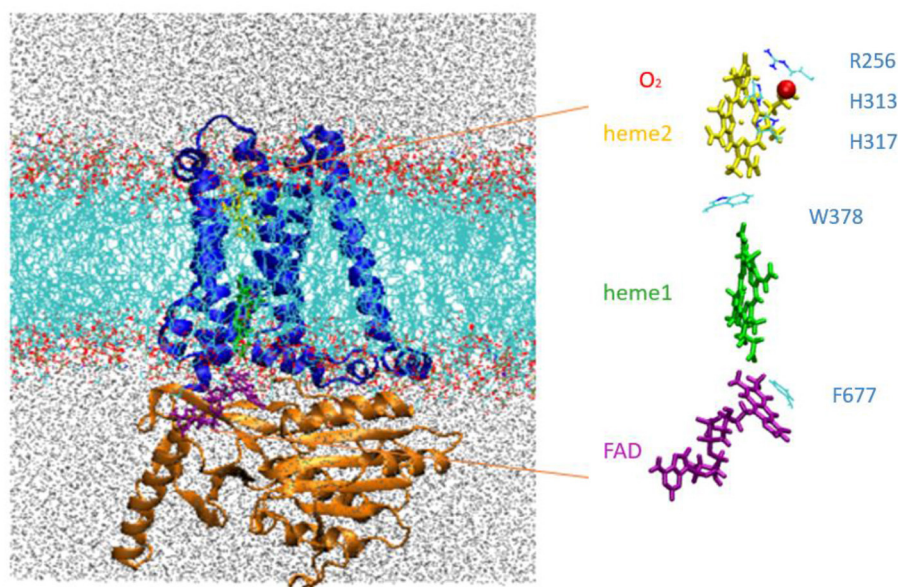


FIGURE 2 | Left, NOX5 catalytic core investigated in this study, composed of the transmembrane domain (in blue) and dehydrogenase domain (in orange) embedded in a lipid bilayer (in light blue and red). Water molecules are shown in gray. Right, insert shows the cofactor FAD (purple), Heme1 (green), Heme2 (yellow) and O₂ (red).

moves back-and-forth between two binding pockets situated near Heme2. When Heme2 is reduced, O₂ dominantly populates the pocket which is the closest to the heme. The electron tunneling pathways afforded by this pocket are one order of magnitude stronger than those emerging when O₂ is present in the more remote pocket, hence providing a way to catalyze the final electron transfer to produce superoxide. Data and scripts to produce key figures and table of this article are available on the Zenodo data base (doi: 10.5281/zenodo.4424142).

BUILDING OF AN ATOMISTIC MODEL FOR NOX5

Our aim is to investigate inter-heme electron transfer. To this end, our approach is to develop an atomistic model of NOX5 inserted within a lipid bilayer based on the recently reported structures of helical transmembrane (TM) and C-terminal cytosolic dehydrogenase (DH) domains from *Cylindrospermum stagnale* NOX5. The initial coordinates of the TM and DH domains were taken from the Protein Data Bank structures with codes 5O0T (2.0 Å resolution) and 5O0X (2.2 Å resolution), respectively. We start by detailing the protocol we have followed to set-up the system and to carry out molecular dynamics simulations. In the following section we will focus on electron transfer modeling.

Molecular Dynamics Simulation of NOX Proteins

Preparation of the Simulation System

The MD simulations were carried out for an extended system comprising the NOX protein catalytic core embedded in a model

phospholipid membrane and solvated with an ionic aqueous solution as shown in **Figure 2**. Magnani et al. (2017) identified a putative cavity to bind a dioxygen molecule in the vicinity of Heme2 (see the red bead on **Figure 2**, right). In our simulations this cavity is filled either by a dioxygen molecule or by a water molecule (see below).

Construction of a Full-Length NOX5 Model

In the experiments that achieved crystallization of the DH domain, a short amino acid sequence PWLELAAA was added after the C-terminal Phe693 residue to enhance thermal stability and FAD retention (Magnani et al., 2017). We removed this artificial additional sequence in our model. On the other hand, 27 amino acid residues were missing in the N-terminal calcium-binding EF-hand domain (GAQQKSDMKSSSTLFVAMDLMHQETKVD), for which no homology modeling template was available. We used the PSIPRED server (Buchan and Jones, 2019) to predict the secondary structure of this segment. The central part of this sequence is predicted to form an alpha helix. MODELLER (Šali and Blundell, 1993) was used to add this missing part, however the resulting models did not form an alpha-helix. This segment is only present in the NOX5 branch of the family, and is replaced by e.g., an 11-residue stretch in a NOX4. So, we constructed a NOX4-like variant, by deleting SSTLFVAMDLMHQET and only keeping GAQQKSDMKVD (Resid 605–615). This shorter sequence was modeled *ab initio* with MODELLER. 20 models were built and assessed based on their DOPE (Discrete Optimized Protein Energy) score (Shen and Sali, 2006). Differences between the 20 models were small: the RMSD difference between the model with best score and

worst is 0.19 Å. We considered that 20 models are enough to build this missing part and we chose the model with the best score. We do not expect this assumption to influence the study of the ET process between two hemes, since the distance between the reconstructed loop and Heme1 is 35 Å.

In ref. Magnani et al. (2017), the X-ray structures of the two DH and TM domains were obtained separately, and docked together with some user-defined restraints using the Haddock server (Dominguez et al., 2003; van Zundert et al., 2016). We have followed the same docking strategies. Specifically, Asn288 (B-loop of TM), Lys361 (D-loop of TM), Thr520 (B-loop binding region of DH), and Phe677 (flavin-interacting C terminus of DH) were defined as “active” residues (preferentially placed at the interface by Haddock). Moreover, we constrained the edge-to-edge distance between FAD and Heme1 to be within 2.5 Å. We also constrained Phe677 to be close to the isoalloxazine ring of FAD with a face-to-face π -stacking interaction (Figure 2). The distance between Lys412 (C terminus of TM) and Glu413 (N terminus of DH) was constrained to 2 Å. The best docked complex (Haddock score of -2.5) was then fused by creating a covalent bond between Lys412 and Glu413. The geometry of the model was further validated by the Qmean server (Benkert et al., 2011) for model quality estimation. Our model obtained a QMEAN Z-score of -1.97 . We can consider this score as satisfactory since the Duox1 cryo-EM structure has a slightly worse Z-score of -2.65 .

The interface between the transmembrane and dehydrogenase domains was the main unknown when building our full-length model. Recent cryo-EM structures of the homologous Duox1 protein contain both domains, and offer a basis for comparison (Sun, 2020). We find that when aligning the transmembrane domain, our model of the dehydrogenase domain is rotated by 60° with respect to the equivalent domain in the 7D3E structure of the human DUOX1-DUOX1A1 complex (Supplementary Figure 1). During the simulations, the relative orientation of the two domains fluctuates by up to 11° from the initial model.

Construction of the Extended System

The docking structure was used as initial coordinates of the catalytic core. All amino acid residues were assigned a standard protonation state at pH 7. All histidine residues were singly protonated at the N δ sites based on the inspection of inter-residue interactions. The importance of the lipid metabolism was evidenced in NOX activities, although the regulatory role of the lipid membrane properties remains unclear. Membrane properties (charges, thickness, composition, lipid raft formation) have been shown to affect the NOX2 enzyme functioning (Shao et al., 2003; Souabni et al., 2014, 2017). Moreover, the phospholipid composition changes during NOX2 activation (Magalhaes and Glogauer, 2010; Br  chard et al., 2012; Joly et al., 2020). We made the choice of building a membrane with 1-Palmitoyl-2-oleoyl-sn-glycero-3-(phosphorac-(1-glycerol)) (POPG) and 1-palmitoyl-2-oleoyl-sn-glycero-3-phosphoethanolamine (POPE) in 4 to 1 proportions with CHARMMGUI (Jo et al., 2008; Brooks et al., 2009; Lee et al., 2016). Note that this membrane composition is one among

many possibilities that could have been considered. The OPM (orientations of proteins in membranes) orientation of the TM domain has been used as starting point for membrane insertion. The protein membrane system was solvated with 38,341 water molecules in a hexagonal prism unit cell ($a,b,c = 135\text{Å}, 117\text{Å}, 112\text{Å}$, $\alpha, \beta, \gamma = 90, 90, 120^\circ$). The system was neutralized electrically by adding 451 Na $^+$ and 98 Cl $^-$ ions to obtain a 0.15 M NaCl solution.

Force Field Parameters

Standard protein residues and lipids were modeled using the CHARMM36 force field (Lee et al., 2016). We used the TIP3P water model (MacKerell et al., 1998). Force field parameters for the heme cofactor in ferrous and ferric states and for FADH \bullet have been developed by our groups and can be found in **Supplementary Materials**. In this study, we consider two distinct redox states associated to the inter-hemes electron transfer (see next section): Heme1-Fe(II)/Heme2-Fe(III) and Heme1-Fe(III)/Heme2-Fe(II). In some simulations, a single dioxygen molecule was placed in the cavity shaped by the propionate groups of Heme2 and by residues Arg256, His313 and His317 as shown in Figure 2. This cavity has been previously proposed to host dioxygen prior to its reduction. Following the methodology proposed in Ref. Javanainen et al. (2017, 2020), we placed a charged dummy atom holding a 0.452 electric charge in between the oxygen nuclei, each holding a -0.226 electric charge in order to reproduce the quadrupole moment of the dioxygen molecule. A restraint energy term was added to the total potential energy with the Colvar module (Fiorin et al., 2013) of NAMD (Phillips et al., 2005, 2020) to maintain the dioxygen molecule within the pocket during the MD simulations (details are given later in the text).

Simulation Protocol

Initial equilibration and production phase were carried out using the NAMD program (Phillips et al., 2020). We carried out MD simulations for two different systems. One system includes the presence of O $_2$ in the aforementioned cavity, while the other is without dioxygen. We conducted in each case MD simulations for the system in the initial and final redox states, represented by different partial charge distributions on heme and iron moieties. The protein membrane system was equilibrated with a standard procedure as suggested from CHARMM-GUI (Jo et al., 2008; Lee et al., 2016). The equilibration phase has been carried out in the isothermal–isobaric ensemble (NPT) under periodic boundary conditions with six cycles of 25, 25, 25, 200, 200, 200 ps by gradually releasing harmonic restraints around the initial positions of protein backbone and membrane lipid atoms at 310 K and 1 bar. For protein, the harmonic restraints force constants of each cycle were set to 10.0, 5.0, 2.5, 1.5, 1.0, and 0.5 kcal/mol/Å 2 , while membrane lipid restraints were applied with force constants of 5.0, 5.0, 2.0, 1.0, 0.2, and 0 kcal/mol/Å 2 . The integration time step was set to 1 fs for the first three cycles and then increased to 2 fs for the last three cycles. All bonds involving H are fixed in length. To maintain planarity of the membrane, the center of mass of the lipid head groups in the upper and lower layers had their positions restrained in the z

direction to +19 and −19 Å relative to the center of mass of the bilayer by application of a constraining potential with a force constant of 5.0, 5.0, 2.0, 1.0, 0.2, and 0 kcal/mol/Å². The particle-mesh Ewald (PME) method was used for the calculation of electrostatic interactions. Non-bonding interactions were treated using a cutoff of 12.0 Å. Pressure was controlled by the Nose-Hoover Langevin piston method (Phillips et al., 2005) while the temperature was controlled by Langevin dynamics.

Production runs in the canonical ensemble (NVT) were carried out for 300 ns for each redox state. Geometries were saved every 2 ps to sample the vertical energy gap. We also conducted two 100 ns MD simulations for each state with the same equilibrated structure but different initial velocities to assess the variability of the computed ET parameters with respect to the initial conditions of the simulation. Altogether, we generated a set of 12 MD simulations, 6 for each state (with and without oxygen), with 3 replicas of 300, 100, and 100 ns for each state, respectively, and two charge distributions each representing the initial and final redox states.

Analysis of Protein Stability

The protein backbone root-mean-square deviation (RMSD) time series calculated during MD simulations are shown in **Supplementary Figure 2**. The docking structure is taken as reference for the RMSD calculation. Panels (a) to (c) correspond to the MD with oxygen present, while panels (d) to (f) are without O₂. Black (resp. red) curves correspond to dynamics performed in the initial (resp. final) redox states. For all simulations, the RMSD stays under around 4 Å, assessing a slight distortion with respect to the initial structural model. Only in the 300 ns-long MD simulation without O₂ in the initial redox state a small drift toward higher values of RMSD is seen at the end of the simulation.

Analysis of NOX5 in the Membrane

We have assessed the stability of the insertion of the transmembrane domain of the protein in the lipid bilayer by computing the membrane thickness and the relative position of the protein in the bilayer throughout the simulations. The membrane thickness is estimated by the distance between the center-of-mass of upper and lower lipids. It is stable during all the MD simulations with a fluctuation of less than 2 Å (**Supplementary Figure 3**). We use the distance between the center of mass of the membrane and the center of mass of the transmembrane part of the protein to measure the relative position of the protein inside the bilayer. Its evolution in all the MD simulations is shown in **Supplementary Figure 4**. It is found to be stable with fluctuations less than 6 Å and no apparent drift on the hundreds of ns timescale.

Heme-to-heme Electron Transfer

Having assessed the stability of the *in-silico* model of NOX5 inserted in a lipid membrane, we focus in this section on the heme-to-heme electron transfer. We follow the framework of the Marcus Theory of electron transfer to evaluate the free energy of the reaction (ΔA°) and the reorganization energy (λ) (Marcus and Sutin, 1985). Warshel et al. showed that both quantities

can be obtained from microscopic simulations under the Linear Response Approximation as (King and Warshel, 1990):

$$\Delta A^0 = \frac{1}{2} (\langle \Delta E \rangle_i + \langle \Delta E \rangle_f) \quad (1)$$

$$\lambda^{St} = \frac{1}{2} (\langle \Delta E \rangle_i - \langle \Delta E \rangle_f) \quad (2)$$

where ΔE is the diabatic energy gap, that is the difference in potential energy of the system in the initial and final redox state ($\Delta E = E_f - E_i$), or alternatively said when the transferred electron sits on Heme1 or Heme2, respectively. Note that ΔE is calculated for a given set of nuclear coordinates and is therefore referred to as a vertical energy gap. $\langle \dots \rangle_x$ refers to an average performed over a canonical ensemble of configurations of the system in redox state x (i or f). ΔE can be decomposed into a contribution coming from the heme cofactors (inner-sphere contribution), from the environment (outer-sphere contribution) and from a coupling term between them. The latter refers to the mutual polarization (E^{mp}) that differs for the two redox states: $\Delta E = \Delta E^{is} + \Delta E^{os} + \Delta E^{mp}$. Neglecting ΔE^{mp} , a separation of the total free energy of the reaction as $\Delta A = \Delta A^{is} + \Delta A^{os}$ is obtained. This approximation has been tested in other heme proteins and turned out to be reasonable (Blumberger, 2008). We adopt it here, too. Furthermore, as ET is taking place between two chemically identical hemes, $\Delta A^{is} = 0$, therefore $\Delta A \approx \Delta A^{os}$.

The reorganization energy calculated with Equation 2 is referred to as the Stokes reorganization energy, hence the upper script *St*. The fluctuation of the energy gap can also be used to define the reorganization energy:

$$\lambda_x^{var} = \frac{var(\Delta E_x)}{2k_B T} \quad (3)$$

In Equation 3, ΔE_x is the energy gap computed over a trajectory performed in the state x (i or f). From MD simulations performed on each electronic state involved in the ET, one obtains two different values: λ_i^{var} and λ_f^{var} . If the LRA and the ergodic principle apply, the three definitions of the reorganization energy coincide: $\lambda^{St} = \lambda_i^{var} = \lambda_f^{var}$. A simple measure of non-ergodicity can be obtained as:

$$\chi_G = \frac{\lambda_i^{var} + \lambda_f^{var}}{2\lambda^{St}} \quad (4)$$

Values of χ_G close to 1 correspond to ergodic systems.

Neglecting ΔE^{mp} as above, reorganization energy can be decomposed into two contributions: $\lambda = \lambda^{is} + \lambda^{os}$. λ^{os} has been evaluated by Eqs. 2 and 3 using force field-based interaction energies computed between the two hemes and the environment. λ^{is} has been evaluated by Density Functional Theory calculation (see **Supplementary Material** for details). The geometries of the heme cofactors including the apical and axial histidine ligands (modeled as methyl-imidazoles) have been optimized and λ^{is} has been calculated as:

$$\lambda^{is} = 2 \cdot \left(\frac{E_{gR}^O - E_{gR}^R + E_{gO}^R - E_{gO}^O}{2} \right) \quad (5)$$

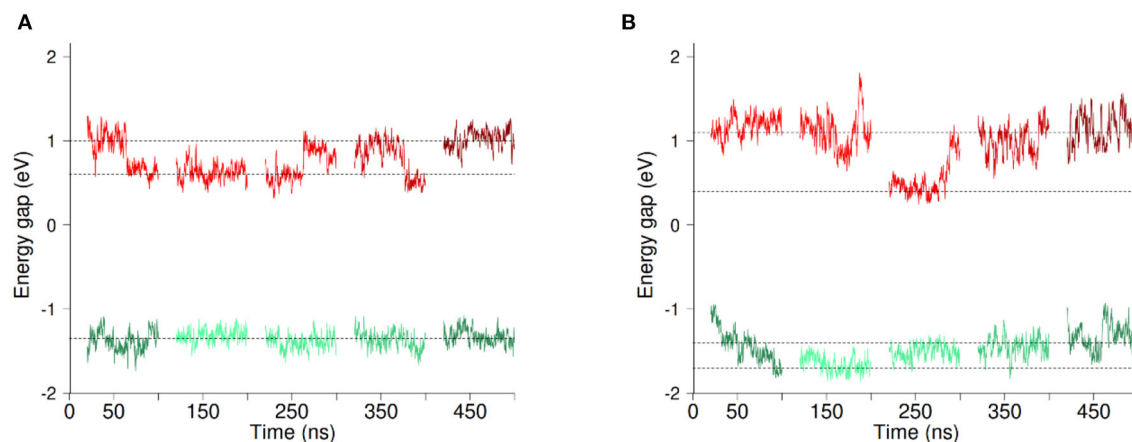


FIGURE 3 | Evolution of the vertical energy gap ΔE ($E_f - E_i$) along MD simulations with O_2 (A) and without O_2 (B). Each line section represents 80ns of MD simulation. The first three sections correspond to parts of the 300ns-long simulation (Set 1–3) while the two last sections come from the two independent 100ns-long replica simulations (Set 4 and 5). Energy gaps computed based on simulations in the initial (resp. final) redox state are shown in red (resp. green). Data shown correspond to running averages of ΔE for clarity. Horizontal lines are guides to the eye.

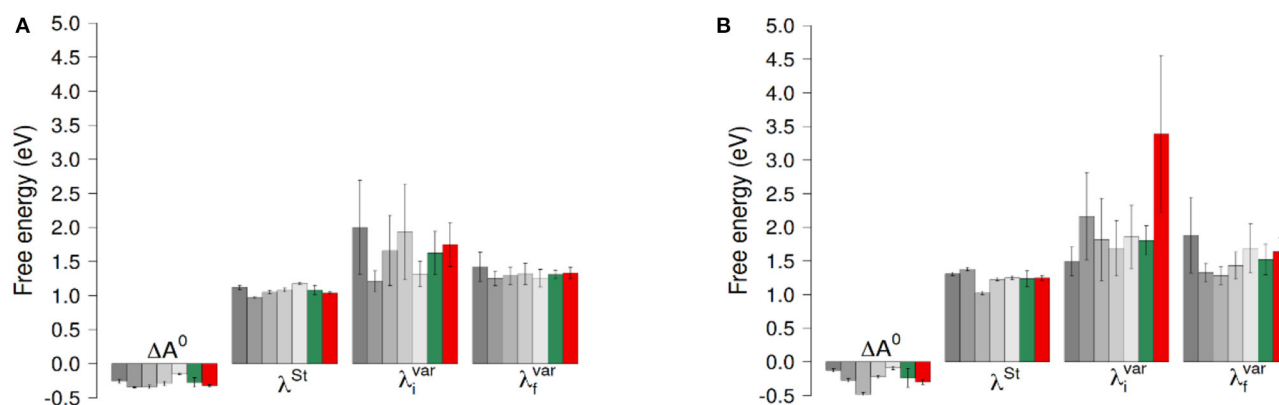


FIGURE 4 | ET reaction free energies and outer-sphere reorganization energies of the ET between hemes with O_2 (A) and without O_2 (B). The gray bars represent values obtained for the five 100ns-long data sets. The green bars are the results of a block average using the data of these five data sets. The red bars correspond to values obtained using the full 300ns-long trajectory. Error bars correspond to twice the uncertainty.

E_{gX}^X stands for the energy of the heme in the redox state X ($O \vee R$) in the equilibrium geometry gX . We obtained a value of 0.10 eV for λ^{is} . For each system (with or without O_2) we have computed ET thermodynamic parameters using the full 300 ns-long MD simulations, discarding the first 20 ns. In order to assess the variability of ET parameters with respect to the sampling, we have split the 300 ns-long simulations into three segments of 100 ns. Adding the two small 100 ns-long simulations, we have access to 5 sets of data that we consider to be independent, hereafter referred to as Set1 to Set 5. From these datasets, we have computed ET thermodynamic parameters, discarding each time the first 20ns, considered as an equilibration time. A block analysis over the 5 obtained sets of values has finally been performed. The results obtained for Heme1 to Heme2 ET are summarized in **Figures 3, 4** (all the individual numerical values are given in **Supplementary Table 1**).

Figure 3 presents the evolution of the energy gaps ΔE in the five data sets Set1 to Set5 with O_2 (panel a) or without O_2 (panel b), computed in the initial (in red) and final (in green) redox states. We begin by describing the results in presence of dioxygen. The data clearly shows that fluctuations of the energy gap are greater in the initial redox state (in red). What is more, a clear bimodality appears for the energy gaps in this redox state, with ΔE oscillating around two values, which are indicated with horizontal dotted lines in **Figure 3**. This oscillation seems to take place at the scale of tens of ns. No clear-cut localized change in structure of the protein and/or its environment could be found to account for this bimodality. That said, we decomposed ΔE into different contributions, namely TM domain, DH domain, environment (water, membrane and counter ions) and cofactors (FAD, hemes, O_2). The result of this decomposition is shown in **Supplementary Figures 5, 6**

for simulations in presence and absence of O₂ respectively. For the initial redox state we recover a bimodality when considering the contributions from the TM domain and from the environment. Longer simulations could help to decipher the origin of the bimodality of ΔE . It could come from slow concerted motion involving the TM and the lipids composing the membrane and its solvation layer. On the other hand, the other components (FAD, Hemes, O₂, DH domain) don't exhibit any bimodality in the energy gap distributions. In addition, these results are independent on the presence or not of dioxygen in the cavity.

ET reaction free energies obtained with Equation 1 are negative whatever data set is used to compute them, with values ranging roughly from -0.5 to -0.1 eV (see **Figure 4** and **Supplementary Table 1**), indicating that the ET from Heme1 to Heme2 is favorable. The values obtained from the full 300 ns-long MD simulations or from the five 100 ns-long datasets are consistent (green and red bars in **Figure 4**). Because of the larger fluctuations in ΔE , values of ΔA^0 obtained without O₂ are more dispersed (see e.g., **Figure 4**). However, the average values obtained for the two systems are similar within the uncertainties of the calculations (-0.28 eV and -0.24 eV respectively with and without O₂). Outer-sphere reorganization energies are presented in **Figure 4**, calculated with Equation 2 (λ^{St}) or Equation 3 (λ_i^{var} and λ_f^{var}). λ^{St} values lie between 1 and 1.4 eV, with averages of 1.04 and 1.24 eV for λ^{St} respectively with and without O₂. Note that these reorganization energies are computed with a non-polarizable forcefield. Accounting for electrostatic induction is expected to decrease the values of the reorganization energies by 30% approximately (Blumberger, 2008). Once again one observes greater fluctuations in the values when O₂ is not bound to Heme2. This is especially the case when one considers λ_x^{var} values computed over the 300 ns-long MD simulations in the initial electronic state. This observation should be taken with caution as the duration of the simulation is likely not to be long enough with respect to the slow degree of freedom that is responsible for the bimodality in ΔE . Whichever way they are computed, reorganization energies are greater in absence of dioxygen (see **Supplementary Table 1**). This dependency may arise because the presence of O₂ "rigidifies" the environment around Heme2, lowering the structural differences between both electronic states, noting that the uncertainties of the mean values are large, respectively 0.07 and 0.24 eV. Further investigations with longer simulations or more replicas should help to ascertain these conclusions more strongly. Values of λ_x^{var} are found to be greater than λ^{St} for every dataset, leading to χ_G values between 1.1 and 2.0, most of the time lying between 1.3 and 1.5. For simulations without O₂, the long 300 ns MD simulations gives rise to a much larger λ_i^{var} (ca. 3.5 eV, red bar in **Figure 4**, right). This high value, associated to a large statistical uncertainty (1.17 eV, **Supplementary Table 1**) results from the bimodality in the energy gap distribution which is apparent in **Figure 3**. Together with the low values obtained for λ^{os} , this finding reveals that the structural reorganization around the two hemes is somewhat moderate, since much larger χ_G values have been reported (Matyushov, 2015).

We have decomposed ΔA^0 and λ^{St} into contributions arising from the molecular components of the system, namely the TM and DH domains, FAD, the Hemes, the counter-ions, the membrane and the solvent (**Supplementary Table 2**). It turns out that the negative ΔA^0 results from a balance between positive and negative contributions. With the current membrane composition (POPG/POPE in 4:1 proportion), the TM domain and membrane largely disfavor inter-heme ET (1.52 ± 0.18 and 0.60 ± 0.14 eV, respectively, considering the average over the five sets of trajectories), while water and counter-ions provide a net driving force for ET (-0.27 ± 0.12 and -1.42 ± 0.68 , respectively). We can thus extrapolate that a change of membrane composition, especially if it incorporates more of less charged lipids would directly impact inter-heme ET. Interestingly, the DH domain has little influence on ΔA^0 and marginally reorganizes upon electron transfer. As in our model the DH domain might have a non-physiological orientation with respect to the TM domain in view of the recent cryo-EM structure of DUOX1 (see above, and **Supplementary Figure 1**), this result is reassuring regarding our estimates of inter-heme ET thermodynamics, *i.e.*, the precise orientation of the DH domain marginally determines these parameters, likely because the DH is far away from the inter-heme region.

Electron Tunneling Pathways

We have carried out tunneling pathway analyses along MD trajectories with the pathway model of Beratan and co-workers. This model is built on the assumption that the electron tunnels from the electron donor to the acceptor along a pathway that is defined as a succession of covalent or hydrogen bonds and of through space contacts (Beratan et al., 1987). The decay of the electronic coupling associated with a given pathway is expressed as the product of multiplication of a constant contact coupling ($H_{if}^{contact}$) by a factor (ϵ_{tot}) that reflects the attenuation of the coupling caused by the presence of intervening medium between the donor and the acceptor. ϵ_{tot} depends on the number of covalent or hydrogen bonds (denoted N_c and N_{hb} , respectively) and of through-space jumps (N_{ts}) composing the electron transfer pathway. This factor is calculated according to a set of mathematical expressions empirically calibrated by the authors of the model (Onuchic and Beratan, 1990; Beratan et al., 1991).

$$H_{if} = H_{if}^{contact} \epsilon_{tot} \quad (6)$$

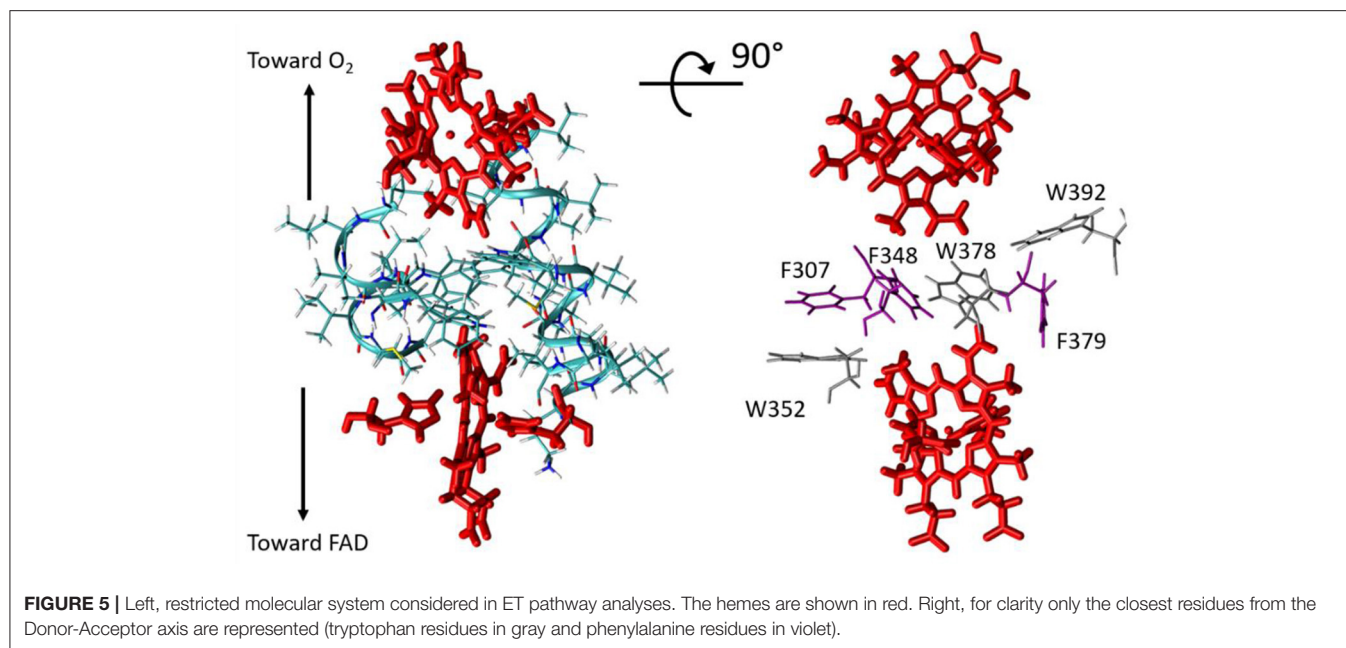
$$\epsilon_{tot} = \prod_{N_c} \epsilon_c \times \prod_{N_{hb}} \epsilon_{hb} \times \prod_{N_{ts}} \epsilon_{ts} \quad (7)$$

$$\epsilon_c = 0.6 \quad (8)$$

$$\epsilon_{hb} = 0.36 \times \exp[-\beta_S (R_H - 2.8)] \quad (9)$$

$$\epsilon_{ts} = 0.6 \times \exp[-\beta_S (R_S - 1.4)] \quad (10)$$

R_S is the atom-atom distance for through-space jumps, R_H is the hydrogen bond length (taking the inter-heavy atom distance) and β_S is a characteristic decay factor. The latter was originally parametrized in the 1990's to a value of 1.7 \AA^{-1} , but later investigations suggested that a value of 1.1 \AA^{-1} enables better



agreement with quantum chemistry calculations (Prytkova et al., 2005). This is the value we have used here. Covalent bonds within the porphyrin aromatic rings were made fully conductive (*i.e.*, setting $\epsilon_c = 1$ between two such atoms) in our analysis, so that the PM results do not depend on the particular choice of the donor/acceptor atom within the two hemes. The best pathway was identified for each analyzed structure using the Dijkstra algorithm (Dijkstra, 1959) with an in-house program (de la Lande et al., 2010; El Hammi et al., 2012). Our program (i) seeks for the pathway producing the most efficient electronic coupling with the Dijkstra algorithm, (ii) decomposes the total pathway over covalent, through-hydrogen-bond and through-space interactions (iii) indicates which amino-acid residues or other molecules are involved in tunneling pathways, (iv) provides adequate files for visual representation of the pathways with the VMD program. Structures were extracted from MD simulation trajectories every 20 ps. To make the pathway search tractable, the structure was preliminarily pruned to include only the atoms susceptible to take part in the tunneling process, that is residues not lying too far from the direct inter-heme axis. The pruned sub-system comprises the two hemes and their axial ligands (His299, His313, His372, His385) as well as residues Leu268, Ile269, Lys300, Leu301, Val302, Gly303, Gln304, Val305, Met306, Phe307, Ala308, Leu309, Ala310, Ile311, Val312, Leu345, Leu346, Val347, Phe348, Ile349, Ile350, Met351, Trp352, Trp378, Phe379, Trp392 (**Figure 5**). As seen on the picture, the hemes are separated by a layer of five aromatic amino acids, among which Trp378, as highlighted in Magnani et al. (2017) but also Phe307, Phe348, Trp352, Phe379, and Trp392.

Results are collected in **Table 1** and on **Figure 6**. Two types of pathways are identified over the duration of the MD simulations. The first one is running through Trp378, while the other is running through Phe348 as illustrated by the green and red tubes in **Figure 6**. They connect the hemes by the edge of the porphyrin

TABLE 1 | Semi-empirical pathway analyses of tunneling matrix elements mediating inter-heme electron transfer. $\langle H_{if}^{PM} \rangle$ are given in eV².

Path	(%)	$\langle \epsilon_{tot} \rangle$	σ^2	$\langle H_{if}^{PM} \rangle$ eV	$\langle \epsilon_{tot}^2 \rangle$	R_{coh}^{cl}
Fe²⁺/Fe³⁺						
Trp378	92	$2.04 \cdot 10^{-5}$	$7.44 \cdot 10^{-11}$	—	—	—
Phe348	7	$3.06 \cdot 10^{-5}$	$2.58 \cdot 10^{-10}$	—	—	—
Total	100	$2.12 \cdot 10^{-5}$	$9.62 \cdot 10^{-11}$	$3.75 \cdot 10^{-6}$	$5.43 \cdot 10^{-10}$	0.82
Fe³⁺/Fe²⁺						
Trp378	56	$2.32 \cdot 10^{-5}$	$7.83 \cdot 10^{-11}$	—	—	—
Phe348	44	$3.93 \cdot 10^{-5}$	$2.75 \cdot 10^{-10}$	—	—	—
Total	100	$3.04 \cdot 10^{-5}$	$2.30 \cdot 10^{-10}$	$5.40 \cdot 10^{-6}$	$1.15 \cdot 10^{-9}$	0.80

plane. Our simulations thus confirm the expectation that Trp378 plays a key role in mediating inter-heme tunneling, but also reveal the occurrence of pathways running through Phe348. As seen on the distributions depicted in **Figure 6**, the tunneling pathways running through Phe348 are in general slightly more efficient than those running through Trp378. The respective distributions among the two kinds of pathways seem to depend on the redox state but it is difficult to find a rational in terms of structure of the intervening medium, and both kinds of pathways give rise to rather similar decay factors. Overall, the average decay factor equals to $2.11 \cdot 10^{-5}$ with a standard deviation of $9.98 \cdot 10^{-6}$ when analyzing MD trajectories of the Fe²⁺/Fe³⁺ redox state, and to $3.03 \cdot 10^{-5}$ and $1.52 \cdot 10^{-5}$ for the Fe³⁺/Fe²⁺ redox state.

As $\langle \epsilon_{tot}^2 \rangle = \langle \epsilon_{tot} \rangle^2 + \sigma^2$ with $\sigma^2 = \langle (\epsilon_{tot} - \langle \epsilon_{tot} \rangle)^2 \rangle$, the ratio R_{coh}^{cl} defined as $R_{coh}^{cl} = \langle \epsilon_{tot} \rangle^2 / \langle \epsilon_{tot}^2 \rangle$ permits to assess if tunneling is governed by fluctuations of the electronic coupling or by its average (Balabin and Onuchic, 2000; Balabin et al., 2012).

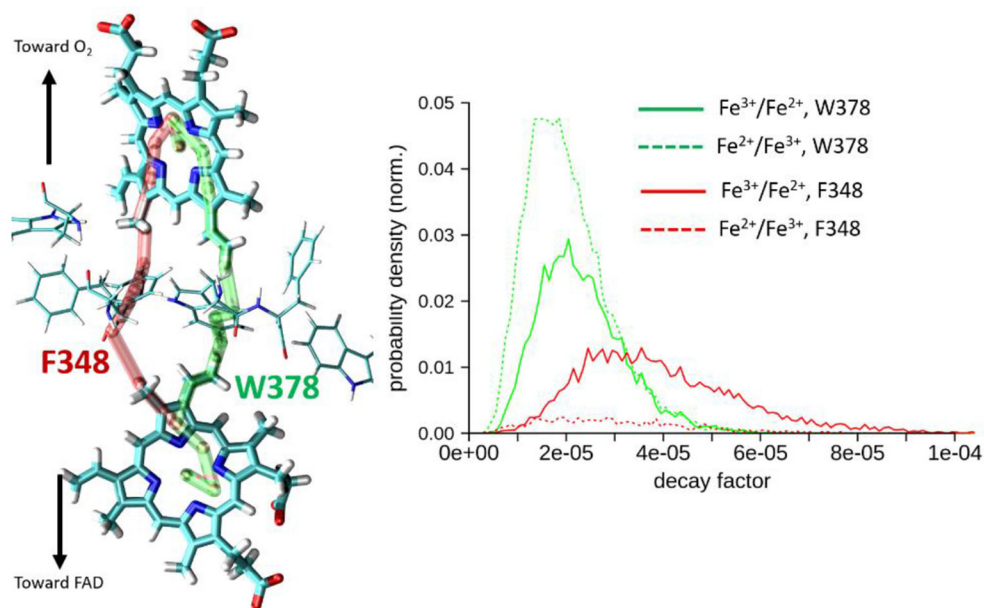


FIGURE 6 | Left, illustration of the two types of pathways encountered for heme-to-heme ET in NOX5 running either through Trp378 (in green) or through Phe348 (in red). Right, distributions of tunneling decay factors for MD simulations in the $\text{Fe}^{2+}/\text{Fe}^{3+}$ and $\text{Fe}^{3+}/\text{Fe}^{2+}$ redox states (in dashed and plane lines respectively), deconvoluted by pathway types.

If R_{coh}^{cl} approaches unity it means that $\langle \varepsilon_{tot} \rangle^2 \gg \sigma^2$, tunneling is governed by the average value. On the other hand, if R_{coh}^{cl} approaches 0.5, it means that $\langle \varepsilon_{tot} \rangle^2 \ll \sigma^2$, i.e. tunneling is likely to be dominated by the fluctuations. We obtain values larger than 0.8 suggesting tunneling is actually dominated by a single kind of pathway in both cases. This observation is consistent with the fact that almost all pathways run through Trp378 or Phe348. Note that R_{coh}^{cl} is a classical coherence-like parameter in the sense that it is calculated from ε_{tot} provided by the semi-empirical pathway model. R_{coh}^{cl} does not explicitly capture fine quantum effects like interferences among competing tunneling pathways running through the intervening medium (Prytkova et al., 2007). The pathway does not give access to H_{if} , but to the decay ε_{tot} caused by the presence of an intervening medium (see the first equation). A crude estimation of the absolute coupling may still be obtained by setting $H_{if}^{contact}$ to $4.3 \cdot 10^{13}$ Hz (0.177829 eV) (as in Prytkova et al., 2005), yielding an average value of $3.75 \cdot 10^{-6}$ eV for $\langle H_{if}^{PM} \rangle$ from MD trajectories of the $\text{Fe}^{2+}/\text{Fe}^{3+}$ state.

Probing the Putative O_2 -accessible Cavity and Tunneling Pathways

The authors of Magnani et al. (2017) identified a putative cavity to bind the dioxygen molecule in the vicinity of Heme2 (right insert in Figure 2). In the simulation without O_2 , we saw that a water molecule occupied this cavity, that is shaped by residues Arg256, His313, and His317 and Heme2 (Figure 7). We replaced this water molecule with a dioxygen molecule to perform MD simulations with O_2 . First attempts to run simulations without

constraint on O_2 position lead to its escape from the protein matrix. This may be due to the fact that there is only one dioxygen molecule in the system and/or to the fact that the protein has not had enough time to accommodate to the O_2 molecule. Since we are interested in the impact of O_2 binding on the dynamics of the protein and on the ET parameters, we decided to constrain O_2 to remain in the cavity. To this end we used Colvar options in NAMD. We defined a distance between the center of mass (COM) of the cavity and O_2 [hereafter referred to as $d(\text{O}_2\text{-COM})$]. We added a boundary semi-harmonic potential restraint applying on this distance when it is more than 5 Å and with a force constant of 20 kcal/mol/Å².

Figure 7C shows the histograms of this distance in the initial and final electronic states for the 300 ns-long MD simulations. A bimodal structure appears with two different positions of O_2 around the cavity. The oscillations of O_2 between these two positions occur at the timescale of few ns. The first position is O_2 inserted inside the cavity with $d(\text{O}_2\text{-COM})$ of around 2.5 Å (Figure 7A) and a distance between O_2 and the Fe atom of Heme2 ($d(\text{O}_2\text{-Fe})$) around 5.5 Å. The other one corresponds to O_2 lying on the edge of the cavity with $d(\text{O}_2\text{-COM})$ of around 4.3 Å and $d(\text{O}_2\text{-Fe})$ around 8.5 Å (Figure 7B). The relative proportion of occupancy of the two sites is reversed in the two electronic states. After the electron transfer (in red), O_2 is more often close to Heme2 than in the initial state (black).

To explore possible implications of the existence of these two connected cavities for electron tunneling pathways connecting Heme2 to O_2 , we have carried out pathway analyses as in the previous section, but enlarging the pruned system to encompass amino acid residues from the binding pocket. We have analyzed

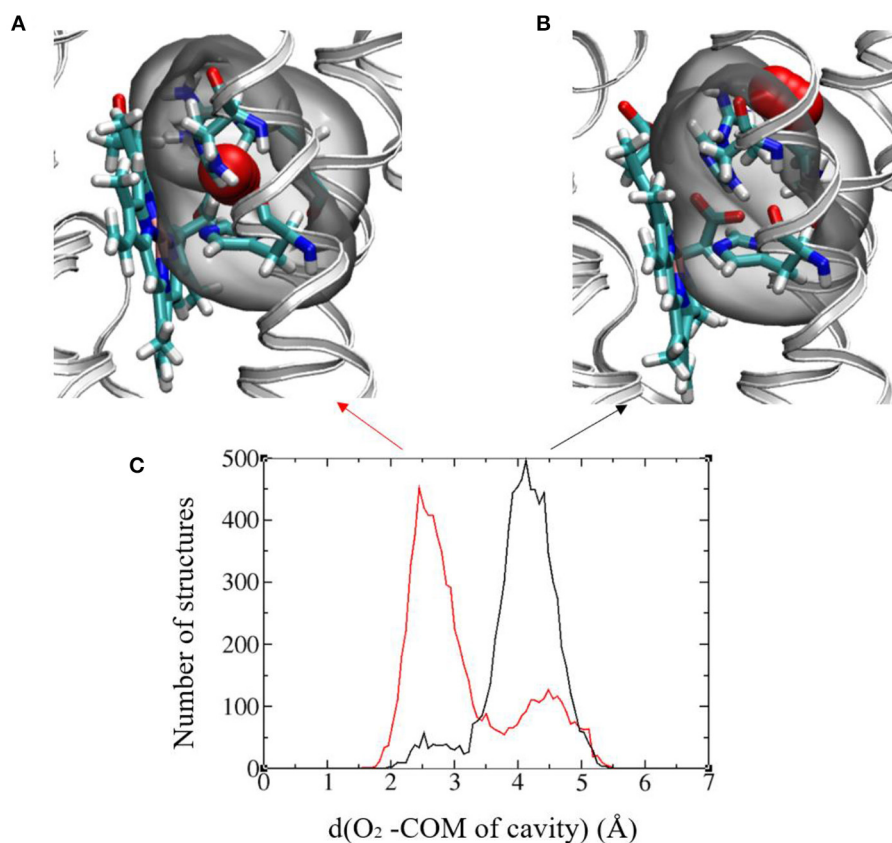


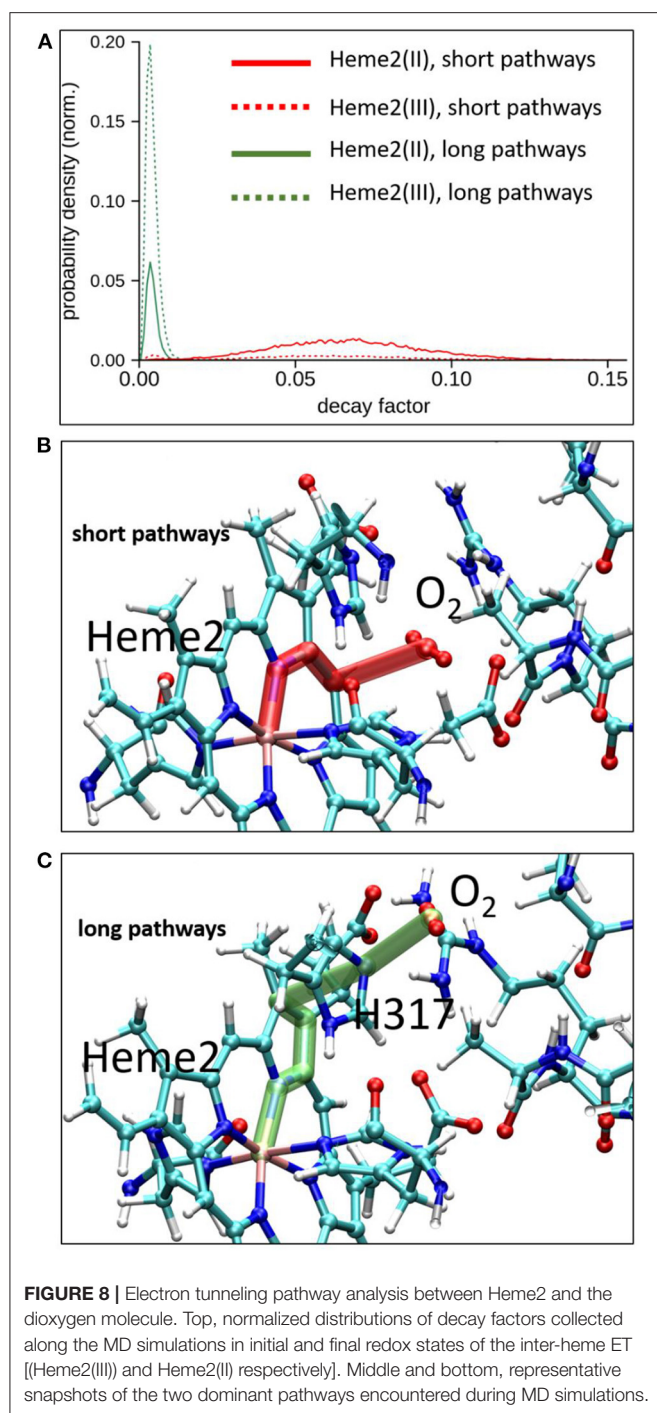
FIGURE 7 | (A) and (B) Images showing the two favored O₂ positions with respect to the binding cavity. The protein backbone is represented in gray ribbon and the cavity is highlighted in all-atom representation: Arg256, His313, and His317 and Heme2, O₂ (in red). The cavity in gray bubble. (C) Histograms of the distance between O₂ and the center of mass (COM) of the cavity in the initial (black) and final (red) redox states. Results from the 300ns-long MD runs.

all the MD simulations (in the initial and final electronic states of the inter-heme ET). Two kinds of pathways are identified. The “short pathway” type implies a direct through-space jump from the porphyrin ring to O₂. It is illustrated in **Figure 8** (middle). The “long pathway” involves an intermediate passage through His317 before jumping to O₂. The short pathways are associated to an average decay factor of 0.065 while the long pathways are associated to an average decay factor of 0.004, which is directly correlated to the respective lengths of the pathways. Interestingly, the short pathways are predominant when Heme2 is reduced, while the long pathways are dominant when Heme2 is oxidized. This could be a piece of the mechanism ensuring superoxide production catalysis. When Heme2 is reduced, thus ready to transfer an electron to a dioxygen molecule, the latter binds closer to the porphyrin ring, hence enabling very fast tunneling. The molecular origin of the dynamical control of the position shifting is not completely clear. From our simulations, it appears that the positively charged arginine Arg256 and histidine His317 play a role in this process. The conformations accessible to Arg256 in both redox states are similar. There is no frank residue repositioning upon Heme2 reduction. On the other hand, while Arg256 is almost exclusively hydrogen bonded to the propionate moieties in the ferrous state, it also often

makes alternative hydrogen bonds to His317 in the ferric state (**Supplementary Figure 8**). In such situations, the cavity for O₂ binding close to Heme2 is inaccessible. Further simulations will be needed to fully explain this behavior.

DISCUSSION AND CONCLUSION

This study reports the first molecular simulations of a NOX system inserted into a lipid bilayer membrane. Starting from separate experimental structures of the DH and TM domains of NOX5, we have built a fused model of the full protein. This model is stable in MD simulations at the timescale of hundreds of nanoseconds. The interface between the two domains involves the same residues as in the very recent cryo-EM structures of the homologous protein DUOX1, however the DH domain has a different orientation in our model. We have focused on electron transfer between Heme1 and Heme2 within the TM domain, and on the impact of O₂ on ET thermodynamics parameters. Dioxygen binding in the vicinity of Heme 2 appears to reduce the fluctuations of the energy difference between the two redox states involved in the ET, leading to more stable values of ET parameters. In both cases, O₂ binding doesn't



significantly alter the thermodynamics of inter-heme electron transfer. Negative values of the redox free energies on the order of few tenths of eV have been obtained, corresponding to spontaneous ET. Outer-sphere reorganization energies of about 1.1–1.3 eV (including contributions of the inner and outer-spheres) have been observed. Decomposition of these thermodynamics parameters over the molecular components of the system has provided additional insight. First, the DH has little impact on the inter-heme ET, suggesting that the relative

orientation of the DH with respect to the cryo-EM structure is not a major concern for the present study of inter-heme ET. Second, we have highlighted the subtle balance existing between the protein matrix, the membrane, the water and the counter-ions. Our results should stimulate other studies aiming at investigating for instance the effect of membrane composition on inter-heme ET. Considering that outer-sphere reorganization energies have been calculated with a non-polarizable forcefield and are thus overestimated by *ca.* 30%, the values obtained fall within the range of values (0.7–1.0 eV) obtained recently for inter-heme ET within multi-hemic protein (Breuer et al., 2012). We have finally evaluated the tunneling coupling matrix element to fall within the μ eV based on the tunneling pathway model (Beratan et al., 1991; Prytkova et al., 2005). We have been able to confirm the important role of Trp378 and Phe348 to sustain electron tunneling between the two hemes.

Dioxygen reduction by electron transfer is another essential part of NOX5 function that remains unclear though of prominent importance to understand the NOX machinery. It was suggested from Electron Paramagnetic Resonance and Raman spectroscopies (Yamaguchi et al., 1989; Hurst et al., 1991; Ueno et al., 1991; Fujii et al., 1999) that since Heme2 is hexacoordinated Heme2-to-O₂ ET is likely to proceed via an outer-sphere mechanism. This hypothesis was corroborated by stopped-flow and rapid-scanning spectroscopy oxidation-reduction kinetics on porcine neutrophils (Isogai et al., 1995). The identification of a putative binding cavity in the 3D structure of NOX5 further supports this hypothesis (Magnani et al., 2017). In NOX5, the cavity is formed by Arg256, His313, and His317. We have investigated the localization of dioxygen near Heme2 by means of molecular dynamics simulations. Our simulations revealed that the cavity deduced from the X-ray structure is actually flexible, offering two possible binding sites, one being closer to the heme than the other, while the other is more accessible to solvent. The occupancy of these two sites depends on the redox states of the two hemes. When Heme2 is in a reduced state, the close position of O₂ is largely favored. Importantly, this occupancy shift is coupled to the emergence of ten-times more efficient electron tunneling pathways than when O₂ is positioned in the remote cavity. This 10-fold increase of tunneling matrix element would induce a 100-fold increase of ET rate from Heme2 to O₂, therefore providing a powerful mean to catalyze superoxide production. We speculate that Arg256 is playing a central role in this process, since this positively charged residue necessarily rearranges when Heme2 is reduced. On the other hand, our MD simulations don't reveal any dramatic cavity shape modifications, but more subtle rearrangements. The stability of the hydrogen bond network among Arg256, His317, and the Heme2's propionate groups that shape the cavity appears to be sensitive to the charge present on Heme2. Further investigations will be needed to fully decipher this mechanism. Our study thus provides a possible mechanistic explanation to the experimental results reported in Magnani et al. (2017) indicating that the oxidation rate in R256S and H317R mutants were at least fivefold lower than observed for wild type. We now need to investigate the thermodynamics of this ET, including the possibility of spin-inversion on Heme2 cofactor as suggested by some authors

(Doussière et al., 1996; Maturana et al., 2001), as well as the mechanism of primary binding of dioxygen into the remote cavity when Heme2 is oxidized.

This work is the first step toward a global investigation of the mechanism of superoxide production by the NOX machinery using molecular simulation. Many aspects deserve further analysis (computation of kinetic parameters, study of the electron transfers between FAD and Heme1, influence of lipid composition and/or mutation of key residues sustaining ETs in NOX...). The refinement of computational methods (such as the use of polarizable forcefields) will allow us to ascertain the conclusions drawn in this study, but the results obtained here open the path to a better understanding of NOX.

DATA AVAILABILITY STATEMENT

The datasets presented in this study can be found in online repositories. The names of the repository/repositories and accession number(s) can be found below: doi: 10.5281/zenodo.4424142; https://zenodo.org/record/4424142#.X_ciUyXjLeM/b.

AUTHOR CONTRIBUTIONS

MB, JH, and AL designed research. XW performed research. XW, JH, FC and AL carried out complementary analyses. All

authors discussed and analyzed research data. All authors wrote the manuscript.

FUNDING

Computational work was performed using HPC resources from GENCI (Grant Number A0070701714) and from LBT-HPC thanks to support from Geoffrey Letessier. This work was supported by the Initiative d'Excellence program from the French State (Grant DYNAMO, ANR-11-LABX-0011 and Grant CACSICE, ANR-11-EQPX-0008). MB thanks Sesame Ile-de-France for co-funding the display wall used for data analysis.

ACKNOWLEDGMENTS

We are grateful to Prof. Mattevi who provided us with early pdb file containing atomic coordinates of the NOX5 3D model they built and that turned very useful to initiate our work.

SUPPLEMENTARY MATERIAL

The Supplementary Material for this article can be found online at: <https://www.frontiersin.org/articles/10.3389/fchem.2021.650651/full#supplementary-material>

REFERENCES

- Balabin, I. A., Hu, X., and Beratan, D. N. (2012). Exploring biological electron transfer pathway dynamics with the pathways plugin for VMD. *J. Comput. Chem.* 33, 906–910. doi: 10.1002/jcc.22927
- Balabin, I. A., and Onuchic, J. N. (2000). Dynamically controlled protein tunneling paths in photosynthetic reaction centers. *Science* 290, 114–117. doi: 10.1126/science.290.5489.114
- Bedard, K., and Krause, K.-H. (2007). The NOX family of ROS-generating NADPH oxidases: physiology and pathophysiology. *Physiol. Rev.* 87, 245–313. doi: 10.1152/physrev.00044.2005
- Bedard, K., Lardy, B., and Krause, K.-H. (2007). NOX family NADPH oxidases: not just in mammals. *Biochimica* 89, 1107–1112. doi: 10.1016/j.biochi.2007.01.012
- Benkert, P., Biasini, M., and Schwede, T. (2011). Toward the estimation of the absolute quality of individual protein structure models. *Bioinformatics*, 27, 343–350. doi: 10.1093/bioinformatics/btq662
- Beratan, D. N., Betts, J. N., and Onuchic, J. N. (1991). Protein electron transfer rates set by the bridging secondary and tertiary structure. *Science* 252, 1285–1288. doi: 10.1126/science.1656523
- Beratan, D. N., Liu, C., Migliore, A., Polizzi, N. F., Skourtis, S. S., Zhang, P., et al. (2015). Charge transfer in dynamical biosystems, or the treachery of (static) images. *Acc. Chem. Res.* 48, 474–481. doi: 10.1021/ar500271d
- Beratan, D. N., Onuchic, J. N., and Hopfield, J. J. (1987). Electron tunneling through covalent and noncovalent pathways in proteins. *J. Chem. Phys.* 86, 4488–4498. doi: 10.1063/1.452723
- Blumberger, J. (2008). Free energies for biological electron transfer from QM/MM calculation: method, application and critical assessment. *Phys. Chem. Chem. Phys.* 10, 5651–5667. doi: 10.1039/b807444e
- Bréchar, S., Plançon, S., and Tschirhart, E. J. (2012). New insights into the regulation of neutrophil NADPH oxidase activity in the phagosome: a focus on the role of lipid and Ca²⁺ signaling. *Antioxid. Redox Signal.* 18, 661–676. doi: 10.1089/ars.2012.4773
- Breuer, M., Zarzycki, P., Shi, L., Clarke, T. A., Edwards, M. J., Butt, J. N., et al. (2012). Molecular structure and free energy landscape for electron transport in the decahaem cytochrome MtrF. *Biochem. Soc. Trans.* 40, 1198–1203. doi: 10.1042/BST20120139
- Brooks, C. L., Brooks, A. D. III, Mackerell L. Jr, Nilsson, R. J., Petrella, B., Roux, Y., et al. (2009). The biomolecular simulation program. *J. Comput. Chem.* 30, 1545–1614. doi: 10.1002/jcc.21287
- Buchan, D. W. A., and Jones, D. T. (2019). The PSIPRED protein analysis workbench: 20 years on. *Nucl. Acid Res.* 47, W402–W407. doi: 10.1093/nar/gkz297
- Cross, A. R., Rae, J., and Curnutte, J. T. (1995). Cytochrome b of the neutrophil superoxide-generating system contains two nonidentical hemes: POTENTIOMETRIC STUDIES OF A MUTANT FORM OF Gp91. *J. Biol. Chem.* 270, 17075–17077. doi: 10.1074/jbc.270.29.17075
- de la Lande, A., Babcock, N. S., Rezáč, J., Sanders, B. C., and Salahub, D. R. (2010). Surface residues dynamically organize water bridges to enhance electron transfer between proteins. *Proc. Natl. Acad. Soc.* 107, 11799–11804. doi: 10.1073/pnas.0914457107
- de la Lande, A., Babcock, N. S., Rezáč, J., Sanders, B. C., and Salahub, D. R. (2013). Surface residues dynamically organize water bridges to enhance electron transfer between proteins. *Proc. Natl. Acad. Soc.* 110, 1136–1137. doi: 10.1073/pnas.1220833110
- Dijkstra, E. W. (1959). A note on two problems in connexion with graphs. *Numer. Math.* No. 1, 269:BF01386390. doi: 10.1007/BF01386390
- Dominguez, C., Boelens, R., and Bonvin, A. M. J. J. (2003). HADDOCK: a protein-protein docking approach based on biochemical or biophysical information. *J. Am. Chem. Soc.* 125, 1731–1737. doi: 10.1021/ja026939x
- Doussière, J., Gaillard, J., and Vignais, P. V. (1996). Electron transfer across the O²-generating flavocytochrome b of neutrophils. Evidence for a transition from a low-spin state to a high-spin state of the heme iron component. *Biochemistry* 35, 13400–13410. doi: 10.1021/bi960916b
- El Hammi, E., Houee-Levin, C., Rezac, J., Levy, B., Demachy, I., Baciou, L., et al. (2012). New insights into the mechanism of electron transfer within

- flavohemoglobins: tunnelling pathways, packing density, thermodynamic and kinetic analyses. *Phys. Chem. Chem. Phys.* 14, 13872–13880. doi: 10.1039/c2cp41261f
- Fiorin, G., Klein, M. L., and Hénin, J. (2013). Using collective variables to drive molecular dynamics simulations. *null* 111, 3345–3362. doi: 10.1080/00268976.2013.813594
- Fujii, H., Finnegan, M. G., and Johnson, M. K. (1999). The active form of the ferric heme in neutrophil cytochrome B558 is low-spin in the reconstituted cell-free system in the presence of amphiphil. *J. Biochem.* 126, 708–714. doi: 10.1093/oxfordjournals.jbchem.a022507
- Geiszt, M., and Leto, T. L. (2004). The NOX family of NAD(P)H oxidases: host defense and beyond. *J. Biol. Chem.* 279, 51715–51718. doi: 10.1074/jbc.R400024200
- Hajjar, C., Cherrier, M. V., Dias Mirandela, G., Petit-Hartlein, I., Stasia, M. J., Fontecilla-Camps, J. C., et al. (2017). The NOX family of proteins is also present in bacteria. *mBio*, 8:e01487–e01417. doi: 10.1128/mBio.01487-17
- Hurst, J. K., Loehr, T. M., Curnutte, J. T., and Rosen, H. (1991). Resonance raman and electron paramagnetic resonance structural investigations of neutrophil cytochrome B558. *J. Biol. Chem.* 266, 1627–1634. doi: 10.1016/S0021-9258(18)52340-1
- Isogai, Y., Iizuka, T., and Shiro, Y. (1995). The mechanism of electron donation to molecular oxygen by phagocytic cytochrome B558. *J. Biol. Chem.* 270, 7853–7857. doi: 10.1074/jbc.270.14.7853
- Javanainen, M., Vattulainen, I., and Monticelli, L. (2017). On atomistic models for molecular oxygen. *J. Phys. Chem. B*, 121, 518–528. doi: 10.1021/acs.jpcc.6b11183
- Javanainen, M., Vattulainen, I., and Monticelli, L. (2020). Correction to “on atomistic models for molecular oxygen”. *J. Phys. Chem. B* 124, 6943–6946. doi: 10.1021/acs.jpcc.0c06376
- Jo, S., Kim, T., Iyer, V. G., and Im, W. (2008). CHARMM-GUI: a web-based graphical user interface for CHARMM. *J. Comput. Chem.* 29, 1859–1865. doi: 10.1002/jcc.20945
- Joly, J., Hudik, E., Lecart, S., Roos, D., Verkuiljen, P., Wrona, D., et al. (2020). Membrane dynamics and organization of the phagocyte NADPH oxidase in PLB-985 cells. *Front. Cell Dev. Biol.* 8:1295. doi: 10.3389/fcell.2020.608600
- King, G., and Warshel, A. (1990). Investigation of the free energy functions for electron transfer reactions. *J. Chem. Phys.* 93, 8682–8692. doi: 10.1063/1.459255
- Lee, J., Cheng, X., Swails, J. M., Yeom, M. S., Eastman, P. K., Lemkul, J. A., et al. (2016). CHARMM-GUI input generator for NAMD, GROMACS, AMBER, OpenMM, and CHARMM/OpenMM simulations using the CHARMM36 additive force field. *J. Chem. Theory Comput.* 12, 405–413. doi: 10.1021/acs.jctc.5b.00935
- MacKerell, A. D., Bashford, D., Bellott, M., Dunbrack, R. L., Evanseck, J. D., Field, M. J., et al. (1998). All-atom empirical potential for molecular modeling and dynamics studies of proteins. *J. Phys. Chem. B* 102, 3586–3616. doi: 10.1021/jp973084f
- Magalhaes, M. A. O., and Glogauer, M. (2010). Pivotal advance: phospholipids determine net membrane surface charge resulting in differential localization of active Rac1 and Rac2. *J. Leuk. Biol.* 87, 545–555. doi: 10.1189/jlb.0609390
- Magnani, F., Nenci, S., Millana Fananas, E., Ceccon, M., Romero, E., Fraaije, M. W., et al. (2017). Crystal structures and atomic model of NADPH oxidase. *Proc. Natl. Acad. Sci.* 114, 6764–6769. doi: 10.1073/pnas.1702293114
- Marcus, R. A., and Sutin, N. (1985). Electron transfers in chemistry and biology. *Biochim. Biophys. Acta* 811, 265–322. doi: 10.1016/0304-4173(85)90014-X
- Maturana, A., Arnaudeau, S., Ryser, S., Banfi, B., Hossle, J. P., Schlegel, W., et al. (2001). Heme histidine ligands within Gp91 Phox modulate proton conduction by the phagocyte NADPH oxidase. *J. Biol. Chem.* 276, 30277–30284. doi: 10.1074/jbc.M010438200
- Matyushov, D. (2015). Protein electron transfer: is biology (thermo) dynamic? *J. Phys. Condens. Matter*, 27:473001. doi: 10.1088/0953-8984/27/47/473001
- Onuchic, J. N., and Beratan, D. N. (1990). A predictive theoretical model for electron tunneling pathways in proteins. *J. Chem. Phys.* 92, 722–733. doi: 10.1063/1.458426
- Phillips, J. C., Braun, R., Wang, W., Gumbart, J., Tajkhorshid, E., Villa, E., et al. (2005). Scalable molecular dynamics with NAMD. *J. Comput. Chem.* 26, 1781–1802. doi: 10.1002/jcc.20289
- Phillips, J. C., Hardy, D. J., Maia, J. D. C., Stone, J. E., Ribeiro, J. V., Bernardi, R. C., et al. (2020). Scalable molecular dynamics on CPU and GPU architectures with NAMD. *J. Chem. Phys.* 153:044130. doi: 10.1063/5.0014475
- Prytkova, T. R., Kurnikov, I. V., Beratan, D. N. (2005). Ab initio based calculations of electron-transfer rates in metalloproteins. *J. Phys. Chem. B* 109, 1618–1625. doi: 10.1021/jp0457491
- Prytkova, T. R., Kurnikov, I. V., and Beratan, D. N. (2007). Coupling coherence distinguishes structure sensitivity in protein electron transfer. *Science* 315, 622–625. doi: 10.1126/science.1134862
- Šali, A., and Blundell, T. L. (1993). Comparative protein modelling by satisfaction of spatial restraints. *J. Mol. Biol.* 234, 779–815. doi: 10.1006/jmbi.1993.1626
- Shao, D., Segal, A. W., and Dekker, L. V. (2003). Lipid rafts determine efficiency of NADPH oxidase activation in neutrophils. *FEBS Lett.* 550, 101–106. doi: 10.1016/S0014-5793(03)00845-7
- Shen, M., and Sali, A. (2006). Statistical potential for assessment and prediction of protein structures. *Prot. Sci.* 15, 2507–2524. doi: 10.1110/ps.062416606
- Souabni, H., Machillot, P., and Baciou, L. (2014). Contribution of lipid environment to NADPH oxidase activity: influence of sterol. *Biochemistry* 107, 33–42. doi: 10.1016/j.biochi.2014.10.006
- Souabni, H., Wien, F., Bizouarn, T., Houée-Levin, C., Réfrégiers, M., and Baciou, L. (2017). The physicochemical properties of membranes correlate with the NADPH oxidase activity. *Biochim. Biophys. Acta.* 1861, 3520–3530. doi: 10.1016/j.bbagen.2016.06.028
- Sumimoto, H. (2008). Structure regulation and evolution of NOX-family NADPH oxidases that produce reactive oxygen species. *FEBS J.* 275, 3249–3277. doi: 10.1111/j.1742-4658.2008.06488.x
- Sun, J. (2020). Structures of mouse DUOX1–DUOX1 provide mechanistic insights into enzyme activation and regulation. *Nat. Struct. Mol. Biol.* 27, 1086–1093. doi: 10.1038/s41594-020-0501-x
- Ueno, I., Fujii, S., Ohya-Nishiguchi, H., Iizuka, T., and Kanegasaki, S. (1991). Characterization of neutrophil B-type cytochrome *in situ* by electron paramagnetic resonance spectroscopy. *FEBS Lett.* 281, 130–132. doi: 10.1016/0014-5793(91)80375-D
- van Zundert, G. C. P., Rodrigues, J. P. G. L. M., Trellet, M., Schmitz, C., Kastiris, P. L., Karaca, E., et al. (2016). The HADDOCK2.2 web server: user-friendly integrative modeling of biomolecular complexes. *J. Mol. Biol.* 428, 720–725. doi: 10.1016/j.jmb.2015.09.014
- Yamaguchi, T., Hayakawa, T., Kaneda, M., Kakinuma, K., and Yoshikawa, A. (1989). Purification and some properties of the small subunit of cytochrome B558 from human neutrophils. *J. Biol. Chem.* 264, 112–118. doi: 10.1016/S0021-9258(17)31230-9

Conflict of Interest: The authors declare that the research was conducted in the absence of any commercial or financial relationships that could be construed as a potential conflict of interest.

Copyright © 2021 Wu, Hénin, Baciou, Baaden, Cailliez and de la Lande. This is an open-access article distributed under the terms of the Creative Commons Attribution License (CC BY). The use, distribution or reproduction in other forums is permitted, provided the original author(s) and the copyright owner(s) are credited and that the original publication in this journal is cited, in accordance with accepted academic practice. No use, distribution or reproduction is permitted which does not comply with these terms.



The High-Spin Heme b_L Mutant Exposes Dominant Reaction Leading to the Formation of the Semiquinone Spin-Coupled to the $[2Fe-2S]^+$ Cluster at the Q_o Site of *Rhodobacter capsulatus* Cytochrome bc_1

OPEN ACCESS

Edited by:

Petra Hellwig,
Université de Strasbourg,
France

Reviewed by:

Frauke Baymann,
CNRS UMR7281 Bioénergétique et
Ingénierie des Protéines, France
Di Xia,
National Institutes of Health (NIH),
United States

*Correspondence:

Artur Osyczka
artur.osyczka@uj.edu.pl

[†]These authors have contributed
equally to this work

Specialty section:

This article was submitted to
Theoretical and Computational
Chemistry,
a section of the journal
Frontiers in Chemistry

Received: 26 January 2021

Accepted: 19 April 2021

Published: 07 May 2021

Citation:

Sarewicz M, Pintscher S, Bujnowicz L,
Wolska M,
Artur Osyczka (2021) The High-Spin
Heme b_L Mutant Exposes Dominant
Reaction Leading to the Formation of
the Semiquinone Spin-Coupled to the
 $[2Fe-2S]^+$ Cluster at the Q_o Site of
Rhodobacter capsulatus
Cytochrome bc_1 .
Front. Chem. 9:658877.
doi: 10.3389/fchem.2021.658877

Marcin Sarewicz, Sebastian Pintscher[†], Łukasz Bujnowicz[†], Małgorzata Wolska and
Artur Osyczka *

Department of Molecular Biophysics, Faculty of Biochemistry, Biophysics and Biotechnology, Jagiellonian University,
Kraków, Poland

Cytochrome bc_1 (mitochondrial complex III) catalyzes electron transfer from quinols to cytochrome c and couples this reaction with proton translocation across lipid membrane; thus, it contributes to the generation of protonmotive force used for the synthesis of ATP. The energetic efficiency of the enzyme relies on a bifurcation reaction taking place at the Q_o site which upon oxidation of ubiquinol directs one electron to the Rieske $2Fe2S$ cluster and the other to heme b_L . The molecular mechanism of this reaction remains unclear. A semiquinone spin-coupled to the reduced $2Fe2S$ cluster ($SQ_o-2Fe2S$) was identified as a state associated with the operation of the Q_o site. To get insights into the mechanism of the formation of this state, we first constructed a mutant in which one of the histidine ligands of the iron ion of heme b_L *Rhodobacter capsulatus* cytochrome bc_1 was replaced by asparagine (H198N). This converted the low-spin, low-potential heme into the high-spin, high-potential species which is unable to support enzymatic turnover. We performed a comparative analysis of redox titrations of antimycin-supplemented bacterial photosynthetic membranes containing native enzyme and the mutant. The titrations revealed that H198N failed to generate detectable amounts of $SQ_o-2Fe2S$ under neither equilibrium (in dark) nor nonequilibrium (in light), whereas the native enzyme generated clearly detectable $SQ_o-2Fe2S$ in light. This provided further support for the mechanism in which the back electron transfer from heme b_L to a ubiquinone bound at the Q_o site is mainly responsible for the formation of semiquinone trapped in the $SQ_o-2Fe2S$ state in *R. capsulatus* cytochrome bc_1 .

Keywords: cytochrome bc_1 (complex III), electron transfer, quinol oxidation, semiquinone, electron paramagnetic resonance

Abbreviations: Cyt bc_1 , cytochrome bc_1 ; Q, quinone (general); QH₂, quinol (general); UQ, ubiquinone; UQH₂, ubihydroquinone; RC, reaction center; $2Fe2S$, $[2Fe-2S]$ Rieske iron-sulfur cluster; SQ_o , semiquinone at the Q_o site; $SQ_o-2Fe2S$, semiquinone spin-coupled to the reduced $2Fe2S$.

INTRODUCTION

The cytochrome *bc*₁ complex (Cyt*bc*₁) is one of the enzymes involved in energy conversion that takes place in mitochondria and many prokaryotic respiratory chains and anoxygenic photosynthesis (Berry et al., 2000; Crofts, 2004; Sarewicz and Osyczka, 2015). Structurally and functionally very similar to Cyt*bc*₁—cytochrome *b*₆*f* is a central enzyme of oxygenic photosynthesis in cyanobacteria and plants (Darrouzet et al., 2004; Baniulis et al., 2008; Hasan et al., 2013; Cramer and Hasan, 2016). Cyt*bc*₁ catalyzes electron transfer from membrane-soluble electron carriers—quinone (Q) derivatives (usually ubiquinones) (Al-Attar and de Vries, 2013) to water-soluble electron carrier: cytochrome *c* (Bertini et al., 2006). The energy released during enzymatic reduction of cytochrome *c* by ubiquinol (UQH₂) is used to transfer protons across the membrane, contributing to building up the protonmotive force (Hunte et al., 2003). Cyt*bc*₁ is not operating as a typical proton pump that uses special proton channels but it utilizes quinone molecules to transport protons across the lipid bilayers (Al-Attar and de Vries, 2013). This transport is carried out by coupling two opposite redox reactions of quinones at the two catalytic sites that are located within the enzyme structure at the opposite sides of the membrane (Mitchell, 1975; Crofts et al., 1983). The UQH₂ oxidation site (Q_o site) is located close to the *p* side of the membrane (the positively charged side), while the UQ-reduction site (Q_i site) is located close to the *n* side of the membrane (the negatively charged side) (Xia et al., 1997; Crofts and Berry, 1998). The Q_o and Q_i sites are electronically connected by two low-potential, low-spin hemes *b*: heme *b*_L [*E*_{m,7} ~ -120 mV in *R. capsulatus* (Zhang et al., 2008)], which is adjacent to the Q_o site and heme *b*_H [*E*_{m,7} ~ +60 mV], which is adjacent to the Q_i site. The oxidation of UQH₂ at the Q_o site is accompanied by the release of two protons to the bulk water at the *p* side. Oppositely, the reduction taking place at the Q_i site is associated with uptake of two protons from the *n* side of the membrane. This way the protons are transported through the membrane along with pairs of diffusing UQH₂/UQ molecules.

The reduction of UQ at the Q_i site is a sequential process, involving two consecutive electron transfers from the same cofactor (heme *b*_H). A stable semiquinone is an intermediate of this reaction (Robertson et al., 1984; Jünemann et al., 1998; Dikanov et al., 2004) and, as implicated from recent studies, a mechanism of its stabilization might involve polarization of charges within the ring (Pintscher et al., 2020). On the other hand, the oxidation of UQH₂ at the Q_o site directs two electrons derived from the UQH₂ into two separate cofactor chains. In this so-called electron bifurcation reaction one electron is transferred on the Rieske [2Fe-2S] cluster (2Fe2S) and further, through cytochrome *c*₁ onto a water-soluble cytochrome *c* (or *c*₂ in some bacteria, such as the *Rhodobacter* strains). The second electron is transferred to heme *b*_L and subsequently through heme *b*_H it reaches the Q_i site where UQ is reduced first to semiquinone form (USQ_i) and then to UQH₂.

Despite a long history of studying the mechanism of electron bifurcation, the involvement of a semiquinone intermediate (USQ_o) in this reaction is still unclear and thus a matter of

intense discussion (Osyczka et al., 2004; Osyczka et al., 2005; Cape et al., 2007; Zhang et al., 2007; Zhu et al., 2007; Crofts et al., 2013; Sarewicz et al., 2013; Crofts et al., 2017; Sarewicz et al., 2021). A general agreement has been reached that a superoxide generation by Cyt*bc*₁ results from a reaction of USQ_o with molecular oxygen (Boveris and Cadenas, 1975; Ksenzenko et al., 1983; Muller et al., 2002; Borek et al., 2008; Dröse and Brandt, 2008; Sarewicz et al., 2010; Pagacz et al., 2021). However, trapping the intermediate USQ_o radical during the UQH₂ oxidation and its detection by electron paramagnetic resonance (EPR) has been proven difficult and obtained results have often been disputable or contradictory (de Vries et al., 1981; Jünemann et al., 1998; Cape et al., 2006; Cape et al., 2007; Zhang et al., 2007; Zhu et al., 2007; Sarewicz et al., 2013; Vennam et al., 2013; Victoria et al., 2013; Pietras et al., 2016; Crofts et al., 2017; Sarewicz et al., 2017; Sarewicz et al., 2018; Bujnowicz et al., 2019). Additionally, the inability to generate USQ_o in the equilibrium redox titrations (Takamiya and Dutton, 1979; Sarewicz et al., 2018) implicated a concept of a high instability of the semiquinone and its reactivity was proposed to be a reason for superoxide production by Cyt*bc*₁.

Detection of a small amount of USQ_o under nonequilibrium conditions in isolated, antimycin-inhibited Cyt*bc*₁ has been reported in a few studies (Cape et al., 2007; Zhang et al., 2007; Vennam et al., 2013; Victoria et al., 2013). The presence of USQ_o in Cyt*bc*₁ samples was assigned to a stigmatellin-sensitive, X-band EPR signal which is typical of an organic radical with a nearly isotropic *g* value ~2.0 (Cape et al., 2007; Vennam et al., 2013). Although experimental evidences were not presented, generation of this signal was assumed to be associated with the oxidation of UQH₂ by the 2Fe2S cluster under conditions in which the resulting USQ_o was unable to donate electron to heme *b*_L as this heme, in antimycin-inhibited enzyme, was expected to be in the reduced state after two consecutive electron transfers from the Q_o site (Cape et al., 2007; Crofts et al., 2017).

Our previous work reported an unusual EPR signal with an average *g* value less than 2, which originated from the Q_o site of the antimycin-inhibited Cyt*bc*₁, isolated from *Rhodobacter capsulatus* (Sarewicz et al., 2013; Sarewicz et al., 2017; Bujnowicz et al., 2019). This signal was detected only when the Q_o site was able to catalyze the UQH₂ oxidation and the cytochrome *c* reduction before the system reached equilibrium. The signal was not present in the samples containing specific inhibitors of the Q_o site (stigmatellin, myxothiazol, famoxadone, azoxystrobin, kresoxim-methyl, etc.), nor in the mutants with disabled Q_o site (like, for example, *cyt**b*:G158W). Simulations of the EPR spectra suggested that this signal results from the spin-spin exchange interactions between USQ_o and the reduced 2Fe2S (it is thus referred to as SQ_o-2Fe2S) with approximated *J* constant ~3.6 GHz (Sarewicz et al., 2013). This suggestion was further supported by the observations that the *g* values of the SQ_o-2Fe2S state were frequency-dependent—they changed upon increasing the microwave frequency from X-band ~9.4 to Q-band ~33.5 GHz. At X-band, the most prominent “derivative-shaped” transition of SQ_o-2Fe2S in Cyt*bc*₁ was detected at *g* = ~1.94 and was found to shift to ~1.96 at Q-band. Remarkably, the SQ_o-2Fe2S signal was also detected in isolated but non-inhibited spinach cytochrome *b*₆*f* during the

oxidation of synthetic decylplastoquinol and the reduction of plastocyanin (Sarewicz et al., 2017).

Our subsequent work revealed that the SQ_o-2Fe₂S signal can be generated in antimycin-supplemented native chromatophore membranes isolated from *R. capsulatus*, in which the reactions at the Q_o site are triggered by the photosynthetic reaction center (RC) (Sarewicz et al., 2018). In these experiments, the characteristic transitions of the SQ_o-2Fe₂S state with a readily detectable maximum in continuous wave X-band spectra at $g = 1.95$ were detected during the redox-titration of chromatophores in relatively narrow ranges of the external redox potential (E_h). However, the signal appears only when the chromatophores are illuminated by continuous light during the titrations, which keeps the RC activated to supply substrates for the Q_o site. Similar titrations performed in dark, i.e. without activation of RC (equilibrium conditions), do not lead to the generation of SQ_o-2Fe₂S. Clearly, in membranes, similarly to isolated Cytbc₁, the SQ_o-2Fe₂S state corresponds to one of the states of the enzyme that can be populated to detectable levels only under nonequilibrium conditions.

One of the most important observations regarding the enzymatic state of *Rhodobacter capsulatus* Cytbc₁ is that the SQ_o-2Fe₂S state is detected in samples in which heme b_L remains oxidized (Sarewicz et al., 2013; Sarewicz et al., 2018). This suggests that in those experiments, the reaction sequence leading to the formation of the SQ_o-2Fe₂S state begins with the electron transfer from the reduced heme b_L to the UQ molecule bound at the Q_o site. The resulting SQ_o then interacts with the reduced 2Fe₂S that is present at the Q_o site. However, a direct evidence supporting this mechanism has not yet been provided. Furthermore, the SQ_o can, in principle, also be formed in another reaction: electron transfer from UQH₂ to oxidized 2Fe₂S, which would also result in the formation of the SQ_o-2Fe₂S state if the subsequent electron transfer from SQ_o to heme b_L is (somehow) blocked. In this work, we addressed this issue with a series of experiments performed with the histidine ligand mutant of *R. capsulatus* in which the heme b_L was inactivated. The mutation of choice was patterned after the previous study with closely related *Rhodobacter sphaeroides* where replacing the histidine ligand with asparagine (cyt*b*:H198N) was found to result in a loss of spectral properties of heme b_L typical of WT Cytbc₁ and in a complete loss of the enzymatic activity (Yang et al., 2008). We found that in *R. capsulatus* the H198N mutation converted the low-spin heme b_L into the high-spin heme unable to transfer electron from SQ_o to heme b_H , and such conditions were tested for the efficiency of SQ_o-2Fe₂S generation in chromatophores in dark or illuminated by light. The tests failed to detect the spin-spin-coupled SQ_o-2Fe₂S state in H198N even in chromatophores activated by light, which we considered an indication that electron transfer from heme b_L to the UQ molecule at the Q_o site is mainly responsible for creating conditions that ultimately lead to the formation of *R. capsulatus*.

MATERIALS AND METHODS

Construction of the H198N Mutant

The H198N mutant of *Rhodobacter capsulatus* containing the H198N mutation in cytochrome *b* subunit was generated using

the genetic system described previously (Atta-Asafo-Adjei and Daldal, 1991). Mutation H198N was constructed by the QuikChange site-directed mutagenesis kit from Stratagene using pPET1-ST (Czapla et al., 2012b) as the template, and the mutagenic forward H198N-F: 5'-TTC TTC TCG CTG AAC TAT CTG CTG CCC TTC G -3' and reverse H198N-R 5'-GGG CAG CAG ATA GTT CAG CGA GAA GAA GCG G -3' oligonucleotides. After sequencing, the *Xma*I/*Sfu*I fragment of pPET1-ST-H198N plasmid bearing the desired mutation and no other mutations was exchanged with its wild-type counterparts in pMTS1. This created the expression vector pMTS1-ST-H198N that was introduced into *R. capsulatus* MT-RBC1 strain (*petABC*-operon deletion background) via triparental crosses (Atta-Asafo-Adjei and Daldal, 1991). The presence of H198N mutation was confirmed by sequencing the plasmid DNA isolated from the mutated *R. capsulatus* strain (H198N mutant).

Isolation of Chromatophores

Chromatophores from *R. capsulatus* strains were prepared as described in detail by Sarewicz et al. (2018). Briefly, bacterial cultures were grown heterotrophically under semiaerobic conditions on the MPYE medium. After 48 h of growing the bacteria cells were centrifuged for 30 min at 6,641 g and the pellet resuspended in buffer containing 50 mM MOPS (pH 7), 100 mM KCl, and 1 mM EDTA, followed by the addition of protease inhibitors (benzamidine, PMSF, and 6-aminocaproic acid). The cells' suspension was then passed two times through French Press® with pressure maintained between 11 and 15 MPa. Bacterial lysate was then centrifuged for 30 min at 24,104g and the obtained supernatant was then ultra-centrifuged at 244,062g for 1.5 h. The pellet containing isolated chromatophores was resuspended and homogenized in 50 mM bicine buffer (pH 8) containing 100 mM KCl and 1 mM EDTA.

Redox Titrations

The prepared chromatophores membranes containing WT and mutant H198N Cytbc₁ were supplemented with antimycin at a final concentration of 0.15 mM and redox titrated under anaerobic conditions in dark. The solutions contained the following redox mediators: 50 μ M 2,3,5,6-tetramethyl-1,4-phenylenediamine (DAD), 50 μ M 1,2-naphthoquinone (NQ), 50 μ M 1,2-naphthoquinone-4-sulfonate (NQS), 12.5 μ M phenazine ethosulfate (PES), 25 μ M phenazine methosulfate (PMS), 50 μ M duroquinone (DQ), 12.5 μ M indigotrisulfonate (ITS), 50 μ M anthraquinone-2-sulfonic acid (AQS), 50 μ M 2-hydroxy-1,4-naphthoquinone (HNQ), and 50 μ M benzyl viologen (BV). The external redox potential (E_h) of the buffer was adjusted by injection of small volumes of sodium dithionite or potassium ferricyanide solutions. In dark equilibrium redox titration for each E_h about ~200 μ L of the chromatophore solution was collected and injected to an argon-flushed EPR quartz tube and then subsequently frozen in cold isopentane. The illuminated samples were prepared by inserting the EPR tube containing chromatophores to a home-built cylindrical chamber blocked at the bottom with a piston connected to an

electromagnet. The chamber contained 43 diodes (OSRICA3131A by Optosupply), having a single emission band at 850 nm, that were built in the walls of the chamber. The tubes were illuminated for 5 s and then were released to cold isopentane bath by pulling the piston of the electromagnet. A freezing time was estimated to be ~1–2 s. With this method a maximum level of SQ_o-2Fe2S is reached after 2 s of illumination, as determined for chromatophores containing antimycin-inhibited WT Cytbc₁. A decay time constant of the SQ_o-2Fe2S state after switching off the light is about 1.8 s⁻¹, which means that not more than ~60% of the SQ_o-2Fe2S state can be trapped after 1–2 s of the deadtime associated with the freezing of the samples.

We note that isolation of chromatophores required special care to prevent loss of cytochrome *c*₂ during the cell centrifugations with an excessive RCF. This is because the formation of the SQ_o-2Fe2S center in light-activated chromatophores was found to be sensitive to the coupling of RC with Cytbc₁ by cytochrome *c*₂. This effect is illustrated in **Supplementary Figure S1**, which demonstrates a decrease or even complete disappearance of the SQ_o-2Fe2S state in chromatophores having a shortage of cytochrome *c*₂. A partial restoration of the signal is possible upon the addition of external horse cytochrome *c* to the chromatophores followed by the sonication of the samples.

Preparation of Isolated WT and H198N Enzymes

Cytbc₁ complexes were isolated from detergent-solubilized chromatophores by Strep-tag[®] affinity chromatography, using the procedure described by Czapla et al. (2012a). Purity of the isolated proteins was checked with SDS-PAGE (**Supplementary Figure S2**). Cytbc₁ samples were concentrated on centrifugal filter units and dialyzed against buffer composed of 50 mM Tris (pH 8), 100 mM NaCl, 1 mM EDTA, 20% glycerol (v/v), and 0.01% (m/m) DDM. The concentration of the isolated cytochrome *b*_{c1} was determined as described by Valkova-Valchanova et al. (1998).

EPR Measurements

All the measurements were performed using a Bruker ElexSys E580 spectrometer equipped with a super-HighQ (SQHE0511) resonator and ESR900 cryostat unit (Oxford Instruments). The chromatophore membranes were measured using the parameters described by Sarewicz et al. (2018). Briefly, the temperature of the measured samples was 20 K, microwave power of 2 mW and frequency 9.4 GHz, modulation amplitude of 14.36 G, sweep width of 926.8 G, sweep time of 40.96 s, and time constant of 81.92 ms. The number of scans was usually 1–3 depending on the signal-to-noise (S/N) ratio. The registered spectra were processed and analyzed using the Eleana EPR program.

The isolated WT and H198N Cytbc₁ complexes were measured as follows. The X-band EPR spectra of low- and high-field transitions of hemes were measured at 10 K, with 2 mW microwave power, frequency of 9.4 GHz, and modulation amplitude of 6 G. The X-band EPR spectra of the

2Fe2S cluster was measured at 30 K with 0.65 mW microwave power and modulation amplitude of 16 G.

RESULTS AND DISCUSSION

H198N Mutant Incorporates a High-Potential, High-Spin Heme *b*_L

Cytbc₁ contains the low-potential [*E*_{m,7} = ~-120 mV (Zhang et al., 2008)], low-spin (L-S) heme *b*_L which is axially coordinated by two histidine side chains: H97 and H198 (*R. capsulatus* numbering of cytb subunit) (Berry et al., 2004). This heme is diamagnetic in the reduced state and, together with a higher potential (*E*_m = +60 mV) heme *b*_H, contributes to the absorbance band with a maximum at ~560 nm of the fully reduced WT Cytbc₁ (**Figure 1A**, left, black). A replacement of histidine 198 to non-liganding asparagine is expected to significantly alter properties of heme *b*_L or even prevent its incorporation into the protein, as previously reported for the ligand mutants of hemes *b* in *R. capsulatus* and *R. sphaeroides* (Yang et al., 2008). Indeed, the optical spectrum of the H198N mutant in *R. capsulatus* constructed in this work (^{Rc}H198N) exhibits a significant decrease in the absorbance at ~560 nm (**Figure 1A**, right, black), consistent with the previous observation on the analogical H198N mutant in *Rhodobacter sphaeroides* (^{Rs}H198N) (Yang et al., 2008). Such a decrease suggests that one of the L-S hemes *b* might be missing, as was concluded for the ^{Rs}H198N mutant. However, along with the disappearance of the absorption band at ~560 nm we note an additional absorption maximum at ~590 nm present in both the ascorbate- and dithionite-reduced samples containing ^{Rc}H198N. This band was not seen in WT and suggested that it is associated with a change in the heme ligand in the ^{Rc}H198N mutant.

Low-temperature X-band EPR spectra for isolated WT and the H198N mutant for air-oxidized samples are compared in **Figure 1B**. WT Cytbc₁ shows the *g*_z transitions typical of highly anisotropic low-spin (HALS) hemes at *g* = 3.77 and 3.45 (**Figure 1B**, black), originating from the oxidized, low-spin hemes *b*_L and *b*_H, respectively (Salerno, 1984; Finnegan et al., 1996). From those two transitions, only the *g* = 3.45 originating from heme *b*_H was detected in H198N mutant (**Figure 1B**, gray), indicating that this heme was properly assembled into the protein core and retained its native bis-his axial ligation. The missing *g* = 3.77 transition was consistent with the expected lack of HALS heme *b*_L with his-his axial ligation. Instead, a relatively intense transition at *g* = ~5.96 and a much weaker at *g* = ~2 were detected revealing that in ^{Rc}H198N, the HALS heme *b*_L was converted into an axial, high-spin (H-S) form. Given the fact that other centers contribute to the EPR signal in the region of *g* = 5.96, the heterogeneity, if any, of the spin state of heme *b*_L in the mutant cannot be evaluated.

To get insights into the redox properties of hemes *b* in the H198N mutant, we analyzed the relaxation properties of a semiquinone formed at the Q_i site, which, as reported recently, strongly depend on whether the electron preferentially stays on heme *b*_H or heme *b*_L, thus can be used to estimate the relative difference in equilibrium redox potentials between these hemes (Pintscher et al., 2018). The results, discussed in detail in SI (**Supplementary Figures S3 and S4**), revealed that heme *b*_L in

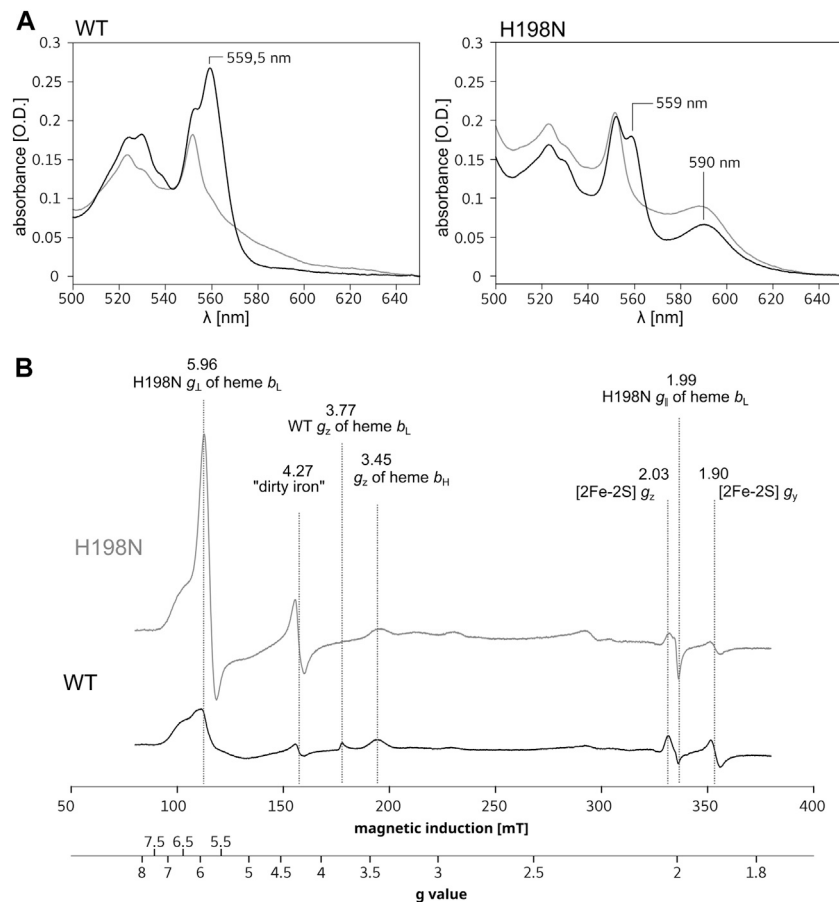


FIGURE 1 | Comparison of spectra for isolated WT and H198N mutants of Cytbc₁. **(A)** Optical spectra of WT (left) and H198N mutant (right) measured for ascorbate (gray) and dithionite-reduced (black) Cytbc₁. Maximum at ~560 nm originates from absorption of hemes b . Additional absorption band at ~590 nm is likely to originate from heme b_L with changed ligand in H198N mutant. **(B)** X-band EPR spectra of air-oxidized WT (black) and H198N mutant (gray) measured at 10 K. In the range between ~70 and ~160 mT the contribution from high-spin iron centers is detected. In the range between ~160 and 200 mT, the g_z transitions of HALS hemes b transitions are detected, while the reduced 2Fe2S contributes to transitions at the magnetic field above ~320 mT.

the mutant has a redox potential much more positive than the native HALS heme b_H (Pintscher et al., 2018). Furthermore, the $g = 5.96$ transition disappeared when the Rc H198N Cytbc₁ was reduced by a synthetic substrate—decylubiquinol (Supplementary Figure S5), which suggests that heme b_L in Rc H198N mutant has a much higher redox midpoint potential than heme b_L of the wild type.

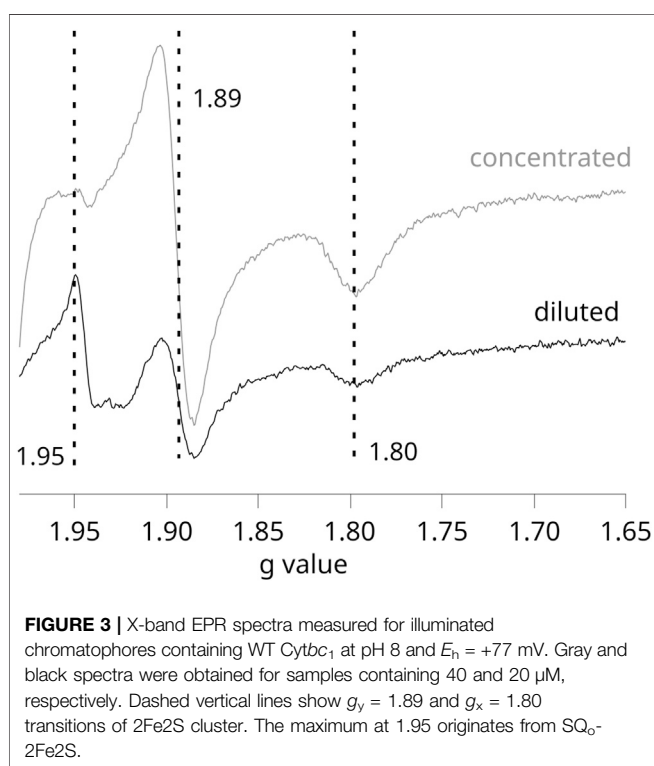
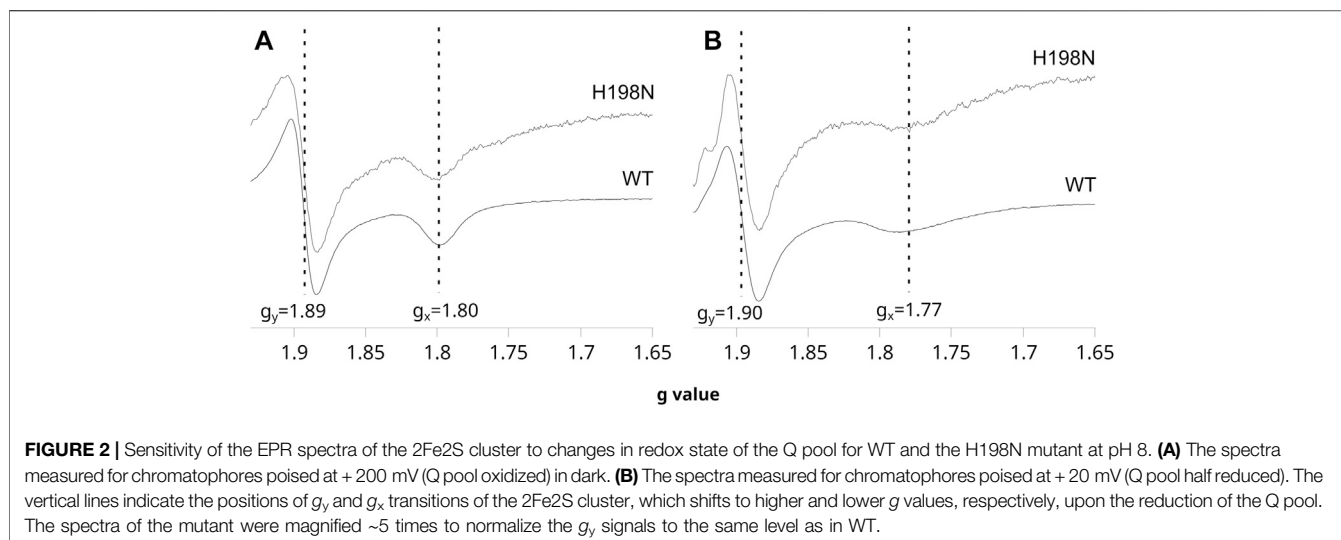
H198N Mutant Binds Properly UQ to the Q_o Site

The shape of the CW EPR spectra of the reduced 2Fe2S cluster in chromatophores is sensitive to the type of molecule that occupies the Q_o site. In particular, the relatively narrow g_x transition at 1.80 indicates that UQ is bound at this site and interacts with the cluster, whereas a more broad $g_x = 1.77$ indicates the presence of UQH₂ in the Q_o site (Robertson et al., 1993; Ding et al., 1995; Cooley et al., 2004; Sharp et al., 1999). This change in g_x transition is so characteristic that it was often used in evaluating the effects of mutations on the binding of ubiquinone molecules to the catalytic site, or in the redox titrations of ubiquinones in the membranes

(Cooley et al., 2004; Osyczka et al., 2006). As shown in Figure 2A, the CW EPR spectra of the ascorbate-reduced 2Fe2S cluster in chromatophores containing WT and H198N Cytbc₁ were similar and both exhibited clear $g_x = 1.80$ transition when the Q pool was fully oxidized (at high E_h). Furthermore, reducing the Q pool, upon decreasing the external redox potential, changed the g_x from 1.80 to ~1.77 in both WT and the mutant protein (Figure 2B). These observations indicate that UQ and UQH₂ can bind to the Q_o site of the mutant in the same way as in WT [see references Cooley et al. (2004), Osyczka et al. (2006) for details]. This feature, along with the specifically altered redox properties of heme b_L described earlier, made H198N an attractive mutant for the mechanistic analysis of the formation of the SQ_o-2Fe2S state.

Controlling the Efficiency of SQ_o-2Fe2S Generation in Illuminated Chromatophores

In our previous studies we established a general methodology for monitoring the formation of the SQ_o-2Fe2S state in chromatophore membranes (Sarewicz et al., 2018). We found that this state can be



detected by CW EPR during the redox titrations of chromatophores containing antimycin-inhibited Cytbc₁ only under nonequilibrium conditions when the photosynthetic reaction center and allied Cytbc₁ were kept activated by continuous light during the titration. The same experiments performed in dark (equilibrium conditions) do not lead to the formation of SQ_o-2Fe2S at detectable levels (Sarewicz et al., 2018).

Given that in these experiments, the formation of SQ_o-2Fe2S strongly depends on the activation level of RC, any comparative redox titrations of chromatophores illuminated by continuous

light (nonequilibrium conditions) require careful controls to assure that conditions for the generation of the SQ_o-2Fe2S signal and its detection were equally met in each of the studied cases. We found that the most important factor influencing the efficiency of SQ_o-2Fe2S generation in chromatophores was the optical transparency for the light that activates RC. This effect is shown in **Figure 3**, which compares the two EPR spectra obtained for the concentrated (gray) and diluted (black) samples of the same batch of chromatophores (containing 40 and 20 μ M cytochrome c_1 , respectively).

This example emphasizes that the SQ_o-2Fe2S signal ($g = 1.95$) can be lost in the more concentrated sample despite improvement in the signal-to-noise ratio, and this is related to the fact that the activation of RC is much weaker due to increased opacity of the solution. The weaker light activation of RC in the more concentrated samples was also reflected in the measured UQ/UQH₂ average redox midpoint potential, which, despite illumination of the sample, approached those detected in dark. Thus, the titrations of the SQ_o-2Fe2S signal on illuminated chromatophores required sufficiently diluted samples. However, after diluting the samples, a measurement of the redox state of hemes b by EPR is compromised due to the fact that the amplitudes of these hemes are relatively very weak. We found that at the concentrations of Cytbc₁ at which hemes b became clearly detectable by EPR, the SQ_o-2Fe2S signal started to disappear due to increase of the opacity of the samples. Therefore, the experiments were limited to a relatively narrow range of Cytbc₁ concentrations that allowed efficient activation of RC and, at the same time, a detection of relatively good-quality EPR spectra.

Light-Activated RC Interacts With H198N in Chromatophores and Imposes a Shift in Apparent Midpoint Potential of the 2Fe2S Cluster

In view of the observation that the efficiency of SQ_o-2Fe2S generation in the light-activated WT chromatophores strongly

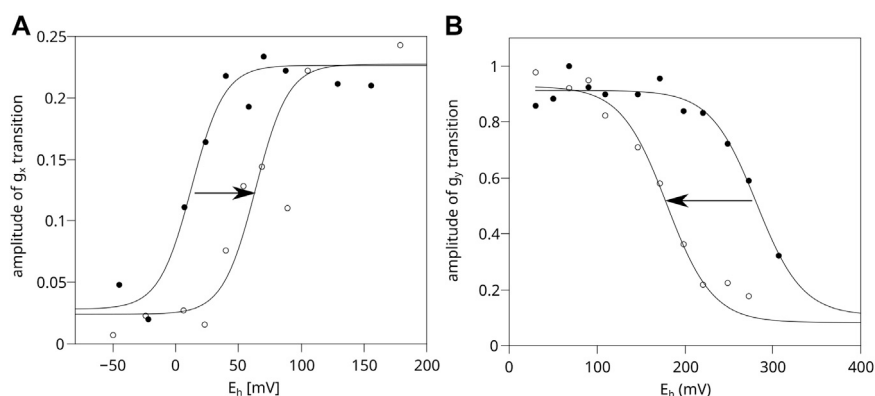


FIGURE 4 | Comparison of efficiency of light activation of RC in chromatophores containing WT and H198N mutant of *Cytbc*₁. **(A)** Amplitude of the normalized g_x transition of the 2Fe2S cluster of WT *Cytbc*₁, which is proportional to the amount of UQ in the Q pool in dark (closed circles) and in illuminated samples (open circles). The experimental data points were simulated using an appropriate Nernst equation with $n = 2$. **(B)** Amplitude of the g_y transition of the 2Fe2S cluster measured for the illuminated chromatophores containing H198N mutant of *Cytbc*₁ (open circles) and chromatophores in dark (closed circles).

depends on the optical transparency of the samples (see the paragraph above), it became apparent that prior to comparing WT and the H198N mutant, it was necessary to verify that RC in both WT and the H198N mutant containing chromatophores were sufficiently well activated by light and, consequently, both the systems were pushed out of equilibrium. Furthermore, it was necessary to apply a verification method that was independent of the analysis of the SQ_o-2Fe2S signal. One such possibility relates to the fact that light activation affects the redox state of the membranous Q pool. Changes in the redox state of the Q pool can be monitored by measuring a progressive decrease in the amplitude of the normalized $g_x = 1.80$ transition of the 2Fe2S cluster as the Q pool becomes progressively reduced (Sarewicz et al., 2018). Illumination leads to the electron transfer from the cytochrome c_2 pool to the Q pool and the extent of the transfer is reflected in a shift in the Nernst curve of UQ/UQH₂ couple toward higher values. Thus, the shift confirms the activation level of RC.

Figure 4A shows that in chromatophores containing WT *Cytbc*₁ at a concentration equal to 20 μ M cytochrome c_1 (corresponding to black spectrum of **Figure 3**), the obtained equilibrium redox potential of UQ/UQH₂ couple in dark shifts by approximately +60 mV upon the activation of RC by light. Clearly, the optical transparency of the chromatophores in this case was enough to allow sufficient RC activation. In a more concentrated sample (corresponding to the gray spectrum of **Figure 3**) the measured UQ/UQH₂ average redox midpoint potential was similar in light and in dark, and the lack of the shift (lack of activation of RC) was concomitant with the lack of the SQ_o-2Fe2S signal (data not shown).

In the case of the H198N mutant, the expression level of *Cytbc*₁ was found to be lower by approximately 2–3 folds than WT (data not shown). Thus, after concentrating the H198N chromatophores to reach 20 μ M of cytochrome c_1 , the samples became too opaque to allow efficient activation of RC. As a result, the illumination of the samples did not lead to a shift of the UQ/UQH₂ Nernst curve toward a higher value (data not shown).

Therefore, the chromatophores containing H198N must have been diluted to 10 μ M of cytochrome c_1 to reach the optical transparency similar to that of WT chromatophores. This, in turn, exerted a negative effect of the quality of the measured EPR spectra of 2Fe2S cluster, and the reliable measurement of g_x transition was not possible, precluding the possibility of monitoring activation level by determining the shift in the redox state of Q pool.

Instead, we monitored the extent of 2Fe2S oxidation upon activation of RC by comparing the amplitude of the relatively strong g_y transition of the 2Fe2S cluster, as a function of E_h for illuminated chromatophores with those measured in dark. Illumination of H198N chromatophores imposed a shift of the Nernst curve with the midpoint potential of the 2Fe2S cluster from approximately +300 mV (in dark) to approximately +180 mV (in light) (**Figure 4B**, dashed and solid lines, respectively). This shift was an expected effect if RC had been efficiently activated and able to oxidize the whole chain of high-potential cofactors connecting RC and *Cytbc*₁ (i.e., cytochrome c_2/c_1 and 2Fe2S). We note that similar shift in the 2Fe2S cluster can be observed in WT chromatophores; however, *Cytbc*₁ must be inhibited by myxothiazol (i.e., it is not observed in non-inhibited *Cytbc*₁). This inhibitor binds at the Q_o site and prevents oxidation of UQH₂ at this site; however, it does not impair the movement of the 2Fe2S cluster nor its interaction with other components of the high-potential chains (Kim et al., 1998; Darrouzet et al., 2000; Esser et al., 2004; Osyczka et al., 2004; Sarewicz et al., 2009; Cieluch et al., 2010). Thus, the observed shift in H198N chromatophores not only confirms the activation of RC, but also indicates that the components of the high-potential chain in this mutant are functionally linked with RC. At the same time, these components remain decoupled from the low-potential chain of *Cytbc*₁ because of the enzymatic incompetence of mutated heme b_L (with the net effect similar to the presence of myxothiazol in the Q_o site of the native enzyme). We note that the observed shift in the 2Fe2S cluster induced by light activation of RC is interesting itself, and it will be discussed elsewhere.

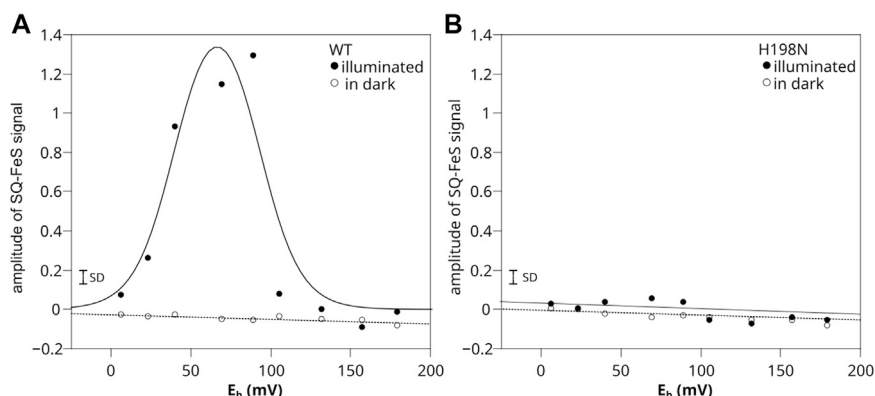


FIGURE 5 | Comparison of SQ_o-2Fe₂S generation in chromatophores containing WT **(A)** and H198N mutant **(B)** of Cytbc₁. Amplitude of SQ_o-2Fe₂S was measured for illuminated samples (closed circles) and titrated in dark (open circles). Optical transparencies were the same for A and B, and the concentrations of cytochrome c₁ were 20 and 10 μM, respectively. The solid line in A represents the fit of $f_{SQ_o-2Fe_2S} = f_A / \{1 + \exp [0.039n (E_h - E_1)] + \exp [0.039n (E_2 - E_h)]\}$ function described in detail by Sarewicz et al. (2018). The fit yielded $E_1 = +92 \pm 8$ mV and $E_2 = +40 \pm 7$ mV for $n = 2$ and $f_A = 1.7 \pm 0.4$. The small bar denoted marked as SD shows the typical uncertainty of the amplitude reads and includes the baseline and the noise of the EPR spectrum. It does not include uncertainty related to changes in efficiency of SQ_o-2Fe₂S generation dominated by variations in light activation and/or changes in the freezing time.

H198N Fails to Generate Detectable Amounts of SQ_o-2Fe₂S Spin-Coupled State

Having established the conditions for meaningful comparison of WT and H198N chromatophores (see the previous paragraphs), we performed a series of redox titrations that screened for the SQ_o-2Fe₂S state in the H198N mutant.

The results for WT chromatophores were consistent with the previous observations (Sarewicz et al., 2018) (**Figure 5A**). When titrations were performed in light at pH 8, the SQ_o-2Fe₂S was detected within the range of E_h below +150 mV and above 0 mV (with the maximum amplitude at $E_h \sim +66$ mV) (closed circles). The SQ_o-2Fe₂S was not detected in this range of E_h when similar titrations were performed in dark (open circles).

Remarkably, in titrations performed with chromatophores containing H198N instead of WT Cytbc₁, the SQ_o-2Fe₂S was not detected at all, regardless of whether the experiment was conducted in light or in dark (**Figure 5B**). A corollary of this result on the mechanisms of the formation of the SQ_o-2Fe₂S state in antimycin-inhibited WT Cytbc₁ is discussed below.

The H198N Mutation Implicates That Semireverse Mechanisms of SQ_o-2Fe₂S Formation Are Dominant in WT Cytbc₁

Let us consider two possible mechanisms of the formation of SQ_o-2Fe₂S in antimycin-inhibited Cytbc₁ shown schematically in **Figure 6**. In each of these two scenarios it is assumed that heme b_H is already reduced after the oxidation of the first UQH₂ molecule at the Q_o site. This heme cannot be reoxidized by electron transfer to the Q_i site, because this site is occupied by antimycin.

The first mechanism assumes the sequence of reactions schematically shown in **Figure 6A**. The UQH₂ binds at the Q_o site where it undergoes one-electron oxidation by 2Fe₂S forming an unstable semiquinone, SQ_o (transition 1a). This semiquinone immediately donates electron to heme b_L and the resulting UQ

molecule is then replaced with next UQH₂ (transition 2a in **Figure 6A**). As the Q_i site is blocked by antimycin, both hemes b_H and b_L cannot be reoxidized by electron transfer to the Q_i site. Thus, SQ_o formed upon the oxidation of the second UQH₂ molecule by the 2Fe₂S cluster is unable to donate electron to heme b_L and SQ_o and the reduced cluster forms spin-coupled state (transition 3a). Because this reaction corresponds to uncompleted oxidation of UQH₂ in the forward direction of the operation of the Q_o site, it is referred to as a *semiforward* reaction.

The second scenario assumes the sequence of reactions schematically shown in **Figure 6B**. The UQH₂ molecule at the Q_o site undergoes oxidation and two electrons are transferred to the 2Fe₂S cluster and heme b_L , leading to UQ bound at the Q_o site. Since the electron transfer from heme b_L to heme b_H is not possible, the electron from heme b_L is transferred back to the UQ molecule forming SQ_o. At the same time the reduced 2Fe₂S cluster is still at the position close to the Q_o site and is able to interact with SQ_o. As a result the SQ_o-2Fe₂S state is generated. Because this reaction corresponds to uncompleted reduction of UQH₂ in the reverse direction of the operation of the Q_o site, it is referred to as a *semireverse* reaction.

The role of heme b_L in the formation of SQ_o-2Fe₂S is different for both the mechanisms. The *semiforward* reaction occurs when heme b_L is unable to accept the electron from SQ_o; thus, the redox-active heme b_L is not required for the formation of the SQ_o-2Fe₂S state. Conversely, the *semireverse* reaction obligatorily requires presence of the redox-active heme b_L to enable back electron transfer to the Q_o site to form the SQ_o-2Fe₂S.

In view of these considerations, H198N provided an attractive opportunity to test the contribution of the *semireverse* reaction to the formation of the SQ_o-2Fe₂S state. The high-spin, high-potential heme b_L in this mutant, once accepting the electron, will preferably stay reduced, and thus is unable to pass electron further to heme b_H at a significant rate. This means that its redox activity required for the catalytic turnover is lost. At the same time, this heme is unable to transfer electron back to the Q_o site. It

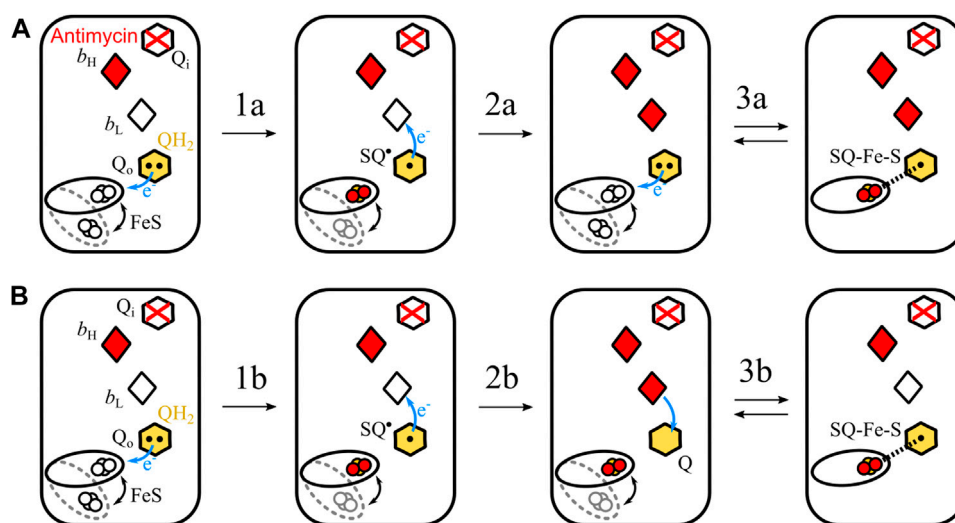


FIGURE 6 | Simplified scheme of two possible reactions of SQ_o-2Fe2S formation. **(A)** The *semiforward* mechanism of UQH₂ oxidation by the 2Fe2S cluster at the time when heme *b_L* is unable to accept electron (because of being already reduced) from resulting SQ_o, leading to the creation of the SQ_o-2Fe2S state. **(B)** The *semireverse* mechanism assumes that the reduced heme *b_L* donates electrons to UQ at the time when the reduced 2Fe2S is close to the Q_o site. This leads to the creation of the SQ_o-2Fe2S state. According to the mechanism shown in A, the redox-active heme *b_L* is not necessary, while the mechanism shown in B requires heme *b_L* for the generation of the SQ_o-2Fe2S state.

follows that the H198N mutant provides conditions that should favor the formation of the SQ_o-2Fe2S if the *semiforward* reaction is a dominant mechanism, but should discourage the formation of SQ_o-2Fe2S if the *semireverse* reaction is dominant. Thus, if the SQ_o-2Fe2S state was detected in the H198N mutant of Cytbc₁, then both *semiforward* and *semireverse* would be potentially responsible for the formation of this state. This was clearly not the case. The observation that the H198N mutation leads to complete disappearance of the SQ_o-2Fe2S signal under the tested conditions implies that the *semireverse* reaction can be considered the dominant mechanism for the formation of this state in WT Cytbc₁. This mechanism involves electron transfer from heme *b_L* back to the ubiquinone bound to the Q_o site followed by its interaction with the reduced 2Fe2S cluster.

We note that this scenario prevails even if heme *b_L* was able to pass electron to heme *b_H* at a significant rate in H198N, which, given that antimycin was present at the Q_i site, would eventually lead to a reduction of both hemes *b_L* and *b_H*. In this case, as long as heme *b_L* was unable to transfer electron back to the Q_o site, the SQ_o-2Fe2S signal would still be absent if occurrence of the *semireverse* reaction was required to generate it.

We also note that our conclusion requires an assumption that proton paths and proton transfers are not different in the H198N mutant and WT Cytbc₁. In addition, one should bear in mind that there is still a possibility that the SQ_o-2Fe2S state can be generated in the H198N mutant but it was not detected in our experiments. This would mean that either the efficiency of its formation, i.e., contribution of the *semiforward* mechanism is much lower than the contribution of the *semireverse* mechanism, or the lifetime of the SQ_o-2Fe2S state under conditions of altered ligand of heme *b_L* is much shorter than the lifetime of this state in WT. If so, then the decay of the SQ_o-2Fe2S state must have taken place within the deadtime of the method (i.e., before a

sample became frozen, see the Materials and Methods). If this alternative explanation was true, it would immediately suggest a change in a mechanism of SQ_o-2Fe2S formation when properties of heme *b_L* were altered in the mutant. In other words, the presence of oxidized heme *b_L* in antimycin-inhibited Cytbc₁ from *R. capsulatus* would greatly stabilize the SQ_o-2Fe2S state, whereas the reduced or disabled heme *b_L* would eliminate or greatly destabilize this state.

SUMMARY AND CONCLUSION

In this work we constructed a mutant H198N that targeted one of the His ligands of heme *b_L*. We found that this mutation leads to the conversion of HALS heme *b_L* into the high-spin and high-potential form, which was indicated from the analysis of optical and EPR spectra of isolated enzymes. While H198N binds properly the substrates at the Q_o site, the specific redox properties of heme *b_L* in this mutant made the heme unable to transfer electrons to heme *b_H* on a catalytically relevant timescale. Consequently, the enzymatic activity of Cytbc₁ in H198N was lost. We then used this mutant to test the formation of the SQ_o-2Fe2S state under nonequilibrium conditions (light-activated chromatophores) when heme *b_L* cannot perform normal electron-relay function between the Q_o site and heme *b_H*.

Careful analysis of various chromatophore samples established that the SQ_o-2Fe2S signal can be efficiently generated in illuminated chromatophores containing antimycin-inhibited WT Cytbc₁, provided that the samples are optically transparent and cytochrome *c₂* molecules were not lost during the preparation of the chromatophores. Monitoring of the apparent shift in the midpoint potential of the UQ/UQH₂ couple induced by light

activation of RC provides convenient means for verifying the effectiveness of setting the nonequilibrium conditions in the analyzed samples, independently of the analysis of the SQ_o-2Fe₂S signal. In H198N chromatophores, for which this method turned out to be unsuitable, imposing the nonequilibrium conditions was found to result in a large, negative shift of the apparent E_m of the 2Fe₂S cluster (a similar shift in the apparent redox midpoint potential of the 2Fe₂S cluster was observed in WT Cytbc₁ inhibited by myxothiazol). This provided an alternative method for verifying the effectiveness of light activation of RC and additionally confirmed their efficient coupling with Cytbc₁ via cytochrome c_2 resulting in the oxidation of 2Fe₂S.

Comparative redox titrations of light-induced WT and H198N chromatophores revealed that the H198N mutant failed to form detectable amounts of the SQ_o-2Fe₂S state under the same conditions at which WT Cytbc₁ generated a large amount of SQ_o-2Fe₂S. This failure implicates that the *semireverse* mechanism that leads to the SQ_o-2Fe₂S state is the dominant over the *semiforward* reaction in WT Cytbc₁ (Sarewicz et al., 2010). According to the *semireverse* mechanism, the electron transfer from the low-spin heme b_L to the UQ bound at the Q_o site (*semireverse* reaction) results in the formation of the semiquinone that is spin-coupled to the reduced 2Fe₂S, forming the SQ_o-2Fe₂S state detectable by EPR.

DATA AVAILABILITY STATEMENT

The raw data supporting the conclusion of this article will be made available by the authors, without undue reservation.

REFERENCES

- Al-Attar, S., and de Vries, S. (2013). Energy Transduction by Respiratory Metallo-Enzymes: From Molecular Mechanism to Cell Physiology. *Coord. Chem. Rev.* 257, 64–80. doi:10.1016/j.ccr.2012.05.022
- Atta-Asafo-Adjei, E., and Daldal, F. (1991). Size of the Amino Acid Side Chain at Position 158 of Cytochrome B Is Critical for an Active Cytochrome Bc₁ Complex and for Photosynthetic Growth of Rhodospirillum rubrum. *Proc. Natl. Acad. Sci.* 88, 492–496. doi:10.1073/pnas.88.2.492
- Baniulis, D., Yamashita, E., Zhang, H., Hasan, S. S., and Cramer, W. A. (2008). Structure-Function of the Cytochrome b₆f Complex. *Photochem. Photobiol.* 84, 1349–1358. doi:10.1111/j.1751-1097.2008.00444.x
- Berry, E. A., Guergova-Kuras, M., Huang, L.-S., and Crofts, A. R. (2000). Structure and Function of Cytochrome b₆f Complexes. *Annu. Rev. Biochem.* 69, 1005–1075. doi:10.1146/annurev.biochem.69.1.1005
- Berry, E. A., Huang, L.-S., Saechao, L. K., Pon, N. G., Valkova-Valchanova, M., and Daldal, F. (2004). X-Ray Structure of Rhodospirillum rubrum Cytochrome Bc₁: Comparison with its Mitochondrial and Chloroplast Counterparts. *Photosynth. Res.* 81, 251–275. doi:10.1023/b:pres.0000036888.18223.0e
- Bertini, I., Cavallaro, G., and Rosato, A. (2006). Cytochrome C: Occurrence and Functions. *Chem. Rev.* 106, 90–115. doi:10.1021/cr050241v
- Borek, A., Sarewicz, M., and Osyczka, A. (2008). Movement of the Iron-Sulfur Head Domain of Cytochrome b₆f Transiently Opens the Catalytic Qo Site for Reaction with Oxygen. *Biochemistry* 47, 12365–12370. doi:10.1021/bi801207f
- Boveris, A., and Cadenas, E. (1975). Mitochondrial Production of Superoxide Anions and its Relationship to the Antimycin Insensitive Respiration. *FEBS Lett.* 54, 311–314. doi:10.1016/0014-5793(75)80928-8
- Bujnowicz, L., Borek, A., Kuleta, P., Sarewicz, M., Osyczka, A., and Osyczka, A. (2019). Suppression of Superoxide Production by a Spin-spin Coupling between Semiquinone and the Rieske Cluster in Cytochrome bc₁. *FEBS Lett.* 593, 3–12. doi:10.1002/1873-3468.13296
- Cape, J. L., Bowman, M. K., and Kramer, D. M. (2007). A Semiquinone Intermediate Generated at the Q_o Site of the Cytochrome bc₁ Complex: Importance for the Q-Cycle and Superoxide Production. *Proc. Natl. Acad. Sci.* 104, 7887–7892. doi:10.1073/pnas.0702621104
- Cape, J. L., Bowman, M. K., and Kramer, D. M. (2006). Understanding the Cytochrome bc Complexes by what They Don't Do. The Q-Cycle at 30. *Trends Plant Sci.* 11, 46–55. doi:10.1016/j.tplants.2005.11.007
- Cieluch, E., Pietryga, K., Sarewicz, M., and Osyczka, A. (2010). Visualizing Changes in Electron Distribution in Coupled Chains of Cytochrome bc₁ by Modifying Barrier for Electron Transfer between the FeS Cluster and Heme c(1). *Biochim. Biophys. Acta (Bba) - Bioenerg.* 1797, 296–303. doi:10.1016/j.bbabi.2009.11.003
- Cooley, J. W., Roberts, A. G., Bowman, M. K., Kramer, D. M., and Daldal, F. (2004). The Raised Midpoint Potential of the [2Fe₂S] Cluster of Cytochrome bc₁ Is Mediated by Both the Qo Site Occupants and the Head Domain Position of the Fe-S Protein Subunit. *Biochemistry* 43, 2217–2227. doi:10.1021/bi035938u
- Cramer, W. A., and Hasan, S. S. (2016). "Structure-Function of the Cytochrome B₆F Lipoprotein Complex," in *Cytochrome Complexes Evol. Struct. Energy Transduction, Signal*. Editors W. A. Cramer and T. Kallas (Dordrecht: Springer), 177–207. doi:10.1007/978-94-017-7481-9_9
- Crofts, A. R., and Berry, E. A. (1998). Structure and Function of the Cytochrome Bc₁ Complex of Mitochondria and Photosynthetic Bacteria. *Curr. Opin. Struct. Biol.* 8, 501–509. doi:10.1016/s0959-440x(98)80129-2
- Crofts, A. R., Hong, S., Wilson, C., Burton, R., Victoria, D., Harrison, C., et al. (2013). The Mechanism of Ubiquinol Oxidation at the Qo-Site of the Cytochrome bc₁ Complex. *Biochim. Biophys. Acta (Bba) - Bioenerg.* 1827, 1362–1377. doi:10.1016/j.bbabi.2013.01.009

AUTHOR CONTRIBUTIONS

MS designed experiments, performed EPR measurements, contributed to construction of illumination chamber, analyzed data, and wrote the manuscript. SP isolated and analyzed spectral properties of the mutant protein, and participated in writing the manuscript. LB designed electronic parts of illumination chamber and performed EPR measurements. MW isolated chromatophores and performed redox titrations. AO discussed data and wrote the manuscript.

FUNDING

This work was funded by National Science Centre, Poland, Grant No. 2015/18/A/NZ1/00046 to A.O.

ACKNOWLEDGMENTS

We would like to thank Dr. Ewelina Cieluch for preparing the H198N mutant of cytochrome bc₁. We would like to thank Dr. Robert Ekiert for SDS page analysis of isolated proteins.

SUPPLEMENTARY MATERIAL

The Supplementary Material for this article can be found online at: <https://www.frontiersin.org/articles/10.3389/fchem.2021.658877/full#supplementary-material>

- Crofts, A. R., Meinhardt, S. W., Jones, K. R., and Snozzi, M. (1983). The Role of the Quinone Pool in the Cyclic Electron-Transfer Chain of *Rhodospseudomonas Sphaeroides* A Modified Q-Cycle Mechanism. *Biochim. Biophys. Acta (Bba) - Bioenerg.* 723, 202–218. doi:10.1016/0005-2728(83)90120-2
- Crofts, A. R., Rose, S. W., Burton, R. L., Desai, A. V., Kenis, P. J. A., and Dikanov, S. A. (2017). The Q-Cycle Mechanism of the bc₁ Complex: A Biologist's Perspective on Atomistic Studies. *J. Phys. Chem. B* 121, 3701–3717. doi:10.1021/acs.jpcc.6b10524
- Crofts, A. R. (2004). The Cytochrome bc₁ Complex: Function in the Context of Structure. *Annu. Rev. Physiol.* 66, 689–733. doi:10.1146/annurev.physiol.66.032102.150251
- Czapla, M., Borek, A., Sarewicz, M., and Osyczka, A. (2012a). Enzymatic Activities of Isolated Cytochrome Bc₁-like Complexes Containing Fused Cytochrome B Subunits with Asymmetrically Inactivated Segments of Electron Transfer Chains. *Biochemistry* 51, 829–835. doi:10.1021/bi2016316
- Czapla, M., Borek, A., Sarewicz, M., and Osyczka, A. (2012b). Fusing Two Cytochromes B of *Rhodobacter Capsulatus* Cytochrome Bc 1 Using Various Linkers Defines a Set of Protein Templates for Asymmetric Mutagenesis. *Protein Eng. Des. Sel.* 25. doi:10.1093/protein/gzr055
- Darrouzet, E., Cooley, J. W., and Daldal, F. (2004). The Cytochrome bc₁ Complex and its Homologue the b(6) f Complex: Similarities and Differences. *Photosynth. Res.* 79, 25–44. doi:10.1023/b:pres.0000011926.47778.4e
- Darrouzet, E., Valkova-Valchanova, M., Moser, C. C., Dutton, P. L., and Daldal, F. (2000). Uncovering the [2Fe2S] Domain Movement in Cytochrome Bc₁ and its Implications for Energy Conversion. *Proc. Natl. Acad. Sci.* 97, 4567–4572. doi:10.1073/pnas.97.9.4567
- de Vries, S., Albracht, S. P., Berden, J. A., and Slater, E. C. (1981). A New Species of Bound Ubisemiquinone Anion in QH₂: Cytochrome C Oxidoreductase. *J. Biol. Chem.* 256, 11996–11998. doi:10.1016/s0021-9258(18)43222-x
- Dikanov, S. A., Samoilova, R. I., Kolling, D. R. J., Holland, J. T., and Crofts, A. R. (2004). Hydrogen Bonds Involved in Binding the Qi-Site Semiquinone in the Bc₁ Complex, Identified through Deuterium Exchange Using Pulsed EPR. *J. Biol. Chem.* 279, 15814–15823. doi:10.1074/jbc.m313417200
- Ding, H., Moser, C. C., Robertson, D. E., Tokito, M. K., Daldal, F., and Dutton, P. L. (1995). Ubiquinone Pair in the Qo Site Central to the Primary Energy Conversion Reactions of Cytochrome Bc₁ Complex. *Biochemistry* 34, 15979–15996. doi:10.1021/bi00049a012
- Dröse, S., and Brandt, U. (2008). The Mechanism of Mitochondrial Superoxide Production by the Cytochrome Bc₁ Complex. *J. Biol. Chem.* 283, 21649–21654. doi:10.1074/jbc.m803236200
- Esser, L., Quinn, B., Li, Y.-F., Zhang, M., Elberry, M., Yu, L., et al. (2004). Crystallographic Studies of Quinol Oxidation Site Inhibitors: A Modified Classification of Inhibitors for the Cytochrome Bc 1 Complex. *J. Mol. Biol.* 341, 281–302. doi:10.1016/j.jmb.2004.05.065
- Finnegan, M. G., Knaff, D. B., Qin, H., Gray, K. A., Daldal, F., Yu, L., et al. (1996). Axial Heme Ligation in the Cytochrome Bc₁ Complexes of Mitochondrial and Photosynthetic Membranes. A Near-Infrared Magnetic Circular Dichroism and Electron Paramagnetic Resonance Study. *Biochim. Biophys. Acta (Bba) - Bioenerg.* 1274, 9–20. doi:10.1016/0005-2728(95)00155-7
- Hasan, S. S., Yamashita, E., and Cramer, W. A. (2013). Transmembrane Signaling and Assembly of the Cytochrome B6f-Lipidic Charge Transfer Complex. *Biochim. Biophys. Acta (Bba) - Bioenerg.* 1827, 1295–1308. doi:10.1016/j.bbabi.2013.03.002
- Hunte, C., Palsdottir, H., and Trumpower, B. L. (2003). Protonmotive Pathways and Mechanisms in the Cytochrome Bc 1 Complex. *FEBS Lett.* 545, 39–46. doi:10.1016/s0014-5793(03)00391-0
- Jünemann, S., Heathcote, P., and Rich, P. R. (1998). On the Mechanism of Quinol Oxidation in Thebc₁ Complex. *J. Biol. Chem.* 273, 21603–21607. doi:10.1074/jbc.273.34.21603
- Kim, H., Xia, D., Yu, C.-A., Xia, J.-Z., Kachurin, A. M., Zhang, L., et al. (1998). Inhibitor Binding Changes Domain Mobility in the Iron-Sulfur Protein of the Mitochondrial Bc₁ Complex from Bovine Heart. *Proc. Natl. Acad. Sci.* 95, 8026–8033. doi:10.1073/pnas.95.14.8026
- Ksenzenko, M., Konstantinov, A. A., Khomutov, G. B., Tikhonov, A. N., and Ruuge, E. K. (1983). Effect of Electron Transfer Inhibitors on Superoxide Generation in the Cytochrome Bc 1 Site of the Mitochondrial Respiratory Chain. *FEBS Lett.* 155, 19–24. doi:10.1016/0014-5793(83)80200-2
- Mitchell, P. (1975). The Protonmotive Q Cycle: A General Formulation. *FEBS Lett.* 59, 137–139. doi:10.1016/0014-5793(75)80359-0
- Muller, F., Crofts, A. R., and Kramer, D. M. (2002). Multiple Q-Cycle Bypass Reactions at the Qo Site of the Cytochrome bc₁ Complex†. *Biochemistry* 41, 7866–7874. doi:10.1021/bi025581e
- Osyczka, A., Moser, C. C., Daldal, F., and Dutton, P. L. (2004). Reversible Redox Energy Coupling in Electron Transfer Chains. *Nature* 427, 607–612. doi:10.1038/nature02242
- Osyczka, A., Moser, C. C., and Dutton, P. L. (2005). Fixing the Q Cycle. *Trends Biochem. Sci.* 30, 176–182. doi:10.1016/j.tibs.2005.02.001
- Osyczka, A., Zhang, H., Mathé, C., Rich, P. R., Moser, C. C., and Dutton, P. L. (2006). Role of the PEWY Glutamate in Hydroquinone–Quinone Oxidation–Reduction Catalysis in the Qo Site of Cytochrome Bc₁. *Biochemistry* 45, 10492–10503. doi:10.1021/bi060013a
- Pagacz, J., Broniec, A., Wolska, M., Osyczka, A., and Borek, A. (2021). ROS Signaling Capacity of Cytochrome bc₁: Opposing Effects of Adaptive and Pathogenic Mitochondrial Mutations. *Free Radic. Biol. Med.* 163, 243–254. doi:10.1016/j.freeradbiomed.2020.12.019
- Pietras, R., Sarewicz, M., and Osyczka, A. (2016). Distinct Properties of Semiquinone Species Detected at the Ubiquinol Oxidation Q_o Site of Cytochrome Bc₁ and Their Mechanistic Implications. *J. R. Soc. Interf.* 13, 1–11. doi:10.1098/rsif.2016.0133
- Pintscher, S., Pietras, R., Sarewicz, M., and Osyczka, A. (2018). Electron Sweep across Four B-Hemes of Cytochrome Bc₁ Revealed by Unusual Paramagnetic Properties of the Qi Semiquinone Intermediate. *Biochim. Biophys. Acta (Bba) - Bioenerg.* 1859, 459–469. doi:10.1016/j.bbabi.2018.03.010
- Pintscher, S., Wójcik-Augustyn, A., Sarewicz, M., and Osyczka, A. (2020). Charge Polarization Imposed by the Binding Site Facilitates Enzymatic Redox Reactions of Quinone. *Biochim. Biophys. Acta (Bba) - Bioenerg.* 1861, 148216. doi:10.1016/j.bbabi.2020.148216
- Robertson, D. E., Ding, H., Chelminski, P. R., Slaughter, C., Hsu, J., Moomaw, C., et al. (1993). Hydrubiquinone–Cytochrome C₂ Oxidoreductase from *Rhodobacter Capsulatus*: Definition of a Minimal, Functional Isolated Preparation. *Biochemistry* 32, 1310–1317. doi:10.1021/bi00056a016
- Robertson, D. E., Prince, R. C., Bowyer, J. R., Matsuura, K., Dutton, P. L., and Ohnishi, T. (1984). Thermodynamic Properties of the Semiquinone and its Binding Site in the Ubiquinol–Cytochrome C (C₂) Oxidoreductase of Respiratory and Photosynthetic Systems. *J. Biol. Chem.* 259, 1758–1763. doi:10.1016/s0021-9258(17)43472-7
- Salerno, J. C. (1984). Cytochrome Electron Spin Resonance Line Shapes, Ligand Fields, and Components Stoichiometry in Ubiquinol–Cytochrome C Oxidoreductase. *J. Biol. Chem.* 259, 2331–2336. doi:10.1016/s0021-9258(17)43356-4
- Sarewicz, M., Borek, A., Cieluch, E., Świerczek, M., and Osyczka, A. (2010). Discrimination between Two Possible Reaction Sequences that Create Potential Risk of Generation of Deleterious Radicals by Cytochrome Bc₁. *Biochim. Biophys. Acta (Bba) - Bioenerg.* 1797, 1820–1827. doi:10.1016/j.bbabi.2010.07.005
- Sarewicz, M., Bujnowicz, Ł., Bhaduri, S., Singh, S. K., Cramer, W. A., and Osyczka, A. (2017). Metastable Radical State, Nonreactive with Oxygen, Is Inherent to Catalysis by Respiratory and Photosynthetic Cytochromes Bc₁/b₆f. *Proc. Natl. Acad. Sci. USA* 114, 1323–1328. doi:10.1073/pnas.1618840114
- Sarewicz, M., Bujnowicz, Ł., and Osyczka, A. (2018). Generation of semiquinone-[2Fe-2S]+ Spin-Coupled Center at the Qo Site of Cytochrome Bc₁ in Redox-Poised, Illuminated Photosynthetic Membranes from *Rhodobacter Capsulatus*. *Biochim. Biophys. Acta (Bba) - Bioenerg.* 1859, 145–153. doi:10.1016/j.bbabi.2017.11.006
- Sarewicz, M., Dutka, M., Froncisz, W., and Osyczka, A. (2009). Magnetic Interactions Sense Changes in Distance between Heme b_L and the Iron–Sulfur Cluster in Cytochrome bc₁. *Biochemistry* 48, 5708–5720. doi:10.1021/bi900511b
- Sarewicz, M., Dutka, M., Pintscher, S., and Osyczka, A. (2013). Triplet State of the Semiquinone–Rieske Cluster as an Intermediate of Electronic Bifurcation Catalyzed by Cytochrome Bc₁. *Biochemistry* 52, 6388–6395. doi:10.1021/bi400624m
- Sarewicz, M., and Osyczka, A. (2015). Electronic Connection between the Quinone and Cytochrome C Redox Pools and its Role in Regulation of Mitochondrial Electron Transport and Redox Signaling. *Physiol. Rev.* 95, 219–243. doi:10.1152/physrev.00006.2014

- Sarewicz, M., Pintscher, S., Pietras, R., Borek, A., Bujnowicz, L., Hanke, G., et al. (2021). Catalytic Reactions and Energy Conservation in the Cytochrome Bc1 and B6F Complexes of Energy-Transducing Membranes. *Chem. Rev.* 121, 2020–2108. doi:10.1021/acs.chemrev.0c00712
- Sharp, R. E., Palmitessa, A., Gibney, B. R., White, J. L., Moser, C. C., Daldal, F., et al. (1999). Ubiquinone Binding Capacity of the Rhodobacter capsulatus Cytochrome bc1 Complex: Effect of Diphenylamine, a Weak Binding Q Site Inhibitor. *Biochemistry* 38, 3440–3446. doi:10.1021/bi982639+
- Takamiya, K.-I., and Dutton, P. L. (1979). Ubiquinone in Rhodospseudomonas Sphaeroides. Some Thermodynamic Properties. *Biochim. Biophys. Acta (Bba) - Bioenerg.* 546, 1–16. doi:10.1016/0005-2728(79)90166-x
- Valkova-Valchanova, M. B., Saribas, A. S., Gibney, B. R., Dutton, P. L., and Daldal, F. (1998). Isolation and Characterization of a Two-Subunit Cytochrome b_c1 Subcomplex from Rhodobacter Capsulatus and Reconstitution of its Ubihydroquinone Oxidation (Qo) Site with Purified Fe-S Protein Subunit. *Biochemistry* 37, 16242–16251. doi:10.1021/bi981651z
- Vennam, P. R., Fisher, N., Krzyaniak, M. D., Kramer, D. M., and Bowman, M. K. (2013). A Caged, Destabilized, Free Radical Intermediate in the Q-Cycle. *ChemBioChem* 14, 1745–1753. doi:10.1002/cbic.201300265
- Victoria, D., Burton, R., and Crofts, A. R. (2013). Role of the -PEWY-Glutamate in Catalysis at the Qo-Site of the Cyt Bc1 Complex. *Biochim. Biophys. Acta (Bba) - Bioenerg.* 1827, 365–386. doi:10.1016/j.bbabo.2012.10.012
- Xia, D., Yu, C.-A., Kim, H., Xia, J.-Z., Kachurin, A. M., Zhang, L., et al. (1997). Crystal Structure of the Cytochrome bc1 Complex from Bovine Heart Mitochondria. *Science* 277, 60–66. doi:10.1126/science.277.5322.60
- Yang, S., Ma, H.-W., Yu, L., and Yu, C.-A. (2008). On the Mechanism of Quinol Oxidation at the QP Site in the Cytochrome Bc1 Complex. *J. Biol. Chem.* 283, 28767–28776. doi:10.1074/jbc.m803013200
- Zhang, H., Chobot, S. E., Osyczka, A., Wraight, C. A., Dutton, P. L., and Moser, C. C. (2008). Quinone and Non-quinone Redox Couples in Complex III. *J. Bioenerg. Biomembr.* 40, 493–499. doi:10.1007/s10863-008-9174-6
- Zhang, H., Osyczka, A., Dutton, P. L., and Moser, C. C. (2007). Exposing the Complex III Qo Semiquinone Radical. *Biochim. Biophys. Acta (Bba) - Bioenerg.* 1767, 883–887. doi:10.1016/j.bbabo.2007.04.004
- Zhu, J., Egawa, T., Yeh, S.-R., Yu, L., and Yu, C.-A. (2007). Simultaneous Reduction of Iron-Sulfur Protein and Cytochrome bL during Ubiquinol Oxidation in Cytochrome Bc1 Complex. *Proc. Natl. Acad. Sci.* 104, 4864–4869. doi:10.1073/pnas.0607812104

Conflict of Interest: The authors declare that the research was conducted in the absence of any commercial or financial relationships that could be construed as a potential conflict of interest.

Copyright © 2021 Sarewicz, Pintscher, Bujnowicz, Wolska and Artur Osyczka. This is an open-access article distributed under the terms of the Creative Commons Attribution License (CC BY). The use, distribution or reproduction in other forums is permitted, provided the original author(s) and the copyright owner(s) are credited and that the original publication in this journal is cited, in accordance with accepted academic practice. No use, distribution or reproduction is permitted which does not comply with these terms.



A Quinol Anion as Catalytic Intermediate Coupling Proton Translocation With Electron Transfer in *E. coli* Respiratory Complex I

Franziska Nuber, Luca Mérono, Sabrina Oppermann, Johannes Schimpf, Daniel Wohlwend and Thorsten Friedrich*

Institut für Biochemie, Albert-Ludwigs-Universität, Freiburg, Germany

OPEN ACCESS

Edited by:

Petra Hellwig,
Université de Strasbourg, France

Reviewed by:

Hideto Miyoshi,
Kyoto University, Japan
Francisco Solano,
University of Murcia, Spain

*Correspondence:

Thorsten Friedrich
Friedrich@bio.chemie.uni-freiburg.de

Specialty section:

This article was submitted to
Chemical Biology,
a section of the journal
Frontiers in Chemistry

Received: 01 March 2021

Accepted: 09 April 2021

Published: 07 May 2021

Citation:

Nuber F, Mérono L, Oppermann S,
Schimpf J, Wohlwend D and
Friedrich T (2021) A Quinol Anion as
Catalytic Intermediate Coupling
Proton Translocation With Electron
Transfer in *E. coli* Respiratory Complex
I. *Front. Chem.* 9:672969.
doi: 10.3389/fchem.2021.672969

Energy-converting NADH:ubiquinone oxidoreductase, respiratory complex I, plays a major role in cellular energy metabolism. It couples NADH oxidation and quinone reduction with the translocation of protons across the membrane, thus contributing to the protonmotive force. Complex I has an overall L-shaped structure with a peripheral arm catalyzing electron transfer and a membrane arm engaged in proton translocation. Although both reactions are arranged spatially separated, they are tightly coupled by a mechanism that is not fully understood. Using redox-difference UV-vis spectroscopy, an unknown redox component was identified in *Escherichia coli* complex I as reported earlier. A comparison of its spectrum with those obtained for different quinone species indicates features of a quinol anion. The re-oxidation kinetics of the quinol anion intermediate is significantly slower in the D213G^H variant that was previously shown to operate with disturbed quinone chemistry. Addition of the quinone-site inhibitor piericidin A led to strongly decreased absorption peaks in the difference spectrum. A hypothesis for a mechanism of proton-coupled electron transfer with the quinol anion as catalytically important intermediate in complex I is discussed.

Keywords: NADH dehydrogenase, respiratory complex I, bioenergetics, proton-coupled electron transfer, quinone chemistry, *Escherichia coli*

INTRODUCTION

The universal cellular energy currency adenosine triphosphate (ATP) is mainly produced by oxidative phosphorylation, a process that couples electron transfer with ATP synthesis. Electrons from reducing equivalents that are produced during catabolism are transferred in an exergonic reaction to oxygen to produce water. The released energy is used in an endergonic reaction to pump protons across the membrane, thus, establishing the protonmotive force (pmf). The pmf in turn drives ATP synthesis by ATP Synthase (Mitchell, 1961). Complex I contributes to the pmf by coupling NADH oxidation and quinone (Q) reduction with the translocation of protons across the membrane. The two reactions find a reflection in the two distinct structural parts, the peripheral arm, catalyzing the electron transfer reaction, and the membrane arm, conducting proton translocation (Hirst, 2013; Sazanov, 2015; Cabrera-Orefice et al., 2018; Parey et al., 2019). Mammalian complex I is a complicated machinery consisting of up to 45 subunits, while bacteria contain a simpler version comprising in general 14 subunits. These 14 subunits are conserved in

all species containing an energy-converting NADH:Q oxidoreductase and they represent the core subunits required for catalytic activity of complex I (Gnandt et al., 2016). The structure of complex I from several organisms is known from either X-ray crystallography or single-particle electron cryo-microscopy (cryo-EM), at resolutions not exceeding 3.2 Å (Agip et al., 2019). Recent cryo-EM studies yielded structures of the mitochondrial complex from a yeast and from ovine at 2.7 and 2.3 Å, respectively (Grba and Hirst, 2020; Kampjut and Sazanov, 2020).

Still, coupling of the exergonic electron transfer reaction in the peripheral arm with the endergonic proton translocation in the membrane arm is not fully understood. NADH is oxidized at the tip of the peripheral arm and the electrons are transferred from a flavin mononucleotide (FMN), the primary electron acceptor, via a chain of iron-sulfur (Fe/S)-clusters to the Q reduction site in ~ 100 Å distance. Q binds in 12 Å distance to the most distal iron-sulfur cluster, called N2, that is located ~ 15 Å above the membrane surface. The unique Q binding site is a narrow tunnel protruding deep into the enzyme and it is made up of subunits from both arms. The membrane arm extends over 180 Å in the lipid bilayer and provides four putative proton channels. These proton channels are connected to each other and to the Q binding site by a chain of charged amino acid residues located in the center of the membrane arm (Baradaran et al., 2013). Although these findings lay the foundations for a recent and elegant proposal of a proton translocation mechanism by the membrane arm (Kaila, 2018), the process that couples both reactions is still under debate. It was shown experimentally and supported by molecular dynamics (MD) simulations that the redox energy contained in NADH is almost completely transferred to the Q (Sharma et al., 2015; Wikström et al., 2015). This leads to the conclusion that it is the Q chemistry that drives proton translocation by complex I. However, the underlying molecular mechanism remains so far elusive.

More than 20 years ago, when no high resolution structure of complex I was available, the group of Hanns Weiss proposed the presence of a hitherto undetected redox group in the bacterial *Escherichia coli* and the mitochondrial *Neurospora crassa* complex I from UV-vis redox-difference spectroscopy (Friedrich et al., 1998, 2000; Schulte et al., 1998). Complex I is rapidly reduced by NADH preventing the spectral identification of individual redox components (Bakker and Albracht, 1986). To kinetically resolve contributions of the individual redox groups to the UV-vis spectrum, the slower re-oxidation of the reduced enzyme was investigated. These experiments led to the detection of an unknown redox group in complex I called “X” that was reducible with NADH and that was suspected to be involved in electron transfer from cluster N2 to ubiquinone. It was speculated that it might represent a post-translationally modified amino acid (Friedrich et al., 1998, 2000; Schulte et al., 1998). These data fell into oblivion in the course of time. Furthermore, recent structural data showed that such a postulated modified amino acid residue is not present in the complex. However, the important quinone chemistry implies the presence of several quinone species in complex I.

Here, we used a novel protocol for the preparation of *E. coli* complex I to re-investigate the findings obtained more than 20 years ago. The preparation is reduced with NADH and re-oxidized by oxygen from residual atmospheric gas within the assay buffer leading to a kinetic resolution of some of the redox-components. Indeed, just as described, after re-oxidation of the FMN and the Fe/S-clusters, the absorbance of a residual component was detectable. The UV-vis difference spectrum resembles very much the one of the QH⁻ anion. In the presence of the specific Q-site inhibitor piericidin A, the absorbance of this component is significantly diminished. Furthermore, the re-oxidation kinetics of the component is significantly decelerated in the D213G^H variant (the superscript denotes the corresponding subunit of *E. coli* complex I). Notably, it is particularly a disturbed Q chemistry that diminishes electron transfer and proton translocation (Nuber et al., manuscript submitted). Both activities showed a significant lag-phase not detected with the wild type complex. This lag-phase is most likely caused by a hampered Q reduction. Unexpectedly, the absorbance of the putative QH⁻ anion was not bleached by the oxidation of neither the wild type nor the variant complex. Based on our data we discuss that a quinol anion is a catalytically important intermediate in the mechanism coupling electron transfer with proton translocation.

MATERIALS AND METHODS

Cell Growth

BW25113Δ*ndh nuo::ntpII FRT* (Burschel et al., 2019) was transformed either with pBAD*nuo_{his}nuoF* containing the *nuo*-operon encoding the wild type enzyme decorated with a His-tag or with pBAD*nuo_{His}nuoF* D213G^H encoding the variant. Cells were grown in autoinduction medium while shaking (180 rpm, New Brunswick Innova 44, Eppendorf). At an OD₆₀₀ of ~ 4.0 cells were harvested by centrifugation ($3,913 \cdot g$, 15 min, 4°C; JLA 8.1000, Avanti J-26 XP, Beckman Coulter), shock frozen in liquid nitrogen and stored at -80°C .

Preparation of *E. coli* Complex I

All steps were performed at 4°C. Frozen cells were suspended in A-buffer [1:5 (w/v), 50 mM MES/NaOH, pH 6.0; 50 mM NaCl] supplemented with PMSF (1:1,000, w/v) and 2–3 mg DNase I. Cells were homogenized and disrupted by passing them three times through an EmulsiFlex-C5 (1,000 bar, 4°C, Avestin). The membrane fraction was obtained by differential centrifugation (low speed at $9500 \cdot g$, 20 min, 4°C; A8. 24, RC-5 Superspeed Refrigerated Centrifuge, Sorvall Instruments and high speed at $201,240 \cdot g$, 70 min, 4°C, 60 Ti, L8-M Ultrafuge, Beckman). Membranes were suspended in A_{6.8}^{*}-buffer (A-buffer at pH 6.8 plus 5 mM MgCl₂; 2 mL buffer per g membrane), shock frozen in liquid nitrogen and stored at -80°C . Membrane proteins were solubilized from the membranes by dropwise addition of lauryl maltose neopentyl glycol (LMNG; Anatrace) to a final concentration of 2% (w/v). After 60 min incubation at room temperature, non-solubilized remnants were removed by centrifugation ($201,240 \cdot g$, 15 min, 4°C, 60 Ti, L8-M Ultrafuge, Beckman). Elution buffer [50 mM MES/NaOH, pH 6.8; 50 mM

NaCl; 5 mM MgCl₂; 0.5 M imidazole; 10% (w/v) glycerol and 0.005% (w/v) LMNG] was added to a final concentration of 20 mM imidazole. Subsequently, the protein was loaded onto a Probond Ni²⁺ affinity chromatography column equilibrated in binding-buffer [50 mM MES/NaOH, pH 6.8; 50 mM NaCl; 5 mM MgCl₂; 20 mM imidazole; 10% (w/v) glycerol and 0.005% (w/v) LMNG]. After a washing step at 116 mM imidazole, bound proteins were eluted in a single elution step at 308 mM imidazole. Peak fractions were concentrated by ultrafiltration (Amicon Ultra, 100 kDa MWCO; 3,800 · g, 4°C, A-4-44, Eppendorf 5804 R) and loaded onto a Superose 6 size exclusion chromatography column in A_{MNG}^{*} buffer [A buffer plus 5 mM MgCl₂; 10% (w/v) glycerol and 0.005% (w/v) LMNG]. Peak fractions of the eluate were concentrated by ultrafiltration, shock frozen in liquid nitrogen and stored at −80°C.

UV-vis Spectroscopy

UV-vis spectra were recorded with a diode-array UV-vis spectrophotometer (TIDAS II, J&M) using quartz suprasil cuvettes with a path length of 1 cm (Hellma Analytics, Müllheim, Germany). The spectra of the quinone species were recorded in water:ethanol (20:80, v/v) using a 60 μM solution of decyl-ubiquinone (Sigma). Decyl-ubiquinone was reduced at anoxic conditions with a 5-fold molar excess of NaBH₄ and the solution was titrated to pH 7 with 0.1 M HCl. Decyl-ubiquinol was deprotonated by an addition of 0.2 M NaOH.

For measurements with complex I and the D213G^H variant, 1 μM protein in A_{MNG}^{*}-buffer was placed in a stirred cuvette and a spectrum was recorded. The entire sample was set to zero absorbance and a stable baseline was obtained within 30 s. Then, the sample was reduced by an addition of a 10-fold molar excess of NADH (Sigma). Reduction and re-oxidation of complex I was followed by the absorbance at 450 nm and the oxidation of NADH by oxygen dissolved in the buffer at 340 nm. NADH was oxidized faster than the enzyme within about 1 min allowing for the calculation of a redox-difference spectrum of a partly reduced enzyme (Friedrich et al., 2000). To measure the inhibition by piericidin A (Sigma) the protein and the buffer were placed in the stirred cuvette and an ethanolic solution of piericidin A (10 mM) was added. The mixture was incubated at room temperature for 5 min to allow binding of the inhibitor and after that, the reaction was started by an addition of NADH as described above. As control, the equivalent volume of ethanol (10 μL) was added to an aliquot of the preparation and the reaction was started after 5 min incubation.

Analytical Procedures

The NADH/ferricyanide oxidoreductase activity was measured as decrease of the ferricyanide concentration over time at 410 nm (macro cuvette QS, d = 1 cm, Hellma Analytics; TIDAS II, J&M Analytik AG). One milliliter ferricyanide (1 mM final concentration) in A^{*}-buffer was mixed with 200 μM NADH and after the onset of a stable baseline, the reaction was started by adding 5 μL of the fractions of the chromatographic columns. The NADH/ferricyanide oxidoreductase activity was calculated according to the Lambert–Beer law using a molar extinction coefficient for ferricyanide of 1 mM^{−1} · cm^{−1} (Friedrich et al.,

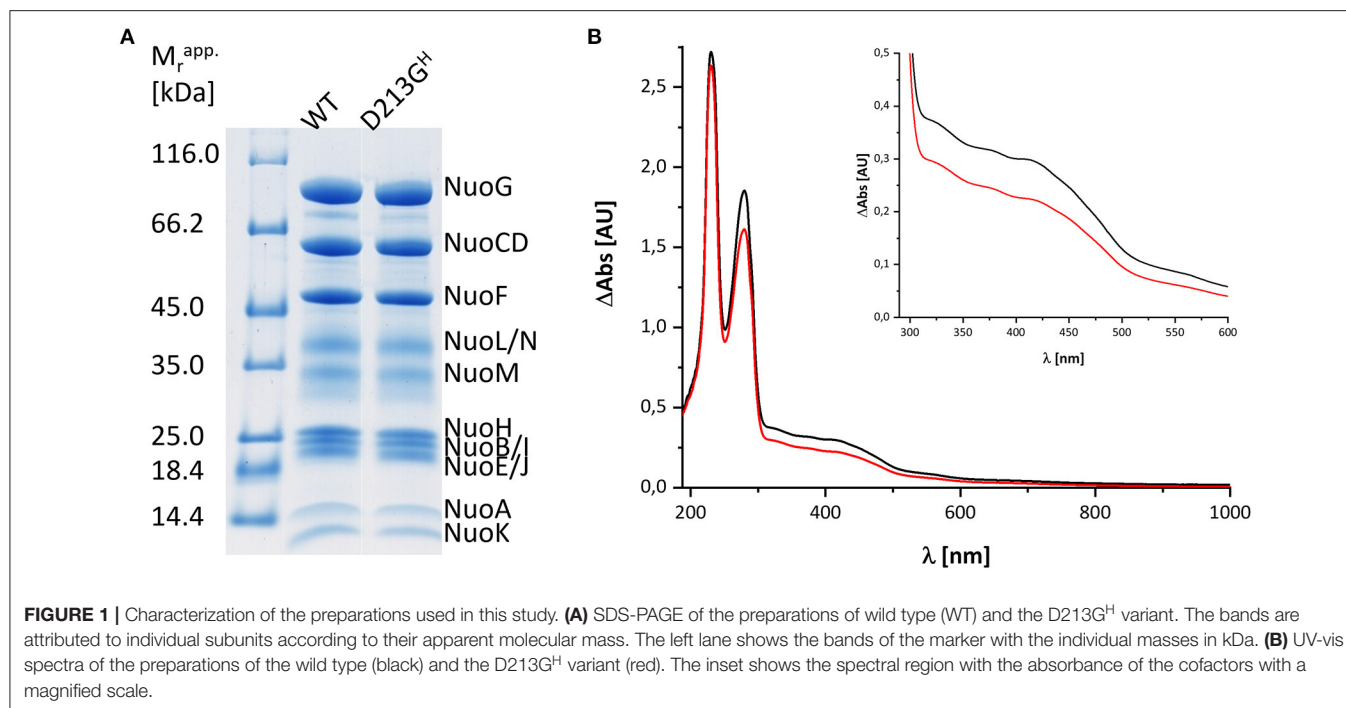
1989). SDS polyacrylamide gel electrophoresis (SDS-PAGE) was performed according to Schagger and von Jagow (1987). NADH:decyl-Q oxidoreductase activity and proton translocation measured as quench of the 9-amino-6-chloro-2-methoxyacridine (ACMA) fluorescence were determined as described (Mühlbauer et al., 2020). The proton gradient across the proteoliposome membrane was dissipated by an addition of 10 μM carbonyl cyanide 3-chlorophenylhydrazone (CCCP).

RESULTS

Spectrum of a Redox Component in *E. coli* Complex I Beyond Cluster N2

Bacterial complex I from *E. coli* is made up of 13 different subunits that are encoded in the *nuo*-operon. In *E. coli*, the genes *nuoC* and *nuoD* are fused to a single gene *nuoCD* (Braun et al., 1998). We routinely use a host strain that chromosomally lacks the *nuo*-genes and that is transformed with a pBAD overexpression plasmid containing the entire *nuo*-operon, facilitating manipulation of the *nuo*-genes (Mühlbauer et al., 2020). For fast enzyme purification, the sequence of a His-tag is fused N-terminally to NuoF. A stable and homogeneous preparation of the complex produced from the *nuo*-operon on the plasmid is obtained in the presence of the detergent LMNG by affinity- and size-exclusion-chromatography resulting in sufficient material of excellent quality for spectroscopic analysis (Figure 1). The preparation differs in nearly all aspects from that used for the spectroscopic investigations 20 years ago: First, both the host strain and the expression plasmid used to produce the complex are different and second, chromatography media and the detergent have changed. To address the question whether the UV-vis redox-difference spectrum of the novel preparation of the *E. coli* complex I still provides an indication for a component that is neither the FMN nor an Fe/S cluster, we repeated the experiments following the re-oxidation of a preparation that was reduced with NADH.

Figure 2 shows the reduction of complex I by NADH and its subsequent re-oxidation by oxygen from the air dissolved in the buffer. The oxidation of NADH is followed at 340 nm and the redox state of the complex by its absorbance at 450 nm. Although, the absorption of the redox groups of complex I is partly masked by the spectral contributions from NADH at the beginning of the reaction, this changes after ~1 min, when the added NADH is fully oxidized: while the spectrum lacks potential contributions from NADH at 340 nm being indicative for full NADH oxidation, residual features between 290 and 600 nm suggest that the complex is still partly reduced (Figure 2B). The additional absorbance with two broad negative peaks at 334 and 418 nm that extends up to 550 nm derives from the two tetranuclear Fe/S clusters on NuoI (Rasmussen et al., 2001). Admittedly, the strong positive absorbance of the remaining NAD⁺ dominates the spectrum at wavelength shorter than 290 nm. However, the spectral range from 290 to 600 nm remained unaffected by NAD⁺ accumulation rendering the redox-difference spectrum in that range suitable for a reliable evaluation (Figure 2). The spectrum is characterized by a positive peak around 305 nm and a broad



negative absorbance around 440 nm. Thus, the UV-vis difference spectrum obtained with the new preparation looks very similar to that detected in *N. crassa* and *E. coli* complex I more than 20 years ago. Noteworthy, the absorbance at 450 nm does not return to its original zero value, opposed to what was reported in the early experiments. This might be due to the capability of the novel preparation to catalyze the energy conversion step (Mühlbauer et al., 2020). The pmf that is lacking in this experiment would therefore be needed to drive the reverse reaction. The capability of the old preparations to catalyze proton-coupled electron transfer was never measured. We will further elaborate on this below.

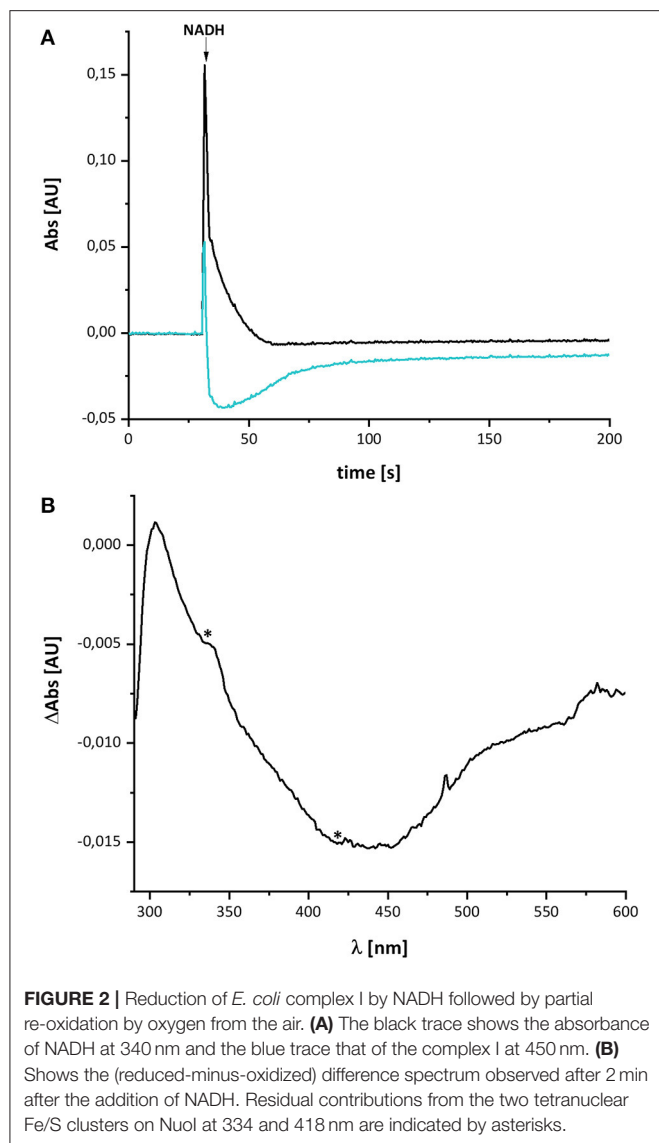
Spectra of Various decyl-Ubiquinone Species

The spectral signature of a component that stayed partly reduced after re-oxidation of NADH-reduced complex I indicates the presence of another component in complex I beyond the FMN and the Fe/S-clusters. In the original publications, it was proposed that this component may reflect the presence of a redox-active post-translationally modified amino acid such as a quinoid group found in quinoproteins (Friedrich et al., 1998, 2000; Schulte et al., 1998; Williamson et al., 2014). Recently, the structure of ovine complex I was determined at 2.3 Å resolution (Kampjut and Sazanov, 2020). At this resolution, the structure actually shows that complex I does not contain a posttranslationally modified amino acid residue with a quinoid structure. However, the simplest explanation for the UV-vis spectrum is that it represents a Q species tightly bound to complex I. This seems feasible as our preparation contains

about 0.5 mol Q/mol enzyme. Furthermore, the spectrum of the unknown component is reminiscent of the spectrum of the ubiquinol anion that has been recorded in water/ethanol (20:80, v:v; Rich and Bendall, 1980). To compare the spectra of the quinone species with the spectrum of the unknown redox component detected in complex I, we recorded the UV-vis spectra of decyl-Q in (20:80, v:v) water/ethanol with the same diode array photometer (Figure 3).

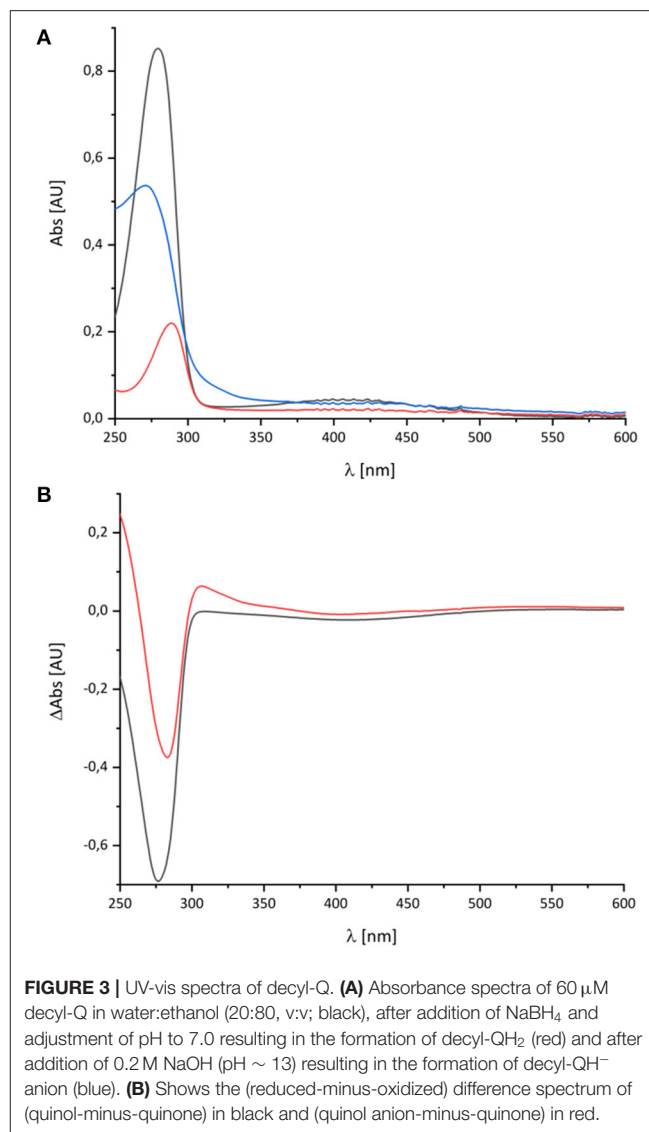
As reported in the literature, the oxidized Q featured an absorbance maximum at 280 nm and a broad positive absorbance around 420 nm (Figure 3). This very sample was reduced by an addition of NaBH₄ and titrated to pH 7.0 by 0.1 M HCl leading to the typical QH₂ spectrum with a maximum at 290 nm and a very minor broad positive absorbance from 360 to 480 nm (Figure 3). Deprotonating this species by adding 0.2 M NaOH resulted in a pH of about 13 and, consecutively, to the formation of the QH⁻ anion. The UV-vis spectrum of the QH⁻ anion is dominated by a maximum at 275 nm and a broad positive absorbance in the vis-region (Figure 3).

The UV-vis spectrum of the component detected in complex I represents its (reduced-minus-oxidized) difference spectrum (Figure 2). Therefore, we calculated the (quinol-minus-quinone) and the (quinol anion-minus-quinone) difference spectra (Figure 3). It turned out that the difference spectrum detected in complex I is rather similar to the calculated difference spectrum of the QH⁻ anion minus the quinone. It shows a positive peak at 307 nm and a broad negative absorbance between 330 and 600 nm (Figure 3). Thus, it is reasonable to assume that the catalytic intermediate detected in the reaction cycle of complex I is a QH⁻ anion (Figure 4).



Re-oxidation of the NADH-Reduced D213G^H Variant

Recently, we characterized a complex I variant that showed a prominent lag-phase in activity attributed to a disturbed Q reduction (Nuber et al., manuscript submitted). In humans, the mutation D199G within the mitochondrially encoded subunit ND1 was detected in a patient, who suffered from exercise intolerance and nephropathy in his 40 s. This position is homologous to position D213 on subunit NuoH in *E. coli* complex I (**Supplementary Figure 1**). The corresponding mutation was introduced into *E. coli*, resulting in the D213G^H variant. The variant was stably assembled and enzymatically active although with a diminished reaction rate. Most importantly, the D213G^H variant showed a prominent lag-phase in electron transfer and proton translocation and its maximal turnover was reached only after ~1 min (**Figure 5**). By contrast, the wild type enzyme is active in both respects right



after substrate addition. It might be possible that the disturbed Q chemistry of the variant is related to the reaction of the putative QH⁻ anion and, hence, that its re-oxidation is also delayed to the same extent as the electron transfer and proton translocation activity.

The variant was prepared from the mutant strain in full analogy to the procedure applied to the parental strain. Not surprisingly, the SDS-PAGE and UV-vis spectrum of the preparation were virtually identical to that of the wild type complex (**Figure 1**). This sample was subjected to the same procedure of reduction and re-oxidation as the wild type complex (**Figure 6**). The UV-vis difference spectrum obtained with the variant also featured the positive peak around 305 nm and the broad negative absorbance around 440 nm. Thus, the difference spectra obtained with the wild type complex and the D213G^H variant are very similar to each other (**Figures 4, 6**). As observed for the wild type, the variant was quickly reduced by NADH and rapidly re-oxidized within 60 sec (**Figure 6**). Just as before,

the absorbance at 450 nm did not return to its original value suggesting an incomplete re-oxidation of the NADH-reduced variant. While both preparations, wild type and variant, are reduced to nearly the same extent, a small difference in the minimum of the two traces recorded at 450 nm after NADH addition was observed, presumably caused by slight differences in enzyme concentration (Figure 7). Remarkably, however, the variant is re-oxidized much slower than the original enzyme (Figure 7). Thus, not only the forward, but also the reverse reaction is hampered in the variant.

Effect of Piericidin A on the Redox-Difference Spectrum

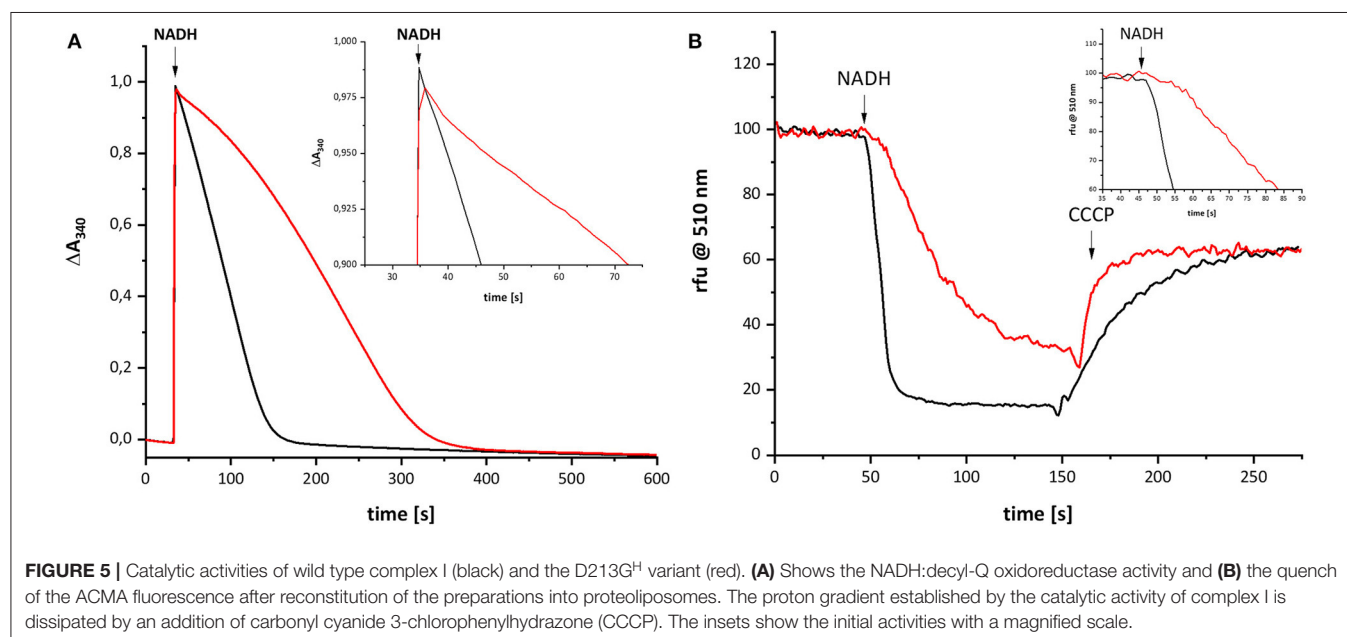
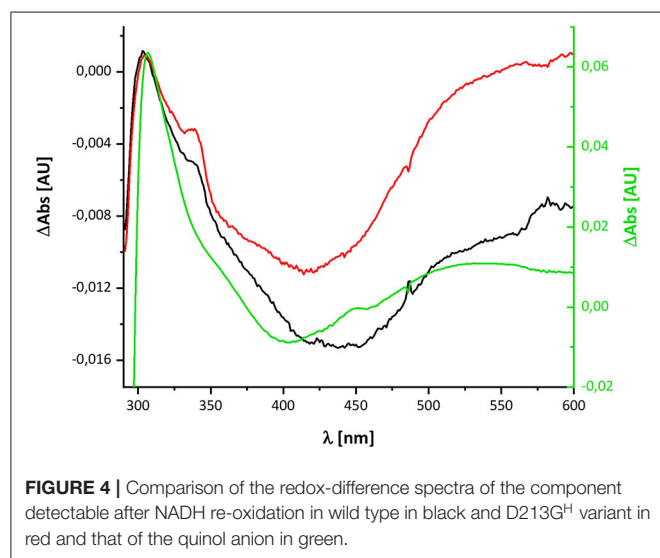
In case the UV-vis difference spectrum indeed reflected the formation of a quinol anion within the Q binding-cavity, the

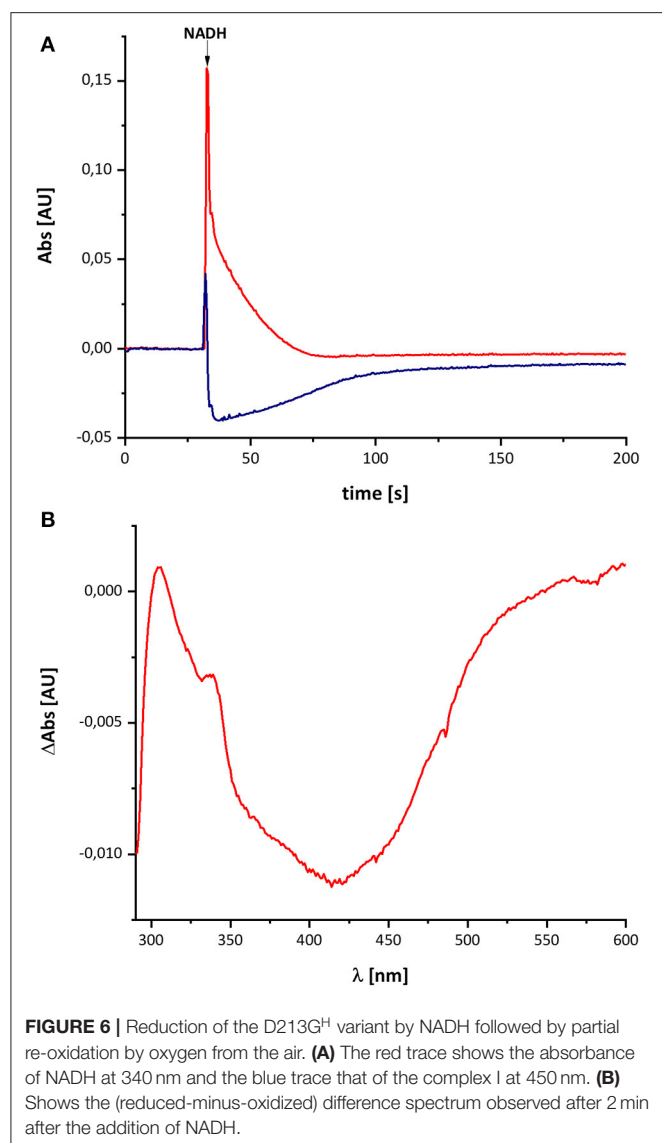
spectrum should be influenced by an addition of a specific Q-site inhibitor such as piericidin A (Bridges et al., 2020). We performed the assay as described above with complex I in a buffer containing 10 μ M piericidin A and used an aliquot of the same preparation incubated with the equivalent volume of ethanol as control (Figure 8). Due to the lack of lipids and a Q regenerating system in the assay, the *E. coli* complex I exhibits a rather low activity of 2.5 U/mg protein. This activity is inhibited to 60% (1.57 U/mg protein) by an addition of 10 μ M piericidin A under these assay conditions. The piericidin A treated complex was quickly reduced to the same extent as the ethanol-treated control but it re-oxidized substantially faster. The UV-vis difference spectrum of the inhibited complex is similar to the one obtained from the ethanol-treated control, but its peaks are significantly smaller, although both measurements were performed using the same protein concentrations. Relative to the absorbance at 600 nm, the positive peak at 305 nm was about one fifth of that of the control (Figure 8). The broad negative absorbance from 350 to 550 nm is diminished only by about 20%. This is due to the strong residual absorbance of the two Fe/S clusters on NuoI that mainly contribute to this spectral region (Rasmussen et al., 2001). The absorbance at 305 nm is not completely bleached by 10 μ M piericidin A due to the incomplete inhibition.

In contrast to the other measurements, the absorbance at 450 nm of the piericidin A treated enzyme returned to its original value, indicating that the NADH-reduced complex is fully re-oxidized. A possible explanation for this finding is provided in the section Discussion.

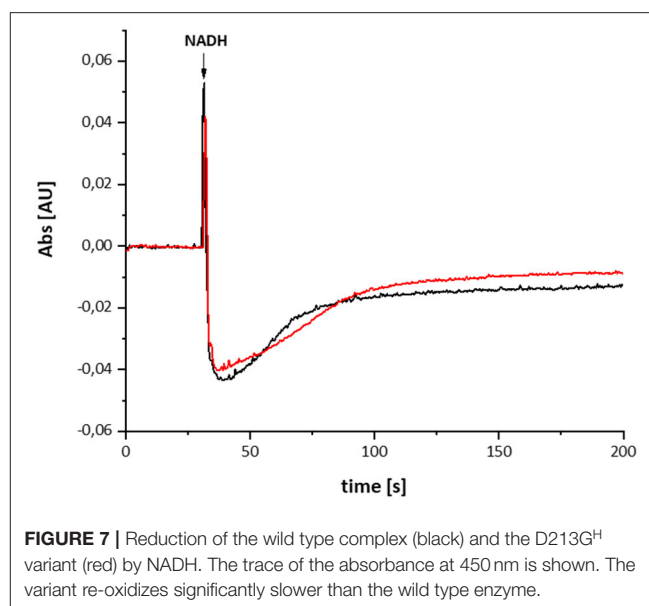
DISCUSSION

Here, we have re-investigated the UV-vis spectroscopic experiments from the Hanns Weiss lab that were conducted more than 20 years ago (Friedrich et al., 1998, 2000; Schulte et al., 1998). We were able to reproduce the data with a completely





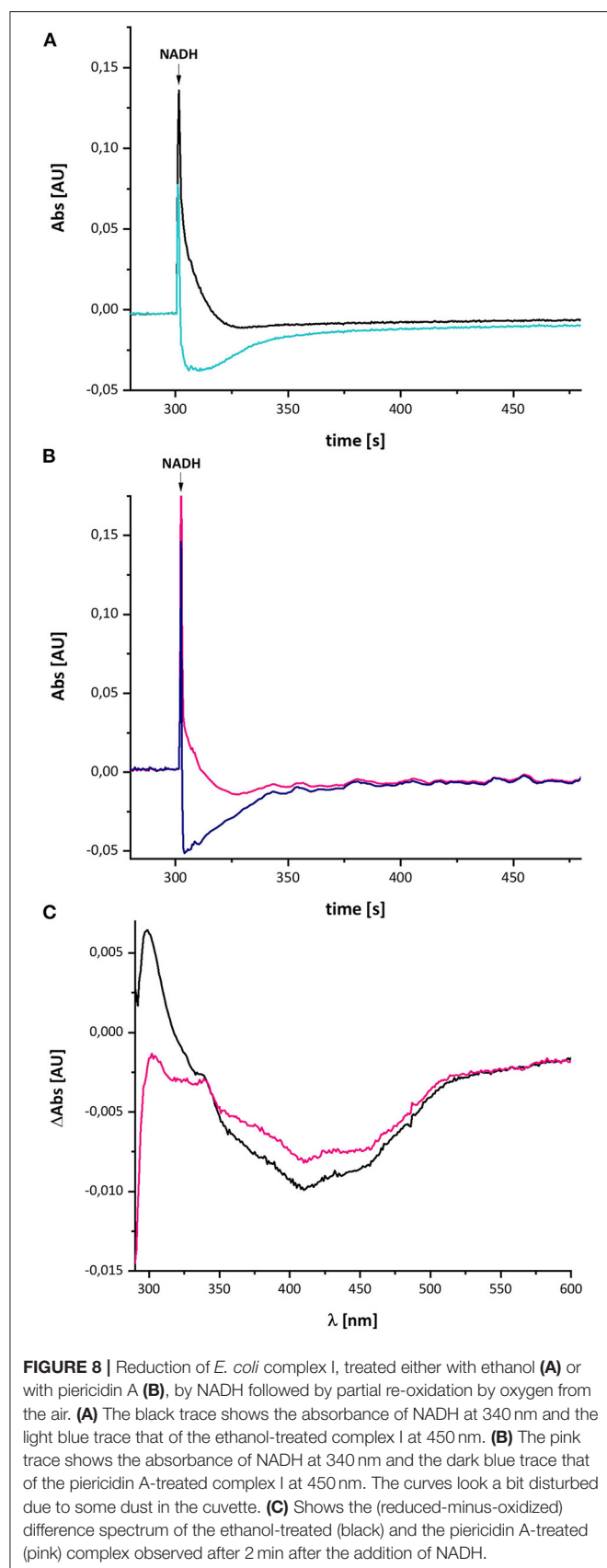
novel preparation of the *E. coli* complex I and obtained a UV-vis redox-difference spectrum of a complex I component highly similar to the one that was called “X” in the first reports (Figures 2, 5, 6). The spectrum is characterized by a positive absorption band around 305 nm and a very broad negative absorbance around 425 nm (Figures 4, 8). In the past, the spectrum was interpreted to derive from a modified amino acid that mediates electron transfer between the distal Fe/S-cluster N2 and the substrate Q. However, recent insights into the molecular structure of complex I from various organisms by X-ray crystallography and cryo-EM render this assumption obsolete (Agip et al., 2019). A simple answer to the question of the molecular identity of the group “X” is that it represents a quinol anion that is playing a role in the catalytic cycle of complex I. The postulate of a QH⁻ anion is supported by the similar UV-vis redox-difference spectra of the group “X” and of the QH⁻ anion (Figures 3, 4; Rich and Bendall, 1980). In



addition, two semiquinone radicals were reported to be involved in the reaction cycle of complex I (Ohnishi et al., 2018). However, the signal of the dominant species called Q_{Nf} depends on the presence of the pmf. Here, the enzyme was investigated in detergent, not in proteoliposomes, spheroplasts or SMPs, hence in the absence of a pmf. Consequently, radical signals were not observed (De Vries et al., 2015). The quinone species detected here can, thus, not reflect a radical state of the quinone.

In addition, it was published that signals of the Q methoxy groups are expected to be detectable in the FT-IR difference spectrum when reducing the oxidized Q to QH₂ (Hellwig et al., 1999). Initially, we speculated that the unknown group acts as a converter of two one-electron-transfers to one two-electron transfer reaction, implying its transition from the oxidized to its fully reduced form. Due to the lack of IR modes specific for the methoxy groups in previously published FT-IR redox difference spectra (Friedrich et al., 2000), we concluded at that time that the unknown redox group is not Q bound to complex I. Here, we now propose that the UV-vis difference spectrum reflects the generation of a quinol anion (Figure 9). Importantly, this non-redox process will not cause the raise of the signals of the methoxy groups (Hellwig et al., 1999), so that the published FT-IR difference spectrum of the unknown group (Friedrich et al., 2000) is in line with the proposal that the spectrum stems from a quinol anion. The interpretation of the UV-vis difference spectrum as QH⁻ anion is further supported by the significant decrease of its spectral amplitude in the presence of the Q-site specific inhibitor piericidin A (Figure 8). As piericidin A competes with Q for the same binding site (Bridges et al., 2020; Gutiérrez-Fernández et al., 2020), a smaller signal is expected.

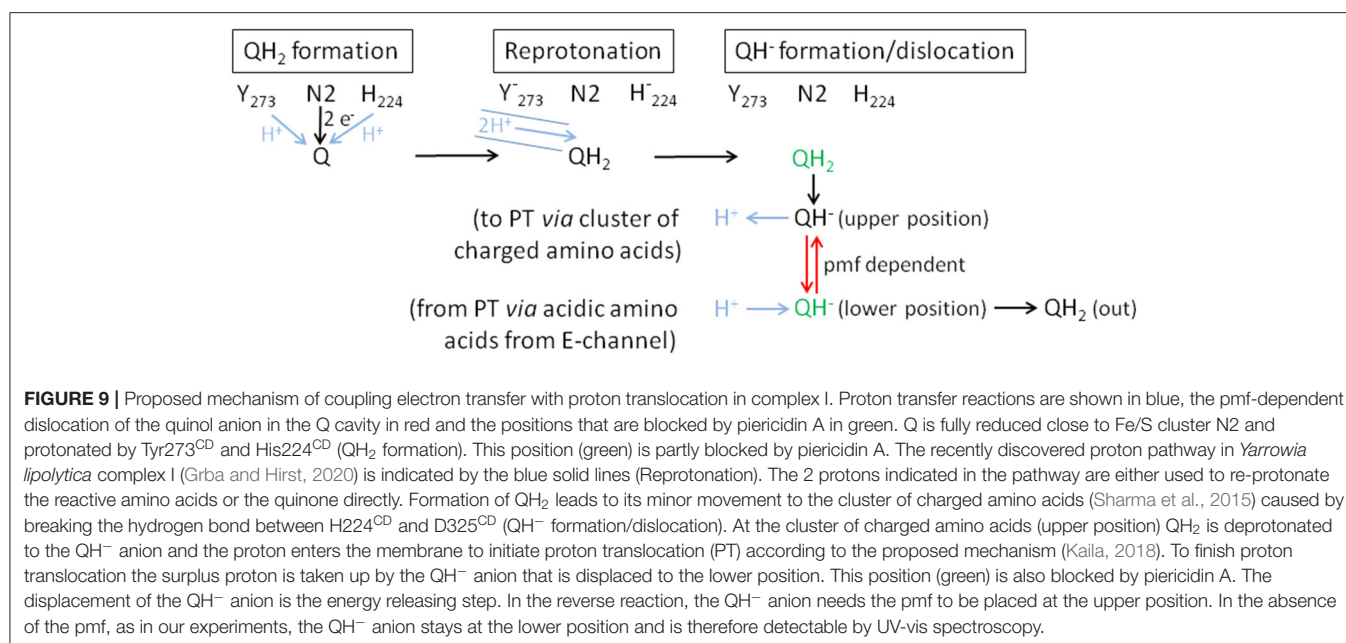
The difference between the re-oxidation kinetics reported in the previous work from the Weiss group and those presented here is the incomplete re-oxidation of the NADH-reduced complex over time. In the old experiments, after reduction of the enzyme



by either NADH or dithionite, the complex was fully oxidized by atmospheric oxygen. In the experiments shown here, the residual absorbance of the putative QH^- anion is detectable for more than 10 min and does not disappear (Figures 2, 6). We hypothesize that the perseverance of the absorbance is connected to the capability of the new preparation to catalyze the energy converting step of the overall reaction (Mühlbauer et al., 2020), a property that has not been investigated with the preparations 20 years ago. Indeed, we propose that the QH^- anion is a catalytic intermediate of the reaction cycle coupling electron transfer and proton translocation in the complex. We suggest that coupling is mediated by the QH^- anion, which has to change its position in the quinone binding cavity to become protonated in the reverse reaction and then re-oxidized as will be explained below. Since this change in position would be the energy converting step, its reversal depends on the presence of the pmf. Thus, the QH^- anion is not re-oxidized in our experiments due to lack of a driving force (Figure 9).

According to MD simulations the first and second electron transfer reactions from Fe/S-cluster N2 to Q are isoenergetic leading to a redox potential of bound ubiquinone of about -260 mV (Sharma et al., 2015; Gamiz-Hernandez et al., 2017; Warnau et al., 2018). This is close to the experimentally determined value of about -295 mV (Hielscher et al., 2013) and <-300 mV (Verkhovskaya and Wikström, 2014). Consequently, it is generally accepted that proton translocation is driven by the quinone chemistry. Structural data and MD simulations imply that the quinone binding cavity comprises at least two positions for quinone binding (Verkhovsky et al., 2012; Baradaran et al., 2013; Wikström et al., 2015; Haapanen et al., 2019; Parey et al., 2019; Grba and Hirst, 2020; Kampjut and Sazanov, 2020). The substrate Q binds in 12 \AA distance to cluster N2. Its quinoid head group is hydrogen-bonded by the conserved residues Y273^{CD} and H224^{CD} (Tocilescu et al., 2010). In this position, Q is reduced by sequential electron transfer from cluster N2 and protonated by these two residues. We propose that the Q is fully reduced and protonated to QH_2 at this site (Figure 9). MD simulations suggest that formation of the anionic form of the two amino acid residues binding Q induces conformational changes enabling a path to the E-channel (Gutiérrez-Fernández et al., 2020). A recently discovered water-channel may be used to re-protonate the involved tyrosine and histidine residues (Grba and Hirst, 2020).

Protonation of Q by H224^{CD} leads to the breaking of a hydrogen bond between H224^{CD} and the neighboring D325^{CD} (Sharma et al., 2015; Warnau et al., 2018; Kampjut and Sazanov, 2020). This induces a conformational move enabling the dissociation of QH_2 that then most likely moves toward a nearby cluster of charged amino acids. It was proposed that QH_2 movement may initiate proton pumping (Sharma et al., 2015) by a change of dipolar interactions within the membrane arm (Kaila, 2018). The cluster of charged amino acid residues connects the quinone binding site with the E-channel, the putative proton translocation pathway closest to the peripheral arm. MD simulations and cryo-EM show that this region is hydrated (Haapanen and Sharma, 2017; Grba and Hirst, 2020). Electrostatic calculations indicate that the movement of QH_2



may change the protonation state of nearby titratable residues (Sharma et al., 2015; Gamiz-Hernandez et al., 2017; Haapanen and Sharma, 2017; Warnau et al., 2018; Haapanen et al., 2019), possibly enabling the deprotonation of QH₂ to the QH⁻ anion that we propose to be a relevant intermediate. The cluster of charged amino acids might thus function as a proton relay system that deprotonates QH₂. Position D213^H is part of the cluster of charged amino acid residues, providing a possible explanation of the disturbed Q reduction in the D213G^H variant (Nuber et al., manuscript submitted). The proton released from QH₂ in its “upper position” is subsequently transferred to the E-channel leading to a “proton push” that initiates a cascade of changing dipolar interactions, which is transmitted all along the membrane arm (Kaila, 2018). The “wave” of changing dipolar interactions is reflected at the end of the membrane arm and travels back toward the peripheral arm, leading to proton uptake from the N-side and to proton release to the P-side (Kaila, 2018). This process ends with a surplus proton that might be localized on an acidic amino acid residue of the E-channel. According to our proposal, the QH⁻ anion formed at the cluster of charged amino acids moves to its second Q binding site, the “lower position,” in the quinone binding cavity close to the E-channel leading to a “proton pull.” Here, the surplus proton from one of the acidic amino acids is taken up by the QH⁻ anion and the resulting QH₂ finally leaves the quinone binding cavity.

Remarkably, the absorbance at 450 nm of complex I returns to its original value about 3 min after NADH addition only in the presence of piericidin A (Figure 8). We interpret this finding as the capability of piericidin A to also block the second QH⁻ anion binding site (its “lower position”), preventing its displacement within the Q cavity. A second binding site for piericidin A was modeled in mouse complex I (Bridges et al., 2020). This binding

site roughly corresponds to the position of the second Q binding site in *Thermus thermophilus* (Warnau et al., 2018) and *Yarrowia lipolytica* (Haapanen et al., 2019; Parey et al., 2019). According to our proposal, the QH⁻ anion is re-protonated at this “lower position.” We propose that in the presence of piericidin A, a residual amount of QH⁻ is formed in the “upper position,” however, the anion cannot move to the “lower position” that is blocked by the inhibitor. Correspondingly, the QH⁻ anion can be fully re-oxidized in the reverse reaction at the “upper position” (Figure 9). In the reverse reaction, it will gain a proton from the cluster of charged amino acids and can be deprotonated and re-oxidized in the position close to cluster N2 without the need of the pmf enabling its shift to the “upper position” (Figure 9).

According to our hypothesis, the movement of the QH⁻ anion is the energy converting step in complex I. This is a variation of the two-stroke model proposed by Brandt (2011) in which the semiquinone anion (Q^{•-}) is transferred by conformational changes from a destabilizing to a stabilizing state inducing the translocation of two protons. In the next step the QH⁻ anion is formed in an environment leading to a pK_a of the QH⁻ anion of about 11.5. The transfer to a different environment by a conformational change results in a pK_a of about 8. The second transition is connected to the translocation of another two protons (Brandt, 2011). This “two-stroke” mechanism requires the presence of only two proton pathways in the membrane arm. Accordingly, our model is a “one stroke” model in which the energy obtained from the displacement of the QH⁻ anion drives translocation of four protons through four proton pathways (one proton per pathway) according to the mechanism provided by Kaila (2018). The latter mechanism, however, needs to be initiated by a yet unknown “proton push” and depends on a “proton pull” at the end of one catalytic cycle. Here, we

propose two different states of the QH[−] anion at two different binding positions and assume that its movement provides the energy for proton translocation. The “proton push” initiated by the formation of the QH[−] anion places the electrostatic interactions of the charged amino acids in the membrane arm in a position, which allows for a loaded spring type mechanism, so that the “proton pull” resulting in the protonation of the QH[−] anion ultimately leads to proton translocation. In order to achieve this, the QH[−] anion has to change its position in the quinone binding cavity from the position close to cluster N2 (“upper position”) to a position close to the E-channel (“lower position”). In terms of the temporal arrangement of these steps within the reaction cycle of complex I, the initial reduction of the complex by NADH leads to the formation of QH₂ at the upper position. Now, the quinol is deprotonated at the cluster of charged amino acids including position D213 and the QH[−] anion moves to the lower position. If electrons are now withdrawn from the complex at the NADH binding site, for instance through the action of molecular oxygen, the FMN and the Fe/S clusters are re-oxidized. However, this has no impact on the QH[−] anion as it cannot move to the upper position due to the lack of the pmf. That explains why the UV-vis absorbance of the QH[−] anion remains after NADH, FMN and the Fe/S clusters have been oxidized. As a consequence of our model, energy coupling in complex I does not involve a previously proposed electron transfer step (Brandt, 2011; Wikström et al., 2015), but instead is solely mediated by a sequence of deprotonation and protonation reactions and the movement of the quinol anion.

DATA AVAILABILITY STATEMENT

The raw data supporting the conclusions of this article will be made available by the authors, without undue reservation.

REFERENCES

- Agip, A.-N. A., Blaza, J. N., Fedor, J. G., and Hirst, J. (2019). Mammalian Respiratory Complex I through the lens of Cryo-EM. *Annu. Rev. Biophys.* 48, 165–184. doi: 10.1146/annurev-biophys-052118-115704
- Bakker, P. T. A., and Albracht, S. P. J. (1986). Evidence for two independent pathways of electron transfer in mitochondrial NADH:Q oxidoreductase. *Biochim. Biophys. Acta* 850, 413–422. doi: 10.1016/0005-2728(86)90109-X
- Baradaran, R., Berrisford, J. M., Minhas, G. S., and Sazanov, L. A. (2013). Crystal structure of the entire respiratory complex I. *Nature* 494, 443–448. doi: 10.1038/nature11871
- Brandt, U. (2011). A two-state stabilization-change mechanism for proton-pumping complex I. *Biochim. Biophys. Acta* 1807, 1364–1369. doi: 10.1016/j.bbabo.2011.04.006
- Braun, M., Bungert, S., and Friedrich, T. (1998). Characterization of the overproduced NADH dehydrogenase fragment of the NADH:ubiquinone oxidoreductase (complex I) from *Escherichia coli*. *Biochemistry* 37, 1861–1867. doi: 10.1021/bi971176p
- Bridges, H. R., Fedor, J. G., Blaza, J. N., Di Luca, A., Jussupow, A., Jarman, O. D., et al. (2020). Structure of inhibitor-bound mammalian complex I. *Nat. Commun.* 11:5261. doi: 10.1038/s41467-020-18950-3
- Burschel, S., Kreuzer Decovic, D., Nuber, F., Stiller, M., Hofmann, M., Zupok, A., et al. (2019). Iron-sulfur cluster carrier proteins involved in the assembly of

AUTHOR CONTRIBUTIONS

FN and TF recorded and calculated the enzyme spectra. LM and TF recorded and calculated the quinone spectra. JS established the novel preparation protocol. FN purified the enzymes. FN and SO made the variant. TF and DW wrote the manuscript with the help of all authors and TF designed the study. All authors contributed to the article and approved the submitted version.

FUNDING

This work was funded by Deutsche Forschungsgemeinschaft (DFG) through grants 278002225/RTG 2202 and SPP1927 (FR 1140/11-2).

DEDICATION

Dedicated to Prof. Dr. Hanns Weiss on the occasion of his 80th birthday.

ACKNOWLEDGMENTS

We would like to thank Prof. Petra Hellwig, University of Strasbourg, France, for helpful discussions and Prof. Dr. Hanns Weiss for his creative and farsighted idea to use old fashioned UV-vis spectroscopy to investigate the mechanism of complex I.

SUPPLEMENTARY MATERIAL

The Supplementary Material for this article can be found online at: <https://www.frontiersin.org/articles/10.3389/fchem.2021.672969/full#supplementary-material>

Escherichia coli NADH:ubiquinone oxidoreductase (complex I). *Mol. Microbiol.* 111, 31–45. doi: 10.1111/mmi.14137

- Cabrera-Orefice, A., Yoga, E. G., Wirth, C., Siegmund, K., Zwicker, K., Guerrero-Castillo, S., et al. (2018). Locking loop movement in the ubiquinone pocket of complex I disengages the proton pumps. *Nat. Commun.* 9:4500. doi: 10.1038/s41467-018-06955-y
- De Vries, S., Dörner, K., Stramprecht, M. F. J., and Friedrich, T. (2015). Electron tunneling rates in Complex I are tuned for efficient energy conversion. *Angew. Chem. Int. Ed.* 54, 2844–2848. doi: 10.1002/anie.201410967
- Friedrich, T., Abelman, A., Brors, B., Guénebaud, V., Kintscher, L., Leonard, K., et al. (1998). Redox components and structure of the respiratory NADH:Ubiquinone oxidoreductase (complex I). *Biochim. Biophys. Acta* 1365, 215–219. doi: 10.1016/S0005-2728(98)00070-X
- Friedrich, T., Brors, B., Hellwig, P., Kintscher, L., Scheide, D., Schulte, U., et al. (2000). Characterization of two novel redox groups in the respiratory NADH:ubiquinone oxidoreductase (complex I). *Biochim. Biophys. Acta* 1459, 305–310. doi: 10.1016/S0005-2728(00)0165-1
- Friedrich, T., Hofhaus, G., Ise, W., Nehls, U., Schmitz, B., and Weiss, H. (1989). A small isoform of NADH:ubiquinone oxidoreductase (complex I) without mitochondrially encoded subunits is made in chloramphenicol-treated *Neurospora crassa*. *Eur. J. Biochem.* 180, 173–180. doi: 10.1111/j.1432-1033.1989.tb14629.x

- Gamiz-Hernandez, A. P., Jussupow, A., Johansson, M. P., and Kaila, V. R. I. (2017). Terminal Electron-proton transfer dynamics in the quinone reduction of respiratory complex I. *J. Am. Chem. Soc.* 139, 16282–16288. doi: 10.1021/jacs.7b08486
- Gnandt, E., Dörner, K., Strampraad, M. F. J., de Vries, S., and Friedrich, T. (2016). The multitude of iron-sulfur clusters in respiratory complex I. *Biochim. Biophys. Acta* 1857, 1068–1072. doi: 10.1016/j.bbabi.2016.02.018
- Grba, D. N., and Hirst, J. (2020). Mitochondrial complex I structure reveals ordered water molecules for catalysis and proton translocation. *Nat. Struct. Mol. Biol.* 27, 892–900. doi: 10.1038/s41594-020-0473-x
- Gutiérrez-Fernández, J., Kaszuba, K., Minhas, G. S., Baradaran, R., Tambalo, M., Gallagher, D. T., et al. (2020). Key role of quinone in the mechanism of respiratory complex I. *Nat. Commun.* 11:4135. doi: 10.1038/s41467-020-17957-0
- Haapanen, O., Djurabekova, A., and Sharma, V. (2019). Role of second quinone binding site in proton pumping by respiratory complex I. *Front. Chem.* 7:221. doi: 10.3389/fchem.2019.00221
- Haapanen, O., and Sharma, V. (2017). Role of water and protein dynamics in proton pumping by respiratory complex I. *Sci. Rep.* 7:7747. doi: 10.1038/s41598-017-07930-1
- Hellwig, P., Mogi, T., Tomson, F. L., Gennis, R. B., Iwata, J., Miyoshi, H., et al. (1999). Vibrational modes of ubiquinone in cytochrome bo3 from *Escherichia coli* identified by fourier transform infrared difference spectroscopy and specific ¹³C labeling. *Biochemistry* 38, 14683–14689. doi: 10.1021/bi991267h
- Hielscher, R., Yegres, M., Voicescu, M., Gnandt, E., Friedrich, T., and Hellwig, P. (2013). Characterization of two quinone radicals in the NADH:ubiquinone oxidoreductase from *Escherichia coli* by a combined fluorescence spectroscopic and electrochemical approach. *Biochemistry* 52, 8993–9000. doi: 10.1021/bi4009903
- Hirst, J. (2013). Mitochondrial complex I. *Annu. Rev. Biochem.* 82, 551–575. doi: 10.1146/annurev-biochem-070511-103700
- Kaila, V. R. I. (2018). Long-range proton-coupled electron transfer in biological energy conversion: towards mechanistic understanding of respiratory complex I. *J. R. Soc. Interface* 15:20170916. doi: 10.1098/rsif.2017.0916
- Kampjut, D., and Sazanov, L. A. (2020). The coupling mechanism of mammalian respiratory complex I. *Science* 370:eabc4209. doi: 10.1126/science.abc4209
- Mitchell, P. (1961). Coupling of phosphorylation to electron and hydrogen transfer by a chemi-osmotic type of mechanism. *Nature* 191, 144–148. doi: 10.1038/191144a0
- Mühlbauer, M. E., Saura, P., Nuber, F., Di Luca, A., Friedrich, T., and Kaila, V. R. I. (2020). Water-gated proton transfer dynamics in respiratory complex I. *J. Am. Chem. Soc.* 142, 13718–13728. doi: 10.1021/jacs.0c02789
- Ohnishi, T., Ohnishi, S. T., and Salerno, J. C. (2018). Five decades of research on mitochondrial NADH-quinone oxidoreductase (complex I). *Biol. Chem.* 399, 1249–1264. doi: 10.1515/hsz-2018-0164
- Parey, K., Haapanen, O., Sharma, V., Köfeler, H., Züllig, T., Prinz, S., et al. (2019). High-resolution cryo-EM structures of respiratory complex I: mechanism, assembly, and disease. *Sci. Adv.* 5:eaax9484. doi: 10.1126/sciadv.aax9484
- Rasmussen, T., Scheide, D., Brors, B., Kintscher, L., Weiss, H., and Friedrich, T. (2001). Identification of two tetranuclear FeS clusters on the ferredoxin-type subunit of NADH:ubiquinone oxidoreductase (complex I). *Biochemistry* 40, 6124–6131. doi: 10.1021/bi0026977
- Rich, P. R., and Bendall, D. S. (1980). The redox potentials of the b-type cytochromes of higher plant chloroplasts. *Biochim. Biophys. Acta* 592, 506–518.
- Sazanov, L. A. (2015). A giant molecular proton pump: structure and mechanism of respiratory complex I. *Nat. Rev. Mol. Cell. Biol.* 16, 375–388. doi: 10.1038/nrm3997
- Schägger, H., and von Jagow, G. (1987). Tricine-sodium dodecyl sulfate-polyacrylamide gel electrophoresis for the separation of proteins in the range from 1 to 100 kDa. *Anal. Biochem.* 166, 368–379. doi: 10.1016/0003-2697(87)90587-2
- Schulte, U., Abelman, A., Amling, N., Brors, B., Friedrich, T., Kintscher, L., et al. (1998). Analysis of the redox groups of mitochondrial NADH:ubiquinone oxidoreductase (complex I) by UV/VIS-spectroscopy. *BioFactors* 8, 177–186. doi: 10.1002/biof.5520080303
- Sharma, V., Belevich, G., Gamiz-Hernandez, A. P., Róg, T., Vattulainen, I., Verkhovskaya, M. L., et al. (2015). Redox-induced activation of the proton pump in the respiratory complex I. *Proc. Natl. Acad. Sci. U.S.A.* 112, 11571–11576. doi: 10.1073/pnas.1503761112
- Tocilescu, M. A., Zickermann, V., Zwicker, K., and Brandt, U. (2010). Quinone binding and reduction by respiratory complex I. *Biochim. Biophys. Acta* 1797, 1883–1890. doi: 10.1016/j.bbabi.2010.05.009
- Verkhovskaya, M., and Wikström, M. (2014). Oxidoreduction properties of bound ubiquinone in Complex I from *Escherichia coli*. *Biochim. Biophys. Acta* 1837, 246–250. doi: 10.1016/j.bbabi.2013.11.001
- Verkhovsky, M., Bloch, D. A., and Verkhovskaya, M. (2012). Tightly-bound ubiquinone in the *Escherichia coli* respiratory complex I. *Biochim. Biophys. Acta* 1817, 1550–1556. doi: 10.1016/j.bbabi.2012.04.013
- Warnau, J., Sharma, V., Gamiz-Hernandez, A. P., Di Luca, A., Haapanen, O., Vattulainen, I., et al. (2018). Redox-coupled quinone dynamics in the respiratory complex I. *Proc. Natl. Acad. Sci. U. S. A.* 115, E8413–E8420. doi: 10.1073/pnas.1805468115
- Wikström, M., Sharma, V., Kaila, V. R. I., Hosler, J. P., and Hummer, G. (2015). New perspectives on proton pumping in cellular respiration. *Chem. Rev.* 115, 2196–2221. doi: 10.1021/cr500448t
- Williamson, H. R., Dow, B. A., and Davidson, V. L. (2014). Mechanisms for control of biological electron transfer reactions. *Bioorg. Chem.* 57, 213–221. doi: 10.1016/j.bioorg.2014.06.006

Conflict of Interest: The authors declare that the research was conducted in the absence of any commercial or financial relationships that could be construed as a potential conflict of interest.

Copyright © 2021 Nuber, Mérono, Oppermann, Schimpf, Wohlwend and Friedrich. This is an open-access article distributed under the terms of the Creative Commons Attribution License (CC BY). The use, distribution or reproduction in other forums is permitted, provided the original author(s) and the copyright owner(s) are credited and that the original publication in this journal is cited, in accordance with accepted academic practice. No use, distribution or reproduction is permitted which does not comply with these terms.



Modeling the Energy Landscape of Side Reactions in the Cytochrome bc_1 Complex

Peter Husen¹ and Ilia A. Solov'yov^{2*}

¹Department of Physics, Chemistry and Pharmacy, University of Southern Denmark, Odense, Denmark, ²Department of Physics, Carl von Ossietzky Universität Oldenburg, Oldenburg, Germany

Much of the metabolic molecular machinery responsible for energy transduction processes in living organisms revolves around a series of electron and proton transfer processes. The highly redox active enzymes can, however, also pose a risk of unwanted side reactions leading to reactive oxygen species, which are harmful to cells and are a factor in aging and age-related diseases. Using extensive quantum and classical computational modeling, we here show evidence of a particular superoxide production mechanism through stray reactions between molecular oxygen and a semiquinone reaction intermediate bound in the mitochondrial complex III of the electron transport chain, also known as the cytochrome bc_1 complex. Free energy calculations indicate a favorable electron transfer from semiquinone occurring at low rates under normal circumstances. Furthermore, simulations of the product state reveal that superoxide formed at the Q_o -site exclusively leaves the bc_1 complex at the positive side of the membrane and escapes into the intermembrane space of mitochondria, providing a critical clue in further studies of the harmful effects of mitochondrial superoxide production.

Keywords: electron transfer, computational biophysics, molecular dynamics, superoxide, free energy perturbation, quantum chemical modeling, enzymes, proteins

OPEN ACCESS

Edited by:

Vivek Sharma,
University of Helsinki, Finland

Reviewed by:

Andrei Pislakov,
University of Dundee, United Kingdom
Wei-Chun Kao,
University of Freiburg, Germany

*Correspondence:

Ilia A. Solov'yov
ilia.solovyov@uni-oldenburg.de

Specialty section:

This article was submitted to
Theoretical and
Computational Chemistry,
a section of the journal
Frontiers in Chemistry

Received: 18 December 2020

Accepted: 27 April 2021

Published: 19 May 2021

Citation:

Husen P and Solov'yov IA (2021)
Modeling the Energy Landscape of
Side Reactions in the
Cytochrome bc_1 Complex.
Front. Chem. 9:643796.
doi: 10.3389/fchem.2021.643796

1 INTRODUCTION

The cytochrome bc_1 complex is a transmembrane protein complex in the inner mitochondrial membrane of eukaryotes or the plasma membrane of photosynthetically active bacteria. Through its sophisticated reaction cycle, the Q-cycle (Mitchell, 1975; Lhee et al., 2010; Crofts et al., 2017; Barragan et al., 2021) depicted in **Figure 1**, it serves as a crucial energy transducer in the ATP synthesis pathway. It is, however, also suspected to be a source of harmful superoxide production through stray reactions with molecular oxygen, O_2 (Cape et al., 2007; Dröse and Brandt, 2008; Rottenberg et al., 2009; Brand, 2010; Guillaud et al., 2014).

As part of the Q-cycle, an ubiquinol (QH_2) molecule from the membrane is oxidized to ubiquinone (Q) in a bifurcated reaction at one of the two substrate binding sites, the Q_o -site, of the bc_1 complex. It was previously shown (Husen and Solov'yov, 2016; Husen and Solov'yov, 2017) that O_2 molecules can occasionally enter the protein complex through the membrane and become trapped close to the iron-sulfur cluster (Fe_2S_2) at the Q_o binding site of the bc_1 complex during a short-lived state of the Q-cycle, in which a bound QH_2 has been partly oxidized to a semiquinone anion ($Q^{\bullet-}$) at the Q_o -site (Crofts et al., 2003; Barragan et al., 2016). As this reaction intermediate is a radical, it is conceivable that it could react with a nearby oxygen molecule to produce a potentially harmful superoxide anion, $O_2^{\bullet-}$.

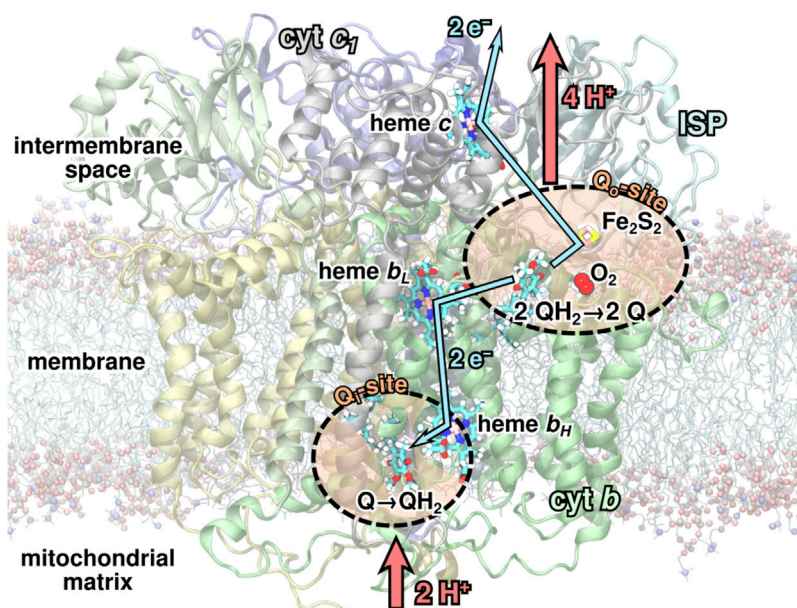


FIGURE 1 | The bc_1 complex and its reaction cycle. During the Q-cycle, two substrate quinol molecules (QH_2) are oxidized to quinone (Q) at the Q_o -site, while one Q is reduced to QH_2 at the Q_i -site of the bc_1 complex. In this process, two protons are absorbed from the negative side of the membrane, and four are released to the positive side, hence maintaining the transmembrane electrochemical gradient. An oxygen molecule may occasionally bind in a pocket near the Q_o -site (Husen and Solov'yov, 2016), which could lead to superoxide production.

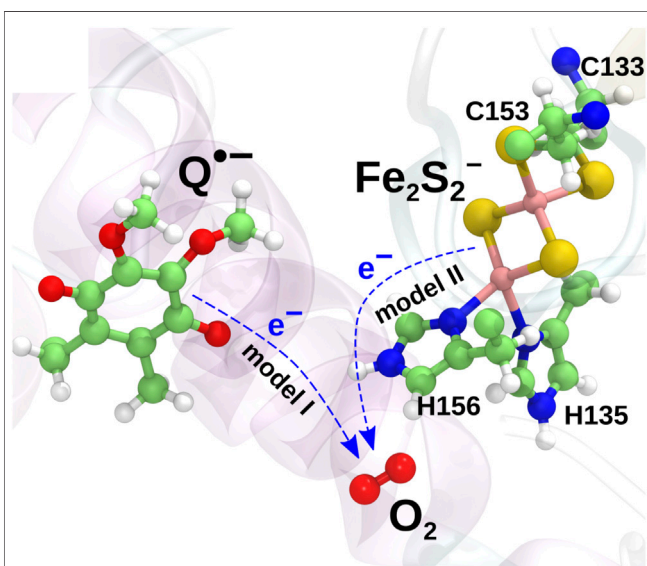
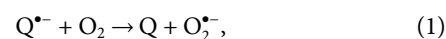


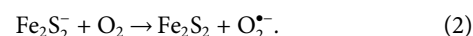
FIGURE 2 | Two charge transfer mechanisms possibly leading to superoxide production. In *model I*, an electron is transferred from the radical semiquinone anion to the O_2 molecule, oxidizing the semiquinone to a neutral quinone. In *model II*, an electron is instead transferred from $Fe_2S_2^-$ to O_2 to yield a superoxide radical.

Earlier computational studies (Salo et al., 2017) have indicated two candidate mechanisms of superoxide production in the bc_1 complex initiated from a state with a radical semiquinone anion

bound at the Q_o -site of the complex and an oxygen molecule trapped at the previously identified binding pocket near Fe_2S_2 Husen and Solov'yov (2016). In the present investigation, these are studied separately as *model I*, in which an electron is transferred from semiquinone to the O_2 molecule,



and *model II*, in which the electron is instead transferred from the iron-sulfur cluster (Fe_2S_2) in the iron-sulfur protein (ISP) subunit of the bc_1 complex:



The two models are illustrated in **Figure 2**. The mechanism described in model II would appear to be prohibited due to the high midpoint redox potential of Fe_2S_2 and can essentially be ruled out from the experimental evidence (Sun and Trumpower, 2003; Bleier and Dröse, 2013). It has, however, been included in the present investigation for completeness, as the reaction is consistently observed in both earlier quantum chemical calculations (Salo et al., 2017) and new extended calculations presented here. The inclusion of this implausible reaction will serve as a test for the model and to shed light on the importance of the local environment, when modeling electron transfer processes.

Studying complex biomolecular processes computationally generally require a range of computational modeling tools covering different time and length scales (Korol et al., 2020). The present work employs several computational modeling

techniques at both the quantum and classical level to characterize the possible reactions leading to superoxide formation at the Q_o -site of the bc_1 complex. Essentially, this study aims to complete an endeavor to computationally model superoxide production at the Q_o -site of the bc_1 complex from O_2 binding to O_2^- unbinding, specifically with anionic semiquinone at the Q_o -site (Husen and Solov'yov, 2016; Husen and Solov'yov, 2017; Salo et al., 2017) to gauge the importance of this mechanism as a contributor to metabolic superoxide production. Firstly, previously reported (Salo et al., 2017) quantum chemical (QC) calculations are repeated with significantly extended sampling over an ensemble of molecular dynamics (MD) simulation snapshots from a previous study (Husen and Solov'yov, 2016) with O_2 bound near Fe_2S_2 , leading to a much more clear classification of electron transfer reactions at the Q_o -site into the two main reactions, models I and II described above, with superoxide as a product. The same calculations are also repeated with a modified cluster model to gauge the sensitivity to the local protein environment of the QC calculations. Secondly, extended MD simulation of the product state of the modeled reactions are carried out to study the binding time and unbinding of superoxide. Lastly, the free energy landscapes of the two reactions are studied using two separate MD-based approaches in order to gauge the feasibility of the reactions and estimate possible rates.

The protonation state of semiquinone at the Q_o -site is debated (Pietras et al., 2016), and the choice of an anionic semiquinone in our model is based on the assumption that it would be the most reactive with oxygen, and some experimental indications exist of this form of semiquinone (Mulikidjanian, 2005; Cape et al., 2007). The anionic form is also interesting for superoxide production, as a proposed protective complex (Pietras et al., 2016; Bujnowicz et al., 2019) with a hydrogen bond between QH^\bullet and the ISP could not be formed in this state, so if both are possible during the Q-cycle, the anionic form would likely be the most relevant for superoxide production. Similarly, the semiquinone at the Q_o -site could alternatively be a result of a semireverse mechanism, where QH_2 has rapidly donated its second electron to heme b_L in the cytochrome b subunit, in accordance with the Q-cycle, but the electron is then later transferred back to the oxidized quinone (Dröse and Brandt, 2008; Sarewicz et al., 2010). The semireverse reaction is in principle also consistent with our model, but it places fewer constraints on the state and position of the Fe_2S_2 -cluster, as it can happen with more delay. Separate computational investigations using the same methodology would be warranted to study mechanisms involving the semireverse reaction or a neutral semiquinone at the Q_o -site as possible contributors to superoxide production.

The combined investigations include all levels of modeling of an important biomolecular process: Diffusion of O_2 , the quantum chemistry of electron transfer and the free energy budget of the complex protein-ligand environment of the hypothetical reaction. Experimental methods can only address the problem much more indirectly, so the details we can get out of modeling are essential to make sure we understand the mechanism and for this, the completeness of the model is essential to allow comparison with experiment.

2 COMPUTATIONAL METHODS

The computational protocols for the quantum chemical modeling and all-atom MD simulations employed in the present work are described in the following sections.

2.1 Quantum Chemical Calculations

The quantum chemical calculations followed the protocol of an earlier study (Salo et al., 2017), but with a significantly increased number of included snapshots to allow improved statistics following the aim of the present investigation. A total of 200 snapshots from an earlier MD simulation (Husen and Solov'yov, 2016) of the membrane embedded bc_1 complex from *Rhodobacter capsulatus* (PDB ID: 1ZRT (Berry et al., 2004)) in presence of molecular oxygen were extracted at random among the parts of the simulated trajectory with O_2 present in the binding pocket near Fe_2S_2 (see **Supplementary Figure S5** in the supplementary material (SM)). A region, illustrated in **Figure 3**, including the bound semiquinone and oxygen molecule, the iron-sulfur cluster and a number of nearby amino acids was extracted from each snapshot and used for quantum chemical calculations. Water molecules were also observed in the vicinity of the O_2 binding position in the earlier simulations (Husen and Solov'yov, 2016), so for each extracted snapshot, the four water molecules closest to the midpoint between TYR302 of the cytochrome b subunit and HIS135 of the ISP subunit were also included in the studied quantum region. The unsaturated bonds in the amino acids were capped with hydrogen. A separate set of calculations was also carried out with the quantum region extended to included the residues V293, P294 and E295 of the cythochrome b subunit. These results of the extended calculations are presented in the SM.

Quantum chemical geometry optimization calculations were carried out in Gaussian 09 (Frisch et al., 2013) using the CAM-B3LYP density functional theory method (Yanai et al., 2004) with the 6-31G basis set (Rassolov et al., 2001) on the extracted quantum region from each sampled MD snapshot. Backbone carbons of the amino acids as well as the carbon atom connecting the ring and the tail of O_2^- were held fixed during the optimization in order to impose the overall conformation sampled from MD, while still allowing the system to relax according to the quantum model. The quantum region was divided into fragments to allow setting the charge and multiplicity for the different molecules and amino acids separately in the initial wavefunction guess. Furthermore, the iron-sulfur cluster was split into separate fragments for each of the four atoms to allow modeling the anti-ferromagnetic coupling between the two iron atoms (Szilagyi and Winslow, 2006). The multiplicities for the two iron atoms were set to five and six, respectively, with anti-parallel spins between the two. The multiplicity of five for one of the irons was due to the fact that this iron atom has accepted the first electron from the bound QH_2 .

The relatively simple 6-31G basis set with no polarization or diffuse functions was chosen despite the inclusion of iron atoms in the model due to the size of the quantum region with a total of 263 atoms, which would have made the calculations unrealistic with a more advanced basis set. The 6-31G basis set has, however,

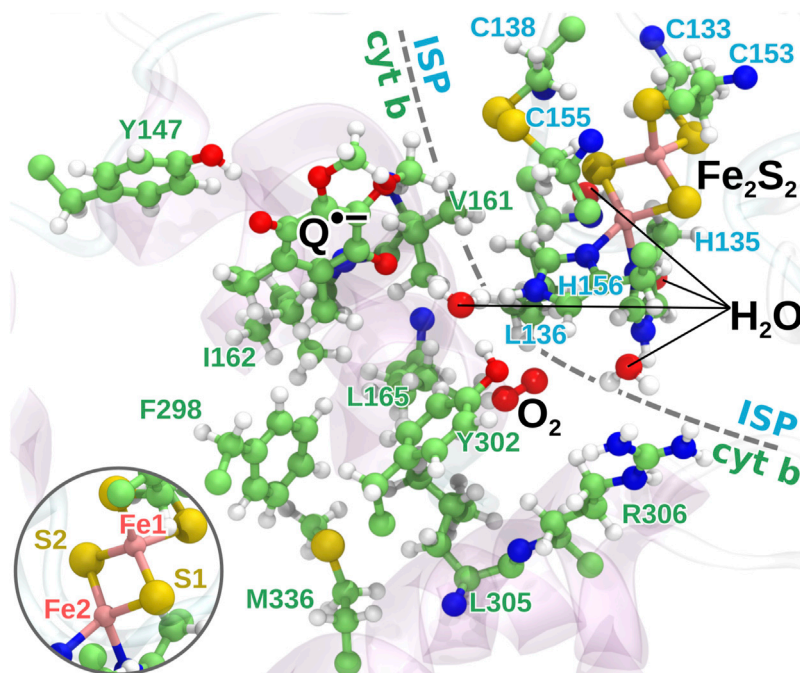


FIGURE 3 | The quantum region used for QC calculations. The region consists of the head group of the semiquinone anion, the iron-sulfur cluster, 16 amino acid residues from the protein, the bound O_2 molecule and four water molecules. The two iron atoms are modeled as having four and five unpaired electrons, respectively, with anti-parallel spin orientation between the two atoms as an initial guess for the QC calculations. Inset: the naming of the iron and sulfur atoms of Fe_2S_2 used in the model.

been shown to be able to model the anti-ferromagnetic coupling in the Fe_2S_2 -cluster (Szilagyi and Winslow, 2006) and the pK_a of its coordinating histidine residues of the ISP (Barragan et al., 2015) correctly, indicating that a reasonable quantum model of the Fe_2S_2 -cluster and its surroundings can be achieved using the basis set.

2.2 Molecular Dynamics Simulations

The MD simulation protocol from earlier studies (Barragan et al., 2015; Husen and Solov'yov, 2016) was adopted, such that equilibrated structures and simulated trajectories from those studies were employed for the further modeling and analysis in the present investigation. Briefly, the X-ray crystal structure of the bc_1 complex from *Rhodobacter capsulatus* (PDB ID: 1ZRT (Berry et al., 2004)) was embedded in a membrane patch consisting of a mixture of phosphatidylcholine (PC 18:2/18:2), phosphatidylethanolamine (PE 18:2/18:2) and cardiolipin (CL 18:2/18:2/18:2) with a total of 102 CL, 406 PC and 342 PE lipids. The histidines of the protein were all considered δ -protonated, except for H135 and H156 of the ISP, which are coordinating the Fe_2S_2 -cluster through the N_δ -atom. These are instead modeled as ϵ -protonated. Two disulfide bonds were introduced based on inspection of the crystal structure: between C144 and C167 of the cytochrome c_1 subunit and between C138 and C155 of the ISP. The protonation state of H156 upon quinol binding is debated (Crofts et al., 1999; Postila et al., 2013), but as we are modeling the semiquinone state, the histidine would be protonated in either case. Similarly, E295 of cytochrome b was considered as

protonated as it is expected to have received the second proton from oxidation of QH_2 . Finally, ASP252 of cytochrome b was considered protonated as it appears to form a hydrogen bond with PHE248 in the crystal structure. Both protonation states of ASP252 could be relevant in a proposed switching mechanism (Postila et al., 2016) involved in proton transport at the Q_i -site.

The system was solvated in a water box of $197 \text{ \AA} \times 177 \text{ \AA} \times 142 \text{ \AA}$ size, and a concentration of 0.05 mol/L NaCl was added, resulting in a total of 497,562 atoms. In the adopted equilibrated structures (Barragan et al., 2015; Husen and Solov'yov, 2016), the membrane embedded bc_1 complex exhibits a stable conformation, where the transmembrane helical scaffold is filled by the Q_i -site quinones and lipids from the membrane. No water molecules are observed in the transmembrane region. While interactions between cardiolipin and the Q_i -site of the bc_1 complex are reported in the literature (Catucci et al., 2012; Postila et al., 2016), no cardiolipin was found near the Q_i -site in the equilibrated structure. This is most likely due to the fact that lipids were randomly placed in the original simulations (Barragan et al., 2015; Husen and Solov'yov, 2016), and the timescale of lipid diffusion in the membrane is too great to observe proper mixing in realistic MD simulations. However, as the present study focuses on the Q_o -site activity, we are mostly concerned with the overall structural stability in the transmembrane region.

In the present study, the bc_1 complex was modeled using MD simulations in three different redox states: The reactant state with

semiquinone at the Q_o-site and O₂ bound and the product state in model I and II, respectively, with a newly formed superoxide bound. The position of the bound O₂ or O₂^{•−} molecule is depicted in **Supplementary Figure S5** in the SM. All earlier and new simulations have quinone at the Q_i-site. The simulated trajectories for the reactant state were taken from an earlier study (Husen and Solov'yov, 2016), while the simulations of the product state in the two models were carried out in the present investigation. The overall simulation protocol including both previous and new simulations is shown in **Supplementary Table S1**.

The reactant state simulations (Husen and Solov'yov, 2016) included a concentration of molecular oxygen added initially to the water phase in the simulation box to study the dynamics O₂ and identify its potential binding sites in the bc₁ complex. The simulated trajectories were analyzed to identify events of O₂ binding at a particular site near Q^{•−} and Fe₂S₂ at the Q_o-site (see **Supplementary Figure S5**), and the parts of the trajectories with a bound O₂ molecule were extracted and used for the energy sampling in the present investigation and for setting up quantum chemical calculations and product state simulations. A binding event was identified as starting when an oxygen molecule comes within a distance of 9 Å from the Fe₂S₂-cluster and ending when it is last observed within 13 Å of Fe₂S₂ before reaching a threshold distance of 20 Å. This definition allows O₂ to temporarily fluctuate more than 13 Å away, as long as it returns again rather than leaving entirely.

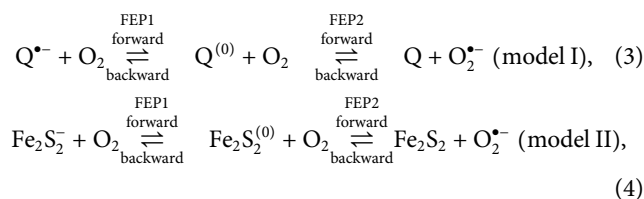
The product state simulations were set up by choosing a simulation snapshot with a trapped O₂ molecule in the binding pocket near Fe₂S₂ and modifying the atomic partial charges and force field parameters to model a product state according to model I and II, respectively, based on earlier parametrizations (Kaszuba et al., 2013; Husen and Solov'yov, 2016) of the involved molecular constituents in different redox states. In model I, the Q_o-site was modeled with a neutral quinone and a negatively charged iron-sulfur cluster, while in model II, a semiquinone anion and a neutral Fe₂S₂ was assumed, as specified in **Supplementary Table S1**. In both cases, the bound O₂ was changed to O₂^{•−}. For each model, 100 replicate MD simulations with O₂^{•−} initially bound were then carried out for long enough to observe it unbind, following an approach previously used to model O₂ binding in proteins (Husen et al., 2019).

MD simulations were performed using NAMD (Phillips et al., 2005) with the CHARMM 36 (MacKerell et al., 1998; MacKerell et al., 2004; Best et al., 2012) force field, and VMD (Humphrey et al., 1996) was used extensively for system construction, data analysis and visualization. The force field parameters and partial charges for the heme groups, iron-sulfur clusters and bound quinones and semiquinones were taken from an earlier study (Kaszuba et al., 2013; Postila et al., 2013), except for the partial charges of Fe₂S₂^{•−} and Q^{•−} which were obtained separately (Husen and Solov'yov, 2016).

2.3 Free Energy Perturbation Simulations

The free energy perturbation (FEP) simulations (Dixit and Chipot, 2001; Woo and Roux, 2005) follow the same protocol as the MD simulations described above, except that constant

pressure, rather than constant volume, is employed in the simulations, and electrostatic interactions were modulated using the alchemical transformation method in NAMD. FEP transformations, where electrostatic interactions were gradually turned on or off through a coupling parameter, λ , were performed to measure the free energy change due to going from reactant to product state, when modeling the reactions in **Eqs. 1, 2** for model I and II, respectively. The van der Waals and bonded interactions were assumed to be essentially unchanged after electron transfer, so the same force-field parameters were used for the product and reactant states, and the van der Waals and bonded interactions were kept fully coupled during the transformations, which simplifies the method considerably. The FEP transformations were carried out in two parts – first turning off electrostatic interactions in the reactant configuration with O₂ bound at the binding pocket near Fe₂S₂, FEP1, and then turning the interactions back on in the product configuration with O₂^{•−} bound in place of O₂ FEP2:



where the “(0)” superscript indicates that all electrostatic interactions are turned off, equivalent to setting all partial charges of atoms to zero.

For model I, the part of the system undergoing the FEP transformation included Q^{•−} at the Q_o-site and the nearby bound O₂ molecule, while for model II, the FEP region included O₂, the iron-sulfur cluster and its coordinating cysteine and histidine residues as well as SER158 of the ISP (implicitly included with Fe₂S₂ in **Eq. 2**), as the partial charges on these residues differ between the modeled charge states of the Fe₂S₂ cluster. Each FEP transformation was carried out in both forward and backward mode, i.e. stepping the coupling parameter, λ , from 0 to 1 and then back again to 0 in 16 steps for each transformation. The simulations were carried out with three settings of the simulation time per λ -window, 10 ps, 1 and 2 ns, to test the sensitivity of the results to the simulation length. The resulting set of 24 FEP calculations is illustrated in **Supplementary Figure S1**: two model reactions, each modeled through two partial transformations (FEP1 and FEP2) and all transformations carried out in both forward and backward mode and for three choices of simulation length. Backward transformations were carried out starting from the atomic coordinates resulting from the corresponding forward transformations, and the FEP2 forward transformations were continued from the end of the FEP1 forward transformations as also illustrated in the figure. The O₂ molecule was restrained to move within a sphere of radius 8 Å and 10 Å for model I and II, respectively, to prevent it from leaving the binding site. For model I, the center of the confined region was defined as the midpoint between the carbonyl carbon atoms of TYR302 of cytochrome b and HIS135 of the ISP, and for model II, the midpoint between

the Fe2 iron atom of Fe_2S_2 (see **Figure 3**) and the nearest of the two unprotonated oxygens of $Q^{\bullet-}$ was used.

The ParseFEP plugin (Liu et al., 2012) of VMD was used to analyze the results of the FEP simulations and produce free energy curves using the Bennet acceptance ratio (BAR) estimator (Bennett, 1976) based on the combined results from forward and backward simulations.

3 RESULTS AND DISCUSSION

The starting point of the present investigation was an earlier computational study (Husen and Solov'yov, 2016) of the dynamics and binding of molecular oxygen inside the bc_1 complex (PDB ID: 1ZRT (Berry et al., 2004)). From these earlier simulations, parts of simulated trajectories with O_2 bound in a pocket near the Q_o -site were extracted and used for the simulations and analysis presented here. First, we discuss the results from quantum chemical modeling of a region around the Q_o -site with O_2 bound, where we generate statistics of local spin densities and identify possible chemical reactions leading to superoxide production. Next, we utilize MD-based approaches to estimate the free energy due to such electron transfer processes. Finally, we estimate the possible superoxide production rate based on the free energy results.

3.1 Quantum Chemical Modeling of the Q_o -Site

A total of 200 snapshots from MD simulations with O_2 trapped close to the Q_o -site of the bc_1 complex were randomly selected, and a 263 atom “quantum region” consisting of the local environment at the Q_o -site (see **Figure 3**) was extracted and analyzed in QC calculations using Gaussian 09 (Frisch et al., 2013; Yanai et al., 2004; Rassolov et al., 2001) following a protocol described previously (Salo et al., 2017). The large number of snapshots was employed to extract ensemble statistics from the earlier MD simulations Husen and Solov'yov (2016) in a local minimum characterized by having O_2 bound in the pocket near Fe_2S_2 depicted in **Supplementary Figure S5** in the SM, while $Q^{\bullet-}$ is bound at the Q_o -site. The need for increased sampling is emphasized by the large variability in outcome from quantum chemical modeling observed earlier (Salo et al., 2017). The QC calculations presented here essentially consist of a geometry optimization using the CAM-B3LYP DFT method using the 6-31G basis set (Rassolov et al., 2001; Yanai et al., 2004) carried out for each extracted snapshot with backbone carbon atoms kept at fixed positions and thereby carrying the conformational variation sampled from MD simulations. The relatively limited 6-31G basis set has earlier been shown to model important properties of iron-sulfur clusters correctly (Szilagyi and Winslow, 2006; Barragan et al., 2015) and was chosen to support the inclusion of a rather large region at the Q_o -site in the quantum model. The limitations of the basis set, lacking diffuse and polarization functions, should however be considered as a source of uncertainty in the results as also discussed below.

In its ground state, O_2 is a triplet diradical, and the two unpaired electrons were modeled in both spin up and spin down configurations, where the unpaired electrons of the iron atom Fe2 of the Fe_2S_2 -cluster (see **Figure 3**) are considered as spin up. The calculations successfully converged for 127 and 114 snapshots, when modeled with O_2 spin up and O_2 spin down, respectively. After geometry optimization, a spontaneous electron transfer to the bound O_2 molecule was observed in some, but not all cases: as can be seen in **Figure 4A**, the spin density of O_2 is either 2 (no charge transfer) or 1 (charge transfer occurred) for the spin up case and -2 and -1 , respectively, for the spin down case. The sign of the spin densities in **Figure 4A** indicate the spin orientation of the fragment, so it can e.g. be observed that the anti-parallel spin between the iron atoms of Fe_2S_2 is maintained after the QC geometry optimization.

To identify the source of the electron transferred to the O_2 molecule, **Figure 4B** shows the difference in local spin density between each of the studied snapshots, where electron transfer to O_2 was observed, and the average of all snapshots with no electron transfer, i.e. the quantity:

$$\Delta s_i = s_i - \langle s \rangle_{\text{no ET}}, \quad i \in \{\text{snapshots with ET}\}. \quad (5)$$

Here, s_i is the local spin density calculated for a snapshot i , where electron transfer was observed, and $\langle s \rangle_{\text{no ET}}$ is the average of the local spin density among all snapshots, where no electron transfer was observed. In the case of O_2 spin up, the electron is consistently transferred from the Fe_2S_2 -cluster (primarily atoms Fe2, S1 and S2, see **Figure 3**), while in the spin down case, the electron comes either fully from the semiquinone anion or again from the Fe_2S_2 -cluster, but this time primarily from the two sulfur atoms. These results confirm earlier findings that an electron can be transferred to O_2 either from $Q^{\bullet-}$ (model I) or from Fe_2S_2 (model II) and its coordinating amino acids (Salo et al., 2017). The extended statistics provided here clearly separates the possible reactions into two principal scenarios, corresponding to the two models studied through MD modeling in the following. A comparison of the initial geometries leading to different electronic configurations after QC calculations, shown in **Supplementary Figure S2** in the SM, revealed that the position of the bound O_2 molecule is important for electron transfer to happen, but no clear deciding geometric features of $Q^{\bullet-}$ or the protein are immediately apparent.

The distributions of total energies of the modeled Q_o -site of the bc_1 complex separated into cases with and without observed charge transfer events are shown in **Figure 5**. The mean energies and standard deviations of the separate distributions are listed in **Table 1** and were used to draw the Gaussian fit functions presented in **Figure 5**. A small number of outlier cases, determined based on an energy threshold, fall well outside the main identified distributions. Various alternative electron transfers, mostly not involving the O_2 molecule, were observed in the outlier cases. In the snapshots leading to electron transfer from $Fe_2S_2^-$ to O_2 (model II), the energy is noticeably lower than for snapshots with no electron transfer, while there is virtually no energy difference in case of electron transfer from $Q^{\bullet-}$ (model I).

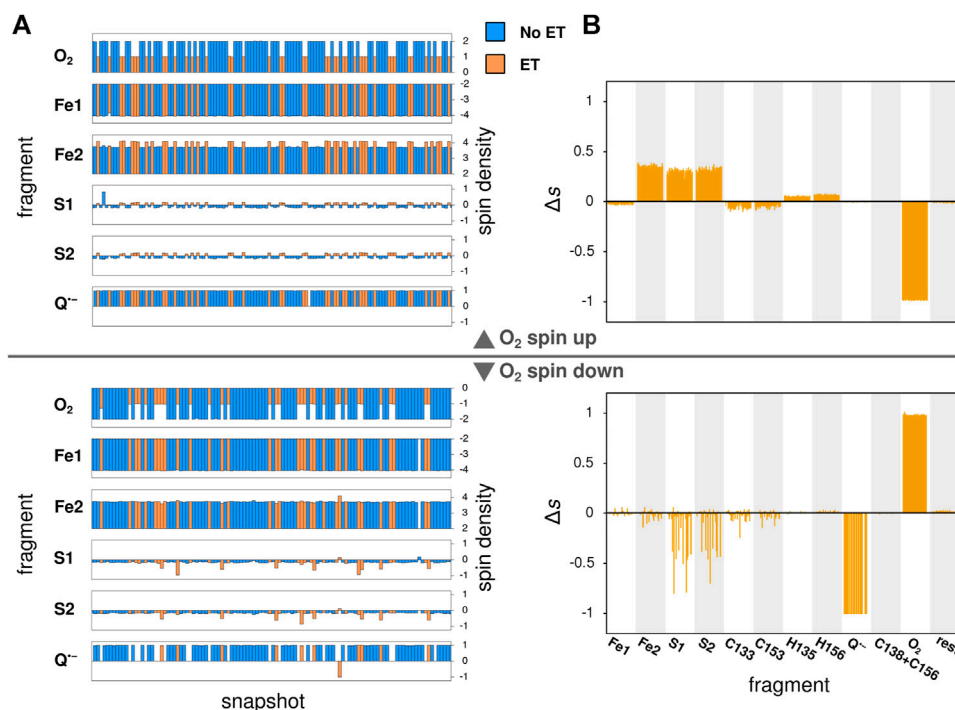


FIGURE 4 | Local spin densities resulting from QC calculations on MD snapshots. **(A)** The local spin densities obtained from QC calculations on MD snapshots with O_2 bound near the Q_o -site. The snapshots where electron transfer to O_2 has occurred, as determined by a change in O_2 spin density, are indicated with orange color, while snapshots with no electron transfer are shown in blue. **(B)** The difference Δs between the local spin density in each snapshot where electron transfer is observed and the average of all snapshots with no electron transfer. The top half of the figure shows the results of QC calculations with O_2 in the spin up state, while the bottom shows results for the spin down state.

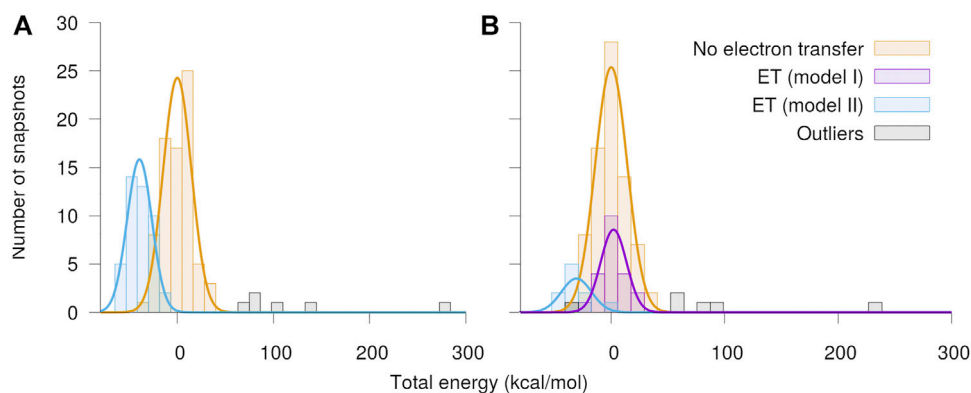


FIGURE 5 | Distribution of total energy of the quantum region after QC geometry optimization. The calculations were performed separately with O_2 assumed to be in the **(A)** spin up and **(B)** spin down state, respectively. The snapshots have been classified into cases with no electron transfer and electron transfer from either the semiquinone (model I) or the Fe_2S_2 -cluster (model II) to O_2 . The energies are shown relative to the mean energy of the snapshots with no charge transfer.

The calculations indicated that both reactions are clearly allowed, when considering the quantum energetics of the Q_o -site alone. In the following, classical MD methods are used to model effects of the local environment in the two model reactions, including binding of $O_2^{\bullet-}$, bc_1 complex reorganization and the free energy of the combined reaction complex. This is in poor

agreement with the experimental evidence, which essentially rules out Fe_2S_2 as an electron donor (Sun and Trumpower, 2003; Bleier and Dröse, 2013). The relatively small quantum region has, however, been isolated in our model, while the effects of the surroundings, i.e. the solvent or, in this case, the protein environment, is likely to play a significant role in electron transfer

TABLE 1 | Energy statistics from the QC geometry optimizations. The table shows the numbers *N* of snapshots along with mean energies $\langle E \rangle$ and standard deviations σ , where no electron transfer or electron transfer according to model I, **Eq. 1**, or model II, **Eq. 2**, was observed following QC geometry optimization of randomly selected MD simulation snapshots. The energies are computed relative to the mean energy of snapshots with no electron transfer observed.

	O ₂ spin up			O ₂ spin down		
	N	$\langle E \rangle$ (kcal/mol)	σ (kcal/mol)	N	$\langle E \rangle$ (kcal/mol)	σ (kcal/mol)
No ET	77	0	14.730	77	0	14.088
ET (model I)	0			21	2.0507	11.399
ET (model II)	44	-39.333	12.906	10	-30.672	13.267
Outliers	6			6		

processes (Moser and Dutton, 1992; Moser et al., 1992; Miyashita et al., 2003).

The size of the studied quantum region and the choice of basis set needed to be balanced due the high computational complexity of QC modeling methods. The modeled region was chosen with proximity to the O₂ molecule bound near the Q_o-site as the main criterion and matches the model studied in an earlier investigation (Salo et al., 2017). To assess the significance of the choice of cluster model on the results from QC modeling, all calculations were repeated using the same MD snapshots, but with the cluster model extended to include E295 from cytochrome b, which is likely to be an important interaction partner with QH₂/Q^{•-}, along with its immediate neighbors, V293 and P294 (Lee et al., 2011; Crofts et al., 2017). The results are shown in **Supplementary Figures S3, S4** as well as **Supplementary Table S2** of the SM. In this case, only three snapshots out of 109 led to the charge transfer described by model I, while the model II reaction remains prevalent in the extended model. The high sensitivity to the choice of included amino acid residues indicates that a limited cluster model is insufficient to reliably and quantitatively model electron transfer processes in a highly complex protein environment. Furthermore, the use of the limited basis set, 6-31G, also introduce uncertainties, but these are likely overshadowed by the uncertainties due to the choice of quantum region. In the present investigation, the results from quantum chemical modeling are ultimately used in an exploratory fashion to identify possible reactions leading to superoxide production: while the initial motivation was the hypothesis that a highly reactive semiquinone anion could react with an oxygen molecule, the frequent observation of electron transfer from Fe₂S₂⁻ led us to include both models in the further free energy calculations.

Aside from the redox states of the potential reaction partners at the Q_o-site, the protonation of the bound semiquinone was also tracked in the extended quantum calculations to test for possible proton transfer back to Q^{•-}. The second proton transfer after binding of QH₂ at the Q_o-site is generally believed to go to E295 (Crofts et al., 2017), either directly or through Y147 as an intermediate (Barragan et al., 2016), so in the extended model, which includes E295, it is conceivable that the proton would be transferred back, if the anionic semiquinone at the Q_o-site is unstable. None of the studied snapshots led to proton transfer

from E295 or Y147, but in around 4% of cases, proton transfer from Y302 to Q^{•-} was observed. In the majority of cases, Q^{•-} thus remained fully deprotonated, so the existence of a local minimum with anionic semiquinone bound at the Q_o-site remains plausible.

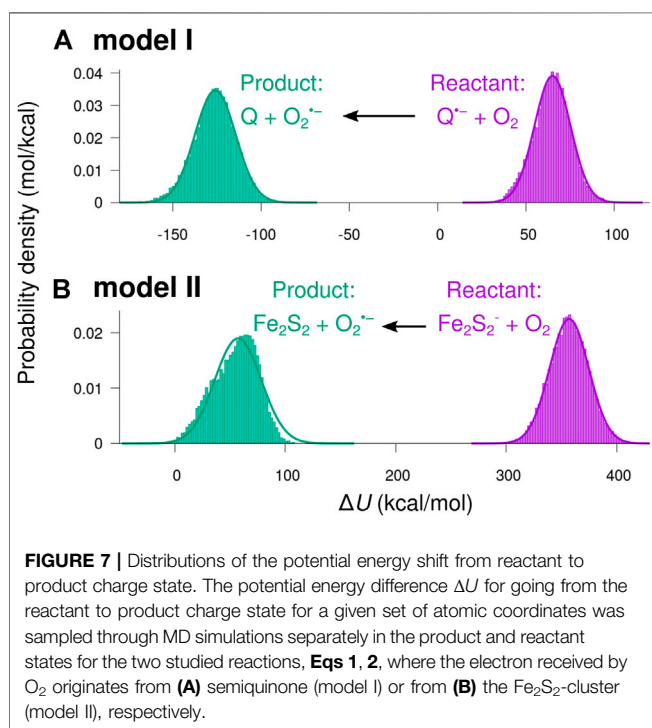
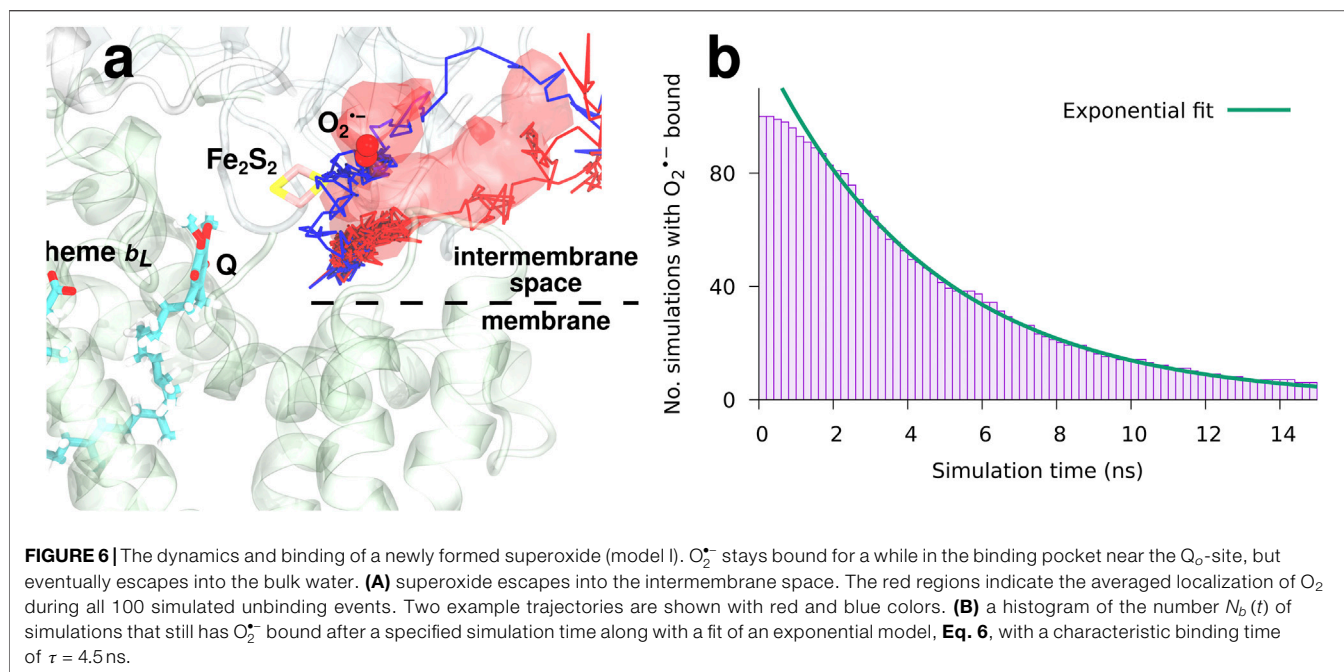
3.2 Unbinding of Superoxide

To study the binding and dynamics of superoxide after an electron transfer event at the Q_o-site, a set of 100 MD simulations starting with O₂^{•-} bound in place of O₂ in the pocket depicted on **Supplementary Figure S5** in the SM were carried out for each of the two models following an approach previously used to model O₂ binding and unbinding in proteins (Husen et al., 2019). All simulations were continued until O₂^{•-} unbinding was observed. O₂^{•-} is indeed able to bind in the same pocket as O₂ near the Q_o-site, where it stays for a while before unbinding as illustrated in **Figure 6** and **Supplementary Figure S5C** for model I. While the neutral O₂ enters the binding pocket from the membrane (Husen and Solov'yov, 2016), O₂^{•-} was found to consistently escape directly into the water phase on the positive side of the membrane, i.e. the intermembrane space in case of mitochondria, in all 100 simulations for each model. Two example trajectories of O₂^{•-} unbinding are shown in **Figure 6A** with red and blue lines, and the red surface is an isosurface of the O₂^{•-} density averaged over all 100 unbinding simulations, i.e. indicating the general localization of the anion during the simulations.

The observed occupancy of O₂^{•-} in the binding position near the Q_o-site of the bc₁ complex, defined as the fraction of simulations that still has O₂^{•-} bound, is shown in **Figure 6B** as a function of simulation time for model I. A fit of an exponential model,

$$N_b(t) = N_0 e^{-\frac{t}{\tau}}, \quad (6)$$

reveals a characteristic binding time of $\tau = 4.5$ ns for model I and $\tau = 1.6$ ns for model II (see **Supplementary Figure S6** in the SM). The fact that O₂^{•-} remains briefly bound points to the existence of a local minimum in the product state of the electron transfer reaction, which puts the free energy analysis in the following on a stronger footing. For both models, the superoxide anion consistently leaves into the positive side of the membrane (the intermembrane space, in case of mitochondria), when it



unbinds. This is unlike the initial binding of the neutral (and non-polar) O_2 molecule, which arrives through the membrane (Husen and Solov'yov, 2016). The finding clearly indicates that mitochondrial superoxide production originating from the bc_1 -complex will primarily emit superoxide into the intermembrane space.

3.3 Reorganization Energy From Classical MD Simulations

In order to construct free energy diagrams of possible electron transfer processes that could lead to superoxide production at the Q_o -site of the bc_1 complex, a number of MD simulations with O_2 bound in the binding pocket near Fe_2S_2 were carried out to sample the potential energy surfaces in the reactant and product states; in particular, the potential energy difference, ΔU , for transferring the system from the reactant to the product charge state for a given set of nuclear coordinates is sampled. The sampled energy histograms are then used to calculate the free energy curves with ΔU serving as the reaction coordinate. The simulations and analysis were carried out for both of the two models of superoxide formation, differing in the source of the electron transferred to O_2 . For both models, simulations from an earlier study (Husen and Solov'yov, 2016) were used in the analysis as the reactant state with O_2 bound near the Q_o -site in the presence of $Q^{\bullet-}$, i.e. after the initial electron transfer from QH_2 in the Q-cycle. Simulations of the product states were then set up with O_2 converted to $O_2^{\bullet-}$ and either $Q^{\bullet-}$ oxidized to Q (model I) or $Fe_2S_2^{\bullet-}$ oxidized to Fe_2S_2 (model II) at the Q_o -site.

Figure 7 shows histograms of the energy difference ΔU sampled from MD simulations. Specifically, ΔU is obtained by calculating the potential energy in a given simulation snapshot, which defines a set of atomic coordinates, $\vec{x}_1, \dots, \vec{x}_N$, by separately assigning atomic partial charges and model parameters describing the system in the reactant and product states:

$$\Delta U(\vec{x}_1, \dots, \vec{x}_N) = U_{\text{product}}(\vec{x}_1, \dots, \vec{x}_N) - U_{\text{reactant}}(\vec{x}_1, \dots, \vec{x}_N). \quad (7)$$

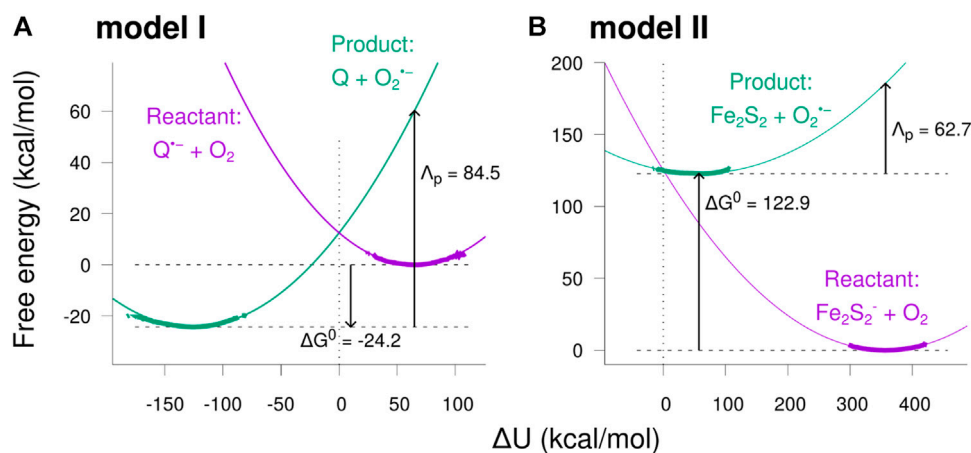


FIGURE 8 | Free energy diagrams for the two model reactions. The free energy was calculated as a function of the potential energy shift ΔU sampled in the MD simulations (see **Figure 7**) in the reactant and product states. **(A)** results for model I, **(B)** results for model II. The thick curves indicate the free energies sampled directly from the simulations, while the thinner curves are the extrapolated parabolas, obtained using **Eq. 10**. The free energy difference ΔG^0 between the reactant and product state minima and the reorganization energy Λ_p calculated in the product state are indicated in the figure, both values in kcal/mol.

The smooth curves in **Figure 7** indicate normal distributions based on the statistical mean values, $\langle \Delta U \rangle$, and standard deviations, σ , from the sampled ΔU distributions:

$$\rho(\Delta U) = \frac{1}{\sqrt{2\pi}\sigma^2} e^{-\frac{(\Delta U - \langle \Delta U \rangle)^2}{2\sigma^2}}. \quad (8)$$

Except for a small skewness for the product state in model II, the sampled ΔU appears to be normal distributed, indicating that the sampling is carried out within a single local minimum of the free energy landscape.

The potential energy difference is a function of atomic coordinates alone and is therefore suitable as a reaction coordinate describing the mechanical reorganization accompanying the modeled electron transfer process (Miyashita and Go, 2000; Miyashita et al., 2003). By sampling ΔU fluctuations in local minima around both product and reactant states, a set of free energy curves can be constructed by taking the logarithm of the densities of states (Warshel, 1982; Miyashita et al., 2003) shown in **Figure 7**:

$$G = -k_B T \ln[\rho(\Delta U)] + \text{constant}. \quad (9)$$

Assuming a normal distribution of ΔU , **Eq. 8**, the free energy curve acquires a parabolic trend:

$$G = \frac{k_B T}{2\sigma^2} (\Delta U - \langle \Delta U \rangle)^2 + G_0. \quad (10)$$

The resulting free energy curves for the studied electron transfer processes are depicted in **Figure 8**. The figure shows the free energy calculated from the sampled histograms in **Figure 7** by using **Eq. 9** with thick lines, while extrapolated parabolas obtained through **Eq. 10** are shown with thin lines. The free energy of the product state was shifted to make the two curves intersect at $\Delta U = 0$ (Miyashita et al., 2003). ΔG^0 shown in the figure is the difference between the minima of the two free energy

TABLE 2 | Free energy parameters and estimated rates obtained from simulations. $\Delta G_{\text{reorg}}^0$ is the free energy difference between the reactant and product state equilibria estimated from the two-state reorganization energy calculations, and Λ_p and Λ_r are the corresponding reorganization energies estimated in the product and reactant state, respectively (see **Figure 8**). ΔG_{FEP}^0 is the free energy change estimated through FEP simulations. k_{et} is the electron transfer rate estimate obtained using ΔG_{FEP}^0 , Λ_p and **Eq. 13**.

	$\Delta G_{\text{reorg}}^0$ (kcal/mol)	Λ_p (kcal/mol)	Λ_r (kcal/mol)	ΔG_{FEP}^0 (kcal/mol)	k_{et} S ⁻¹
Model I	-24.5	84.5	107.9	-21.6	6.1×10^5
Model II	122.9	62.7	88.3	162.7	1.0×10^{-98}

curves, and the reorganization energy, Λ_p , is the energy required to reorganize the atoms of the local environment from their equilibrium position in the product state, i.e. after electron transfer, to correspond to the equilibrium positions in the reactant state. The reorganization energy Λ_p and the similarly defined Λ_r for moving atoms in the reactant state to the equilibrium positions in the product state were observed to differ (see **Table 2**), indicating that the medium fluctuations do not globally follow Gaussian statistics (LeBard and Matyushov, 2010; Martin and Matyushov, 2012; Martin et al., 2013; Matyushov, 2013). The product state value, Λ_p , was used, as the two parabolas intersect at the product state equilibrium when $\Lambda_p = -\Delta G^0$, leading to maximal overlap integral between the reactant and the product harmonic oscillator states (Moser et al., 1992; Moser and Dutton, 1992).

The free energy diagrams in **Figure 8** and the parameters Λ and ΔG^0 could be used to estimate the rate of electron transfers leading to superoxide production using the Marcus theory (Marcus and Sutin, 1985; Page et al., 1999). However, as the sampled ΔU distributions are rather far from directly overlapping, quite extensive extrapolation is involved, which

leads to a high degree of uncertainty in the estimated values of ΔG^0 and Λ_p . To alleviate this uncertainty, a different approach of free energy estimation was employed.

3.4 Free Energy Perturbation Calculations

Instead of connecting the product and reactant states in a single step, an alchemical free energy perturbation (Dixit and Chipot, 2001; Miyashita et al., 2003) (FEP) approach was employed as a second attempt of identifying the free energy change due to an electron transfer to O₂. In this approach, the electrostatic interactions involving O₂/O₂^{•−} and Q^{•−}/Q for model I and Fe₂S₂[−]/Fe₂S₂ (including the coordinating amino acids and SER158 of the ISP) for model II were gradually modulated by a parameter λ during MD simulations, where $\lambda = \lambda_1, \lambda_2, \dots, \lambda_N$ steps between 0 and 1 in a series of simulation windows. First, the electrostatic interactions were turned off in the reactant state. Then, they were turned back on in the product state charge configuration. Only electrostatic interactions were modulated, as no atoms or bonds are introduced or removed in either of the studied reactions, and the van der Waals interactions were assumed to be the same for the two redox states. The total free energy difference between reactant and product state was then calculated by adding up the contributions from each λ -step:

$$\Delta\Delta G_i = -k_B T \ln \langle e^{-\frac{\Delta U_i}{k_B T}} \rangle, \quad \Delta G^0 = \sum_i \Delta\Delta G_i. \quad (11)$$

Here, $\Delta\Delta G_i$ is the change in free energy when stepping the λ parameter from λ_i to λ_{i+1} , and ΔG^0 is the total change in free energy between the reactant and the product states. The sampled variable, ΔU_i , is the difference in potential energy due to changing λ from λ_i to λ_{i+1} for a given set of atomic coordinates, sampled in a simulation with a force field corresponding to $\lambda = \lambda_i$. The FEP transformation is carried out both in forward and backward mode, and the results are combined to produce a single estimate of the free energy change as a function of λ by using the BAR estimator (Bennett, 1976) in the ParseFEP plugin (Liu et al., 2012) of VMD (Humphrey et al., 1996). The results of the individual forward and backward transformations and the BAR estimates are summarized in **Supplementary Tables S3, S4** in the SM. The combined results of the free energy calculations are shown in **Supplementary Figure S7**. The free energy due to the discharging (FEP1) and charging (FEP2) transitions have been connected in the figure, such that the total end-to-end free energy difference in the diagram reflects the total free energy change, ΔG^0 , of the electron transfer reaction. The results are shown for three settings of the simulation length per λ -window. The results are further broken down in **Supplementary Figures S10–S21** of the SM, where distributions of the sampled ΔU_i for each λ step are shown along with the separate free energy curves for the forward and backward simulations. When 1 ns or 2 ns simulation time per λ step is used, the sampled ΔU_i appear as normal distributed, and the forward and backward results are generally in good correspondence with discrepancies up to 5 kcal/mol (see **Supplementary Tables S3, S4**). The effects of the artificial restraints keeping the O₂ molecule from leaving its binding pocket are assumed to be minor, as the O₂ remains naturally

in the bound position during most of the simulations as further discussed in the SM.

The electron transfer from Q^{•−} (model I) leads to a significant decrease in free energy of around 20 kcal/mol, indicating a favorable reaction, while the reaction in model II has a quite high free energy cost of 160 kcal/mol. The reaction free energies are summarized in **Table 2**. The free energy change for the reaction in model I is roughly similar to the result from the reorganization energy sampling (**Figure 8**), while the discrepancy is somewhat bigger for model II. In the latter case, however, both models agree that the free energy cost is so large that the reaction is virtually impossible. The gradual change of potential in the free energy perturbation approach makes sure that the ΔU histograms for a forward and backward step are always overlapping, leading to a much higher confidence in the resulting free energy difference. However, barriers in the free energy landscape and the reorganization energy cannot be obtained using the free energy perturbation method, since an alchemical and unphysical route is used to sample the energy profile.

3.5 Rate of Superoxide Production

The obtained free energy shifts and reorganization energies can be used to estimate the possible rates of the modeled electron transfer processes. Marcus theory (Marcus and Sutin, 1985; Miyashita et al., 2003) predicts the following form of the electron transfer rate constant:

$$k_{et} = \frac{2\pi}{\hbar} |T_{AB}|^2 \frac{1}{\sqrt{4\pi\Lambda k_B T}} \exp\left(-\frac{(\Lambda + \Delta G^0)^2}{4\Lambda k_B T}\right), \quad (12)$$

where $|T_{AB}|$ is the electronic coupling constant between the reactant and product states, Λ is the reorganization energy, and ΔG^0 is the total change in Gibbs free energy between the minima of the two states. $\Lambda = \Lambda_p$ and ΔG^0 can be taken from the reorganization and FEP calculations, respectively. Meanwhile, Dutton and Moser (Moser and Dutton, 1992; Moser et al., 1992) found the following empirical relationship for electron transfers in biomolecules:

$$\log_{10} k_{et} = 15 - 0.6R - 3.1 \frac{(\Delta G + \Lambda)^2}{\Lambda}, \quad (13)$$

where R is the edge-to-edge distance between donor and acceptor in Å, energies are assumed in eV, and the electron transfer rate is in inverse seconds. In the reactant state simulations, the distance between donor and acceptor in model I (the head group of Q^{•−} and the O₂ molecule) fluctuates between 2 and 10 Å. Taking $\Lambda = \Lambda_p$ and $\Delta G^0 = \Delta G_{FEP}^0$ and applying **Eq. 13** individually to 892 snapshots at 10 ps intervals from an O₂ binding event in a simulated trajectory in the reactant state leads to average electron transfer rates of $6.1 \times 10^5 \text{ s}^{-1}$ for model I as listed in **Table 2**. The results for model II indicates that the electron transfer from Fe₂S₂[−] to O₂ is virtually impossible.

The estimated electron transfer rates correspond to the state, where semiquinone and O₂ are simultaneously present at the Q_o-site of the bc₁ complex. The total superoxide production rate, while the bc₁ complex is in the semiquinone state, taking into account binding and unbinding of oxygen molecules can be estimated as:

$$k_{O_2^{\bullet-}|SQ} = k_{bind} \frac{k_{et}}{k_{et} + k_{unbind}}, \quad (14)$$

where k_{bind} and k_{unbind} are the rates of binding and unbinding of O_2 at the binding pocket near the Q_o -site. A previous investigation (Husen and Solov'yov, 2016) estimated the binding and unbinding rates under physiological oxygen concentrations as $k_{bind} = 2 \times 10^5 \text{ s}^{-1}$ and $k_{unbind} = 10^8 \text{ s}^{-1}$, which leads to a superoxide production rate in the semiquinone state for model I of:

$$k_{O_2^{\bullet-}|SQ} \approx 1.2 \times 10^3 \text{ s}^{-1}. \quad (15)$$

This is a very rough order of magnitude estimate, as e.g. using instead the reorganization energy estimate from the reactant state, $\Lambda = \Lambda_r$, yields a two orders of magnitude lower electron transfer rate, but the results clearly indicate that the reaction described in model I is plausible, while the electron transfer from Fe_2S_2 in model II is prohibited due the local protein environment. An experimental study on rat mitochondria (Quinlan et al., 2011) estimated values of $k_{O_2^{\bullet-}|SQ}$ (k_9 in the referenced study (Quinlan et al., 2011)) ranging from 1 to 40 s^{-1} by fits of different kinetic models to experimental superoxide production data, which taking into account the uncertainties, is qualitatively consistent with our computational findings. It should be noted that the rate estimations shown here assume that the bc_1 complex is in a state of the Q-cycle that has semiquinone bound at the Q_o -site. This will most likely only be the case a small fraction of the time (one estimate (Crofts et al., 2006) puts this fraction at $x_{SQ} \approx 4 \times 10^{-8}$), so in reality the superoxide production rate per bc_1 complex will be much lower. This is not so surprising, as under normal conditions the mitochondrial ROS production should be low.

4 CONCLUSION

Quantum chemical modeling confirmed earlier findings (Salo et al., 2017) of two main electron transfer processes leading to superoxide formation at the Q_o -site of the bc_1 complex, which were studied as models I and II, where an electron is donated by either the semiquinone anion, $Q^{\bullet-}$, at the Q_o -site or the iron-sulfur cluster, respectively. The more extended statistics in the present study clearly separates the studied snapshots into cases corresponding to the two electron transfer models as well as cases, where no electron transfer takes place. The shift in energy between the cases with the electron at the donor and acceptor, respectively, indicates a notable decrease in energy for model II, while the electron transfer from $Q^{\bullet-}$ in model I leads to a slight increase. The data from QC calculations alone thus suggests that both reactions are possible, and the model II reaction is rather favorable, which is in contrast to the expected high redox potential of the Fe_2S_2 -cluster. However, including the effects of reorganization of the local protein environment changes this picture dramatically: the free energy contributions due to the local environment were estimated by two separate methods based on classical all-atom MD simulations, leading to values of the free energy difference between reactant and product states of the

studied reactions as well as the corresponding reorganization energies. The free energy contribution obtained through modeling of the entire complex showed that the effects of the local environment is critical. Essentially, the electron transfer from Fe_2S_2 (model II) is virtually impossible, as expected, while the electron transfer from $Q^{\bullet-}$ could happen at low rates. The calculated electron transfer rates are at best rough order of magnitude estimates, but are in reasonable correspondence with available experimental values (Quinlan et al., 2011) and provide evidence pointing to semiquinone at the Q_o -site of the bc_1 complex as a source of mitochondrial ROS production. The computational model could further be used to model other potential superoxide production mechanisms and to study the effects of e.g. mutations on ROS production rates to further connect the computational results with experimental evidence. Additionally, it is found that superoxide produced at the Q_o -site will exclusively escape to the intermembrane space of mitochondria.

DATA AVAILABILITY STATEMENT

The original contributions presented in the study are included in the article/**Supplementary Material**, further inquiries can be directed to the corresponding author.

AUTHOR CONTRIBUTIONS

PH performed the simulations, analyzed the data and prepared the figures. IS supervised the project. Both authors contributed in writing the manuscript.

FUNDING

The authors would like to thank the Independent Research Fund Denmark, the Volkswagen Foundation (Lichtenberg Professorship to IAS), the DFG, German Research Foundation, (GRK1885—Molecular Basis of Sensory Biology and SFB 1372—Magnetoreception and Navigation in Vertebrates) and the Ministry for science and culture of Lower Saxony (Simulations meet experiments on the nanoscale: Opening up the quantum world to artificial intelligence (SMART)). Computational resources for the simulations were provided by the DeIC National HPC Center, SDU, and the CARL Cluster at the Carl-von-Ossietzky University Oldenburg, which is supported by the DFG and the ministry for science and culture of Lower Saxony. The work was supported by the North-German Supercomputing Alliance (HLRN).

SUPPLEMENTARY MATERIAL

The Supplementary Material for this article can be found online at: <https://www.frontiersin.org/articles/10.3389/fchem.2021.643796/full#supplementary-material>

REFERENCES

- Barragan, A. M., Crofts, A. R., Schulten, K., and Solov'yov, I. A. (2015). Identification of Ubiquinol Binding Motifs at the Qo-Site of the Cytochromebc₁Complex. *J. Phys. Chem. B*, 119, 433–447. doi:10.1021/jp510022w
- Barragan, A. M., Schulten, K., and Solov'yov, I. A. (2016). Mechanism of the Primary Charge Transfer Reaction in the Cytochrome bc₁ Complex. *J. Phys. Chem. B*, 120, 11369–11380. doi:10.1021/acs.jpcc.6b07394
- Barragan, A. M., Soudackov, A. V., Luthy-Schulten, Z., Hammes-Schiffer, S., Schulten, K., and Solov'yov, I. A. (2021). Theoretical Description of the Primary Proton-Coupled Electron Transfer Reaction in the Cytochrome Bc₁ Complex. *J. Am. Chem. Soc.* 143, 715–723. doi:10.1021/jacs.0c07799
- Bennett, C. H. (1976). Efficient Estimation of Free Energy Differences from Monte Carlo Data. *J. Comp. Phys.* 22, 245–268. doi:10.1016/0021-9991(76)90078-4
- Berry, E. A., Huang, L.-S., Saechao, L. K., Pon, N. G., Valkova-Valchanova, M., and Daldal, F. (2004). X-Ray Structure of Rhodobacter Capsulatus Cytochrome bc₁: Comparison with its Mitochondrial and Chloroplast Counterparts. *Photosynth. Res.* 81, 251–275. doi:10.1023/b:pres.0000036888.18223.0e
- Best, R. B., Zhu, X., Shim, J., Lopes, P. E. M., Mittal, J., Feig, M., et al. (2012). Optimization of the Additive CHARMM All-Atom Protein Force Field Targeting Improved Sampling of the Backbone ϕ , ψ and Side-Chain χ 1 and χ 2 Dihedral Angles. *J. Chem. Theory Comput.* 8, 3257–3273. doi:10.1021/ct300400x
- Bleier, L., and Dröse, S. (2013). Superoxide Generation by Complex Iii: from Mechanistic Rationales to Functional Consequences. *Biochim. Biophys. Acta*, 1827, 1320–1331. doi:10.1016/j.bbabi.2012.12.002
- Brand, M. D. (2010). The Sites and Topology of Mitochondrial Superoxide Production. *Exp. Gerontol.* 45, 466–472. doi:10.1016/j.exger.2010.01.003
- Bujnowicz, L., Borek, A., Kuleta, P., Sarewicz, M., and Osyczka, A. (2019). Suppression of superoxide production by a spin-spin coupling between semiquinone and the Rieske cluster in cytochrome bc₁. *FEBS Lett.* 593, 3–12. doi:10.1002/1873-3468.13296
- Cape, J. L., Bowman, M. K., and Kramer, D. M. (2007). A semiquinone intermediate generated at the Qo site of the cytochrome bc₁ complex: Importance for the Q-cycle and superoxide production. *Proceed. Nation. Acad. Sci.* 104, 7887–7892. doi:10.1073/pnas.0702621104
- Catucci, L., De Leo, V., Milano, F., Giotta, L., Vitale, R., Agostiano, A., et al. (2012). Oxidoreductase activity of chromatophores and purified cytochrome bc₁ complex from Rhodobacter sphaeroides: a possible role of cardiolipin. *J. Bioenerg. Biomembr.* 44, 487–493. doi:10.1007/s10863-012-9447-y
- Crofts, A. R., Barquera, B., Gennis, R. B., Kuras, R., Guergova-Kuras, M., and Berry, E. A. (1999). Mechanism of Ubiquinol Oxidation by the bc₁Complex: Different Domains of the Quinol Binding Pocket and Their Role in the Mechanism and Binding of Inhibitors. *Biochem.* 38, 15807–15826. doi:10.1021/bi990962m
- Crofts, A. R., Lhee, S., Crofts, S. B., Cheng, J., and Rose, S. (2006). Proton pumping in the bc₁ complex: A new gating mechanism that prevents short circuits. *Biochimica et Biophysica Acta (BBA) - Bioenergetics* 1757, 1019–1034. doi:10.1016/j.bbabi.2006.02.009
- Crofts, A. R., Rose, S. W., Burton, R. L., Desai, A. V., Kenis, P. J. A., and Dikanov, S. A. (2017). The Q-Cycle Mechanism of the bc₁ Complex: A Biologist's Perspective on Atomistic Studies. *J. Phys. Chem. B*, 121, 3701–3717. doi:10.1021/acs.jpcc.6b10524
- Crofts, A. R., Shinkarev, V. P., Kolling, D. R. J., and Hong, S. (2003). The Modified Q-cycle Explains the Apparent Mismatch between the Kinetics of Reduction of Cytochromes c₁ and b_H in the bc₁ Complex. *J. Bio. Chem.* 278, 36191–36201. doi:10.1074/jbc.m305461200
- Dixit, S. B., and Chipot, C. (2001). Can Absolute Free Energies of Association Be Estimated from Molecular Mechanical Simulations? The Biotin–Streptavidin System Revisited. *J. Phys. Chem. A*, 105, 9795–9799. doi:10.1021/jp011878v
- Dröse, S., and Brandt, U. (2008). The Mechanism of Mitochondrial Superoxide Production by the Cytochrome bc₁ Complex. *J. Biol. Chem.* 283, 21649–21654. doi:10.1074/jbc.M803236200
- Frisch, M. J., Trucks, G. W., Schlegel, H. B., Scuseria, G. E., Robb, M. A., Cheeseman, J. R., et al. (2013). *Gaussian 09 Citation*. Wallingford, CT: Gaussian, Inc.
- Guillaud, F., Dröse, S., Kowald, A., Brandt, U., and Klipp, E. (2014). Superoxide production by cytochrome bc₁ complex: A mathematical model. *Biochim. Biophys. Acta*, 1837, 1643–1652. doi:10.1016/j.bbabi.2014.05.358
- Humphrey, W., Dalke, A., and Schulten, K. (1996). VMD: Visual molecular dynamics. *J. Mol. Graph.* 14, 33–38. doi:10.1016/0263-7855(96)00018-5
- Husen, P., Nielsen, C., Martino, C. F., and Solov'yov, I. A. (2019). Molecular Oxygen Binding in the Mitochondrial Electron Transfer Flavoprotein. *J. Chem. Inf. Model.* 59, 4868–4879. doi:10.1021/acs.jcim.9b00702
- Husen, P., and Solov'yov, I. A. (2017). Mutations at the QoSite of the Cytochromebc₁Complex Strongly Affect Oxygen Binding. *J. Phys. Chem. B*, 121, 3308–3317. doi:10.1021/acs.jpcc.6b08226
- Husen, P., and Solov'yov, I. A. (2016). Spontaneous Binding of Molecular Oxygen at the Qo-Site of the bc₁ Complex Could Stimulate Superoxide Formation. *J. Am. Chem. Soc.* 138, 12150–12158. doi:10.1021/jacs.6b04849
- Kaszuba, K., Postila, P. A., Cramariuc, O., Sarewicz, M., Osyczka, A., Vattulainen, I., et al. (2013). Parameterization of the Prosthetic Redox Centers of the Bacterial Cytochrome Bc₁ Complex for Atomistic Molecular Dynamics Simulations. *Theor. Chem. Acc.* 132, 1–13. doi:10.1007/s00214-013-1370-8
- Korol, V., Husen, P., Sjulstok, E., Nielsen, C., Friis, I., Frederiksen, A., et al. (2020). Introducing Viking: A Novel Online Platform for Multiscale Modeling. *ACS Omega* 5, 1254–1260. doi:10.1021/acsomega.9b03802
- LeBard, D. N., and Matyushov, D. V. (2010). Protein-water electrostatics and principles of bioenergetics. *Phys. Chem. Chem. Phys.* 12, 15335–15348. doi:10.1039/c0cp01004a
- Lee, D.-W., El Khoury, Y., Francia, F., Zambelli, B., Ciurli, S., Venturoli, G., et al. (2011). Zinc Inhibition of Bacterial Cytochromebc₁Reveals the Role of Cytochromebe295 in Proton Release at the QoSite. *Biochemistry* 50, 4263–4272. doi:10.1021/bi200230e
- Lhee, S., Kolling, D. R. J., Nair, S. K., Dikanov, S. A., and Crofts, A. R. (2010). Modifications of Protein Environment of the [2Fe-2S] Cluster of the bc₁ Complex. *J. Biol. Chem.* 285, 9233–9248. doi:10.1074/jbc.m109.043505
- Liu, P., Dehez, F., Cai, W., and Chipot, C. (2012). A Toolkit for the Analysis of Free-Energy Perturbation Calculations. *J. Chem. Theory Comput.* 8, 2606–2616. doi:10.1021/ct300242f
- MacKerell, A. D., Feig, M., and Brooks, C. L. (2004). Extending the Treatment of Backbone Energetics in Protein Force Fields: Limitations of Gas-phase Quantum Mechanics in Reproducing Protein Conformational Distributions in Molecular Dynamics Simulations. *J. Comput. Chem.* 25, 1400–1415. doi:10.1002/jcc.20065
- MacKerell, A. D., Jr., Bashford, D., Bellott, M., Dunbrack, R. L., Jr., Evanseck, J. D., Field, M. J., et al. (1998). All-Atom Empirical Potential for Molecular Modeling and Dynamics Studies of Proteins†. *J. Phys. Chem. B*, 102, 3586–3616. doi:10.1021/jp973084f
- Marcus, R. A., and Sutin, N. (1985). Electron transfers in chemistry and biology. *Biochimica et Biophysica Acta (BBA) - Review. Bioenerg.* 811, 265–322. doi:10.1016/0304-4173(85)90014-x
- Martin, D. R., LeBard, D. N., and Matyushov, D. V. (2013). Coulomb Soup of Bioenergetics: Electron Transfer in a Bacterial bc₁ Complex. *J. Phys. Chem. Lett.* 4, 3602–3606. doi:10.1021/jz401910e
- Martin, D. R., and Matyushov, D. V. (2012). Non-gaussian Statistics and Nanosecond Dynamics of Electrostatic Fluctuations Affecting Optical Transitions in Proteins. *J. Phys. Chem. B*, 116, 10294–10300. doi:10.1021/jp305757t
- Matyushov, D. V. (2013). Protein Electron Transfer: Dynamics and Statistics. *J. Chem. Phys.* 139, 025102. doi:10.1063/1.4812788
- Mitchell, P. (1975). The Protonmotive Q Cycle: a General Formulation. *FEBS Lett.* 59, 137–139. doi:10.1016/0014-5793(75)80359-0
- Miyashita, O., and Go, N. (2000). Reorganization Energy of Protein Electron Transfer Reaction: Study with Structural and Frequency Signature. *J. Phys. Chem. B*, 104, 7516–7521. doi:10.1021/jp000865z
- Miyashita, O., Okamura, M. Y., and Onuchic, J. N. (2003). Theoretical Understanding of the Interprotein Electron Transfer between Cytochrome c₂ and the Photosynthetic Reaction Center. *J. Phys. Chem. B*, 107, 1230–1241. doi:10.1021/jp026753k
- Moser, C., and Dutton, P. (1992). Engineering protein structure for electron transfer function in photosynthetic reaction centers. *Biochimica et Biophysica Acta (BBA) - Bioenerg.* 1101, 171–176. doi:10.1016/s0005-2728(05)80012-x

- Moser, C. C., Keske, J. M., Warncke, K., Farid, R. S., and Dutton, P. L. (1992). Nature of Biological Electron Transfer. *Nature* 355, 796–802. doi:10.1038/355796a0
- Mulkidjanian, A. Y. (2005). Ubiquinol oxidation in the cytochrome bc₁ complex: Reaction mechanism and prevention of short-circuiting. *Biochim. Biophys. Acta* 1709, 5–34. doi:10.1016/j.bbabi.2005.03.009
- Page, C. C., Moser, C. C., Chen, X., and Dutton, P. L. (1999). Natural Engineering Principles of Electron Tunnelling in Biological Oxidation-Reduction. *Nature* 402, 47, 52. doi:10.1038/46972
- Phillips, J. C., Braun, R., Wang, W., Gumbart, J., Tajkhorshid, E., Villa, E., et al. (2005). Scalable Molecular Dynamics with NAMD. *J. Comput. Chem.* 26, 1781–1802. doi:10.1002/jcc.20289
- Pietras, R., Sarewicz, M., and Osyczka, A. (2016). Distinct Properties of Semiquinone Species Detected at the Ubiquinol Oxidation Q o Site of Cytochrome bc₁ and Their Mechanistic Implications. *J. R. Soc. Interface* 13, 20160133. doi:10.1098/rsif.2016.0133
- Postila, P. A., Kaszuba, K., Kuleta, P., Vattulainen, I., Sarewicz, M., Osyczka, A., et al. (2016). Atomistic Determinants of Co-enzyme Q Reduction at the Q_r-Site of the Cytochrome bc₁ Complex. *Sci. Rep.* 6, 33607. doi:10.1038/srep33607
- Postila, P. A., Kaszuba, K., Sarewicz, M., Osyczka, A., Vattulainen, I., and Róg, T. (2013). Key Role of Water in Proton Transfer at the Qo-Site of the Cytochrome bc₁ Complex Predicted by Atomistic Molecular Dynamics Simulations. *Biochim. Biophys. Acta* 1827, 761–768. doi:10.1016/j.bbabi.2013.02.005
- Quinlan, C. L., Gerencser, A. A., Treberg, J. R., and Brand, M. D. (2011). The Mechanism of Superoxide Production by the Antimycin-Inhibited Mitochondrial Q-Cycle. *J. Biol. Chem.* 286, 31361–31372. doi:10.1074/jbc.m111.267898
- Rassolov, V. A., Ratner, M. A., Pople, J. A., Redfern, P. C., and Curtiss, L. A. (2001). 6-31g* Basis Set for Third-Row Atoms. *J. Comput. Chem.* 22, 976–984. doi:10.1002/jcc.1058
- Rottenberg, H., Covian, R., and Trumpower, B. L. (2009). Membrane Potential Greatly Enhances Superoxide Generation by the Cytochrome bc₁ Complex Reconstituted into Phospholipid Vesicles. *J. Biol. Chem.* 284, 19203–19210. doi:10.1074/jbc.m109.017376
- Salo, A. B., Husen, P., and Solov'yov, I. A. (2017). Charge Transfer at the Qo-Site of the Cytochrome bc₁ Complex Leads to Superoxide Production. *J. Phys. Chem. B* 121, 1771–1782. doi:10.1021/acs.jpcc.6b10403
- Sarewicz, M., Borek, A., Cieluch, E., Świerczek, M., and Osyczka, A. (2010). Discrimination between two possible reaction sequences that create potential risk of generation of deleterious radicals by cytochrome bc₁. *Biochim. Biophys. Acta (BBA) - Bioenergetics* 1797, 1820–1827. doi:10.1016/j.bbabi.2010.07.005
- Sun, J., and Trumpower, B. L. (2003). Superoxide Anion Generation by the Cytochrome bc₁ Complex. *Archiv. Biochem. Biophys.* 419, 198–206. doi:10.1016/j.abb.2003.08.028
- Szilagyi, R. K., and Winslow, M. A. (2006). On the accuracy of density functional theory for iron-sulfur clusters. *J. Comput. Chem.* 27, 1385–1397. doi:10.1002/jcc.20449
- Warshel, A. (1982). Dynamics of Reactions in Polar Solvents. Semiclassical Trajectory Studies of Electron-Transfer and Proton-Transfer Reactions. *J. Phys. Chem.* 86, 2218–2224. doi:10.1021/j100209a016
- Woo, H.-J., and Roux, B. (2005). Calculation of absolute protein-ligand binding free energy from computer simulations. *Proceedings of the National Academy of Sciences* 102, 6825–6830. doi:10.1073/pnas.0409005102
- Yanai, T., Tew, D. P., and Handy, N. C. (2004). A New Hybrid Exchange-Correlation Functional Using the Coulomb-Attenuating Method (CAM-B3LYP). *Chemical Physics Letters* 393, 51–57. doi:10.1016/j.cplett.2004.06.011

Conflict of Interest: The authors declare that the research was conducted in the absence of any commercial or financial relationships that could be construed as a potential conflict of interest.

Copyright © 2021 Husen and Solov'yov. This is an open-access article distributed under the terms of the Creative Commons Attribution License (CC BY). The use, distribution or reproduction in other forums is permitted, provided the original author(s) and the copyright owner(s) are credited and that the original publication in this journal is cited, in accordance with accepted academic practice. No use, distribution or reproduction is permitted which does not comply with these terms.



Proton-Binding Motifs of Membrane-Bound Proteins: From Bacteriorhodopsin to Spike Protein S

Ana-Nicoleta Bondar*

Freie Universität Berlin, Department of Physics, Theoretical Molecular Biophysics Group, Berlin, Germany

Membrane-bound proteins that change protonation during function use specific protein groups to bind and transfer protons. Knowledge of the identity of the proton-binding groups is of paramount importance to decipher the reaction mechanism of the protein, and protonation states of prominent are studied extensively using experimental and computational approaches. Analyses of model transporters and receptors from different organisms, and with widely different biological functions, indicate common structure-sequence motifs at internal proton-binding sites. Proton-binding dynamic hydrogen-bond networks that are exposed to the bulk might provide alternative proton-binding sites and proton-binding pathways. In this perspective article I discuss protonation coupling and proton binding at internal and external carboxylate sites of proteins that use proton transfer for function. An inter-helical carboxylate-hydroxyl hydrogen-bond motif is present at functionally important sites of membrane proteins from archaea to the brain. External carboxylate-containing H-bond clusters are observed at putative proton-binding sites of protonation-coupled model proteins, raising the question of similar functionality in spike protein S.

Keywords: hydrogen-bonding, proton transfer, proton antenna, membrane transporter, spike protein S

INTRODUCTION

Proton transfer reactions are fundamental to cells from all branches of life. Among proteins that use proton binding and proton transfer for biological function, one of the best studied is bacteriorhodopsin, a small light-driven proton pump of the halophile archaeon *Halobacterium salinarum*. The first three-dimensional structure of bacteriorhodopsin, solved in 1975 by Henderson and Unwin using cryo-Electron Microscopy (cryo-EM), identified the seven transmembrane helices of the protein at a resolution of 7 Å (Henderson and Unwin, 1975). In recent years, structures of bacteriorhodopsin solved with time-resolved serial femtosecond crystallography provided an atomic-resolution movie of structural changes during the proton-transfer reaction cycle (Nango et al., 2016; Weinert et al., 2019). Knowledge derived from simple model systems such as bacteriorhodopsin and other microbial rhodopsins can inform and guide studies of significantly more complex proteins and protein complexes that use protonation change and proton transfer during their reaction cycles (Ernst et al., 2014; Govorunova et al., 2017; Bondar and Lemieux, 2019). An example are the ASIC-like ion channels thought to participate in a cellular pH-sensing mechanism of specialized neurons (Jalalvand et al., 2016; Jalalvand et al., 2018). During ischemia and traumatic brain injury, a drop in extracellular pH and release of glutamate associate with hyperactive N-methyl-D-aspartate (NMDA) receptors and neuronal cell death (Regan et al., 2019).

OPEN ACCESS

Edited by:

Petra Hellwig,
Université de Strasbourg, France

Reviewed by:

Steffen Wolf,
University of Freiburg, Germany
Alexei Stuchebrukhov,
University of California, United States

*Correspondence:

Ana-Nicoleta Bondar
nbondar@zedat.fu-berlin.de

Specialty section:

This article was submitted to
Chemical Biology,
a section of the journal
Frontiers in Chemistry

Received: 26 March 2021

Accepted: 18 May 2021

Published: 31 May 2021

Citation:

Bondar A-N (2021) Proton-Binding
Motifs of Membrane-Bound Proteins:
From Bacteriorhodopsin to Spike
Protein S.
Front. Chem. 9:685761.
doi: 10.3389/fchem.2021.685761

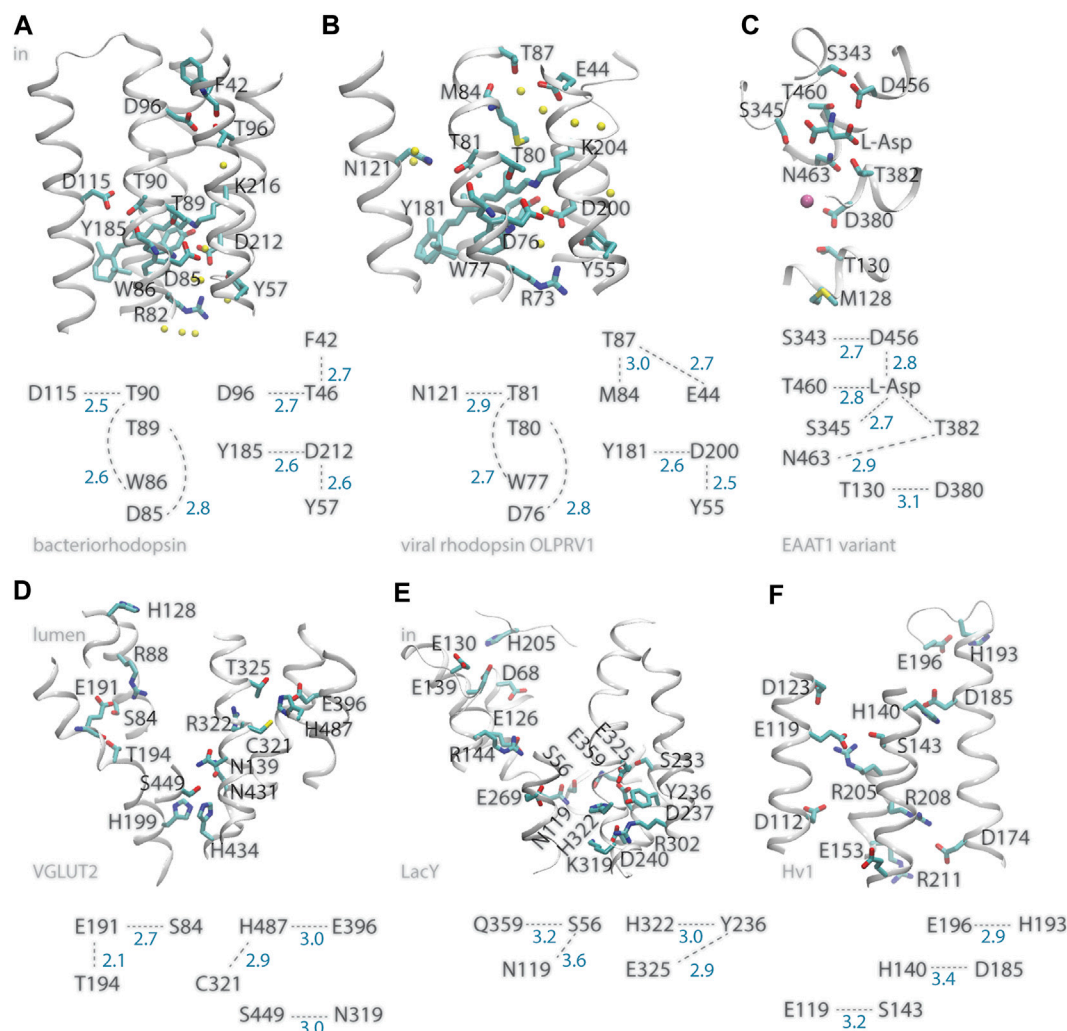


FIGURE 1 | Illustration of inter-helical carboxylate-hydroxyl H-bond motifs. For clarity, only selected backbone groups are shown. Numbers in blue represent H-bond distances in Å. **(A)** The bacteriorhodopsin proton pump, PDB ID:5ZIM (Hasegawa et al., 2018). **(B)** The viral ion channel OLPRV1, PDB ID:7AKY (Zabelskii et al., 2021). **(C)** EAAT1 bound to L-Asp substrate, PDB ID:5LLU (Canul-Tec et al., 2017). **(D)** The glutamate transporter VGLUT2, PDB ID:64VD (Li et al., 2020). **(E)** The LacY symporter, PDB ID:2V8N. **(F)** The Hv1 proton channel, PDB ID:5OKK, molecule #7 (Bayrhuber et al., 2019). All molecular graphics were prepared with Visual Molecular Dynamics, VMD (Humphrey et al., 1996).

pH sensing by proteins is thought to involve the chemical reaction of protonation change of a relatively small number of the titratable groups, typically carboxylate and histidine sidechains (Damaghi et al., 2013; Schönichen et al., 2013). Histidine sidechains, with their nominal pKa of 6.54 ± 0.4 , can titrate at physiological values of cytosolic pH (Schönichen et al., 2013). The pKa value of an amino acid residue may, however, depend strongly on the environment (Thurkill et al., 2006a). For example, whereas the nominal pKa values for aspartic and glutamic acids in solution are, respectively, 3.67 ± 0.4 and 4.25 ± 0.5 (Thurkill et al., 2006b), pKa values as low as 1.56 ± 0.14 and as high as seven were determined with Nuclear Magnetic Resonance (NMR) for aspartic groups of the soluble protein PsbO (Gerland et al., 2020). In this perspective article, common proton-binding and H-bonding motifs are discussed with

examples from simple model systems to more complex proteins.

An Inter-helical Carboxylate-Hydroxyl H-Bond Motif Common to Membrane Transporters and Receptors

Membrane insertion of Asp/Glu groups is energetically costly, with apparent free energy penalties of $\sim 4\text{--}5$ kcal/mol (Xie et al., 2007), and indeed there is only a relatively small probability that Asp and Glu locate in the hydrophobic core of α -helical membrane proteins (Ulmschneider and Sansom, 2001). Presence of carboxylates in transmembrane regions of membrane transporters and receptors is thus of direct interest to evaluate structure-function relationships, particularly for proteins in which these carboxylate groups could be involved

in proton binding and proton transfer. Examples discussed here suggest that internal carboxylates used by membrane proteins for proton binding might be part of common inter-helical H-bond motifs; this could guide studies of other, more complex proteins for which proton-binding groups are yet to be identified.

A prominent example of a membrane transporter that uses internal carboxylates to bind protons is *bacteriorhodopsin*, which for decades has served as model system to study proton pumps (Lanyi, 1999; Herzfeld and Tongue, 2000; Balashov and Ebrey, 2001; Kandori, 2004; Kouyama et al., 2004; Gerwert et al., 2014). The primary proton acceptor group of bacteriorhodopsin is D85 (Metz et al., 1992), a carboxylate within one helical turn of T89, whose sidechain can serve as intermediate carrier for the proton transferred from the Schiff base proton donor to D85 (Bondar et al., 2004; Nango et al., 2016; Ni et al., 2018) (**Figure 1A**). Adjacent to T89, T90 has an inter-helical H-bond with D115, a carboxylate that stays protonated throughout the entire reaction cycle (Metz et al., 1992), and an intra-helical H-bond to the backbone carbonyl of W86 (del Val et al., 2014a). In the structure of the resting state of bacteriorhodopsin (Luecke et al., 1999), the cytoplasmic proton donor D96 (Gerwert et al., 1989) is within inter-helical H-bond distance from the T46 hydroxyl, which is within H-bond distance from the backbone carbonyl of F42 (**Figure 1A**); later during the reaction cycle, rearrangements of hydrophobic sidechains associate with formation of a water chain from D96 to the retinal Schiff base (Weinert et al., 2019). That is, at two internal sites where protons bind, bacteriorhodopsin can have inter-helical carboxylate-hydroxyl H-bonding and intra-helical H-bonding of the Thr hydroxyl group to a backbone carbonyl group (del Val et al., 2014a). The fact that only D96 changes protonation, whereas D115 remains protonated, suggests local protein environment other than with the direct H-bond partner impacts protonation change (del Val et al., 2014a). At the extracellular proton-release side, H-bonding between S193 and E204 depends on the protonation state (Gerwert et al., 2014).

Similar inter-helical carboxylate-hydroxyl motifs were identified in structures of other membrane transporters, such as the *C1C2 channelrhodopsin chimera* and the *sodium pump rhodopsin KR2* (del Val et al., 2014b; Bondar and Smith, 2017; Siemers et al., 2019), the *SERCA calcium pump ATPase*, and the *multidrug transporter AcrB* (del Val et al., 2014a; Bondar and Lemieux, 2019), and can be observed in the recently solved structure of *viral rhodopsin OLPVR1*, a sodium/potassium ion channel (Zabelskii et al., 2021) (**Figure 1B**). Likewise, recently solved structures of *glutamate transporters VGLUT2* (Li et al., 2020) and *EAAT1* (Canul-Tec et al., 2017), which are members of families of neurotransmitter transporters essential for the functioning of the brain (Münster-Wandowski et al., 2016; Martineau et al., 2017), indicate inter-helical carboxylate-hydroxyl motifs at functionally important sites of both transporters: In the structure of VGLUT2, the putative pH sensor E191 (Li et al., 2020) H-bonds to S84 and T194 (**Figure 1D**); in EAAT1, D380 is within H-bond distance from T130 and thus close to M128, a group whose mutation to Arg

inhibits glutamate transport (Chivukala et al., 2020); D456 H-bonds to the L-Asp substrate and to S343—which was noted as a conserved group whose mutation in wild-type EAAT1 inhibits transport (Canul-Tec et al., 2017); L-Asp H-bonds to three Ser/Thr hydroxyl groups (**Figure 1C**).

G-Protein Coupled Receptors (GPCRs) are membrane proteins that mediate communication between cells and their external environments. Protonation change might occur at carboxylate D2.50 (Zhang et al., 2015; Vickery et al., 2018), a carboxylate group part of the sodium-binding site in many class-A GPCRs (Katritch et al., 2014). H-bond networks conserved among static structures of GPCRs show D2.50 paired with S7.46, that is, a carboxylate-hydroxyl pair is present at a functionally important site (Bertalan et al., 2020) [the Ballesteros and Weinstein numbering scheme is used for GPCR groups (Ballesteros and Weinstein, 1995)].

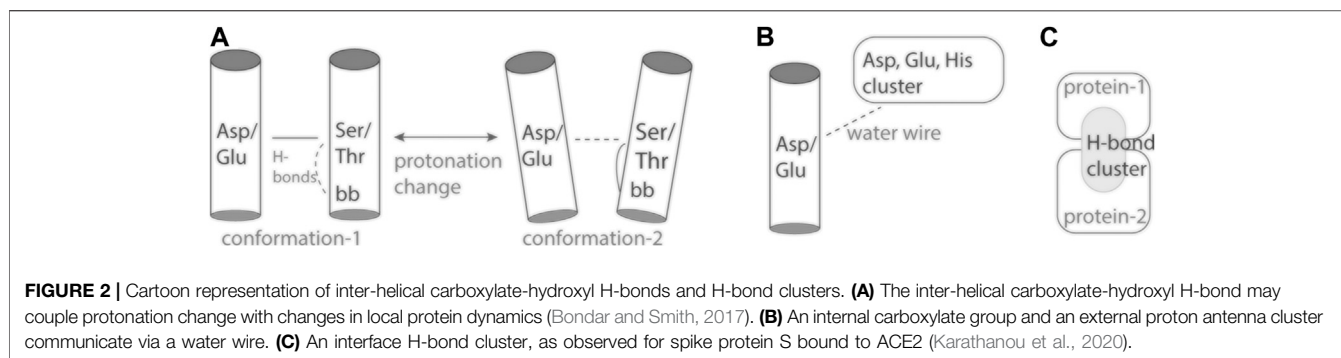
Inter-helical H-bonding between Asp/Glu and Ser/Thr could provide an efficient mechanism to couple protonation change with local protein dynamics (Bondar and Smith 2017). Hydrophobic contacts of non-polar segments of these H-bond partners can reduce H-bond dynamics and strengthen H-bonding (Nemethy et al., 1963; Fernandez and Scheraga, 2003), and alteration of the pKa of an internal carboxylate might require local protein conformational change enabling water access to the carboxylate (Szaraz et al., 1994). In bacteriorhodopsin, the T90-D115 H-bond (**Figure 1A**) is in a local environment with more non-polar contacts than T46-D96, and its H-bond distance experiences smaller-amplitude fluctuations at room temperature (del Val et al., 2014a); the lesser hydrophobic packing near T46-D96 associates with water molecules entering rapidly the vicinity of D96 when the protein is mutated elsewhere (del Val et al., 2014a), and during the reaction cycle of the wild-type pump a file of waters assembles to bridge D96 to the Schiff base proton acceptor (Freier et al., 2011; Weinert et al., 2019).

Protonation change at an inter-helical carboxylate-hydroxyl pair might couple to altered local dynamics of the helix hosting the hydroxyl group: Ser/Thr hydroxyl groups can compete with backbone amide groups for H-bonding to a carbonyl group (Gray and Matthews, 1984; Presta and Rose, 1988), which increases local fluctuations of the helix (del Val et al., 2012). Alternatively, altered helix dynamics might impact local dynamics and hydration of the hydroxyl-carboxylate H-bond (**Figure 2A**).

Other H-Bond Motifs at Internal Proton-Binding Sites of Membrane Transporters

Local H-bonding and hydrophobic packing are likely key mechanisms used by proteins to control protonation of a proton-binding group—and different solutions as to which sidechain serves as H-bond partner for proton-transfer sidechains of membrane transporters appear to exist.

In the *plasma membrane proton pump AHA2*, which is a P-type ATPase, the primary proton donor/acceptor D684 (Buch-Pedersen and Palmgren, 2003) makes an inter-helical



H-bond with an Asn (Pedersen et al., 2007; Guerra and Bondar, 2015; Focht et al., 2017); Likewise, OLPRV1, EAAT1, VGLUT2, and LacY, have at functionally important sites inter-helical bonds between Ser/Thr and Asn instead of Asp (**Figure 1B–E**).

In bacteriorhodopsin D212, which might functions as an intermediate proton carrier (Dioumaev et al., 1999; Phatak et al., 2009) has inter-helical H-bonds with Y57 and Y185 (**Figure 1A**), both important for optimal control of H-bond dynamics in the wild-type pump: mutating either Tyr group alters the kinetics of the reaction cycle (Rath et al., 1993; Govindjee et al., 1995), and Y57F has weak Y185-D212 H-bonding (del Val et al., 2014a). In the *Escherichia coli* proton-galactopyranoside symporter LacY E325, which deprotonates during the reaction cycle (Sahin-Toh and Kaback, 2001; Guan and Kaback, 2006), is part of a local H-bond network with Tyr and His sidechains (**Figure 1E**). Deprotonation of E325 causes protein structure changes that depend on the composition of the surrounding lipid bilayer (Andersson et al., 2012).

Hv1, also known as HVCN1 (human voltage-gated proton channel) is a proton-selective ion channel whose action early after ischemia contributes to brain damage by providing the cancer cell with protons to compensate for the electron-transfer action of phagocytic cell NADPH oxidase (Wu et al., 2012). Proton selectivity of Hv1 requires a carboxylate group at D112 (**Figure 1F**), as some mutants with a neutral group instead Asp or Glu at this position loose proton specificity and became anion selective, and proton specificity could not be recovered when mutating D112 to His (Musset et al., 2011). That Hv1 becomes predominantly anion selective when its proton sensor is neutralized by mutation (Musset et al., 2011) resembles the behavior of bacteriorhodopsin, which from an outward proton pump becomes an inward chloride pump when the primary proton acceptor D85 is mutated to Thr (Sasaki et al., 1995), and underlines the need to decipher the role of electrostatic interactions—of static protein groups and of mobile ions, that govern charge states along the reaction cycle of ion transporters (Song and Gunner, 2014). The recent solution NMR structure of Hv1 reports for the sidechains of D112, R208, and R211 (**Figure 1F**) coordinates modeled by considering steric packing (Bayrhuber et al., 2019), and interactions of internal arginine sidechains can change in the presence of membrane voltage (Geragotelis et al., 2020). This suggests Hv1 has a rather dynamical internal H-bond network.

H-Bond Networks of Histidine Sidechains at Proton-Binding Sites of Membrane Transporters and Receptors

Internal histidine groups can be central to the reaction mechanisms of protonation-coupled transporters and receptors. Examples include 1) H322 of LacY is part of an inter-helical H-bond motif with E325 at a proton-binding site (**Figure 1D**); 2) H128 of VGLU2 is thought to pick up a proton at the lumen side of the membrane, and connect to the E119 proton sensor via a water-filled pore (Li et al., 2020) (**Figure 1**); 3) H140 of Hv1 is a putative binding site for Zn^{2+} (DeCoursey et al., 2016; Bayrhuber et al., 2019), and its inter-helical H-bond partner D185 might be involved in ΔpH -gating (DeCoursey, 2018); 4) A pair of two H37 groups of the influenza channel M2 could participate in a proton-conductance mechanism that involves low-barrier H-bonding (Fu et al., 2020); 5) A cluster of histidine sidechains was proposed to ensure proton-sensing by the ovarian cancer GPCR 1, known as OGR1 or GPR68 (Ludwig et al., 2003; Holzer, 2009). OGR1, and other members of the proton-sensing GPCR subgroup, are activated when the extracellular pH becomes acidic, and histidine protonation couples with protein conformational change (Radu et al., 2004; Wang et al., 2004).

Taken together, the examples above suggest that internal histidine sidechains implicated in proton binding tend to be part of local H-bond clusters with carboxylate and/or other histidine sidechains. An Asp-His pair is also involved in pH sensing by the soluble protein hemoglobin (Srivastava et al., 2007).

Carboxylate Clusters as Proton Antennas on Protein Surfaces

Proton antennas consist of clusters of closely spaced carboxylate, or of carboxylate and histidine groups, which can capture protons and prolong the time protons spend bound at the surface of the protein (Gutman and Nachliel, 1990; Sacks et al., 1998; Ädelroth and Brzezinski, 2004), and deliver a proton to a proton-entry site (Checover et al., 2001) (**Figure 2B**). Putative proton antenna clusters have been identified for bacteriorhodopsin (Checover et al., 2001), cytochrome *c* oxidase (Ädelroth and Brzezinski, 2004), and

for the PsbO subunit of photosystem II (Shutova et al., 2007; Lorch et al., 2015; Kemmler et al., 2019). Surface carboxylates could be part of a pH-dependent conformational switch of PsbO (Bommer et al., 2016), and of a local buffering mechanism used by photosystem II to respond to acidification of the lumen (Gerland et al., 2020). The two carboxylate groups thought to bind the proton are part of a dynamic protein-water H-bond network that extends across the interface between PsbO and another protein subunit of photosystem II (Kemmler et al., 2019).

H-Bond Networks of SARS-CoV-2 Protein S

The acidic environment of the endosome activates membrane fusion of coronaviruses, but it remains unclear whether acidity is required for proteases that cleave protein S to activate fusion, or for the spike protein itself (Heald-Sargent and Gallagher, 2012; Li, 2016). Membrane fusion might also be assisted by calcium binding to conserved negatively charged groups of SARS-CoV spike protein S (Millet and Whittaker, 2018).

Sequences of corona spike proteins S tend to carry significant net negative charges and contain patches rich in carboxylate, or carboxylate and histidine groups (Karathanou et al., 2020), but a discussion of a putative involvement of these patches in ion binding would be speculative. From graph-based analyses we discovered that titratable groups can participate in H-bond clusters that tend to have three-fold compositional symmetry when SARS-CoV-2 protein S is closed (Karathanou et al., 2020). Loss of this three-fold symmetry in the pre-fusion conformation could contribute to conformational selection of one protein S protomer to bind to the ACE2 receptor (Karathanou et al., 2020). An H-bond network that extends across the interface between the Receptor Binding Domain (RBD) of protein S and ACE2 contains N501 (Karathanou et al., 2020), which is mutated to Tyr in the United Kingdom virus variant (Leung et al., 2021). E484, which is mutated to Lys in the South African variant (Tegally et al., 2021), is close in sequence to RBD-Y449, which H-bonds to ACE2-D38 (Karathanou et al., 2020).

Elsewhere on the surface of protein S, intra-molecular H-bonding of D614 would be lost in the D614G virus variant (Korber et al., 2020); this mutation favors enhanced conformational dynamics of the spike protein, which could enable ACE2 binding (Benton et al., 2021). At the C-terminal region of the ectodomain of the closed protein S, a symmetrical H-bond cluster of no fewer than 33 protein groups includes six carboxylates and six histidine sidechains (Karathanou et al., 2020). Close to the R815 proteolytic cleavage site, E819 H-bonds to three Ser/Thr groups in all protomers of the closed and open conformations, and contributes to a large H-bond cluster in a pre-fusion protomer (Karathanou et al., 2020). Cryo-EM data suggest D830 and D843 are part of a pH-dependent switch that enables protein S to adopt, at low pH, a conformation incompatible with binding of particular antibodies (Zhou et al., 2020). Future experiments and computation are needed to evaluate any pH-dependent conformational changes at the interface between protein S and ACE2 (Figure 2C).

CONCLUSION

Proteins across all branches of life rely on proton binding and proton transfer to exert their biological function. As three-dimensional structures of proteins and macro-molecular protein complexes involved in human physiology and disease become available, reasonable predictions of likely proton-binding sites and proton-transfer events are of interest to understand reaction mechanisms and potentially guide drug design. Simpler model proteins inform on H-bonding motifs common at proton-binding sites, and on structural elements that can shape the energetics of proton transfers in heterogeneous protein environments. Examples discussed here (Figure 1) illustrate an inter-helical H-bond carboxylate-hydroxyl motif that can ensure coupling between carboxylate protonation, protein conformational dynamics, and local water accessibility (Figure 2A). On the surface of the protein, carboxylate clusters may transiently bind a proton to then deliver it to an internal proton-binding site (Figure 2B) or for buffering, and participate in pH-dependent conformational switching that could impact protein interactions (Figure 2C). Dissecting the functional role of surface proton-binding clusters would need to account for local water interactions and protein conformational dynamics.

DATA AVAILABILITY STATEMENT

Publicly available datasets were analyzed in this study. This data can be found here: Protein Data Bank, with accession codes as indicated in the article.

AUTHOR CONTRIBUTIONS

A-NB wrote the manuscript and prepared the figures.

FUNDING

European Union's Horizon 2020 research and innovation program, Marie Skłodowska-Curie grant agreement No 860592, Innovative Training Network "Proton and proton-coupled transport". German Cancer Research Foundation (DFG) Collaborative Research Center SFB 1078, project C4.

ACKNOWLEDGMENTS

Research reviewed here was supported in part by the German Research Foundation, DFG, Collaborative Research Center SFB1078 Protonation Dynamics in Protein Function, SFB1078, Project C4. Research supported in part by the Innovative Training Network PROTON founded by the European Commission. I acknowledge support from the Open Access Publication Initiative of the Freie Universität Berlin.

REFERENCES

- Ädelroth, P., and Brzezinski, P. (2004). Surface-mediated Proton-Transfer Reactions in Membrane-Bound Proteins. *Biochim. Biophys. Acta (Bba) - Bioenerg.* 1655, 102–115. doi:10.1016/j.bbabi.2003.10.018
- Andersson, M., Bondar, A.-N., Freitas, J. A., Tobias, D. J., Kaback, H. R., and White, S. H. (2012). Proton-coupled Dynamics in Lactose Permease. *Structure* 20, 1893–1904. doi:10.1016/j.str.2012.08.021
- Balashov, S. P., and Ebrey, T. G. (2001). Trapping and Spectroscopic Identification of the Photointermediates of Bacteriorhodopsin at Low Temperatures. *Photochem. Photobiol.* 73, 453–462. doi:10.1562/0031-8655(2001)0730453TASIoT2.0.CO2
- Ballesteros, J. A., and Weinstein, H. (1995). Integrated Methods for the Construction of Three-Dimensional Models and Computational Probing of Structure-Function Relations in G Protein-Coupled Receptors. *Methods Neurosci.* 25, 366–428. doi:10.1016/s1043-9471(05)80049-7
- Bayrhuber, M., Maslennikov, I., Kwiatkowski, W., Sobol, A., Wierschem, C., Eichmann, C., et al. (2019). Nuclear Magnetic Resonance Solution Structure and Functional Behavior of the Human Proton Channel. *Biochemistry* 58, 4017–4027. doi:10.1021/acs.biochem.9b00471
- Benton, D. J., Wroberl, A. G., Roustan, C., Borg, A., Xu, P., Martin, S. R., et al. (2021). The Effect of the D614G Substitution on the Structure of the Spike Glycoprotein of SARS-CoV-2. *Proc. Natl. Acad. Sci.* 118, e2022586118. doi:10.1073/pnas.2022586118
- Bertalan, É., Lešnik, S., Bren, U., and Bondar, A.-N. (2020). Protein-water Hydrogen-Bond Networks of G Protein-Coupled Receptors: Graph-Based Analyses of Static Structures and Molecular Dynamics. *J. Struct. Biol.* 212, 107634. doi:10.1016/j.jsb.2020.107634
- Bommer, M., Bondar, A.-N., Zouni, A., Dobbek, H., and Dau, H. (2016). Crystallographic and Computational Analysis of the Barrel Part of the PsbO Protein of Photosystem II: Carboxylate-Water Clusters as Putative Proton Transfer Relays and Structural Switches. *Biochemistry* 55, 4626–4635. doi:10.1021/acs.biochem.6b00441
- Bondar, A.-N., Elstner, M., Suhai, S., Smith, J. C., and Fischer, S. (2004). Mechanism of Primary Proton Transfer in Bacteriorhodopsin. *Structure* 12, 1281–1288. doi:10.1016/j.str.2004.04.016
- Bondar, A.-N., and Lemieux, M. J. (2019). Reactions at Biomembrane Interfaces. *Chem. Rev.* 119, 6162–6183. doi:10.1021/acs.chemrev.8b00596
- Bondar, A.-N., and Smith, J. C. (2017). Protonation-state-Coupled Conformational Dynamics in Reaction Mechanisms of Channel and Pump Rhodopsins. *Photochem. Photobiol.* 93, 1336–1344. doi:10.1111/php.12790
- Buch-Pedersen, M. J., and Palmgren, M. G. (2003). Conserved Asp684 in Transmembrane Segment M6 of the Plant Plasma Membrane P-type Proton Pump AHA2 Is a Molecular Determinant of Proton Translocation. *J. Biol. Chem.* 278, 17845–17851. doi:10.1074/jbc.m212729200
- Canul-Tec, J. C., Assal, R., Cirri, E., Legrand, P., Brier, S., Chamot-Rooke, J., et al. (2017). Structure and Allosteric Inhibition of Excitatory Amino Acid Transporter 1. *Nature* 544, 446–451. doi:10.1038/nature22064
- Checover, S., Marantz, Y., Nachliel, E., Gutman, M., Pfeiffer, M., Tittor, J., et al. (2001). Dynamics of the Proton Transfer Reaction on the Cytoplasmic Surface of Bacteriorhodopsin†. *Biochemistry* 40, 4281–4292. doi:10.1021/bi002574m
- Chivukala, A. S., Suslova, M., Kortzak, D., Kovermann, P., and Fahlke, C. (2020). Functional Consequences of SLC1A3 Mutations Associated with Episodic Ataxia 6. *Hum. Mutat.* 1–14. doi:10.1002/humu.24089
- Damaghi, M., Wojtkowiak, J. W., and Gillies, R. J. (2013). pH Sensing and Regulation in Cancer. *Front. Physiol.* 4, 1–10. doi:10.3389/fphys.2013.00370
- DeCoursey, T. E., Morgan, D., Musset, B., and Cherny, V. V. (2016). Insights into the Structure and Function of Hv1 from a Meta-Analysis of Mutation Studies. *J. Gen. Physiol.* 148, 97–118. doi:10.1085/jgp.201611619
- DeCoursey, T. E. (2018). Voltage and pH Sensing by the Voltage-Gated Proton Channel, Hv1. *J. R. Soc. Interf.* 15, 20180108. doi:10.1098/rsif.2018.0108
- Del Val, C., Bondar, L., and Bondar, A.-N. (2014a). Coupling between Inter-helical Hydrogen Bonding and Water Dynamics in a Proton Transporter. *J. Struct. Biol.* 186, 95–111. doi:10.1016/j.jsb.2014.02.010
- Del Val, C., Royuela-Flor, J., Milenkovic, S., and Bondar, A.-N. (2014b). Channelrhodopsins: A Bioinformatics Perspective. *Biochim. Biophys. Acta - Bioenerg.* 1837, 643–655. doi:10.1016/j.bbabi.2013.11.005
- Del Val, C., White, S. H., and Bondar, A.-N. (2012). Ser/Thr Motifs in Transmembrane Proteins: Conservation Patterns and Effects on Local Protein Structure and Dynamics. *J. Membr. Biol.* 245, 717–730. doi:10.1007/s00232-012-9452-4
- Dioumaev, A. K., Brown, L. S., Needleman, R., and Lanyi, J. K. (1999). Fourier Transform Infrared Spectra of a Late Intermediate of the Bacteriorhodopsin Photocycle Suggest Transient Protonation of Asp-212. *Biochemistry* 38, 10070–10078. doi:10.1021/bi990873+
- Ernst, O. P., Lodowski, D. T., Elstner, M., Hegemann, P., Brown, L. S., and Kandori, H. (2014). Microbial and Animal Rhodopsins: Structures, Functions, and Molecular Mechanisms. *Chem. Rev.* 114, 126–163. doi:10.1021/cr4003769
- Fernandez, A., and Scheraga, H. A. (2003). Insufficiently Dehydrated Hydrogen Bonds as Determinants of Protein Interactions. *Proc. Natl. Acad. Sci.* 100, 113–118. doi:10.1073/pnas.0136888100
- Focht, D., Croll, T. I., Pedersen, B. P., and Nissen, P. (2017). Improved Model of Proton Pump crystal Structure Obtained by Interactive Molecular Dynamics Flexible Fitting Expands the Mechanistic Model for Proton Translocation in P-type ATPases. *Front. Physiol.* 8, 202. doi:10.3389/fphys.2017.00202
- Freier, E., Wolf, S., and Gerwert, K. (2011). Proton Transfer via a Transient Linear Water-Molecule Chain in a Membrane Protein. *Proc. Natl. Acad. Sci.* 108, 11435–11439. doi:10.1073/pnas.1104735108
- Fu, R., Miao, Y., Qin, H., and Cross, T. A. (2020). Observation of the Imidazole-Imidazolium Hydrogen Bonds Responsible for Selective Proton Conductance in the Influenza A M2 Channel. *J. Am. Chem. Soc.* 142, 2115–2119. doi:10.1021/jacs.9b09985
- Geragotelis, A. D., Wood, M. L., Göddeke, H., Hong, L., Webster, P. D., Wong, E. K., et al. (2020). Voltage-dependent Structural Models of the Human Hv1 Proton Channel from Long-Timescale Molecular Dynamics Simulations. *Proc. Natl. Acad. Sci. USA* 117, 13490–13498. doi:10.1073/pnas.1920943117
- Gerland, L., Friedrich, D., Hopf, L., Donovan, E. J., Wallmann, A., Erdmann, N., et al. (2020). pH-Dependent Protonation of Surface Carboxylate Groups in PsbO Enables Local Buffering and Triggers Structural Changes. *ChemBioChem* 21, 1597–1604. doi:10.1002/cbic.201900739
- Gerwert, K., Freier, E., and Wolf, S. (2014). The Role of Protein-Bound Water Molecules in Microbial Rhodopsins. *Biochim. Biophys. Acta - Bioenerg.* 1837, 606–613. doi:10.1016/j.bbabi.2013.09.006
- Gerwert, K., Hess, B., Soppa, J., and Oesterhelt, D. (1989). Role of Aspartate-96 in Proton Translocation by Bacteriorhodopsin. *Proc. Natl. Acad. Sci.* 86, 4943–4947. doi:10.1073/pnas.86.13.4943
- Govindjee, R., Kono, M., Balashov, S. P., Imasheva, E., Sheves, M., and Ebrey, T. G. (1995). Effects of Substitution of Tyrosine 57 with Asparagine and Phenylalanine on the Properties of Bacteriorhodopsin. *Biochemistry* 34, 4828–4838. doi:10.1021/bi00014a040
- Govorunova, E. G., Sineshchikov, O. A., Li, H., and Spudich, J. L. (2017). Microbial Rhodopsins: Diversity, Mechanisms, and Optogenetic Applications. *Annu. Rev. Biochem.* 86, 845–872. doi:10.1146/annurev-biochem-101910-144233
- Gray, T. M., and Matthews, B. W. (1984). Intrahelical Hydrogen Bonding of Serine, Threonine and Cysteine Residues within α -helices and its Relevance to Membrane-Bound Proteins. *J. Mol. Biol.* 175, 75–81. doi:10.1016/0022-2836(84)90446-7
- Guan, L., and Kaback, H. R. (2006). Lessons from Lactose Permease. *Annu. Rev. Biophys. Biomol. Struct.* 35, 67–91. doi:10.1146/annurev.biophys.35.040405.102005
- Guerra, F., and Bondar, A.-N. (2015). Dynamics of the Plasma Membrane Proton Pump. *J. Membr. Biol.* 248, 443–453. doi:10.1007/s00232-014-9732-2
- Gutman, M., and Nachliel, E. (1990). The Dynamic Aspects of Proton Transfer Processes. *Biochim. Biophys. Acta (Bba) - Bioenerg.* 1015, 391–414. doi:10.1016/0005-2728(90)90073-d
- Hasegawa, N., Jonotsuka, H., Miki, K., and Takeda, K. (2018). X-ray Structure Analysis of Bacteriorhodopsin at 1.3 Å Resolution. *Sci. Rep.* 8, 13123. doi:10.1038/s41598-018-31370-0
- Heald-Sargent, T., and Gallagher, T. (2012). Ready, Set, Fuse! the Coronavirus Spike Protein and Acquisition of Fusion Competence. *Viruses* 4, 557–580. doi:10.3390/v4040557
- Henderson, R., and Unwin, P. N. T. (1975). Three-dimensional Model of Purple Membrane Obtained by Electron Microscopy. *Nature* 257, 28–32. doi:10.1038/257028a0

- Herzfeld, J., and Tongue, B. (2000). NMR Probes Vectoriality in the Proton-Motive Photocycle of Bacteriorhodopsin: Evidence for an 'Electrostatic Steering' Mechanism. *Biochim. Biophys. Acta* 1460, 95–105. doi:10.1016/s0005-2728(00)00132-8
- Holzer, P. (2009). Acid-sensitive Ion Channels and Receptors. *Handb. Exp. Pharmacol.* 194, 283–332. doi:10.1007/978-3-540-79090-7_9
- Humphrey, W., Dalke, A., and Schulten, K. (1996). VMD: Visual Molecular Dynamics. *J. Mol. Graphics* 14, 33–38. doi:10.1016/0263-7855(96)00018-5
- Jalalvand, E., Robertson, B., Tostivint, H., Löw, P., Wallén, P., and Grillner, S. (2018). Cerebrospinal Fluid-Contacting Neurons Sense pH Changes and Motion in the Hypothalamus. *J. Neurosci.* 38, 7713–7724. doi:10.1523/jneurosci.3359-17.2018
- Jalalvand, E., Robertson, B., Wallén, P., and Grillner, S. (2016). Ciliated Neurons Lining the central Canal Sense Both Fluid Movement and pH through ASIC3. *Nat. Comm.* 7, 10002. doi:10.1038/ncomms10002
- Kandori, H. (2004). Role of Internal Water Molecules in Bacteriorhodopsin. *Biochim. Biophys. Acta* 1460, 177–191. doi:10.1016/s0005-2728(00)00138-9
- Karathanou, K., Lazaratos, M., Bertalan, E., Siemers, M., Buzar, K., Schertler, G. F. X., et al. (2020). A Graph-Based Approach Identifies Dynamic H-Bond Communication Networks in Spike Protein S of SARS-CoV-2. *J. Struct. Biol.* 212, 107617. doi:10.1016/j.jsb.2020.107617
- Katritch, V., Fenalti, G., Abola, E. E., Roth, B. L., Cherezov, V., and Stevens, R. C. (2014). Allosteric Sodium in Class A GPCR Signaling. *Trends Biochem. Sci.* 39, 233–244. doi:10.1016/j.tibs.2014.03.002
- Kemmler, L., Ibrahim, M., Dobbek, H., Zouni, A., and Bondar, A.-N. (2019). Dynamic Water Bridging and Proton Transfer at a Surface Carboxylate Cluster of Photosystem II. *Phys. Chem. Chem. Phys.* 21, 25449–25466. doi:10.1039/c9cp03926k
- Korber, B., Fischer, W. M., Gnanakaran, S., Yoon, H. W., Theiler, J., Abfalterer, W., et al. (2020). Tracking Changes in SARS-CoV-2 Spike: Evidence that D614G Increases Infectivity of the COVID-19 Virus. *Cell* 182, 1–16. doi:10.1016/j.cell.2020.06.043
- Kouyama, T., Nishikawa, T., Tokuhisa, T., and Okumura, H. (2004). Crystal Structure of the L Intermediate of Bacteriorhodopsin: Evidence for Vertical Translocation of a Water Molecule during the Proton Pumping Cycle. *J. Mol. Biol.* 335, 531–546. doi:10.1016/j.jmb.2003.10.068
- Lanyi, J. K. (1999). Bacteriorhodopsin. *Int. Rev. Cytol.* 187, 161–202. doi:10.1016/s0074-7696(08)62418-3
- Leung, K., Shum, M. H. H., Leung, G. M., Lam, T. T. Y., and Wu, J. T. (2021). Early Transmissibility Assessment of the N501Y Mutant Strains of SARS-CoV-2 in the United Kingdom, October to November 2020. *Euro Surveill.* 26, 2002106. doi:10.2807/1560-7917.es.2020.26.1.2002106
- Li, F., Eriksen, J., Finer-Moore, J., Chang, R., Nguyen, P., Bowen, A., et al. (2020). Ion Transport and Regulation in a Synaptic Vesicle Glutamate Transporter. *Science* 368, 893–897. doi:10.1126/science.aba9202
- Li, F. (2016). Structure, Function, and Evolution of Coronavirus Spike Proteins. *Annu. Rev. Virol.* 3, 237–261. doi:10.1146/annurev-virology-110615-042301
- Lorch, S., Capponi, S., Pieront, F., and Bondar, A.-N. (2015). Dynamic Carboxylate/water Networks on the Surface of the PsbO Subunit of Photosystem II. *J. Phys. Chem. B* 119, 12172–12181. doi:10.1021/acs.jpcc.5b06594
- Ludwig, M.-G., Vanek, M., Guerini, D., Gasser, J. A., Jones, C. E., Junker, U., et al. (2003). Proton-sensing G-Protein-Coupled Receptors. *Nature* 425, 93–98. doi:10.1038/nature01905
- Luecke, H., Schobert, B., Richter, H.-T., Cartailler, J.-P., and Lanyi, J. K. (1999). Structure of Bacteriorhodopsin at 1.55 Å Resolution. *J. Mol. Biol.* 291, 899–911. doi:10.1006/jmbi.1999.3027
- Martineau, M., Guzman, R. E., Fahlke, C., and Klingauf, J. (2017). VGLUT1 Functions as a Glutamate/proton Exchanger with Chloride Channel Activity in Hippocampal Glutamatergic Synapses. *Nat. Comm.* 8, 2279. doi:10.1038/s41467-017-02367-6
- Metz, G., Siebert, F., and Engelhard, M. (1992). Asp85 Is the Only Internal Aspartic Acid that Gets Protonated in the M Intermediate and the Purple-To-Blue Transition of Bacteriorhodopsin. A Solid-State ¹³C CP-MAS NMR Investigation. *FEBS Lett.* 303, 237–241. doi:10.1016/0014-5793(92)80528-o
- Millet, J. K., and Whittaker, G. R. (2018). Physiological and Molecular Triggers for SARS-CoV Membrane Fusion and Entry into Host Cells. *Virology* 517, 3–8. doi:10.1016/j.virol.2017.12.015
- Münster-Wandowski, A., Zander, J.-F., Richter, K., and Ahnert-Hilger, G. (2016). Co-existence of Functionally Different Vesicular Neurotransmitter Transporters. *Front. Synaptic Neurosci.* 8. doi:10.3389/fnsyn.2016.00004
- Musset, B., Smith, S. M. E., Rajan, S., Morgan, D., Cherny, V. V., and DeCoursey, T. E. (2011). Aspartate 112 Is the Selectivity Filter of the Human Voltage-Gated Proton Channel. *Nature* 480, 273–277. doi:10.1038/nature10557
- Nango, E., Royant, A., Kubo, M., Nakane, T., Wickstrand, C., Kimura, T., et al. (2016). A Three-Dimensional Movie of Structural Changes in Bacteriorhodopsin. *Science* 354, 1552–1557. doi:10.1126/science.aah3497
- Némethy, G., Steinberg, I. Z., and Scheraga, H. A. (1963). Influence of Water Structure and of Hydrophobic Interactions on the Strength of Side-Chain Hydrogen Bonds in Proteins. *Biopolymers* 1, 43–69. doi:10.1002/bip.360010107
- Ni, Q. Z., Can, T. V., Daviso, E., Griffin, R. G., and Herzfeld, J. (2018). Primary Transfer Step in the Light-Driven Ion Pump Bacteriorhodopsin: An Irreversible U-Turn Revealed by Dynamic Nuclear Polarization-Enhanced Magic Angle Spinning NMR. *J. Am. Chem. Soc.* 140, 4085–4091. doi:10.1021/jacs.8b00022
- Pedersen, B. P., Buch-Pedersen, M. J., Preben Morth, J., Palmgren, M. G., and Nissen, P. (2007). Crystal Structure of the Plasma Membrane Proton Pump. *Nature* 450, 1111–1114. doi:10.1038/nature06417
- Phatak, P., Frähmcke, J. S., Wanko, M., Hoffmann, M., Strodel, P., Smith, J. C., et al. (2009). Long-distance Proton Transfer with a Break in the Bacteriorhodopsin Active Site. *J. Am. Chem. Soc.* 131, 7064–7078. doi:10.1021/ja809767v
- Presta, L., and Rose, G. (1988). Helix Signals in Proteins. *Science* 240, 1632–1641. doi:10.1126/science.2837824
- Radu, C. G., Nijagal, A., McLaughlin, J., Wang, L., and Witte, O. N. (2004). Differential Proton Sensitivity of Related G Protein-Coupled Receptors T Cell Death-Associated Gene 8 and G2A Expressed in Immune Cells. *Proc. Natl. Acad. Sci. U S A* 102, 1632–1637. doi:10.1073/pnas.0409415102
- Rath, P., Krebs, M. P., He, Y., Khorana, H. G., and Rothschild, K. J. (1993). Fourier Transform Raman Spectroscopy of the Bacteriorhodopsin Mutant Tyr-185 Phe: Formation of a Stable O-like Species during Light Adaptation and Detection of its Transient N-like Photoproduct. *Biochemistry* 32, 2272–2281. doi:10.1021/bi00060a020
- Regan, M. C., Zhu, Z., Yuan, H., Myers, S. J., Menaldino, D. S., Tahirovic, Y. A., et al. (2019). Structural Elements of a pH-Sensitive Inhibitor Binding Site in NMDA Receptors. *Nat. Comm.* 10, 321. doi:10.1038/s41467-019-08291-1
- Sacks, V., Marantz, Y., Aagaard, A., Checover, S., Nachliel, E., and Gutman, M. (1998). The Dynamic Feature of the Proton Collecting Antenna of a Protein Surface. *Biochim. Biophys. Acta - Bioenerg.* 1365, 232–240. doi:10.1016/s0005-2728(98)00073-5
- Sahin-Toh, M., and Kaback, H. R. (2001). Arg-302 Facilitates Deprotonation of Glu-325 in the Transport Mechanism of the Lactose Permease from *Escherichia coli*. *Proc. Natl. Acad. Sci.* 98, 6068–6073. doi:10.1073/pnas.111139698
- Sasaki, J., Brown, L., Chon, Y., Kandori, H., Maeda, A., Needleman, R., et al. (1995). Conversion of Bacteriorhodopsin into a Chloride Ion Pump. *Science* 269, 73–75. doi:10.1126/science.7604281
- Schönichen, A., Webb, B. A., Jacobson, M. P., and Barber, D. L. (2013). Considering Protonation as a Posttranslational Modification Regulating Protein Structure and Function. *Annu. Rev. Biophys.* 42, 289–314. doi:10.1146/annurev-biophys-050511-102349
- Shutova, T., Klimov, V. V., Andersson, B., and Samuelsson, G. (2007). A Cluster of Carboxylic Groups in PsbO Protein Is Involved in Proton Transfer from the Water Oxidizing Complex of Photosystem II. *Biochim. Biophys. Acta - Bioenerg.* 1767, 434–440. doi:10.1016/j.bbabi.2007.01.020
- Siemers, M., Lazaratos, M., Karathanou, K., Guerra, F., Brown, L. S., and Bondar, A.-N. (2019). Bridge: A Graph-Based Algorithm to Analyze Dynamic H-Bond Networks in Membrane Proteins. *J. Chem. Theor. Comput.* 15, 6781–6798. doi:10.1021/acs.jctc.9b00697
- Song, Y., and Gunner, M. R. (2014). Halorhodopsin Pumps Cl⁻ and Bacteriorhodopsin Pumps Protons by a Common Mechanism that Uses Conserved Electrostatic Interactions. *Proc. Natl. Acad. Sci. USA* 111, 16377–16382. doi:10.1073/pnas.1411191111
- Srivastava, J., Barber, D. L., and Jacobson, M. P. (2007). Intracellular pH Sensors: Design Principles and Functional Significance. *Physiology* 22, 30–39. doi:10.1152/physiol.00035.2006
- Szárász, S., Oesterheld, D., and Ormos, P. (1994). pH-Induced Structural Changes in Bacteriorhodopsin Studied by Fourier Transform Infrared Spectroscopy. *Biophysical J.* 67, 1706–1712. doi:10.1016/s0006-3495(94)80644-7

- Tegally, H., Wilkinson, E., Giovanetti, M., Iranzadeh, A., Fonseca, V., Giandhari, J., et al. (2021). Emergence of Rapid Spread of a New Severe Acute Respiratory Syndrome-Related Coronavirus 2 (SARS-CoV-2) Lineage with Multiple Spike Mutations in South Africa. [Epub ahead of print]. 10.1101/2020.12.21.20248640
- Thurlkill, R. L., Grimsley, G. R., Scholtz, J. M., and Pace, C. N. (2006a). Hydrogen Bonding Markedly Reduces the pK of Buried Carboxyl Groups in Proteins. *J. Mol. Biol.* 362, 594–604. doi:10.1016/j.jmb.2006.07.056
- Thurlkill, R. L., Grimsley, G. R., Scholtz, J. M., and Pace, C. N. (2006b). pK Values of the Ionizable Groups of Proteins. *Protein Sci.* 15, 1214–1218. doi:10.1110/ps.051840806
- Ulmschneider, M. B., and Sansom, M. S. P. (2001). Amino Acid Distributions in Integral Membrane Protein Structures. *Biochim. Biophys. Acta - Biomembranes* 1512, 1–14. doi:10.1016/s0005-2736(01)00299-1
- Vickery, O. N., Carvalheda, C. A., Zaidi, S. A., Pislakov, A. V., Katritch, V., and Zachariae, U. (2018). Intracellular Transfer of Na⁺ in an Active-State G-Protein-Coupled Receptor. *Structure* 26, 171–180. doi:10.1016/j.str.2017.11.013
- Wang, J.-Q., Kon, J., Mogi, C., Tobo, M., Damirin, A., Sato, K., et al. (2004). TDAG8 Is a Proton-Sensing and Psychosine-Sensitive G-Protein-Coupled Receptor. *J. Biol. Chem.* 279, 45626–45633. doi:10.1074/jbc.m406966200
- Weinert, T., Skopintsev, P., James, D., Dworkowski, F., Panepucci, E., Kekilli, D., et al. (2019). Proton Uptake Mechanism in Bacteriorhodopsin Captured by Serial Synchrotron Crystallography. *Science* 365, 61–65. doi:10.1126/science.aaw8634
- Wu, L.-J., Wu, G., Sharif, M. R. A., Baker, A., Jia, Y., Fahey, F. H., et al. (2012). The Voltage-Gated Proton Channel Hv1 Enhances Brain Damage from Ischemic Stroke. *Nat. Neurosci.* 15, 565–573. doi:10.1038/nn.3059
- Xie, K., Hessa, T., Seppälä, S., Rapp, M., Von Heijne, G., and Dalbey, R. E. (2007). Features of Transmembrane Segments that Promote the Lateral Release from the Translocase into the Lipid Phase. *Biochemistry* 46, 15153–15161. doi:10.1021/bi701398y
- Zabelskii, D., Alekseev, A., Kovalev, K., Rankovic, V., Balandin, T., Soloviov, D., et al. (2021). Viral Rhodopsins 1 Are an Unique Family of Light-Gated Cation Channels. *Nat. Commun.* 11, 5707. doi:10.1038/s41467-020-19457-7
- Zhang, X. C., Cao, C., Zhou, Y., and Zhao, Y. (2015). Proton Transfer-Mediated GPCR Activation. *Protein Cell* 6, 12–17. doi:10.1007/s13238-014-0106-4
- Zhou, T., Tsybovsky, Y., Gorman, J., Rapp, M., Cerutti, G., Chuang, G.-Y., et al. (2020). Cryo-EM Structures of SARS-CoV-2 Spike without and with ACE2 Reveal a pH-dependent Switch to Mediate Endosomal Positioning of Receptor-Binding Domains. *Cell Host Microbe* 28, 867–879. doi:10.1016/j.chom.2020.11.004

Conflict of Interest: The author declares that the research was conducted in the absence of any commercial or financial relationships that could be construed as a potential conflict of interest.

Copyright © 2021 Bondar. This is an open-access article distributed under the terms of the Creative Commons Attribution License (CC BY). The use, distribution or reproduction in other forums is permitted, provided the original author(s) and the copyright owner(s) are credited and that the original publication in this journal is cited, in accordance with accepted academic practice. No use, distribution or reproduction is permitted which does not comply with these terms.



A Voltammetric Perspective of Multi-Electron and Proton Transfer in Protein Redox Chemistry: Insights From Computational Analysis of *Escherichia coli* HypD Fourier Transformed Alternating Current Voltammetry

OPEN ACCESS

Edited by:

Petra Imhof,
University of Erlangen Nuremberg,
Germany

Reviewed by:

Rubin Gulaboski,
Goce Delcev University, North
Macedonia
Vincent Fourmond,
CNRS UMR7281 Bioénergétique et
Ingénierie des Protéines, France

*Correspondence:

Alison Parkin
alison.parkin@york.ac.uk
David J. Gavaghan
david.gavaghan@cs.ox.ac.uk
Alan M. Bond
alan.bond@monash.edu

Specialty section:

This article was submitted to
Theoretical and Computational
Chemistry,
a section of the journal
Frontiers in Chemistry

Received: 26 February 2021

Accepted: 25 May 2021

Published: 14 June 2021

Citation:

Dale-Evans AR, Robinson MJ,
Lloyd-Laney HO, Gavaghan DJ,
Bond AM and Parkin A (2021) A
Voltammetric Perspective of Multi-
Electron and Proton Transfer in Protein
Redox Chemistry: Insights From
Computational Analysis of *Escherichia*
coli HypD Fourier Transformed
Alternating Current Voltammetry.
Front. Chem. 9:672831.
doi: 10.3389/fchem.2021.672831

Alister R. Dale-Evans¹, Martin J. Robinson¹, Henry O. Lloyd-Laney¹, David J. Gavaghan^{1*}, Alan M. Bond^{2*} and Alison Parkin^{3*}

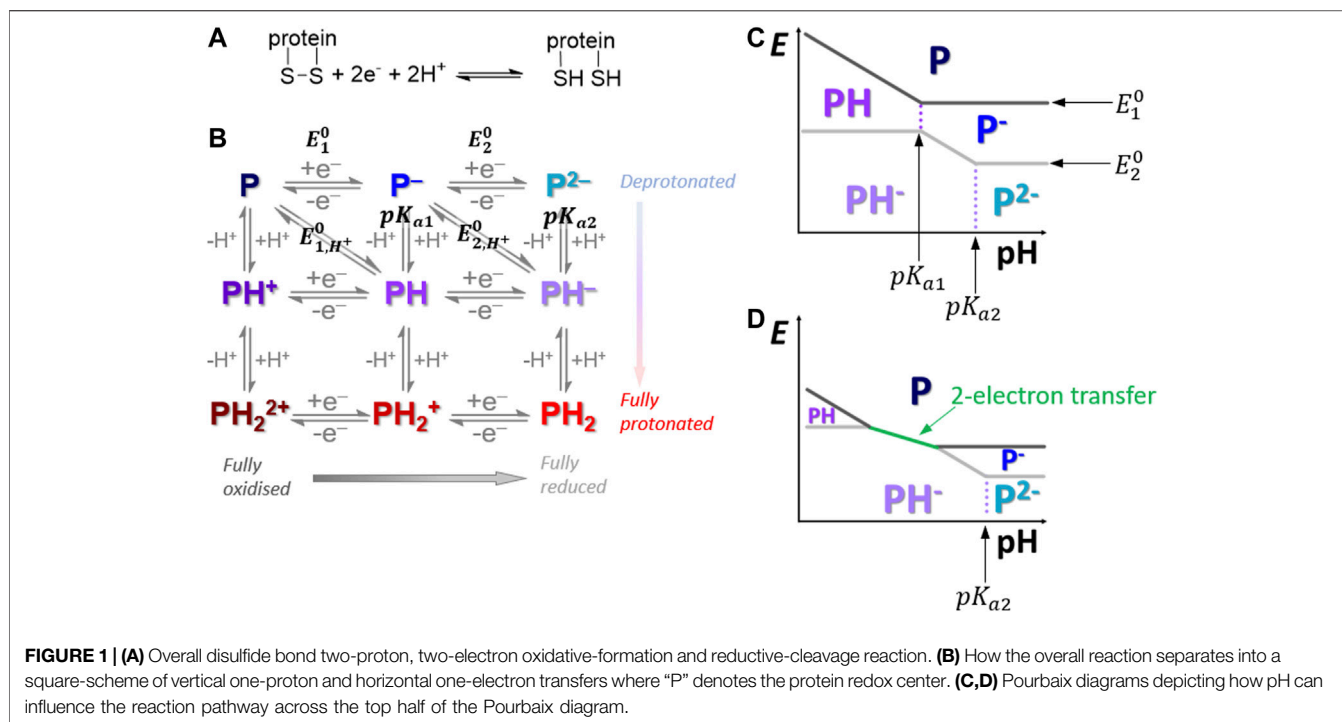
¹Department of Computer Science, University of Oxford, Oxford, United Kingdom, ²School of Chemistry, Monash University, Clayton, VIC, Australia, ³Department of Chemistry, University of York, Heslington, United Kingdom

This paper explores the impact of pH on the mechanism of reversible disulfide bond (CysS-SCys) reductive breaking and oxidative formation in *Escherichia coli* hydrogenase maturation factor HypD, a protein which forms a highly stable adsorbed film on a graphite electrode. To achieve this, low frequency (8.96 Hz) Fourier transformed alternating current voltammetric (FTACV) experimental data was used in combination with modelling approaches based on Butler-Volmer theory with a dual polynomial capacitance model, utilizing an automated two-step fitting process conducted within a Bayesian framework. We previously showed that at pH 6.0 the protein data is best modelled by a redox reaction of two separate, stepwise one-electron, one-proton transfers with slightly “crossed” apparent reduction potentials that incorporate electron and proton transfer terms ($E_{app2}^0 > E_{app1}^0$). Remarkably, rather than collapsing to a concerted two-electron redox reaction at more extreme pH, the same two-stepwise one-electron transfer model with $E_{app2}^0 > E_{app1}^0$ continues to provide the best fit to FTACV data measured across a proton concentration range from pH 4.0 to pH 9.0. A similar, small level of crossover in reversible potentials is also displayed in overall two-electron transitions in other proteins and enzymes, and this provides access to a small but finite amount of the one electron reduced intermediate state.

Keywords: protein electrochemistry, ac voltammetry, surface confined voltammetry, proton-coupled electron-transfer, *Escherichia coli* HypD, disulfide redox

INTRODUCTION

The redox chemistry of metalloenzymes and metalloproteins frequently occurs *via* multiple electron transfer events coupled to proton transfer (Hirst, 2006; Weinberg et al., 2012; Savéant and Costentin, 2019). For example, many of the enzymes which underpin photosynthesis and have application in artificial biological solar fuel production (i.e., Photosystem II, hydrogenases, and carbon monoxide dehydrogenases) rely on the efficient, concerted movement of protons and electrons to ensure



product selectivity (Evans et al., 2019). Protein film electrochemistry (PFE) has been shown to be a powerful technique to probe the redox biochemistry of such proton-coupled electron transfer reactions (Armstrong et al., 1997; Hirst, 2006; Fourmond and Léger, 2017). As we have demonstrated previously (Adamson et al., 2017b), *Escherichia coli* hydrogenase maturation factor HypD (elsewhere "H2ase-MFHypD"), an enzyme which is important in the biosynthesis of hydrogenases (Nutschan et al., 2019), acts as a relatively simple example of such biological proton-coupled electron transfer redox chemistry. When H2ase-MFHypD was immobilized on a graphite electrode we could use both classical direct current cyclic voltammetry (DCV, involving a linear potential-time ramp) as well as large amplitude Fourier transform alternating current voltammetry (FTACV, utilizing a sine-wave plus linear-ramp voltage-time oscillation) to observe reversible disulfide bond reductive cleavage and oxidative formation (Supplementary Figure S1), a reaction that is considered to be a net two-proton, two-electron reaction at near-neutral pH (Figure 1A) (Adamson et al., 2017b).

An advantage of using FTACV over DCV in dynamic electrochemical measurements is that the higher order harmonic current-time responses (isolated by the sequence of Fourier transformation of the total current, band selection of current at a certain frequency, and inverse Fourier transformation) emphasize the response of fast electron transfer processes, i.e., current from rapid electron transfer processes can be separated from that arising from slower processes (Zhang and Bond, 2007; Adamson et al., 2017a). The isolation of fast electron transfer current from other contributions becomes particularly powerful when FTACV is

applied to PFE (Adamson et al., 2017a; Zouraris et al., 2018). This is attributed to the fact that in many PFE studies when looking at the DC/fundamental harmonic current there is a low ratio of Faradaic signal from non-catalytic electron transfer processes relative to the capacitive background charging current. This arises because the large footprint of the protein molecule only allows a low surface coverage of redox active biomolecules to be present on the electrode surface (Hirst, 2006; Adamson et al., 2017a; Fourmond and Léger, 2017). As a result of these benefits, large amplitude FTACV is beginning to be adopted by the electrochemical community and is now being used in multiple laboratories (Zhang et al., 2018; Zouraris et al., 2018; Kumari and Adeboju, 2019; Zheng et al., 2019). In this study, as well as exploiting access to the much improved faradaic-to-charging current ratio, we specifically demonstrate the utility of the technique in distinguishing reaction mechanisms of the kind showcased initially in our previous work (Adamson et al., 2017b). Use of AC techniques to distinguish mechanisms that give rise to similar voltammetric data is an area of increasing research as shown by the recent use of square-wave voltammetry to distinguish between one and two-step reaction mechanisms (Gulaboski, 2019; Gulaboski and Mirceski, 2020; Guziejewski, 2020).

In this study, although H2ase-MFHypD serves as an extremely useful test system for developing our data analysis techniques for probing disulfide mechanisms, it is not possible to conclude if this redox-driven bond making/breaking is relevant to the physiological function of the enzyme (Adamson et al., 2017b; Nutschan et al., 2019). However, there are a multitude of proteins and enzymes where the disulfide chemistry is vitally important and *in vitro* electrochemical studies do provide a useful insight

into the *in vivo* biological chemistry, as demonstrated by the comprehensive study by Bewley et al. (Bewley et al., 2015).

In our previous publication (Adamson et al., 2017b), PF-FTACV H2ase-MFHypD data collected at pH 6.0 was analyzed using automated solver methods to address the inverse problem, i.e., return a set of reaction model parameter values which generated a simulated dataset that provides a “best fit” to the experimental data, as quantified by an objective function that measured the least squares distance between the experimental and simulated data (Adamson et al., 2017b). Based on this analysis we concluded that at pH 6.0 solution conditions the overall H2ase-MFHypD redox reaction was most accurately modelled as two separate one-electron, one-proton steps with very similar associated reversible potentials (Adamson et al., 2017b). We therefore considered that at pH 6.0 the overall reaction proceeded from the top-left to the bottom-right of the square scheme shown in **Figure 1B** (Adamson et al., 2017b).

The best fit parameters for modelling H2ase-MFHypD FTACV at pH 6.0 and low frequency were consistent with the reaction proceeding under equilibrium conditions and the second electron transfer having an apparent reversible potential value (E_{app} , a potential term relating to the equilibrium point of an electrochemical-chemical “EC” process comprising electron transfer and chemical steps) more positive than for the first process by about 10 mV (Laviron, 1980; Adamson et al., 2017b). This is broadly observed across many two-electron transfer biological processes, and generally the redox crossover between the separate potential values is sufficiently small to permit a finite potential window to exist in which the intermediate one-electron state can be detected, as predicted by the Nernst equation (**Supplementary Figure S2**) (Lopez-Tenes et al., 2014; Evans et al., 2019).

As in **Figure 1B**, in proton-coupled electron transfer reactions the formal potential associated with an overall proton-electron equilibrium reaction is often denoted a value of E_{n,H^+}^0 as it is derived from a combination of E_n^0 , the potential associated with the n th electron-transfer, and pK_{an} , the equilibrium position of the associated protonation process (Laviron, 1980; Bond, 2002). As shown by **Figures 1C,D**, the origin of “crossed” one-proton, one-electron potential values, i.e., E_{2,H^+}^0 , the equilibrium value for adding a second electron and a proton, being more positive than E_{1,H^+}^0 , the equilibrium value for adding a first electron and a proton, can be rationalized by considering that although E_2^0 will be negative relative to E_1^0 (simplistically ascribed to the increased charge repulsion between the one-electron reduced state P^- and the second electron relative to the oxidized “P” state and the first electron), if the species P^{2-} is a stronger base than P^- (i.e., $pK_{a2} > pK_{a1}$, as is usually the case due to electrostatic attraction), then as solutions become more acidic the ordering of the potentials can change from E_{2,H^+}^0 more negative than E_{1,H^+}^0 , to equal values and, ultimately, E_{2,H^+}^0 more positive than E_{1,H^+}^0 , i.e., “crossed” potentials. At sufficiently high potential crossover, i.e., when E_{2,H^+}^0 is sufficiently more positive than E_{1,H^+}^0 , the two-stepwise one-electron scenario is equivalent to the simultaneous two-electron transfer, as is shown by **Figure 1D** and the Nernst plots in **Supplementary Figure S2**. This is thoroughly described

and derived in the seminal paper on a 9-member square scheme by Laviron (Laviron, 1983).

In our earlier work on H2ase-MFHypD (Adamson et al., 2017b), although we collected experimental data from pH 4.0 to pH 9.0 (**Supplementary Figure S3**), we did not explore the impact of proton availability on the conserved appropriateness of a stepwise two-sequential, one-electron transfer model, or on the tuning of the redox-potential crossover; this is the focus of the work presented here. We aim to establish if the same reaction model is appropriate under alkaline solution conditions (up to pH 9.0) and acidic solution conditions (down to pH 4.0) by comparing the accuracy with which a simulated dataset provides a “best fit” to the experimental data using either a two-stepwise one-electron transfer reaction model ($n_1 = n_2 = 1$) or a one-concerted two-electron transfer model ($n_3 = 2$). We also explore if an equilibrium reaction model is appropriate across the entire pH range. Overall, we are therefore probing how proton availability in the bulk solution-phase impacts the mechanism of biological redox chemistry, as well as showcasing the power of FTACV in allowing differentiation between reaction models.

MATERIALS AND METHODS

Electrochemistry Measurements

All data was collected in our previous study (Adamson et al., 2017b), all experiments were conducted at 25°C and all potentials are reported vs. the standard hydrogen electrode (SHE). An example of raw experimental data and verification of protein adherence can be seen in **Supplementary Figure S11**. In FTACV the input potential as a function of time, $E(t)$, is formulated as **Eq. 1**.

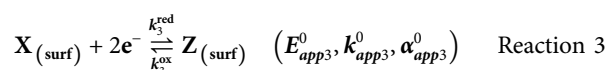
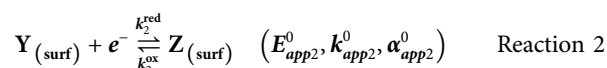
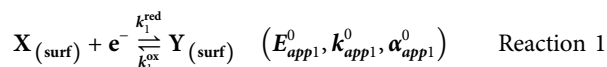
$$E(t) = E_{dc}(t) + \Delta E \sin(\omega t + \eta). \quad (1)$$

The term $E_{dc}(t)$ describes dc contributions to the overall input potential. In all the experimental data shown the dc scan rate (ν) was 22.4 mV s⁻¹. The second term, $\Delta E \sin(\omega t + \eta)$, describes the ac contribution to the FTACV experiment; ΔE is the amplitude of the sine wave and in all experimental data in the paper $\Delta E = 150$ mV. The term ω denotes the angular frequency, where $\omega = 2\pi f$; f is the frequency of the sine wave and in all experimental data in the paper $f = 8.96$ Hz. Finally, the term η indicates the phase, the values of which are determined *via* fittings to the experimental data detailed below.

Mathematical Model of the Faradaic Current

Modelling has been undertaken to calculate the Faradaic current output from the FTACV interrogation of a two-sequential one-electron transfer process described by Reaction 1 and Reaction 2 (referred to as the $n_1 = n_2 = 1$ process), and a concerted two-electron process, as given by Reaction 3 (elsewhere designated $n_3 = 2$). Other researchers have published work on the experimental measurement and theoretical modelling of solution phase voltammetry of such electrochemical-electrochemical stepwise

multiple electron transfer processes (Evans, 2008; Lopez-Tenes et al., 2014). We, and others, have published a number of analogous studies on surface confined species such as the H2ase-MFHypD system we describe here (Finklea, 2001; Lee et al., 2011; Stevenson et al., 2012; Robinson et al., 2018; Robinson et al., 2019).



It is assumed that protonation reactions accompanying the electron transfer are reversible (diffusion controlled) which allows modelling to be undertaken by combining the E^0 , K_a and pH terms of a reaction into an apparent E_{app}^0 value which is defined as the reversible potential. The reaction processes are treated as quasi-reversible with k_{app}^0 , the electrode kinetics parameters describing the electron transfer rate constant at E_{app}^0 , and the charge transfer coefficient α_{app}^0 being added to the model via the Butler-Volmer relationship (Bard and Faulkner, 2001). The Faradaic current term is scaled by the total amount of H2ase-MFHypD on the electrode surface and therefore the parameter Γ , denoting the surface coverage per unit area of protein on the electrode, is also incorporated into the Faradaic current models with a value of 0.03 cm^2 used to account for the geometric surface area of the electrode tip.

As detailed in the Results, an advantage of analyzing H2ase-MFHypD FTACV data compared to other proton coupled electron transfer protein systems is that we show that we are in a parameter regime where we do not have to incorporate kinetic dispersion into our simulation model; this avoids a substantial additional computational cost, as shown previously (Lloyd-Laney et al., 2021b). For simplicity, and as shown previously (Adamson et al., 2017b), we can also neglect a possible small contribution from thermodynamic dispersion (Léger et al., 2002; Morris et al., 2015); this is advantageous as it makes the data fitting computationally less demanding (and therefore faster), and it also decreases the number of models which must be compared (Lloyd-Laney et al., 2021b).

Two-step Approach to Solving the Inverse Problem

To extract the reaction model parameter values which gave the “best fit” between the experimental electrochemical data and either a simulation of the two-sequential one-electron transfer model ($n_1 = n_2 = 1$) or a simulation of the consecutive two-electron transfer model ($n_3 = 2$) a two-step process was used, based on that described in our previous work (Adamson et al., 2017b). This two-step process takes advantage of the fact that the total current recorded in an experiment is a sum of both the Faradaic current arising from the redox reaction under interrogation and non-Faradaic background capacitive charging current contributions.

First, using analysis in the time-domain, we determined the parameter values which gave the best fit between a simulated non-Faradaic capacitance current trace (see **Supplementary Material** for details of the third order polynomial “capacitance” model) and regions of the experimental current trace with little or no Faradaic contribution (**Supplementary Figures S5, S6**) by performing 10 optimizations per experimental dataset and recording the parameter value combination which gave the minimal sum of square difference between the simulated capacitance current and the experimental current. Amongst other parameters, this enabled the determination of “best fit” values for the uncompensated resistance, R_u . Secondly, using Fourier transformation to convert the total current trace into the frequency domain, full models were used to simulate both a non-Faradaic capacitance-current component using the pre-determined “capacitance” and R_u parameter values, and find the “best fit” Faradaic reaction model parameters using either the model for two-stepwise one-electron transfers ($n_1 = n_2 = 1$) or the model for one-concerted two-electron transfer ($n_3 = 2$). A phase parameter, η , and the protein density on the electrode surface, Γ , were also determined in this latter process. Again, 10 optimizations were performed for each experimental current trace and the “best fit” values were defined as those which gave a minimal value for an Euclidean distance objective function that measures the difference between simulated Fourier transformed current and Fourier transformed experimental current.

Full details of the mathematical model, as well as a more in-depth description of the optimization methods used to solve the inverse problem are provided in the **Supplementary Material** (Gavaghan et al., 2018; Clerx et al., 2019; Harris et al., 2020; Gundry et al., 2021).

RESULTS

Model Verification

The models and the inference methods used in this study were extensively verified based on synthetic data studies and the reproduction of results from the literature, as detailed in Verification of computational methods in the **Supplementary Material**.

Two-Sequential One-Electron Transfer Reaction Model Vs. Concerted Two Electron Transfer Model

The two-step fitting process described in the Materials and Methods was used to extract “best fit” parameter values for the pH 4.0, 5.0, 6.0, 7.0, 8.0, and 9.0 experimental H2ase-MFHypD FTACV data using the non-Faradaic capacitance-current model described in the **Supplementary Material** and both a two-sequential one-electron transfer reaction model (Reaction 1 and Reaction 2, $n_1 = n_2 = 1$) and the consecutive two-electron transfer model (Reaction 3, $n_3 = 2$) to account for the Faradaic current. As previously (Adamson et al., 2017b), an objective function was used to quantify the distance between the total experimental current and the simulated data, denoted as $\ell_{fq}(x)$. **Table 1** summarizes the

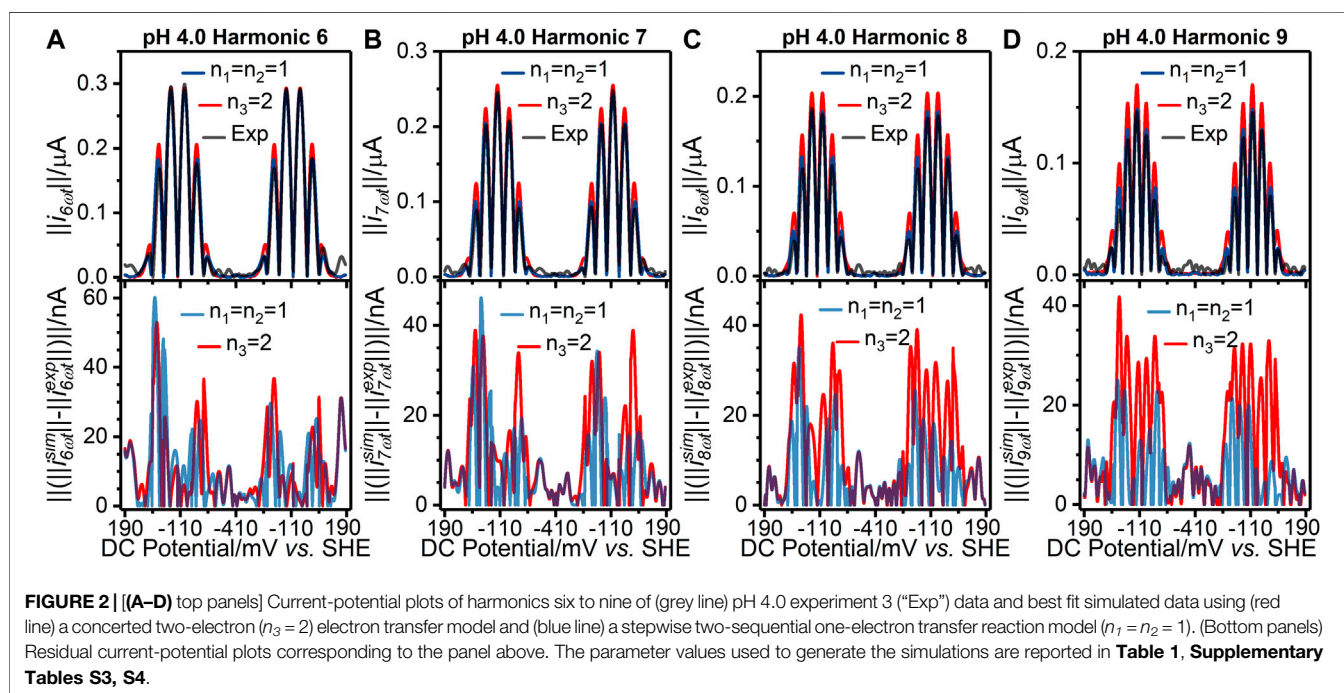
TABLE 1 | Best fit parameter values extracted when the two-sequential one-electron transfer model ($n_1 = n_2 = 1$) is used to simulate three repeated $v = 22.4 \text{ mV s}^{-1}$, $f = 8.96 \text{ Hz}$, $\Delta E = 150 \text{ mV}$ H2ase-MFHypD FTACV experiments (Exp. 1, 2, and 3) at each of the pH values 4.0, 5.0, 6.0, 7.0, 8.0, and 9.0.

pH	Exp.	k_{app1}^0/s^{-1}	k_{app2}^0/s^{-1}	$E_{app1}^0/\text{mV vs. SHE}$	$E_{app2}^0/\text{mV vs. SHE}$	η^b/rad	$\Gamma/\text{pmol cm}^{-2}$	$\ell_{iq}(x)/10^4$
4.0	1	4,000	4,000	-95.9	-95.2	2.13e-3	3.46	1.656
	2	2034	4,000	-96.9	-93.8	-2.85e-3	3.40	1.619
	3	1791	4,000	-98.5	-92.3	1.03e-3	3.32	1.635
5.0	1	2,939	4,000	-156	-149	2.26e-2	3.53	1.666
	2	2,175	4,000	-155	-149	1.81e-3	3.57	1.594
	3	4,000	4,000	-154	-150	-6.26e-3	3.55	1.607
6.0	1	4,000	4,000	-215	-206	3.64e-2	3.51	2.433
	2	1888	4,000	-213	-207	2.69e-2	3.56	1.684
	3	4,000	4,000	-214	-206	1.21e-2	3.49	1.679
7.0	1	4,000	4,000	-273	-250	6.56e-2	4.31	1.800
	2	4,000	797.8	-280	-243	1.05e-1	4.18	1.692
	3	4,000	4,000	-272	250	5.84e-2	4.27	1.674
8.0	1	4,000	4,000	-314	-289	8.20e-2	4.02	1.800
	2	4,000	4,000	-314	-288	7.77e-2	3.97	1.632
	3	4,000	4,000	-313	-289	7.24e-2	3.97	1.642
9.0	1	4,000	4,000	-348	-326	5.15e-2	4.29	1.783
	2	4,000	4,000	-348	-326	3.84e-2	4.25	1.656
	3	4,000	4,000	-348	-326	3.24e-2	4.22	1.650

^aThe rate constants are reported to highlight that the reaction appears to be under equilibrium conditions across all experiments, these parameter values are therefore not well defined as the model is converging to the Nernstian limit.

^bThe phase was fitted about 2π in our previous work, and about 0 in this study. Therefore, although tabulated values may appear different, they are in accord.

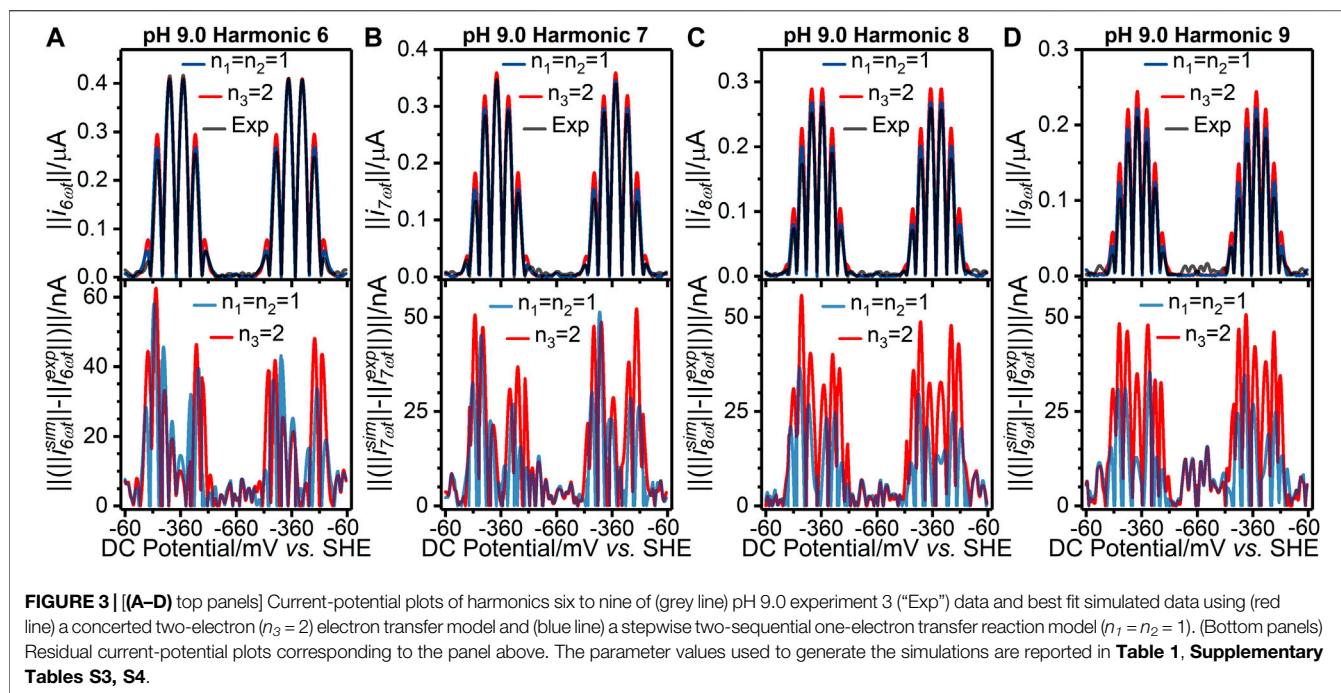
The rate constants^a, k_{app1}^0 and k_{app2}^0 , and the objective function ($\ell_{iq}(x)$) are reported to 4 S.F., all other parameters are reported to 3 S.F. Phase shift^b, η , and electrode coverage, Γ , are experiment dependent parameters rather than electron-transfer reaction parameters but affect the resulting Faradaic signal.



best fit reaction model parameter values obtained from using the two-sequential one-electron transfer model to simulate each of three experiments at pH 4.0, 5.0, 6.0, 7.0, 8.0, and 9.0; the equivalent values for the concerted two-electron reaction model are reported in **Supplementary Table S3** and the best

fit non-Faradaic capacitance-current parameter values are reported in **Supplementary Table S4**.

As shown in **Supplementary Tables S1, S2**, the values of the objective function for the best fits from the two-sequential one-electron transfer model ($n_1 = n_2 = 1$) are consistently lower than



those for the concerted two-electron transfer model ($n_3 = 2$) across the entire pH range 4.0–9.0. The better fit of the $n_1 = n_2 = 1$ model can also be visualized *via* the residuals plotted in **Figure 2** and **Figure 3** for the pH 4.0, and 9.0 data, respectively; plots of the pH 5.0, 6.0, 7.0, and 8.0 data are shown in **Supplementary Figure S8**. The better fit of the $n_1 = n_2 = 1$ electron transfer model vs. the $n_3 = 2$ electron reaction model in itself gives some confidence that this is the more likely of the two to be a correct reflection of physical reality, although it is not conclusive evidence since the better fitting model contains more free parameters (six vs. four). However, further strong evidence in favor of the correctness of the two-sequential one-electron transfer model can be seen by considering the higher harmonics of the experimental data as shown in **Figures 2, 3**, and **Supplementart Figure S8**. The fact that at least nine well defined harmonics are accessible for the reduction of surface confined H2ase-MFHypD is remarkable. This provides compelling evidence that the reduction of surface confined H2ase-MFHypD is an extremely fast process with both electron transfer and coupled protonation reactions being reversible or very close to reversible on the time scale of even the ninth harmonic of the AC voltammetric experiment. Thus, the data is strongly characteristic of a kinetic parameter approaching the reversible limit of Nernstian kinetics. This is consistent with the “best-fit” kinetic regime of the two-sequential one-electron transfer model ($n_1 = n_2 = 1$); as detailed below, all the electron transfer rates fall into the reversible regime (**Table 1**). Conversely, the concerted two-electron transfer model ($n_3 = 2$) yields best-fit electron transfer (k_{app}^0) values in the range 120–280 s^{-1} , indicating the kinetic parameter is being optimized to a physically unrealistic value, consistent with model mis-specification (**Supplementary Table S3**).

Figure 4 further illustrates the mis-specification of the concerted two-electron transfer model ($n_3 = 2$) by comparing data generated with a k_{app}^0 value of 200 s^{-1} (similar to the best-fit values in **Supplementary Table S3**) to that generated with k_{app}^0 value of 3,000 s^{-1} (this generates voltammetry approaching that predicted for the reversible Nernstian regime). A clear distinction between the reversible ($k_{app}^0 = 3,000 s^{-1}$) and quasi-reversible regimes ($k_{app}^0 = 200 s^{-1}$) is that in the former case the higher order AC harmonic signals for reversible electron transfer are characterized by well separated peaks and currents that drop to zero between each peak, whereas these features are lacking in the latter case, with loss in resolution of the outermost peaks being particularly evident (**Figure 4**). The relatively low values of the recovered “best-fit” k_{app}^0 kinetic parameters in **Supplementary Table S3** therefore give strong evidence that the concerted two-electron transfer model is mis-specified for analyzing H2ase-MFHypD data as it fails to capture key features in the high harmonic current across the range pH 4.0–9.0, as summarized in **Supplementary Figure S10**.

The best fit non-Faradaic capacitance-current parameters values give good estimates of background capacitance, as illustrated by **Supplementary Figure S9**. The polynomial parameters reported are not expected to be identical to our previous work as the model has been improved to better describe the underlying capacitance differences between the oxidative and reductive DC sweep directions (see **Supplementary Material**). However, the best fit values are of a comparable magnitude and as expected no significant trends are observed as a function of pH (**Supplementary Table S4**). In our previous work, the analysis of electrochemical impedance spectroscopy data collected at pH 6.0 was used to generate an estimate of the uncompensated resistance, $R_u \approx 27 \Omega$ (Adamson

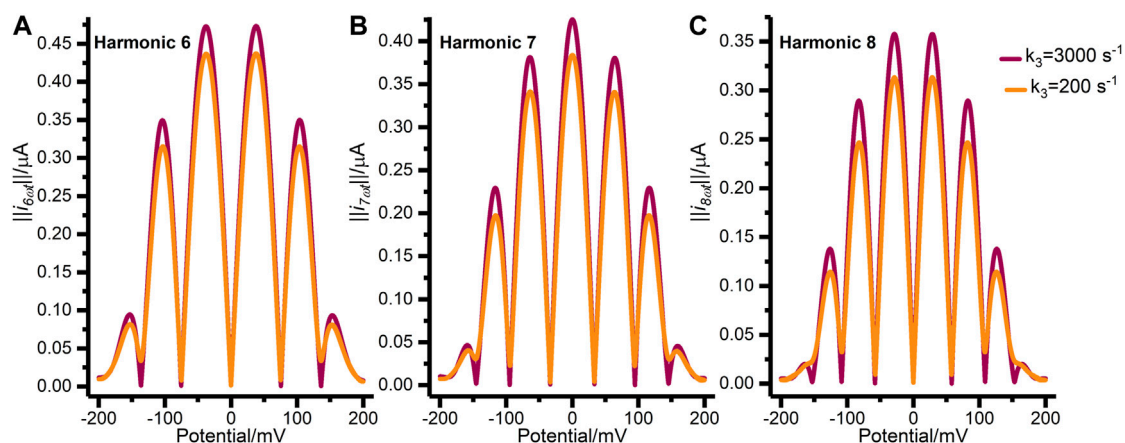


FIGURE 4 | Synthetic FTACV data showing (A) harmonic 6, (B) harmonic 7, and (C) harmonic 8 generated by the concerted two-electron transfer model with $k_3 = 3,000 \text{ s}^{-1}$ (purple) and $k_3 = 200 \text{ s}^{-1}$ (orange). The other parameters used to generate these harmonics were: $E_{\text{start}} = 200 \text{ mV}$, $E_{\text{reverse}} = -200 \text{ mV}$, $f = 9.0 \text{ Hz}$, $\Delta E = 150 \text{ mV}$, $\eta = 0.0 \text{ rad s}^{-1}$, $\zeta = 1.0$, $F_0 = 3.5 \text{ pmol}$, $S = 0.03 \text{ cm}^2$, $v = -22.4 \text{ mVs}^{-1}$, $T = 298 \text{ K}$, $\alpha_3 = 0.5$, and uncompensated resistance and capacitance were set to zero.

et al., 2017b), and this single value was used in all the modelling. In the current study, R_u was fitted for every experiment and these values can be seen to vary between from 9 to 120Ω (Supplementary Table S4), sitting well within the expected range. Indeed, given that the fitting method is insensitive to Ohmic IR drop within this range of uncompensated resistance (Supplementary Figure S16), no significance can be ascribed to fluctuations in these values.

Within the three experimental measurements made at the same pH, the best fit $n_1 = n_2 = 1$ model parameter values are generally self-consistent. Results for E_{app1}^0 and E_{app2}^0 are particularly consistent as a function of pH, and across all pH values $E_{\text{app1}}^0 < E_{\text{app2}}^0$ (more in-depth analysis of the impact of pH follows later). The calculated coverage of H2ase-MFHypD on the electrode surface (Γ) is well within the sensible expected experimental range, varying between ~ 3.3 – 4.3 pmol , as is consistent with a monolayer coverage of protein (Adamson et al., 2017b). As expected, the E_{app1}^0 , E_{app2}^0 and Γ “best fit” $n_1 = n_2 = 1$ model parameter values for the pH 6.0 dataset are consistent with those from our previous work (Adamson et al., 2017b). Furthermore, the range covered by E_{app1}^0 and E_{app2}^0 ($\sim 250 \text{ mV}$, from -95.2 to -348 mV) is consistent with previously observed mid-point potentials of disulfide bonds ($\sim 300 \text{ mV}$) (Chivers et al., 1997; Chobot et al., 2007; Bewley et al., 2015).

In our earlier work, we demonstrated that it was not possible to determine the electron transfer rate constants at pH 6.0 because the reaction reached equilibrium under the experimental conditions. This explains why experiment 1 and 3 of the pH 6.0 dataset return k_{app1}^0 and k_{app2}^0 values at the upper boundary limits that were set for these parameters ($4,000 \text{ s}^{-1}$, Supplementary Figure S7). As shown in Table 1, these rate constant boundary limits are also returned for both electron transfer processes for at least one experimental run at each pH, suggesting that across the pH range 4.0–9.0 the k_{app1}^0 and k_{app2}^0 values may be too fast to be determined using FTACV data

recorded at a frequency of 8.96 Hz . This was further investigated as shown in Figure 5; using the $n_1 = n_2 = 1$ model to simulate pH 4.0 experiment 3 and pH 9.0 experiment 3, the k_{app1}^0 and k_{app2}^0 values were varied between 0 s^{-1} and $4,000 \text{ s}^{-1}$ but all other model input parameters were held at their best fit values. From this analysis we see that the “quality of fit”, as determined by the objective function, is substantially unchanged above a lower rate limit of $\sim 2000 \text{ s}^{-1}$, suggesting that all the experiments were conducted at a sufficiently slow timescale that the rapid biological redox process of the H2ase-MFHypD disulfide bond are under thermodynamic control.

We have not modelled the impact of either kinetic or thermodynamic dispersion when fitting the data in this work (Figures 2, 3, and Supplementary Figure S8). By definition, kinetic dispersion is not possible for a fully reversible electron transfer process that is fully described by the Nernst thermodynamic relationship. Furthermore, the experimental data shows none of the hallmarks of significant thermodynamic dispersion — a broadening of the harmonics, and substantial reduction in current amplitude of the higher harmonics relative to the non-dispersed case (Lloyd-Laney et al., 2021a). Since the harmonic simulations generated without dispersion in Figures 2, 3, and Supplementary Figure S8 provide such an excellent fit to the experimental harmonics, it is concluded that the contribution of thermodynamic dispersion is negligible.

E_{app} Versus pH

Figure 6 shows how the E_{app1}^0 and E_{app2}^0 best-fit values for the two-sequential one-electron ($n_1 = n_2 = 1$) reaction model from Table 1 change as a function of pH. We observe “crossed” potentials over the entire pH range (i.e., $E_{\text{app2}}^0 > E_{\text{app1}}^0$), although the potential difference notably changes, with the E_{app1}^0 and E_{app2}^0 values being within 10 mV of one another at pH 4.0, 5.0, and 6.0, then E_{app2}^0 exceeding E_{app1}^0 by about 25 mV at pH 7.0, 8.0, and 9.0. To probe this further we have used the infrastructure of the “PINTS” Python library (Clerx et al., 2019) to fit the pH vs. E_{app} values

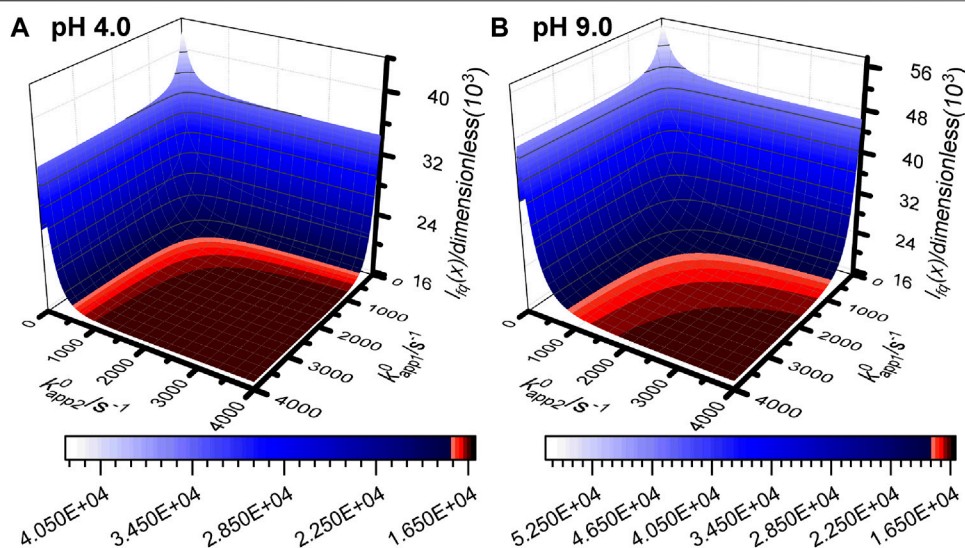


FIGURE 5 | Objective function surface for (A) pH 4.0 experiment 3 and (B) pH 9.0 experiment 3 calculated using simulated data from the $n_1 = n_2 = 1$ reaction model with all input parameters set to the best fit values from **Table 1** and **Supplementary Table S4** except k_{app1}^0 and k_{app2}^0 which are varied between 0 s^{-1} and $4,000 \text{ s}^{-1}$ and sampled every 20 s^{-1} .

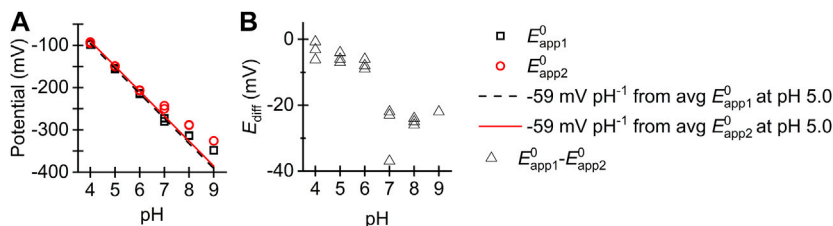


FIGURE 6 | (A) Plot of (black square) E_{app1}^0 and (red circle) E_{app2}^0 values from **Table 1** vs. pH. Overlaid are -59 mV per pH lines extrapolated from the average point values at pH 5.0 for (black dashed line) E_{app1}^0 and (red solid line) E_{app2}^0 . (B) Plot of difference between best fit E_{app1}^0 and E_{app2}^0 values as a function of pH.

as inferred above (**Table 1**) to **Eqs. 2, 3** taken from the literature (Hirst, 2006). From this approach we have inferred best fit point estimates for the characteristic pK_a values of the square scheme in **Figure 1** (note that, with reference to **Figure 1**, pK_{a1} is equivalent to pK_{aD} and pK_{a2} is equivalent to pK_{aE}), along with the true reversible potentials, E_1^0 and E_2^0 , and the standard deviation of the noise on the reversible potentials $\sigma_{E_1^0}$ and $\sigma_{E_2^0}$. Twenty optimizations were performed to maximize a Gaussian log likelihood with best fit parameters reported in **Figure 7B**. Additionally, parameter posterior distributions were sampled using an Adaptive Metropolis Markov Chain Monte Carlo (MCMC) method from the “PINTS” Python library, with the range of the inferred posterior distributions shown in **Figure 7C**. The full details of the inference approach used, along with figures detailing the posterior distributions can be found in the **Supplementary Material**.

$$E_{app1}^0 = E_1^0 - \frac{RT}{F} \ln \left[\left(1 + \frac{[H^+]}{K_{aB}} + \frac{[H^+]^2}{K_{aA}K_{aB}} \right) \div \left(1 + \frac{[H^+]}{K_{aD}} + \frac{[H^+]^2}{K_{aC}K_{aD}} \right) \right] \quad (2)$$

$$E_{app2}^0 = E_2^0 - \frac{RT}{F} \ln \left[\left(1 + \frac{[H^+]}{K_{aD}} + \frac{[H^+]^2}{K_{aC}K_{aD}} \right) \div \left(1 + \frac{[H^+]}{K_{aF}} + \frac{[H^+]^2}{K_{aE}K_{aF}} \right) \right] \quad (3)$$

DISCUSSION

Our Results indicate that across the pH range 4.0–9.0 H2ase-MFHypD maintains the same two-sequential one-electron transfer redox reaction, i.e., the Faradaic current detected in our FTACV experiments is attributable to the enzyme undergoing a redox process described by Reaction 1 and Reaction 2, converting from a fully oxidized state into a fully reduced state *via* the addition of one-electron to generate an intermediate state that accepts a second electron.

In the pH regime 4.0–6.0 the apparent potentials associated with the first and second electron transfer, E_{app1}^0 and E_{app2}^0 , respectively, both alter with a gradient of approximately -59 mV per pH unit (**Figure 6**). The rates of the two stepwise redox-state interconversion processes are reversible on the timescale of our 8.96 Hz FTACV experiment, indicating that

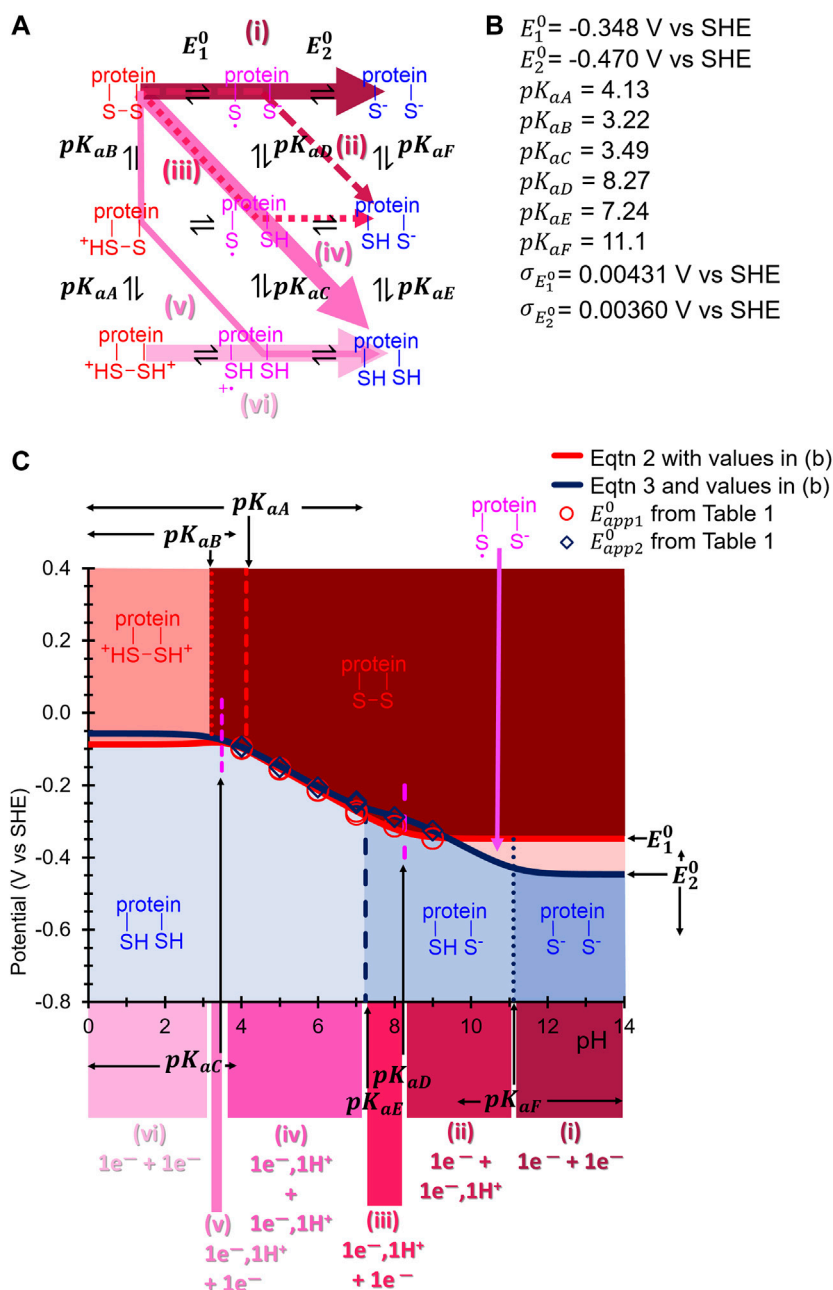


FIGURE 7 | (A) Square scheme from **Figure 1B** updated to show the appropriate pK_a and E^0 symbols associated with each protonation and electron-transfer reaction, respectively, of H2ase-MFHypD. Coloured arrows indicate the suggested reaction path taken through the scheme at different pH values. **(B)** Best fit inferred pK_a and E_1^0 , E_2^0 (potential values at the most alkaline pH) are calculated as described in the text. **(C)** E_{app1}^0 and E_{app2}^0 vs. pH data from **Table 1** plotted along with predicted E_1^0 , E_2^0 and pK_a values shown in **(B)**. The predicted protein state is indicated by background colour and associated label within the area of the plot, and the predicted square scheme path is indicated by regions of colour underneath the x-axis which correspond to the arrow colours in **(A)**. The MCMC calculated parameter distribution range is shown about each parameter name in **(C)** where the distribution is wide enough to allow it to be shown in this manner.

the experiment can be interpreted using the Nernst equation. Taken together, this evidence is consistent with the notion that in the pH range 4.0–6.0 each electron transfer is associated with a proton transfer, as derived by Laviron and many others (Laviron, 1980, 1983; Hirst, 2006; Costentin et al., 2009; Weinberg et al., 2012). Thus, in this pH regime the reaction is consistent with

moving diagonally through the Pourbaix diagram in **Figure 1**. Therefore, from pH 4.0 to 6.0 the disulfide bond redox reaction observed in our experiments is consistent with the most oxidized state being a CysS-SCys species (the deprotonated, fully oxidized “P” species in **Figure 1**) that accepts one-electron and one-proton to form a radical intermediate (“PH” in **Figure 1**), this

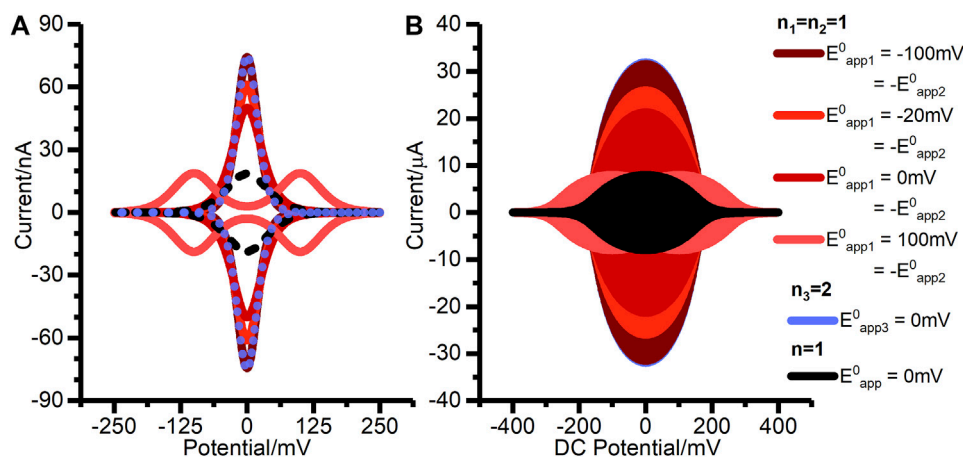


FIGURE 8 | Simulated (A) DCV, and (B) FTACV outputs for two-stepwise one-electron transfer processes ($n_1 = n_2 = 1$) when (solid pink line) $E_{app1}^0 > E_{app2}^0$ (solid light red line) $E_{app1}^0 = E_{app2}^0$, and (solid orange and dark red lines) $E_{app2}^0 > E_{app1}^0$. The data is also compared to (dashed black line) a single, reversible one electron transfer ($n = 1$), and (dotted blue line) a single, reversible two-electron ($n_3 = 2$) transfer. For the DCV simulations in (A) all electron transfer rate constants were set to $10,000 \text{ s}^{-1}$, while for the simulations FTACV in (B) all electron transfer rate constants were set to $100,000 \text{ s}^{-1}$. The other parameters used for these simulations were: $\eta = 0.0 \text{ rad s}^{-1}$, $\zeta = 1.0$, $\Gamma_0 = 10.0 \text{ pmol}$, $S = 0.01 \text{ cm}^2$, $v = -20 \text{ mVs}^{-1}$, $T = 298.15 \text{ K}$, all α values were set to 0.5, and uncompensated resistance and capacitance were set to zero. For (A) $E_{start} = 250 \text{ mV}$, $E_{reverse} = -250 \text{ mV}$, $f = 0.0 \text{ Hz}$, and $\Delta E = 0 \text{ mV}$ while for (B) $E_{start} = 400 \text{ mV}$, $E_{reverse} = -400 \text{ mV}$, $f = 9.0 \text{ Hz}$, and $\Delta E = 150 \text{ mV}$. The $n = 1$ simulations were completed using the two-stepwise one-electron transfer model and setting the second rate constant (k_{app2}^0) to zero.

intermediate is further reduced by one-proton and one-electron to form the CysSH HSCys reduced species (“PH₂” in **Figure 1**).

Although the net reaction is consistent with **Figure 1A**, we find that a concerted two-electron, two-proton mechanism is not appropriate, i.e., the classic double-headed arrow of organic chemistry does not accurately describe the reaction. A quasi-reversible concerted two-electron model is found to be mis-specified, as described in the Results. **Figure 8** shows a theoretical comparison of the DCV and FTACV output from reversible concerted two-electron transfer compared to reversible two sequential one-electron transfers in the regimes of $E_{app1}^0 = E_{app2}^0$ and $E_{app1}^0 = E_{app2}^0 + 40 \text{ mV}$ ($E_{app1}^0 = -20 \text{ mV} = -E_{app2}^0$ in **Figure 8**) and this analysis confirms that the two reversible reaction types will be distinguishable (the plot shows that the reaction models have converged when $E_{app1}^0 = -100 \text{ mV} = -E_{app2}^0$, i.e., when $E_{app2}^0 = E_{app1}^0 + 200 \text{ mV}$). Therefore, detectable amounts of the intermediate radical generated during the redox reaction of H2ase-MFHypD will exist at the midpoint potential defined by averaging E_{app1}^0 and E_{app2}^0 (**Supplementary Figure S2**). This is consistent with the observation of radical species in EPR experiments designed to probe X-ray damage in crystallography experiments on disulfide-containing proteins (Sutton et al., 2013), and also with observations of reactions between simple disulfides and one-electron reducing agents (Hoffman and Hayon, 1972).

When constructing **Figure 8** we found that the magnitude of the electron transfer rate constant required to achieve model convergence in the $E_{app1}^0 = -100 \text{ mV} = -E_{app2}^0$ regime is considerably greater for FTACV than for DCV. Thus, while rate constants of $10,000 \text{ s}^{-1}$ were used for the DCV plot in **Figure 8A**, equivalent values of $100,000 \text{ s}^{-1}$ were used for the FTACV simulations. This larger rate constant is needed as model convergence is only possible when in the reversible regime. This

highlights the utility of the FTACV technique in differentiating between reaction types, although it is notable that this theoretical consideration does not account for noise, resistance, dispersion, or background current contributions, all of which limit the accuracy of reaction model determination (Lee et al., 2011; Stevenson et al., 2012; Adamson et al., 2017a; Adamson et al., 2017b; Lloyd-Laney et al., 2021b). The effects of noise and background current contribution on real data are particularly well illustrated in our previous work on H2ase-MFHypD, which shows that many of the difficulties in model differentiation from DCV data are removed in FTACV analysis due to the increased ratio of Faradaic to capacitive current in FTACV.

In amino acid reference tables, cysteine residues are ascribed an average pK_a value of 8.5 (Poole, 2015), suggesting that under sufficiently alkali conditions the reductive cleavage of a disulfide linkage should collapse into a two-electron, zero-proton regime, equivalent to the top line of the Pourbaix diagram in **Figure 1**. The increased gap between E_{app1}^0 and E_{app2}^0 at pH 7.0, 8.0, and 9.0 relative to the more acidic conditions (see **Table 1** and **Figure 6**) is consistent with a change in the ratio of protons to electrons at pH ≥ 6.0 and when we fit the data to **Eqs. 2, 3** we derive a pK_a value of 7.3 for deprotonation of the CysSH HSCys reduced state, and a pK_a of 8.3 for deprotonation of the CysS HSCys intermediate oxidation state species. The lack of the experimental data in the regimes of $3.5 < \text{pH} < 9.5$ means that we cannot be confident in the accuracy of the remaining 4 pK_a values detailed in **Figure 7** (**Supplementary Figure S14A** for posterior distributions). However, from the ranges shown in **Figure 7** (and **Supplementary Figure S14A**) it can be seen that the ordering of pK_{aD}, pK_{aE}, and pK_{aF} is very unlikely to change, while there is some uncertainty around the ordering of pK_{aA}, pK_{aB}, and pK_{aC}. Consequently, even though the E_{app} data is sparse and exclusively at equilibrium, we can still make predictions

about the likely possible paths through the square scheme within H2ase-MFHypD. This illustrates the power of our approach. In addition, it suggests that high-frequency data, where specific estimates of the kinetic parameter can be obtained, along with the possibility of determining proton transfer rates, will be an even richer source of biological information.

With this in mind, we wish to draw the reader's attention to the incredible role that the protein matrix must play in ensuring a highly consistent redox reaction mechanism is maintained over a range of solution protonation values from 10^{-4} to 10^{-9} M. Clearly the secondary protein structure plays a vital role in mediating the protonation environment to enable Biology to precisely tune the disulfide chemistry so that the E_{app1}^0 and E_{app2}^0 values remain remarkably in concert across a very wide range. The fact that the redox chemistry of H2ase-MFHypD is consistent with the "classical" treatment of proton-coupled electron transfer *via* a square-scheme description of separated, stepwise EC processes across such a wide pH window is notable because at pH 9.0 so few protons are available. Thus, this work offers further evidence to the hypothesis that establishing stable radical one-electron reduced intermediates is a conserved feature in much of the two-electron redox chemistry seen in biology (Evans et al., 2019).

There are examples of related voltammetric behaviour outside that of biologically relevant molecules. A well-studied example is the reduction of solution soluble and surface confined polyoxometalates as a function of acid concentration. For example, the DC cyclic voltammetry for reduction of $[\text{P}_2\text{W}_{18}\text{O}_{62}]^{6-}$ in acetonitrile provides an extensive series of well separated one-electron reduction processes. On addition of sufficient acid, the processes converge into apparently multi-electron transfer processes (Prenzler et al., 1999). However, detailed voltammetry simulations based on one-electron transfer steps model the initial two reactions very well over the acid concentration range. The acid dependence and simulation details for this and related polyoxometalates have been reviewed (Bond, 2002). A fully analogous situation to the present study (Robinson et al., 2018; Robinson et al., 2019) has been demonstrated to apply for surface confined reduction of $[\text{PMo}_{12}\text{O}_{40}]^{3-}$; in highly acid media it is shown to be well modelled by treatment as two closely spaced one-electron reduction steps rather than a simultaneous two-electron reduction processes. Conversely, more exotic electron-proton transfer schemes like the elegant "wedge" scenario are necessary for describing electron and proton transfer *via* an

intermediate H-bond complex in some organic molecules (Clare et al., 2019).

DATA AVAILABILITY STATEMENT

The datasets presented in this study can be found in online repositories. The names of the repository/repositories and accession number(s) can be found below: https://github.com/alisterde/HypD_low_freq_pH_analysis

AUTHOR CONTRIBUTIONS

AD-E carried out all the modelling work and wrote the first draft of the manuscript, MR and HL-L provided expertise in model construction and method verification. All authors contributed to the design of the project and the writing of the final paper.

FUNDING

This work was supported by funding from the Biotechnology and Biological Sciences Research Council (UKRI-BBSRC, grant number BB/T008784/1) which AD-E gratefully acknowledges. MR and DG gratefully acknowledge support from the EPSRC SABS:R3 Centre for Doctoral Training (EP/S024093/1). HL-L gratefully acknowledges funding from the EPSRC and BBSRC Centre for Doctoral Training in Synthetic Biology (grant no. EP/L016494/1). AB, DG and AP thank the Australian Research Council for financial support that facilitated this international collaboration under the auspices of Discovery Program Grant No. DP170101535.

ACKNOWLEDGMENTS

We thank Dr. Hope Adamson for her expert work in obtaining the original dataset.

SUPPLEMENTARY MATERIAL

The Supplementary Material for this article can be found online at: <https://www.frontiersin.org/articles/10.3389/fchem.2021.672831/full#supplementary-material>

REFERENCES

- Adamson, H., Bond, A. M., and Parkin, A. (2017a). Probing Biological Redox Chemistry with Large Amplitude Fourier Transformed Ac Voltammetry. *Chem. Commun.* 53 (69), 9519–9533. doi:10.1039/C7CC03870D
- Adamson, H., Robinson, M., Bond, P. S., Soboh, B., Gillow, K., Simonov, A. N., et al. (2017b). Analysis of HypD Disulfide Redox Chemistry via Optimization of Fourier Transformed Ac Voltammetric Data. *Anal. Chem.* 89 (3), 1565–1573. doi:10.1021/acs.analchem.6b03589
- Armstrong, F. A., Heering, H. A., and Hirst, J. (1997). Reaction of Complex Metalloproteins Studied by Protein-Film Voltammetry. *Chem. Soc. Rev.* 26 (3), 169–179. doi:10.1039/CS9972600169
- Bard, A. J., and Faulkner, L. R. (2001). *Electrochemical Methods: Fundamentals and Applications*. 2nd Edition. New York, NY: John Wiley & Sons, Incorporated.
- Bewley, K. D., Dey, M., Bjork, R. E., Mitra, S., Chobot, S. E., Drennan, C. L., et al. (2015). Rheostat Re-wired: Alternative Hypotheses for the Control of Thioredoxin Reduction Potentials. *PLOS ONE* 10 (4), e0122466. doi:10.1371/journal.pone.0122466
- Bond, A. M. (2002). *Broadening Electrochemical Horizons: Principles and Illustration of Voltammetric and Related Techniques*. Oxford, United Kingdom: Oxford University Press.

- Chivers, P. T., Prehoda, K. E., and Raines, R. T. (1997). The CXXC Motif: A Rheostat in the Active Site. *Biochemistry* 36 (14), 4061–4066. doi:10.1021/bi9628580
- Chobot, S. E., Hernandez, H. H., Drennan, C. L., and Elliott, S. J. (2007). Direct Electrochemical Characterization of Archaeal Thioredoxins. *Angew. Chem. Int. Ed.* 46 (22), 4145–4147. doi:10.1002/anie.200604620
- Clare, L. A., Pham, T. D., Rafou, L. A., Buenaventura, A. G., Scott, T. R., Mikhaylova, V., et al. (2019). The Role of H-Bonding in Nonconcerted Proton-Coupled Electron Transfer: Explaining the Voltammetry of Phenylenediamines in the Presence of Weak Bases in Acetonitrile. *J. Phys. Chem. C* 123 (38), 23390–23402. doi:10.1021/acs.jpcc.9b06825
- Clerx, M., Robinson, M., Lambert, B., Lei, C. L., Ghosh, S., Mirams, G. R., et al. (2019). Probabilistic Inference on Noisy Time Series (PINTS). *J. Open Res. Softw.* 7 (1), Article 23. doi:10.5334/jors.252
- Costentin, C., Robert, M., Savéant, J.-M., and Teillout, A.-L. (2009). Concerted Proton-Coupled Electron Transfers in Aquo/hydroxo/oxo Metal Complexes: Electrochemistry of $[\text{Os}^{\text{II}}(\text{bpy})_2\text{py}(\text{OH}_2)]^{2+}$ in Water. *Proc. Natl. Acad. Sci.* 106 (29), 11829. doi:10.1073/pnas.0905020106
- Evans, D. H. (2008). One-Electron and Two-Electron Transfers in Electrochemistry and Homogeneous Solution Reactions. *Chem. Rev.* 108 (7), 2113–2144. doi:10.1021/cr068066l
- Evans, R. M., Siritanaratkul, B., Megarity, C. F., Pandey, K., Esterle, T. F., Badiani, S., et al. (2019). The Value of Enzymes in Solar Fuels Research - Efficient Electrocatalysts through Evolution. *Chem. Soc. Rev.* 48 (7), 2039–2052. doi:10.1039/C8CS00546J
- Finklea, H. O. (2001). Consequences of a Potential-dependent Transfer Coefficient in Ac Voltammetry and in Coupled Electron-Proton Transfer for Attached Redox Couples. *J. Electroanalytical Chem.* 495 (2), 79–86. doi:10.1016/S0022-0728(00)00399-5
- Fourmond, V., and Léger, C. (2017). Modelling the Voltammetry of Adsorbed Enzymes and Molecular Catalysts. *Curr. Opin. Electrochemistry* 1 (1), 110–120. doi:10.1016/j.coelec.2016.11.002
- Gavaghan, D. J., Cooper, J., Daly, A. C., Gill, C., Gillow, K., Robinson, M., et al. (2018). Use of Bayesian Inference for Parameter Recovery in DC and AC Voltammetry. *ChemElectroChem* 5 (6), 917–935. doi:10.1002/celec.201700678
- Gulaboski, R., and Mirceski, V. (2020). Simple Voltammetric Approach for Characterization of Two-step Surface Electrode Mechanism in Protein-Film Voltammetry. *J. Solid State. Electrochem.* 24 (11), 2723–2732. doi:10.1007/s10008-020-04563-9
- Gulaboski, R. (2019). Theoretical Contribution towards Understanding Specific Behaviour of “Simple” Protein-film Reactions in Square-wave Voltammetry. *Electroanalysis* 31 (3), 545–553. doi:10.1002/elan.201800739
- Gundry, L., Guo, S.-X., Kennedy, G., Keith, J., Robinson, M., Gavaghan, D., et al. (2021). Recent Advances and Future Perspectives for Automated Parameterisation, Bayesian Inference and Machine Learning in Voltammetry. *Chem. Commun.* 57, 1855–1870. doi:10.1039/D0CC07549C
- Guziejewski, D. (2020). Electrode Mechanisms with Coupled Chemical Reaction - Amplitude Effect in Square-Wave Voltammetry. *J. Electroanalytical Chem.* 870, 114186. doi:10.1016/j.jelechem.2020.114186
- Harris, C. R., Millman, K. J., van der Walt, S. J., Gommers, R., Virtanen, P., Cournapeau, D., et al. (2020). Array Programming with NumPy. *Nature* 585 (7825), 357–362. doi:10.1038/s41586-020-2649-2
- Hirst, J. (2006). Elucidating the Mechanisms of Coupled Electron Transfer and Catalytic Reactions by Protein Film Voltammetry. *Biochim. Biophys. Acta (Bba) - Bioenerg.* 1757 (4), 225–239. doi:10.1016/j.bbabi.2006.04.002
- Hoffman, M. Z., and Hayon, E. (1972). One-electron Reduction of the Disulfide Linkage in Aqueous Solution. Formation, Protonation, and Decay Kinetics of the RSSR- Radical. *J. Am. Chem. Soc.* 94 (23), 7950–7957. doi:10.1021/ja00778a002
- Kumari, P., and Adeboju, S. B. (2019). Fabrication of a Novel DNA Affinity Biosensor Based on Hybridisation Induced Current by Electrostatic Repulsion of Silicotungstic Acid as a Redox Indicator. *Talanta* 194, 127–133. doi:10.1016/j.talanta.2018.09.074
- Laviron, E. (1983). Electrochemical Reactions with Protonations at Equilibrium. *J. Electroanalytical Chem. Interfacial Electrochemistry* 146 (1), 15–36. doi:10.1016/S0022-0728(83)80110-7
- Laviron, E. (1980). Theoretical study of a $1e, 1H^+$ surface electrochemical reaction (four-member square scheme) when the protonation reactions are at equilibrium. *J. Electroanalytical Chem. Interfacial Electrochemistry* 109 (1), 57–67. doi:10.1016/S0022-0728(80)80106-9
- Lee, C.-Y., Stevenson, G. P., Parkin, A., Roessler, M. M., Baker, R. E., Gillow, K., et al. (2011). Theoretical and Experimental Investigation of Surface-Confined Two-center Metalloproteins by Large-Amplitude Fourier Transformed AC Voltammetry. *J. Electroanalytical Chem.* 656 (1), 293–303. doi:10.1016/j.jelechem.2010.08.012
- Léger, C., Jones, A. K., Albracht, S. P. J., and Armstrong, F. A. (2002). Effect of a Dispersion of Interfacial Electron Transfer Rates on Steady State Catalytic Electron Transport in [NiFe]-Hydrogenase and Other Enzymes. *J. Phys. Chem. B* 106 (50), 13058–13063. doi:10.1021/jp0265687
- Lloyd-Laney, H. O., Robinson, M. J., Bond, A. M., Parkin, A., and Gavaghan, D. J. (2021a). A Spotter's Guide to Dispersion in Non-catalytic Surface-Confined Voltammetry Experiments. *J. Electroanalytical Chem.* 894, 115204. doi:10.1016/j.jelechem.2021.115204
- Lloyd-Laney, H. O., Yates, N. D. J., Robinson, M. J., Hewson, A. R., Firth, J. D., Elton, D. M., et al. (2021b). Using Purely Sinusoidal Voltammetry for Rapid Inference of Surface-Confined Electrochemical Reaction Parameters. *Anal. Chem.* 93 (4), 2062–2071. doi:10.1021/acs.analchem.0c03774
- Lopez-Tenes, M., Gonzalez, J., and Molina, A. (2014). Two-Electron Transfer Reactions in Electrochemistry for Solution-Soluble and Surface-Confined Molecules: A Common Approach. *J. Phys. Chem. C* 118 (23), 12312–12324. doi:10.1021/jp5025763
- Morris, G. P., Baker, R. E., Gillow, K., Davis, J. J., Gavaghan, D. J., and Bond, A. M. (2015). Theoretical Analysis of the Relative Significance of Thermodynamic and Kinetic Dispersion in the DC and AC Voltammetry of Surface-Confined Molecules. *Langmuir* 31 (17), 4996–5004. doi:10.1021/la5042635
- Nutschan, K., Golbik, R. P., and Sawers, R. G. (2019). The Iron-Sulfur-containing HypC-HypD Scaffold Complex of the [NiFe]-hydrogenase Maturation Machinery Is an ATPase. *FEBS Open Bio* 9 (12), 2072–2079. doi:10.1002/2211-5463.12743
- Poole, L. B. (2015). The Basics of Thiols and Cysteines in Redox Biology and Chemistry. *Free Radic. Biol. Med.* 80, 148–157. doi:10.1016/j.freeradbiomed.2014.11.013
- Prenzler, P. D., Boskovic, C., Bond, A. M., and Wedd, A. G. (1999). Coupled Electron- and Proton-Transfer Processes in the Reduction of α -[P2W18O62]6- and α -[H2W12O40]6-As Revealed by Simulation of Cyclic Voltammograms. *Anal. Chem.* 71 (17), 3650–3656. doi:10.1021/ac9814290
- Robinson, M., Ounnunkad, K., Zhang, J., Gavaghan, D., and Bond, A. (2018). Integration of Heuristic and Automated Parametrization of Three Unresolved Two-Electron Surface-Confined Polyoxometalate Reduction Processes by AC Voltammetry. *ChemElectroChem* 5 (23), 3771–3785. doi:10.1002/celec.201800950
- Robinson, M., Ounnunkad, K., Zhang, J., Gavaghan, D., and Bond, A. M. (2019). Models and Their Limitations in the Voltammetric Parameterization of the Six-Electron Surface-Confined Reduction of $[\text{PMo}_{12}\text{O}_{40}]^{3-}$ at Glassy Carbon and Boron-Doped Diamond Electrodes. *ChemElectroChem* 6 (21), 5499–5510. doi:10.1002/celec.201901415
- Savéant, J. M., and Costentin, C. (2019). “Proton-Coupled Electron Transfers,” in *Elements of Molecular and Biomolecular Electrochemistry*. Editors J. M. Savéant and C. Costentin, 259–284.
- Stevenson, G. P., Lee, C.-Y., Kennedy, G. F., Parkin, A., Baker, R. E., Gillow, K., et al. (2012). Theoretical Analysis of the Two-Electron Transfer Reaction and Experimental Studies with Surface-Confined Cytochrome C Peroxidase Using Large-Amplitude Fourier Transformed AC Voltammetry. *Langmuir* 28 (25), 9864–9877. doi:10.1021/la205037e
- Sutton, K. A., Black, P. J., Mercer, K. R., Garman, E. F., Owen, R. L., Snell, E. H., et al. (2013). Insights into the Mechanism of X-ray-induced Disulfide-Bond Cleavage in Lysozyme Crystals Based on EPR, Optical Absorption and X-ray Diffraction Studies. *Acta Crystallogr. D Biol. Cryst.* 69 (12), 2381–2394. doi:10.1107/S0907444913022117
- Weinberg, D. R., Gagliardi, C. J., Hull, J. F., Murphy, C. F., Kent, C. A., Westlake, B. C., et al. (2012). Proton-Coupled Electron Transfer. *Chem. Rev.* 112 (7), 4016–4093. doi:10.1021/cr200177j
- Zhang, J., and Bond, A. M. (2007). Theoretical Studies of Large Amplitude Alternating Current Voltammetry for a Reversible Surface-Confined Electron

- Transfer Process Coupled to a Pseudo First-Order Electrocatalytic Process. *J. Electroanalytical Chem.* 600 (1), 23–34. doi:10.1016/j.jelechem.2006.02.023
- Zhang, Y., Zhang, X., Ling, Y., Li, F., Bond, A. M., and Zhang, J. (2018). Controllable Synthesis of Few-Layer Bismuth Subcarbonate by Electrochemical Exfoliation for Enhanced CO₂ Reduction Performance. *Angew. Chem. Int. Ed.* 57 (40), 13283–13287. doi:10.1002/anie.201807466
- Zheng, F., Lawrence, N. S., Hartshorne, R. S., and Fisher, A. C. (2019). Voltammetric and Electrosynthetic Triggered Gel Formation. *Electrochimica Acta* 296, 1095–1101. doi:10.1016/j.electacta.2018.11.146
- Zouraris, D., Dimarogona, M., Karnaouri, A., Topakas, E., and Karantonis, A. (2018). Direct Electron Transfer of Lytic Polysaccharide Monooxygenases (LPMOs) and Determination of Their Formal Potentials by Large Amplitude Fourier Transform Alternating Current Cyclic Voltammetry. *Bioelectrochemistry* 124, 149–155. doi:10.1016/j.bioelechem.2018.07.009
- Conflict of Interest:** The authors declare that the research was conducted in the absence of any commercial or financial relationships that could be construed as a potential conflict of interest.
- Copyright © 2021 Dale-Evans, Robinson, Lloyd-Laney, Gavaghan, Bond and Parkin. This is an open-access article distributed under the terms of the Creative Commons Attribution License (CC BY). The use, distribution or reproduction in other forums is permitted, provided the original author(s) and the copyright owner(s) are credited and that the original publication in this journal is cited, in accordance with accepted academic practice. No use, distribution or reproduction is permitted which does not comply with these terms.



Protein Motifs for Proton Transfers That Build the Transmembrane Proton Gradient

Divya Kaur^{1,2†}, Umesh Khaniya^{2,3†}, Yingying Zhang^{2,3†} and M. R. Gunner^{1,2,3*}

¹Department of Chemistry, The Graduate Center, City University of New York, New York, NY, United States, ²Department of Physics, City College of New York, New York, NY, United States, ³Department of Physics, The Graduate Center, City University of New York, New York, NY, United States

OPEN ACCESS

Edited by:

Vivek Sharma,
University of Helsinki, Finland

Reviewed by:

Ville Kaila,
Stockholm University, Sweden
Thomas E. DeCoursey,
Rush University, United States

*Correspondence:

M. R. Gunner
mgunner@ccny.cuny.edu

[†]These authors have contributed
equally to this work and share first
authorship

Specialty section:

This article was submitted to
Theoretical and Computational
Chemistry,
a section of the journal
Frontiers in Chemistry

Received: 30 January 2021

Accepted: 31 May 2021

Published: 15 June 2021

Citation:

Kaur D, Khaniya U, Zhang Y and
Gunner MR (2021) Protein Motifs for
Proton Transfers That Build the
Transmembrane Proton Gradient.
Front. Chem. 9:660954.
doi: 10.3389/fchem.2021.660954

Biological membranes are barriers to polar molecules, so membrane embedded proteins control the transfers between cellular compartments. Protein controlled transport moves substrates and activates cellular signaling cascades. In addition, the electrochemical gradient across mitochondrial, bacterial and chloroplast membranes, is a key source of stored cellular energy. This is generated by electron, proton and ion transfers through proteins. The gradient is used to fuel ATP synthesis and to drive active transport. Here the mechanisms by which protons move into the buried active sites of Photosystem II (PSII), bacterial RCs (bRCs) and through the proton pumps, Bacteriorhodopsin (bR), Complex I and Cytochrome c oxidase (CcO), are reviewed. These proteins all use water filled proton transfer paths. The proton pumps, that move protons uphill from low to high concentration compartments, also utilize Proton Loading Sites (PLS), that transiently load and unload protons and gates, which block backflow of protons. PLS and gates should be synchronized so PLS proton affinity is high when the gate opens to the side with few protons and low when the path is open to the high concentration side. Proton transfer paths in the proteins we describe have different design features. Linear paths are seen with a unique entry and exit and a relatively straight path between them. Alternatively, paths can be complex with a tangle of possible routes. Likewise, PLS can be a single residue that changes protonation state or a cluster of residues with multiple charge and tautomer states.

Keywords: proton transfer pathways, bacteriorhodopsin, photosystem II, bacterial reaction center, complex I, cytochrome c oxidase, Grotthuss mechanism

INTRODUCTION

Protons serve as substrate or product in many chemical and biological reactions. In proteins, protons often travel 10 Å or more from the surface to reach an active site. Proton gradients across the membranes of bacteria, mitochondria and chloroplasts contribute to the electrochemical gradients, $\Delta\Psi$, used to store cellular energy (Mitchell, 1961; Rich, 2008; Nicholls, 2010; Gunner et al., 2013). The proton gradient can be generated by vectorial electron transfer, where reactants are oxidized and reduced on different sides of the membrane. Here the electrons cross the membrane, but the protons only move to or from the separated redox sites. In contrast, proton pumps transfer protons through the transmembrane proteins, requiring mechanisms to avoid downhill proton transfer.

Regardless of the mechanism a protein uses, it takes energy to build a proton gradient. The input energy is light in photosynthetic proteins (Cardona et al., 2012; Ge and Gunner, 2016; Cardona and Rutherford, 2019), redox reactions in the electron transfer chain (Kaila and Hummer, 2011), ATP hydrolysis (Vasanthakumar and Rubinstein, 2020) or the dissipation of the gradient of another ion (Fowler et al., 2015; Brandt, 2019). The protons flow down the electrochemical gradient then fuel processes such as ATP synthesis in F_1/F_0 ATPase (Walker et al., 1991; Futai et al., 2012; Yanagisawa and Frasca, 2017) and the active transport of ions and metabolites (Accardi and Piccolo, 2010; Gunner et al., 2013).

To build the gradient, protons are transferred from the more negative, N-side of the membrane, where they are at lower concentration (higher pH) to the positive, P-side where they are at higher concentration (lower pH). The P-side is in the periplasm of bacteria, the outer membrane space of mitochondria and in the lumen on the inside of the chloroplast thylakoid membrane. The N-side is toward the bacterial cytoplasm, the mitochondrial matrix and the chloroplast stroma. The electrochemical gradient, $\Delta\Psi$, is made up of the gradient of protons (the ΔpH) but also has contributions from other ions, adding to a voltage change, ΔV , across the membrane (Decoursey, 2003). The $\Delta\Psi$ across a given membrane determines the energy needed to push a proton uphill in the protein pumps described here or the energy liberated when protons run from P- to N-side as used for ATP synthesis.

Although we refer to “protons”, H^+ does not travel alone. Rather it is associated with a water (hydronium, H_3O^+) or two water molecules as a Zundel cation (H_5O_2^+) or as a larger, Eigen complex (H_9O_4^+) (Agmon, 1995; Wraight, 2006; Farahvash and Stuchebrukhov, 2018). In proteins, the proton can also be bound to redox cofactors, to acidic or basic residues or trapped as a stabilized hydronium (Xu and Voth, 2006; Freier et al., 2011; Ikeda et al., 2017).

Protons move through a chain of oriented molecules by a Grotthuss proton transfer mechanism (Agmon, 1995; Cukierman, 2006; de Grotthuss, 2006; DeCoursey and Hosler, 2014). An active group in the middle of the chain is: 1) a hydrogen bond donor to the next group in the direction of proton transfer and 2) has a lone pair of electrons that is a hydrogen bond acceptor from the neighbor toward the proton input side. In the Grotthuss mechanism no proton moves more than one bond, as the proton acceptor takes ownership from the neighboring proton donor. However, overall the coupled transfers lead to a proton rapidly leaving the input side and appearing at the end of the chain. There are many reviews of the chemistry of proton transfer reactions as well as of proton transfer reactions in proteins (Hammes-Schiffer, 2001; Pomès and Roux, 2002; Blomberg and Siegbahn, 2006; Swanson et al., 2007; Knight and Voth, 2012; Ishikita and Saito, 2014; Miyake and Rolandi, 2015; Wikström et al., 2015; Sakashita et al., 2020).

Two requirements create barriers for Grotthuss proton transfers. First, the chain of hydrogen bonds between proton donors and acceptors needs to be pre-organized. Then, once the proton has transferred, the hydrogen bonds are arranged to return the proton back to the origin, not to move another

proton in the same direction. The hydrogen bonded chain needs to fully reorient for the next proton to transfer, so overall proton flux is limited by this slow “hop and turn” process (Nagle and Morowitz, 1978).

Vectorial proton coupled electron transfer. Proteins such as PSII, cytochromes bc_1 and b_6f use vectorial electron transfer reactions where oxidation and reduction reactions are spatially separated to add to the proton gradient. Thus, oxidation occurs on the P-side, where protons are released because the loss of an electron lowers the oxidized product pK_a below the pH of the nearby compartment. Reduction occurs on the N-side, where reduction shifts the product pK_a to be higher than the compartment pH (Rich, 2008; Nicholls, 2010; Gunner et al., 2013; Gunner and Koder, 2017). Within the protein, a sequence of electron tunneling reactions pass the electrons 30 Å or more between the terminal electron donor and acceptor (Gray and Winkler, 2003; Moser et al., 2006). The interior electron transfer reactions are not coupled to gain or loss of protons. Thus, a proton gradient is generated without moving protons through the membrane by a redox loop mechanism as suggested by Mitchell (Mitchell, 1977). The intra-membrane, middle of these proteins are mostly non-polar side chains with few associated water molecules, so discourage proton transfer. However, as will be seen in the discussion of PSII and bRCs, the sites of final, proton coupled oxidation or reduction can be 10 Å or more from the surface, requiring long-range proton transfer to move the protons to the active site.

Proton pumps. The proton pumps include the well-studied, light-driven Bacteriorhodopsin (Balashov, 2000; Luecke, 2000), Complex I (Mathiesen and Hägerhäll, 2002; Hirst, 2013; Sazanov, 2014) and the heme copper oxidase (HuCuOx) family (Kaila et al., 2010; Lee and Ådelroth, 2013). To ensure protons move in the correct direction pumps require three elements. These are proton transfer paths, as found in vectorial electron transfer proteins. However, pumps need Proton Loading Sites, PLS, placed along the proton transfer path, and gates. PLS transiently change their proton affinity to load a proton when the gate is open to the N-side and releases it when it is open to the P-side. Pathway gating and proton loading must be synchronized to guard against energy dissipating proton transfer from P- to N-side.

This review will compare and contrast the residues that make up the proton transfer elements in three light activated proteins: Bacteriorhodopsin (bR) and the photosynthetic proteins, Photosystem II (PSII) and the purple non-sulfur photosynthetic bacterial reactions centers (bRCs) and in the proton pumps Complex I and Cytochrome c oxidase, which are the first and last protein in the erobic electron transfer chain.

Overview of Proton Transfer Paths

The role of the different residues in proton transfer paths. The review will describe the residues found along proton transfer paths. Water is the quintessential Grotthuss competent molecule so water filled channels through protein structures often trace the proton transfer paths. However, some side chains can be a part of a proton transfer chain. Hydroxyl residues are well established in

proton transfer paths, such as in Green Fluorescent Protein, GFP, which has a Ser on the short proton transfer path (Brejc et al., 1997; Donati et al., 2018). A neutral His has a proton on N_ϵ with a lone pair on N_δ (or the proton/lone pair swap positions). It can accept a proton from one side of the imidazole and donate a proton from the other side. His plays this role in proton transfer in the M2 proton channel (Wang et al., 1995) and in carbonic anhydrase (Tu et al., 1989). Histidine analogs have been used in synthetic electron coupled proton transfer chains that lead to the Grotthuss transfer of a proton over long distances (Odella et al., 2018; Odella et al., 2019). Ionized side chains cannot be both a hydrogen bond donor and acceptor as required for Grotthuss proton transfer (Ge and Gunner, 2016; Lazaridis and Hummer, 2017; Duster and Lin, 2019). Thus, deprotonated Asp⁻ and Glu⁻ are hydrogen bond acceptors but have no proton to donate, while protonated His⁺, Lys⁺ or Arg⁺ have no lone pairs to accept a proton. This review will show examples where acidic and basic residues are found as PLS in the proton transfer chain, serving as meta-stable intermediates that can cycle between loaded (protonated) and unloaded states. Polar residues such as Asn, Gln and Trp are found to anchor the hydrogen bond chain, but are unlikely to be active elements in Grotthuss proton transfer chains (Hammes-Schiffer, 2001; Goings et al., 2020), while non-polar residues are insulators stopping water penetration and proton leaks.

Linear vs. complex proton transfer paths. As proton transfers have been investigated in different proteins, we have found they can take place via linear or complex paths. Linear paths, as defined here, have a single entry and exit and a well-defined road between them. There are limited branches, which never deviate far from the main path. Linear paths can often be identified in a protein structure that includes well resolved water molecules (Sharpe and Ferguson-Miller, 2008; Sazanov, 2015). Mutation of a single entry or exit residue can block proton transfer.

However, representative structures will be shown to reveal interior regions with tangled webs of polar and protonatable groups and many water molecules (Krammer et al., 2009; Cai et al., 2020; Khaniya et al., 2020). These complex proton transfer paths provide multiple choices for protons to follow. Here mutations of individual residue may lead to partial loss of activity, generating ambiguous results that neither fully confirm nor deny their role. The proteins reviewed here use linear and complex paths in different regions of the overall transfer of protons through the membrane.

Proton Loading Sites

Type of Residues That Can Serve as PLS

A successful pump takes a proton through the protein from the N-side to the P-side, even though it is thermodynamically unfavorable. A PLS must transiently hold protons with gates open to the N-side and to be released to the P-side, synchronized with a turnover time of microseconds to milliseconds (Balashov, 2000; Kaila et al., 2010). The PLS is thus a residue or cluster of residues whose proton affinity changes dramatically between different reaction intermediates (**Supplementary Material S2**). The carboxylic acids, Asp, Glu and heme propionic acids are the

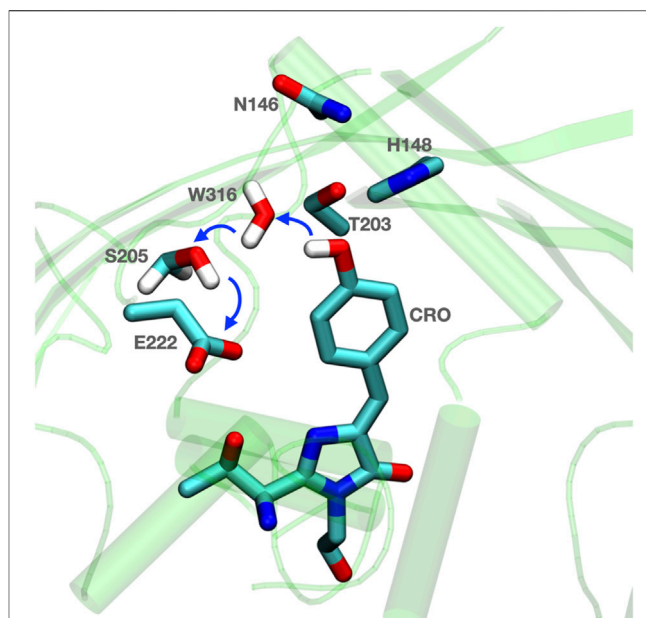


FIGURE 1 | Residues are prearranged for Grotthuss proton transfer in GFP. Blue thick arrows show direction of proton transfer from chromophore (CRO) to E222 via water (W316) and S205. The surrounding H148 and N146 can help to anchor the active proton transfer path. The coordinates for *Equorea victoria* GFP are from PDB ID: 1EMA (Ormö et al., 1996).

most common PLS components in the proteins described here. They are found as single site PLS as well as PLS clusters. His and Lys are more often found coupled to acidic residues in clusters. H_3O^+ , trapped between several acidic residues has been suggested to be part of PLS clusters (Freier et al., 2011; Kovalevsky et al., 2011; Supekar et al., 2016). However, the pK_a for Arg⁺ to lose a proton is as high as that of water or a hydroxyl side chain (Fitch et al., 2015). Thus, the protonated Arg can help stabilize the negative charge but is unlikely to lose a proton in a PLS.

PLS clusters. The PLS and complex proton transfer paths often have regions with many interacting, buried ionizable and polar residues (Lancaster et al., 1996; Kannt et al., 1998). For a PLS cluster with n protonatable residues there are $n+1$ charge states and 2^n microstates, which identify the number and distribution of protons (Gunner et al., 2020). The charge ranges from $-N_{acids}$ (the number of acids) (assuming all bases are neutral) to $+N_{bases}$ (number of bases) (assuming all acids are neutral). Tautomers are protonation microstates with the same charge but different proton locations. With m protons distributed over n binding sites in a PLS there are:

$$\frac{n!}{m!(n-m)!} \quad (1)$$

tautomers. The relative energies of the different tautomers determine the proton positions within the loaded and unloaded clusters. This review will describe examples of mechanisms by which PLS can change their protein affinity to load and unload protons.

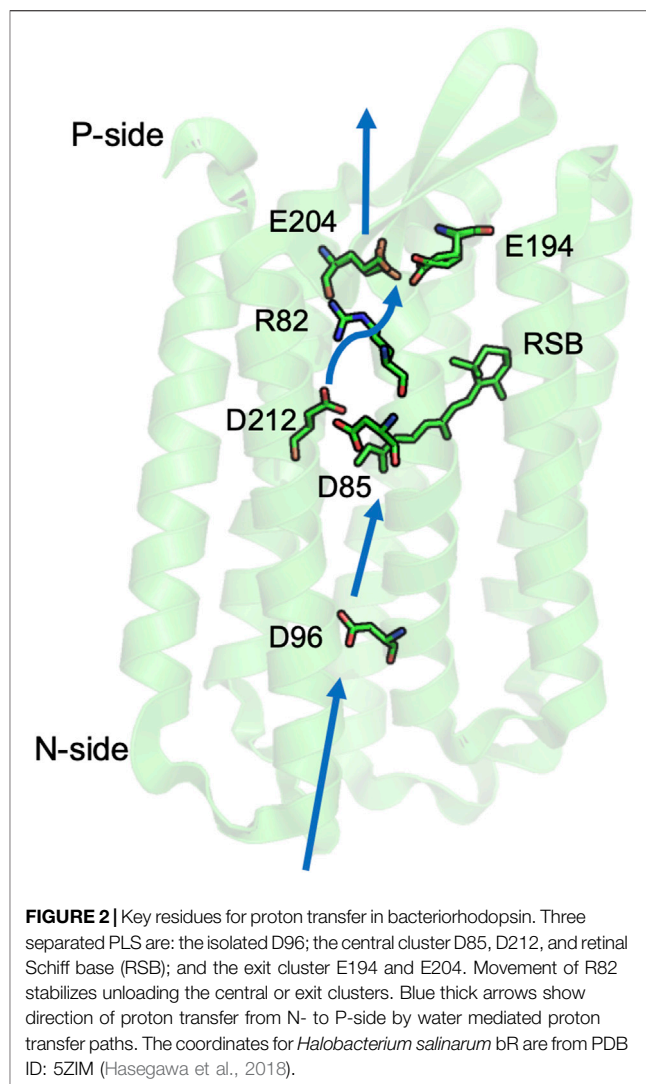
MODEL SYSTEMS

Green Fluorescent Protein (GFP). GFP provides a simple example of the role of side chains in and around the proton transfer path (**Figure 1**). It also shows how fast protons can transfer via a pre-organized Grotthuss competent chain (Brejc et al., 1997; Zimmer, 2009; Donati et al., 2018). GFP is well studied as it has revolutionized cell biology. When introduced into a genome it is co-expressed with a specific protein of interest and its characteristic fluorescence allows the targeted protein to be localized within a living cell. The chromophore in GFP is a photoacid that absorbs light in the near UV and emits in the green (Zhou and Han, 2018). The large Stokes shift results from the ground state absorption and excited state emission occurring from molecules with different charges. Thus, in the ground state the chromophore is the PLS, while Glu 222 is the proton acceptor when the chromophore proton affinity is diminished by excitation. In this system the path for rapid proton release must be ready to carry the proton away prior to relaxation of the chromophore (Chattoraj et al., 1996).

The proton is transferred through bound water and Ser 205 to Glu 222. A nearby His 148, Thr 203 and Asn 146 are on the outskirts of the proton transfer wire (Stoner-Ma et al., 2005; Di Donato et al., 2011). These provide a polar residue fence to pre-orient the hydrogen bond network. As the protein is light activated experiments can synchronize the protein for kinetic measurements to follow changes in the hydrogen bonding network. The proton arrives on the Glu in less than 10 ps (Donati et al., 2018). Vibrational spectroscopy shows that there are rapid changes in hydrogen bond orientation that precede proton transfer, presumably to fine tune the hydrogen bond connections for Grotthuss proton transfer. The kinetic transients are distinguished as rearrangements, which do not have a kinetic isotope effect, and proton transfers, which do (Di Donato et al., 2011).

Gramicidin (gA). The gA channel is a proton and cation conducting channel that has been used to study proton transfer through a linear water wire, with no intervening side chains. gA is made of two short β -strand peptides, capped on N- and C-terminal ends. The N-termini meet in the center of the membrane. In the β -helix the side chains are to the outside, with sufficient space to hold a linear chain of ≈ 8 water molecules in the middle of the helix. gA is an antibiotic, allowing protons and other cations to cross, depolarizing the cell's electrochemical gradient (Kelkar and Chattopadhyay, 2007; Li et al., 2016). The simplicity of this system has made it ideal for the experimental (Dorman and Jordan, 2004; Ryu et al., 2015; Paulino et al., 2020) and computational (Roux, 2002; Allen et al., 2004; Till et al., 2008; Lazaridis and Hummer, 2017; Zhang et al., 2020) studies of the Grotthuss proton transfer mechanism.

The water molecules in gA form hydrogen bonds with the two neighboring water molecules and with the amides of the surrounding peptides. The balance of the water-water and water-amide interactions determines the stability of the water wire, the stability of an excess proton within the wire and the barrier for flipping the wire orientation once a proton has



translocated to transport another proton via the hop and turn mechanism. The rate determining step for transfer can be initially orienting the water molecules or flipping the oriented water dipoles to the correct direction (Pomès and Roux, 2002; Agmon et al., 2016; Bozdaganyan et al., 2019).

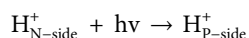
Recent computer simulations showed a rather substantial sensitivity of the water wire orientation to the force field and simulation method (Zhang et al., 2020). In molecular dynamics simulations, with a classical force field the water molecules are fully aligned within the channel with rare flips from one orientation to the other. In contrast, MD with a the Drude polarizable force field shows more disorganized water molecules. Monte Carlo sampling with a Continuum Electrostatic force field also show relatively disorganized water chain. Thus, the balance of the forces that determine the orientation of the water molecules are such that different simulation conditions induce different behavior.

Experiments have also supported a range of structures for water in the channel. The experimentally derived rate of proton translocation through the channel under a transmembrane

voltage gradient appears to be diffusion limited ($\approx 2 \times 10^9 \text{ s}^{-1}$) even at pH 0 (Cukierman, 2000; Decoursey, 2003). The reorientation of the water chain is likely to be the rate determining step in Grotthuss proton transfer (Pomès and Roux, 1998). In the MD simulations with a classical force field the water chain flips its direction at $\approx 4 \times 10^8 \text{ s}^{-1}$ and this process is faster with the Drude force field. Thus, the simulations are in general agreement with the measured rate of proton transfer. However, recent solid-state NMR studies show a well-organized water-wire with flip rates on the millisecond time scale, which would suggest very slow turnover for proton transfers. The NMR studies point to hydrogen bonds between water molecules and amides near the first and last turns of each β -helix leading to this stability. Thus, despite the simplicity of its structure, bR remains a protein where our understanding of the channel water structure and the mechanism of proton transport remains incomplete.

BACTERIORHODOPSIN

bR is the simplest and best studied proton pump (Balashov, 2000; Baudry et al., 2001; Gunner et al., 2006; Lanyi, 2006; Lórenz-Fonfría et al., 2008; Clemens et al., 2011). The bacteriorhodopsin family uses retinal not chlorophyll based photoactivation to fuel proton or ion pumping (Figure 2). Absorption of a 568 nm photon initiates a reaction cycle that removes a proton from the cell interior (N-side) and releases one to the outside (P-side) adding to the proton gradient. The overall reaction is simply:



The proton transfers are driven by the light induced conformational changes of the retinal from all trans to 13-cis, which is coupled to small changes in the helical packing in the protein core. There are three PLS in bR that illustrate different mechanisms to control PLS protonation and the connection to the proton transfer path.

Characterization of proton transfer intermediates. In light activated proteins such as GFP, bR, PSII and bRCs experiments can follow the sequential reaction mechanism since the flash of light used to start the reaction synchronizes the population. Time resolved visible and IR spectroscopy, combined with site directed mutations allow assignment of kinetic features to individual residues. bR intermediates were identified with the proton resting on acidic amino acids making up three well separated PLSs, each with metastable intermediates with different ionization states (Balashov, 2000; Lórenz-Fonfría and Kandori, 2009; Lórenz-Fonfría et al., 2011; Lórenz-Fonfría and Heberle, 2014). These intermediates clearly demonstrate the role of transient resting places for protons. Changes occur in times ranging from the picosecond transitions that trap the photon's energy in the isomerized retinal to the milliseconds required to complete the full photocycle.

In bR, it is possible to crystallize protein trapped in different intermediates by a combination of mutation and temperature changes (Edmonds and Luecke, 2004; Hirai et al., 2009; Wickstrand et al., 2015). Simulations using these structures have shown that the calculated equilibrium proton distribution

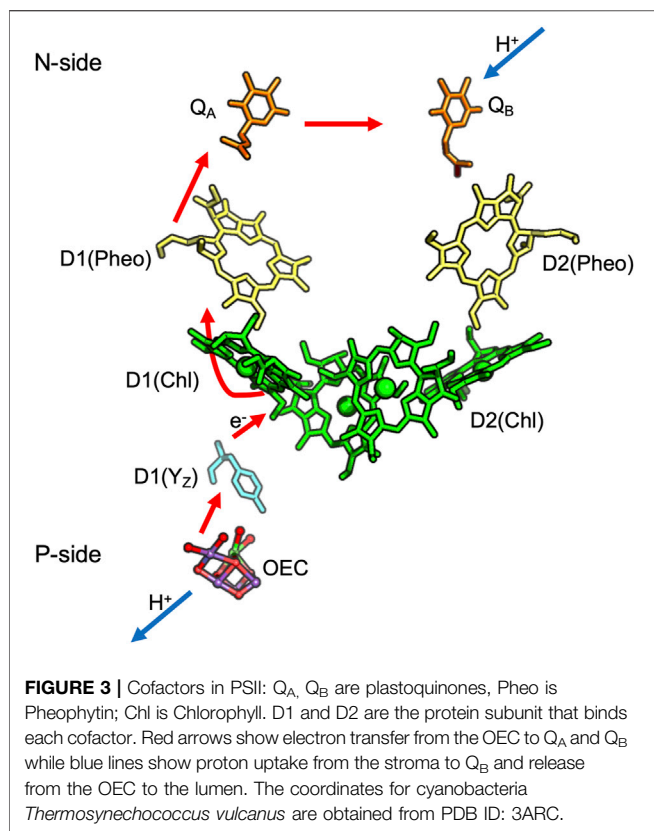
changes between intermediates as expected (Bashford and Gerwert, 1992; Spassov et al., 2001; Onufriev et al., 2003; Song et al., 2003; Song and Gunner, 2014). More recent time resolved crystal structures have been obtained using X-ray free electron lasers (XFEL) (Nogly et al., 2018; Wickstrand et al., 2019). These structures show many of the motions of water molecules and side chains and helices seen in earlier trapped structures. However, as the XFEL structures are not in deeply trapped intermediates, the dynamic structures provide additional information. However, as the transitions between photocycle intermediates are not all well separated in time, the XFEL structures each contain a mixture of states.

bR Demonstrates the Character of Simple and Cluster PLS

The central cluster tautomer shift. The central cluster consists of three residues: the retinal Schiff base (RSB), Asp 85 and Asp 212, which binds one proton on the RSB in the ground state (RSBH^+ : Asp 85⁻: Asp 212⁻). Light absorption leads to isomerization of the retinal, which rotates the RSB from facing the P-side to the N-side, leaving the proton on Asp 85 (M state: RSB: Asp85H: Asp 212⁻). This transition demonstrates a feature of a cluster PLS, as it moves between states with different proton distributions (tautomers) while retaining the same number of protons. The redistribution of the proton coupled to the retinal isomerization serves as a gate as it changes the direction of proton access. Thus, a proton will be passed from the trans-RSB to Asp85 toward the P-side, while later a proton is bound to the 13-cis RSB from the N-side (Bondar et al., 2007; Clemens et al., 2011; Wolter et al., 2013). The retinal returns to the P-side facing trans isomer only after it has bound the proton (Balashov, 2000).

A complex PLS can trap a proton on multiple sites. The complex exit cluster PLS, with Glu 194 and 204, has multiple tautomers for the proton loaded state. IR spectroscopy (Daldrop et al., 2018) and simulations (Bashford and Gerwert, 1992; Spassov et al., 2001; Phatak et al., 2008) support a protonated water stabilized by the two anionic glutamic acids, while the proton can also be trapped by a hydrogen bonded pair with one acid protonated and a water nearby (Song et al., 2003; Phatak et al., 2008). An advantage of using a cluster PLS is that it can use the multiple ways to store the proton to be less sensitive to mutation. If one of the Glu is mutated to an Asp the cluster is no longer properly positioned to trap a hydronium so the water cation IR signature is lost. The proton is now trapped on an acid, thereby retaining PLS function (Balashov, 2000; Gerwert et al., 2014).

An isolated acidic PLS requires hydration to lose its proton. Asp 96 on the N-side of bR plays a key role in proton transport (Miller and Oesterhelt, 1990). Asp 96 is an isolated PLS, as it is not in a cluster with other protonatable residues and has few hydrogen bonding opportunities to residues beyond Thr46 in the neighborhood. In the neutral, unloaded structure, there are few nearby water molecules and the acid is very stable in its neutral, loaded state (Gerwert et al., 2014; Wolf et al., 2014). A combination of time resolved IR and MD simulations show that isomerization of the retinal, 10 Å from Asp96, and the transfer of



the proton from RSBH⁺ to the nearby Asp 85 leads to formation of a linear water chain on the N-side (Freier et al., 2011). The water molecules provide a proton transfer path, and also stabilize the negative charge on Asp 96 so that it can release a proton to the RSB near the end of the photocycle. Thus, a single site PLS cannot change its proton affinity by small movements of the polar and charged groups. Here flooding the site with water is required to both stabilize the charged Asp⁻ and to open the gate for proton release by connecting it to the proton transfer path.

PHOTOSYSTEM II

PSII (Umena et al., 2011) is a multi-subunit protein pigment complex present in the thylakoid membrane of plants and cyanobacteria (Cox et al., 2013; Vinyard and Brudvig, 2017; Pantazis, 2018). The reaction is initiated by chlorophyll excitation with a 680 nm photon. Water is the primary electron donor and plastoquinone, PQ, is the final electron acceptor (Figure 3) (McEvoy and Brudvig, 2006). The overall reaction is:



The Oxygen Evolving Complex (OEC), an inorganic Mn₄CaO₅ cluster, catalyzes water oxidation following four sequential oxidations of the cluster (through five S-states) releasing O₂ (Suga et al., 2019). The OEC is ≈20 Å from the

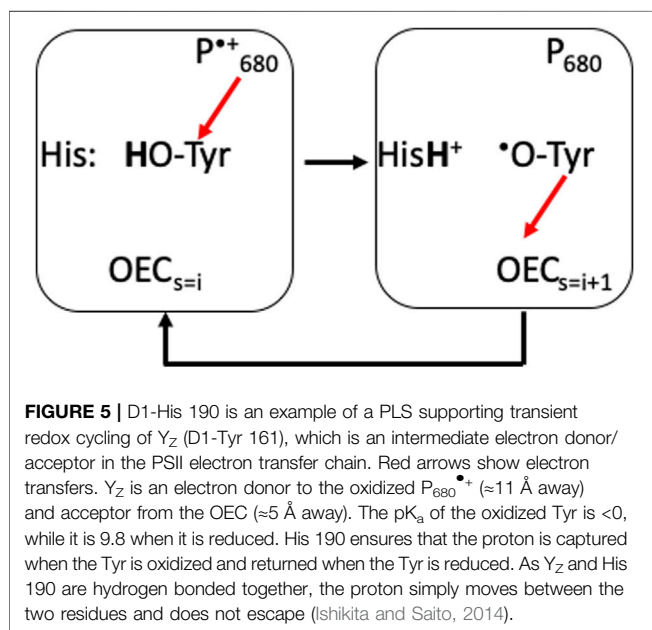
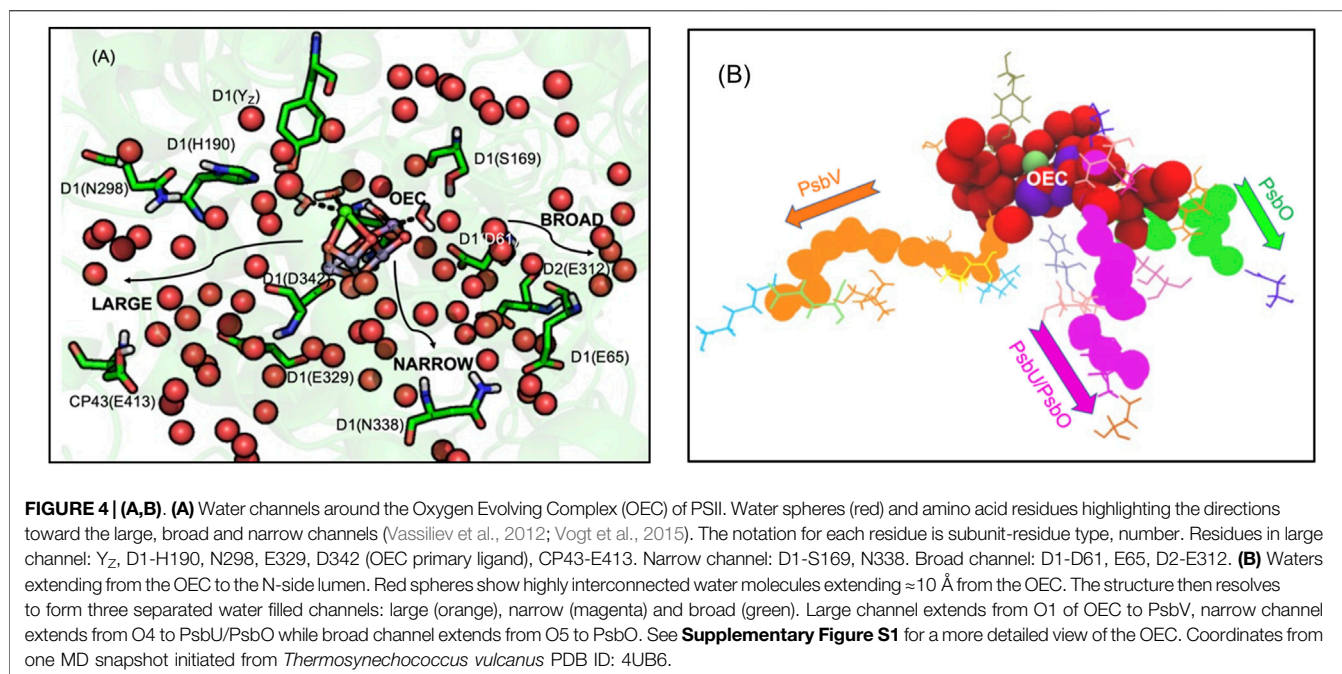
surface, requiring paths for water entry and O₂ and proton release. The region around the OEC is filled with water molecules that separate into three discrete water-filled channels moving to the lumen (Figures 4A,B) (Vassiliev et al., 2012; Vogt et al., 2015). On the electron acceptor side, Q_B in PSII is quite close to the stroma requiring only a short proton transfer path to bring in protons (Saito et al., 2013).

Proton Paths to the P-Side Near the OEC in PSII

Three water filled paths. Proton transfer paths combine Grotthuss competent water molecules and residues with protonatable groups to serve as transient proton loading sites. The proton release paths in PSII are dominated by water molecules, requiring minimal assistance from residues. There are three identified water filled channels leading from the OEC to the lumen (Figure 4A) (Vassiliev et al., 2012; Vogt et al., 2015). The narrow channel originates from one side of the Mn₄ water ligands and extends through the PsbU/PsbO subunits (Figure 4B). The broad channel originates from the other side of Mn₄, extending to the PsbO subunit, while the large channel originates from the OEC Ca water ligands leading to the PsbV subunit (Vassiliev et al., 2012; Vogt et al., 2015). These channels can provide paths for the transfer of the four product protons and O₂ to the lumen and entry of the two substrate water molecules.

Which path does the proton take? With so many choices, an open question is which channel is best suited for proton transfer to the surface. Various simulation techniques have explored the nature of the water channels. Molecular dynamics investigations (Vassiliev et al., 2012) and quantum chemical studies (Retegan et al., 2016) favored the narrow channel for substrate water delivery. QM/MM studies (Saito et al., 2015) supported proton transport through the narrow channel. Continuum electrostatics calculations considered the proton affinity of residues lining the broad channel, finding increasing proton affinity, lowering the barrier for proton transfer, nearer the channel exit (Ishikita et al., 2006). Steered MD calculations (Vassiliev et al., 2012) found the large channel favorable for O₂ transport and the narrow channel for substrate water delivery. However, other experimental and computational studies favored the large channel for proton transport (Chrysina et al., 2011; Nakamura et al., 2014; Sakamoto et al., 2017) or for substrate water delivery (McEvoy and Brudvig, 2004; Isobe et al., 2015; Shoji et al., 2015; Ugur et al., 2016; Kim and Debus, 2017). Thus, despite experimental and computational studies, a consensus for the role of each channel is yet to be established (Pantazis, 2018).

While earlier studies focused on individual linear paths, network analysis provides a somewhat different view of the connectivity of the water networks near the OEC (Kaur et al., 2021). These studies indicate that beyond ≈10–12 Å from the cofactor the three paths do become well separated as indicated by inspection of the structures. However, closer to the OEC all water molecules are highly interconnected. A proton from any of the Mn terminal water ligands or any of the oxygens that bridge the OEC Mn (except O2 and O3) can find its way to any of the three channels (Figure 4B) (Kaur et al., 2021). Comparing the proton

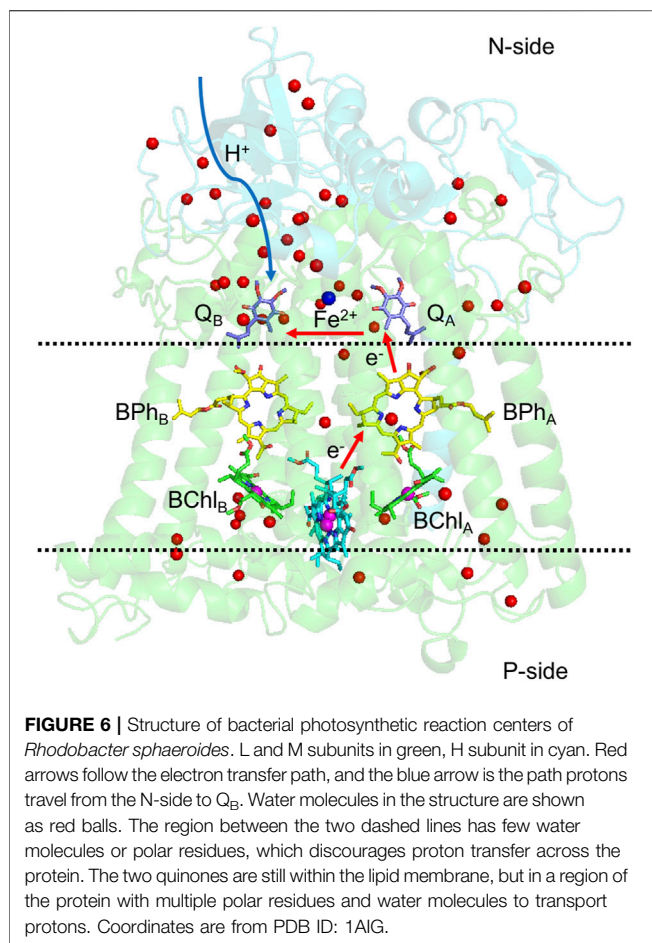


affinity of H₃O⁺ placed on individual water molecules in the three separated paths shows the broad channel as being more hospitable to the positive charge as suggested earlier (Ishikita et al., 2006; Bondar and Dau, 2012).

Mutations and time resolved IR difference spectroscopy support a complex proton transfer path near the OEC. The question is how to characterize a highly interconnected proton transfer path dominated by water molecules. FTIR-difference spectra followed through the cycle of reactions that lead to oxygen evolution shows changes in an extensive hydrogen bonding

network around the cofactor. For example, FTIR-difference spectra shows a carboxylate peak (near 1,747 cm⁻¹) whose proton affinity decreases in the step in the OEC oxidation cycle where a proton is not released to the lumen (S₁ to S₂) (Debus, 2015). This feature is lost when mutations are made of residues separated by ≈ 20 Å including D1-Asp61Ala, D1-Glu65Ala, D2-Glu312Ala, D1-Arg334Ala, D1-Glu329Gln (Figure 4). Mutation of each of these residues disrupts the hydrogen bond network and blocks or slows O₂ evolution (Service et al., 2010; Debus, 2014). All of these residues are found in the network analysis that revealed the connections of all water molecules near the OEC (Kaur et al., 2021).

PLS used for proton coupled electron transfer near the OEC. PSII provides an example of the use of a PLS to stabilize the redox reactions of an intermediate on a longer electron transfer chain. Through the S-state cycle the redox active Tyr161, Y_Z, is the electron donor to the oxidized chlorophyll, P₆₈₀^{•+}. Y_Z^{•+} is then reduced by the OEC (Figure 5) (Lavergne and Junge, 1993). The pK_a of an oxidized Tyr is -2 (Tommos and Babcock, 2000), so Y_Z^{•+} will lose its proton. D1-His 190 serves as a PLS, trapping the proton for the microseconds to several milliseconds that Y_Z is oxidized (Figure 5) (Rappaport et al., 1994). This His has a low enough proton affinity that it is neutral in the ground state, yet its proton affinity is higher than the oxidized Y_Z[•]. The protein must block the proton from being lost to the lumen from the His. A tight hydrogen bond between the Tyr and the His helps as does the presence of polar, but non-proton conducting residues such as D1-Asn 298 surrounding the pair (Saito et al., 2011). The proton is shuttled between the Tyr cofactor and its adjacent PLS, never moving in or out of the protein, while the electron is passed from the OEC to P₆₈₀ via Y_Z (Figure 5) (Saito et al., 2011; Ishikita and Saito, 2014).



Gates in proton transfer pathways in proteins that are not pumps. A gate along proton transfer path guards against unwanted proton transfers. An inhibitory gate can be identified in PSII, where a chloride ion helps to keep the entrance to the broad channel open by preventing a salt bridge between D1-Asp 61 and D2-Lys 317. Experiments show chloride depletion blocks the advancement of S-state transition beyond S_2 (Ono et al., 1986; Pokhrel and Brudvig, 2014). Simulations show depletion of chloride leads to formation of a salt bridge between D1-Asp 61 and D2-Lys 317 hindering proton loss (Rivalta et al., 2011; Amin et al., 2016; Kaur et al., 2019).

Fences support a proton path. The sides of the water filled channels contain residues such as Asn and Arg (e.g., D1-Asn 87 and CP43-Arg 357). These cannot participate in Grotthuss proton transfers, nor are their pK_a in a range that would let them be PLS. Rather, these residues can anchor, the hydrogen bond connections, orienting the water molecules. One example that has been investigated is D1-Asn 298 near the OEC. Mutating this residue influences oxygen evolution (Kuroda et al., 2014) and the FTIR spectrum of the OEC network (Nagao et al., 2017; Chrysina et al., 2019). Simulations show the Asn changes the orientation of its side chain amide dipole in the transition from S_2 to S_3 leading to rearrangement of the hydrogen bond network (Chrysina et al., 2019).

BACTERIAL REACTION CENTER

The reaction center, bRC, of the purple non-sulfur bacteria is the first membrane protein whose structure was solved at atomic resolution (Deisenhofer et al., 1985). RCs are light activated proteins so as with GFP, bR and PSII, time resolved measurements allow individual steps in the series of electron and/or proton transfer reactions to be monitored by time-resolved spectroscopy, showing the individual steps in the reactions (Okamura et al., 2000; Wraight, 2006).

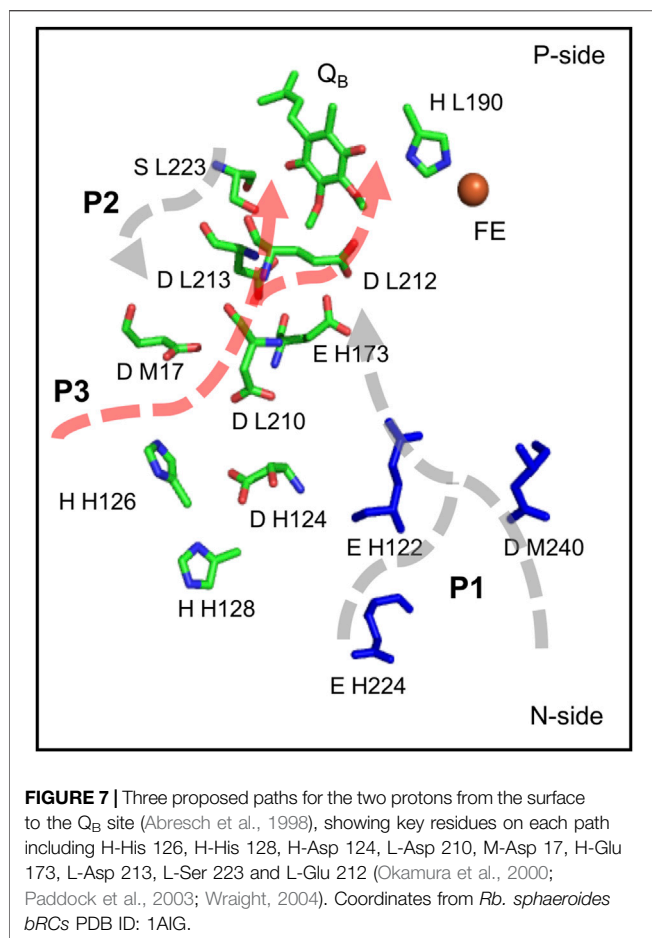
bRCs and PSII are Type II reaction centers where a fully reduced, QH_2 is the final product. The quinol dissociates into the membrane to serve as the substrate of the b_6f complex in oxygenic photosynthesis and the bc_1 complex in bacteria (Cardona et al., 2012; Cardona and Rutherford, 2019). The D1 and D2 subunits of PSII are related to the L and M subunits in bRCs (Raymond and Blankenship, 2004). The bacterial systems use a photon, in the range of 860–960 nm. Thus, they do not have enough energy to carry out the PSII reaction, which uses a 680 nm photon to fuel the uphill transfer of electrons from water to quinone (Heathcote et al., 2002). The primary electron donor in bRCs is periplasmic (P-side) cytochrome c. The redox reactions of cytochrome c are not coupled to proton binding/release. The overall reaction is:



In contrast to PSII, which has a very short distance to the N-side, bRCs have an H subunit, capping the N-side of the protein, requiring a much longer path for the protons to reach the Q_B site (Figure 6).

Quinones as a model redox coupled proton transfer reactant. Electrons move one at a time between cofactors in proteins generating free radical intermediates. While some cofactors such as chlorophylls, hemes, iron sulfur clusters and Tyr are stable one electron redox cofactors, unpaired electrons are often sources of toxic reactive oxygen intermediates (Weisz et al., 2017). Quinones function as single electron donors/acceptors within proteins, but accumulate two electrons and protons (Paddock et al., 2003; Müh et al., 2012). These lipid soluble cofactors thus transport electrons from many proteins including PSII, bRCs and complex I described here to the bc_1 complex in mitochondria and bacteria or b_6f complexes in chloroplasts as electrons move down the electron transfer chains.

As quinones cycle between oxidized quinone (Q), semiquinone ($Q^{\bullet-}$) and fully reduced quinol (QH_2) their proton affinity changes. The quinone pK_a is <0 , it is <5 for the semiquinone (Zhu and Gunner, 2005; Gunner et al., 2008; Hasegawa et al., 2017). Hence, the anionic semiquinone is often the stable state within the protein. However, the generation of $Q^{\bullet-}$ can trigger proton binding to nearby residues (Graige et al., 1996; Abresch et al., 1998; Alexov and Gunner, 1999; Paddock et al., 2003). The pK_a s for the fully reduced quinol is >10 so the second Q_B reduction is coupled to binding two protons to the cofactor. The difference in the hydrogen bonding pattern for the two quinone carbonyls and two quinol hydroxyls promote quinone dissociation in PSII (Shevela et al., 2012; Saito et al., 2013). As will be described below, in Complex I quinone reduction leads to a



large conformational change that trigger proton pumping through distant pathways (Gupta et al., 2020; Gutiérrez-Fernández et al., 2020; Kampjut and Sazanov, 2020).

The quinone electrochemistry is modified within the protein, but the underlying proton affinity of each redox state in the isolated compound strongly influences the order in which protons are bound. The sequence of reactions in bRCs (Graige et al., 1996) and likely in PSII is: 1) Q_B is first reduced to the anionic semiquinone. The negative potential causes protons to be bound to nearby amino acids (Okamura and Feher, 1992; Wraight, 2006; Gunner et al., 2008); 2) uphill protonation of the semiquinone is the rate-determining step preceding the second reduction; 3) reduction is followed by binding a second proton and release of the quinol.

Proton transfer pathways to Q_B in bRCs. The proton transfer paths to Q_B have been well studied (Abresch et al., 1998; Okamura et al., 2000). These are different than those described above near the OEC, as residues play a much larger role in the network. However, they are similar in that there is a tangled complex of proton transfer paths. There is a large number of acidic and basic residues buried in the protein near Q_B that influence the electrochemistry of the quinone and provide paths for proton transfer (Figure 7) (Sebban et al., 1995; Lancaster et al., 1996; Abresch et al., 1998; Alexov and Gunner, 1999; Rabenstein

et al., 2000). FTIR difference spectra obtained on Q_A and Q_B reduction shows broad features characteristic of a polarized, interconnected hydrogen bonded network of water molecules and amino acids around the two quinones (Breton and Nabedryk, 1998). L-Asp 210 and Asp 213 may share a proton in the ground state, serving as a PLS. Protonating one of the acids removes a negative charge, stabilizing the semiquinone $Q_B^{\bullet-}$ and keeping a proton available for passage to the quinone itself (Lancaster et al., 1996; Alexov and Gunner, 1999; Ishikita et al., 2003). The mutants L-Asp213Asn and L-Ser223Ala slow the rate of this reaction, with the mutation of L-Asp 213 having a bigger impact (Paddock et al., 1994; Paddock et al., 1995). In the absence of L-Asp 213, H-Glu 173 may provide an alternative location for the proton in this extended PLS (Paddock et al., 2003). Thus, this web of acidic residues combines the functions of a cluster PLS and complex proton transfer path.

L-Glu 212, which is a protonated PLS in the ground state, provides the second proton to Q_B (Wraight, 2004). The pK_a of the Glu is ≈ 10 , trapping a proton near the quinone in the ground state ready when needed (Kleinfeld et al., 1984; Okamura and Feher, 1992). The mutant L-Glu212Gln does not affect the delivery of the first proton, supporting this site being neutral in the presence of Q_B^- . However, the transfer of the second proton is totally blocked, indicating L-Glu 212 is a unique single site PLS (Paddock et al., 1989; Shinkarev et al., 1993; P. H.; McPherson et al., 1994; Okamura et al., 2000; Wraight, 2004).

Three possible paths. The complex web of acidic and other polar residues near Q_B leads to the question of what is the route for proton transfer from the N-side surface to the quinone binding site. The crystal structures reveal three likely paths (Figure 7) (Abresch et al., 1998). The longest path, P1, is ≈ 20 Å long. It enters the protein near H-Asp 224 or M-Asp 240 and passes to L-Glu 212, which provides the second proton to Q_B . P2, also ≈ 20 Å long, starts near M-Tyr 3 and moves via H-Glu 173 to L-Asp 213, which donates the first proton to Q_B . P3 is the shortest path, with only ≈ 7 Å between L-Asp 213 and the surface M-Asp 17 with one water molecule in the middle (Abresch et al., 1998).

Surface PLS as a proton collection site. RCs also have a well characterized external cluster near the entrance to P3 made up of H-Asp 124, H-His 126, H-His 128. The cluster is a proposed proton collection site (Utschig et al., 1998; Paddock et al., 1999; Okamura et al., 2000) (Figure 7). Zn^{2+} or Cd^{2+} bind here and slow proton transfer to Q_B . Clusters of protonatable groups near the surface of proton transfer paths are found in other proteins. A similar proton accumulation site is found in the D-channel (Cai et al., 2018). The broad channel in PSII exits to a cluster of surface acidic residues that can trap the released proton (Bondar and Dau, 2012; Kaur et al., 2021).

P3 appears to carry protons in wild-type bRCs. Mutation of L-Asp 210 and M-Asp 17, have a larger impact when Zn^{2+} or Cd^{2+} are present, showing an additive effect of multiple changes to this pathway. However even with P3 blocked, protons still enter to Q_B , indicating that other routes can serve as pathways, but with slower transfer rates (Okamura et al., 2000). Thus, in the tangled potential proton transfer network, multiple paths are possible, but some are preferred.

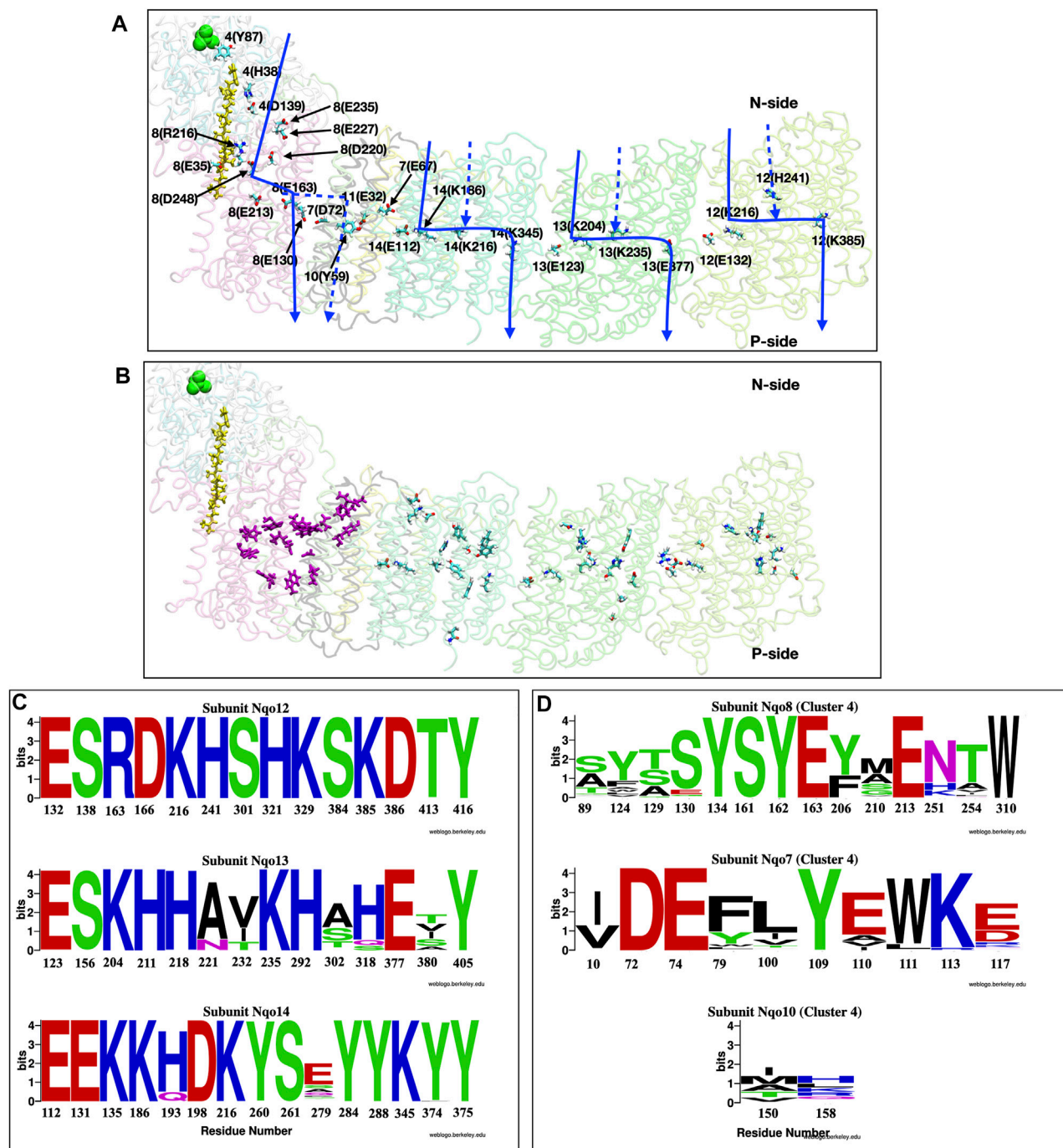


FIGURE 8 | (A,B) Structure of the full membrane domain of complex I and only the Nqo4 subunit of the periplasmic domain from *T. thermophilus* [PDB ID: 4HEA (Baradaran et al., 2013)] highlighting proton transfer paths. **(A)** Residues that have been proposed to be important for proton pumping are shown as sticks and labeled as subunit number (one letter amino acid designation-residue number). Quinone is yellow and N2 of each Iron Sulfur cluster is green. Approximate locations of putative proton transfer paths are blue arrows and dashed lines show alternative, proposed paths. **(B)** Residues that are included in the conservation analysis. Purple sticks: E channel cluster in the center of the protein [Cluster 4 in (Khaniya et al., 2020)]; Sticks colored by atom type: antiporter residues (Baradaran et al., 2013; Di Luca et al., 2017; Haapanen and Sharma, 2017; Gutiérrez-Fernández et al., 2020). **(C,D)** Conservation analysis shown as Weblogo (Crooks, 2004) representation of multiple sequence alignment of 1,000 complex I sequences (Johnson et al., 2008; Sievers et al., 2011). **(C)** Residues in the three linear antiporter pathways in Nqo12 (Top), Nqo13 (Middle) and Nqo14 (Bottom) subunits. **(D)** Residues in the E-channel cluster 4. Residues from Nqo8 (Top), Nqo7 (Middle) and Nqo10 (Bottom).

NADH-UBIQUINONE OXIDOREDUCTASE (COMPLEX I)

Complex I is the first and the largest protein in the aerobic respiratory electron transfer chain of bacteria and mitochondria (Brandt et al., 2003; Hirst, 2013; Sazanov, 2015; Kaila, 2018). Within the protein electrons are transferred from NADH to a flavin and through a series of Iron Sulfur (FeS) complexes to a quinone (Verkhovskaya et al., 2008; Efremov et al., 2010; Hirst, 2013; Zickermann et al., 2015). The overall reaction is:



The quinone, Q, is often ubiquinone but can be menaquinone in bacteria such as *Thermus thermophilus*, the source of the protein for the first complete crystal structure (Baradaran et al., 2013). The transfer of the two electrons, which occurs in the N-side peripheral arm, leads to the pumping of four protons from the N- to P-side of the membrane embedded portion of the protein (Figure 8).

Complex I combines elements of two disparate proteins. The long, peripheral arm is likely derived from a soluble hydrogenase and three of the proton channels are related to Mrp Na-H antiporters (denoted antiporter channels), however, the fourth, E-channel, is unique to Complex I and its close relatives (Efremov and Sazanov, 2012; Brandt, 2019). Complex I is remarkable, as the tightly coupled electron transfer and proton pumping elements are separated by as much as 300 Å from the NADH binding site, at the end of the peripheral arm, to the distal proton pumping subunit (Baradaran et al., 2013; Kaila, 2018). Quinone binding and reduction lead to a rotation of the soluble arm that connects the redox reactions to proton pumping in some way (Gupta et al., 2020; Gutiérrez-Fernández et al., 2020; Kampjut and Sazanov, 2020).

Antiporter: simple pathway. Complex I provides examples of both simple and complex proton transfer pathways. There are four proton paths, three through the antiporter subunits and one through the E-channel (Hirst, 2013; Ripple et al., 2013; Sazanov, 2015; Di Luca et al., 2017; Haapanen and Sharma, 2018; Saura and Kaila, 2019). The crystal structures show likely, linear paths through each antiporter subunit (Efremov and Sazanov, 2011; Baradaran et al., 2013; Zickermann et al., 2015) which have chain of well conserved acidic and basic residues in the center running parallel to the membrane (Figures 8A,B) (Fearnley and Walker, 1992; Torres-Bacete et al., 2007; Efremov and Sazanov, 2012). Recognizable water chains leading to the N- and P-sides are seen in computational studies (Kaila et al., 2014; Di Luca et al., 2017; Haapanen and Sharma, 2017; Röpke et al., 2020). Moving along each pathway from the N-side is a Glu/Lys pair then a central Lys followed by either a Lys or Glu (Baradaran et al., 2013; Kaila, 2018). Their protonation states change as the proton is handed from one ionizable residue to the next. Thus, the antiporter channels are simple linear proton transfer paths.

With a linear proton transfer path, it is often possible to identify a unique gating element. Simulations have been carried out to investigate the behavior of Complex I with different protonation states for these residues (Kaila et al., 2014; Di

Luca et al., 2017; Haapanen and Sharma, 2017). Increasing the net charge in the interior leads to water molecules being brought into the protein in MD trajectories and they are expelled when the charges are neutralized (Kaila et al., 2014; Hummer and Wikström, 2016; Di Luca et al., 2017). These hydration/dehydration changes will gate proton transfer through the channels, similar to that described above for Asp96 in bR. They can be validated by seeing waters in different locations in structures trapped in different intermediates or by interpretation of IR spectroscopy (Lórenz-Fonfría et al., 2008). However, a buried charge will attract water in MD simulations so it is important that the residue protonation states be correctly assigned in the simulation (Hummer and Wikström, 2016).

Comparison of the structures of Complex I from different organisms shows conservation of the P-side proton release paths in the antiporter subunits. However, on the N-side MD studies (Kaila et al., 2014; Di Luca et al., 2017; Haapanen and Sharma, 2017) found a pathway similar to one identified in the crystal structure of *Y. lipolytica* (Zickermann et al., 2015) Complex I but different from the one proposed from the *T. thermophilus* (Sazanov, 2015) crystal structure. Thus, it is not known if the exit path is conserved. Similar changes in pathways through evolution are also found comparing A- and B-type CcO as will be described below.

E-channel: A complex proton transfer path. In contrast to the linear proton transfer path seen through the three antiporter subunits, the fourth proton travels through a path directly under the periplasmic arm denoted the E-channel. This region has a web of water molecules and polar and protonatable residues characteristic of a complex proton transfer path with several PLS clusters (Di Luca et al., 2017; Saura and Kaila, 2019; Gutiérrez-Fernández et al., 2020; Khaniya et al., 2020). There are several competing proposals for the proton transfer path through the E-channel. It has been suggested to use subunits Nqo10 and Nqo11 (Efremov and Sazanov, 2011; Zickermann et al., 2015) or subunit Nqo8 (Baradaran et al., 2013). Various computational studies also provide different answers (Kaila et al., 2014; Di Luca et al., 2017; Haapanen and Sharma, 2017). This uncertainty about the route is characteristic of complex proton transfer paths. There is a growing consensus that residues in subunits Nqo7, 8, 10 and 11 are important for E-channel function (Figure 8A). Network analysis, which can accommodate complexity, has proposed a complete path through subunit Nqo4 and Nqo8 at the N-side entry, moving through subunit Nqo8 and Nqo7 in the center, and exiting through subunit Nqo10 and Nqo11 (Khaniya et al., 2020).

Role of quinone in Complex I as a gate. Complex I is able to couple the energy releasing redox reactions in the peripheral arm to the energy requiring proton pumping through four, distant well separated pumping sites (Baradaran et al., 2013; Kaila, 2018). The quinone binding site in complex I is ≈25–30 Å above the membrane surface, which is different from its location in any other quinone dependent membrane protein (Baradaran et al., 2013; Zickermann et al., 2015). Quinone binding leads to the rotation and tilt of the peripheral arm (Gutiérrez-Fernández et al., 2020). MD simulations (Gamiz-Hernandez et al., 2017; Warnau et al., 2018; Gupta et al., 2020) and Monte Carlo sampling (Khaniya et al., 2020) find changes in the connectivity of the hydrogen bond network that depend on the presence and redox

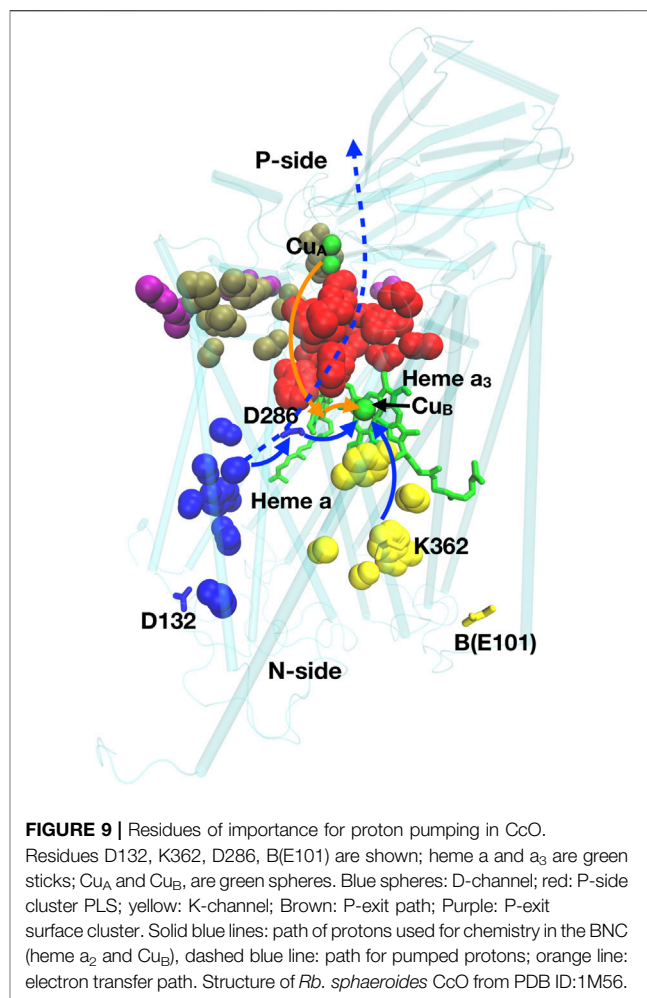
state of the quinone. Movement of subunit Nqo4 and Nqo8 leads to changes in the E-channel hydrogen bond network that propagate into the first antiporter channel by a distortion near Nqo10 (Tyr 59) (Gutiérrez-Fernández et al., 2020). The shifts in hydrogen bond network and residue protonation initiated by the quinone reactions thus yield changes in the interaction between the key Glu/Lys residues in the very distant antiporter channels (Efremov and Sazanov, 2011; Kampjut and Sazanov, 2020). This web of long-range communication is not needed in smaller proteins such as CcO, described below, where the change in electrostatic potential due to the redox reactions can directly modify PLS proton affinity coupled to proton pumping.

MD trajectories show quinone binding influences the E-channel by enriching the number of hydrogen bonds near the N-side, which are proposed to open the channel for proton uptake (Gupta et al., 2020; Khaniya et al., 2020). However, when QH₂ is bound the charge of conserved residues change leading to modification of the water wires in the proton transfer channels (Gamiz-Hernandez et al., 2017; Kaila, 2018). The E-channel central region has extended clusters of protonatable residues including Nqo7 (Asp 72), 8 (Glu 130), 8 (Glu 163), 8 (Glu 213) (Khaniya et al., 2020) [the nomenclature uses residue numbering from the *T. thermophilus* complex I in the form as Nqo subunit (residues)].

Beyond the central cluster of polar residues there is a hydrophobic barrier that blocks the proton transfer to the P-side in the E-channel. Thus, while there have been several studies of the proton entry, connections are rarely drawn from the center to the P-side (Baradaran et al., 2013; Kaila et al., 2014; Zickermann et al., 2015; Di Luca et al., 2017; Haapanen and Sharma, 2017). Network analysis of the hydrogen bonds made in MD trajectories suggests several paths that rely on transient wetting events (Khaniya et al., 2020). One lies near Nqo7 (Tyr 7) and 8 (Tyr 124). Another possibility is from Nqo8 (Glu 130) to 10 (Tyr 59) (Gutiérrez-Fernández et al., 2020; Steiner and Sazanov, 2020). However, these proposed bridging residues are not well conserved. Thus, what permits the proton to cross the hydrophobic barrier, and whether it conserved through Complex I evolution, is still an open question. A similar hydrophobic barrier is also seen in the voltage-sensing domain (VSD) of voltage-gated ion channels. Here mutations of the hydrophobic residues make the system leaky, showing the importance of non-polar residues to block uncontrolled proton transfers (Banh et al., 2019).

Residue conservation. The conservation and sensitivity of residues to mutation can provide evidence that there is a unique pathway for protons. The multisequence alignment of the residues in the linear paths through the three antiporter subunits (Baradaran et al., 2013; Di Luca et al., 2017; Haapanen and Sharma, 2017; Gutiérrez-Fernández et al., 2020) were compared with that found for the central cluster in the complex E-channel pathway (cluster 4 residues) (Khaniya et al., 2020). The WebLogo (Crooks, 2004) provides a graphical comparison of the results (Figures 8C,D). The residues along the linear antiporter paths are highly conserved. In contrast, the E-channel central cluster shows much weaker conservation, suggesting that, while the cluster as a whole must function, individual residues may not be uniquely important.

Mutation The sensitivity to mutation may also distinguish linear from complex proton transfer paths. Thus, mutation of

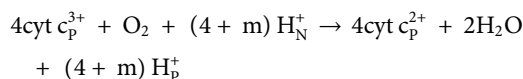


residues along a linear path should severely impair activity. In contrast, a complex path may be less sensitive as there are multiple routes for the proton, though as shown above for bRCs, not all need be equally favorable. Many of the residues in the well-defined antiporter channels have been subjected to site-directed mutations. Mutation of the residues shown in (Figure 8A) severely reduce quinone oxidoreductase activity that is tightly coupled to proton transfer since there is no alternative paths for proton transport (Torres-Bacete et al., 2007; Euro et al., 2008; Michel et al., 2011). However, the E-channel is more complex and there is less consensus about the path. Mutations of proposed E-channel residues often modify but do not kill activity (Taylor et al., 2002; Yang et al., 2009).

CYTOCHROME C OXIDASE

CcO is a proton pump belonging to the heme-copper oxidase superfamily (Kaila et al., 2010; Liang et al., 2017; Kaur et al., 2019). The energy for proton pumping comes from electrons from cytochrome c (Cyt c) reducing O₂ to water in the binuclear (Heme & Cu) center (BNC), located in the protein center (Figure 9). The BNC is reduced stepwise, one at a time to

store four electrons. O₂ reduction takes place in one step in the fully reduced BNC (Kaila et al., 2010; Cai et al., 2020). O₂ production likewise takes place in one step in the fully oxidized OEC of PSII. This mechanism protects against the release of toxic reactive oxygen intermediates. The overall reaction is:



Four electrons come from the cytochrome c on the P-side, and four protons from the N-side to the BNC for chemistry. *m* is the number of protons pumped across the membrane. There are several related classes of CcO, denoted A, B and C. The A-type CcO is found from bacteria to mammals, while B- and C-type are found in bacteria that live at low O₂ levels. In the A-type CcO, *m* = 4. B- and C- type CcOs differ in the types of heme used and in the number of protons pumped/electron, with *m* generally less than four (Lee et al., 2012). CcO provides examples of simple and complex proton transfer paths and simple and cluster PLS as well as a gate generated by hydration/dehydration changes.

Proton transfer paths through CcO. In the A-type CcO two linear water filled channels (D- and K-channels) are seen. Each has an essential ionizable residue at the entry on the N-side and at the end near the BNC, but none within the channels. The D-channel has Asp 132 at the entry and the essential, isolated Glu 286 as the PLS (Wikström et al., 2000; Brändén et al., 2001). The K channel has Lys 362 near the BNC and B-Glu 101 near the entry (Ma et al., 1999; Brändén et al., 2002). The buried Glu and Lys are both isolated in hydrophobic parts of the protein. In the ground states, their proton affinity has shifted so both are neutral (*Rb. sphaeroides* CcO numbering used here).

The D-channel carries six of the eight protons in the A-type CcO reaction cycle, while the K-channel carries two. At the center of CcO is heme a and heme a₃ and Cu_B of the active site BNC. As the retinal does in bR, the large cofactors may help to block proton transfer through the protein. The protons from the K channel exit into the BNC to be added to the reduced product water, while the D channel exits between the two hemes. The importance of these linear pathways were demonstrated by mutation of the residues at the beginning and end of the channels leading to loss of activity (Jünemann et al., 1997; Qian et al., 1997; Mills and Ferguson-Miller, 2002). Oddly, the D-channel is missing in B- and C-type CcOs, with only a K-channel remaining (Lee et al., 2012). Thus, as suggested in complex I, proton transfer paths may shift through evolution. In the B- and C- type CcOs it remains unclear how the pumped protons move around the active site to be delivered to the P-side.

Complex proton transfer pathways. The P-side of all CcOs has a tangled cluster of strongly interacting polar and protonatable residues that do not provide an obvious single exit path, although linear paths have been suggested (Popović and Stuchebrukhov, 2005; Björck et al., 2019). The hydrogen bond network on the P-side of A- and B-type CcO, was analyzed using Monte Carlo sampling and network analysis (Cai et al., 2018; Cai et al., 2020). Calculations were initiated with experimental crystal structures as well as with snapshots from MD trajectories carried out in different redox states of the hemes and protonation states of key residues. This analysis recognized a linear proton transfer path through the D-channel in the A-type CcO. A very

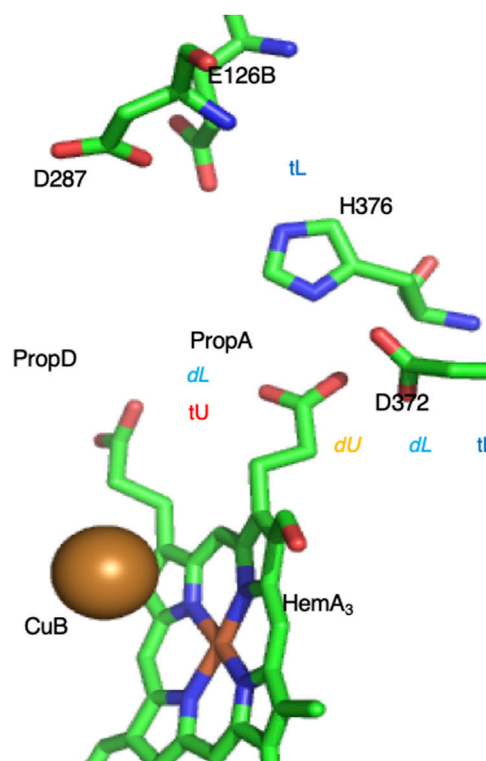


FIGURE 10 | Complex PLS on the P-side of the B-type CcO. The proton moves between Prop A [trapped unloaded (tU), with very low proton affinity] to D372 [dynamic unloaded (dU)] where electron transfer to Heme A₃ or Cu_B in the BNC active site 15 Å distant will lead to proton loading into the cluster (Cai et al., 2020). In the loaded state one proton is on D372. If the second proton is on PropA the system is dynamic (dL), so addition of a proton to the product water trapped in the BNC leads to the PLS unloading. If the second proton is on H386 the cluster proton affinity is too high to lose a proton (tL). The intra-cluster distances determine the relative energy of the loaded and unloaded tautomers. The crystal structure is likely trapped in the loaded state. Structure of *Th. thermophilus* CcO from PDB ID:3S8F.

large cluster of interconnected residues was identified as the P-side PLS (**Figure 9**). This cluster exits through several paths to a region near the cytochrome c binding site. Thus, there is an exit region not a unique exit for protons in this complex path.

Single residue PLS in CcO. Glu 286 is located at the top of the D-channel of A-type CcO (Kaila et al., 2010). It is isolated from other protonatable residues so forms a simple PLS. It plays an essential role, releasing a proton to the BNC for chemistry and to a P-side PLS cluster for pumping. The X-ray crystal structures show it is in a dry region and all simulation techniques give it a high proton affinity as there is nothing in the structure to stabilize an anionic residue (Hummer and Wikström, 2016). Measurements found a pK_a of ≈10 for turnover that is assigned to Glu286 (Namslaue et al., 2003). However, MD simulations showed protonation of a propionic acid in the P-side PLS breaks a hydrogen bond and opens a cavity which then fills with water (Goyal et al., 2013; Son et al., 2017).

The hydration of the water cavity near Glu 286 also serves as a gate for the proton transfer pathway. In the crystal structures and in protein equilibrated in MD trajectories without the water cavity

there is no exit found from the D-channel to the P-side PLS. Thus, the closed cavity blocks the backflow of protons (Cai et al., 2018). However, when the cavity is hydrated Glu 286 becomes well connected to the extensive PLS cluster on the P-side. Changes in hydration also help control the proton transfer from Glu 286 to the BNC (Wikström et al., 2003). Thus, hydration tunes the proton affinity of an isolated residue and serves as a gate in the proton transfer pathway, a pattern described for Asp 96 in bR and for the antiporter subunits in complex I.

The role of tautomer shifts in a complex PLS. A proton pump must regulate the thermodynamics of PLS loading and unloading, and then change proton affinity when the reaction progresses. This requires tuning the free energy difference between the loaded and unloaded states at the pH of interest as well as the shift in this value as the protein goes through the reaction cycle (See fuller description in **Supplementary Material S1**). The PLS must remain in the appropriate loaded/unloaded state until the reaction has progressed and the accessibility of N- and P-side is modified by the gates opening/closing (Kim et al., 2007; Kim et al., 2009; Kim and Hummer, 2012; Stuchebrukhov, 2018; Stuchebrukhov, 2019). The challenge is to find the changes that can trap, hold and then release the proton. An analysis of the proton distribution in the PLS cluster in B-type CcO provides some insight into the atomic details of one mechanism.

On the P-side of the B-type CcO, an extended cluster of six residues was found to behave as a PLS (**Figure 10**) (Cai et al., 2020). The unloaded PLS has one proton bound (net charge -4) while the loaded cluster has two protons. The protein surrounding the PLS provides sufficient long-range positive potential to stabilize the cluster negative charge. There are six tautomers with one proton and 12 with two protons distributed over the six residues (**Eq. 1**). By investigating the proton affinity of different tautomers in snapshots derived from MD trajectories it was found that a shift in the hydrogen bond pattern changes the tautomer selected. This resulted in dynamic states where a loaded and unloaded state are close in energy so changes at the active site lead to proton binding or release. However, the BNC is ≈ 15 Å from the PLS and the change in the BNC do not shift the PLS proton affinity enough to fully load a proton to the PLS cluster. This behavior is seen **Supplementary Figures S2A,B** when there is only a small shift in proton affinity in a group with a pK_a near the pH (**Supplementary Figure S2C**, middle titration). The problem of incomplete loading/unloading appears to be solved by moving the bound protons and rearranging the hydrogen bonding pattern, which is described as a tautomer trap. This leads to the PLS being trapped loaded or unloaded because the cluster proton affinity is either too high or too low (**Supplementary Figure S2C**, right-most titration) or unloaded (**Supplementary Figure S2C**, left-most titration).

The proton shift in the CcO complex PLS shows how a tautomer trap can solve the problem that a PLS, which is sensitive to changes in the protein, may not strongly trap the proton. Thus, in active structures, the change in proton affinity due to the BNC will lead to some changes in the PLS protonation state. But this shift in free energy is insufficient to reliably move the PLS between being fully loaded and unloaded (**Supplementary Figure S2**). Then a tautomer shift moves the PLS from the dynamic configuration (where the proton was bound or lost) to the stable, fully loaded or unloaded locked configuration. This mechanism may be similar to activation and inactivation process in

voltage gated ion channels, where conformational changes occur when the channels are an active open state, then block the channel and transit to inactive state (Aldrich, 2001). A tautomer trap is only available to a PLS cluster, it is not possible in a single residue PLS.

CONCLUSION

The structure of multiple proton transfer paths in several proteins that add to the transmembrane electrochemical gradient show a range of motifs. Thus, they can be simple linear paths as found in the D- and K- channels of CcO and the antiporter subunits of complex I. They can also be complex paths as seen on the P-side of CcO and the E-channel of complex I. Paths can be filled with water so that a proton never needs to use a side chain as found around the OEC in PSII or to be handed through a mixture of side chains and water molecules as found in GFP and in bRCs. With simple, single site PLS, as at the exit from the D-channel and the N-side of bR, changes far from the PLS trigger water influx that leads to proton release and production of a water chain to ferry protons. A similar mechanism is used in the antiporter subunits of complex I. In contrast, in the PLS cluster on the proton release side of bR and CcO, small, local rearrangements of a cluster of strongly interacting residues leads to large changes in proton affinity to cause the PLS to load and unload.

Thus, the framework that proteins will have proton transfer paths, Proton Loading Sites (PLS) and gates allows the analysis of each of these proteins. However, the motifs vary in the residues that make up the needed elements and in their complexity. Each proton pump reviewed here use structures with different complexity for different parts of the proton transfer paths. The advantages of different motifs remain to be determined.

AUTHOR CONTRIBUTIONS

DK, UK, YZ, and MG contributed to the draft preparation. DK, UK, and YZ contributed equally. MG reviewed and edited the manuscript.

FUNDING

The authors would like to acknowledge the funds from the Department of Energy Basic Energy Sciences grant number DE-SC0001423 and the National Science Foundation grant MCB-1519640.

ACKNOWLEDGMENTS

We would like to thank Xiuhong Cai and Junjun Mao for many helpful discussions.

SUPPLEMENTARY MATERIAL

The Supplementary Material for this article can be found online at: <https://www.frontiersin.org/articles/10.3389/fchem.2021.660954/full#supplementary-material>

REFERENCES

- Abresch, E. C., Paddock, M. L., Stowell, M. H. B., McPhillips, T. M., Axelrod, H. L., Soltis, S. M., et al. (1998). Identification of Proton Transfer Pathways in the X-ray crystal Structure of the Bacterial Reaction center from *Rhodobacter Sphaeroides*. *Photosyn. Res.* 55, 119–125. doi:10.1023/a:1006047519260
- Accardi, A., and Picollo, A. (2010). CLC Channels and Transporters: Proteins with Borderline Personalities. *Biochim. Biophys. Acta (Bba) - Biomembranes* 1798, 1457–1464. doi:10.1016/j.bbame.2010.02.022
- Agmon, N., Bakker, H. J., Campen, R. K., Henchman, R. H., Pohl, P., Roke, S., et al. (2016). Protons and Hydroxide Ions in Aqueous Systems. *Chem. Rev.* 116, 7642–7672. doi:10.1021/acs.chemrev.5b00736
- Agmon, N. (1995). The Grotthuss Mechanism. *Chem. Phys. Lett.* 244, 456–462. doi:10.1016/0009-2614(95)00905-J
- Aldrich, R. W. (2001). Fifty Years of Inactivation. *Nature* 411, 643–644. doi:10.1038/35079705
- Alexov, E. G., and Gunner, M. R. (1999). Calculated Protein and Proton Motions Coupled to Electron Transfer: Electron Transfer from QA-To QB in Bacterial Photosynthetic Reaction Centers†. *Biochemistry* 38, 8253–8270. doi:10.1021/bi982700a
- Allen, T. W., Andersen, O. S., and Roux, B. (2004). Energetics of Ion Conduction through the Gramicidin Channel. *Proc. Natl. Acad. Sci.* 101, 117–122. doi:10.1073/pnas.2635314100
- Amin, M., Pokhrel, R., Brudvig, G. W., Badawi, A., and Obayya, S. S. A. (2016). Effect of Chloride Depletion on the Magnetic Properties and the Redox Leveling of the Oxygen-Evolving Complex in Photosystem II. *J. Phys. Chem. B* 120, 4243–4248. doi:10.1021/acs.jpcc.6b03545
- Balashov, S. P. (2000). Protonation Reactions and Their Coupling in Bacteriorhodopsin. *Biochim. Biophys. Acta (Bba) - Bioenerg.* 1460, 75–94. doi:10.1016/S0005-2728(00)00131-6
- Banh, R., Cherny, V. V., Morgan, D., Musset, B., Thomas, S., Kulleperuma, K., et al. (2019). Hydrophobic Gasket Mutation Produces Gating Pore Currents in Closed Human Voltage-Gated Proton Channels. *Proc. Natl. Acad. Sci. U.S.A.* 116, 18951–18961. doi:10.1073/pnas.1905462116
- Baradaran, R., Berrisford, J. M., Minhas, G. S., and Sazanov, L. A. (2013). Crystal Structure of the Entire Respiratory Complex I. *Nature* 494, 443–448. doi:10.1038/nature11871
- Bashford, D., and Gerwert, K. (1992). Electrostatic Calculations of the pKa Values of Ionizable Groups in Bacteriorhodopsin. *J. Mol. Biol.* 224, 473–486. doi:10.1016/0022-2836(92)91009-e
- Baudry, J., Tajkhorshid, E., Molnar, F., Phillips, J., and Schulten, K. (2001). Molecular Dynamics Study of Bacteriorhodopsin and the Purple Membrane. *J. Phys. Chem. B* 105, 905–918. doi:10.1021/jp000898e
- Björck, M. L., Vilhjálmssdóttir, J., Hartley, A. M., Meunier, B., Näsvisk Öjemyr, L., Maréchal, A., et al. (2019). Proton-transfer Pathways in the Mitochondrial S. cerevisiae Cytochrome C Oxidase. *Sci. Rep.* 9, 20207. doi:10.1038/s41598-019-56648-9
- Blomberg, M. R. A., and Siegbahn, P. E. M. (2006). Quantum Chemistry Applied to the Mechanisms of Transition Metal Containing Enzymes-Cytochrome Oxidase, a Particularly Challenging Case. *J. Comput. Chem.* 27, 1373–1384. doi:10.1002/jcc.20448
- Bondar, A.-N., and Dau, H. (2012). Extended Protein/water H-Bond Networks in Photosynthetic Water Oxidation. *Biochim. Biophys. Acta (Bba) - Bioenerg.* 1817, 1177–1190. doi:10.1016/j.bbabi.2012.03.031
- Bondar, A.-N., Suhai, S., Fischer, S., Smith, J. C., and Elstner, M. (2007). Suppression of the Back Proton-Transfer from Asp85 to the Retinal Schiff Base in Bacteriorhodopsin: A Theoretical Analysis of Structural Elements. *J. Struct. Biol.* 157, 454–469. doi:10.1016/j.jsb.2006.10.007
- Bozdaganyan, M. E., Lokmatikov, A. V., Voskoboinikova, N., Cherepanov, D. A., Steinhoff, H.-J., Shaitan, K. V., et al. (2019). Proton Leakage across Lipid Bilayers: Oxygen Atoms of Phospholipid Ester Linkers Align Water Molecules into Transmembrane Water Wires. *Biochim. Biophys. Acta (Bba) - Bioenerg.* 1860, 439–451. doi:10.1016/j.bbabi.2019.03.001
- Brändén, M., Sigurdson, H., Namlauer, A., Gennis, R. B., Ädelroth, P., and Brzezinski, P. (2001). On the Role of the K-Proton Transfer Pathway in Cytochrome C Oxidase. *Proc. Natl. Acad. Sci.* 98, 5013–5018. doi:10.1073/pnas.081088398
- Brändén, M., Tomson, F., Gennis, R. B., and Brzezinski, P. (2002). The Entry Point of the K-Proton-Transfer Pathway in Cytochrome Oxidase†. *Biochemistry* 41, 10794–10798. doi:10.1021/bi026093+
- Brandt, U., Kersch, S., Dröse, S., Zwicker, K., and Zickermann, V. (2003). Proton Pumping by NADH:ubiquinone Oxidoreductase. A Redox Driven Conformational Change Mechanism? *FEBS Lett.* 545, 9–17. doi:10.1016/S0014-5793(03)00387-9
- Brandt, U. (2019). Adaptations of an Ancient Modular Machine. *Science* 363, 230–231. doi:10.1126/science.aaw0493
- Brejč, K., Sixma, T. K., Kitts, P. A., Kain, S. R., Tsien, R. Y., Ormo, M., et al. (1997). Structural Basis for Dual Excitation and Photoisomerization of the Aequorea victoria green Fluorescent Protein. *Proc. Natl. Acad. Sci.* 94, 2306–2311. doi:10.1073/pnas.94.6.2306
- Breton, J., and Nabeudryk, E. (1998). Proton Uptake upon Quinone Reduction in Bacterial Reaction Centers: IR Signature and Possible Participation of a Highly Polarizable Hydrogen Bond Network. *Photosyn. Res.* 55, 301–307. doi:10.1023/a:1005972514425
- Cai, X., Haider, K., Lu, J., Radic, S., Son, C. Y., Cui, Q., et al. (2018). Network Analysis of a Proposed Exit Pathway for Protons to the P-Side of Cytochrome C Oxidase. *Biochim. Biophys. Acta (Bba) - Bioenerg.* 1859, 997–1005. doi:10.1016/j.bbabi.2018.05.010
- Cai, X., Son, C. Y., Mao, J., Kaur, D., Zhang, Y., Khaniya, U., et al. (2020). Identifying the Proton Loading Site Cluster in the Ba Cytochrome C Oxidase that Loads and Traps Protons. *Biochim. Biophys. Acta (Bba) - Bioenerg.* 1861, 148239. doi:10.1016/j.bbabi.2020.148239
- Cardona, T., and Rutherford, A. W. (2019). Evolution of Photochemical Reaction Centres: More Twists? *Trends Plant Sci.* 24, 1008–1021. doi:10.1016/j.tplants.2019.06.016
- Cardona, T., Sedoud, A., Cox, N., and Rutherford, A. W. (2012). Charge Separation in Photosystem II: a Comparative and Evolutionary Overview. *Biochim. Biophys. Acta (Bba) - Bioenerg.* 1817, 26–43. doi:10.1016/j.bbabi.2011.07.012
- Chatteraj, M., King, B. A., Bublitz, G. U., and Boxer, S. G. (1996). Ultra-Fast Excited State Dynamics in Green Fluorescent Protein: Multiple States and Proton Transfer. *Proc. Natl. Acad. Sci.* 93, 8362–8367. doi:10.1073/pnas.93.16.8362
- Chrysina, M., Zahariou, G., Sanakis, Y., Ioannidis, N., and Petrouleas, V. (2011). Conformational Changes of the Intermediate of the S2 to S3 Transition in Photosystem II. *J. Photochem. Photobiol. B: Biol.* 104, 72–79. doi:10.1016/j.jphotobiol.2011.02.012
- Chrysina, M., de Mendonça Silva, J. C., Zahariou, G., Pantazis, D. A., and Ioannidis, N. (2019). Protein Translocation via Tautomerization of Asn298 during the S2-S3 State Transition in the Oxygen-Evolving Complex of Photosystem II. *J. Phys. Chem. B* 123, 3068–3078. doi:10.1021/acs.jpcc.9b02317
- Clemens, M., Phatak, P., Cui, Q., Bondar, A.-N., and Elstner, M. (2011). Role of Arg82 in the Early Steps of the Bacteriorhodopsin Proton-Pumping Cycle. *J. Phys. Chem. B* 115, 7129–7135. doi:10.1021/jp201865k
- Cox, N., Pantazis, D. A., Neese, F., and Lubitz, W. (2013). Biological Water Oxidation. *Acc. Chem. Res.* 46, 1588–1596. doi:10.1021/ar3003249
- Crooks, G. E. (2004). WebLogo: A Sequence Logo Generator. *Genome Res.* 14, 1188–1190. doi:10.1101/gr.849004
- Cukierman, S. (2000). Proton Mobilities in Water and in Different Stereoisomers of Covalently Linked Gramicidin A Channels. *Biophysical J.* 78, 1825–1834. doi:10.1016/S0006-3495(00)76732-4
- Cukierman, S. (2006). Et Tu, Grotthuss! and Other Unfinished Stories. *Biochim. Biophys. Acta (Bba) - Bioenerg.* 1757, 876–885. doi:10.1016/j.bbabi.2005.12.001
- Daldrop, J. O., Saita, M., Heyden, M., Lorenz-Fonfria, V. A., Heberle, J., and Netz, R. R. (2018). Orientation of Non-spherical Protonated Water Clusters Revealed by Infrared Absorption Dichroism. *Nat. Commun.* 9, 311. doi:10.1038/s41467-017-02669-9
- de Grotthuss, C. J. T. (2006). Memoir on the Decomposition of Water and of the Bodies that it Holds in Solution by Means of Galvanic Electricity. *Biochim. Biophys. Acta (Bba) - Bioenerg.* 1757, 871–875. doi:10.1016/j.bbabi.2006.07.004
- Debus, R. J. (2014). Evidence from FTIR Difference Spectroscopy that D1-Asp61 Influences the Water Reactions of the Oxygen-Evolving Mn4CaO5 Cluster of Photosystem II. *Biochemistry* 53, 2941–2955. doi:10.1021/bi500309f

- Debus, R. J. (2015). FTIR Studies of Metal Ligands, Networks of Hydrogen Bonds, and Water Molecules Near the Active Site Mn₄CaO₅ Cluster in Photosystem II. *Biochim. Biophys. Acta (Bba) - Bioenerg.* 1847, 19–34. doi:10.1016/j.bbabbio.2014.07.007
- DeCoursey, T. E., and Hosler, J. (2014). Philosophy of Voltage-Gated Proton Channels. *J. R. Soc. Interf.* 11, 20130799. doi:10.1098/rsif.2013.0799
- Decoursey, T. E. (2003). Voltage-Gated Proton Channels and Other Proton Transfer Pathways. *Physiol. Rev.* 83, 475–579. doi:10.1152/physrev.00028.2002
- Deisenhofer, J., Epp, O., Miki, K., Huber, R., and Michel, H. (1985). Structure of the Protein Subunits in the Photosynthetic Reaction centre of Rhodospseudomonas Viridis at 3 Å Resolution. *Nature* 318, 618–624. doi:10.1038/318618a0
- Di Donato, M., van Wilderen, L. J. G. W., Van Stokkum, I. H. M., Stuart, T. C., Kennis, J. T. M., Hellingwerf, K. J., et al. (2011). Proton Transfer Events in GFP. *Phys. Chem. Chem. Phys.* 13, 16295. doi:10.1039/c1cp20387h
- Di Luca, A., Gamiz-Hernandez, A. P., and Kaila, V. R. I. (2017). Symmetry-related Proton Transfer Pathways in Respiratory Complex I. *Proc. Natl. Acad. Sci. U.S.A.* 114, E6314–E6321. doi:10.1073/pnas.1706278114
- Donati, G., Petrone, A., Caruso, P., and Rega, N. (2018). The Mechanism of a green Fluorescent Protein Proton Shuttle Unveiled in the Time-Resolved Frequency Domain by Excited State Ab Initio Dynamics. *Chem. Sci.* 9, 1126–1135. doi:10.1039/C7SC02803B
- Dorman, V. L., and Jordan, P. C. (2004). Ionic Permeation Free Energy in Gramicidin: A Semimicroscopic Perspective. *Biophysical J.* 86, 3529–3541. doi:10.1529/biophysj.103.039214
- Duster, A. W., and Lin, H. (2019). Tracking Proton Transfer through Titratable Amino Acid Side Chains in Adaptive QM/MM Simulations. *J. Chem. Theor. Comput.* 15, 5794–5809. doi:10.1021/acs.jctc.9b00649
- Edmonds, B. W., and Luecke, H. (2004). Atomic Resolution Structures and the Mechanism of Ion Pumping in Bacteriorhodopsin. *Front. Biosci.* 9, 1556–1566. doi:10.2741/1264
- Efremov, R. G., and Sazanov, L. A. (2011). Structure of the Membrane Domain of Respiratory Complex I. *Nature* 476, 414–420. doi:10.1038/nature10330
- Efremov, R. G., and Sazanov, L. A. (2012). The Coupling Mechanism of Respiratory Complex I - A Structural and Evolutionary Perspective. *Biochim. Biophys. Acta (Bba) - Bioenerg.* 1817, 1785–1795. doi:10.1016/j.bbabbio.2012.02.015
- Efremov, R. G., Baradaran, R., and Sazanov, L. A. (2010). The Architecture of Respiratory Complex I. *Nature* 465, 441–445. doi:10.1038/nature09066
- Euro, L., Belevich, G., Verkhovskiy, M. I., Wikström, M., and Verkhovskaya, M. (2008). Conserved Lysine Residues of the Membrane Subunit NuoM Are Involved in Energy Conversion by the Proton-Pumping NADH:ubiquinone Oxidoreductase (Complex I). *Biochim. Biophys. Acta (Bba) - Bioenerg.* 1777, 1166–1172. doi:10.1016/j.bbabbio.2008.06.001
- Farahvash, A., and Stuchebrukhov, A. (2018). Investigating the Many Roles of Internal Water in Cytochrome C Oxidase. *J. Phys. Chem. B* 122, 7625–7635. doi:10.1021/acs.jpcc.7b11920
- Fearnley, I. M., and Walker, J. E. (1992). Conservation of Sequences of Subunits of Mitochondrial Complex I and Their Relationships with Other Proteins. *Biochim. Biophys. Acta (Bba) - Bioenerg.* 1140, 105–134. doi:10.1016/0005-2728(92)90001-I
- Fitch, C. A., Platzer, G., Okon, M., Garcia-Moreno E., B. B., and McIntosh, L. P. (2015). Arginine: Its pK_a Revisited. *Protein Sci.* 24, 752–761. doi:10.1002/pro.2647
- Fowler, P. W., Orwick-Rydmark, M., Radestock, S., Solcan, N., Dijkman, P. M., Lyons, J. A., et al. (2015). Gating Topology of the Proton-Coupled Oligopeptide Symporters. *Structure* 23, 290–301. doi:10.1016/j.str.2014.12.012
- Freier, E., Wolf, S., and Gerwert, K. (2011). Proton Transfer via a Transient Linear Water-Molecule Chain in a Membrane Protein. *Proc. Natl. Acad. Sci.* 108, 11435–11439. doi:10.1073/pnas.1104735108
- Futai, M., Nakanishi-Matsui, M., Okamoto, H., Sekiya, M., and Nakamoto, R. K. (2012). Rotational Catalysis in Proton Pumping ATPases: From *E. coli* F₁-ATPase to Mammalian V-ATPase. *Biochim. Biophys. Acta (Bba) - Bioenerg.* 1817, 1711–1721. doi:10.1016/j.bbabbio.2012.03.015
- Gamiz-Hernandez, A. P., Jussupow, A., Johansson, M. P., and Kaila, V. R. I. (2017). Terminal Electron-Proton Transfer Dynamics in the Quinone Reduction of Respiratory Complex I. *J. Am. Chem. Soc.* 139, 16282–16288. doi:10.1021/jacs.7b08486
- Ge, X., and Gunner, M. R. (2016). Unraveling the Mechanism of Proton Translocation in the Extracellular Half-Channel of Bacteriorhodopsin. *Proteins* 84, 639–654. doi:10.1002/prot.25013
- Gerwert, K., Freier, E., and Wolf, S. (2014). The Role of Protein-Bound Water Molecules in Microbial Rhodopsins. *Biochim. Biophys. Acta (Bba) - Bioenerg.* 1837, 606–613. doi:10.1016/j.bbabbio.2013.09.006
- Goings, J. J., Li, P., Zhu, Q., and Hammes-Schiffer, S. (2020). Formation of an Unusual Glutamine Tautomer in a Blue Light Using Flavin Photocycle Characterizes the Light-Adapted State. *Proc. Natl. Acad. Sci. USA* 117, 26626–26632. doi:10.1073/pnas.2016719117
- Goyal, P., Lu, J., Yang, S., Gunner, M. R., and Cui, Q. (2013). Changing Hydration Level in an Internal Cavity Modulates the Proton Affinity of a Key Glutamate in Cytochrome C Oxidase. *Proc. Natl. Acad. Sci.* 110, 18886–18891. doi:10.1073/pnas.1313908110
- Graige, M. S., Paddock, M. L., Bruce, J. M., Feher, G., and Okamura, M. Y. (1996). Mechanism of Proton-Coupled Electron Transfer for Quinone (QB) Reduction in Reaction Centers of *Rb. Sphaeroides*. *J. Am. Chem. Soc.* 118, 9005–9016. doi:10.1021/ja960056m
- Gray, H. B., and Winkler, J. R. (2003). Electron Tunneling through Proteins. *Quart. Rev. Biophys.* 36, 341–372. doi:10.1017/S0033583503003913
- Gunner, M. R., and Koder, R. (2017). The Design Features Cells Use to Build Their Transmembrane Proton Gradient. *Phys. Biol.* 14, 013001. doi:10.1088/1478-3975/14/1/013001
- Gunner, M. R., Mao, J., Song, Y., and Kim, J. (2006). Factors Influencing the Energetics of Electron and Proton Transfers in Proteins. What Can Be Learned from Calculations. *Biochim. Biophys. Acta (Bba) - Bioenerg.* 1757, 942–968. doi:10.1016/j.bbabbio.2006.06.005
- Gunner, M. R., Madeo, J., and Zhu, Z. (2008). Modification of Quinone Electrochemistry by the Proteins in the Biological Electron Transfer Chains: Examples from Photosynthetic Reaction Centers. *J. Bioenerg. Biomembr.* 40, 509–519. doi:10.1007/s10863-008-9179-1
- Gunner, M. R., Amin, M., Zhu, X., and Lu, J. (2013). Molecular Mechanisms for Generating Transmembrane Proton Gradients. *Biochim. Biophys. Acta (Bba) - Bioenerg.* 1827, 892–913. doi:10.1016/j.bbabbio.2013.03.001
- Gunner, M. R., Murakami, T., Rustenburg, A. S., Isik, M., and Chodera, J. D. (2020). Standard State Free Energies, Not pK_as, Are Ideal for Describing Small Molecule Protonation and Tautomeric States. *J. Comput. Aided Mol. Des.* 34, 561–573. doi:10.1007/s10822-020-00280-7
- Gupta, C., Khaniya, U., Chan, C. K., Dehez, F., Shekhar, M., Gunner, M. R., et al. (2020). Charge Transfer and Chemo-Mechanical Coupling in Respiratory Complex I. *J. Am. Chem. Soc.* 142, 9220–9230. doi:10.1021/jacs.9b13450
- Gutiérrez-Fernández, J., Kaszuba, K., Minhas, G. S., Baradaran, R., Tambalo, M., Gallagher, D. T., et al. (2020). Key Role of Quinone in the Mechanism of Respiratory Complex I. *Nat. Commun.* 11, 4135. doi:10.1038/s41467-020-17957-0
- Haapanen, O., and Sharma, V. (2017). Role of Water and Protein Dynamics in Proton Pumping by Respiratory Complex I. *Sci. Rep.* 7, 7747. doi:10.1038/s41598-017-07930-1
- Haapanen, O., and Sharma, V. (2018). A Modeling and Simulation Perspective on the Mechanism and Function of Respiratory Complex I. *Biochim. Biophys. Acta (Bba) - Bioenerg.* 1859, 510–523. doi:10.1016/j.bbabbio.2018.04.001
- Hammes-Schiffer, S. (2001). Theoretical Perspectives on Proton-Coupled Electron Transfer Reactions. *Acc. Chem. Res.* 34, 273–281. doi:10.1021/ar990117
- Hasegawa, R., Saito, K., Takaoka, T., and Ishikita, H. (2017). pK_a of Ubiquinone, Menaquinone, Phylloquinone, Plastoquinone, and Rhodoquinone in Aqueous Solution. *Photosynth. Res.* 133, 297–304. doi:10.1007/s11120-017-0382-y
- Hasegawa, N., Jonotsuka, H., Miki, K., and Takeda, K. (2018). X-ray Structure Analysis of Bacteriorhodopsin at 1.3 Å Resolution. *Sci. Rep.* 8, 13123. doi:10.1038/s41598-018-31370-0
- Heathcote, P., Fyfe, P. K., and Jones, M. R. (2002). Reaction Centres: the Structure and Evolution of Biological Solar Power. *Trends Biochem. Sci.* 27, 79–87. doi:10.1016/s0968-0004(01)02034-5
- Hirai, T., Subramaniam, S., and Lanyi, J. K. (2009). Structural Snapshots of Conformational Changes in a Seven-helix Membrane Protein: Lessons from Bacteriorhodopsin. *Curr. Opin. Struct. Biol.* 19, 433–439. doi:10.1016/j.sbi.2009.07.009
- Hirst, J. (2013). Mitochondrial Complex I. *Annu. Rev. Biochem.* 82, 551–575. doi:10.1146/annurev-biochem-070511-103700

- Hummer, G., and Wikström, M. (2016). Molecular Simulation and Modeling of Complex I. *Biochim. Biophys. Acta (Bba) - Bioenerg.* 1857, 915–921. doi:10.1016/j.bbabi.2016.01.005
- Ikeda, T., Saito, K., Hasegawa, R., and Ishikita, H. (2017). The Existence of an Isolated Hydronium Ion in the Interior of Proteins. *Angew. Chem.* 129, 9279–9282. doi:10.1002/ange.201705512
- Ishikita, H., and Saito, K. (2014). Proton Transfer Reactions and Hydrogen-Bond Networks in Protein Environments. *J. R. Soc. Interf.* 11, 20130518. doi:10.1098/rsif.2013.0518
- Ishikita, H., Morra, G., and Knapp, E.-W. (2003). Redox Potential of Quinones in Photosynthetic Reaction Centers from Rhodospirillum rubrum: Dependence on Protonation of Glu-L212 and Asp-L213. *Biochemistry* 42, 3882–3892. doi:10.1021/bi026781t
- Ishikita, H., Saenger, W., Loll, B., Biesiadka, J., and Knapp, E.-W. (2006). Energetics of a Possible Proton Exit Pathway for Water Oxidation in Photosystem II. *Biochemistry* 45, 2063–2071. doi:10.1021/bi051615h
- Isobe, H., Shoji, M., Shen, J.-R., and Yamaguchi, K. (2015). Strong Coupling between the Hydrogen Bonding Environment and Redox Chemistry during the S2 to S3 Transition in the Oxygen-Evolving Complex of Photosystem II. *J. Phys. Chem. B* 119, 13922–13933. doi:10.1021/acs.jpcc.5b05740
- Johnson, M., Zaretskaya, I., Raytselis, Y., Merezhuk, Y., McGinnis, S., and Madden, T. L. (2008). NCBI BLAST: a Better Web Interface. *Nucleic Acids Res.* 36, W5–W9. doi:10.1093/nar/gkn201
- Jünemann, S., Meunier, B., Gennis, R. B., and Rich, P. R. (1997). Effects of Mutation of the Conserved Lysine-362 in Cytochrome Oxidase from Rhodospirillum rubrum. *Biochemistry* 36, 14456–14464. doi:10.1021/bi971458p
- Kaila, V. R. I., and Hummer, G. (2011). Energetics of Direct and Water-Mediated Proton-Coupled Electron Transfer. *J. Am. Chem. Soc.* 133, 19040–19043. doi:10.1021/ja2082262
- Kaila, V. R. I., Verkhovsky, M. I., and Wikström, M. (2010). Proton-coupled Electron Transfer in Cytochrome Oxidase. *Chem. Rev.* 110, 7062–7081. doi:10.1021/cr1002003
- Kaila, V. R. I., Wikström, M., and Hummer, G. (2014). Electrostatics, Hydration, and Proton Transfer Dynamics in the Membrane Domain of Respiratory Complex I. *Proc. Natl. Acad. Sci.* 111, 6988–6993. doi:10.1073/pnas.1319156111
- Kaila, V. R. I. (2018). Long-range Proton-Coupled Electron Transfer in Biological Energy Conversion: towards Mechanistic Understanding of Respiratory Complex I. *J. R. Soc. Interf.* 15, 20170916. doi:10.1098/rsif.2017.0916
- Kampjut, D., and Sazanov, L. A. (2020). The Coupling Mechanism of Mammalian Respiratory Complex I. *Science* 370, eabc4209. doi:10.1126/science.abc4209
- Kannt, A., D. Lancaster, C. R., and Michel, H. (1998). The Role of Electrostatic Interactions for Cytochrome C Oxidase Function. *J. Bioenerg. Biomembr.* 30, 81–87. doi:10.1023/A:1020563629032
- Kaur, D., Cai, X., Khaniya, U., Zhang, Y., Mao, J., Mandal, M., et al. (2019). Tracing the Pathways of Waters and Protons in Photosystem II and Cytochrome C Oxidase. *Inorganics* 7, 14. doi:10.3390/inorganics7020014
- Kaur, D., Zhang, Y., Reiss, K. M., Mandal, M., Brudvig, G. W., Batista, V. S., et al. (2021). Proton Exit Pathways Surrounding the Oxygen Evolving Complex of Photosystem II. *Biochim. Biophys. Acta Bioenerg.* 1862, 148446. doi:10.1016/j.bbabi.2021.148446
- Kelkar, D. A., and Chattopadhyay, A. (2007). The Gramicidin Ion Channel: A Model Membrane Protein. *Biochim. Biophys. Acta (Bba) - Biomembranes* 1768, 2011–2025. doi:10.1016/j.bbame.2007.05.011
- Khaniya, U., Gupta, C., Cai, X., Mao, J., Kaur, D., Zhang, Y., et al. (2020). Hydrogen Bond Network Analysis Reveals the Pathway for the Proton Transfer in the E-Channel of *T. thermophilus* Complex I. *Biochim. Biophys. Acta (Bba) - Bioenerg.* 1861, 148240. doi:10.1016/j.bbabi.2020.148240
- Kim, C. J., and Debus, R. J. (2017). Evidence from FTIR Difference Spectroscopy that a Substrate H₂O Molecule for O₂ Formation in Photosystem II Is provided by the Ca Ion of the Catalytic Mn₄CaO₅ Cluster. *Biochemistry* 56, 2558–2570. doi:10.1021/acs.biochem.6b01278
- Kim, Y. C., and Hummer, G. (2012). Proton-pumping Mechanism of Cytochrome C Oxidase: A Kinetic Master-Equation Approach. *Biochim. Biophys. Acta (Bba) - Bioenerg.* 1817, 526–536. doi:10.1016/j.bbabi.2011.09.004
- Kim, Y. C., Wikström, M., and Hummer, G. (2007). Kinetic Models of Redox-Coupled Proton Pumping. *Proc. Natl. Acad. Sci.* 104, 2169–2174. doi:10.1073/pnas.0611114104
- Kim, Y. C., Wikström, M., and Hummer, G. (2009). Kinetic Gating of the Proton Pump in Cytochrome C Oxidase. *Proc. Natl. Acad. Sci.* 106, 13707–13712. doi:10.1073/pnas.0903938106
- Kleinfeld, D., Okamura, M. Y., and Feher, G. (1984). Electron Transfer in Reaction Centers of Rhodospirillum rubrum Sphaeroides. I. Determination of the Charge Recombination Pathway of D+QAQ-B and Free Energy and Kinetic Relations between Q-AQB and QAQ-B. *Biochim. Biophys. Acta (Bba) - Bioenerg.* 766, 126–140. doi:10.1016/0005-2728(84)90224-x
- Knight, C., and Voth, G. A. (2012). The Curious Case of the Hydrated Proton. *Acc. Chem. Res.* 45, 101–109. doi:10.1021/ar200140h
- Kovalevsky, A. Y., Hanson, B. L., Mason, S. A., Yoshida, T., Fisher, S. Z., Mustyakimov, M., et al. (2011). Identification of the Elusive Hydronium Ion Exchanging Roles with a Proton in an Enzyme at Lower pH Values. *Angew. Chem. Int. Ed.* 50, 7520–7523. doi:10.1002/anie.201101753
- Krammer, E.-M., Till, M. S., Sebban, P., and Ullmann, G. M. (2009). Proton-Transfer Pathways in Photosynthetic Reaction Centers Analyzed by Profile Hidden Markov Models and Network Calculations. *J. Mol. Biol.* 388, 631–643. doi:10.1016/j.jmb.2009.03.020
- Kuroda, H., Kodama, N., Sun, X.-Y., Ozawa, S.-i., and Takahashi, Y. (2014). Requirement for Asn298 on D1 Protein for Oxygen Evolution: Analyses by Exhaustive Amino Acid Substitution in the green Alga *Chlamydomonas Reinhardtii*. *Plant Cell Physiol* 55, 1266–1275. doi:10.1093/pcp/pcu073
- Lancaster, C. R., Michel, H., Honig, B., and Gunner, M. R. (1996). Calculated Coupling of Electron and Proton Transfer in the Photosynthetic Reaction center of *Rhodospirillum rubrum*. *Biophysical J.* 70, 2469–2492. doi:10.1016/S0006-3495(96)79820-X
- Lanyi, J. K. (2006). Proton Transfers in the Bacteriorhodopsin Photocycle. *Biochim. Biophys. Acta (Bba) - Bioenerg.* 1757, 1012–1018. doi:10.1016/j.bbabi.2005.11.003
- Lavergne, J. R. M., and Junge, W. (1993). Proton Release during the Redox Cycle of the Water Oxidase. *Photosynth. Res.* 38, 279–296. doi:10.1007/BF00046752
- Lazaridis, T., and Hummer, G. (2017). Classical Molecular Dynamics with Mobile Protons. *J. Chem. Inf. Model.* 57, 2833–2845. doi:10.1021/acs.jcim.7b00603
- Lee, H. J., and Ådelroth, P. (2013). The Heme-Copper Oxidase Superfamily Shares a Zn²⁺-Binding Motif at the Entrance to a Proton Pathway. *FEBS Lett.* 587, 770–774. doi:10.1016/j.febslet.2013.01.069
- Lee, H. J., Reimann, J., Huang, Y., and Ådelroth, P. (2012). Functional Proton Transfer Pathways in the Heme-Copper Oxidase Superfamily. *Biochim. Biophys. Acta (Bba) - Bioenerg.* 1817, 537–544. doi:10.1016/j.bbabi.2011.10.007
- Li, H., Anuwongcharoen, N., Malik, A., Prachayasittikul, V., Wikberg, J., and Nantasenamat, C. (2016). Roles of D-Amino Acids on the Bioactivity of Host Defense Peptides. *IJMS* 17, 1023. doi:10.3390/ijms17071023
- Liang, R., Swanson, J. M. J., Wikström, M., and Voth, G. A. (2017). Understanding the Essential Proton-Pumping Kinetic gates and Decoupling Mutations in Cytochrome C Oxidase. *Proc. Natl. Acad. Sci. USA* 114, 5924–5929. doi:10.1073/pnas.1703654114
- Lórenz-Fonfría, V. A., and Heberle, J. (2014). Channelrhodopsin Unchained: Structure and Mechanism of a Light-Gated Cation Channel. *Biochim. Biophys. Acta (Bba) - Bioenerg.* 1837, 626–642. doi:10.1016/j.bbabi.2013.10.014
- Lórenz-Fonfría, V. A., and Kandori, H. (2009). Spectroscopic and Kinetic Evidence on How Bacteriorhodopsin Accomplishes Vectorial Proton Transport under Functional Conditions. *J. Am. Chem. Soc.* 131, 5891–5901. doi:10.1021/ja900334c
- Lórenz-Fonfría, V. A., Furutani, Y., and Kandori, H. (2008). Active Internal Waters in the Bacteriorhodopsin Photocycle. A Comparative Study of the L and M Intermediates at Room and Cryogenic Temperatures by Infrared Spectroscopy†. *Biochemistry* 47, 4071–4081. doi:10.1021/bi7024063
- Lórenz-Fonfría, V. A., Kandori, H., and Padrós, E. (2011). Probing Specific Molecular Processes and Intermediates by Time-Resolved Fourier Transform Infrared Spectroscopy: Application to the Bacteriorhodopsin Photocycle. *J. Phys. Chem. B* 115, 7972–7985. doi:10.1021/jp201739w
- Luecke, H. (2000). Atomic Resolution Structures of Bacteriorhodopsin Photocycle Intermediates: the Role of Discrete Water Molecules in the Function of This Light-Driven Ion Pump. *Biochim. Biophys. Acta (Bba) - Bioenerg.* 1460, 133–156. doi:10.1016/S0005-2728(00)00135-3

- Ma, J., Tsatsos, P. H., Zaslavsky, D., Barquera, B., Thomas, J. W., Katsonouri, A., et al. (1999). Glutamate-89 in Subunit II of Cytochrome_b3 from *Escherichia coli* Is Required for the Function of the Heme-Copper Oxidase†. *Biochemistry* 38, 15150–15156. doi:10.1021/bi991764y
- Mathiesen, C., and Hägerhäll, C. (2002). Transmembrane Topology of the NuoL, M and N Subunits of NADH:quinone Oxidoreductase and Their Homologues Among Membrane-Bound Hydrogenases and Bona Fide Antiporters. *Biochim. Biophys. Acta (Bba) - Bioenerg.* 1556, 121–132. doi:10.1016/S0005-2728(02)00343-2
- McEvoy, J. P., and Brudvig, G. W. (2004). Structure-based Mechanism of Photosynthetic Water Oxidation. *Phys. Chem. Chem. Phys.* 6, 4754–4763. doi:10.1039/B407500E
- McEvoy, J. P., and Brudvig, G. W. (2006). Water-splitting Chemistry of Photosystem II. *Chem. Rev.* 106, 4455–4483. doi:10.1021/cr0204294
- McPherson, P. H., Schoenfeld, M., Paddock, M. L., Okamura, M. Y., and Feher, G. (1994). Protonation and Free Energy Changes Associated with Formation of QBH₂ in Native and Glu-L212 Fwdarw. Gln Mutant Reaction Centers from Rhodospirillum rubrum. *Biochemistry* 33, 1181–1193. doi:10.1021/bi00171a018
- Michel, J., DeLeon-Rangel, J., Zhu, S., Van Ree, K., and Vik, S. B. (2011). Mutagenesis of the L, M, and N Subunits of Complex I from *Escherichia coli* Indicates a Common Role in Function. *PLoS One* 6, e17420. doi:10.1371/journal.pone.0017420
- Miller, A., and Oesterhelt, D. (1990). Kinetic Optimization of Bacteriorhodopsin by Aspartic Acid 96 as an Internal Proton Donor. *Biochim. Biophys. Acta (Bba) - Bioenerg.* 1020, 57–64. doi:10.1016/0005-2728(90)90093-J
- Mills, D. A., and Ferguson-Miller, S. (2002). Influence of Structure, pH and Membrane Potential on Proton Movement in Cytochrome Oxidase. *Biochim. Biophys. Acta (Bba) - Bioenerg.* 1555, 96–100. doi:10.1016/S0005-2728(02)00261-X
- Mitchell, P. (1961). Coupling of Phosphorylation to Electron and Hydrogen Transfer by a Chemi-Osmotic Type of Mechanism. *Nature* 191, 144–148. doi:10.1038/191144a0
- Mitchell, P. (1977). Vectorial Chemiosmotic Processes. *Annu. Rev. Biochem.* 46, 996–1005. doi:10.1146/annurev.bi.46.070177.005024
- Miyake, T., and Rolandi, M. (2015). Grothuss Mechanisms: from Proton Transport in Proton Wires to Bioprotonic Devices. *J. Phys. Condens. Matter* 28, 023001. doi:10.1088/0953-8984/28/2/023001
- Moser, C. C., Farid, T. A., Chobot, S. E., and Dutton, P. L. (2006). Electron Tunneling Chains of Mitochondria. *Biochim. Biophys. Acta (Bba) - Bioenerg.* 1757, 1096–1109. doi:10.1016/j.bbabi.2006.04.015
- Müh, F., Glöckner, C., Hellmich, J., and Zouni, A. (2012). Light-induced Quinone Reduction in Photosystem II. *Biochim. Biophys. Acta (Bba) - Bioenerg.* 1817, 44–65. doi:10.1016/j.bbabi.2011.05.021
- Nagao, R., Ueoka-Nakanishi, H., and Noguchi, T. (2017). D1-Asn-298 in Photosystem II Is Involved in a Hydrogen-Bond Network Near the Redox-Active Tyrosine YZ for Proton Exit during Water Oxidation. *J. Biol. Chem.* 292, 20046–20057. doi:10.1074/jbc.M117.815183
- Nagle, J. F., and Morowitz, H. J. (1978). Molecular Mechanisms for Proton Transport in Membranes. *Proc. Natl. Acad. Sci.* 75, 298–302. doi:10.1073/pnas.75.1.298
- Nakamura, S., Nagao, R., Takahashi, R., and Noguchi, T. (2014). Fourier Transform Infrared Detection of a Polarizable Proton Trapped between Photooxidized Tyrosine YZ and a Coupled Histidine in Photosystem II: Relevance to the Proton Transfer Mechanism of Water Oxidation. *Biochemistry* 53, 3131–3144. doi:10.1021/bi500237y
- Namslauer, A., Aagaard, A., Katsonouri, A., and Brzezinski, P. (2003). Intramolecular Proton-Transfer Reactions in a Membrane-Bound Proton Pump: The Effect of pH on the Peroxy to Ferryl Transition in Cytochrome Oxidase†. *Biochemistry* 42, 1488–1498. doi:10.1021/bi026524o
- Nicholls, D. G. (2010). Mitochondrial Ion Circuits. *Essays Biochem.* 47, 25–35. doi:10.1042/bse0470025
- Nogly, P., Weinert, T., James, D., Carbajo, S., Ozerov, D., Furrer, A., et al. (2018). Retinal Isomerization in Bacteriorhodopsin Captured by a Femtosecond X-ray Laser. *Science* 361, eaat0094. doi:10.1126/science.aat0094
- Odella, E., Mora, S. J., Wadsworth, B. L., Huynh, M. T., Goings, J. J., Liddell, P. A., et al. (2018). Controlling Proton-Coupled Electron Transfer in Bioinspired Artificial Photosynthetic Relays. *J. Am. Chem. Soc.* 140, 15450–15460. doi:10.1021/jacs.8b09724
- Odella, E., Wadsworth, B. L., Mora, S. J., Goings, J. J., Huynh, M. T., Gust, D., et al. (2019). Proton-Coupled Electron Transfer Drives Long-Range Proton Translocation in Bioinspired Systems. *J. Am. Chem. Soc.* 141, 14057–14061. doi:10.1021/jacs.9b06978
- Okamura, M. Y., and Feher, G. (1992). Proton Transfer in Reaction Centers from Photosynthetic Bacteria. *Annu. Rev. Biochem.* 61, 861–896. doi:10.1146/annurev.bi.61.070192.004241
- Okamura, M. Y., Paddock, M. L., Graige, M. S., and Feher, G. (2000). Proton and Electron Transfer in Bacterial Reaction Centers. *Biochim. Biophys. Acta (Bba) - Bioenerg.* 1458, 148–163. doi:10.1016/S0005-2728(00)00065-7
- Ono, T., Zimmermann, J. L., Inoue, Y., and Rutherford, A. W. (1986). EPR Evidence for a Modified S-State Transition in Chloride-Depleted Photosystem II. *Biochim. Biophys. Acta (Bba) - Bioenerg.* 851, 193–201. doi:10.1016/0005-2728(86)90125-8
- Onufriev, A., Smolyanov, A., and Bashford, D. (2003). Proton Affinity Changes Driving Unidirectional Proton Transport in the Bacteriorhodopsin Photocycle. *J. Mol. Biol.* 332, 1183–1193. doi:10.1016/s0022-2836(03)00903-3
- Ormö, M., Cubitt, A. B., Kallio, K., Gross, L. A., Tsien, R. Y., and Remington, S. J. (1996). Crystal Structure of the *Aequorea victoria* Green Fluorescent Protein. *Science* 273, 1392–1395. doi:10.1126/science.273.5280.1392
- Paddock, M. L., Rongey, S. H., Feher, G., and Okamura, M. Y. (1989). Pathway of Proton Transfer in Bacterial Reaction Centers: Replacement of Glutamic Acid 212 in the L Subunit by Glutamine Inhibits Quinone (Secondary Acceptor) Turnover. *Pnas* 86, 6602–6606. doi:10.1073/pnas.86.17.6602
- Paddock, M. L., Rongey, S. H., McPherson, P. H., Juth, A., Feher, G., and Okamura, M. Y. (1994). Pathway of Proton Transfer in Bacterial Reaction Centers: Role of Aspartate-L213 in Proton Transfers Associated with Reduction of Quinone to Dihydroquinone. *Biochemistry* 33, 734–745. doi:10.1021/bi00169a015
- Paddock, M. L., Feher, G., and Okamura, M. Y. (1995). Pathway of Proton Transfer in Bacterial Reaction Centers: Further Investigations on the Role of Ser-L223 Studied by Site-Directed Mutagenesis. *Biochemistry* 34, 15742–15750. doi:10.1021/bi00048a019
- Paddock, M. L., Graige, M. S., Feher, G., and Okamura, M. Y. (1999). Identification of the Proton Pathway in Bacterial Reaction Centers: Inhibition of Proton Transfer by Binding of Zn²⁺ or Cd²⁺. *Proc. Natl. Acad. Sci.* 96, 6183–6188. doi:10.1073/pnas.96.11.6183
- Paddock, M. L., Feher, G., and Okamura, M. Y. (2003). Proton Transfer Pathways and Mechanism in Bacterial Reaction Centers. *FEBS Lett.* 555, 45–50. doi:10.1016/S0014-5793(03)01149-9
- Pantazis, D. A. (2018). Missing Pieces in the Puzzle of Biological Water Oxidation. *ACS Catal.* 8, 9477–9507. doi:10.1021/acscatal.8b01928
- Paulino, J., Yi, M., Hung, I., Gan, Z., Wang, X., Chekmenev, E. Y., et al. (2020). Functional Stability of Water Wire-Carbonyl Interactions in an Ion Channel. *Proc. Natl. Acad. Sci. U.S.A.* 117, 11908–11915. doi:10.1073/pnas.2001083117
- Phatak, P., Ghosh, N., Yu, H., Cui, Q., and Elstner, M. (2008). Amino Acids with an Intermolecular Proton Bond as Proton Storage Site in Bacteriorhodopsin. *Proc. Natl. Acad. Sci.* 105, 19672–19677. doi:10.1073/pnas.0810712105
- Pokhrel, R., and Brudvig, G. W. (2014). Oxygen-evolving Complex of Photosystem II: Correlating Structure with Spectroscopy. *Phys. Chem. Chem. Phys.* 16, 11812–11821. doi:10.1039/C4CP00493K
- Pomès, R., and Roux, B. (1998). Free Energy Profiles for H⁺ Conduction along Hydrogen-Bonded Chains of Water Molecules. *Biophysical J.* 75, 33–40. doi:10.1016/S0006-3495(98)77492-2
- Pomès, R., and Roux, B. (2002). Molecular Mechanism of H⁺ Conduction in the Single-File Water Chain of the Gramicidin Channel. *Biophysical J.* 82, 2304–2316. doi:10.1016/s0006-3495(02)75576-8
- Popović, D. M., and Stuchebrukhov, A. A. (2005). Proton Exit Channels in Bovine Cytochrome C Oxidase. *J. Phys. Chem. B* 109, 1999–2006. doi:10.1021/jp0464371
- Qian, J., Shi, W., Pressler, M., Hoganson, C., Mills, D., Babcock, G. T., et al. (1997). Aspartate-407 in Rhodospirillum rubrum Cytochrome Oxidase Is Not Required for Proton Pumping or Manganese Binding†. *Biochemistry* 36, 2539–2543. doi:10.1021/bi962721+
- Rabenstein, B., Ullmann, G. M., and Knapp, E.-W. (2000). Electron Transfer between the Quinones in the Photosynthetic Reaction Center and its Coupling

- to Conformational Changes†. *Biochemistry* 39, 10487–10496. doi:10.1021/bi000413c
- Rappaport, F., Blanchard-Desce, M., and Lavergne, J. (1994). Kinetics of Electron Transfer and Electrochromic Change during the Redox Transitions of the Photosynthetic Oxygen-Evolving Complex. *Biochim. Biophys. Acta (Bba) - Bioenerg.* 1184, 178–192. doi:10.1016/0005-2728(94)90222-4
- Raymond, J., and Blankenship, R. E. (2004). The Evolutionary Development of the Protein Complement of Photosystem 2. *Biochim. Biophys. Acta (Bba) - Bioenerg.* 1655, 133–139. doi:10.1016/j.bbabo.2003.10.015
- Retegan, M., Krewald, V., Mamedov, F., Neese, F., Lubitz, W., Cox, N., et al. (2016). A Five-Coordinate Mn(IV) Intermediate in Biological Water Oxidation: Spectroscopic Signature and a Pivot Mechanism for Water Binding. *Chem. Sci.* 7, 72–84. doi:10.1039/c5sc03124a
- Rich, P. R. (2008). A Perspective on Peter Mitchell and the Chemiosmotic Theory. *J. Bioenerg. Biomembr.* 40, 407–410. doi:10.1007/s10863-008-9173-7
- Ripple, M. O., Kim, N., and Springett, R. (2013). Mammalian Complex I Pumps 4 Protons Per 2 Electrons at High and Physiological Proton Motive Force in Living Cells*. *J. Biol. Chem.* 288, 5374–5380. doi:10.1074/jbc.M112.438945
- Rivalta, I., Amin, M., Lubert, S., Vassiliev, S., Pokhrel, R., Umena, Y., et al. (2011). Structural-Functional Role of Chloride in Photosystem II. *Biochemistry* 50, 6312–6315. doi:10.1021/bi200685w
- Röpke, M., Saura, P., Riepl, D., Pövelin, M. C., and Kaila, V. R. I. (2020). Functional Water Wires Catalyze Long-Range Proton Pumping in the Mammalian Respiratory Complex I. *J. Am. Chem. Soc.* 142, 21758–21766. doi:10.1021/jacs.0c09209
- Roux, B. (2002). Computational Studies of the Gramicidin Channel. *Acc. Chem. Res.* 35, 366–375. doi:10.1021/ar010028v
- Ryu, H., Lee, H., Iwata, S., Choi, S., Ki Kim, M., Kim, Y.-R., et al. (2015). Investigation of Ion Channel Activities of Gramicidin A in the Presence of Ionic Liquids Using Model Cell Membranes. *Sci. Rep.* 5, 11935. doi:10.1038/srep11935
- Saito, K., Shen, J.-R., Ishida, T., and Ishikita, H. (2011). Short Hydrogen Bond between Redox-Active Tyrosine YZand D1-His190 in the Photosystem II Crystal Structure. *Biochemistry* 50, 9836–9844. doi:10.1021/bi201366j
- Saito, K., Rutherford, A. W., and Ishikita, H. (2013). Mechanism of Proton-Coupled Quinone Reduction in Photosystem II. *Proc. Natl. Acad. Sci.* 110, 954–959. doi:10.1073/pnas.1212957110
- Saito, K., William Rutherford, A., and Ishikita, H. (2015). Energetics of Proton Release on the First Oxidation Step in the Water-Oxidizing Enzyme. *Nat. Commun.* 6, 8488. doi:10.1038/ncomms9488
- Sakamoto, H., Shimizu, T., Nagao, R., and Noguchi, T. (2017). Monitoring the Reaction Process during the S2 → S3 Transition in Photosynthetic Water Oxidation Using Time-Resolved Infrared Spectroscopy. *J. Am. Chem. Soc.* 139, 2022–2029. doi:10.1021/jacs.6b11989
- Sakashita, N., Ishikita, H., and Saito, K. (2020). Rigidly Hydrogen-Bonded Water Molecules Facilitate Proton Transfer in Photosystem II. *Phys. Chem. Chem. Phys.* 22, 15831–15841. doi:10.1039/D0CP00295J
- Saura, P., and Kaila, V. R. I. (2019). Molecular Dynamics and Structural Models of the Cyanobacterial NDH-1 Complex. *Biochim. Biophys. Acta (Bba) - Bioenerg.* 1860, 201–208. doi:10.1016/j.bbabo.2018.11.010
- Sazanov, L. A. (2014). The Mechanism of Coupling between Electron Transfer and Proton Translocation in Respiratory Complex I. *J. Bioenerg. Biomembr.* 46, 247–253. doi:10.1007/s10863-014-9554-z
- Sazanov, L. A. (2015). A Giant Molecular Proton Pump: Structure and Mechanism of Respiratory Complex I. *Nat. Rev. Mol. Cell Biol.* 16, 375–388. doi:10.1038/nrm3997
- Sebban, P., Maróti, P., Schiffer, M., and Hanson, D. K. (1995). Electrostatic Dominoes: Long Distance Propagation of Mutational Effects in Photosynthetic Reaction Centers of *Rhodobacter Capsulatus*. *Biochemistry* 34, 8390–8397. doi:10.1021/bi00026a021
- Service, R. J., Hillier, W., and Debus, R. J. (2010). Evidence from FTIR Difference Spectroscopy of an Extensive Network of Hydrogen Bonds Near the Oxygen-Evolving Mn4Ca Cluster of Photosystem II Involving D1-Glu65, D2-Glu312, and D1-Glu329. *Biochemistry* 49, 6655–6669. doi:10.1021/bi100730d
- Sharpe, M. A., and Ferguson-Miller, S. (2008). A Chemically Explicit Model for the Mechanism of Proton Pumping in Heme-Copper Oxidases. *J. Bioenerg. Biomembr.* 40, 541–549. doi:10.1007/s10863-008-9182-6
- Shevela, D., Eaton-Rye, J. J., Shen, J.-R., and Govindjee, G. (2012). Photosystem II and the Unique Role of Bicarbonate: A Historical Perspective. *Biochim. Biophys. Acta (Bba) - Bioenerg.* 1817, 1134–1151. doi:10.1016/j.bbabo.2012.04.003
- Shinkarev, V. P., Takahashi, E., and Wraight, C. A. (1993). Flash-induced Electric Potential Generation in Wild Type and L212EQ Mutant Chromatophores of *Rhodobacter Sphaeroides*: QBH2 Is Not Released from L212EQ Mutant Reaction Centers. *Biochim. Biophys. Acta (Bba) - Bioenerg.* 1142, 214–216. doi:10.1016/0005-2728(93)90106-P
- Shoji, M., Isobe, H., and Yamaguchi, K. (2015). QM/MM Study of the S2 to S3 Transition Reaction in the Oxygen-Evolving Complex of Photosystem II. *Chem. Phys. Lett.* 636, 172–179. doi:10.1016/j.cplett.2015.07.039
- Sievers, F., Wilm, A., Dineen, D., Gibson, T. J., Karplus, K., Li, W., et al. (2011). Fast, Scalable Generation of High-quality Protein Multiple Sequence Alignments Using Clustal Omega. *Mol. Syst. Biol.* 7, 539. doi:10.1038/msb.2011.75
- Son, C. Y., Yethiraj, A., and Cui, Q. (2017). Cavity Hydration Dynamics in Cytochrome C Oxidase and Functional Implications. *Proc. Natl. Acad. Sci. U.S.A.* 114, E8830–E8836. doi:10.1073/pnas.1707922114
- Song, Y., and Gunner, M. R. (2014). Halorhodopsin Pumps Cl-And Bacteriorhodopsin Pumps Protons by a Common Mechanism that Uses Conserved Electrostatic Interactions. *Proc. Natl. Acad. Sci. U.S.A.* 111, 16377–16382. doi:10.1073/pnas.1411191111
- Song, Y., Mao, J., and Gunner, M. R. (2003). Calculation of Proton Transfers in Bacteriorhodopsin bR and M Intermediates†. *Biochemistry* 42, 9875–9888. doi:10.1021/bi034482d
- Spassov, V. Z., Luecke, H., Gerwert, K., and Bashford, D. (2001). pKa calculations suggest storage of an excess proton in a hydrogen-bonded water network in bacteriorhodopsin 1. Edited by G. von Heijne. *J. Mol. Biol.* 312, 203–219. doi:10.1006/jmbi.2001.4902
- Steiner, J., and Sazanov, L. (2020). Structure and Mechanism of the Mrp Complex, an Ancient Cation/proton Antiporter. *eLife* 9, e59407. doi:10.7554/eLife.59407
- Stoner-Ma, D., Jaye, A. A., Matousek, P., Towrie, M., Meech, S. R., and Tonge, P. J. (2005). Observation of Excited-State Proton Transfer in Green Fluorescent Protein Using Ultrafast Vibrational Spectroscopy. *J. Am. Chem. Soc.* 127, 2864–2865. doi:10.1021/ja042466d
- Stuchebrukhov, A. A. (2018). Redox-Driven Proton Pumps of the Respiratory Chain. *Biophysical J.* 115, 830–840. doi:10.1016/j.bpj.2018.07.022
- Stuchebrukhov, A. A. (2019). Kinetics and Efficiency of Energy-Transducing Enzymes. *J. Phys. Chem. B* 123, 9456–9465. doi:10.1021/acs.jpbc.9b08191
- Suga, M., Akita, F., Yamashita, K., Nakajima, Y., Ueno, G., Li, H., et al. (2019). An Oxy/oxo Mechanism for Oxygen-Oxygen Coupling in PSII Revealed by an X-ray Free-Electron Laser. *Science* 366, 334–338. doi:10.1126/science.aax6998
- Supekar, S., Gamiz-Hernandez, A. P., and Kaila, V. R. I. (2016). A Protonated Water Cluster as a Transient Proton-Loading Site in Cytochrome cOxidase. *Angew. Chem. Int. Ed.* 55, 11940–11944. doi:10.1002/anie.201603606
- Swanson, J. M. J., Maupin, C. M., Chen, H., Petersen, M. K., Xu, J., Wu, Y., et al. (2007). Proton Solvation and Transport in Aqueous and Biomolecular Systems: Insights from Computer Simulations. *J. Phys. Chem. B* 111, 4300–4314. doi:10.1021/jp070104x
- Taylor, R. W., Morris, A. A., Hutchinson, M., and Turnbull, D. M. (2002). Leigh Disease Associated with a Novel Mitochondrial DNA ND5 Mutation. *Eur. J. Hum. Genet.* 10, 141–144. doi:10.1038/sj.ejhg.5200773
- Till, M. S., Essigke, T., Becker, T., and Ullmann, G. M. (2008). Simulating the Proton Transfer in Gramicidin A by a Sequential Dynamical Monte Carlo Method. *J. Phys. Chem. B* 112, 13401–13410. doi:10.1021/jp801477b
- Tommos, C., and Babcock, G. T. (2000). Proton and Hydrogen Currents in Photosynthetic Water Oxidation. *Biochim. Biophys. Acta (Bba) - Bioenerg.* 1458, 199–219. doi:10.1016/S0005-2728(00)00069-4
- Torres-Bacete, J., Nakamaru-Ogiso, E., Matsuno-Yagi, A., and Yagi, T. (2007). Characterization of the NuoM (ND4) Subunit in *Escherichia coli* NDH-1. *J. Biol. Chem.* 282, 36914–36922. doi:10.1074/jbc.M707855200
- Tu, C. K., Silverman, D. N., Forsman, C., Jonsson, B. H., and Lindskog, S. (1989). Role of Histidine 64 in the Catalytic Mechanism of Human Carbonic Anhydrase II Studied with a Site-specific Mutant. *Biochemistry* 28, 7913–7918. doi:10.1021/bi00445a054
- Ugur, I., Rutherford, A. W., and Kaila, V. R. I. (2016). Redox-coupled Substrate Water Reorganization in the Active Site of Photosystem II-The Role of Calcium

- in Substrate Water Delivery. *Biochim. Biophys. Acta (Bba) - Bioenerg.* 1857, 740–748. doi:10.1016/j.bbabi.2016.01.015
- Umena, Y., Kawakami, K., Shen, J.-R., and Kamiya, N. (2011). Crystal Structure of Oxygen-Evolving Photosystem II at a Resolution of 1.9 Å. *Nature* 473, 55–60. doi:10.1038/nature09913
- Utschig, L. M., Ohgashi, Y., Thurnauer, M. C., and Tiede, D. M. (1998). A New Metal-Binding Site in Photosynthetic Bacterial Reaction Centers that Modulates Q_Ato Q_BElectron Transfer†. *Biochemistry* 37, 8278–8281. doi:10.1021/bi980395n
- Vasanthakumar, T., and Rubinstein, J. L. (2020). Structure and Roles of V-type ATPases. *Trends Biochem. Sci.* 45, 295–307. doi:10.1016/j.tibs.2019.12.007
- Vassiliev, S., Zaraiskaya, T., and Bruce, D. (2012). Exploring the Energetics of Water Permeation in Photosystem II by Multiple Steered Molecular Dynamics Simulations. *Biochim. Biophys. Acta (Bba) - Bioenerg.* 1817, 1671–1678. doi:10.1016/j.bbabi.2012.05.016
- Verkhovskaya, M. L., Belevich, N., Euro, L., Wikström, M., and Verkhovsky, M. I. (2008). Real-time Electron Transfer in Respiratory Complex I. *Proc. Natl. Acad. Sci.* 105, 3763–3767. doi:10.1073/pnas.0711249105
- Vinyard, D. J., and Brudvig, G. W. (2017). Progress toward a Molecular Mechanism of Water Oxidation in Photosystem II. *Annu. Rev. Phys. Chem.* 68, 101–116. doi:10.1146/annurev-physchem-052516-044820
- Vogt, L., Ertem, M. Z., Pal, R., Brudvig, G. W., and Batista, V. S. (2015). Computational Insights on Crystal Structures of the Oxygen-Evolving Complex of Photosystem II with Either Ca²⁺ or Sr²⁺ Substituted by Sr²⁺. *Biochemistry* 54, 820–825. doi:10.1021/bi5011706
- Walker, J. E., Lutter, R., Dupuis, A., and Runswick, M. J. (1991). Identification of the Subunits of F₁F₀-ATPase from Bovine Heart Mitochondria. *Biochemistry* 30, 5369–5378. doi:10.1021/bi00236a007
- Wang, C., Lamb, R. A., and Pinto, L. H. (1995). Activation of the M2 Ion Channel of Influenza Virus: a Role for the Transmembrane Domain Histidine Residue. *Biophysical J.* 69, 1363–1371. doi:10.1016/S0006-3495(95)80003-2
- Warnau, J., Sharma, V., Gamiz-Hernandez, A. P., Di Luca, A., Haapanen, O., Vattulainen, I., et al. (2018). Redox-coupled Quinone Dynamics in the Respiratory Complex I. *Proc. Natl. Acad. Sci. U.S.A.* 115, E8413–E8420. doi:10.1073/pnas.1805468115
- Weisz, D. A., Gross, M. L., and Pakrasi, H. B. (2017). Reactive Oxygen Species Leave a Damage Trail that Reveals Water Channels in Photosystem II. *Sci. Adv.* 3, eaao3013. doi:10.1126/sciadv.aao3013
- Wickstrand, C., Dods, R., Royant, A., and Neutze, R. (2015). Bacteriorhodopsin: Would the Real Structural Intermediates Please Stand up? *Biochim. Biophys. Acta (Bba) - Gen. Subjects* 1850, 536–553. doi:10.1016/j.bbagen.2014.05.021
- Wickstrand, C., Nogly, P., Nango, E., Iwata, S., Standfuss, J., and Neutze, R. (2019). Bacteriorhodopsin: Structural Insights Revealed Using X-Ray Lasers and Synchrotron Radiation. *Annu. Rev. Biochem.* 88, 59–83. doi:10.1146/annurev-biochem-013118-111327
- Wikström, M., Jasaitis, A., Backgren, C., Puustinen, A., and Verkhovsky, M. I. (2000). The Role of the D- and K-Pathways of Proton Transfer in the Function of the Haem-Copper Oxidases. *Biochim. Biophys. Acta (Bba) - Bioenerg.* 1459, 514–520. doi:10.1016/s0005-2728(00)00191-2
- Wikström, M., Verkhovsky, M. I., and Hummer, G. (2003). Water-gated Mechanism of Proton Translocation by Cytochrome C Oxidase. *Biochim. Biophys. Acta (Bba) - Bioenerg.* 1604, 61–65. doi:10.1016/s0005-2728(03)00041-0
- Wikström, M., Sharma, V., Kaila, V. R. I., Hosler, J. P., and Hummer, G. (2015). New Perspectives on Proton Pumping in Cellular Respiration. *Chem. Rev.* 115, 2196–2221. doi:10.1021/cr500448t
- Wolf, S., Freier, E., and Gerwert, K. (2014). A Delocalized Proton-Binding Site within a Membrane Protein. *Biophysical J.* 107, 174–184. doi:10.1016/j.bpj.2014.05.019
- Wolter, T., Welke, K., Phatak, P., Bondar, A.-N., and Elstner, M. (2013). Excitation Energies of a Water-Bridged Twisted Retinal Structure in the Bacteriorhodopsin Proton Pump: a Theoretical Investigation. *Phys. Chem. Chem. Phys.* 15, 12582. doi:10.1039/c3cp44280b
- Wraight, C. A. (2004). Proton and Electron Transfer in the Acceptor Quinone Complex of Photosynthetic Reaction Centers from Rhodospirillum rubrum. *Front. Biosci.* 9, 309–337. doi:10.2741/1236
- Wraight, C. A. (2006). Chance and Design-Proton Transfer in Water, Channels and Bioenergetic Proteins. *Biochim. Biophys. Acta (Bba) - Bioenerg.* 1757, 886–912. doi:10.1016/j.bbabi.2006.06.017
- Xu, J., and Voth, G. A. (2006). Free Energy Profiles for H⁺ Conduction in the D-Pathway of Cytochrome C Oxidase: A Study of the Wild Type and N98D Mutant Enzymes. *Biochim. Biophys. Acta (Bba) - Bioenerg.* 1757, 852–859. doi:10.1016/j.bbabi.2006.05.028
- Yanagisawa, S., and Frasch, W. D. (2017). Protonation-dependent Stepped Rotation of the F₁-type ATP Synthase C-Ring Observed by Single-Molecule Measurements. *J. Biol. Chem.* 292, 17093–17100. doi:10.1074/jbc.M117.799940
- Yang, J., Zhu, Y., Tong, Y., Chen, L., Liu, L., Zhang, Z., et al. (2009). Confirmation of the Mitochondrial ND1 Gene Mutation G3635A as a Primary LHON Mutation. *Biochem. Biophysical Res. Commun.* 386, 50–54. doi:10.1016/j.bbrc.2009.05.127
- Zhang, Y., Haider, K., Kaur, D., Ngo, V. A., Cai, X., Mao, J., et al. (2020). Characterizing the Water Wire in the Gramicidin Channel Found by Monte Carlo Sampling Using Continuum Electrostatics and in Molecular Dynamics Trajectories with Conventional or Polarizable Force fields. *J. Theor. Comput. Chem.*, 2042001. doi:10.1142/S0219633620420018
- Zhou, P., and Han, K. (2018). Unraveling the Detailed Mechanism of Excited-State Proton Transfer. *Acc. Chem. Res.* 51, 1681–1690. doi:10.1021/acs.accounts.8b00172
- Zhu, Z., and Gunner, M. R. (2005). Energetics of Quinone-dependent Electron and Proton Transfers in Rhodospirillum rubrum Photosynthetic Reaction Centers. *Biochemistry* 44, 82–96. doi:10.1021/bi048348k
- Zickermann, V., Wirth, C., Nasiri, H., Siegmund, K., Schwalbe, H., Hunte, C., et al. (2015). Mechanistic Insight from the crystal Structure of Mitochondrial Complex I. *Science* 347, 44–49. doi:10.1126/science.1259859
- Zimmer, M. (2009). GFP: from Jellyfish to the Nobel Prize and beyond. *Chem. Soc. Rev.* 38, 2823–2832. doi:10.1039/b904023d

Conflict of Interest: The authors declare that the research was conducted in the absence of any commercial or financial relationships that could be construed as a potential conflict of interest.

Copyright © 2021 Kaur, Khaniya, Zhang and Gunner. This is an open-access article distributed under the terms of the Creative Commons Attribution License (CC BY). The use, distribution or reproduction in other forums is permitted, provided the original author(s) and the copyright owner(s) are credited and that the original publication in this journal is cited, in accordance with accepted academic practice. No use, distribution or reproduction is permitted which does not comply with these terms.

Advantages of publishing in Frontiers



OPEN ACCESS

Articles are free to read
for greatest visibility
and readership



FAST PUBLICATION

Around 90 days
from submission
to decision



HIGH QUALITY PEER-REVIEW

Rigorous, collaborative,
and constructive
peer-review



TRANSPARENT PEER-REVIEW

Editors and reviewers
acknowledged by name
on published articles

Frontiers

Avenue du Tribunal-Fédéral 34
1005 Lausanne | Switzerland

Visit us: www.frontiersin.org

Contact us: frontiersin.org/about/contact



REPRODUCIBILITY OF RESEARCH

Support open data
and methods to enhance
research reproducibility



DIGITAL PUBLISHING

Articles designed
for optimal readership
across devices



FOLLOW US

@frontiersin



IMPACT METRICS

Advanced article metrics
track visibility across
digital media



EXTENSIVE PROMOTION

Marketing
and promotion
of impactful research



LOOP RESEARCH NETWORK

Our network
increases your
article's readership